

SERIES ON SEMICONDUCTOR  
SCIENCE AND TECHNOLOGY

*Series Editors*

R.J. Nicholas University of Oxford  
H. Kamimura University of Tokyo

## SERIES ON SEMICONDUCTOR SCIENCE AND TECHNOLOGY

---

1. M. Jaros: *Physics and applications of semiconductor microstructures*
2. V.N. Dobrovolsky and V.G. Litovchenko: *Surface electronic transport phenomena in semiconductors*
3. M.J. Kelly: *Low-dimensional semiconductors*
4. P.K. Basu: *Theory of optical processes in semiconductors*
5. N. Balkan: *Hot electrons in semiconductors*
6. B. Gil: *Group III nitride semiconductor compounds: physics and applications*
7. M. Sugawara: *Plasma etching*
8. M. Balkanski and R.F. Wallis: *Semiconductor physics and applications*
9. B. Gil: *Low-dimensional nitride semiconductors*
10. L.J. Challis: *Electron–phonon interaction in low-dimensional structures*

# Electron–Phonon Interaction in Low-Dimensional Structures

*Edited by*

**Lawrence Challis**

*Emeritus Professor of Physics  
University of Nottingham*

**OXFORD**  
UNIVERSITY PRESS

**OXFORD**  
UNIVERSITY PRESS

Great Clarendon Street, Oxford, OX2 6DP,  
United Kingdom

Oxford University Press is a department of the University of Oxford.  
It furthers the University's objective of excellence in research, scholarship,  
and education by publishing worldwide. Oxford is a registered trade mark of  
Oxford University Press in the UK and in certain other countries

© Oxford University Press 2003

The moral rights of the authors have been asserted

Some rights reserved. No part of this publication may be reproduced, stored in  
a retrieval system, or transmitted, in any form or by any means, for commercial purposes,  
without the prior permission in writing of Oxford University Press, or as expressly permitted  
by law, by licence or under terms agreed with the appropriate reprographics  
rights organization.



This is an open access publication. Except where otherwise noted, this work is distributed  
under and subject to the terms of a Creative Commons Attribution 4.0 International License  
(CC BY 4.0) a copy of which is available at <https://creativecommons.org/licenses/by/4.0/>

This title has been made available on an Open Access basis  
through the sponsorship of SCOAP3.



Published in the United States of America by Oxford University Press  
198 Madison Avenue, New York, NY 10016, United States of America

British Library Cataloguing in Publication Data

Data available

Library of Congress Control Number: 0000000000

ISBN 978-0-19-850732-1

Printed in Great Britain by  
Clays Ltd, St Ives plc

This book is dedicated to my collaborators and students  
and to my wife, Jennifer, for her unstinting support and  
encouragement



# Contents

---

List of Contributors	ix
<b>1</b> Introduction	1
<b>L.J. Challis</b>	
<b>2</b> Energy relaxation by hot two-dimensional carriers in zero magnetic field	5
<b>A.J. Kent and J.K. Wigmore</b>	
2.1 Experimental principles	5
2.2 Emission of acoustic phonons by 2D carriers	13
2.3 Energy relaxation via optic phonons	27
2.4 Phonon pulse measurements	38
2.5 Higher subband occupancy	49
2.6 Other 2D systems	51
2.7 Conclusions	53
<b>3</b> Phonon interactions with magnetically quantized two-dimensional carrier systems: the integer and fractional quantum Hall states	59
<b>C.J. Mellor, W. Dietsche, and L.J. Challis</b>	
3.1 Introduction	59
3.2 Ballistic phonon techniques	63
3.3 Theoretical investigations of phonon interaction with magnetically quantized 2DEGs	64
3.4 Experimental studies of the phonon emission from magnetically quantized 2DEGs	69
3.5 Experimental studies of phonon absorption by magnetically quantized 2DEGs	75
3.6 Introduction to the FQHE	80
3.7 Electron–phonon interaction in the fractional quantum Hall regime	82
3.8 SAW studies of quantum Hall states	90
3.9 Conclusions	107
<b>4</b> Carrier–phonon interactions in semiconductor quantum dots and wires	115
<b>S.A. Cavill, P. Hawker, and A.J. Kent</b>	
4.1 Introduction	115

4.2	Electron–phonon interaction in QWRs	116
4.3	QDs	137
4.4	Conclusions	145
<b>5</b>	<b>Phonon drag thermopower of low-dimensional systems</b>	<b>149</b>
	<b>R. Fletcher, E. Zaremba, and U. Zeitler</b>	
5.1	General introduction	149
5.2	Experimental results at zero magnetic field	165
5.3	Behaviour of 2D systems in magnetic fields	173
5.4	Conclusions and outlook	180
<b>6</b>	<b>Phonon-assisted tunnelling</b>	<b>185</b>
	<b>F.F. Ouali and L.J. Challis</b>	
6.1	Introduction	185
6.2	DBRTDs and TBRTDs	187
6.3	SLs	209
6.4	Related transport processes	227
6.5	Conclusions	231
<b>7</b>	<b>Exciton–phonon interaction in quantum wells</b>	<b>239</b>
	<b>A.V. Akimov</b>	
7.1	Introduction	239
7.2	Role of phonons in exciton dynamics	247
7.3	Heating of 2D exciton gas by non-equilibrium acoustic phonons	254
7.4	Acoustic phonon-assisted tunnelling in double QWs	260
7.5	Conclusions and outlook	264
<b>8</b>	<b>Quantized thermal conductance of acoustic phonons in nanowires</b>	<b>269</b>
	<b>M.P. Blencowe</b>	
8.1	Introduction	269
8.2	Derivation of the Landauer formula for the thermal conductance	270
8.3	Measurement of the quantum of thermal conductance	275
8.4	Conclusion	281
	<i>Index</i>	283
	<i>Applications</i>	286

# Contributors

---

## **A.V. Akimov**

Ioffe Physical-Technical Institute,  
26 Polytechnicheskaya str,  
194021, St Petersburg,  
Russia  
e-mail: akimov.os@mail.ioffe.ru

## **M.P. Blencowe**

Department of Physics and Astronomy,  
Dartmouth College,  
Hanover, NH 03755,  
USA  
e-mail: miles.p.blencowe@dartmouth.edu

## **S.A. Cavill**

School of Physics and Astronomy,  
University of Nottingham,  
Nottingham NG7 2RD,  
UK  
e-mail: stuart.cavill@nottingham.ac.uk

## **L.J. Challis**

School of Physics and Astronomy,  
University of Nottingham,  
Nottingham NG7 2RD,  
UK  
e-mail: lawrie.challis@nottingham.ac.uk

## **W. Dietsche**

Max-Planck-Institut für Festkörperforschung,  
Heisenbergstr. 1,  
70569 Stuttgart,  
Germany  
e-mail: w.dietsche@fkf.mpg.de

**R. Fletcher**

Department of Physics,  
Queen's University,  
99 University Avenue,  
Kingston,  
Ontario,  
K7L 3N6,  
Canada  
e-mail: fletcher@physics.queensu.ca

**P. Hawker**

School of Physics and Astronomy,  
University of Nottingham,  
Nottingham NG7 2RD,  
UK  
e-mail: philip.hawker@nottingham.ac.uk

**A.J. Kent**

School of Physics and Astronomy,  
University of Nottingham,  
Nottingham NG7 2RD,  
UK  
e-mail: anthony.kent@nottingham.ac.uk

**C.J. Mellor**

School of Physics and Astronomy,  
University of Nottingham,  
Nottingham NG7 2RD,  
UK  
e-mail: chris.mellor@nottingham.ac.uk

**F.F. Ouali**

Bookham Technology Plc,  
Caswell,  
Towcester,  
Northamptonshire,  
NN12 8EQ,  
UK  
e-mail: fouzia.ouali@bookham.com

**J.K. Wigmore**

Department of Physics,  
University of Lancaster,  
Bailrigg,

Lancaster,  
LA1 4YW,  
UK  
e-mail: k.wigmore@lancaster.ac.uk

**E. Zaremba**

Department of Physics,  
Queen's University,  
99 University Avenue,  
Kingston,  
Ontario,  
K7L 3N6,  
Canada  
e-mail: zaremba@sparky.phy.queensu.ca

**U. Zeitler**

HFML  
Toernooiveld 7  
6525 ED Nijmegen  
The Netherlands  
e-mail: zeitler@sci.kun.nl



# 1 Introduction

L.J. Challis

---

The development of techniques capable of producing semiconducting structures made from layers whose thickness can be as small as a nanometre has stimulated a wealth of new physics and led to the production of a wide range of electronic and optoelectronic devices. Further advances have been made using techniques that allow these two-dimensional (2D) systems to be formed into quantum wires, one-dimensional (1D) systems, in which electronic motion is essentially restricted to one direction, and quantum dots, zero-dimensional (0D) systems, which can be thought of as artificial atoms.

This book concerns the interaction between the electrons and holes confined within these low-dimensional structures and the phonons that are present within and around the confined regions. The new physics of these structures primarily involves their electronic properties. However, an appreciation of the role of the phonons is frequently needed if this physics is to be understood in any detail. So while a first discussion of the quantum Hall effect does not involve the electron–phonon interaction, the manifestation of the quantized Hall resistance  $R_H$  through the dissipation of the Joule heat,  $I^2 R_H$ , near the contacts evidently does and phonons are also intimately associated with the processes leading to breakdown when the critical current is exceeded. The room temperature mobility of 2D electron gases is limited by phonon scattering and phonons provide the principal channel of energy exchange between the confined electrons and their surroundings. Indeed, these two properties have a major effect on both the physics and the device performance of low-dimensional structures. But phonons have many other roles: for example non-radiative recombination involving phonons can greatly reduce the efficiency of optoelectronic devices, phonon-assisted tunnelling between quantum wells is an essential feature of the operation of the quantum cascade laser, and, at much lower frequencies, the interaction of surface acoustic waves with confined electrons could lead to new devices and even a new current standard.

The efficiencies of energy transfer and electron–phonon scattering are determined by the rates at which electron momentum and energy are transferred to the phonons and these are often very different from those in bulk material. The nature of the vibrational modes may be affected by the presence of the nanostructure and new optic modes may arise. However, the major differences are not usually due to these effects but to the changes in the electronic structure resulting from confinement and the modifications that result in the requirements set by momentum conservation. So while momentum must be conserved in all three orthogonal directions in a three-dimensional (3D) electron system, this is no longer the case when the dimensionality is reduced. For example, in a 2D electron system, momentum has to be conserved within the 2D plane but not necessarily perpendicular to it, at least for changes less than a value set by the confinement width.

The coupling mechanisms themselves are not significantly different from those in bulk material. Electrons still interact with acoustic phonons through deformation potential and piezoelectric coupling and with optic modes through a mechanism normally described by the Fröhlich Hamiltonian. Screening of these interactions is, however, strongly affected by the dimensionality of the system.

The methods used to obtain experimental information on the nature of the electron–phonon coupling in low-dimensional structures include optical and transport techniques similar to those used very successfully in studies of bulk material. The most widely used optical technique has been photoluminescence, both steady state and time dependent, and this technique has been particularly effective in studies of interaction with optic phonons. It has also often been used in conjunction with transport methods, for example to study the response of electrons heated by a current pulse. Transport techniques have been used to study the energy and momentum loss from an electron system to both acoustic and optic phonons and this can provide very direct information on properties such as the coupling between optic phonons and cyclotron modes. But confined structures are also very well suited to techniques involving the use of phonons as probes of the electronic properties—phonon techniques. Phonons interact much more strongly with electrons than photons of the same frequency and they have energies and momenta that are often well matched to those of the confined carriers. So they can be used to obtain direct information on electronic properties ranging from the confinement width to the dispersion curve of quasiparticles in the fractional quantum Hall state.

Because of their short lifetimes, optic phonons cannot be studied very effectively using phonon techniques and the main application of these techniques has been to acoustic phonons. The lifetimes of acoustic phonons become relatively long at low temperatures so that they can travel unattenuated to detectors placed on the opposite face of the substrate. Phonon techniques cannot always match the precision of optical methods but they can reveal details of the emission and absorption and other aspects of electronic systems that cannot be obtained in any other way. For example, the rate of energy loss (phonon emission) from a heated 2D electron gas can be determined by a transport technique. Measurements are made of the rise in electron temperature  $T_e$  produced by a known amount of power (Joule heat) and these can be used to determine the total energy loss as a function of the difference in temperature between the electrons and phonons. The temperature dependences of the loss rate are, however, not a unique signature for the processes involved (e.g. the theoretical dependence for screened piezoelectric electron–phonon coupling is the same as that for unscreened deformation potential coupling), although changes in the dependence can indicate the temperatures at which a switch occurs from predominantly piezoelectric coupling to deformation potential coupling and eventually from predominantly acoustic mode to optic mode emission. So, to determine how much of this energy is emitted as longitudinal acoustic (LA) phonons and how much as transverse acoustic (TA) phonons one needs to look directly at the emitted phonons. The two polarizations travel with different velocities and hence arrive at the detector at different times allowing measurements to be made of their relative intensities and how these change with the parameters of the electron system. Imaging methods have been developed to measure the angular distribution of the phonon emission or absorption and

spectroscopic techniques are starting to provide information on frequency distributions although there is still much to do here.

The book covers the confined structures of most current interest: 2D systems, quantum wires, quantum dots, resonant tunnelling devices, and superlattices. Phonon emission and absorption are given considerable attention as are studies of momentum transfer to the electron system, phonon drag, which is most apparent in the thermoelectric power. Chapters are also devoted to phonon-assisted tunnelling, in which a tunnelling electron simultaneously absorbs or emits a phonon, and to exciton–phonon interaction. One topic that seemed appropriate to include, even though it does not at this stage involve electron–phonon coupling, is that of the quantized thermal conductance that occurs in free-standing nanowires.

It has already been noted that the electron–phonon interaction can play an important part in the properties of low-dimensional devices and it had originally been the intention to devote a separate chapter to this topic. It became clear though that this would be difficult given the variety of devices and the corresponding range of physics involved. So the approach has been to discuss the applications together with the physics within the appropriate chapter and to include a separate index to allow easier access to discussion of a particular device or application.

I should like to thank Professor Robin Nicholas and the Oxford University Press for inviting me to edit this book and am particularly grateful to my fellow authors for agreeing to contribute to it, for the quality of their contributions, and for their tolerance and cooperation in responding to my requests. I should like to add my gratitude to those who helped them or gave them permission to use figures from published work; they are recorded individually within each chapter. Finally I should like to acknowledge, with very many thanks, support from the Leverhulme Trust through the award of an Emeritus Fellowship and from the School of Physics and Astronomy of the University of Nottingham.



# 2 Energy relaxation by hot two-dimensional carriers in zero magnetic field

A.J. Kent and J.K. Wigmore

---

## 2.1 Experimental principles

### 2.1.1 Introduction

The measurement of energy relaxation and loss provides a powerful method of probing the carrier–phonon interaction for two-dimensional (2D) electrons and holes. In addition, the process of energy relaxation has a strong influence on the performance of electronic and optical devices based on low-dimensional structures (LDSs). Over the last two decades the topic has been the focus of intensive experimental and theoretical investigation, the progress of which has been charted specifically through two series of international conferences, Phonon Scattering in Condensed Matter, and Hot Carriers in Semiconductors. In this chapter we shall describe the basic principles of energy relaxation by 2D carriers and summarize current understanding. We shall concentrate on relaxation in zero or low (non-quantizing) magnetic fields; the phenomena and their interpretation at high magnetic fields are more complicated and will be described in later chapters. We shall begin by discussing experimental principles, since these also define the framework within which the theoretical description is formulated. Next the basic theory will be reviewed for the interaction of 2D electrons first with acoustic phonons, which is operative at the lowest carrier temperatures, and then with optic phonons, which are expected to dominate the process for highly excited carriers. Finally in this chapter a selection of recent results obtained for important materials and structures by phonon pulse techniques, an important new tool, will be summarized and compared with the theoretical models. For further details on energy relaxation the reader is recommended to consult also reviews by Ridley [1], Shah [2], and Balkan [3].

### 2.1.2 Basic principles

A number of different techniques have been used to study energy relaxation of two-dimensional electron gases (2DEGs). They may be divided approximately into transport and optical methods, but details overlap and it will be helpful first to summarize the different regimes of the energy relaxation process itself. The objective of all measurements is ultimately to determine the mean energy loss rate per carrier,  $P_c$ , of the excited carriers under given conditions of excitation. Most generally this quantity can be written as

$$P_c = \frac{\int_0^\infty (dE/dt) f(E) g(E) dE}{\int_0^\infty f(E) g(E) dE} \quad (2.1)$$

where  $(dE/dt)$  is the rate of energy loss for a single carrier of energy  $E$ ,  $f(E)$  is the energy distribution function, and  $g(E)$  the density of states. The situation is greatly simplified if the excited carriers can be regarded as being in internal thermal equilibrium at a temperature raised relative to that of the crystal lattice [4]. It was shown by Anderson *et al.* [5] that this approximation, the so-called electron temperature model (ETM), is valid when the electron–electron scattering time,  $\tau_{ee}$ , is significantly less than the energy loss time,  $\tau_i$ , of the carriers. Then the excited carrier distribution has the form of a Fermi–Dirac distribution defined by a single, raised, temperature,  $T_c$ . The condition for the ETM is satisfied in most experimental situations, excepting extremes such as low carrier densities, high excitation levels, and subpicosecond time scales. The primary aim of experiments carried out in the hot carrier regime is to determine the value of  $P_c$  corresponding to a particular value of  $T_c$  at a given lattice temperature,  $T_L$ . It should be noted that although energy relaxation takes place predominantly through emission of phonons and phonon-related excitations, a much smaller (by orders of magnitude) though detectable amount of infrared radiation is also produced. Hot carrier techniques have also been widely used to study the electron–phonon interaction in three-dimensional (3D) systems. Carrier heating effects can be observed more easily in 2D systems because momentum relaxation is much smaller relative to energy relaxation as a result of the lower defect concentration in LDS materials.

Within the ETM framework, there are two alternative strategies for determining  $P_c$  and  $T_c$ , steady state and dynamic. The principle of the former is that an energy balance situation is created between input power and energy loss, resulting in a constant  $T_c$ . Measurements using steady-state excitation of carriers are invariably carried out via electrical transport, since it is straightforward to determine directly the input power, in contrast to optical absorption when it is extremely difficult. The major experimental problem in steady-state measurements is then to determine  $T_c$ , as will be discussed below. In the dynamic technique the carrier system is excited by optical pulses which are short compared with  $\tau_i$  but long compared to  $\tau_{ee}$ , so that the ETM remains valid. The measured quantity is then the variation with time of  $T_c$ , the so-called cooling curve, from which it is possible to obtain the value of  $P_c$  at any given value of  $T_c$ . We may note also that transport techniques are generally used to measure energy loss at low excited carrier temperatures, in the range of relaxation via acoustic phonon emission. Optical techniques have sufficient sensitivity only at relatively high levels of energy loss, typically in the range of optic phonon emission. Since for steady-state transport the data reflect an average taken over the whole carrier distribution, the interpretation relies on the validity of the ETM. In contrast, optical techniques can provide spectroscopic information on the energy distribution of the excited carriers, and hence explore beyond the simple hot carrier picture.

### 2.1.3 Transport techniques

We shall now discuss in more detail the experimental techniques. The energy balance situation occurring in steady-state experiments can be described via the expression [5]

$$\tau_i P_{IN} = \int_{T_L}^{T_c} C(T) dT \quad (2.2)$$

where  $P_{\text{IN}}$  is the power input per electron, equal to the energy loss rate, and  $C(T)$  is the thermal capacity per electron. In a typical steady-state experiment the carriers are directly heated via an electric field, either DC [6] or using short pulses in order to minimize lattice heating [7]. Then  $P_c$  can be determined directly through the expression

$$P_c = P_{\text{IN}} = e\mu F^2 \quad (2.3)$$

where  $F$  is the electric field and  $\mu$  the carrier mobility.

Several different methods have been employed to determine  $T_c$ . It was initially suggested that the intrinsic temperature dependence of the mobility of the 2DEG could be used as a thermometer to determine carrier temperature [5, 8]. The small-signal resistance of a sample measured as a function of lattice temperature is compared with its resistance at the base lattice temperature as a function of applied electric field. However, such a calibration relies on the assumption that  $\mu$  depends only on  $T_c$  and not on  $T_L$ ; that is, the major source of momentum relaxation should be elastic scattering due to defects, and the contribution from phonon scattering should be negligible. For the inversion layer 2DEG in the Si MOSFET the mobility is indeed dominated by elastic scattering from charged impurities. Hence in this material the assumption is valid to high temperatures. However, in modulation-doped GaAs/AlGaAs heterostructures defect scattering is much reduced so that phonon effects make a significant contribution at relatively low temperatures, and the above assumption cannot be relied on. Shah *et al.* [9] highlighted the discrepancies that can arise by measuring  $T_c$  independently via photoluminescence as illustrated in Fig. 2.1. Without the effect of phonon scattering the two curves would be identical. The actual temperature at which the method becomes unreliable will depend on the particular material and sample. Hawker *et al.* [10] have described a method of estimating the

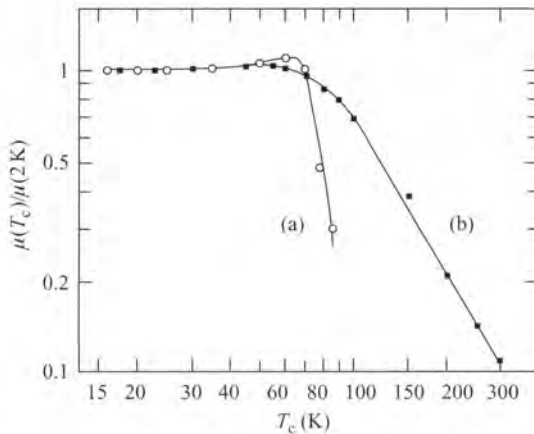


**Fig. 2.1** Variation with carrier temperature  $T_c$  of mobility  $\mu$  of a typical GaAs/AlGaAs 2DEG (a) heated by electric field at a lattice temperature  $T_L$  of 2 K, with  $T_c$  measured by photoluminescence, and (b) in equilibrium with the lattice, so that  $T_c$  is equal to the varying  $T_L$ . In the absence of phonon effects the curves should coincide (Shah *et al.* [9]).

potential discrepancy for a particular sample under given conditions. Notwithstanding the potential uncertainties, this method for determining  $T_c$  has been widely used in steady-state transport experiments, without correction.

A second technique for determining carrier temperature is via the amplitude of the Shubnikov–de Haas oscillations in magnetoresistance in weak magnetic fields [11–13]. The amplitude of the oscillations in a weak magnetic field depends on temperature according to the expression [14]

$$\frac{\Delta\rho}{\rho} = \frac{2\omega_c^2\tau^2}{1 + \omega_c^2\tau^2} \frac{\chi}{\sinh\chi} \exp\left(-\frac{\pi}{\omega_c\tau}\right). \quad (2.4)$$

Here  $\chi$  is  $2\pi^2k_B T_c/h\omega_c$ , where  $\omega_c$  is the cyclotron frequency and  $\tau$  is the (elastic) scattering time. The expression is valid for  $\omega_c^2\tau^2 \leq 1$  and, as long as  $\tau$  does not depend on other experimental parameters such as applied electric or magnetic fields, provides an absolute determination of  $T_c$ . Unfortunately this assumption cannot be generally relied on, and it is more usual to calibrate the amplitude against an ambient temperature variation obtained under equilibrium conditions. Hence the same difficulty arises as for the mobility technique described above, and the results are valid only for temperatures at which lattice heating can be neglected. However, more significantly, at the low magnetic fields required for Eq. (2.4) to be valid ( $< 1$  T) the oscillations become too weak to measure at temperatures above 10–20 K. A typical set of data is given in Fig. 2.2 showing the effect of increasing electric field, and hence carrier temperature, on the amplitude of the oscillations [13].

Although most energy is lost by the 2DEG in the form of phonons or other solid-state excitations, a detectable amount is emitted as infrared radiation. There have been several attempts to determine the carrier temperature by measuring the emitted infrared flux,

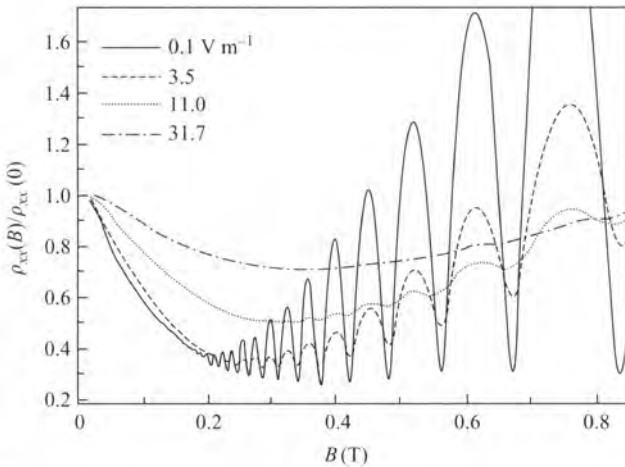


**Fig. 2.2** Shubnikov–de Haas oscillations in resistivity  $\rho_{xx}$  as a function of magnetic field  $B$  observed at a lattice temperature of 500 mK showing the effect of varying electric field, and hence carrier temperature (Leadley *et al.* [13]).

either the total intensity determined by the Stefan–Boltzmann law, or the relative flux density at two different wavelengths given by the Planck distribution. The experiments are difficult, and vary in detail. Höpfel and Weimann [15] measured the electric field dependence of the IR flux using two different detectors, high-purity n-GaAs at  $35\text{ cm}^{-1}$  and Ga-doped Ge at  $100\text{ cm}^{-1}$ . Akimov *et al.* [16] improved the sensitivity of the basic technique by pulse modulation. In contrast Hirakawa *et al.* [17] used a wide-band detector together with an InSb cyclotron resonance filter.

### 2.1.4 Phonon pulse techniques

Instead of detecting the photons emitted by the hot 2DEG, a more detailed picture of the energy relaxation process may be obtained by observing the phonons which are the primary channel of energy loss [10, 18]. Phonon pulse measurements of electron–phonon interactions in low-dimensional systems evolved from the early heat pulse experiments used to study acoustic phonon transport in dielectric crystals [19]. At low (liquid helium) temperatures, the propagation of subterahertz phonons is ballistic over macroscopic distances in substrates of high crystal quality. Typically, in good-quality semi-insulating GaAs substrates used for semiconductor manufacture, 1 THz acoustic phonons have a mean free path of about 1  $\mu\text{m}$  [20]. The main value of pulse phonon measurements is that they allow the resolution of the different acoustic phonon modes, longitudinal (LA), fast transverse (FTA) and slow transverse (STA), owing to the difference in their speeds. Additionally, it is possible to obtain information about the angular dependence of the phonon emission and absorption using the phonon imaging technique [21]. The data obtained in pulse phonon measurements are complementary to those obtained by other means. Pulse phonon measurements do not give information about the overall energy loss rates, but mode and angle dependence measurements give direct information about the fundamental electron (hole)–phonon coupling processes.

Pulse phonon experiments fall into three categories: phonon emission, phonon absorption, and phonon drag. All three have been used to study 2D electrons in LDSs, but because we are concerned here with energy relaxation of hot electrons, we shall consider only emission measurements. For examples of phonon absorption and drag measurements of 2D carrier systems see respectively [22] and [23].

The basic experimental arrangement for making phonon emission measurements is shown in Fig. 2.3. A sample consists of a small 2D electron device (e.g. Si-MOS transistor or GaAs HEMT) fabricated on the semiconductor substrate by the standard methods and a phonon detector on the opposite side of the substrate. The sample is cooled to liquid helium temperatures and electrons in the device are heated above the background (lattice) temperature by application of a short electrical or optical pulse. In the experiments reviewed here, electrical heating was used. To permit resolution of the different phonon modes in standard wafers 0.4 mm thick, it is necessary to use an excitation pulse of less than 20 ns in duration. The excitation pulse is produced by a high-speed pulse generator connected to the device via a length of RF coaxial cable. To determine the power dissipated in the device,  $P_D$ , the amplitudes of the forward (from the pulse generator),  $V_f$ , and reflected (from the device),  $V_r$ , voltage pulses on the cable are measured. Then

$$P_D = \frac{V_f^2 - V_r^2}{Z_0} \quad (2.5)$$

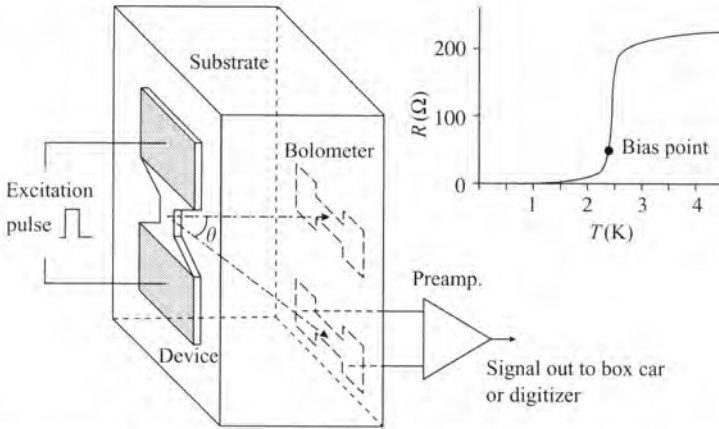


**Fig. 2.3** Geometry of a phonon emission experiment. Two bolometers (phonon detectors) are shown, one is directly opposite the active area of the device and one is at angle  $\theta$  to the device normal. The inset shows the resistance  $R$  of a typical aluminium bolometer around its superconducting transition and the steady-state bias point is indicated.

where  $Z_0$  is the characteristic impedance of the cable, normally 50  $\Omega$ . The average power dissipated per carrier in the device is given by Eq. (2.3). Owing to fast electron–electron scattering, the electron system rapidly reaches internal equilibrium at a temperature  $T_c > T_L$  and the heating effect of the voltage pulse is balanced by energy loss due to phonon emission.

Emitted phonons with frequencies  $\lesssim 1$  THz propagate ballistically to the detector. The most common type of detector is the superconducting bolometer. This consists of a thin film of metal (commonly aluminium) evaporated on the polished wafer surface. The bolometer has a superconducting transition temperature,  $T_0$ , in the range 1.5–4 K. Close to  $T_0$ , the bolometer resistance depends strongly on temperature (inset to Fig. 2.3), and so the small temperature rise caused by the incident phonons is converted to an electrical signal. The thermal mass of a superconducting bolometer is very small and its resistance can be easily matched to the 50  $\Omega$  characteristic impedance of the coaxial cable connecting it to the preamplifier at room temperature. These factors give the superconducting bolometer a very fast (nanosecond) response time. By careful analysis of the bolometer characteristics, it is possible to deconvolve a bolometer response function and so obtain quantitative information about the incident phonon flux [24]. The disadvantages of the superconducting bolometer are that it has a small dynamic range, it will not work in a magnetic field, and it gives no information about the energy spectrum of the detected phonons. Other types of detectors have been developed to overcome these problems. Cadmium sulphide bolometers [25] can operate in a magnetic field and have a very large dynamic range. They are, however, less sensitive than superconducting Al bolometers and a little slower ( $\sim 10$  ns response). Superconducting tunnel junctions offer some spectral resolution of the phonons [26]. They exhibit a low frequency threshold determined by the superconducting energy gap of the junction material. For aluminium junctions this is at  $\sim 100$  GHz and for lead junctions at  $\sim 650$  GHz. The upper frequency

limit is due to phonon scattering in the substrate. The frequency response is therefore very broad, 0.1–1 THz for an Al junction on standard GaAs wafers 0.4 mm thick, but rather narrower, 0.65–1 THz, for Pb junctions. Disadvantages of tunnel junctions are that they can be hard to fabricate reliably, do not work in a magnetic field, and are fixed frequency devices, that is not tuneable. More recently, a tuneable detector having spectral resolution based on phonon-assisted vertical transport in a superlattice structure has been demonstrated [27]. However, this type of detector has not yet been applied to the study of energy relaxation by low-dimensional electrons. To obtain information about the direction dependence of the phonon emission, discrete bolometers are fabricated in different positions relative to the device. Alternative methods based on large-area CdS bolometers [28], superconducting strip bolometers [29] and tunnel junctions [30] have been used to make images (phonographs) of the phonon emission.

After some stages of low-noise amplification, the phonon signal is recorded and analysed with nanosecond temporal resolution using a gated integrator (boxcar) or a high-speed analogue-to-digital converter and signal averager. Figure 2.4 shows a typical phonon pulse signal emitted by electrically heated carriers in a GaAs quantum well and detected by a superconducting aluminium bolometer. The LA and TA phonon pulses are clearly resolved in this trace.

### 2.1.5 Optical techniques

Transport techniques, including phonon pulse experiments, are generally limited to carrier temperatures below around 50 K, the onset of optic phonon emission. Above this temperature sample heating becomes excessive, although experiments using submicrosecond pulses have been reported reaching carrier temperatures up to 200 K [31]. In addition, as noted earlier, the mobility method of determining carrier temperature also becomes unreliable, and optical techniques are normally used for the regime of higher

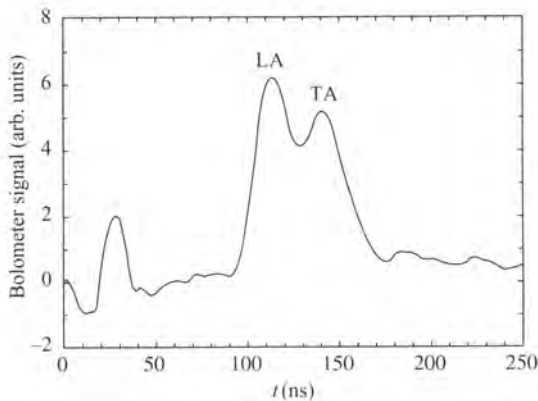


**Fig. 2.4** Typical bolometer signal for phonon emission by a 2DEG in a GaAs quantum well. The signal in the first 40 ns after the start of the excitation pulse at time  $t = 0$  is due to electromagnetic breakthrough of the pulse. The longitudinal (LA) phonons arrive at 90 ns followed by the transverse (TA) phonon pulse at 130 ns.

carrier temperatures. The most widely used method for determining  $T_c$  is photoluminescence (PL) spectroscopy, by means of which the spectral distribution of the carriers is measured directly from the emitted optical flux. Steady-state experiments combining electrical excitation of 2D carriers with photoluminescent determination of their energy distribution have been carried out, for example by Shah *et al.* [32], Yang *et al.* [33], and Balkan *et al.* [34]. The active region of the sample containing the hot carriers is excited by a low-power CW laser at a wavelength close to the bandgap of the material. Information on the carrier distribution is obtained from spectral analysis of the light generated by recombination of the excited carriers.

The above technique, a hybrid of transport and optical, has not been widely used because of the limited sensitivity of the PL spectroscopy below  $\sim 50$  K, together with the problem of CW electrical heating of carriers at higher temperatures. Through a more sophisticated experimental arrangement, PL measurements can be made on a very short (picosecond) time scale, so that the evolution of the hot carrier distribution can be followed. The picosecond resolution can be obtained by a streak camera, or by gated mixing of the photoluminescence with a delayed fraction of the exciting laser [35, 36]. Thus it is possible to plot the dynamic cooling curve of the carriers, that is the evolution of carrier temperature with time. The rate of change of temperature obtained from the cooling curve can be related to energy loss rate per carrier through the expression

$$P_c = C(T) \frac{dT_c}{dt}. \quad (2.6)$$

Data obtained by this technique are shown in Fig. 2.5. The value of  $T_c$  is obtained from the gradient of the high-energy Maxwell–Boltzmann tail of the distribution. However, it is clear that the technique also has the capability of measuring the full distribution of the hot carriers, and hence of testing the basic validity of the ETM itself.

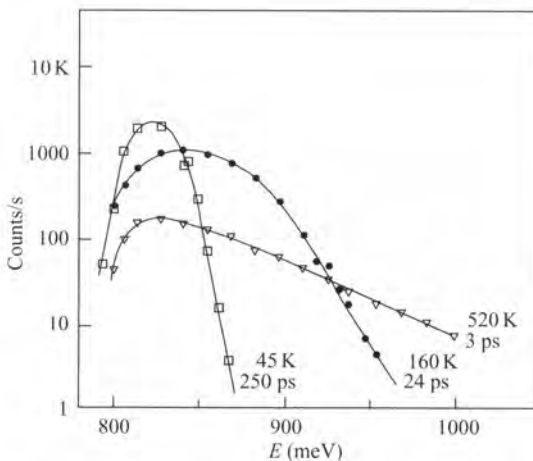


**Fig. 2.5** Luminescence spectra taken at various time delays between excitation and measurement and hence at different carrier temperatures, from which the cooling curve can be constructed [36].

Input for the cooling curve approach described by Eq. (2.6) can also be obtained by monitoring some temperature-dependent feature of the semiconductor sample following picosecond time-scale excitation of the carriers. In the most common form of ‘pump and probe’ spectroscopy the output pulse train from an ultrafast laser is split into low- and high-power components. The carriers are excited by the high-power train, whilst the low power is used to probe some optical parameter of the system, such as absorption coefficient [37], or Raman scattering [38] which can be modelled in terms of the time-dependent temperature and carrier density. A complication is that this may produce intensity-dependent populations of both electrons and holes, occupying several subbands of a low dimensional system. A summary of ultrafast laser techniques is given by Shah [39].

With the advent of femtosecond laser excitation, it is now possible to investigate earlier stages of the energy relaxation process, on a time scale much shorter than  $\tau_1$ , and hence follow the initial non-thermal evolution of the carrier distribution. As a conclusion to this section, it is instructive to summarize the time scales of carrier interaction processes. Defined by exciting pulse length the framework can be considered in terms of four overlapping regimes. In the coherent regime, the time scale is so rapid ( $<200$  fs) that coherence is maintained between the optical electric field and the excitations created, both real and virtual. Such effects are beyond the scope of the present work, and the reader is referred to reviews by Bron [40] and Ryan [41] for further details. There are many scattering processes which destroy the initial coherence so that for rather longer optical pulse lengths  $<2$  ps the resulting excitations are not coherent but are still in a non-equilibrium state; this is the non-thermal regime. The hot carrier regime, discussed earlier and described by the ETM, arises for excitation on the 1–100 ps time scale. Finally, at the end of the hot carrier stage, all the carriers, phonons and excitations are in thermal equilibrium with each other, the so-called isothermal regime.

## 2.2 Emission of acoustic phonons by 2D carriers

### 2.2.1 Introduction: 2D electron gases

In this section we shall consider theoretically the interaction of 2D electrons with bulk (3D) acoustic phonons. First we shall develop the theory of carrier–phonon interactions following the standard approach used in previous studies, for example Payne *et al.* [8], Shinba *et al.* [42, 43], Ridley [44], Price [45], Karpus [46], Rothenfusser *et al.* [47], Vass [48], and Challis *et al.* [49]. We shall then summarize the main results of the standard model.

In deriving the following expressions for the electron–acoustic phonon coupling it has been assumed that the electrons are embedded in the bulk of the semiconductor and that interface and surface effects are negligible. In reality the 2D electrons are found at roughly a typical phonon wavelength from the interface. However, since usually the materials on each side of the interface have similar acoustic properties, the assumption is a reasonable one.

For a general review of the physics of 2D electron gases see Ando *et al.* [50]. In low-dimensional semiconductor structures such as the MOS inversion layer, heterojunction

and quantum well, electrons are confined in the (growth)  $z$ -direction and are free to move in the  $xy$ -plane. The electron eigenfunctions are given by

$$\psi(\mathbf{r}) = (L_x L_y)^{-1/2} \psi_n(z) \exp(ik_x x) \exp(ik_y y) \quad (2.7)$$

where  $(L_x L_y)$  is the area and  $\psi_n(z)$  are the wave functions for motion in the  $z$ -direction. The corresponding energy eigenvalues are

$$E = E_n + \frac{\hbar^2}{2m^*} (k_x^2 + k_y^2) \quad (2.8)$$

where  $E_n$  is the energy of the  $n$ th 2D subband. In temperature terms, the energy separation between the lowest 2D subbands is a few hundred kelvin in typical structures. Therefore, at the low temperatures we are concerned with here and at moderate electron concentrations it is only necessary to consider electrons in the lowest (ground state) subband, that is  $n = 1$ . In MOS inversion layers and heterojunctions, the confining potential is approximately triangular in shape and the ground state variational wave function  $\psi_1(z)$  is given by Stern and Howard [51]:

$$\psi_1(z) = \frac{1}{\sqrt{2a_0^3}} z \exp\left(\frac{-z}{2a_0}\right) \quad (2.9)$$

where  $3a_0$  is the average separation of the electrons from the semiconductor–oxide interface for MOS devices or the heterointerface in semiconductor heterojunctions. In quantum well devices the electrons are confined in an approximately infinite square well between two heterointerfaces at  $z = 0$  and  $z = w$ ; the ground state  $z$ -wave function is given by

$$\psi_1(z) = \sqrt{\frac{2}{w}} \sin\left(\frac{\pi z}{w}\right). \quad (2.10)$$

### 2.2.2 Acoustic phonon emission theory

We start by considering an electron, which is initially in a quantum state described by its wavevector,  $\mathbf{k}$ . When the electron emits or absorbs an acoustic phonon of wavevector  $\mathbf{q}$  the electron is scattered into a new state  $\mathbf{k}'$ , where  $\mathbf{k} = \mathbf{k}' + \mathbf{q}$ . In this process the electron relaxes momentum  $\hbar\mathbf{q}$  and energy  $\hbar\omega_{\mathbf{q},\lambda}$ , where  $\omega_{\mathbf{q},\lambda}$  is the phonon frequency. For a gas of weakly interacting electrons characterized by an electron temperature  $T_c$ , in a semiconductor at a bulk (lattice) temperature  $T_L$ , we have to consider the balance of phonon emission and absorption processes. Here we are mainly interested in the case  $T_c > T_L$  where there is a net loss of energy by the electron system. Using standard time-dependent perturbation theory (see e.g. Landau and Lifshitz [52]), we can write the following expression for the electron energy relaxation rate,  $P_{\mathbf{q},\lambda}$ , into a phonon mode, described by wavevector  $\mathbf{q}$  and polarization  $\lambda$  ( $\lambda =$  longitudinal, fast transverse, or slow transverse):

$$P_{\mathbf{q},\lambda} = \hbar\omega_{\mathbf{q},\lambda} \Lambda_{\mathbf{k}}^{\mathbf{q},\lambda} \quad (2.11)$$

where the phonon emission rate

$$\Lambda_k^{q,\lambda} = g_s g_v \sum_{k,k'} \left( f_k (1 - f_{k'}) [N_{q,\lambda}(T_L) + 1] W_k^{k',\lambda} - f_{k'} (1 - f_k) N_{q,\lambda}(T_L) W_{k,\lambda}^{k'} \right). \quad (2.12)$$

Here  $N_{q,\lambda}(T_L)$  is the (Bose–Einstein) occupation number for phonon mode  $\mathbf{q}$  at the lattice temperature;  $f_k$  and  $f_{k'}$  are the electron (Fermi–Dirac) distribution functions;  $g_s$  and  $g_v$  are, respectively, the spin and valley degeneracies of the electron states;  $W_k^{k',\lambda}$  and  $W_{k,\lambda}^{k'}$  are the transition probabilities for phonon emission and absorption processes respectively. We are interested only in spontaneous phonon emission for which the transition probability given by Fermi's golden rule is

$$W_k^{k',\lambda} = W_{k,\lambda}^{k'} = \frac{2\pi}{\hbar} |M_k^{k',\lambda}|^2 \delta(E_k - E_{k'} - \hbar\omega_{q,\lambda}) \quad (2.13)$$

where  $E_k$  and  $E_{k'}$  are the energies of electron states  $\mathbf{k}$  and  $\mathbf{k}'$  respectively, the  $\delta$ -function accounts for energy conservation, and  $M_k^{k',\lambda}$  is the electron–phonon coupling matrix element

$$M_k^{k',\lambda} = \langle \mathbf{k}' | V_{e-p} | \mathbf{k} \rangle. \quad (2.14)$$

Here  $V_{e-p}$  is the electron–phonon interaction potential.

Using Eqs (2.12) and (2.13), and the identity,  $f_k (1 - f_{k'}) = (f_{k'} - f_k) N_{q,\lambda}(T_c)$ , we may write Eq. (2.11) in a more convenient form

$$P_{q,\lambda} = 2\pi\omega_{q,\lambda} g_s g_v \{ N_{q,\lambda}(T_c) - N_{q,\lambda}(T_L) \} \times \sum_{k,k'} \left( (f_{k'} - f_k) |M_k^{k',\lambda}|^2 \delta(E_k - E_{k'} - \hbar\omega_{q,\lambda}) \right). \quad (2.15)$$

### 2.2.3 Deformation potential coupling

It is now necessary to involve the detailed mechanisms of the electron–phonon interaction. We first consider deformation potential (DP) coupling which is present in all semiconductor crystals. As we shall see later, piezoelectric coupling also occurs for some materials such as GaAs.

In a (100)-oriented silicon MOS device with two conduction band minima, the deformation potential due to an oscillating displacement  $\mathbf{U}(\mathbf{r})$  is written [53]

$$V_{\text{def}}(\mathbf{r}) = \Xi_d \nabla \cdot \mathbf{U} + \Xi_u \frac{\partial U_z}{\partial z} \quad (2.16)$$

where  $\Xi_d$  and  $\Xi_u$  are respectively the uniaxial and hydrostatic coupling constants. In contrast, in (001) GaAs heterojunctions, the conduction band is parabolic with a single minimum and so  $\Xi_u = 0$ .

The displacement vector  $\mathbf{U}(\mathbf{r})$  due to a phonon  $(\mathbf{q}, \lambda)$  is given by

$$\mathbf{U}(\mathbf{r}) = \left( \frac{\hbar}{2\rho\Omega\omega_{q,\lambda}} \right)^{1/2} [a_{q,\lambda} \exp(i\mathbf{q} \cdot \mathbf{r}) + a_{q,\lambda}^\dagger \exp(-i\mathbf{q} \cdot \mathbf{r})] \mathbf{e}_{q,\lambda} \quad (2.17)$$

where  $\rho$  is the crystal density,  $\Omega$  its volume,  $\mathbf{e}_{q,\lambda}$  the phonon polarization vector, and  $a_{q,\lambda}$  and  $a_{q,\lambda}^\dagger$  are respectively the annihilation and creation operators for phonon mode  $(\mathbf{q}, \lambda)$ . Therefore, for emission of DP coupled phonons

$$V_{e-p} = -i \left( \frac{\hbar}{2\rho\Omega\omega_{q,\lambda}} \right)^{1/2} [\Xi_d \mathbf{q} \cdot \mathbf{e}_{q,\lambda} + \Xi_u q_z (\mathbf{e}_{q,\lambda})_z] a_{q,\lambda}^\dagger \exp(-i\mathbf{q} \cdot \mathbf{r}). \quad (2.18)$$

Using Eqs (2.7) and (2.18), the DP matrix element can be calculated

$$\begin{aligned} M_{\mathbf{k}}^{k',\lambda} &= \langle \mathbf{k}' | V_{e-p} | \mathbf{k} \rangle = \frac{-i}{L_x L_y} \left( \frac{\hbar}{2\rho\Omega\omega_{q,\lambda}} \right)^{1/2} [\Xi_d \mathbf{q} \cdot \mathbf{e}_{q,\lambda} + \Xi_u q_z (\mathbf{e}_{q,\lambda})_z] \\ &\times \int_{-L_x/2}^{L_x/2} dx \exp[-i(k_x - k_{x'} - q_x)x] \\ &\times \int_{-L_y/2}^{L_y/2} dy \exp[-i(k_y - k_{y'} - q_y)y] \\ &\times \int_0^\infty dz |\psi_1(z)|^2 \exp(-iq_z z). \end{aligned} \quad (2.19)$$

The integrals over  $x$  and  $y$  give zero unless  $q_x = k_x - k_{x'}$  and  $q_y = k_y - k_{y'}$ , satisfying the requirement that when a phonon is emitted, momentum is conserved in the plane of the 2DEG. The integral over  $z$  is known as the bound state form factor,  $F(q_z)$ , and for the case of a heterojunction,  $F(q_z) = (1 - iq_z a_0)^{-3}$  for the ground state. The form factor places an upper limit on the magnitude of  $q_z$  that can be emitted and accounts for momentum non-conservation in the confinement ( $z$ )-direction. The squared matrix element may therefore be written

$$|M_{\mathbf{k}}^{k',\lambda}|^2 = \frac{\hbar \Xi_d^2 q}{2\rho\Omega s_\lambda} \chi^2(\theta) |F(q_z)|^2 \delta_{\mathbf{k}, \mathbf{k}'+\mathbf{q}_\parallel} \quad (2.20)$$

where  $s_\lambda$  is the velocity of sound for polarization  $\lambda$ ;  $\chi(\theta)$  is a dimensionless anisotropy parameter given in Table 2.1, ( $\theta$  is the direction of the phonon  $\mathbf{q}$ -vector relative to the normal to the 2DEG plane, as shown in Fig. 2.6);  $q = |\mathbf{q}|$ ; the form factor  $|F(q_z)|^2 = (1 + q_z^2 a_0^2)^{-3}$  and is shown in Fig. 2.7 for  $a_0 = 4$  nm. The  $\delta$ -function term,  $\delta_{\mathbf{k}, \mathbf{k}'+\mathbf{q}_\parallel}$  ( $q_\parallel = q \sin \theta$  is the in-plane component of the phonon wavevector), accounts for the in-plane momentum conservation condition and requires (Fig. 2.6)

$$k'^2 = k^2 + q_\parallel^2 - 2kq_\parallel \cos \phi \quad (2.21)$$

**Table 2.1**  $\chi(\theta)$

	LA mode	TA mode, $\mathbf{e}_{q,\lambda}$ parallel to 2DEG plane	TA mode, $\mathbf{e}_{q,\lambda}$ out of plane
Si-MOS	$1 + (\Xi_u/\Xi_d) \cos^2 \theta$	$(\Xi_u/\Xi_d) \sin \theta \cos \theta$	0
GaAs/GaN	1	0	0

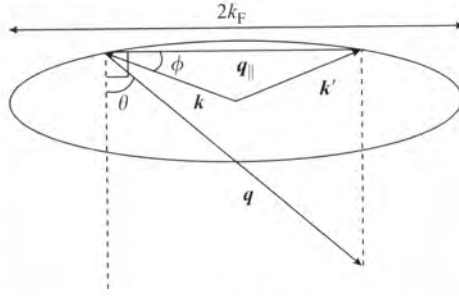


**Fig. 2.6** In-plane  $k$ -space geometry of a 2D electron-phonon scattering event.

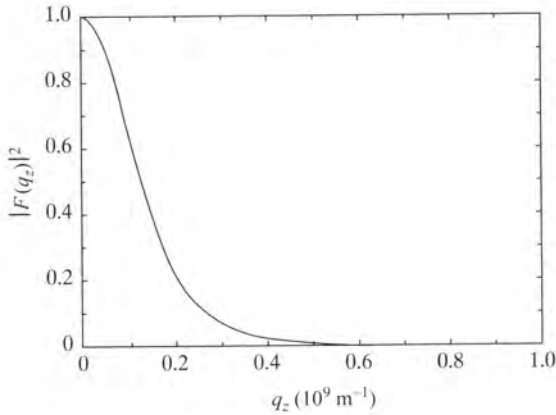


**Fig. 2.7** The form factor for 2D electrons in a GaAs heterojunction with  $a_0 = 4 \text{ nm}$ .

where  $k = |\mathbf{k}|$  and  $k' = |\mathbf{k}'|$ . Remembering that energy is also conserved in the emission or absorption of a phonon, that is  $\hbar\omega_{q,\lambda} = \hbar q s_\lambda = (\hbar^2/2m^*)(k'^2 - k^2)$ , and that  $k' \approx k \approx k_F = (4\pi n_s/g_s g_v)^{1/2}$  where  $n_s$  is the 2D electron areal density, the condition for  $\delta_{\mathbf{k},\mathbf{k}'+\mathbf{q}_\parallel}$  gives

$$\frac{s_\lambda}{v_F} \sin^{-1} \theta - \frac{q_\parallel}{2k_F} = \cos \phi \leq 1 \quad (2.22)$$

where  $v_F$  is the Fermi velocity and  $k_F$  the Fermi wavevector. We see that the electron-phonon interaction is effectively cut off in two angular ranges: at large angles where  $q_\parallel > 2k_F$ , this is the so-called  $2k_F$  in-plane momentum conservation cut-off, and at small angles where  $\sin \theta < s_\lambda/v_F$ . The latter means that the matrix element, coupling orthogonal electron states, vanishes for  $q_\parallel \rightarrow 0$ .

Changing the sum over all  $k$ -states in Eq. (2.15) to an integral and substituting Eq. (2.20) for the DP matrix element, we obtain

$$P_{q,\lambda} = g_s g_v \frac{\hbar \Xi_d^2 q^2}{2\rho\Omega} \chi^2(\theta) |F(q_z)|^2 (N_{q,\lambda}(T_c) - N_{q,\lambda}(T_L)) \times \frac{A}{4\pi^2} \int d^2\mathbf{k} (f_{k'} - f_k) \delta_{k,k'+q_\parallel} \delta(E_k - E_{k'} - \hbar\omega_{q,\lambda}) \quad (2.23)$$

where  $A$  is the 2DEG area. Considering only the integral in Eq. (2.23), using  $E_k = \hbar^2 k^2 / 2m^*$  and  $\delta(ax) = a^{-1} \delta(x)$  we write

$$I_{k,k'} = \frac{2m^*}{\hbar^2} \int d^2\mathbf{k} (f_{k'} - f_k) \delta_{k,k'+q_\parallel} \delta\left(k^2 - k'^2 - \frac{2m^* q v_\lambda}{\hbar}\right). \quad (2.24)$$

The condition  $\delta_{k,k'+q_\parallel}$  means that Eq. (2.21) can be used to substitute for  $k'$ , and writing  $d^2\mathbf{k} = k dk d\phi$  the integral becomes

$$I_{k,k'} = \frac{2m^*}{\hbar^2 q_\parallel} \int dk \int d\phi (f_{k'} - f_k) \delta\left(\cos\phi - \frac{k_0}{k}\right) \quad (2.25)$$

where  $k_0 = (q_\parallel/2) + (m^* s_\lambda / \hbar \sin\theta)$ . Now substituting  $d\phi = -d(\cos\phi) / \sin\phi = -d(\cos\phi) / (1 - \cos^2\phi)^{1/2}$  enables the integral over  $d\phi$  to be performed giving

$$I_{k,k'} = -\frac{2m^*}{\hbar^2 q_\parallel} \int_{k_0}^{\infty} dk \frac{(f_{k'} - f_k)}{\sqrt{1 - k_0^2/k^2}}. \quad (2.26)$$

Therefore, expressing the integral (2.26) in terms of the electron energy  $E_k = \hbar^2 k^2 / 2m^*$ , the power lost into mode  $(q, \lambda)$  per unit area of 2DEG due to deformation potential coupling is given by

$$P_{q,\lambda} = \frac{g_s g_v m^{*3/2} \Xi_d^2 \chi^2(\theta) |F(q_z)|^2 q^2}{2\sqrt{2}\pi \hbar^2 \rho \Omega q_\parallel} [N_{q,\lambda}(T_c) - N_{q,\lambda}(T_L)] \int_{E_0}^{\infty} \frac{(f_{E'} - f_E) dE}{(E_{k'} - E_{k_0})^{1/2}}. \quad (2.27)$$

The units of  $P_{q,\lambda}$  are  $\text{W m}^{-2} \text{sr}^{-1}$ .

While Eq. (2.27) was derived for a heterojunction, the expression for a quantum well (QW) structure is identical except for the form factor,  $|F(q_z)|^2$ . Using the wave function in Eq. (10) gives

$$|F(q_z)|^2 = \left( \frac{4\pi^2}{q_z^3 w^3 - 4q_z w \pi^2} \right)^2 [\sin^2 q_z w - (1 - \cos q_z w)^2]. \quad (2.28)$$

This is shown in Fig. 2.8 for a QW of width  $w = 12$  nm; the  $q_z$  cut-off occurs at  $q_z \approx \pi/w$ .

Notice that the form factor cut-off occurs at a higher value of  $q_z$  than in the case of a heterojunction. This is despite the fact that the ‘thickness’ of the electron wave function is approximately the same in a 12 nm QW as it is in a heterojunction with  $a_0 = 4$  nm. The form factor and value of the  $q_z$  cut-off are very sensitive to the shape of the electron wave function (see also Section 2.4.3).

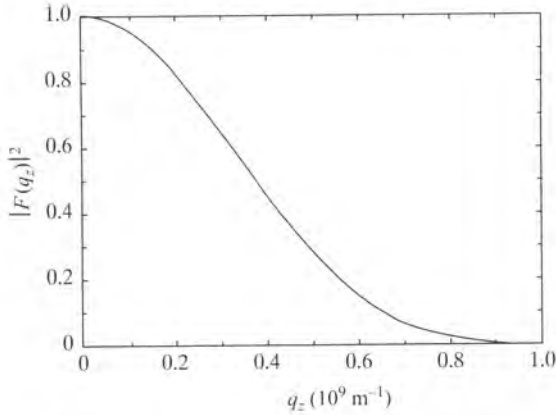


**Fig. 2.8** Form factor for a GaAs quantum well with width  $w = 12$  nm. The  $z$ -extent of the electron charge distribution is similar to that for the  $a_0 = 4$  nm heterojunction shown in Fig. 2.7, but the cut-off is at a larger wavevector owing to the different shape of the confinement potential.

#### 2.2.4 Piezoelectric coupling

Certain compound semiconductor crystals with no centre of inversion symmetry, such as GaAs, GaN, and their alloys, are piezoelectric. When such a crystal is strained, an electric polarization field is produced. Following the method of Mahan [54, 55], the strain  $S$  and electric field are related by

$$\varepsilon_{lm} F_m = e_{lmn} S_{nn} \quad (2.29)$$

where  $e_{lmn}$  are the components of the piezoelectric tensor, often written in the reduced form  $e_{lk}$  ( $l, k = 1, \dots, 6$ ) due to symmetry,  $\varepsilon$  is the dielectric tensor, and summation over repeated indices is assumed. The electric field will cause coupling between lattice distortions and the electrons. The strain may be expressed in terms of the lattice displacement  $U(\mathbf{r})$

$$S_{mn} = \frac{1}{2} \left( \frac{\partial U_m}{\partial x_n} + \frac{\partial U_n}{\partial x_m} \right) = \frac{1}{2} \left( \frac{\hbar}{2\rho\Omega\omega_{q,\lambda}} \right)^{1/2} \times [a_{q,\lambda} \exp(i\mathbf{q} \cdot \mathbf{r}) + a_{q,\lambda}^\dagger \exp(-i\mathbf{q} \cdot \mathbf{r})] [(\mathbf{e}_{q,\lambda})_m q_n + (\mathbf{e}_{q,\lambda})_n q_m]. \quad (2.30)$$

The piezoelectric field is longitudinal and parallel to the direction of the phonon wave vector  $\mathbf{q}$ , and hence may be expressed in terms of a potential  $V(\mathbf{r}) = V_q \exp(-i\mathbf{q} \cdot \mathbf{r})$ :

$$eF_m = -\nabla_m V(\mathbf{r}) = iq_m V_q \exp(-i\mathbf{q} \cdot \mathbf{r}). \quad (2.31)$$

Hence, the piezoelectric matrix elements may be calculated

$$|M_k^{k',\lambda}|^2 = \frac{\hbar}{2\rho\Omega\omega_{q,\lambda}} \left( \frac{ee_{lmn}q_l(\mathbf{e}_{q,\lambda})_m q_n}{q_l \varepsilon_{lm} q_m} \right)^2 |F(q_z)|^2 \delta_{\mathbf{k},\mathbf{k}'+\mathbf{q}_\parallel}. \quad (2.32)$$

In semiconductors such as GaAs, with the zincblende crystal structure, the piezoelectric tensor has only one independent non-zero component  $e_{14} = e_{25} = e_{36}$  and furthermore the dielectric constant is isotropic, so the matrix element becomes

$$|M_k^{k',\lambda}|^2 = \frac{\hbar}{2\rho\Omega q s_\lambda} \left( \frac{e e_{14}}{\varepsilon} \right)^2 |F(q_z)|^2 \delta_{k,k'+q_\parallel} \times \left( \frac{q_x q_y (\mathbf{e}_{q,\lambda})_z + q_y q_z (\mathbf{e}_{q,\lambda})_x + q_z q_x (\mathbf{e}_{q,\lambda})_y}{q^2} \right)^2 \quad (2.33)$$

which is highly dependent on the direction of the phonon wavevector. In Eq. (2.33)  $x$ ,  $y$ , and  $z$  refer to the crystallographic axes [100], [010], and [001] with  $z$  ([001]) perpendicular to the 2DEG.

Following the same procedure described in Section 2.2.3, the phonon emission per steradian, per unit 2DEG area, is calculated:

$$P_{q,\lambda} = \frac{g_s m^{*3/2} |F(q_z)|^2}{2\sqrt{2}\pi \hbar^2 \rho \Omega q_\parallel} \left( \frac{e e_{14}}{\varepsilon} \right)^2 \left( \frac{q_x q_y (\mathbf{e}_{q,\lambda})_z + q_y q_z (\mathbf{e}_{q,\lambda})_x + q_z q_x (\mathbf{e}_{q,\lambda})_y}{q^2} \right)^2 \times [N_{q,\lambda}(T_c) - N_{q,\lambda}(T_L)] \int_{E_0}^{\infty} \frac{(f_{E'} - f_E) dE}{(E_{k'} - E_{k_0})^{1/2}}. \quad (2.34)$$

In semiconductor structures with the wurtzite structure, a notable example (because of its technological applications) being GaN grown epitaxially on sapphire, the non-zero elements of the piezoelectric tensor are  $e_{31} = e_{32}$ ,  $e_{15} = e_{24}$ , and  $e_{33}$ . The dielectric tensor has two non-zero elements  $\varepsilon_{11}$  and  $\varepsilon_{33}$ . Therefore, in this case the phonon emission is given by

$$P_{q,\lambda} = \frac{g_s m^{*3/2} e^2 |F(q_z)|^2}{2\sqrt{2}\pi \hbar^2 \rho \Omega q_\parallel} \times \left( \frac{e_{15}(q_x^2 + q_y^2)(\mathbf{e}_{q,\lambda})_z + e_{33} q_z^2 (\mathbf{e}_{q,\lambda})_z + (e_{15} + e_{31}) q_z [q_x (\mathbf{e}_{q,\lambda})_x + q_y (\mathbf{e}_{q,\lambda})_y]}{\varepsilon_{11}(q_x^2 + q_y^2) + \varepsilon_{33} q_z^2} \right)^2 \times [N_{q,\lambda}(T_c) - N_{q,\lambda}(T_L)] \int_{E_0}^{\infty} \frac{(f_{E'} - f_E) dE}{(E_{k'} - E_{k_0})^{1/2}}. \quad (2.35)$$

### 2.2.5 Screening of the interaction potentials

So far we have ignored screening of the electron–phonon interaction potentials. At low electron temperatures, screening of the DP and piezoelectric (PE) interactions by the free carriers has the effect of reducing the phonon emission as the absolute value of the characteristic thermal phonon wavevector  $q = k_B T_c / \hbar s_\lambda$  becomes smaller than the Thomas–Fermi screening radius,  $r_s = 2\pi \varepsilon \hbar^2 / m^* e^2$ . To account for this we can multiply Eqs (2.27), (2.34), and (2.35) by a screening factor  $S_{q,\lambda}$ . Using the long-wavelength limit of the Lindhard formula for the dielectric function of free 2D electrons [50], we obtain

$$S_{q,\lambda} = \left( \frac{r_s q_\parallel}{H + r_s q_\parallel} \right)^2 \quad (2.36)$$

where the form factor  $H$  is obtained by integrating over the electronic  $z$ -wave function:

$$H = \int dz' |\psi(z')|^2 \int dz |\psi(z)|^2 \exp(-q_{\parallel}|z - z'|). \quad (2.37)$$

In systems with weak electron confinement the approximation  $H = 1$  can be made, resulting in the quasistatic screening approximation. It is clear from Eq. (2.36) that the effect of screening is much greater for small  $q_{\parallel}$ , that is at low frequencies, and for phonon emission in a direction near-perpendicular to the 2DEG.

A more complete, dynamical, approach to screening, which is applicable to shorter wavelengths, considers electron–electron interactions in the random phase approximation. An electron is assumed to be subject to a field,  $\mathbf{E}(\omega_{q,\lambda}, \mathbf{q}) = \mathbf{E}_0 \exp[i(\mathbf{q} \cdot \mathbf{r} - \omega t)]$ , which is the sum of contributions from an external field, in this case due to a phonon, and the induced polarization field,  $\mathbf{P}(\omega_{q,\lambda}, \mathbf{q})$ , of the electron system. If the external field is sufficiently weak, then linear response can be assumed, and hence

$$\mathbf{P}(\omega_{q,\lambda}, \mathbf{q}) = \chi(\omega_{q,\lambda}, \mathbf{q}) \mathbf{E}(\omega_{q,\lambda}, \mathbf{q}) g(z) \quad (2.38)$$

where  $g(z)$  describes the charge distribution of the electrons. Following the method of Ehrenreich and Cohen [56], the polarizability of the 2D sheet is calculated:

$$\chi(\omega_{q,\lambda}, \mathbf{q}_{\parallel}) = \frac{e^2}{q^2 L_x L_y} \lim_{\delta \rightarrow 0} \sum_k \frac{f_{\mathbf{k}}(T_c) - f_{\mathbf{k}+\mathbf{q}_{\parallel}}(T_c)}{E_{\mathbf{k}+\mathbf{q}_{\parallel}} - E_{\mathbf{k}} - \hbar\omega_{q,\lambda} - i\delta}. \quad (2.39)$$

Lehmann *et al.* [57] calculated numerically the phonon emission by 2D electrons including dynamical screening. They obtained better agreement with experimental measurements of the ratio LA : TA of the emitted phonon modes than that using the quasistatic screening approximation. However, for many purposes, using the long-wavelength Lindhard formula is found [58] to give nearly identical results to the dynamical screening model and is computationally less complex.

## 2.2.6 Some predictions of the standard model

In this section we shall use the expressions derived above to calculate some characteristic features of the phonon emission by a 2DEG. As an example system we choose the GaAs/AlGaAs heterojunction commonly used in the manufacture of high electron mobility transistors (HEMTs) and microwave devices for mobile communications. The parameters used in the calculations are shown in Table 2.2.

**Table 2.2** Calculation parameters for GaAs

$g_s$	$g_v$	$m^*/m_e$	$\Xi_d$ (eV)	$e_{14}$ (C m) <sup>-2</sup>	$\epsilon_r$	$a_0$ (m)	$\rho$ (kg m <sup>-3</sup> )	$s_L$ (m s <sup>-1</sup> )	$s_T$ (ms <sup>-1</sup> )
2	1	0.067	9	0.16	13	$7.1 \times 10^{-4} N_s^{-1/3}$	5320	5000	3300

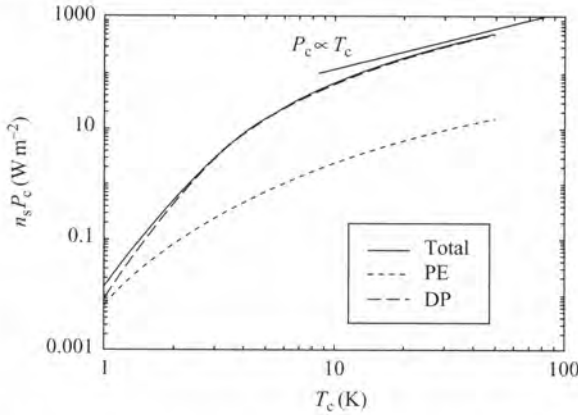


**Fig. 2.9** Calculated energy relaxation rate due to acoustic phonon emission for a 2DEG in a GaAs heterojunction with  $n_s = 5 \times 10^{15} \text{ m}^{-2}$ . The contributions from deformation potential (DP) and piezoelectric (PE) scattering are shown separately.

To calculate the total energy lost by phonon emission in watts per carrier, summing  $P_{q,\lambda}$  over all phonon modes is necessary with the result

$$P_c = \frac{1}{n_s} \sum_{\lambda} \int d\Omega_0 \int dq P_{q,\lambda} \frac{q^2 \Omega}{(2\pi)^3} \quad (2.40)$$

where  $\Omega q^2 d\Omega_0 dq / (2\pi)^3$  is the number of normal modes in the volume of phase space  $q^2 d\Omega_0 dq$ ;  $d\Omega_0$  is the element of solid angle into which the phonons are emitted. Usually it is necessary to evaluate the expression for  $P_c$  numerically.

Figure 2.9 shows the results of the calculation of power loss per unit area  $n_s P_c(T_c)$  in the electron temperature range 1 to 50 K. The lattice temperature is 0.3 K and the 2DEG areal electron density  $n_s = 5 \times 10^{15} \text{ m}^{-2}$ . DP-coupled LA modes make by far the largest contribution to  $P_c$  in this temperature range. The PE interaction becomes dominant at much lower temperatures,  $T_c < 1$  K. At high electron temperatures,  $T_c > 2\hbar k_{\text{FS}\lambda} / k_B$ ,  $P_c$  is seen to vary linearly with  $T_c$  for both DP and PE coupling. In this high-temperature range, known as the equipartition regime, the energy of the emitted phonons is smaller than the mean thermal energy of the electrons because of the  $1/a_0$  and  $2k_{\text{F}}$  cut-offs. Here the Bose–Einstein factor,  $N_{q,\lambda}(T)$ , can be approximated to  $k_B T / \hbar q s_{\lambda}$  giving the linear temperature dependence of  $P_c$  which persists to much higher temperatures than shown in Fig. 2.9. The curve is terminated at 50 K because in GaAs this is the temperature at which optic phonon emission is expected to become important. At very low temperatures,  $T_c \lesssim 1$  K, the peak in the thermal distribution of the emitted phonons is below the cut-offs and we find a power law dependence  $P_c \propto T_c^{n+1}$  arising from the integral  $\int q^n N_{q,\lambda}(T) dq$ . Following the method described for the case of a 3DEG by Ridley [59], it is possible to derive analytic expressions for  $P_c(T_c)$  at low electron temperature.

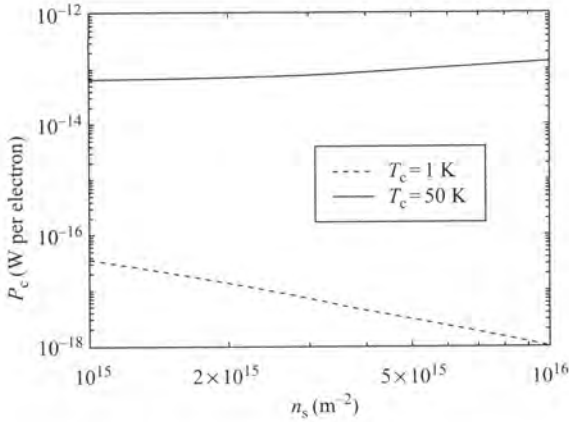


**Fig. 2.10** Total power dissipated per electron in a GaAs heterojunction as a function of the electron density at electron temperatures of 1 K and 50 K.

For DP-coupled phonons

$$P_c = \frac{m^{*2} \Xi_d^2 k_B^7 r_s^2 90 \zeta(7)}{\pi^2 \hbar^9 \rho s_\lambda^6 k_F n_s} (T_c^7 - T_L^7) \quad (2.41)$$

where  $\zeta$  is the Riemann zeta function. For PE-coupled phonons

$$P_c = \frac{K m^{*2} (ee_{14})^2 k_B^5 r_s^2 \zeta(5)}{512 \pi^2 \hbar^7 \rho \varepsilon^2 s_\lambda^4 k_F n_s} (T_c^5 - T_L^5) \quad (2.42)$$

where  $K = 135$  for the LA mode and  $K = 393$  for the TA mode.

Figure 2.10 shows the dependence on electron density of  $P_c$  at high and low electron temperatures. In the equipartition regime ( $T_c = 50$  K) increasing the density leads to a weak increase of  $P_c$ . This is due to the increased momentum space for carrier-phonon scattering since the in-plane ( $2k_F$ ) and perpendicular ( $1/a_0$ ) cut-offs increase as  $n_s^{1/2}$  and  $n_s^{1/3}$  respectively. At low temperatures ( $T_c \sim 1$  K)  $P_c$  decreases with increasing electron density. In fact, by substituting  $k_F = (2\pi n_s)^{1/2}$  in Eqs (2.41) and (2.42) we obtain at low temperatures  $P_c \propto n_s^{-3/2}$ .

The angular ( $\theta$ ) dependence of the DP-coupled LA phonon emission by a heterojunction, with  $n_s = 5 \times 10^{15} \text{ m}^{-2}$ , is shown for different electron temperatures in Fig. 2.11(a). To aid comparison with the results of heat pulse experiments to be reviewed later, the graph shows the power per electron emitted into a particular mode by a point source and falling on a small detector, of area  $dA$ , on the wafer surface opposite the heterojunction (by small we mean the linear dimension of the detector is much less than the wafer thickness). This is given by  $P_{\text{det}} = (1/n_s) \int dq q^2 \Omega P_{(q,\lambda)} d\Omega_0 / (2\pi)^3$ , where  $d\Omega_0 = dA \cos(\theta) / r^2$ , and  $r$  is the distance between the source and the detector:  $r = t / \cos(\theta)$  and  $t$  is the wafer thickness.

For all temperatures the emission falls sharply to zero at very small angles:  $\theta < \theta_c = \sin^{-1}(s_\lambda / v_F)$ , as discussed in Section 2.2.3. At small angles, below the peak but above

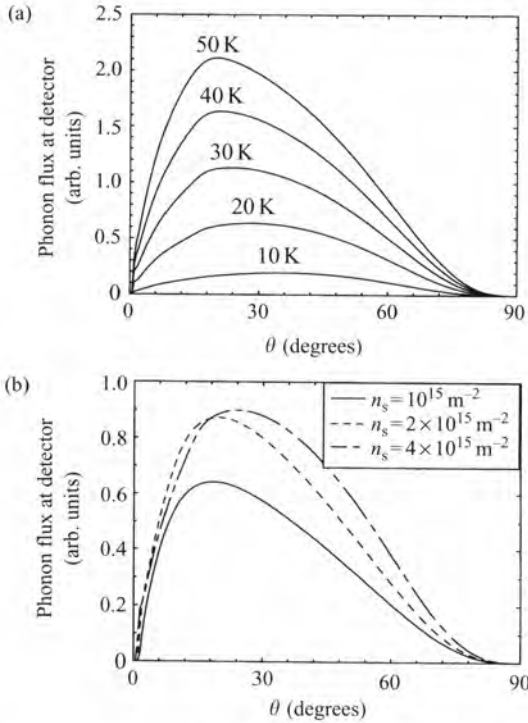


**Fig. 2.11** (a) Angle,  $\theta$ , dependence of the DP-coupled phonon emission by a 2DEG,  $n_s = 5 \times 10^{15} \text{ m}^{-2}$ , in a GaAs heterojunction at several different electron temperatures. As  $T_e$  is increased the peak in the emission moves to smaller angles due to the effect of the  $2k_F$  cut-off. (b) Angle,  $\theta$ , dependence of the DP-coupled phonon emission by a 2DEG in a GaAs heterojunction at  $T_e = 25 \text{ K}$  and for several electron densities. As  $n_s$  is increased the peak in the emission moves to larger angles due to the increased value of the  $2k_F$  cut-off.

$\theta_c$ ,  $q_{\parallel}$  becomes small and the emission is reduced by screening. If screening were not included in the calculations, the  $1/q_{\parallel}$  dependence in Eq. (2.27) would cause a very sharp peak near  $\theta_c$ . At large angles,  $P_c$  is reduced by the factor  $dA \cos(\theta)/r^2$  arising from the source detector geometry. For  $T_c \lesssim 20 \text{ K}$ , the angle at which the peak in  $P_{\text{det}}(\theta)$  occurs becomes smaller as  $T_c$  is increased. This is because the average thermal energy of the electrons is increased and, to conserve energy, the wavevector  $q$  of the emitted phonons must increase. Therefore, as a result of the  $2k_F$  cut-off in  $q_{\parallel}$ , the phonons must be emitted at smaller angles. In the equipartition range,  $T_e > 20 \text{ K}$ , the peak position is independent of temperature because  $q$  no longer depends on the mean thermal energy of the electrons but is determined by the  $2k_F$  and  $1/a_0$  cut-offs.

The  $n_s$  dependence of  $P_{\text{det}}$  at constant electron temperature,  $T_c = 25 \text{ K}$ , is shown in Fig. 2.11(b). It is seen that the peak of the emission moves to smaller angles as  $n_s$  is reduced. This is due to the weak decrease of  $2k_F$  with  $n_s$  ( $k_F \propto n_s^{1/2}$ ) which cuts off emission at large angles. The  $q_z$  ( $1/a_0$ ) cut-off in emission at small angles is more weakly dependent on  $n_s$ : for a heterojunction,  $a_0^{-1} \propto n_s^{1/3}$ . Therefore, the effect of this

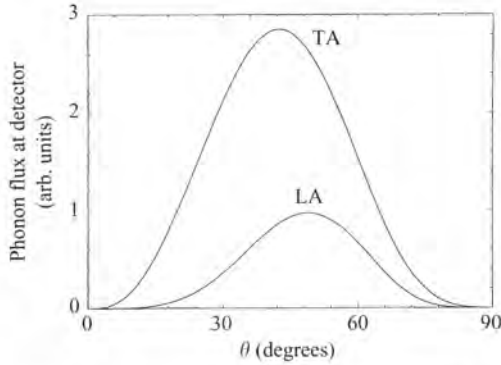


**Fig. 2.12** Angle,  $\theta$ , dependence of the phonon emission by a 2DEG,  $n_s = 5 \times 10^{15} \text{ m}^{-2}$ , in a GaAs heterojunction for PE coupling to LA and TA modes separately.

cut-off, which is to push the peak to larger angles as  $n_s$  is reduced, is not strong enough to compensate fully for the effect of the  $2k_F$  cut-off.

The angular dependence of the emission of PE-coupled modes, shown in Fig. 2.12, is dominated by the anisotropy of the PE matrix element and the source/detector geometry. For PE coupling the effects of changing  $n_s$  and  $T_c$  are weak compared with DP-coupled emission. Unlike that for the DP interaction, the PE-coupled emission also depends on the in-plane angle  $\phi$ , Eq. (2.33), being a maximum for  $q$  emitted in the (110) plane.

### 2.2.7 Effects of strong impurity scattering

In the theoretical analysis of Section 2.2, it was implicit that the electron mean free path for impurity and defect scattering was much longer than the emitted phonon wavelength. This is not always the case in very low-mobility samples or at very low electron temperatures for which  $q_{\parallel}l \ll 1$ , where  $l$  is the electron mean free path. Under these conditions, known either as the dirty limit or the diffusive regime, the electron-phonon interaction is modified by the action of strong impurity scattering. A qualitative picture of why this is so can be obtained by considering the motion of an electron under the influence of a fluctuating potential of period  $\omega^{-1}$ , such as produced by a phonon. The effect of the strong impurity scattering for which  $\tau^{-1} > \omega$ , where  $\tau^{-1} (=v_F/l)$  is the impurity scattering rate, is to ‘damp’ the electron’s response to the potential variations. For electrons interacting with a phonon of wavevector  $q$  and having  $s_{\lambda} \ll v_F$ , the condition  $\omega\tau < 1$  may be written as  $q_{\parallel}l \ll 1$ . In a typical GaAs 2DEG having an electron density of  $10^{15} \text{ m}^{-2}$  and mobility  $50 \text{ m}^2 \text{ V}^{-1} \text{ s}^{-1}$ ,  $q_{\parallel}l \approx 1$  corresponds to an electron temperature ( $T_{c1} \sim \hbar q_{\parallel} s_{\lambda} / 3k_B$ ) of only 10 mK, so that the dirty limit is not reached in practice. However,  $T_{c1} \propto \mu^{-1}$  and so in much lower mobility samples, such as GaN heterostructures for which the best reported mobilities are 2–3 orders of magnitude less than for GaAs, the dirty limit is applicable at higher temperatures.

A theory of electron-phonon interaction in dirty metals was developed by Altshuler and Aronov [60]. They showed that, in the diffusive regime, the electron-phonon coupling is ‘dressed’ by a factor  $\sim \tau^{-1} (i\omega + Dq_{\parallel}^2)^{-1}$  arising from the impurity scattering,

where  $D (=v_F^2\tau/2)$  is the electron diffusion coefficient. Screening is also affected by strong impurity scattering because the electrons in a disordered medium cannot move rapidly enough in response to the electric fields produced by the phonons. This means that the commonly used long-wavelength limit of the dielectric function (see Section 2.2.5) is not appropriate in this regime and, as pointed out by Chow *et al.* [61], dynamical screening must be used. In the diffusive regime, the dielectric function is given by [60]

$$\varepsilon(\omega, \mathbf{q}) = 1 + \frac{HDq_{\parallel}}{r_s(i\omega + Dq_{\parallel}^2)}. \quad (2.43)$$

It should be noted that the long-wavelength limit,  $\omega \rightarrow 0$ , of Eq. (2.43) is  $\varepsilon^2(0, \mathbf{q}) = S_{q,\lambda}$ , as given in Eq. (2.36).

Kveshchenko and Reiser [62] calculated the energy loss rate in a GaAs heterojunction in the dirty limit. They considered emission of PE-coupled phonons which is dominant at the low electron temperatures involved and arrived at the following result, in the notation of this book:

$$P_c = \frac{863\pi m^*}{15n_s\rho s_{\lambda}^3 D\hbar^5} \left(\frac{r_s e e_{14}}{\varepsilon}\right)^2 k_B^4 (T_c^4 - T_L^4). \quad (2.44)$$

We see that, in the dirty limit, the energy loss rate is proportional to  $T_c^4 - T_L^4$  instead of  $T_c^5 - T_L^5$  that was obtained for PE coupling in a clean system, Eq. (2.42). This is related to the loss of a power of  $q$  in the integral  $\int q^n N_{q,\lambda}(T) dq$ , due to the exact cancellation of the factor  $(i\omega + Dq_{\parallel}^2)$  from the impurity correction to the electron-phonon coupling with an identical one in  $\varepsilon(\omega, \mathbf{q})$ . Though not immediately obvious from Eq. (2.44), the energy loss rate is also enhanced by one or two orders of magnitude compared with a clean system.

Similar results were obtained in the calculations by Chow *et al.* [63] who also obtained good agreement with their experimental measurements on low-mobility GaAs heterostructures. In the experiments, they used the device resistance as a thermometer to measure  $T_c$ . The low-temperature ( $T = 0.3$  K) mobility of the samples used was dependent on the 2D electron density which was varied by illuminating the sample. The lowest mobility they obtained was about  $0.2 \text{ m}^2 \text{ V}^{-1} \text{ s}^{-1}$  at  $n_s \approx 5 \times 10^{14} \text{ m}^{-2}$ , corresponding to  $ql \sim 1$  at  $T_c \approx 0.7$  K. They observed the transition to a  $T_c^4$  dependence of  $P_c$  starting at about 300 mK, in fair agreement with this estimate.

Experimental measurements of the energy loss by low mobility 2DEGs in delta-doped GaAs were made by Fletcher *et al.* [64]. A range of samples having electron densities in the range  $1\text{--}2 \times 10^{16} \text{ m}^{-2}$  were investigated, all having  $\mu < 0.1 \text{ m}^2 \text{ V}^{-1} \text{ s}^{-1}$  at 4.2 K. The electron temperature was measured by using the device conductance as a thermometer. They observed a  $T_c^4$  dependence of the energy loss rate below 1 K in all samples. In the lowest mobility samples the  $T_c^4$  dependence continued up to 2 or 3 K. The transition between the ‘clean’ and ‘dirty’ regimes was found to occur at  $q_{\parallel}l \approx 0.35$ .

Little is currently known about phonon emission in samples of extremely low mobility, where the mean free path is less than, or comparable with, the Fermi wavelength ( $k_F l \lesssim 1$ ). The condition  $k_F l \sim 1$  is usually taken as the transition between the weak and strong localization (hopping) regimes. Under these conditions  $k_F$  is not a good quantum number and it is expected that the in-plane momentum conservation ( $2k_F$ ) condition

should be relaxed. Additionally we might expect that screening will become much less effective. The combined effect of these might be to increase the strength of the emission and weaken the temperature dependence to  $T_c^3$  for PE coupling and  $T_c^5$  for DP coupling. The onset of linear temperature dependence (equipartition) may be moved to much higher temperature. More experimental and theoretical work is required in this regime.

## 2.3 Energy relaxation via optic phonons

### 2.3.1 Introduction

As described above in Section 2.2, at the lowest temperatures 2D carriers lose energy via acoustic phonon emission. In the present section we shall deal with other processes that take effect at higher temperatures, primarily relaxation via emission of optic phonons. We shall concentrate on polar semiconductors, particularly GaAs, for which optic phonon emission is an important factor in determining the efficiency of both transport and optical devices [65, 66]. Energy relaxation via optic phonon emission in these materials is simpler to model than the acoustic phonon process, for several reasons. First, the dominant mechanism is the polar Fröhlich interaction, which couples only to longitudinal optic (LO) phonons. The deformation potential and piezoelectric interactions are relatively much weaker. Furthermore, because the Fermi wavevector of the 2D electrons in GaAs structures is close to the Brillouin zone centre, the emitted LO phonons can be regarded as all having the same energy. At low concentrations and at carrier temperatures sufficiently high for optic phonon emission to dominate, it is reasonable to assume also that Maxwell–Boltzmann statistics apply, and, more questionably, that the electron–phonon interaction is unscreened. The above scenario defines what we may call the standard model for energy loss by optic phonon emission. Finally, as long as the carrier temperature is small compared with the equivalent of the LO phonon energy, the expression for 2D energy loss via optic phonon emission reduces to a simple exponential form.

Although the standard model describes qualitatively many of the observed features of 2DEG energy relaxation, measured values of relaxation rates have often been found to vary with the parameters of the LDS, for example with carrier density and layer thickness. It is believed that most of these discrepancies can be understood in terms of three specific phenomena which modify the basic process. First, in a simple heterojunction, the relatively weak confinement is expected to have only a relatively minor effect on optic phonon emission from the 2DEG. However, in multilayer structures, such as quantum wells, and especially in structures of lower dimensions such as quantum dots having clear structural confinement, optic phonon emission may be significantly modified. The effective rate of energy relaxation may also be reduced by the reabsorption of emitted optic phonons before they themselves have had time to decay through anharmonic downconversion. The hot phonon effect, as it is called, is more pronounced at lower lattice temperatures and higher carrier densities. Finally, many results suggest that a simple description via the bare electron–phonon interaction is not adequate, and that it is important to take into account electron–electron interactions in the Fermi gas. As described in the previous section, for acoustic phonons this can be achieved via a static screening model, but for

optic modes the screening is dynamic, giving rise also to anti-screening and frequency shifts. Such many-body effects can be described in terms of coupled plasmon–phonon modes which provide an important alternative channel for 2D energy loss.

### 2.3.2 Standard model

We shall first use the standard model to derive an expression for the energy loss via optic phonons in the absence of these complicating effects, and then describe how each of them modifies the simple picture. The principles have been described previously by many authors, for example Ferry [67], Riddoch and Ridley [68], Price [69], and Ridley [70]. If we consider non-interacting electrons obeying classical Maxwell–Boltzmann statistics, the power loss per electron at a carrier temperature,  $T_c$ , from such system has been given by Conwell [4], who used it to derive the equivalent result for optic phonon emission from a 3D electron gas:

$$P_c = \frac{\int_{\hbar\omega_{\text{LO}}}^{\infty} g(E)P(E)\exp(-E/k_{\text{B}}T_c) dE}{\int_0^{\infty} g(E)\exp(-E/k_{\text{B}}T_c) dE}. \quad (2.45)$$

Here  $g(E)$  is the electronic density of states, and  $P(E)$  is the energy loss rate by a single electron with energy  $E$ , given by Fermi's golden rule

$$P(E) = \frac{2\pi}{\hbar} \sum_{\mathbf{q}} \hbar\omega_{\text{LO}} M_{\mathbf{q}}^2 \delta(E_{\mathbf{k}'} - E_{\mathbf{k}} + \hbar\omega_{\text{LO}}), \quad (2.46)$$

where  $\hbar\omega_{\text{LO}}$  and  $\mathbf{q}$  are the LO phonon energy and wavevector,  $\mathbf{k}$  and  $\mathbf{k}'$  are the initial and final wavevectors of the electron, where  $\mathbf{k} - \mathbf{k}' = \mathbf{q}$ , and  $M_{\mathbf{q}}$  is the electron–phonon matrix element. The electron–phonon interaction with bulk LO phonons in GaAs occurs via the Fröhlich interaction, which results from the longitudinal contrary displacement  $u_{\text{LO}}$  of the two crystal sublattices of opposite charge in the structure. The electric field  $E_{\text{LO}}$  produced by this displacement can be written as  $E_{\text{LO}} = -Fu_{\text{LO}}$ , where

$$F = -[4\pi N M \omega_{\text{LO}}^2 (\varepsilon_{\infty}^{-1} - \varepsilon_s^{-1})]^{1/2}, \quad (2.47)$$

and  $N$  is the number of unit cells per unit volume of the crystal,  $M$  is the reduced mass of the primitive unit cell,  $\omega_{\text{LO}}$  is the LO phonon frequency, and  $\varepsilon_{\infty}$  and  $\varepsilon_s$  are respectively the high- and low-frequency values of the dielectric constant of the material. The matrix elements of the Fröhlich interaction for a 2DEG can be shown to be [71]

$$M_{\mathbf{q}}^2 = \frac{2\pi e^2 \hbar\omega_{\text{LO}}}{q_{\parallel}^2 - q_z^2} \left( \frac{1}{\varepsilon_{\infty}} - \frac{1}{\varepsilon_s} \right) \int_{-\infty}^{\infty} \psi_z^* \exp(iq_z z) \psi_z dz, \quad (2.48)$$

where  $q_{\parallel}$  and  $q_z$  are respectively the components of the phonon wavevector parallel and perpendicular to the plane of the 2DEG, and  $\psi_z$  is the bound state wave function of the electron associated with quantised  $z$ -motion. In the standard model it is assumed that electron motion is purely two-dimensional, so that  $\int_{-\infty}^{\infty} \psi_z^* \exp(iq_z z) \psi_z dz = 1$ .

For the 3D situation the wavevector of the emitted phonon can be in any direction, but in two dimensions momentum within the 2DEG plane must be conserved so that  $E_k - E_{k'} = \hbar\omega_{\text{LO}}$ , and the absolute value of  $q_{\parallel}$  is restricted to lie within the range

$$k \left[ 1 - \left( 1 - \frac{\hbar\omega_{\text{LO}}}{E_k} \right)^{1/2} \right] \leq q_{\parallel} \leq k \left[ 1 + \left( 1 - \frac{\hbar\omega_{\text{LO}}}{E_k} \right)^{1/2} \right]. \quad (2.49)$$

It is straightforward to write the summation over final phonon states,  $\sum_{\mathbf{q}}$  in Eq. (2.46) in terms of integrals over  $q_{\parallel}$ ,  $q_z$ , and  $\phi$ , the angle between  $k$  and  $q_{\parallel}$ . Then Eq. (2.46) becomes

$$P(E) = \frac{\omega_{\text{LO}}}{2\pi} \int_0^{\infty} q_{\parallel} dq_{\parallel} \int_0^{2\pi} d\phi \int_0^{\infty} M_q^2 \delta \left[ \frac{\hbar^2(k - q_{\parallel})^2}{2m^*} - \frac{\hbar^2 k^2}{2m^*} + \hbar\omega_{\text{LO}} \right] dq_z, \quad (2.50)$$

and hence

$$P(E) = \frac{m^* e^2 \omega_{\text{LO}}^2}{\pi k} \left( \frac{1}{\varepsilon_{\infty}} - \frac{1}{\varepsilon_s} \right) \int_0^{\infty} dq_{\parallel} \int_0^{2\pi} \delta \left( \cos \phi - \frac{q_{\parallel}}{2k} - \frac{\gamma k}{2q_{\parallel}} \right) d\phi \\ \times \int_0^{\infty} \frac{dq_z}{q_{\parallel}^2 + q_z^2}, \quad (2.51)$$

where  $\gamma$  is equal to  $\hbar\omega_{\text{LO}}/E_k$ . Evaluating the integrals over  $q_{\parallel}$  and  $q_z$  and transforming that over  $\phi$  yields

$$P(E) = (2\alpha\omega_{\text{LO}})(\hbar\omega_{\text{LO}})I(\gamma), \quad (2.52)$$

where

$$I(\gamma) = \gamma^{1/2} \int_{1/2(1-\sqrt{1-\gamma})}^{1/2(1+\sqrt{1-\gamma})} \frac{dx}{\sqrt{x^2 - (x^2 - \gamma/4)^2}}. \quad (2.53)$$

The definite integral in Eq. (2.53) is a slow function of  $\gamma$  around  $\gamma = 1$ . It is necessary to determine its behaviour only around  $\gamma = 1$ , the threshold for optic phonon emission, where its value is  $\pi$ .

In Eq. (2.52) the quantity

$$\alpha = \frac{e^2}{\hbar} \sqrt{\frac{m^*}{2\hbar\omega_{\text{LO}}}} \left( \frac{1}{\varepsilon_{\infty}} - \frac{1}{\varepsilon_s} \right)$$

is the dimensionless Fröhlich coupling constant, which may be taken as an indicator of the strength of electron–phonon coupling in specific materials. For GaAs it has the value 0.07, InSb 0.03, InAs 0.05, InP 0.08, and GaN 0.25, all of which reflect weak coupling and justify the use of a perturbation approach to the present calculations. Thus we obtain

$$P(E) = (2\pi\alpha\omega_{\text{LO}})(\hbar\omega_{\text{LO}}) \left( \frac{\hbar\omega_{\text{LO}}}{E} \right)^{1/2}. \quad (2.54)$$

Finally, since  $g(E)$  is constant for 2D carriers, if  $kT_c \ll \hbar\omega_{LO}$  it is straightforward to evaluate Eq. (2.45) to obtain an expression for  $P_c$ :

$$P_c = \frac{\hbar\omega_{LO}}{\tau_{LO}} \exp\left(\frac{-\hbar\omega_{LO}}{k_B T_c}\right), \quad (2.55)$$

where  $\tau_{LO}$  is the energy relaxation time given by

$$\tau_{LO} = (\pi\alpha\omega_{LO})^{-1}. \quad (2.56)$$

For GaAs this gives a value for  $\tau_{LO} = 80$  fs. For comparison, the corresponding 3D expression for  $\tau_{LO}$  is  $(2\alpha\omega_{LO})^{-1}$ .

### 2.3.3 Hot phonon effect

Thus the standard model of optic phonon emission by a 2DEG predicts that the energy loss should follow a simple exponential dependence on carrier temperature, with a prefactor which is completely determined by the model parameters. Whilst this exponential dependence has been widely observed with the correct dependence on optic phonon energy, in many investigations the magnitude of the energy loss is found to be smaller than predicted, sometimes greatly so. The situation is illustrated in Fig. 2.13 [32], which shows typical results obtained for GaAs/AlGaAs quantum wells, in which the measured loss rate is almost an order of magnitude smaller than the calculated value for the appropriate carrier temperature. The effect is observed for both 2D and

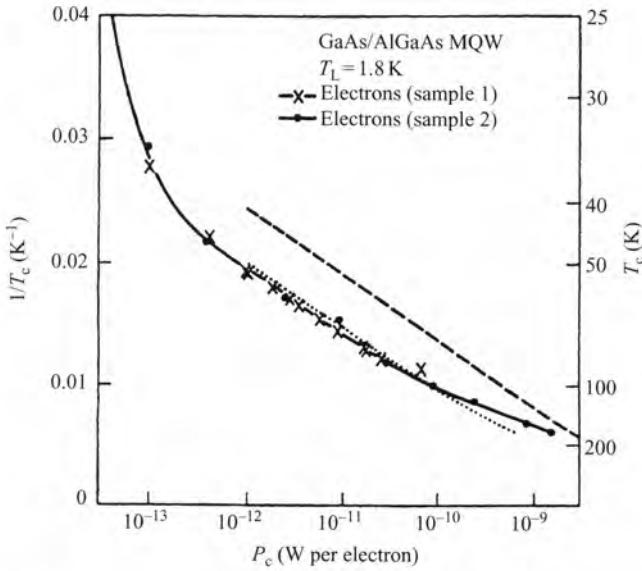


**Fig. 2.13** Energy loss rate per carrier  $P_c$  plotted as a function of inverse carrier temperature  $T_c^{-1}$  for electrons in GaAs/AlGaAs multiple quantum well structures. Solid line, experiment; dashed line, standard theory; dotted line, with hot phonons [32].

3D carriers: it is more pronounced at higher carrier densities and in layer structures, but becomes weaker at higher lattice temperatures. It is seen in both optical and transport measurements [7] and indeed was first observed several decades ago in high electric field studies of Ge [4]. The phenomenon is known as the ‘hot phonon’ effect; for a recent review see Balkan [3].

In the context of the standard model the problem arises through the implicit assumption that the existing population of the mode into which the phonons are being emitted is equal to zero. Although this assumption would be justified for optic phonons which are in thermal equilibrium at the lattice temperature, in practice the quasistationary population may be greatly increased by the input due to the energy loss process itself. That is, optic phonons are created at a rate faster than that at which they can decay and redistribute their energy throughout the whole phonon bath. It is well known that the first stage of this process takes place via anharmonic decay into two acoustic phonons on a time scale of  $\tau_{\text{ph}}$  which is long compared with 80 fs, the rate at which the optic phonons are initially being generated. In bulk GaAs at low temperatures,  $\tau_{\text{ph}}$  is known to be in the range 7–10 ps from experiments by Kash and Tsang [38], von der Linde *et al.* [72], Kash *et al.* [73], and Vallée and Bogani [74, 75]. There is some evidence that  $\tau_{\text{ph}}$  may be shorter for low-dimensional structures: 1–2 ps in an HEMT structure [7], and 5 ps in quantum wells [76, 77].

As the result of the relatively slow anharmonic decay, a non-equilibrium optic phonon distribution is built up which may be shifted in momentum space following the drifting hot 2DEG. The consequence is that optic phonons are reabsorbed by the electron gas, with a net overall reduction in the energy relaxation rate. The momentum relaxation rate and hence the mobility of the material may also be affected, depending on the amount of elastic scattering present in the material. However, whilst this effect is of great importance for high-field device applications, it is not relevant to the present discussion and the interested reader is referred to the review by Ridley [78].

The term ‘hot phonon’ is misleading since it incorrectly implies that the non-equilibrium optic phonons can be described in terms of a thermal spectrum. The non-equilibrium phonon distribution can indeed be defined by an occupation number,  $N_q$ , but this may not necessarily relate to a Planck distribution. The discussion below follows the structure developed by Kogan in his original description of energy loss via optic phonons [79]. In this approach, instead of the energy loss rate being calculated as an average over the carrier distribution as in Eq. (2.45), the steady-state value of  $N_q$  is determined. A kinetic equation is written to describe the rate of change of  $N_q$  as a balance between, on the one hand, net input due to emission by the carriers, taking into account reabsorption, and on the other hand output via decay into lower frequency phonons. Thus, instead of Eq. (2.45), the energy relaxation rate is written as

$$P_c = \sum_q \hbar\omega_{\text{LO}} \frac{N_q - N_0}{\tau_{\text{ph}}}, \quad (2.57)$$

where  $N_0$  is the equilibrium population of the optic phonons, and  $N_q$  is determined from

$$\frac{dN_q}{dt} = R_{\text{em}}(N_q + 1) - R_{\text{abs}}N_q - \frac{N_q - N_0}{\tau_{\text{ph}}}, \quad (2.58)$$

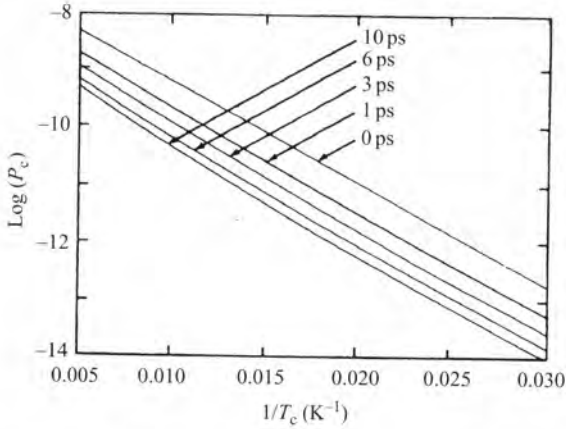


**Fig. 2.14** Dependence of calculated energy loss rate per carrier  $P_c$  on inverse carrier temperature for different assumed values of  $\tau_{\text{ph}}$  at a carrier concentration of  $7 \times 10^{15} \text{ m}^{-2}$  [93].

by setting  $dN_q/dt$  equal to zero. In this expression  $R_{\text{em}}$  and  $R_{\text{abs}}$  are the phonon emission and absorption rates. We may write [80]

$$R_{\text{em}} = R_q \exp\left(-\frac{\hbar\omega_{\text{LO}}}{k_B T_c}\right) \quad (2.59)$$

whence we obtain the result

$$P_c = \hbar\omega_{\text{LO}} \exp\left(-\frac{\hbar\omega_{\text{LO}}}{k_B T_c}\right) \sum_q \frac{R_q}{1 + \tau_{\text{ph}} [R_{\text{abs}} - R_q \exp(-\hbar\omega_{\text{LO}}/k_B T_c)]_q}. \quad (2.60)$$

If, as is commonly assumed,  $R_{\text{em}}$  and  $R_{\text{abs}}$  are related through the principle of detailed balance, with the implication of thermal equilibrium, then Eq. (2.60) becomes

$$P_c = \hbar\omega_{\text{LO}} \exp\left(-\frac{\hbar\omega_{\text{LO}}}{k_B T_c}\right) \sum_q \frac{R_q}{1 + \tau_{\text{ph}} R_q}, \quad (2.61)$$

which in the absence of hot phonon effects reduces to Eq. (2.55) with  $\tau_{\text{LO}}^{-1} = \sum_q R_q$ .

To illustrate the hot phonon effect for a GaAs/AlGaAs heterojunction, Fig. 2.14 shows the relationship calculated using Eq. (2.61) between  $\ln P_c$  and  $T^{-1}$  for different assumed values of  $\tau_{\text{ph}}$  at a carrier concentration of  $n_s = 7 \times 10^{15} \text{ m}^{-2}$  [81]. It is clear from the figure that increasing  $\tau_{\text{ph}}$  from 0 to 10 ps reduces the power loss by an order of magnitude.

The assumption of detailed balance is questionable since it ignores the complex physics of the reabsorption process. For instance, energy and wavevector conservation may restrict the available electron states for reabsorption, since following phonon emission the electron distribution will be rapidly relaxed by electron–electron scattering. Indeed, Eq. (2.61) does not predict correctly the observed dependence of the hot phonon effect on carrier density and lattice temperature, whilst Eq. (2.60) may do so. The hot phonon effect is stronger for higher carrier density because  $R_{\text{abs}}$  increases with carrier density,

thus reducing  $P_c$ . Conversely, the denominator in Eq. (2.60) is decreased by increasing temperature through the exponential factor, thus increasing  $P_c$ . For quantitative modelling of specific materials and situations, more realistic and complex methods than this simple model are required, and in general it is necessary to solve the complete system of coupled Boltzmann equations for carriers and phonons [82]. There have been three different approaches to this problem: direct numerical integration, Monte Carlo technique, and the method of moments. The reader is referred to reviews by Shah [39], Potz and Kocevar [83], and Goodnick and Lugli [84], for further details.

### 2.3.4 Coupled plasmon–phonon modes

The standard model of optic phonon emission ignores interactions between the 2D carriers, but there is increasing evidence that at higher carrier concentrations energy relaxation is significantly modified by many-body effects, particularly the excitation of coupled plasmon–optic phonon modes. This process has been explored extensively in theoretical work, especially by Das Sarma and co-workers. Yet coupled mode excitation has not generally been taken into account as a relaxation mechanism because of the assumption that the coupled modes themselves could lose energy only by re-exciting single electrons, with no net loss to the lattice. Recent work by Kozorezov *et al.* [85], Al Jawhari *et al.* [86], and Wigmore *et al.* [87] suggest that this restriction is unwarranted.

Plasmons may be thought of as collective modes of the 2D gas with energies given by the zeros of the total dielectric function, thus  $\varepsilon(\chi, \omega) = 0$  [51], where  $\chi$  and  $\omega$  are the wavevector and frequency of the mode. Then

$$\varepsilon(\chi, \omega) = \varepsilon_b - V(\chi)\Pi_0(\chi, \omega), \quad (2.62)$$

where  $\varepsilon_b$  is the bare dielectric constant,  $V(\chi) = 2\pi e^2/\chi$  is the Fourier transform of the unscreened electron–electron interaction potential, and  $\Pi_0(\chi, \omega)$  is the polarizability of the 2D electron layer. The solution of Eq. (2.62) when  $\omega_p/\chi \gg v_F$  gives the dependence of the plasmon frequency  $\omega_p$  on wavevector  $\chi$  as

$$\chi^2 = \frac{\varepsilon_b \omega_p^2}{c^2} + \left( \frac{\omega_p^2}{a} \right)^2, \quad (2.63)$$

where  $a = 2\pi n_s e^2/m^* \varepsilon_b$ . For small values of  $\chi$ , the second term on the right is negligible so that  $\omega_p \propto \chi$ , whilst for larger values of  $\chi$ , the second term on the right dominates, giving  $\omega_p \propto \chi^{1/2}$ . In principle plasmons can exist also at larger wavevectors, but over most of this range the excitations are heavily attenuated and decay to electron–hole pairs, a process known as Landau damping. Reviews of experimental and theoretical work on plasmons in 2D systems have been given by Theis [88] and Ando *et al.* [50].

If their energies are close, the plasmons and LO phonons interact via the Fröhlich mechanism to give coupled modes. In bulk GaAs this occurs at a bulk carrier concentration of around  $5 \times 10^{23} \text{ m}^{-3}$ . The 2D coupled mode system in a GaAs/AlGaAs heterojunction is well understood as the result of work by Chaplik and Krashenninnikov [89], Das Sarma and Madhukar [90, 91], and Wu Xiaoguang *et al.* [92]. The effect of

the dielectric background is incorporated by writing  $\epsilon_b$  in Eq. (2.62) as

$$\epsilon_b = \epsilon_\infty \frac{(\omega^2 - \omega_{LO}^2)}{(\omega^2 - \omega_{TO}^2)}, \quad (2.64)$$

where  $\epsilon_\infty$  is the high-frequency dielectric constant of the background medium and  $\omega_{LO}$  and  $\omega_{TO}$  are the LO and TO phonon frequencies of GaAs. Consequently Eq. (2.62) may be rewritten as

$$\epsilon(\kappa, \omega) = \epsilon_\infty \frac{(\omega^2 - \omega_{LO}^2)}{(\omega^2 - \omega_{TO}^2)} - V(\chi)\Pi_0(\chi, \omega). \quad (2.65)$$

The new modes are then obtained by setting the real part of Eq. (2.65) to zero, giving in the small wavevector limit (i.e.  $\chi \ll k_F$ ) three modes as follows:

$$\omega_+ = \omega_{LO} + \frac{(\omega_{LO}^2 - \omega_{TO}^2)}{\omega_{LO}^3} \sqrt{2} r_s \frac{\kappa}{4}; \quad (2.66)$$

$$\omega_-^{(1)} = \frac{\omega_{TO}}{\omega_{LO}} \left( \frac{r_s \kappa}{2} \right)^{1/2}; \quad (2.67)$$

$$\omega_-^{(2)} = \kappa - \frac{\kappa^2}{2}, \quad (2.68)$$

where  $\omega_+$ , the phonon-like mode, and  $\omega_-^{(1)}$ , the plasmon-like mode, are undamped, whilst  $\omega_-^{(2)}$  lies in the electron-hole pair excitation region and is heavily attenuated. In the limit  $\kappa \gg 1$  only one mode is obtained, having the dispersion relation

$$\omega_+ = \omega_{LO} + \frac{(\omega_{LO}^2 - \omega_{TO}^2)}{\omega_{LO}} \frac{\sqrt{2} r_s}{\kappa^3}. \quad (2.69)$$

In all the above expressions, following [92],  $\kappa$  is the wavevector expressed in units of  $k_F$  and  $\omega$ ,  $\omega_{LO}$ , and  $\omega_{TO}$  in terms of  $2E_F/\hbar$ . The various features are illustrated in Fig. 2.15 which shows the coupled mode dispersion curves for a 2DEG with carrier density of  $10^{16} \text{ m}^{-2}$ .

For a degenerate system, where quantum Fermi statistics describe the distribution of the hot 2DEG, the above simple model becomes inapplicable, and Das Sarma *et al.* [93] developed a many-body theory within which plasmon-phonon coupled modes arise internally. Their full treatment is beyond the scope of this review, but the broad conclusions of the classical approach described here are not altered. It should be noted that the dispersion curves obtained above are based on the zero-temperature dielectric constants. In order to analyse the system at finite temperature, Eq. (2.62) should be replaced by

$$\epsilon(\kappa, \omega) = \epsilon_b(\omega) - V(\chi)\Pi_0(\chi, \omega, T, \mu), \quad (2.70)$$

where  $\mu$  is the chemical potential. In principle, this correction may not be negligible at high excited carrier temperatures.

At the lowest temperatures and wavevectors only the  $\omega_-^{(1)}$  branch is excited, since  $\omega_-^{(2)}$  is non-propagating and  $\omega_+$  has no states below the LO phonon energy. Although

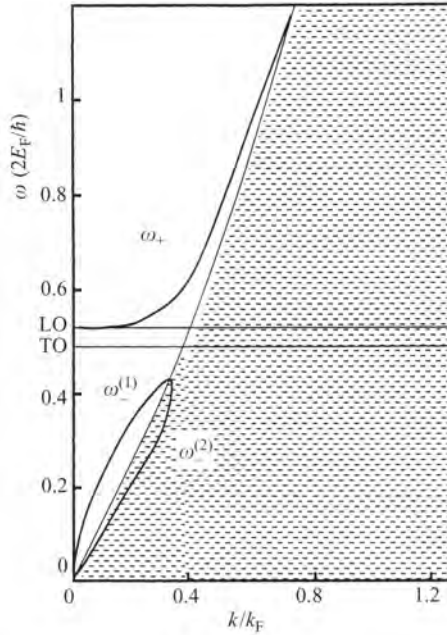


**Fig. 2.15** Coupled mode dispersion curves for a GaAs/AlGaAs 2DEG at an electron density of  $10^{16} \text{ m}^{-2}$ . From [92].

the  $\omega_-^{(1)}$  dispersion curve extends continuously from  $\kappa = 0$ , conservation of energy and momentum gives rise to the existence of a threshold frequency,  $\Omega_-$ , below which the mode cannot be excited through emission by a single hot electron. For a given sheet density, the value of  $\Omega_-$  and the corresponding reduced wavevector threshold,  $\kappa_-$ , can be obtained by solving Eq. (2.65) simultaneously with the condition derived from requirements of energy and momentum conservation

$$\Omega_- = \frac{2E_F}{\hbar} \left( \frac{\kappa_-^2}{2} + \kappa_- \right). \quad (2.71)$$

It is straightforward to calculate that over the range of concentrations  $10^{14}$  to  $10^{15} \text{ m}^{-2}$  the value of energy corresponding to  $\Omega_-$  varies from 16 to 32 meV. Thus  $\Omega_-$  lies below the LO optic phonon energy, and will be excited at carrier temperatures lower than the threshold for the latter. The number of electrons able to excite modes above the threshold  $\Omega_-$  is a rapid function of electron temperature, and Das Sarma *et al.* [80, 94, 95] showed that for a typical carrier density of  $3 \times 10^{15} \text{ m}^{-2}$  the carrier temperature at which the transfer of energy into the  $\omega_-^{(1)}$  mode overtakes that due to direct acoustic phonon emission is around 20 K. At higher carrier densities the value of  $\Omega_-$  begins to approach the LO phonon frequency, so that excitation occurs at a carrier temperature only slightly below that corresponding to the onset of LO phonon emission. Thus the effects of coupled mode excitation should be greatest at low carrier densities and low temperatures, below the optic phonon onset.

The existence of a well-defined threshold for excitation of the  $\omega_-^{(1)}$  mode suggests that, as a first approximation, energy loss via this channel may be written

$$P_{c-} = \frac{\hbar\Omega_-}{\tau_-} \exp\left(-\frac{\hbar\Omega_-}{k_B T_c}\right), \quad (2.72)$$

where  $\tau_-$  is the effective emission time for this process. Strictly Eq. (2.72) should contain an integral over all frequencies above  $\Omega_-$ , but the distribution will fall rapidly with increasing frequency. At higher carrier temperatures and input powers, eventually sufficient electrons will be able to excite also the bulk LO phonon mode, and at higher energies still, the phonon-like coupled mode,  $\omega_+$ , for which a threshold energy,  $\Omega_+$ , also exists for excitation by a single electron. However, for most carrier concentrations  $\Omega_{LO}$  and  $\Omega_+$  lie close to one another so that as a first approximation the total power loss per carrier, ignoring acoustic phonon emission, may be written as

$$P_c = \frac{\hbar\Omega_-}{\tau_-} \exp\left(-\frac{\hbar\Omega_-}{k_B T_c}\right) + \frac{\hbar\Omega_{LO}}{\tau_{LO}} \exp\left(-\frac{\hbar\Omega_{LO}}{k_B T_c}\right). \quad (2.73)$$

Of course, in a particular situation the effective value of  $\tau_{LO}$  may be determined by reabsorption, as described earlier.

The crucial parameter in Eq. (2.73) is  $\tau_-$ . Assuming polar coupling via the phonon component of the coupled mode, Das Sarma *et al.* [80, 94, 95] calculated the rate of emission of the bare  $\omega_-^{(1)}$  mode, that is neglecting reabsorption. They used this figure to model the effect of coupled mode excitation on energy loss from a GaAs/AlGaAs 2DEG for various carrier concentrations, as shown in Fig. 2.16. Until recently it was believed that the effective value of  $\tau_-$  would be greatly increased from the calculated value by reabsorption, since it was believed that the  $\omega_-^{(1)}$  mode could decay only through re-excitation of electron-hole pairs. However Kozorezov *et al.* [85] showed theoretically that the strongest decay channel of the  $\omega_-^{(1)}$  mode is via emission of a pair of phonons.

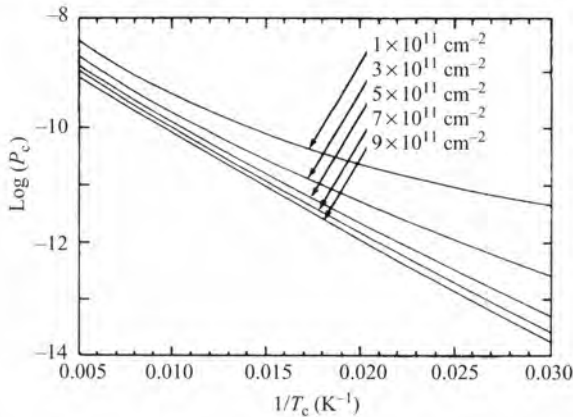


**Fig. 2.16** Calculated dependence of energy loss rate per electron into the  $\omega_-^{(1)}$  mode as a function of carrier density in the absence of reabsorption [94].

The process can take place through the second-order dipole moment and lattice anharmonicity, and since these quantities are well known for GaAs it is possible to make an estimate of the decay time of the  $\omega_{-}^{(1)}$  mode as approximately 1 ps. At low temperatures other processes such as collision damping and excitation of electron-hole pairs may be neglected. The temperature range in which coupled mode excitation is expected to dominate 2DEG energy relaxation (20–60 K) is a difficult one for most optical and transport techniques. However, recent IR [17] and phonon emission experiments [86, 96], to be described in Section 2.4, have provided convincing evidence for the existence of this loss channel.

### 2.3.5 Effects of phonon confinement

Finally we shall consider briefly the effects of phonon confinement on the conclusions reached so far in this section. Of course confinement is a necessary prerequisite for the existence of a 2DEG, but the specific form of  $\psi_z$ , the bound state wave function of the electron associated with quantized  $z$ -motion, will vary depending, for instance, on the structure of a heterojunction or the width and barrier height of a quantum well. As discussed earlier, and by Ridley [44] and Price [69], such variations can be taken into account explicitly in the evaluation of  $M_q^2$ , through the form factor  $\int_{-\infty}^{+\infty} \psi_z^* \exp(iq_z z) \psi_z dz$ . However, the form of  $M_q^2$  is also modified in a layer structure by the effects of phonon confinement.

In determining the characteristics of energy loss in layered semiconductor microstructures there are two separate problems. First it is necessary to model the normal modes of the specific structure into which the carriers may couple. In addition to bulk phonons, these include confined and localized interface modes, together with coupled modes such as polaritons, depending on carrier density. Such localization occurs because of the abrupt discontinuities in dielectric constant that occur at heterointerfaces. The second problem is to formulate the details of the electron-phonon interaction since the bulk expression for the Fröhlich interaction is inappropriate. There have been two different approaches to calculating the normal modes. The first is to model the structure as a dielectric, elastic, continuum [97], the so-called slab model, whilst the second uses lattice dynamical methods applied to a linear chain model of the structure [98]. A further controversy relates to the boundary conditions to be applied at the interfaces, whether they should be electromagnetic or purely elastic. For comparison with theory, Raman scattering measurements have been made on many different structures [99].

One reason for the current, strong interest in this area is the major technical objective of reducing energy loss from carriers, and hence enhancing the electron temperature in electronic devices or the excited state population in lasers based on LDS. In two dimensions there appears to be little difference between energy loss rate calculated on the basis of confined and interface modes, and that due to 3D bulk phonons [100]. The difference is greater in structures of lower dimensions, but far larger effects are attributable to hot phonons. For further details on all aspects of phonon confinement the reader is referred to reviews by Ridley [1, 101] and Leburton *et al.* [102].

## 2.4 Phonon pulse measurements

### 2.4.1 Phonon emission by 2DEGs

The first reported phonon emission measurements were made by Chin *et al.* [103]. Their sample was based on a modulation-doped GaAs/AlGaAs heterojunction having a 2DEG density of  $3.6 \times 10^{15} \text{ m}^{-2}$  and a low-temperature mobility of  $>100 \text{ m}^2 \text{ V}^{-1} \text{ s}^{-1}$ . The electrons in the device, of active area  $0.1 \text{ mm}^2$ , were heated using electrical pulses and the emitted phonons detected by a superconducting aluminium bolometer on the back face of the  $0.5 \text{ mm}$  GaAs wafer opposite the device. At low power ( $\approx 1 \text{ pW/electron}$ ), a sharp ballistic phonon pulse was detected at the expected flight time for TA phonons and no LA signal was seen. On the basis of these results and the assumption that the DP couples only to LA modes in GaAs, while PE coupling is very weak for LA phonons, they concluded that PE coupling must be dominant at low power. However, this conclusion appears to contradict the standard theory which finds that at  $1 \text{ pW/electron}$ , corresponding to electron temperatures of about  $40 \text{ K}$ , emission of DP-coupled LA phonons makes by far the largest contribution to the energy loss. Additionally, it was predicted for emission directions close to  $[001]$  that the PE coupling is extremely weak (see Fig. 2.12). At powers above about  $1 \text{ pW/electron}$ , the signal developed a long tail that, at even higher powers, developed into a broad delayed peak. This secondary peak became totally dominant at the highest powers. Chin *et al.* argued that the appearance of the long tail was due to the emission of optic phonons which subsequently downconverted to large wavevector TA phonons (see Fig. 2.17) and propagated diffusively and dispersively to the bolometer giving the tail signal. The broad peak which developed at the highest power was attributed to the formation of the so-called phonon ‘hot spot’ [104] in which the optic phonons do not decay fast enough to escape the vicinity of the electron gas and so can be reabsorbed.

The pioneering work of Chin *et al.* was followed by further studies of phonon emission by electrons in GaAs/AlGaAs heterostructures: Hawker *et al.* [105] used a spatially

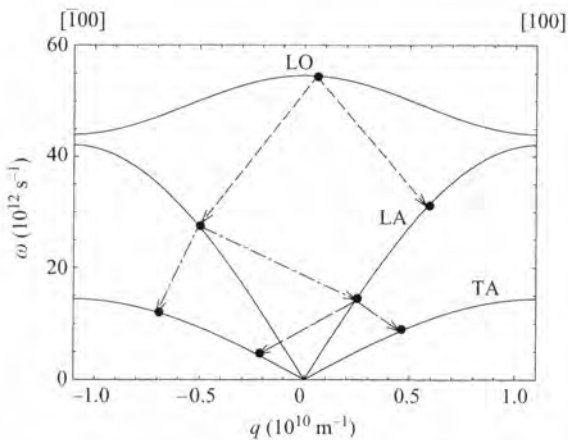


**Fig. 2.17** Schematic diagram showing one possible LO phonon downconversion route ending in TA phonons. It is predicted that the whole process is complete after a few nanoseconds.

resolving CdS bolometer to study the angle and magnetic field dependence of the emission by a 2DEG in a GaAs heterojunction. The heterojunction had a 2DEG density of  $4.7 \times 10^{15} \text{ m}^{-2}$  and a 4.2 K mobility of  $25 \text{ m}^2 \text{ V}^{-1} \text{ s}^{-1}$  and was grown on a substrate 5 mm thick to improve the phonon mode and angle resolution. Like Chin *et al.* they also observed only TA phonons at a detector directly opposite the 2DEG device. However, the lowest excitation power used was 21 pW/electron and at this power considerable optical phonon emission will take place. Therefore the TA decay products of emitted optic phonons were likely to make a significant contribution to the detected signal. This was evident in the angular dependence measurements which showed 'smearing' of the focusing structures due to diffusive phonon transport, and also in measurements of the emission as a function of magnetic field which showed clear magnetophonon resonances [106].

Hawker *et al.* [10], Wigmore *et al.* [18, 107], and Danilchenko *et al.* [108] took advantage of the rapid advancements in the speed and performance of electronic instrumentation during the 1990s to make more detailed measurements of the phonon emission by 2DEGs in GaAs heterojunctions, HEMTs, and delta-doped structures. In common with the earlier experiments, the LA mode was either absent from the heat pulse signals or at least very much weaker than predicted theoretically. It was suggested at the time that the effects of phonon focusing and the chosen experimental geometry were mainly responsible for this. For phonons propagating close to [001] the TA signal is enhanced by a factor of about 20 relative to the LA signal due to focusing. Therefore, even if both modes were emitted in equal proportions, the TA mode would be much stronger at the detector. However, in the measurements of Wigmore *et al.* using a bolometer at 30 degrees to the 2DEG normal [001], the LA mode was also found to be anomalously small compared with TA even though, in this direction, there is no focusing enhancement of TA relative to LA phonons.

These groups also measured the power at which the apparent crossover between acoustic and optic phonon emission occurred. The crossover point was identified from the change in the dependence of the ballistic TA signal intensity on the power dissipated in the device, see Fig. 2.18. The bolometer signal is proportional to the phonon flux falling on it, so it is expected that the signal should vary as  $\alpha P_c^n$ , where  $n \approx 1$ . However, it was found that the value of  $\alpha$  reduced at a particular value of  $P_c$ , which means less energy was reaching the bolometer at the ballistic flight time. This was attributed to the onset of emission of optical phonons, their decay products reaching the bolometer slightly later. Using this technique, Hawker *et al.* [10] measured the crossover as 5 pW/electron in a device having a 2DEG density of  $4.5 \times 10^{15} \text{ m}^{-2}$  whilst Wigmore *et al.* [18] obtained 2.3 pW/electron at  $2.65 \times 10^{15} \text{ m}^{-2}$ .

Rothenfusser *et al.* [47] studied the phonon emission by 2D electrons in silicon MOS devices. They used aluminium and lead superconducting tunnel junctions to give information about the frequency spectrum of the emitted phonons. Their experiments measured the detector signal as a function of the 2D sheet electron concentration which is dependent on the applied gate bias. In contrast to the case of GaAs, both phonon modes LA and TA were detected. The results showed the effect of the  $2k_F$  cut-off of the electron-phonon interaction due to in-plane momentum conservation requirements. When a degenerate 2D electron gas emits phonons, the maximum in-plane component of the phonon wavevector,  $q_{\parallel}$ , corresponds to electron transitions directly across the 2D Fermi circle

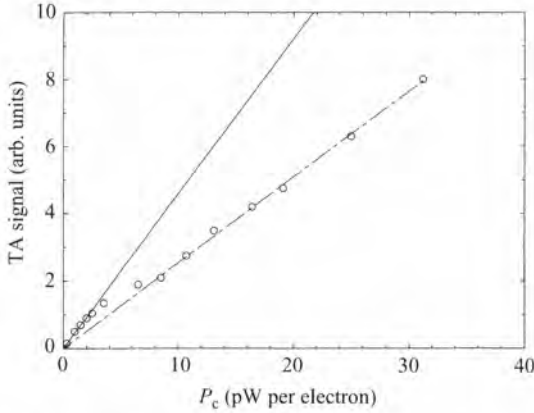


**Fig. 2.18** TA signal height as a function of power dissipation (per electron) in a GaAs heterojunction with  $n_s = 4.5 \times 10^{15} \text{ m}^{-2}$ . The change in slope occurring at approximately 3 pW/electron was associated with the onset of optic phonon emission.

of diameter (in  $k$ -space) of  $2k_F$ . Ignoring the perpendicular  $1/a_0$  cut-off, the maximum possible frequency of a phonon emitted at angle  $\theta$  to the normal to the 2D gas is

$$\nu_{\max} = \left( \frac{k_F s \lambda}{\pi \sin \theta} \right). \quad (2.74)$$

In a silicon MOS device with both spin and valley degeneracy,  $k_F = (\pi n_s)^{1/2}$ . So, for a Pb detector at  $\theta = 54$  degrees with a low-frequency detection threshold of 650 GHz, the TA signal would increase rapidly at  $n_s = 4 \times 10^{16} \text{ m}^{-2}$ . This is close to what Rothenfusser *et al.* observed in their experiment. For detectors at  $\theta = 39$  degrees and  $\theta = 23$  degrees the signal increase moved to lower values of  $n_s$  as predicted by Eq. (2.74).

Images of the emission from a 2D electron gas in MOS structures were made using extended tunnel junction detectors [109] and CdS bolometers [110]. The images showed a higher concentration of phonon flux in a direction normal to the 2DEG than could be explained by phonon focusing effects alone. This directional dependence of the phonon emission was due to the  $2k_F$  cut-off restricting emission at large angles convolved with the phonon focusing effects in the substrate. These effects are clearly illustrated by Fig. 2.19, in which images of the LA phonon emission from electrons in a (001) multiple quantum well (MQW) and from a heated metal film are compared. In both cases optical excitation was used: the focused spot ( $\approx 30 \mu\text{m}$  diameter) from a pulsed (12 ns duration)  $\lambda = 524 \text{ nm}$  laser was shone on the sample and the phonons detected using a superconducting bolometer on the opposite side of the wafer. Images were made by raster scanning the laser spot over the top of the sample. The image made using the metal film source shows the weak LA focusing features: a slight flux enhancement in directions at roughly 45 degrees to [001] and a defocusing close to [001]. However, in the image made using the MQW, the peak of the emission is directed near normal to the well despite the competing effects of phonon focusing. At the low light intensity used to

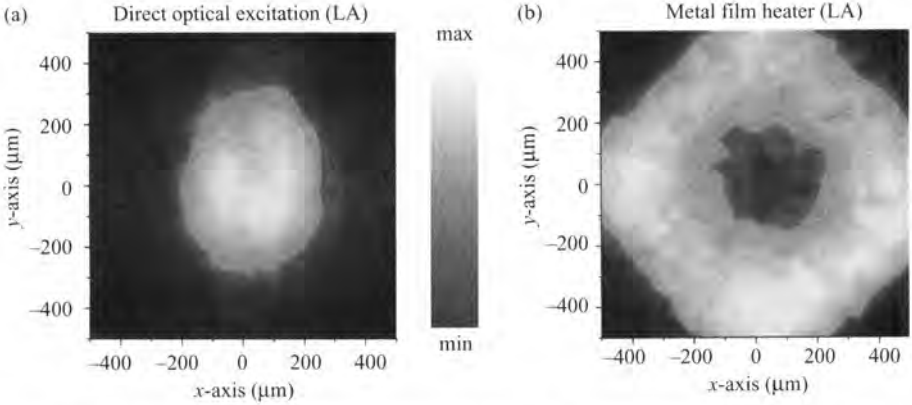


**Fig. 2.19** (a) Image of the LA phonon emission by optically excited carriers in a (001) GaAs quantum well. The bolometer is located at the centre of the image. (b) For comparison, the image for laser heating of a metal film on a GaAs substrate. It is clear that the emission by 2D electrons is channelled into a narrower range of angles close to [001] due to in-plane ( $2k_F$ ) momentum conservation.

excite the MQW sample, the average 2D carrier density per QW is not large,  $\sim 10^{15} \text{ m}^{-2}$ , and so the  $2k_F$  cut-off will occur at small angles,  $\theta \sim 10$  degrees for 1 THz LA phonons.

#### 2.4.2 The role of acoustic anisotropy

The most obvious effect of the anisotropic elastic properties of the substrate material is the so-called ‘focusing’ of the emitted phonons. In some cubic materials, for example Si and GaAs, phonon focusing can be particularly strong for TA modes propagating close to axes of high crystalline symmetry (e.g. [100]). Focusing is easily taken account of in the theory. Once the initial distribution of wavevector directions of the emitted phonons has been worked out, Monte Carlo methods can be used to determine the angular distribution of the phonon energy flux in the substrate [111]. The result is a significant modification of the angular distribution of phonon flux compared with the isotropic approximation. For example, the TA signal is enhanced at a detector directly opposite a (001) 2DEG. The actual enhancement depends on the precise size and orientation of the detector. Typically the focusing enhancement of the TA mode is about 20 times. Incorporation of focusing enhancement factors was, however, unable to account for the TA : LA ratio observed in heat pulse measurements. Furthermore, phonon focusing does not affect the overall energy relaxation rate.

Not included in the standard model is the effect of acoustic anisotropy on the electron–phonon coupling matrix elements. This can have very significant consequences for the emission anisotropy and the overall energy loss rate. To understand why, it is necessary to consider very carefully what is meant when describing phonons as LA or TA polarized. In the isotropic approximation, longitudinal phonons are polarized parallel to their wavevector direction and transverse phonons are polarized perpendicular to their wavevector direction. For both modes their wavevector and energy propagation directions are collinear. However, in experiments on real anisotropic systems, the modes

identified as ‘longitudinal’ are those which have the highest speed and so reach the detector first. For these phonons, the polarization and wavevector directions are not necessarily exactly perpendicular, they may have a small transverse component. Similarly, the modes identified as ‘transverse’ simply because they are slower can possess a significant longitudinal component of the polarization. In directions of strong phonon focusing (e.g. close to [100] in GaAs),  $\mathbf{q} \cdot \mathbf{e}_{q,\lambda} \neq 0$  for these ‘transverse’ phonons and so they are able to couple to the 2D electron system via the DP interaction, Eq. (2.19). This will further enhance the TA signal compared with an isotropic system in which the electrons would only couple to LA phonons via the DP. However, DP coupling to TA modes represents only a small contribution to the overall energy loss and it is partly compensated by the reduction in DP-coupled LA emission due to the small transverse component of the LA mode.

Acoustic anisotropy was included in calculations of the energy relaxation rate by 2D carriers by Jasiukiewicz and Karpus [112]. They found that at high temperatures (equipartition regime) including acoustic anisotropy had no effect on the energy relaxation rate. However, at low electron temperatures, in the Bloch–Grüneisen regime, differences of up to 30 per cent with the traditional (isotropic continuum) model were found. Lehmann *et al.* [57] included the effects of acoustic anisotropy of the coupling matrix elements and also focusing to calculate the ratio of LA and TA phonons emitted by 2D carriers in (001) and (311) GaAs heterojunctions. Using a (311) device allowed the geometry of the detector with respect to the 2DEG plane to be kept constant while the effect of focusing would be different for phonon propagation near [311] than for an (001) device. The calculations also took into account details of the size, shape, and position of the bolometer opposite the device.

Results of the standard theory, including only focusing and the device–detector geometry, are compared in Table 2.3 with those of the modified theory, including acoustic anisotropy in the matrix elements, together with the experimental measurements. Although not in perfect agreement, inclusion of acoustic anisotropy in the calculations gives results that are much closer to the measurements than the standard theory.

### 2.4.3 Carrier confinement and wave function shape

The total energy loss rates and mode and angular dependence of the emission are strongly influenced by the form factor  $|F(q_z)|^2$ . This was convincingly shown in a study of the phonon emission by 2D electrons in GaAs quantum wells of varying width [58].

**Table 2.3** Comparison of the ratio LA : TA detected by a bolometer directly opposite the device with the standard theory (i.e. not including acoustic anisotropy), and the theory including acoustic anisotropy

Substrate surface	Wafer thickness (mm)	LA : TA, experiment	LA : TA, standard theory	LA : TA, theory including acoustic anisotropy
(001)	0.38	$\leq 0.05$	3.5	0.036
(311)	0.28	0.53	13	0.70

The Fang–Howard variational wave function, Eq. (2.9), has been widely used to describe the  $z$ -carrier confinement in single heterojunction devices because it gives good values for the  $z$ -energy levels and because it is easy to use in calculations, often allowing analytic solutions. The form factor for a bound state described by the Fang–Howard wave function has a very severe effect on the phonon emission near normal to the 2DEG. If we define the cut-off wavevector for phonon emission in the  $z$ -direction as the value when  $|F(q_z)|^2 = 0.5$ , that is when  $q_z = (2a_0)^{-1}$ , then, for a typical GaAs 2DEG with  $n_s = 5 \times 10^{15} \text{ m}^{-2}$ ,  $a_0 \approx 4 \text{ nm}$  and the phonon emission is cut-off at 100 GHz for LA phonons and 70 GHz for TA phonons. Taking into account penetration of the electron wave function into the GaAs/AlGaAs barrier, which is necessary since it is not really an infinite potential step, gives a broader wave function and so an even more severe cut-off.

Because the electron–phonon interaction is so sensitive to the shape of the electron wave function, it would be appropriate to use a more realistic form in calculations of the phonon emission. One such one-parameter form which was found to be closer to the numerical, self-consistent, solution was proposed by Takada and Uemura [113]:

$$\psi_1(z) = \sqrt{\frac{3}{2a_0^3}} z \exp\left[-\frac{1}{2}\left(\frac{z}{a_0}\right)^{3/2}\right]. \quad (2.75)$$

Using this wave function, the form factor must be calculated numerically. Figure 2.20 shows  $|F(q_z)|^2$  as a function of  $q_z a_0$  using Eq. (2.75) and, for comparison, using the Fang–Howard wave function. For the wave function in Eq. (2.75), the cut-off is at  $q_z = 1.2/a_0$  which corresponds to 240 GHz for LA modes for  $a_0 = 4 \text{ nm}$ . This more than doubles the volume of momentum space available for phonon emission and increases the calculated energy relaxation rate by a factor of approximately 2 also.

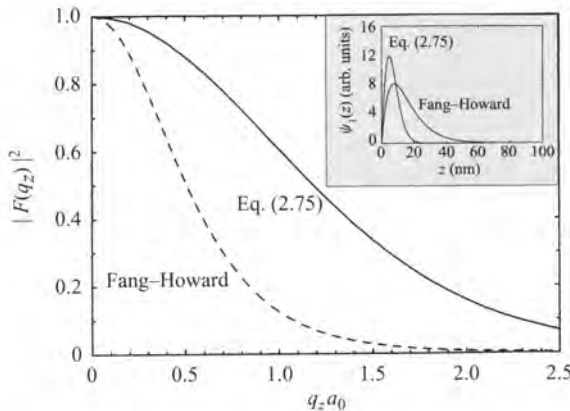


**Fig. 2.20** Form factors,  $|F(q_z)|^2$ , for Fang–Howard wave function, Eq. (2.9), and Takada–Uemura wave function Eq. (2.75), showing how a small difference in wave function shape strongly affects the form factor. The  $z$ -wave functions  $\psi_1(z)$  given by Eqs (2.9) and (2.75) are shown in the inset.

An improved functional form for  $\psi_1(z)$  can be obtained by solving exactly the Schrödinger equation with a linear potential  $V(z) = e\alpha z$  for  $z > 0$  and  $V(z) = \infty$  for  $z \leq 0$ :

$$\psi_1(z) = \text{Ai} \left\{ \frac{2m^*e\alpha}{\hbar^2} \left[ z - \left( \frac{6.391\hbar^2}{m^*e\alpha} \right)^{1/3} \right] \right\}, \quad (2.76)$$

where  $\text{Ai}(x)$  are the Airy functions. Using this form of the wave function has also been shown to give an increase, by a factor of about 2, in the overall energy loss rate [114].

Taken with the effects of acoustic anisotropy, the increase in energy loss rates predicted by using a more realistic electron wave function go a long way towards accounting for the difference between predictions of the standard theory and experimental results [115].

Phonon emission measurements have also been made on 2DEGs in GaAs quantum wells (QWs) [116], [117], and [118]. In contrast to the measurements on heterojunction devices, a strong LA signal was detected directly opposite the 2DEG. This was attributed to the stronger carrier confinement in QWs leading to an increased value of the perpendicular momentum conservation ( $1/a_0$ ) cut-off. To see why this leads to increased LA emission refer to Fig. 2.21, which shows unscreened matrix elements for PE and DP plotted as a function of the phonon wavevector. At low wavevectors,  $< 10^8 \text{ m}^{-1}$ , PE coupling dominates and this favours the emission of TA phonons, while above  $q = 10^8 \text{ m}^{-1}$  DP coupling takes over and this leads to stronger LA emission. The form factor  $|F(q_z)|^2$  for a heterojunction with  $n_s = 5 \times 10^{15} \text{ m}^{-2}$  cuts off the emission perpendicular to the 2DEG at  $q_z \approx 10^8 \text{ m}^{-1}$ , that is before DP coupling can become dominant. On the other hand, in a QW of width 5 nm, the perpendicular cut-off is at  $q_z \approx 6 \times 10^8 \text{ m}^{-1}$  and so strong LA emission in a direction perpendicular to the 2DEG is possible.

Cross [58] made systematic measurements of the ratio of intensities LA : TA and the crossover to optic emission as a function of well width in the range 12 nm down to 3 nm. Figure 2.22 shows the ratio of intensities at a detector directly opposite the 2DEG as a function of  $w$ . As the well narrows, LA emission at first increases relative to TA as expected, but then falls when  $w < 5 \text{ nm}$ . For  $w < 5 \text{ nm}$ , the perpendicular cut-off is above

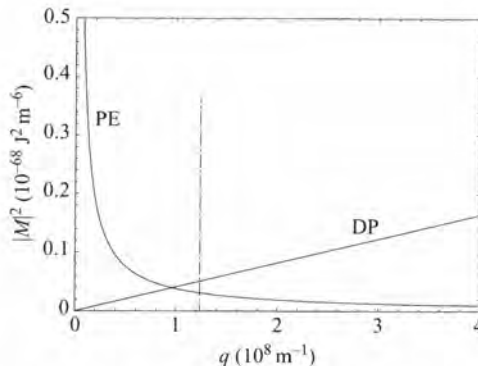


**Fig. 2.21** Squared matrix elements for unscreened DP and (spatially averaged) PE coupling as a function of magnitude of the phonon wavevector,  $q$ , for a heterojunction with  $n_s = 5 \times 10^{15} \text{ m}^{-2}$ . Also shown is the position of the perpendicular cut-off for phonon emission.

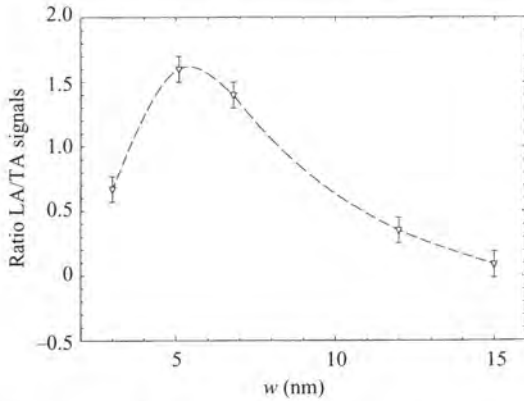


**Fig. 2.22** Ratio of LA : TA signal heights for phonons emitted by electrons in a GaAs quantum well as a function of well width  $w$ .

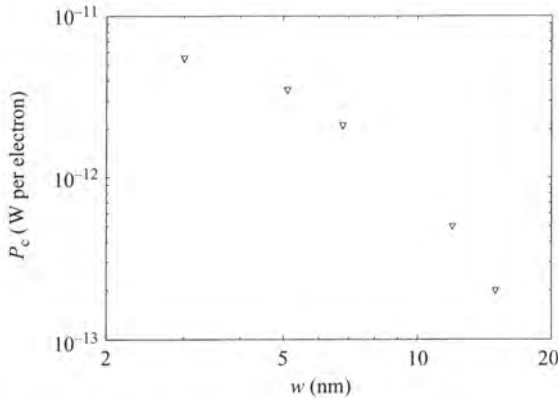


**Fig. 2.23** Power dissipation per electron in a GaAs quantum well at the crossover between acoustic and optic phonon emission (i.e.  $T_e = 50$  K), as a function of the well width.

the peak in the thermal phonon distribution corresponding to the carrier temperature and no further increase in the ratio of intensities would be expected. However, owing to phonon scattering in the substrate, the high-frequency LA phonons are attenuated as they propagate to the bolometer. Therefore, the ratio of intensities actually falls for very small  $w$ . Another effect of decreasing well width is to increase the value of  $P_c$  at which crossover occurs owing to increased acoustic phonon emission as shown in Fig. 2.23 for  $T_c \approx 50$  K. In the narrower wells the form factor cuts off at larger  $q_z$  and so there is a larger momentum space available for acoustic phonon emission perpendicular to the well. Interestingly, the well width dependence and the absolute values of the crossover are correctly predicted by the standard theory modified to include acoustic anisotropy, indicating that there may be no additional channel for inelastic scattering in QW devices at low temperatures.

### 2.4.4 Evidence for coupled mode relaxation

For hot electron temperatures up to approximately 25 K, although complicated by anisotropy and other effects described above, it is generally accepted that acoustic phonon emission through PE and DP coupling is the dominant mechanism for energy loss from a 2DEG. Equally, at carrier temperatures above around 60 K, if hot phonon effects are taken into account, the magnitude of the energy loss can be explained satisfactorily by LO phonon emission. However, in the intermediate temperature range, 25–60 K, which as we have seen is experimentally a difficult regime, different techniques give inconsistent results which do not agree with either model. The earliest indication of coupled mode relaxation was the inconsistency between results obtained by Shah *et al.* [32] and by Yang *et al.* [33], both groups using photoluminescence to measure carrier temperatures in GaAs/AlGaAs QWs, but in samples of different carrier concentrations. The electron energy loss rate observed by Yang *et al.* at 50 K was an order of magnitude faster than that found by Shah *et al.* in samples of higher carrier densities.

An explanation of the discrepancy in terms of coupled mode excitation was proposed by Das Sarma *et al.* [80], but the wider implications of their results were not generally recognized. Further evidence for the existence of an additional channel of energy loss between 25 and 60 K can be seen in the magnetotransport measurements of  $P_c$  against  $T_c$  obtained by Hirakawa and Sakaki [11], and the IR emission data obtained by Hirakawa *et al.* [17], as shown in Fig. 2.24. However, on these occasions, surprisingly, no attempt was made to interpret the excess energy loss and its sample dependence in terms of coupled modes.

The most compelling evidence for coupled mode excitation has been obtained via phonon pulse measurements, described earlier. In experiments on Ga/AlGaAs

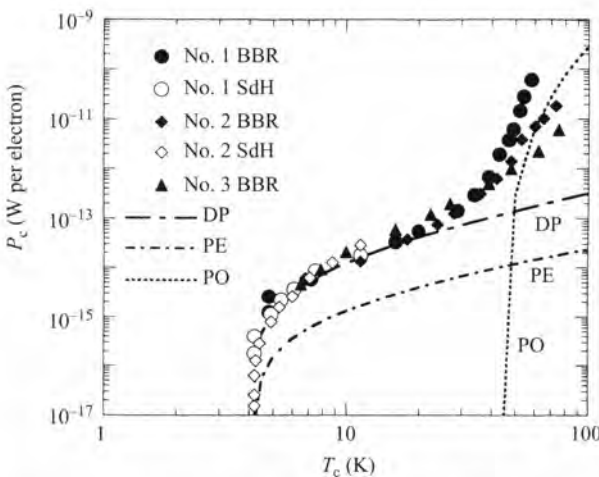


**Fig. 2.24** The energy loss per electron for various 2DEGs as a function of carrier temperature determined by far-infrared emission (BBR) and by magnetotransport (SdH), showing the excess contribution between temperatures of approximately 25 and 60 K [17]. The different mechanisms referred to are DP, PE, and polar optical (PO).

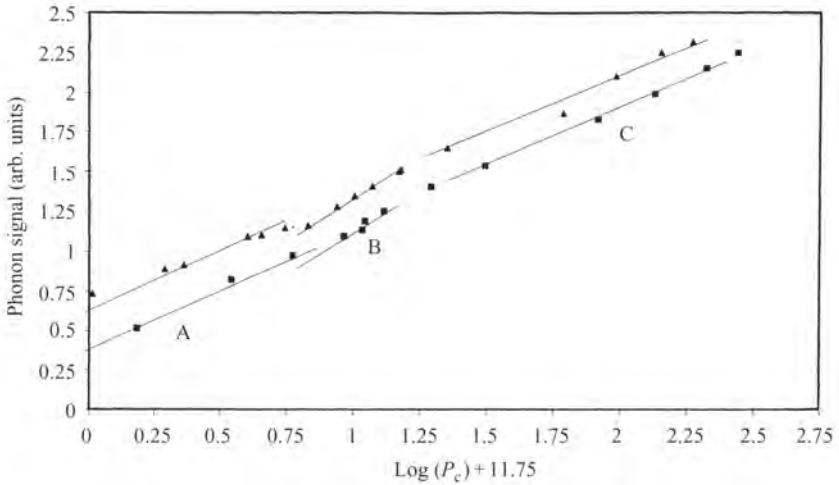


**Fig. 2.25** Emitted transverse acoustic (TA) phonon flux as a function of power loss per carrier  $P_c$ , plotted logarithmically in arbitrary units, showing the two crossovers at  $P_{c1}$  and  $P_{c2}$  for the 2DEG in an HEMT structure. The two data sets correspond to two different carrier concentrations  $3.3 \times 10^{15} \text{ m}^{-2}$  (triangles) and  $2.0 \times 10^{15} \text{ m}^{-2}$  (squares). Although the sets are displaced, the slopes of the corresponding regions A, B, and C are the same, respectively  $0.72 \pm 0.03$ ,  $0.99 \pm 0.03$ , and  $0.69 \pm 0.03$  [96].

heterojunctions, both Hawker *et al.* [10] and Wigmore *et al.* [18, 107] observed a crossover between energy loss regimes which was originally attributed to the onset of optic phonon emission (Fig. 2.18). However, the power level at which the transition occurred was found to be different in the two experiments. Further measurements were made by Al Jawhari *et al.* [86, 96] and Wigmore *et al.* [87] on a series of HEMT structures in which the carrier concentration could be varied by gate depletion. The variation of the phonon flux with  $P_c$  is shown in Fig. 2.25, plotted logarithmically, for a typical sample. At the lowest power levels (region A) the flux increased sublinearly, until at a well-defined value,  $P_{c1}$ , of  $P_c$  the dependence switched to one which is close to linear (region B), corresponding to the crossover. The logarithmic gradient in region A is  $0.72 \pm 0.03$ , and in region B  $0.99 \pm 0.03$ . At a still higher  $P_{c2}$ , the slope switched back to a lower value  $0.69 \pm 0.03$  (region C). Whilst the values  $P_{c1}$  and  $P_{c2}$  varied between samples, within the experimental uncertainties the values of the gradients in the different regions were the same. It was observed also that in region A the pulse shape became gradually broader with increasing power, whilst it remained unchanged throughout regions B and C.

Although the  $P_{c1}$  transition has previously been identified as the crossover from energy loss of the 2DEG by acoustic phonons in region A to that by optic phonons in region B, there are difficulties with this interpretation. Hawker *et al.* [10] determined the electron temperature at the observed crossover to be  $\sim 60$  K, but the measured  $P_c$  at this temperature is an order of magnitude larger than can be explained on the basis of coupling to acoustic phonons using a credible value of  $\Xi_d$ , the deformation potential constant (7 eV). An additional problem is that the deformation potential interaction, which should be the dominant mechanism for acoustic phonons, couples most strongly to LA phonons, whilst even along the (100) axis predominantly TA phonons have been detected.

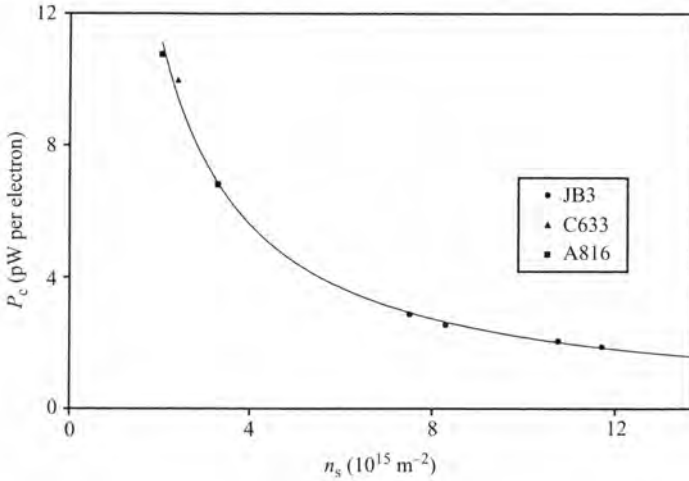


**Fig. 2.26** Phonon pulse data showing the dependence of the coupled mode–optic phonon cross-over for the 2DEGs in three different HEMT structures, as a function of carrier density  $n_s$  [96]. The solid curve is a fit to Eq. (2.73) with  $\tau_- = 1$  ps.

Al Jawhari *et al.* found that the value of  $P_{c1}$  varied rapidly with carrier density, decreasing from 10 to 1 pW per electron as the latter increased from 2 to  $13 \times 10^{15} \text{ m}^{-2}$ . The data are reproduced in Fig. 2.26 [96]. It is seen that the data from all the different 2DEGs, regardless of their origin, lie on a common curve, implying that they can be described in terms of a unified model, which clearly must involve the sheet carrier density. It can be shown that these results are consistent with a mechanism of energy loss via coupled plasmon–optic phonon modes, as described in Section 2.3.4.

Within this model, acoustic phonon emission is overtaken by excitation of the  $\omega_-^{(1)}$  mode at a temperature between 20 and 30 K. This transition is clearly seen in the IR data [17] and has also now been observed in phonon pulse experiments [119]. The feature at  $P_{c1}$  is reinterpreted as the transition from dominant energy loss by excitation of the  $\omega_-^{(1)}$  mode to that by LO phonon emission. The value of  $P_{c1}$  depends on sheet density because of the change in threshold frequency,  $\Omega_-$ , and hence a different electron temperature is required to populate this mode. The experiments yield a value for  $P_c$ , and hence from (2.73)  $\tau_-$  can be obtained in terms of  $\tau_{LO}$ , which is the 2D electron lifetime against optic phonon emission in the presence of phonon reabsorption. The quantity  $\tau_{LO}$  is difficult to calculate, but Al Jawhari *et al.* showed that taking a realistic value for  $\tau_{ph}$  of 3 ps gave a value for  $\tau_{LO}$  typically of 500 fs, and thence 1 ps for  $\tau_-$ . This figure is in good agreement with an estimate made by Kozorezov *et al.* [85], and offers further support for the coupled mode model for energy loss by 2D carriers.

It is plausible that the upper feature observed, at  $P_{c2}$ , is the transition from LO phonon emission to excitation of the  $\omega_+$  mode. Finally, the model also provides a simple explanation for the absence at powers below  $P_c$  of LA phonons, noted earlier. The point is that phonons reaching the detector have not been directly emitted by the hot carriers but have been produced by anharmonic downconversion of the earlier generations of coupled mode decay products. Each downconversion stage favours enhanced production

of TA phonons because of their much larger density of states, thus producing a large excess over LA. In summary, although convincing in many respects, the coupled mode excitation model still leaves many questions unanswered, and it is hoped that the topic will attract wider experimental attention in the near future to answer some of these.

## 2.5 Higher subband occupancy

So far this chapter has been concerned with 2D systems in which only the lowest subband is occupied. However, many practical electronic devices (e.g. HEMTs) work at carrier densities and temperatures where higher subbands can be occupied. In optoelectronic devices (e.g. the QW laser), carriers injected into higher subbands relax to the lowest subband before recombining to emit a photon. Therefore, it is also important to consider the processes of carrier relaxation within higher subbands (intrasubband relaxation) and also between subbands (intersubband relaxation).

Figure 2.27 shows some of the possible scattering processes involving emission of a phonon in a hypothetical quasi-2D system. The carrier is initially in subband  $n$  (in this case  $n = 2$ ) and the final state is in subband  $m$ . Calculation of the emitted power now involves summing over all the possible final states arising from intrasubband ( $m = n$ ) and intersubband ( $m \neq n$ ) transitions. The theoretical treatment of acoustic and optic phonon emission follows closely the methods discussed in the foregoing sections (see e.g. [1, 44, 120, 121]). The main differences are that the electron wavevector in subband  $n$  is given by  $k_n = (1/\hbar)\sqrt{2m^*(E - E_n)}$ , where  $E_n$  is the energy of the bottom of subband  $n$ , and the form factor is given by

$$|F(q_z)|^2 = \left| \int_0^w dz \psi_m^*(z) \psi_n(z) \exp(iq_z z) \right|^2 \quad (2.77)$$

which is shown in Fig. 2.28 for transitions between and within the bottom three subbands in an infinite QW of width  $w$ . Notice that for intersubband transitions,  $|F(q_z)|^2$  is zero

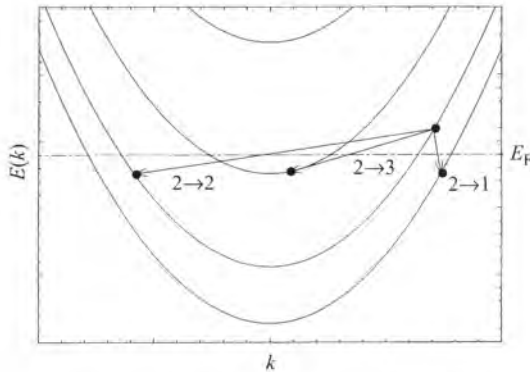


**Fig. 2.27** The 2D electron subbands in an infinite quantum well. Three subbands are shown occupied. Intrasubband and intersubband electronic transitions accompanied by phonon emission are indicated.

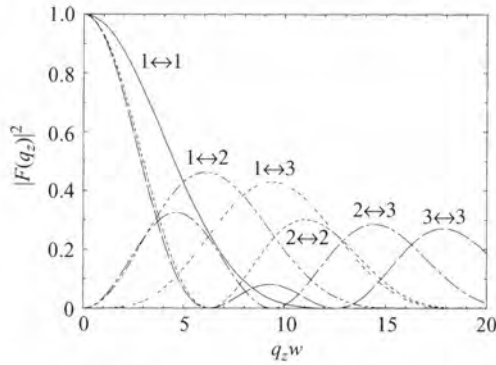


**Fig. 2.28** Form factors,  $|F(q_z)|^2$ , for transitions within and between the lowest three subbands of an infinite quantum well of width  $w$ .

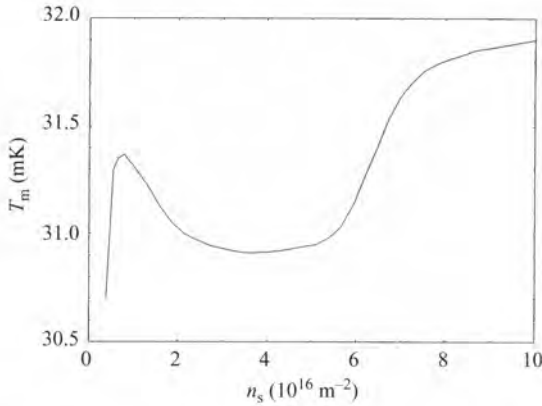


**Fig. 2.29** Temperature rise measured on a resistance thermometer located directly opposite an Si-MOS device as a function of  $n_s$ . The 2DEG is heated by a constant electrical power input of  $47 \mu\text{W}$ .

for  $q_z = 0$  since the carrier states are orthogonal. Transitions within and between higher 2D subbands can involve the emission of phonons having much higher values of  $q_z$  than is possible when only the lowest subband is involved.

Hewett *et al.* [122] observed the acoustic phonon emission from a 2D electron gas in an Si-MOS device at high values  $n_s$  where the lowest and first excited subbands are both occupied. Continuous (not pulsed) electrical excitation was used and the detector, a resistance thermometer, was located directly opposite the device. The fraction of the emitted phonons that fell on the detector increased its temperature by a small amount,  $T_m$ , proportional to the phonon flux. Figure 2.29 shows the dependence of  $T_m$  on  $n_s$  for a constant power input to the 2DEG of  $47 \mu\text{W mm}^{-2}$ . Only the lowest subband was occupied for  $0 < n_s < 5.5 \times 10^{16} \text{ m}^{-2}$  and the fall in  $T_m$  with  $n_s$  and hence  $k_F$  was attributed to the increase in  $q_{||}$  allowed by momentum conservation. The sharp increase in  $T_m$  occurring at  $n_s \simeq 5.5 \times 10^{16} \text{ m}^{-2}$  was attributed to occupation of the excited

subband. The Fermi wavevector in the excited subband will be much smaller than within the ground subband, see Fig. 2.27. Therefore, as a result of the more severe  $2k_F$  cut-off for intrasubband transitions within the excited subband, the emission will be strongly directed in a direction normal to the 2DEG. In pulsed carrier heating measurements using Si-MOS devices, Rothenfusser *et al.* [47] observed an additional signal at  $n_s \simeq 5 \times 10^{16} \text{ m}^{-2}$  which they also attributed to excited subband occupancy.

Hawker *et al.* [123] used the heat pulse technique to study the phonon emission by a 2DEG in a modulation-doped GaAs/(AlGa)As QW 20 nm wide. The carrier density was  $3.2 \times 10^{16} \text{ m}^{-2}$  and two subbands were occupied. Compared with a heterojunction or a wide QW with only one occupied subband, a strong LA signal was observed on a detector directly opposite the device. This was attributed to intersubband electronic transitions. As discussed earlier in this chapter (Section 2.4.3), one reason why the LA signal is usually so weak is that the severe perpendicular cut-off prevents emission of large-wavevector DP-coupled phonons. As shown in Fig. 2.28, much higher values of  $q_z(\text{max})$  are permitted for intersubband transitions. It was found that the crossover to optic phonon emission occurred at  $P_c \sim 3 \text{ pW}$  per carrier. This is about an order of magnitude larger than that of a wide QW with a single occupied subband (Fig. 2.23) and this reflects the increased number of channels for acoustic phonon emission when multiple subbands are occupied.

Intersubband energy relaxation via emission of LO phonons has been studied extensively using a range of optical techniques (see e.g. [76, 124–128], and references therein). Values of the intersubband lifetime obtained in narrow GaAs QWs, having  $E_2 - E_1 > \hbar\omega_{\text{LO}}$ , were typically a few hundred femtoseconds. The results were found to be consistent with optical phonon emission theory allowing for hot phonon effects. Yang and Wilson [129] used transport (magnetotunnelling spectroscopy) measurements to investigate intersubband relaxation in narrow wells. They found the intersubband energy relaxation time was  $\sim 70 \text{ fs}$  and comparable with  $\tau_{\text{LO}}$  (the intrasubband relaxation time) which is much faster than the values obtained in optical measurements. The difference may be due to the absence of hot phonon effects in the tunnelling measurement which was carried out at low current. Intersubband relaxation times were found to be much longer in wide QWs for which the energy-level separation was less than  $\hbar\omega_{\text{LO}}$ . Relaxation times in the range of tens of picoseconds to nanoseconds, depending on such factors as the well width and carrier density, have been measured. Carriers in excited subbands cool rapidly to energies less than  $\hbar\omega_{\text{LO}}$  from the subband edge,  $E_n$ , by intrasubband LO emission. Intersubband relaxation must then take place by acoustic phonon emission which is slow compared with LO emission. Acoustic phonon emission is particularly slow when the subband separation is large (more than a few meV) and the electron-phonon interaction is suppressed by the momentum conservation cut-offs. This slowing of relaxation when  $E_2 - E_1 < \hbar\omega_{\text{LO}}$  is a situation known as the phonon bottleneck and it may have a significant impact on the performance of optoelectronic devices.

## 2.6 Other 2D systems

Most studies of phonon emission by hot 2D carriers have been concerned with 2D electron gases in GaAs and Si devices so this review has concentrated on these. However,

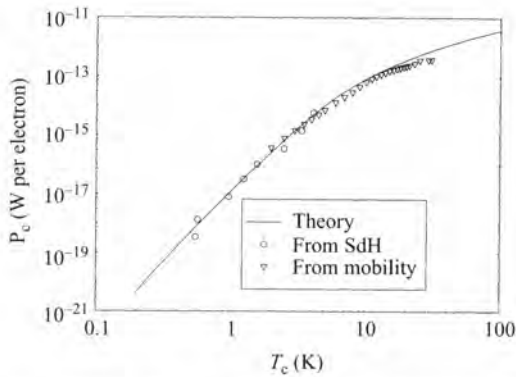


**Fig. 2.30** Energy relaxation rate of a 2DEG in GaN as a function of electron temperature,  $n_s = 5.8 \times 10^{16} \text{ m}^{-2}$ . Also shown is the result of numerical calculation using Eq. (2.35) [134].

measurements have also been made of the phonon emission by 2D hole gases (2DHGs) in p-type GaAs QWs and heterojunctions [130–132]. In contrast to emission by a 2DEG, LA phonons were detected in a direction normal to the 2DHG; this was attributed to the smaller value of  $a_0$  in a 2DHG arising from the larger effective mass of holes. The larger value of effective mass also increases the acoustic phonon emission, see Eqs (2.27) and (2.34), which explains why the crossover to optic phonon emission occurred at about 10 times the power dissipation than in a 2DEG of similar density. Despite the complexity of the 2D hole subband structure in GaAs, it was found that at low enough hole density and low temperatures, the phonon emission theory developed for 2DEGs was applicable. Good agreement with the experimental data was obtained by using the appropriate values of the hole effective mass and DP and PE coupling constants.

Gallium nitride is a relatively new wide-bandgap semiconductor system which is currently the subject of considerable interest owing to its potential applications in blue/UV optoelectronic devices and high-power microwave transistors; for a review see Monemar [133]. The processes of carrier–phonon scattering and energy relaxation are no less important in GaN than in the better understood GaAs, particularly in view of the potential high-temperature applications of GaN. Two properties of GaN that have direct influence on the carrier–phonon interaction are its high optic phonon energy, 92 meV compared with 36 meV in GaAs, and its very strong piezoelectric effect, about three times stronger than in GaAs. One effect of these will be to increase the temperature at which the acoustic–optic phonon emission crossover is expected to occur compared with GaAs. It is also interesting to note that the optic phonon energy relaxation time (Eq. (2.56)) is 8.4 fs, about 10 times less than in GaAs and comparable with the electron–electron scattering time at typical  $n_s$  and so the ETM may not be applicable under certain conditions.

Lee *et al.* [134] have measured the rate of energy relaxation by a 2DEG in a GaN/AlGaIn heterojunction. The sample had a 2DEG density of  $5.8 \times 10^{16} \text{ m}^{-2}$  and 1.4 K mobility of  $1 \text{ m}^2 \text{ V}^{-1} \text{ s}^{-1}$ . The amplitude of Shubnikov–de Haas oscillations was

used as a thermometer to measure  $T_c$ . Measurements were at low temperatures, up to  $T_c = 8$  K, where acoustic phonon emission dominates the energy loss. Data for higher electron temperatures, up to  $\sim 50$  K, were obtained for the same sample by using the mobility as a thermometer [135]. A technique developed by Ouali *et al.* [136] was used to separate the impurity and phonon scattering contributions to the mobility. The results of both sets of measurements are shown in Fig. 2.30 along with theoretical results using Eq. (2.35). No evidence of the onset of optic phonon emission is observed and it appears that PE coupling is dominant in the range of temperatures studied.

Up to the time of writing, there have been no direct phonon emission measurements on 2DEGs in GaN heterostructures. The dissipation and electron temperature at the onset of optic phonon emission have not been measured.

## 2.7 Conclusions

In this chapter we have reviewed the processes by which an excited 2D electron or hole gas in zero magnetic field relaxes back into thermal equilibrium with the lattice. We restricted our discussion to the situation in which the excited distribution itself maintains a thermal equilibrium at a higher temperature, the so-called electron temperature model. At the lowest carrier temperatures, less than approximately 50 K, energy loss takes place through emission of acoustic phonons via deformation potential and piezoelectric coupling. We noted that the basic processes appear to be well understood in this regime and generally good agreement exists between theory and experiment. In this review we have concentrated particularly on the use of phonon pulses to observe features of the energy loss process, such as polarization and angular dependence of the emitted phonons, that are inaccessible to transport and optical techniques. Measurements of these features are especially important in studying the effect of the degree of confinement on energy relaxation, for instance in quantum wells, which is a major outstanding problem.

At sufficiently high carrier temperatures optic phonon emission takes over as the dominant mechanism. The relatively stronger Fröhlich interaction is also potentially simpler than the deformation potential or piezoelectric coupling, since it excites only longitudinal phonons close to the Brillouin zone centre. However, a major problem is that the resulting optic phonons may be immediately reabsorbed by the 2DEG before they are able to downconvert to lower frequency acoustic phonons, a situation known as the hot phonon effect or phonon bottleneck. The effect is complicated and depends on many parameters of the system, particularly carrier density and temperature, so that its understanding for a specific 2D system requires detailed numerical calculation. This is an area of great current activity, since optic phonon emission is an important factor in determining the behaviour of optical and transport devices based on 2DEGs.

A further complication is the energy relaxation due to excitation of coupled plasmon–optic phonon modes in a temperature region overlapping the upper acoustic phonon range and the lower optic phonon range, approximately 25–60 K. It is only recently, through phonon pulse experiments, that evidence for the existence of this loss channel, which has important implications for hot phonon effects also, has been obtained. It is important therefore that confirmation should be obtained of the predicted dependence of energy loss rate on carrier density using other techniques.

Understanding the energy relaxation of 2DEGs is potentially important to the operation of all electronic devices that are based on the properties of carriers in confined structures. The most commercially advanced of these are the high electron mobility transistor (HEMT) and the quantum well double-heterojunction injection laser diode (QWDHILD). The HEMT, also known as the modulation-doped FET (MODFET), makes use of modulation doping to reduce elastic scattering of carriers and hence increase mobility [137]. In the QWDHILD and other reduced dimensional lasers, the mean carrier energy is increased relative to that in three dimensions through the raised density of states, resulting in lower current threshold [138]. Both the HEMT and QWDHILD operate at temperatures which are high enough (above 77 K) for more than one subband to be populated. The quantum cascade laser makes specific use of optical transitions between subbands [139], and it is important that these do not coincide in energy with any optic phonon intersubband transition, otherwise the latter will dominate and kill the laser action [140]. This is discussed in more detail in Chapter 6. A number of hot electron devices have been proposed which depend specifically on the properties of the excited carrier distribution [141] such as resonant tunnelling transistors [142]. A recent review of many of these devices has been given by Mitin *et al.* [143].

The operation of most current devices at frequencies below 1 THz lies within the ETM region, relating to a relaxation time scale of longer than  $\sim 1$  ps, but the research frontier has now advanced to much shorter time scales. In recent years the use of femtosecond pulsed lasers has enabled earlier stages of the energy relaxation process to be investigated, from the initial coherent regime excited on a time scale of femtoseconds, through the non-coherent but still non-equilibrium state at the subpicosecond level, and finally to the thermalized carrier distribution. An interesting question is the extent to which a thermal distribution is established before emission of optic phonons occurs, since the standard model calculation of the bare optic phonon lifetime is 80 fs. However, in many circumstances this figure is greatly increased by the hot phonon effect. The reader is referred to reviews by Bron [40] and Ryan [41] for further details of this important area.

## References

1. Ridley, B.K. (1991). *Rep. Prog. Phys.*, **54**, 169.
2. Shah, J. (ed.) (1992). *Hot carriers in semiconductor nanostructures: physics and applications*, Academic Press, New York.
3. Balkan, N. (ed.) (1998). *Hot electrons in semiconductors: physics and devices*, Oxford University Press, Oxford.
4. Conwell E.M. (1967). *High field transport in semiconductors*, Academic Press, New York.
5. Anderson, P.W., Abrahams, E., and Ramakrishnan, T.V. (1979). *Phys. Rev. Lett.*, **43**, 718.
6. Uren, M.J., Davies, R.A., and Pepper, M. (1980). *J. Phys. C: Solid State Phys.*, **13**, L985.
7. Balkan, N., Gupta, R., Ciechanowska, Z., Ridley, B.K., Peacock, D., Jones, G., Ritchie, D., and Frost, J. (1991). *Semicond. Sci. Technol.*, **6**, 175.
8. Payne, M.C., Davies, R.A., Inkson, J.C., and Pepper, M. (1983). *J. Phys. C: Solid State Phys.*, **16**, L291.
9. Shah, J., Pinczuk, A., Störmer, H.L., Gossard, A.C., and Wiegmann, W. (1983). *Appl. Phys. Lett.*, **42**, 55.
10. Hawker, P., Kent, A.J., Hughes, O.H., and Challis, L.J. (1992). *Semicond. Sci. Technol.*, **7**, B29.

11. Hirakawa, K. and Sakaki, H. (1986). *Appl. Phys. Lett.*, **49**, 889.
12. Manion, S.J., Artaki, M., Emanuel, M.A., Coleman, J.J., and Hess, K. (1987). *Phys. Rev.*, **B35**, 9203.
13. Leadley, D.R., Nicholas, R.J., Harris, J.J., and Foxon, C.T. (1989). *Semicond. Sci. Technol.*, **4**, 879.
14. Ando, T.J. (1974). *J. Phys. Soc. Jpn*, **37**, 1223.
15. Höpfel, R.A. and Weimann, G. (1985). *Appl. Phys. Lett.*, **46**, 291.
16. Akimov, A.V., Challis, L.J., and Mellor, C.J. (1991). *Physica*, **B169**, 563.
17. Hirakawa, K., Grayson, M., Tsui, D.C., and Kurdak, C. (1993). *Phys. Rev.*, **B47**, 16651.
18. Wigmore, J.K., Erol, M., Sahraoui-Tahar, M., Ari, M., Wilkinson, C.D.W., Davies, J.H., Holland, M., and Stanley, C.R. (1993). *Semicond. Sci. Technol.*, **8**, 322.
19. von Gutfeld, R.J. and Nethercot, A.H. (1964). *Phys. Rev. Lett.*, **12**, 641.
20. Ramsbey, M.T., Wolfe, J.P., and Tamura, S. (1988). *Z. Phys.*, **B73**, 167.
21. Wolfe, J.P. (1998). *Imaging phonons: acoustic wave propagation in solids*. Cambridge University Press, Cambridge.
22. Kent, A.J., Strickland, R.E., Strickland, K.R., and Henini, M. (1996). *Phys. Rev.*, **B54**, 2019.
23. Karl, H., Dietsche, W., Fischer, A., and Ploog, K. (1988). *Phys. Rev. Lett.*, **61**, 2360.
24. Edwards, S.C., bin Rani, H., and Wigmore, J.K. (1989). *J. Phys. E: Sci. Instrum.*, **22**, 582.
25. Ishiguro, T. and Morita, S. (1974). *Appl. Phys. Lett.*, **25**, 533.
26. Eisenmenger, W. (1976). In *Physical acoustics 12* (ed. W.P. Mason and R.N. Thurston), Academic Press, New York.
27. Cavill, S.A., Akimov, A.V., Ouali, F.F., Challis, L.J., Kent, A.J., and Henini, M. (1999). *Physica*, **B263-264**, 537.
28. Hurley, D.C., Hardy, G.A., Hawker, P., and Kent, A.J. (1989). *J. Phys. E: Sci. Instrum.*, **22**, 824.
29. Kent, A.J., Strickland, K.R., and Strickland, R.E. (1995). *Meas. Sci. Technol.*, **6**, 1679.
30. Schreyer, H., Dietsche, W., and Kinder, H. (1984). In *Proc. 17th Int. Conf. on low temperature physics* (ed. U. Eckern, A. Schmid, W. Weber, and H. Wuhl), p. 665. North-Holland, Amsterdam.
31. Balkan, N., Ridley, B.K., Emeny, M., and Goodridge, I. (1989). *Semicond. Sci. Technol.*, **4**, 852.
32. Shah, J., Pinczuk, A., Gossard, A.C., and Wiegmann, G. (1985). *Phys. Rev. Lett.*, **54**, 2045.
33. Yang, C.H., Carlson-Swindle, J.M., Lyon, S.A., and Worlock, J.M. (1985). *Phys. Rev. Lett.*, **55**, 2359.
34. Balkan, N., Gupta, R., Daniels, M.E., Ridley, B.K., and Emeny, M. (1990). *Semicond. Sci. Technol.*, **5**, 986.
35. Ryan, J.F., Taylor, R.A., Turberfield, A.J., Maciel, A., Worlock, J.M., Gossard, A.C., and Wiegmann, W. (1984). *Phys. Rev. Lett.*, **53**, 1841.
36. Kash, K. and Shah J. (1984). *Appl. Phys. Lett.*, **45**, 401.
37. Shank, C.V., Fork, R.L., Yen, R., Shah, J., Greene, B.I., Gossard, A.C., and Weisbuch, C. (1983). *Solid State Commun.*, **47**, 981.
38. Kash, J.A. and Tsang, J.C. (1988). *Solid State Electron.*, **31**, 419.
39. Shah, J. (1996). *Ultrafast spectroscopy of semiconductors and semiconductor-nanostructures*, Springer-Verlag, Berlin.
40. Bron, W.E. (ed.) (1993). *Ultrashort processes in solids*, Plenum, New York.
41. Ryan, J.F. (1998). In *Hot electrons in semiconductors: physics and devices* (ed. N. Balkan), p. 183, Oxford University Press, Oxford.
42. Shinba, Y. and Nakamura, K. (1981). *J. Phys. Soc. Jpn*, **50**, 114.
43. Shinba, Y., Nakamura, K., Fukuchi, M., and Sakata, M. (1982). *J. Phys. Soc. Jpn*, **51**, 157.
44. Ridley, B.K. (1982). *J. Phys. C: Solid State Phys.*, **15**, 5899.
45. Price, P.J. (1982). *J. Appl. Phys.*, **53**, 6863.
46. Karpus, V. (1986). *Sov. Phys. Semicond.*, **20**(1), 6.

47. Rothenfusser, M., Köster, L., and Dietsche, W. (1986). *Phys. Rev.*, **B34**, 5518.
48. Vass, E. (1987). *Solid State Commun.*, **61**, 127.
49. Challis, L.J., Toombs, G.A., and Sheard, F.W. (1987). In *Physics of phonons* (ed. T. Paszkiewicz), p. 348, Springer-Verlag, Berlin.
50. Ando, T., Fowler, A.B., and Stern, F. (1982). *Rev. Mod. Phys.*, **54**, 437.
51. Stern, F. and Howard, W.E. (1967). *Phys. Rev.*, **163**, 816.
52. Landau, L.D. and Lifshitz, E.M. (1977). *Quantum mechanics* (3rd edn), Pergamon, Oxford.
53. Herring, C. and Vogt, E. (1956). *Phys. Rev.*, **101**, 944.
54. Mahan, G.D. (1972). In *Polarons in ionic crystals and polar semiconductors* (ed. J.T. Devreese), p. 553, North-Holland, Amsterdam.
55. Mahan, G.D. (1990). *Many particle physics* (2nd edn), Plenum, New York.
56. Ehrenreich, H. and Cohen, M.H. (1959). *Phys. Rev.*, **115**, 786.
57. Lehmann, D., Jasiukiewicz, Cz., and Kent, A.J. (1998). *Physica*, **B249–251**, 718.
58. Cross, A.J. (2001). Ph.D. thesis, University of Nottingham.
59. Ridley, B.K. (1999). *Quantum processes in semiconductors*, Clarendon Press, Oxford.
60. Altshuler, B.L. and Aronov, A.G. (1985). In *Electron–electron interaction in disordered systems* (ed. A.L. Efros and M. Polak), p. 1, North-Holland, Amsterdam.
61. Chow, E., Wei, H.P., Girvin, S.M., and Shayegan, M. (1996). *Phys. Rev. Lett.*, **77**, 1143.
62. Khveshchenko, D.V. and Reizer, M. (1999). *Phys. Rev.*, **B56**, 15822.
63. Chow, E., Wei, H.P., Girvin, S.M., Jan, W., and Cunningham, J.E. (1997). *Phys. Rev.*, **B56**, R1676.
64. Fletcher, R., Feng, Y., Foxon, C.T., and Harris, J.J. (2000). *Phys. Rev.*, **B61**, 2028.
65. Lee, S.C., Galbraith, I., and Pidgeon, C.R. (1995). *Phys. Rev.*, **B52**, 1874.
66. Luryi, S. (1998). In *Hot electrons in semiconductors: physics and devices* (ed. N. Balkan), p. 385, Oxford University Press, Oxford.
67. Ferry, D.K. (1978). *Surface Sci.*, **75**, 86.
68. Riddoch, F.A. and Ridley, B.K. (1983). *J. Phys. C: Solid State Phys.*, **16**, 6971.
69. Price, P.J. (1984). *Phys. Rev.*, **B30**, 2236.
70. Ridley, B.K. (1992). In *Hot carriers in semiconductor nanostructures: physics and applications* (ed. J. Shah), p. 17, Academic Press, New York.
71. Das Sarma, S. and Mason, B.A. (1985). *Ann. Phys. (NY)*, **163**, 78.
72. von der Linde, D., Kuhl, J., and Klingenberg, H. (1980). *Phys. Rev. Lett.*, **44**, 1505.
73. Kash, K., Shah, J., Block, D., Gossard, A.C., and Wiegmann, W. (1985). *Physica*, **B134**, 189.
74. Vallee, F. and Bogani, F. (1991). *Phys. Rev.*, **B43**, 12049.
75. Vallee, F. (1994). *Phys. Rev.*, **B49**, 2460.
76. Tatham, M.C., Ryan, J.F., and Foxon, C.T. (1989). *Phys. Rev. Lett.*, **63**, 1637.
77. De Paula, A.M., Maciel, A.C., Weber, G., Ryan, J.F., Dawson, P., and Foxon, C.T. (1992). *Semicond. Sci. Technol.*, **7**, B120.
78. Ridley, B.K. (1989). *Semicond. Sci. Technol.*, **4**, 1142.
79. Kogan, S.M. (1963). *Sov. Phys.–Solid State*, **4**, 1813.
80. Das Sarma, S., Jain, J.K., and Jalabert, R. (1988). *Phys. Rev.*, **B37**, 1228.
81. Das Sarma, S. (1992). In *Hot carriers in semiconductor nanostructures: physics and applications* (ed. J. Shah), p. 53, Academic Press, New York.
82. Cai, W., Marchetti, M.C., and Lax, M. (1986). *Phys. Rev.*, **B34**, 8573.
83. Potz, W. and Kocevar, P. (1992). In *Hot carriers in semiconductor nanostructures: physics and applications* (ed. J. Shah), p. 87, Academic Press, New York.
84. Goodnick, S.M. and Lugli, P. (1992). In *Hot carriers in semiconductor nanostructures: physics and applications* (ed. J. Shah), p. 191, Academic Press, New York.
85. Kozorezov, A.G., Wigmore, J.K., and Giltrow, M. (1997). *J. Phys. Condens. Matter*, **9**, 4863.

86. Al Jawhari, H.A., Kozorezov, A.G., Sahraoui-Tahar, M., Wigmore, J.K., and Wilkinson, C.D.W. (1999). *Physica*, **B263–264**, 211.
87. Wigmore, J.K., Al Jawhari, H.A., Kozorezov, A.G., and Sahraoui-Tahar, M. (2001). *Proc. 25th Int. Conf. on the physics of semiconductors* (ed. N. Miura and T. Ando), p. 881. Springer-Verlag, Heidelberg.
88. Theis, T.N. (1980). *Surface Sci.*, **98**, 515.
89. Chaplik, A.V. and Krashennnikov, M.V. (1980). *Surf. Sci.*, **98**, 533.
90. Das Sarma, S. and Madhukar, A. (1981). *Phys. Rev.*, **B23**, 805.
91. Das Sarma, S. and Madhukar, A. (1988). *Solid State Electron.*, **31**, 695.
92. Wu Xiaoguang, Peeters, F.M., and de Vreese, J.T. (1988). *Phys. Rev.*, **B32**, 6982.
93. Das Sarma, S., Jain, J.K., and Jalabert, R. (1990). *Phys. Rev.*, **B41**, 3561.
94. Das Sarma, S., Jain, J.K., and Jalabert, R. (1988). *Phys. Rev.*, **B37**, 4560.
95. Das Sarma, S., Jain, J.K., and Jalabert, R. (1988). *Phys. Rev.*, **B37**, 6290.
96. Al Jawhari, H.A. (1999). Ph.D. thesis, Lancaster University
97. Mori, N. and Ando, T. (1989). *Phys. Rev.*, **B40**, 6175.
98. Rucker, H., Molinari, E., and Lugli, P. (1992). *Phys. Rev.*, **B45**, 6747.
99. Fasol, G., Tanaka, M., Sakaki, H., and Horikoshi, Y. (1988). *Phys. Rev.*, **B38**, 6056.
100. Das Sarma, S., Campos, V., Stroschio, M.A., and Kim, K.W. (1992). *Semicond. Sci. Technol.*, **B7**, 60.
101. Ridley, B.K. (1997). *Electrons and phonons in semiconductor multilayers*, Cambridge University Press, Cambridge.
102. Leburton, J.P., Pascual, J., and Sotomayor-Torres, C. (eds) (1993). *Phonons in nanostructures*, Plenum, New York.
103. Chin, M.A., Narayanamurti, V., Stormer, H.L., and Hwang, J.C.M. (1984). In *Phonon scattering in condensed matter* (ed. W. Eisenmenger, K. Laßmann, and S. Döttinger), p. 328, Springer-Verlag, Berlin.
104. Greenstein, M., Tamor, M.A., and Wolfe, J.P. (1982). *Phys. Rev.*, **B26**, 5604.
105. Hawker, P., Kent, A.J., Henini, M., and Hughes, O.H. (1989). *Solid State Electron.*, **32**, 1755.
106. Hawker, P., Kent, A.J., Challis, L.J., Henini, M., and Hughes, O.H. (1989). *J. Phys. Condens. Matter*, **1**, 1153.
107. Wigmore, J.K., Erol, M., Sahraoui-Tahar, M., Wilkinson, C.D.W., Davies, J.H., and Stanley, C. (1991). *Semicond. Sci. Technol.*, **6**, 837.
108. Danilchenko, B., Kilmashov, A., Roshko, S., Asche, M., Hey, R., and Kostial, H. (1994). *J. Phys. Condens. Matter*, **6**, 7955.
109. Dietsche, W. (1986). In *Phonon scattering in condensed matter V* (ed. A.C. Anderson and J.P. Wolfe), p. 366, Springer-Verlag, Berlin.
110. Challis, L.J., Kent, A.J., and Rampton, V.W. (1990). *Semicond. Sci. Technol.*, **5**, 1179.
111. Kent, A.J. (1991). *Physica*, **B169**, 356.
112. Jasiukiewicz, Cz. and Karpus, V. (1996). *Semicond. Sci. Technol.*, **11**, 1777.
113. Takada, Y. and Uemura, Y. (1977). *J. Phys. Soc. Jpn.* **43**, 139.
114. Lehmann, D. and Jasiukiewicz, Cz. (2002). *Proc 10th Int. Conf. on phonon scattering in condensed matter, Physica*, **B316–317**, 226.
115. Lehmann, D., Kent, A.J., Jasiukiewicz, Cz., Cross, A.J., Hawker, P., and Henini, M. (2002). *Phys. Rev.*, **B65**, 085320.
116. Hawker, P., Kent, A.J., Hauser, N., and Jagadish, C. (1995). *Semicond. Sci. Technol.*, **10**, 601.
117. Kent, A.J., Cross, A.J., Hawker, P., and Henini, M. (1997). *Phys. Status Solidi (b)*, **204**, 230.
118. Cross, A.J., Kent, A.J., Hawker, P., Lehmann, D., Jasiukiewicz, Cz., and Henini, M. (1999). *Physica*, **B263–264**, 526.
119. Pentland, I.A. (2000). Ph.D. thesis, University of Nottingham.
120. Ferreira, R. and Bastard, G. (1989). *Phys. Rev.*, **B40**, 1074.

121. Brockelmann, U. and Bastard, G. (1990). *Phys. Rev.*, **B42**, 8947.
122. Hewett, N.P., Russell, P.A., Challis, L.J., Ouali, F.F., Rampton, V.W., Kent, A.J., and Every, A.G. (1989). *Semicond. Sci. Technol.*, **4**, 955.
123. Hawker, P., Kent, A.J., Hauser, N., and Jagadish, C. (1995). *Semicond. Sci. Technol.*, **10**, 601.
124. West, L.C. and Roberts, C.W. (1994). In *Quantum well intersubband transition physics and devices* (ed. H.C. Liu, B.F. Levine, and J.Y. Andersson), p. 501, Kluwer Academic, Dordrecht.
125. Levenson, J.A., Dolique, G., Oudar, J.L., and Abram, I. (1989). *Solid State Electron.*, **32**, 1869.
126. Grahn, H.T., Schneider, H., Rühle, W.W., von Klitzing, K., and Ploog, K. (1990). *Phys. Rev. Lett.*, **64**, 2426.
127. Hunsche, S., Leo, K., Kurz, H., and Köhler, K. (1994). *Phys. Rev.*, **B50**, 5791.
128. Murdin, B.N., Heiss, W., Langerak, C.J.G.M., Lee, S.-C., Galbraith, I., Strasser, G., Gornik, E., Helm, M., and Pidgeon, C.R. (1997). *Phys. Rev.*, **B55**, 5171.
129. Yang, C.H. and Wilson, R.A. (1994). *Semicond. Sci. Technol.*, **9**, 740.
130. Chin, M.A., Narayanamurti, V., Stormer, H.L., and Gossard, A.C. (1985). *Proc. 17th Int. Conf. on the physics of semiconductors* (ed. J. Cahdi and W.A. Harrison), p. 333, Springer-Verlag, Berlin.
131. Strickland, K.R., George, R.E., Henini, M., and Kent, A.J. (1994). *Semicond. Sci. Technol.*, **9**, 786.
132. Kent, A.J., Strickland, R.E., Strickland, K.R., Cross, A.J., Hawker, P., and Henini, M. (1997). *Semicond. Sci. Technol.*, **12**, 849.
133. Monemar, B. (1999). *J. Mater. Sci. Electron. Mater.*, **10**, 227.
134. Lee, K.J., Harris, J.J., Kent, A.J., Wang, T., Sakaki, S., Maude, D.K., and Portal, J.-C. (2001). *Appl. Phys. Lett.*, **78**, 2893.
135. Stanton, N.M., Kent, A.J., Cavill, S.A., Akimov, A.V., Lee, K.J., Harris, J.J., Wang, T., and Sakai, S. (2001). *Phys. Status Solidi (b)*, **228**, 607.
136. Ouali, F.F., Francis, H.R., and Rhodes, H.C. (1999). *Physica*, **B263–264**, 239.
137. Morkoc, H., Unlu, H., and Ji, G. (1991). *Principles and technology of MODFETs*, Wiley, New York.
138. Holonyak, N., Kolbas, R.M., Dupuis, R.D., and Dapkus, P.D. (1980). *IEEE J. Quantum Electron.*, **QE-16**, 170.
139. Capasso, F., Gmachl, C., Sivco, D.L., and Cho, A.Y. (2002). *Phys. Today*, **55**, 34.
140. Lee, S.-C., Galbraith, I., and Pidgeon, C.R. (1995). *Phys. Rev.*, **B52**, 1874.
141. Luryi, S. (1990). In *High speed semiconductor devices* (ed. S.M. Sze), p. 399, Wiley, New York.
142. Yokoyama, N., Ohnishi, H., Mori, T., Takatsu, M., Muto, S., Imamura, K., and Shibatomi, A. (1992). In *Hot carriers in semiconductor nanostructures* (ed. J. Shah), p. 443, Academic Press, San Diego.
143. Mitin, V., Kochelap, V.A., and Stroschio, M.A. (1999). *Quantum heterostructures, microelectronics and optoelectronics*, Cambridge University Press, Cambridge.

# 3 Phonon interactions with magnetically quantized two-dimensional carrier systems: the integer and fractional quantum Hall states

C.J. Mellor, W. Dietsche, and L.J. Challis

---

## 3.1 Introduction

The most spectacular phenomenon in two-dimensional (2D) carrier systems is undoubtedly the quantum Hall effect (QHE) [1, 2]. It is observed at low temperatures in both 2D electron and 2D hole gases (2DEGs and 2DHGs, respectively) of sufficiently high mobility and, since the effect is essentially the same for both, the discussion here uses the term 2DEG to include both cases unless otherwise implied. The origin of the integer quantum Hall effect (IQHE) is the quantization of the electron energies into Landau levels which in real systems are broadened by scattering as shown in Fig. 3.1. Because of the disorder in the system, the states in the tails of the Landau levels become localized while those in the centre of the levels remain extended. The IQHE occurs when an integer number of these levels is filled by electrons so that the Fermi level lies in localized states between them. The condition for this to happen is that there should be an integer number of (spinless) electrons for each flux quantum ( $e/h$ ) passing through the 2DEG. The level filling can be varied by changing either the electron density or the

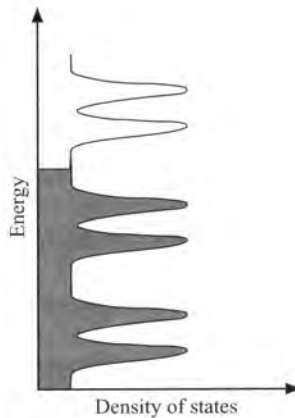


**Fig. 3.1** The energy (Landau) levels of a magnetically quantized 2DEG at low temperatures for a filling factor  $\nu = 4$ . The levels are filled up to the Fermi level and broadened by impurity scattering and disorder. The magnetic field is large enough for the spin sublevels to be resolved. The states between the Landau levels are localized.

external magnetic field. Spin doubles the number of electrons that can occupy a Landau level and, at high enough fields, each Landau level splits into two spin sublevels. The number of filled sublevels is called the filling factor,  $\nu$ . So  $\nu = 2$  describes the situation in which both sublevels of the lowest Landau level are occupied.

The fractional quantum Hall effect (FQHE) is observed at certain rational fractional values of the filling factor. It is also related to the existence of gaps in the electron energy spectrum but this is now the result of electron–electron interactions [3]. The many similarities between the integer and fractional case led to the development of the composite fermion model which offers a unified description of the two effects [4, 5]. The term 2DEG will also be used for these systems in which the electron–electron interactions are important and where the term 2D electron gas might more properly be called 2D electron liquid.

The characteristic properties of both IQHE and FQHE states are that the longitudinal resistance  $R_{xx}$  becomes vanishingly small at low temperatures and, simultaneously, a plateau occurs in the Hall resistance of value  $R_H = h/\nu e^2$ , with  $\nu$  being either integer or fractional, Fig. 3.2. Particularly remarkable is the high precision of this quantization which can approach  $10^{-9}$  in the integer case. The quantization is independent of any of the parameters of the material so that, for example, the measured values of  $R_H$  for an Si-MOSFET device agreed with those for a GaAs device to within less than 1 part in  $10^9$  [7]. This independence from material parameters points to a universal explanation

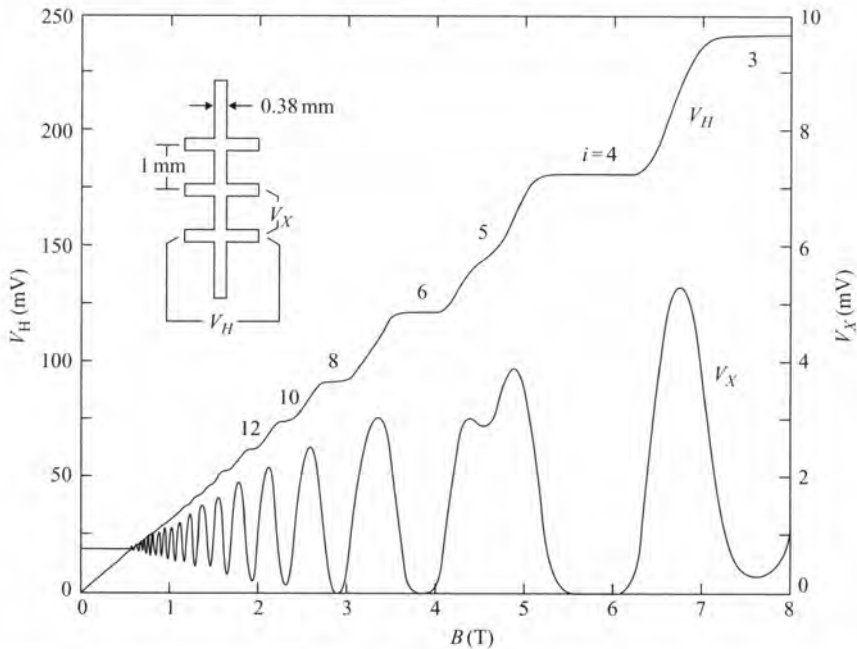


**Fig. 3.2** Magnetotransport in a 2DEG. The IQHE is shown in the transverse resistivity as plateaus in the Hall voltage whilst at the same magnetic fields the longitudinal resistance falls to zero. The features at odd-integer filling factors are noticeably weaker than at even-integer filling factors; this is due to spin splitting of the Landau levels [6].

for the effects. The necessary conditions are the existence of localized states, a high mobility sample, and a temperature that is small compared with the energy gap between Landau levels (integer effect) or the gap due to electron–electron interaction (fractional effect). The QHE has been widely reviewed and there are also several very helpful books [1, 2, 8–10].

This chapter reviews the experimental and theoretical work that has been carried out to investigate the interaction of phonons with magnetically quantized electron systems and with the quantum Hall states. Experimental information has been obtained in a number of ways including transport, Raman, and FIR measurements, but particular attention here is given to the use of acoustic phonons as probes. The phonons include both incoherent ballistic phonons of frequencies 25 GHz and above and coherent surface acoustic waves (SAWs) of frequency less than 12 GHz. The advantages that phonons have are that they interact strongly with electrons and that their energies and momenta (wavelengths) are well matched to the significant parameters of the QHE states. The energies of phonons with frequencies between 25 and 1000 GHz lie between 0.2 and 4 meV, a range that includes both the typical energy gaps of several meV found in the IQHE and the smaller gaps of a few tenths of an meV found in the FQHE. Their wavelength range between 1 and 100 nm includes the characteristic length scale,  $l_B \sim 10$  nm, in both the IQHE and FQHE states, where  $l_B$  is the magnetic length.

Considerable attention has been given in these investigations to the phonon-induced transitions between Landau levels illustrated in Fig. 3.3, the so-called phonon or acoustic cyclotron resonance process. Indeed this chapter reviews not only the work that has been done in the quantum Hall regimes but also work outside these regimes and at currents  $I > I_c$ , the critical current at which breakdown occurs. Phonon-induced transitions involving a change in spin are formally forbidden so the assumption normally made is to consider only those between sublevels with the same spin. Phonon absorption corresponds to the creation of a single particle excitation but studies have also been made of many-particle (plasmon) excitations in the carrier systems. The most prominent example involves the magnetoplasmon excitations in the FQHE regime, in particular

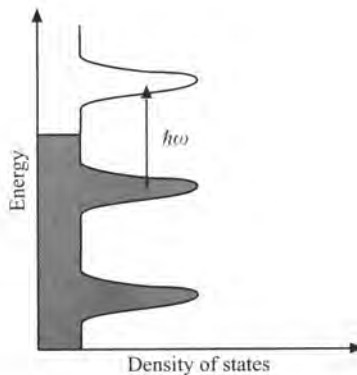
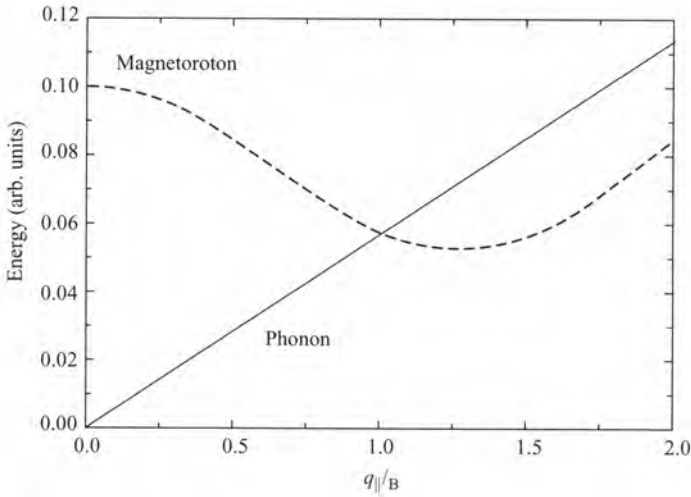
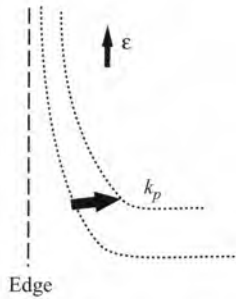


Fig. 3.3 Phonon absorption from inter-Landau level transitions (spin splitting has been omitted).



**Fig. 3.4** The dispersion curves of magnetoplasmon excitations in the FQHE regime and of phonons,  $\varepsilon(q_{||})$ .



**Fig. 3.5** The edgestates of a magnetically quantized 2DEG showing phonon absorption from inter-Landau level transitions (spin splitting has been omitted).

the roton minimum, Fig. 3.4. Studies have also been made of the phonon-induced inter-Landau level excitations requiring low energy but relatively large momentum transfer that are possible at the edges of the samples, Fig. 3.5. At large currents the QHE breaks down and the nearly dissipationless current transport vanishes. The breakdown is evidently related to the onset of phonon emission processes and phonon experiments have helped to elucidate where these processes take place and what type of phonons are being emitted. At small currents the QHE samples are not dissipationless over the full 2DEG area and strong dissipation occurs at 'hot spots' located at the current entry and exit points (Fig. 3.6).

The ballistic phonon work includes studies of both phonon emission and absorption processes and the most widely used arrangements are depicted in Fig. 3.7. The experimental techniques are described in more detail in the next section and Section 3.3 gives an overview of the theoretical work on phonon interaction with magnetically quantized

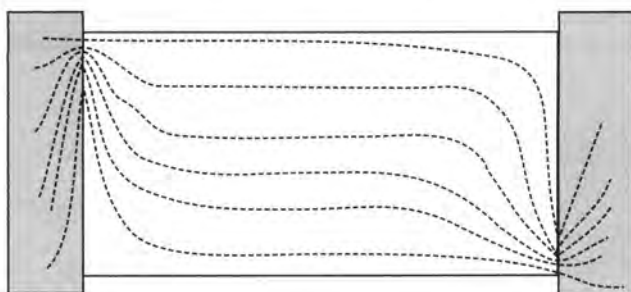


**Fig. 3.6** The current flow through a magnetically quantized 2DEG. The flow lines converge near the corners, hot spots.

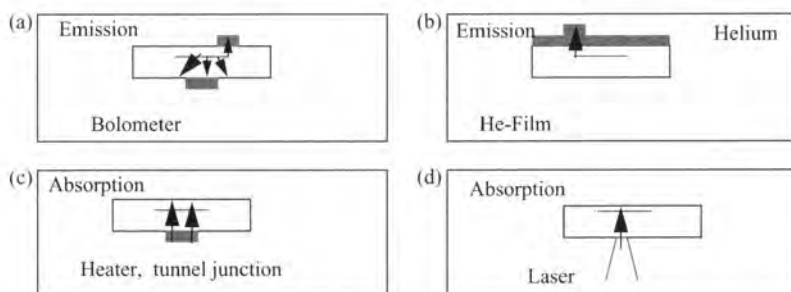


**Fig. 3.7** Examples of experimental arrangements for measuring phonon emission and absorption. Emission is normally measured (a) using a bolometer on the far side of the substrate, but has also been imaged for example by (b) using a helium film and laser-scanned CdS detectors have also been used. Absorption is normally measured (c) using phonons from electrically heated metal films and junctions have also been used. Absorption imaging has been achieved with phonons generated (d) by heating an extended metal film with a laser beam.

2DEGs and on the breakdown of the IQHE. Sections 3.4 and 3.5 review phonon emission and phonon absorption experiments on magnetically quantized 2DEGs and the IQHE. Section 3.6 gives a brief introduction to the FQHE and Section 3.7 describes theoretical and experimental work on the electron-phonon interaction with the FQH states. Section 3.8 reviews the large body of work that has been done using SAWs to study the IQHE and the FQHE states as well as the insulating phase that is observed in high magnetic fields.

## 3.2 Ballistic phonon techniques

The techniques used to study phonon emission and absorption of 2DEGs in the QHE states are broadly similar to those used in zero field and discussed in Chapter 2. The study of phonon emission requires a detector which can be placed either directly onto the face of the substrate immediately above the 2DEG or onto the opposite face. However, since for these experiments the detector needs to operate in high magnetic fields, alternatives

have to be found for the superconducting bolometers normally used in zero field. Carbon and CdS film bolometers have both been found to be effective. They absorb phonons over a wide spectral range and have fast response times ( $<10$  ns) and relatively weak magnetoresistance. Superfluid He films covering the surface of the device have been used to image hot spots and carbon resistors mounted outside the main magnetic field and attached to contacts on the sample have been used to monitor phonon emission. Phonon-induced changes in the photoconductivity of the substrate have provided spectroscopic information on the phonon emission from 2DEGs in Si-MOSFETS.

Phonon absorption has been studied by irradiating the 2DEG sample with heat pulses from metallic film heaters on the far side of the sample. In most experiments the films were heated by current pulses but a movable laser spot has also been used to heat a small area of an extended metal film to obtain spatial resolution. Spectral information on the absorption has been obtained by varying the heater temperature and hence the dominant frequency of the phonons and normal-metal tunnel junctions have also been used as tuneable phonon sources. The 2DEG absorption was measured either directly from the transient change in its resistance produced by the rise in electron temperature (since the resistance can depend non-linearly on the temperature rise, care has to be taken in making quantitative interpretations) or by measuring the transmitted signal using a bolometer on the upper face. If the phonons are incident obliquely, observations can also be made of the drag voltage caused by momentum transfer from the absorbed phonons to the electronic system.

As in zero field, most of the techniques depend on the fact that the substrates, usually GaAs or Si, are essentially transparent to phonons. This appears to be the case for phonon energies below about 4 meV in GaAs and 3 meV in Si (the exact values depend slightly on the thickness of the substrates) but scattering by isotopes and through anharmonicity becomes significant at higher energies. There is in fact evidence of scattering at lower energies attributable to the very small traces of Cr that are present even in nominally Cr-free GaAs substrates [11, 12]. However, this would not appear to be large enough to cause significant problems.

### 3.3 Theoretical investigations of phonon interaction with magnetically quantized 2DEGs

The emission of acoustic phonons, cyclotron phonons, as a result of inter-Landau level transitions was first considered theoretically by Toombs *et al.* [13]. They calculated the phonon matrix elements between electron wavefunctions based on the Landau gauge and then used Fermi's golden rule to determine the transition probabilities. This first treatment gives a somewhat idealized picture since Landau level broadening is neglected but provides useful insight into the emission process. The transition matrix element turns out to be dependent on the phonon momentum in two very important ways. For significant interaction, the phonon wavenumber components perpendicular to the 2DEG plane must be smaller than the inverse width of the electron wave function,  $q_z < a_0^{-1}$ , where  $a_0$  is usually the Fang–Howard parameter, and the components within the plane must be smaller than the inverse magnetic length,  $q_{||} < l_B^{-1}$ . As the magnetic field falls,

this second condition moves smoothly over to the zero-field requirement  $q_{\parallel} < 2k_F$  where  $k_F$  is the Fermi wavenumber. Energy has of course also to be conserved. The physical origin of the  $q$ -dependences is that the sign of the phonon perturbation oscillates over the extent of the electron wave function so that cancellation occurs if either of the two components is too large. Analytically, the dependences are expressed as form factors:

$$|F(q_z, a_0)|^2 \propto \frac{1}{[1 + (a_0 q_z)^2]^3} \quad (3.1)$$

and

$$|I_{nm'}|^2 \propto q_{\parallel}^2 l_B^2 \exp(-q_{\parallel}^2 l_B^2 / 2) \quad (3.2)$$

where

$$l_B = \left( \frac{\hbar}{eB} \right)^{-1/2} = 26/B^{1/2} \text{ nm} \quad (3.3)$$

The wavenumber at the cyclotron frequency  $q_c = \omega_c/s$ , where  $s$  is the sound velocity, increases linearly with  $B$  so that  $q_c$  eventually becomes larger than both  $l_B^{-1}$  and  $a_0^{-1}$ . The effect of these constraints for a 2DEG in GaAs is illustrated in Fig. 3.8. We also consider a typical GaAs heterojunction for which  $a_0 \sim 5 \text{ nm}$  so that  $a_0^{-1} > l_B^{-1}$  for  $B < 25 \text{ T}$ . Below this field, the maximum emission frequency is determined by the condition  $q_c < a_0^{-1}$  and for transverse phonons this requires  $\omega_c/2\pi < 200 \text{ GHz}$  corresponding to  $B < 0.5 \text{ T}$ .  $|I_{nm'}|^2$  has a broad maximum at  $q_{\parallel} l_B \sim \sqrt{2}$  which at  $0.5 \text{ T}$  occurs at an incident angle of  $\sin^{-1}(a_0 l_B^{-1} \sqrt{2}) \sim 10$  degrees. The constraints set by momentum conservation are less restrictive in Si-MOSFETS largely because of the greater effective mass of the electrons ( $m^* = 0.19m_e$  compared with  $0.067m_e$  for electrons moving in the 001 plane of GaAs; for holes on the 311 face of GaAs,  $m^* = 0.38m_e$ ). The cyclotron frequency and the width of the electron wave function both vary inversely with effective mass with the result that  $\omega_c$  is about three times smaller in an Si-MOSFET than in a GaAs heterostructure and  $a_0 \sim 1 \text{ nm}$ . So in Si-MOSFETS, cyclotron phonon emission is possible up to frequencies  $\sim 1000 \text{ GHz}$ , corresponding to  $B \sim 7 \text{ T}$ . Toombs *et al.* showed that significant emission should also occur at  $2\omega_c$ . So while it would seem that

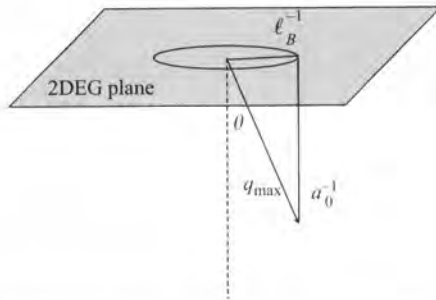


**Fig. 3.8** The effect of the momentum constraints,  $q_z < a_0^{-1}$  and  $q_{\parallel} < l_B^{-1}$  on the cyclotron phonon emission from a magnetically quantized 2DEG. The probability of emission falls strongly for phonon wavevectors that project beyond a cylinder of radius  $l_B^{-1}$  and length  $a_0^{-1}$ .

phonon-induced inter-Landau level transitions would be difficult to observe in 2DEGs in GaAs it should be possible to see them in Si-MOSFETS.

It is interesting to consider what other relaxation processes could occur from excited Landau levels in 2DEGs in GaAs when  $B > 0.5$  T. The severe cut-off set by momentum conservation could in principle be relaxed by uncertainty in the momentum resulting from phonon scattering and indeed impurity-assisted phonon transitions between edge states were considered by Maslov *et al.* [14]. However, the scattering would appear to be far too weak to have a significant effect in this case since, even at 1000 GHz, the phonon mean free paths are  $\sim 100$   $\mu\text{m}$  or so. Another possibility is that the relaxation occurs via two-phonon emission, each phonon of frequency  $\sim \omega_c/2$ , which would be allowed since momentum conservation could be satisfied if the phonons were emitted in approximately opposite directions. The probability of this process was calculated by Fal'ko and Challis [15] and they estimated that the two-phonon process becomes dominant at fields as low as 3 T. The process is still weak, however, for fields of this order and above, so even for relatively modest power inputs, it seems likely that the temperature would rise until optic phonon emission occurred. This would not be constrained significantly by momentum conservation at least for low  $q$  optic phonons. (For multilayer structures, emission of low  $q$  phonons at particular frequencies should also be possible because of zone folding.)

The effect of disorder and hence Landau level broadening on the phonon emission has been considered by several groups [16–20]. They all included disorder by assuming a broadened (usually Gaussian) density of states but the first three groups confined their analysis to intra-Landau level transitions while the last two papers also included inter-Landau level transitions. The analysis by Uchimura and Uemura [16] was used to determine energy loss from Si-MOSFETS while those of Iordanskii and Mutzykantskii [17] and Tamura and Kitagawa [18] were applied to GaAs heterostructures and stimulated by the low-temperature thermal conductivity experiments of Eisenstein *et al.* [21] in which the probability of diffuse scattering was increased by phonon absorption by magnetically quantized 2DEGs at the substrate surfaces. These last two groups both obtained good agreement with experiment although Tamura and Kitagawa found this was only the case if they allowed for the screening of the electron–phonon interaction while this was in fact omitted in the calculations of Uchimura and Uemura, Iordanskii and Mutzykantskii, and Benedict [19, 20]. However, unlike Tamura and Kitagawa, these latter groups all allowed for the effects of two-particle correlation. It would seem of interest for a detailed comparison to be made of the approaches used in these four treatments of phonon-induced intra-Landau level transitions. Benedict also looked at inter-Landau level transitions [19] and applied the analysis to phonon emission from Si-MOSFETS. The effect of including two-particle correlation on cyclotron phonon emission turned out to be rather small and the main differences between his results and those of Toombs *et al.* [13] were broadening effects arising from the Gaussian width of the density of states. He also calculated [20] how the relative contributions of intra- and inter-Landau level transitions varied with the Fermi energy and electron temperature. We note that a broadened density of states was also used by Kent *et al.* to model experimental images of the emission from Si-MOSFETS [22].

The situations considered so far in this discussion assume that the transverse electric fields are small. This is not necessarily the case when the current  $I$  is increased because

of the Hall field  $E_H = IR_H$  across the width of the device. This tilts the Landau levels in this direction and, if this is large enough, causes the energy of the  $n + 1$  level to become equal to that of the  $n$  level at a distance across the width of  $y = \hbar\omega_c/E_H e$ . Eaves and Sheard [23] noted that tunnelling could take place between these levels if there were wavefunction overlap between the two states. This requires  $y \lesssim l_B$ . To conserve momentum the transition would have to be phonon assisted (see Chapter 6) involving the emission of a phonon of wavenumber  $q \sim l_B^{-1}$  and so energy  $\hbar s l_B^{-1}$ . Since this is  $\ll \hbar\omega_c$  the process was referred to as quasielastic inter-Landau level scattering or QUILLS. Eaves and Sheard suggested that the QUILLS process could be responsible for the observed breakdown of the QHE above a critical current [24]. The critical Hall field predicted by the model of  $\sim \hbar\omega_c/e l_B$  was consistent with experimental values for narrow channels [25] but was considerably larger, by perhaps 20, than those found in wider devices [26]. This difference is attributed to inhomogeneity in the recent fluid dynamics model by Eaves [27]. There have been a number of other models for QHE breakdown including one based on local heating [28]. The heating would sustain the dissipation but the model leaves open the question of the microscopic processes leading to its initiation. Presumably in all these models, the dissipated energy will largely be in the form of phonons of energy  $\hbar\omega_c$  and  $\hbar\omega_c/2$ . It also seems plausible that the dissipation that occurs in the hot spots involves the same mechanism as that responsible for quantum Hall breakdown in the bulk of the 2DEG, but this has still to be established. It is of note that detailed theoretical predictions agree that the dissipation in the quantum Hall regime should be concentrated in the corners but they differ as to how it should be distributed between them [29–33].

The steep increase in potential near to the physical edges of the 2DEG that is responsible for confining the electrons causes the Landau levels to bend upwards and form quasi-1D channels [34]; considerable attention has been given to the role of these states in electron transport including the QHE [29]. The interaction of acoustic phonons with these states and its effect on electron relaxation has been considered theoretically by a number of groups and this earlier work is referred to in the papers cited here [14, 32, 35, 36]. The important difference from the bulk of the 2DEG (at least for small Hall fields), as can be seen in Fig. 3.5, is that it should now be possible for intra-Landau level transitions to occur without the need for disorder and for inter-Landau level transitions to be induced by relatively low-energy phonons. The situation has evident similarities to those considered in the QUILLS model and, as in that case, the phonons involved in the tunnelling process would have to have wavenumbers  $q \sim l_B^{-1}$  and hence energies  $\sim \hbar s l_B^{-1}$  which are  $\ll \hbar\omega_c$ . As an example of the treatments we consider that given by McKitterick *et al.* [36] which was stimulated by their experiments that will be discussed later. It focuses on the change in edge-state conductivity produced by a beam of non-equilibrium phonons, ‘phonoconductivity’. The analysis discusses the interesting differences in the phonoconductivity that should occur between a high-field regime,  $q \gg l_B^{-1}$ , in which inter-Landau level transitions are forbidden by momentum conservation so that only intra-Landau level transitions can take place, and a low-field regime  $q \ll l_B^{-1}$  in which both types of transition are allowed.

The change in the processes of energy relaxation that occur when magnetic fields are applied is reflected in the temperature dependence of the power loss from 2DEGs. The interaction between acoustic phonons and 2D carriers in zero field was described in

Chapter 2 and it was noted that in piezoelectric media such as GaAs, the power loss,  $P$ , varies as  $P \sim T^5$  at low temperatures. This temperature dependence is derived using arguments of momentum conservation between the carriers and the emitted phonons. A factor of  $T^3$  comes from the 3D space that is seen by the phonons and the static screening of the carrier–phonon matrix element. The other two factors of  $T$  originate from the mean energy per phonon and the number of electrons that are sufficiently thermally excited to emit a phonon. However, Chow *et al.* [37] found that in the presence of a strong magnetic field the emitted power varied as  $T^4$ . The phonon emission experiments were carried out between  $\nu = 1/3$  and  $2/5$ , two adjacent fractional quantum Hall plateaux, using an electron density of  $6.5 \times 10^{14} \text{ m}^{-2}$  at carrier temperatures between 0.1 and 1 K; the carrier temperatures were determined from  $(d\rho_{xy}/dB)^{\text{max}}$ , where  $\rho_{xy}$  is the Hall resistivity. The same temperature dependence was also seen between plateaux in the integer quantum Hall regime. The efficiency of the emission process was observed to increase with magnetic field. At a substrate temperature of 100 mK the threshold power at which heating of the carriers was observed was four times higher in the integer quantum Hall regime than in the low-field regime and increased by a remarkable factor of 80 between the low-field regime and the fractional quantum Hall regime. These remarkable observations clearly indicate that a new theory of phonon emission is required in strong magnetic fields. They are also very relevant to the practical issues relating to the cooling of 2DEGs at low temperatures.

The theory proposed by the authors is that the carriers in the strong magnetic field regime are in the hydrodynamic limit (dirty limit), that is to say that momentum conservation is lost because of the frequent collisions between the carriers with the intrinsic disorder potential of the substrate. In this limit the 2D carriers act as a black body (albeit with a emissivity less than one) in which the phonons are emitted with the usual  $T^4$  spectrum. For this approach to be valid we must assume that the carriers are in thermal equilibrium with each other at some well-defined temperature. In this hydrodynamic limit, the static screening approximation fails as it is not the static compressibility of the carrier gas that matters (as in Thomas–Fermi screening) but the limited ability of the carriers to redistribute charge quickly. Therefore as the conductivity decreases so the emitted phonon power at a given carrier temperature increases. Evaluating this theory more quantitatively for values of the longitudinal conductivity,  $\sigma_{xx} \sim e^2/h$ , which are typical at the critical point between Hall plateaux, they find that for a current,  $I$ , in the sample the electron temperature,  $T_e$ , is given by

$$T_e = 24.9(\sigma_{xx}\rho_{xx})^{1/4}I^{1/2} \text{ K}$$

which is only  $\sim 4$  per cent lower than the observed values.

As the measurements were made at critical points between quantum Hall plateaux, another possible explanation for the results is that the carrier–carrier correlation time diverges at such points. This explanation also results in a  $T^4$  temperature dependence and so the experiment cannot distinguish between these two explanations. However, the authors report that their sample did not exhibit scaling behaviour in the temperature dependence of the resistivity due to the high mobility of the sample that was used. This fact, along with the close quantitative agreement between the hydrodynamic theory and experiment, would seem to indicate that the hydrodynamic theory is the more reasonable explanation.

The transfer of momentum to the electronic system from phonons incident obliquely onto a 2DEG, phonon drag, has also been investigated theoretically [38–41]. The electrons are accelerated in the direction of the absorbed phonon momenta resulting in the creation of an electric field proportional to the rate of momentum transfer. Some of the experimental studies that will be reported later use imaging techniques to study the angular dependence of the drag voltage and, to allow detailed comparison with this work, the theoretical studies have all included the anisotropy of the electron–phonon interaction as well as phonon focusing effects.

### 3.4 Experimental studies of the phonon emission from magnetically quantized 2DEGs

The studies that have been made focus on two aspects: the location of the dissipation and the frequency spectrum of the phonon emission.

#### 3.4.1 Location of the emission

In zero magnetic field, current flows uniformly through a homogeneous 2DEG. This is no longer true in high magnetic fields ( $\omega_c\tau \gg 1$ ) which, in a typical GaAs heterostructure, requires  $B \gg 0.1$  T. In this case, the current enters and leaves the 2DEG through diagonally opposite corners of the device. Once inside the 2DEG, however, the flow is more or less parallel to the edges of the Hall bar and since the Hall angle,  $\theta_H \sim 90$  degrees, ( $\tan \theta_H$  equals the ratio of the Hall and longitudinal electric fields), the current flows along the equipotentials (Fig. 3.6). This is no longer the case near the corners since  $\theta_H \sim 0$  degree in the metal contacts. So the current crosses the equipotential lines leading to dissipation and hence QHE breakdown. Measurements of the potential distributions by electro-optic techniques have confirmed the existence of these high-field corner regions [42, 43]. In the QHE regime and when  $I < I_c$ , the dissipation is expected to be concentrated almost completely in hot spots at the corners where the current enters and exits [44].

The existence of these hot spots has been studied by phonon experiments on 2DEGs in Si [45, 46] and 2DEGs and 2DHGs in GaAs [47, 48] and using two different and complementary techniques. In one [45, 46, 48, 49] the phonon emission from a hot spot was monitored by the temperature rise on a metal film placed opposite to it and in another, the spatial distribution of the dissipation was imaged using superfluid liquid helium [47, 50]. In the first technique, the power dissipated in the device was held constant and the phonon emission was monitored as the 2DEG was moved in and out of the QHE regime. For Si this was done by sweeping the electron density at a fixed magnetic field, while for GaAs the magnetic field, was swept. In both cases the emission from the entry and exit corner showed quantum oscillations, Fig. 3.9, reaching a maximum each time the 2DEG was in the QHE state. (This became a minimum if the magnetic field were reversed causing the hot spots to move to the two other corners of the rectangular device.) The emission from the two hot spots could be compared by reversing the current direction. For Si, Fig. 3.9(a), it was found that the emission from the entry and exit corners was the same to within experimental error for filling factors between 4 and 32 and over the range

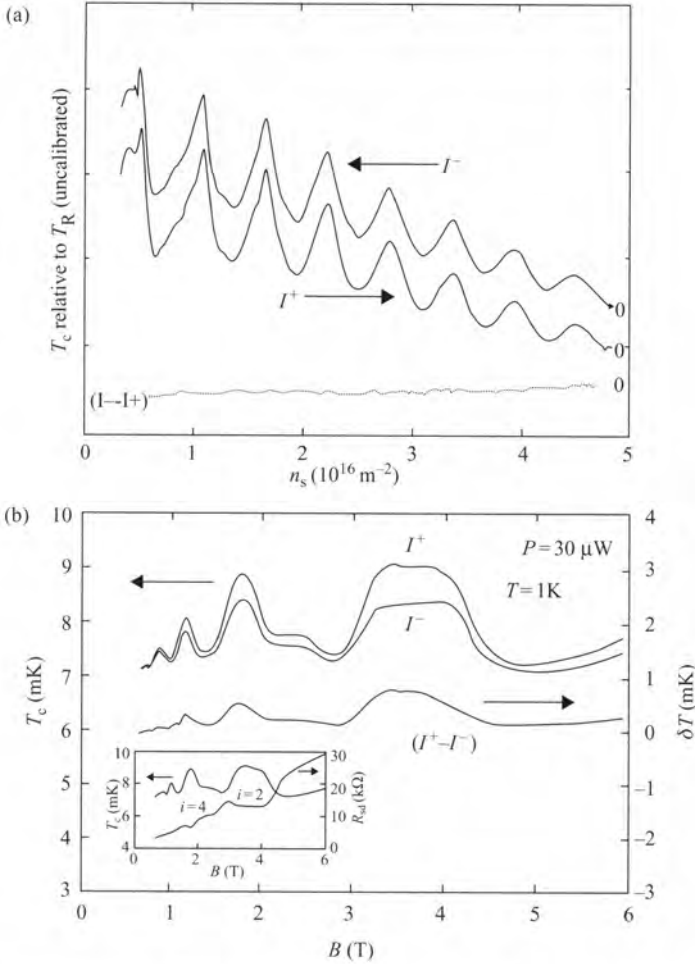


**Fig. 3.9** The change in the phonon emission from a hot spot with filling factor measured by the temperature of a metal film attached to the substrate opposite the hot spot. The changes and their difference are shown for both current directions: (a) data for an Si-MOSFET as a function of gate voltage,  $B = 6\text{ T}$  [46] and (b) for a GaAs heterostructure ( $n_s = 1.9 \times 10^{15} \text{ m}^{-2}$ ) as a function of magnetic field (the difference is shown in the inset in this case) [48].

of power measured from  $0.3$  to  $2000 \mu\text{W}$  corresponding to currents down to  $20 \mu\text{A}$  [46]. For  $\nu = 4$  and  $I = 0.8I_c$ , the error was  $\pm 2$  per cent. Images of the emission obtained using an extended CdS detector also indicated symmetrical emission but the experimental uncertainty was higher [51]. These results contrast with those obtained in four 2DEG devices in GaAs, Fig. 3.9(b). For these, the emission detected was appreciably greater from the electron entry ( $I^+$ ) corner than from the exit corner by amounts which varied from about 20 to 60 per cent depending on the device and the filling factor [48].

The imaging experiments [47] gives quantitative information on the size of the hot spots. The samples contained 2DEG regions of dimensions  $2.5 \times 3 \text{ mm}^2$  and were

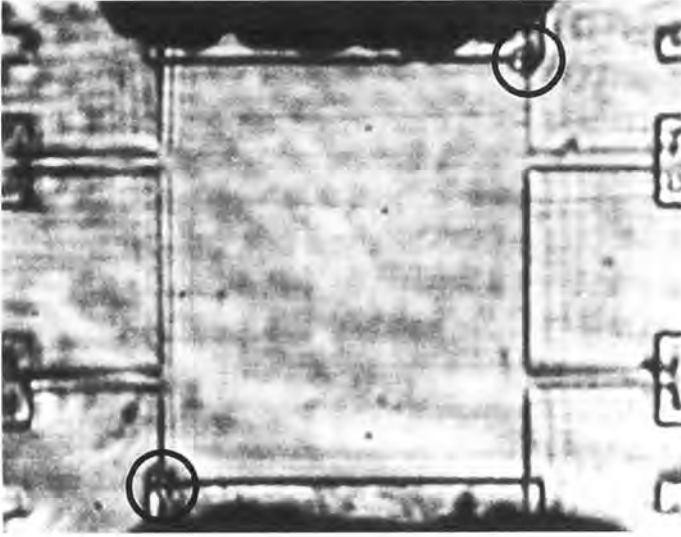


**Fig. 3.10** He film image of a 2DEG Hall bar. The helium drops at the two diagonally opposite corners show the location of the hot spots and their diameters provide upper limits to the hot spot sizes [47].

partially immersed in superfluid helium at  $T \sim 1$  K so that the surface above the 2DEG was coated with a helium film about 100 nm thick. A current  $I < I_c$  was passed through the device and the magnetic field adjusted until the 2DEG was in the integer quantum Hall state; in the GaAs sample, for  $\nu = 2$  this occurred at  $B \sim 8$  T. The dissipation raises the helium temperature above the hot spots increasing the local excitation concentration: the proportion of normal fluid. The viscosity of the normal fluid pins it to the substrate surface so, to correct the local imbalance, superfluid flows towards the hotter region resulting in an increase in the film thickness. (This process is often described in terms of the fountain pressure produced by a temperature difference [52].) The helium drops that formed were directly visible (Fig. 3.10). For a current of  $80 \mu\text{A}$ , the diameters of the two drops in opposite corners were about  $100 \mu\text{m}$  in GaAs. These are expected to be upper limits to the size of the hot spots and so demonstrate the strongly localized nature of the dissipation. Their size also provides an estimate of the electric fields in the hot spots if the plausible assumption is made that the voltage drop between the source and drain contacts,  $V_{SD}$  (the Hall voltage in the QHE state), takes place in a distance roughly equal to the total width of the two hot spots. In the present case this leads to a field of about  $10 \text{ kV m}^{-1}$  which is approximately the same as the field causing the onset of dissipation in the interior of a 2DEG in the QHE state [24, 26, 28]. It seems reasonable to conclude therefore that, in the hot spot region, the current path contracts until the breakdown condition is fulfilled locally and dissipation sets in. At small currents, the diameters of the two drops were nearly identical. If, however, the current exceeded a critical value,  $110 \mu\text{A}$  for the sample shown in Fig. 3.11, the drop at the electron exit point suddenly became much smaller and oscillated irregularly. This asymmetry between the helium

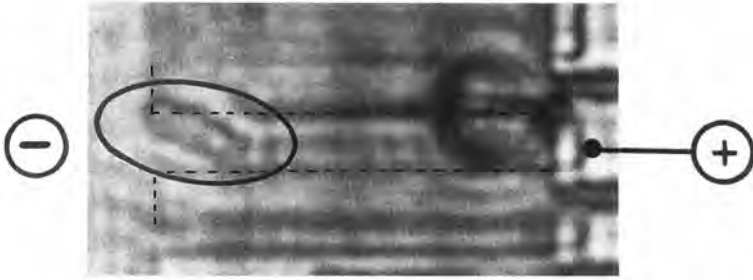


**Fig. 3.11** He film image of a 2DEG showing QHE breakdown within a 200  $\mu\text{m}$  wide strip connecting two large areas. The ellipse shows the helium drop that has formed above the region where breakdown has occurred [54].

drops points to differences in the details of the emission process at the two hot spots also indicated by the measurements of the phonon emission.

The differences between these results for GaAs heterostructures can be reconciled and used to provide information on the location of the dissipation. At the electron entry corner, the electrons would be partially scattered into a higher 2DEG Landau level during the injection from the metal contact. The relaxation back into the lower Landau level by phonon emission will be slow in GaAs, because of the constraints discussed in Section 3.3, and it seems likely therefore that it will take place over a somewhat extended area of 2DEG. Since, though, it will be largely from the 2DEG rather than from the metal contact, the phonons will be emitted predominantly normal to the surface. So in the measurements of the emission signal, most of the phonons will strike the metal film on the opposite face of the substrate. At the exit corner, however, the electrons are injected into a metallic contact where relaxation will be fast. The phonons will also be emitted in all directions since there is very little constraint imposed by momentum conservation and some will miss the metal film on the opposite side. So the smaller emission signal at the exit corner can be ascribed to differences in the angular distribution of the phonons and hence in the nature of the relaxation at the two corners. This model also implies that the dissipation is occurring over a larger area at the entry corner than at the exit corner. Also that, since the helium drops are of similar size below some critical current, the drop sizes are mainly determined by the magnitude of the dissipation rather than the size of the hot spot. This is evidently no longer the case once the dissipation exceeds this critical value. Presumably, the temperature rise of the substrate surface above the smaller exit hot spot becomes high enough for the flow velocity of the superfluid helium passing over it to exceed its critical velocity. The helium would then boil causing the drop size to shrink and become unstable. Estimates suggest that, for a current of 100  $\mu\text{A}$ , the critical diameter is  $\sim 100 \mu\text{m}$ , which is comparable with the value at which the asymmetry developed. The explanation appears to be confirmed by experiments using a focused laser beam which showed that film boiling could be induced if the intensity were high enough [53].

No asymmetry was observed for 2DEGs in Si-MOSFETs either in the drop size [50] or, as discussed earlier, in the detected phonon emission. As discussed in Section 3.3, one-phonon relaxation can readily occur in Si 2DEGs and the electron-phonon coupling

is also appreciably stronger. Therefore much of the electron relaxation seems likely to occur from the 2DEG leading to phonon emission in the normal direction at both corners. This might also have meant that the heated areas would be smaller than in GaAs but no boil-off phenomena were observed. This seems likely to be due to the presence of the metal gate electrode covering the 2DEG and contact regions which would lead to a wider temperature distribution of the surface above the 2DEG.

In both types of experiments, sizeable magneto-oscillations were observed at constant power input with magnetic field while the electric power is kept constant. These suggested that the fraction of dissipation moving from the corners to the interior when the Fermi energy moves from the Landau gap to the centre of a level was typically  $\sim 20$  per cent.

The He film technique was also used by Klass *et al.* [54] to image the breakdown in a GaAs 2DEG for  $B = 7.2$  T and  $\nu = 2$ . Current was passed between two large 2DEG areas through a  $200 \mu\text{m}$  wide strip where breakdown occurred. Evidence for a localized hot area is shown in Fig. 3.11 by the presence of the He drop running diagonally across the strip. The position of this elongated drop moved partially into the strip when the current direction was reversed. The existence of local dissipation that this demonstrates appears to suggest the presence of local electric fields much larger than those that would be present in a homogeneous device. This could help to explain the discrepancies between the critical electric fields predicted by the QUILLS process and those seen in all but narrow channels. No quantitative estimates have yet been made, however.

In summary, these experiments to investigate the location of the dissipation demonstrate that (a) the dissipation is strongly localized near the current entry and exit corners, (b) outside the QHE, a significant part ( $\sim 20$  per cent) of the power is dissipated in the bulk of the 2DEG, and (c) differences in measured values between the entry and exit corners on GaAs samples are unlikely to be due to differences in the amount of power dissipated. The asymmetries observed do, however, show that there are significant differences in the precise location and nature of the dissipation in the two corners. It is also clear that these asymmetries are strongly affected by the slow relaxation rates from excited Landau levels in GaAs since they do not occur in Si-MOSFETS where the relaxation is much faster. These difference in relaxation rates between GaAs and Si-based structures are also apparent in several of the spectroscopic experiments described below. The studies on quantum Hall breakdown suggest the electric fields inside 2DEGs are strongly inhomogeneous. This is in line with measurements using electro-optic techniques and supports suggestions that this is the reason why the critical fields for wide samples are appreciably smaller than those for narrow samples.

### 3.4.2 Frequency spectrum of the phonon emission

The spectrum of the phonons emitted from magnetically quantized 2DEGs is of particular interest because of the information it provides about the dissipative processes in QHE structures. Unfortunately, phonon techniques capable of providing spectral information are scarce but measurements have been made on Si-MOSFETS. The techniques used in the first experiments provided qualitative information only and were for  $I \gtrsim I_c$  [55,56] but the results were clearly consistent with cyclotron phonon emission even up to electron temperatures as high as 100 K. The measurements by Kent *et al.* [55] used the fact that

substrate scattering produces a high frequency cut-off in the transmission. They showed the expected decrease in transmitted signal with magnetic field that would be expected as the cyclotron frequency approached and exceeded the cut-off. Cooper *et al.* [56] observed oscillations of the phonon signal in the normal direction with increasing electron density and hence Fermi energy. These were attributable to the changes in the angular distribution of the phonon emission that would occur as the proportion of inter- and intra-Landau level transitions changed.

Much higher resolution was achieved using the phonon-induced conductivity of the p-type substrate as a detector. Under illumination, the boron dopant atoms are ionized to form  $B^+$  centres and Burger and Lassmann [57] demonstrated that phonons with energies  $\gtrsim 2$  meV release the bound hole causing the substrate conductivity to increase. Later measurements, using a normal-metal tunnel junction as a quasi-monochromatic phonon source, showed that the ionization energy increased with magnetic field as  $E(B) = 1.8 + 1/2\hbar\omega_{ch}$  meV where  $\omega_{ch}$  is the cyclotron frequency of heavy holes in Si [58]. The response of the substrate conductivity to the phonon emission from a 2DEG is shown as a function of magnetic field in Fig. 3.12 [59] for  $\theta = 0$  and 37 degrees ( $\theta$  is the angle of  $B$  to the 2DEG normal). The fields at which arrows marking the signal onsets occur correspond closely with those for which  $E(B) = \hbar\omega_c$  ( $\omega_c \propto B \sin \theta$ ) showing that a significant amount of the phonon emission is at the cyclotron frequency. At higher fields, the signal peaks whenever the 2DEG is in the IQHE regime (shown by the minima in  $R_{xx}$ ) and the emission is almost entirely from the hot spots ( $I < I_c$ ). So the emission at  $\hbar\omega_c$  falls as  $\nu$  moves away from the IQHE regime even though the total emission (dissipation) increases ( $I$  was kept constant) showing that an increasing proportion of the emission is taking place at frequencies less than  $\omega_c$ . This seems reasonable for the bulk of the 2DEG since the Fermi level is within a Landau level and intra-Landau level transitions can occur. However, the decrease in cyclotron phonon emission from the hot spots that this result also implies suggests that their electron temperature falls as the system moves away from the IQHE regime. This might be because the hot spots increase in size so the emission takes place over a larger area. These experiments showed no evidence of emission at  $\hbar\omega_c/2$ ; this would have been seen at  $B \sim 9.2$  T ( $\theta = 0$  degrees) if it had been strong enough. Unfortunately the detector sensitivity was not sufficient to determine whether dissipation still occurred in the 2DEG when  $V_{SD}$  fell below  $\hbar\omega_c/e$  (2 to 4 meV for the conditions used).

A similar spectroscopic technique does not seem possible for GaAs since no acceptor appears to exist with the appropriate properties and it is not known whether the emission from GaAs heterostructures occurs mainly at  $\omega_c$  or  $\omega_c/2$ . The observation of magnetophonon oscillations in the phonon emission does show, however, that optic phonon emission occurs at higher power inputs [60]. Cyclotron *photon* emission has been observed by a number of groups for a range of power inputs from 2DEGs [61–65] in GaAs heterostructures and it seems somewhat surprising perhaps that this should be so significant from 2DEGs given the very much larger volume of phase space for phonon emission. It is, though, consistent with the severe momentum constraints that inhibit phonon emission from 2DEGs in GaAs that have already been discussed. More recently, Kawano *et al.* [66] were able to investigate how the cyclotron photon emission varied along the 2DEG. They found that outside the QHE regime it occurred from both the bulk and the contacts when  $V_{SD} > \hbar\omega_c/2e$ . However, no cyclotron

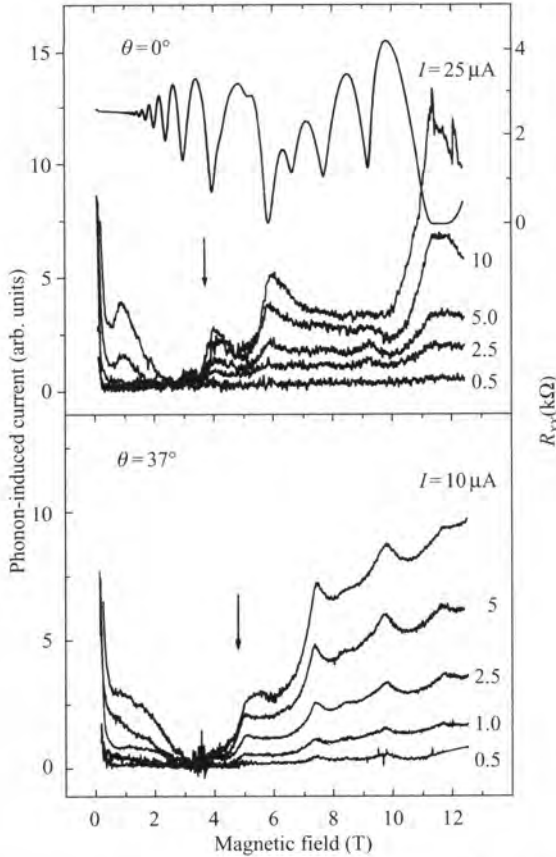


**Fig. 3.12** The change in conductivity of the Si substrate produced by the phonons emitted from an electrically heated 2DEG [59]. The phonon-induced changes are plotted as a function of magnetic field for  $\theta = 0$  and 37 degrees ( $\theta$  is the angle between the field and the normal to the 2DEG). The upper curve also shows  $R_{xx}$ .

emission occurred from the bulk at lower voltages. The implications of this interesting result for the nature of the dissipation mechanisms is fully discussed in their paper.

### 3.5 Experimental studies of phonon absorption by magnetically quantized 2DEGs

The work that has been carried out on phonon absorption in magnetically quantized 2DEGs deals with three issues: the location of the absorption, its frequency dependence, and the momentum transfer from obliquely incident phonons (phonon drag).

### 3.5.1 Location of the absorption

Since the potential distribution and current flow in magnetically quantized 2DEG samples are spatially inhomogeneous, it would be expected that this would be reflected in the spatial variation of the phonon absorption. This could for example arise from variations in the occupation of the Landau levels. In the IQHE regime, it is not known whether, in the hot spots, the Fermi energy lies in the gap and that the dissipation arises, say, as a result of the QUILLS mechanism or within a Landau level so that both intra- and inter-Landau transitions are taking place. However, in the bulk of the 2DEG, the Landau levels are essentially either filled or empty. So in this case, only inter-Landau level transitions are possible and in GaAs, as discussed earlier, these are predicted to couple very weakly to phonons of frequency  $\gtrsim 200$  GHz. This may not be the case at higher currents, though, if the Hall fields are large enough for low-energy QUILLS transitions to occur in the bulk. Absorption should also be very different at the edges of the 2DEG where low energy inter- and intra-Landau level transitions could take place.

A number of experiments to image the spatial variation of the absorption have been carried out by Kent *et al.* in Nottingham using a movable laser spot to generate heat pulses. In low-energy phonon ( $k_B T < \hbar\omega_c$ ) experiments on Si-MOSFETs [51] they found that absorption took place uniformly throughout the sample for non-integral filling factors,  $\nu$ . However, when  $\nu$  was an integer, absorption only occurred when the phonon source was directly opposite the current entry and exit corners. So this behaviour is as expected theoretically except that no edge-state absorption could be detected. This was not the case, however, for GaAs heterostructures. While phonon absorption in the hot spots was still very apparent at integer filling factors, absorption could now also be seen when the phonon source was scanned along the sample edges, Fig. 3.13 [36, 67]. Oscillations with magnetic field occurred in the absorption at the hot spots and edges as expected, Fig. 3.14, although, interestingly, the sign of the changes reversed at 1.3 T. At lower fields the oscillations were negative, the phonon scattering causing reductions in conductance, but they became positive at higher fields. The change in sign was attributed to a change in the dominance of the two classes of transitions predicted between the Landau levels: inter-Landau level transitions decrease the electron velocity while intra-Landau level transitions increase it. The fact that the edge-state transitions could be seen in GaAs, but not in Si-MOSFETs, could either be due to the softer potential of the gated Si-MOSFET devices or to the larger widths of the Landau levels in Si arising from the appreciably lower electron mobility.

### 3.5.2 Frequency dependence of the phonon absorption

The first experiments to provide spectroscopic information on phonon absorption by magnetically quantized 2DEGs were by Eisenstein *et al.* [21]. They measured the thermal conductivity between 0.1 and 1 K along a thin GaAs slab whose surfaces were coated with multilayers containing 2DEGs. The thermal conductivity was found to oscillate with magnetic field and this was attributed to an increase in diffuse scattering caused by phonon absorption. Since  $k_B T \ll \hbar\omega_c$ , the phonons all had energies much less than  $\hbar\omega_c$  so the absorption had to be by intra- rather than inter-Landau level transitions. This was consistent with the fact that the thermal resistance was greatest whenever the Fermi energy was inside a Landau level.

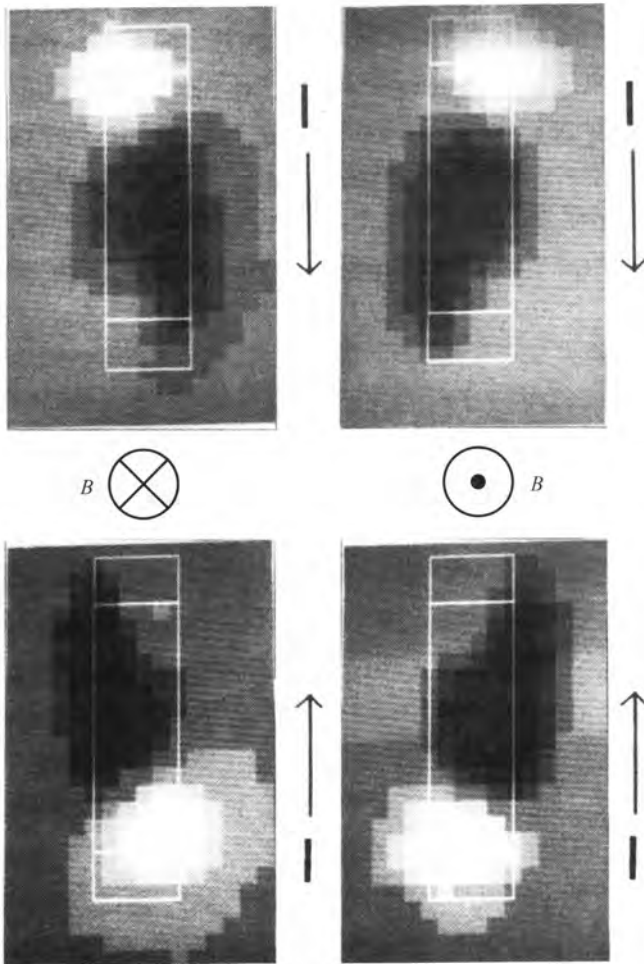


**Fig. 3.13** Phonoconductivity images of the two-terminal resistance of a Hall bar in the IQH state for the four possible permutations of magnetic field and current directions. The dark (light) areas correspond to an increase (decrease) in resistance [67].

The first absorption measurements to observe inter-Landau level or cyclotron phonon transitions were made in Si-MOSFETs by Kent *et al.* using an electrically heated film as a phonon source [68]. Measurements were made as a function of electron density and, for the lower dominant phonon frequencies (heater temperatures), absorption peaks were seen when the Fermi level was inside a Landau level. However, when the dominant phonon frequency was raised, additional peaks appeared between the first peaks when the Fermi level was midway between two Landau levels. This experiment demonstrated that in Si-MOSFETS it was possible to observe absorption from both intra-Landau and inter-Landau level transitions. Another important outcome from this work was that it also confirmed the validity of mismatch theory to obtain the heater temperatures and hence

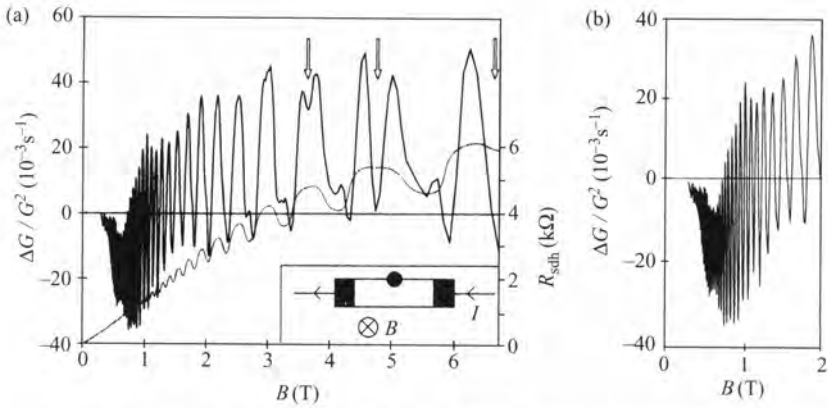


**Fig. 3.14** (a) Magnetic field dependence of the edge-state phonoconductivity of a 2DEG heterostructure [36]. Also shown (dotted line) for comparison are the two-terminal Shubnikov–de Haas oscillations. (b) close-up of the region below 2 T.

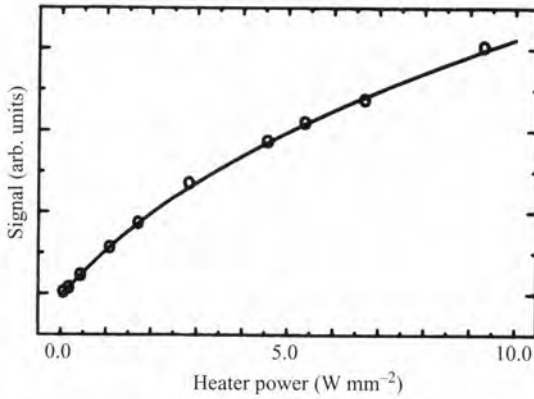


**Fig. 3.15** The signal produced by inter-Landau level absorption at 730 GHz as a function of the input power to the metal phonon source. The solid line normalized at one point is calculated assuming the phonons have a Planckian distribution at a heater temperature determined by acoustic mismatch theory [68].

the phonon spectrum from the input power. This is shown in Fig. 3.15 which plots the absorption signal at the intermediate peaks against heater power. The absorption is due to 730 GHz cyclotron phonons whose intensity is determined by the heater temperature through the Bose–Einstein function. The constant used to relate heater temperature to heater powers to obtain the solid curve in Fig. 3.15 agreed with that calculated from acoustic mismatch theory [69, 70] to within 7 per cent.

Experiments have also been carried out using normal-metal tunnel junction sources with narrower phonon spectra than those from a thermal source. The junctions consist of two metal films separated by an oxide layer and their emission spectrum has a high frequency cut-off proportional to the bias voltage. Quasi-monochromatic phonons can be

separated from the background emission by modulating the bias voltage. The technique had been used successfully above 1 K to measure the ionization energy of holes in  $B^+$  [58] but studies of 2DEGs in GaAs [71] and Si-MOSFETs [72] at 0.4 K were unable to detect any absorption due to cyclotron phonons in either case, which suggested it must be very weak. This is in line with theoretical prediction for GaAs but is surprising for Si-MOSFETs particularly in view of the experiments by Kent *et al.* [68]. The absence of detectable absorption in Si-MOSFETs may then be due to the difficulty of separating the effect of the quasi-monochromatic phonons from the heating by the background phonons. This is increasingly difficult below 1 K because of the poorer contact to the heat bath caused by the increase in the Kapitza resistance to liquid helium with falling temperature [73].

Using ballistic phonon techniques to be discussed later in the context of the FQHE, Schulze-Wischeler *et al.* [74] have studied phonon absorption in the vicinity of  $\nu = 1$ . At exactly  $\nu = 1$  they see no phonon absorption signal; this is as expected since the Landau level spacing is of much greater energy than that of the phonons injected into the substrate. However, at filling factors such as  $\nu = 0.92$  and  $\nu = 1.10$ , they do observe energy absorption by the 2DEG from the injected pulse of non-equilibrium phonons. This implies that slightly away from  $\nu = 1$  there are low-energy excitations of the system which can couple to the phonons. One possibility mentioned by the authors is that these excitations may be related to low-energy spin excitations of the 2DEG known as skyrmions. Whether this is the case and how the spin excitations affect the charged excitations (which in turn alter the resistance of the sample) are matters that need to be addressed by future investigations.

### 3.5.3 Momentum transfer (phonon drag)

The induced electric field resulting from phonon drag is usually obtained by measuring the voltage difference between two contacts although care must be taken both with the choice of geometry and the data interpretation [75]. A typical arrangement uses a 2DEG in the form of a bridge connecting two larger pads. In zero magnetic field, the electric field caused by the drag is given by the voltage between the pads divided by the length of the bridge. However, experiments carried out on magnetically quantized 2DEGs in GaAs heterostructures by Dietzel *et al.* [76, 77] demonstrated the presence of transverse voltages across the width of the bridge as a result of the Nernst–Etingshausen effect seen in thermoelectricity. The longitudinal drag field could, however, still be separated and was shown to be consistent with phonon-induced intra-Landau level transitions. Phonon drag experiments have also been carried out with a scanned laser beam to obtain images of the angular distribution of the phonon absorption strength. Surprisingly, the absorption measured is only weakly dependent on the incident angle of the phonons and shows no sign of the predicted cut-off at  $q_{\parallel} \sim l_B^{-1}$ . This could be because it is masked by focusing effects, but could also be because it is smeared out by Landau level broadening. Phonon drag experiments have also been made on 2DHG systems [41] which have the advantage that the longitudinal drag field is appreciably easier to separate from the transverse field because of its relatively greater size.

### 3.6 Introduction to the FQHE

Soon after the first observation of the FQHE by Tsui *et al.* [78], Laughlin proposed an explanation for the effect in terms of a new, strongly correlated ground state for the 2D carriers which would occur at rational fractional filling factors  $1/m$  where  $m$  is an odd integer [3]. Subsequently, Girvin *et al.* [79] proposed that the excitation spectrum of a Laughlin state would have a finite energy gap at small wavevector (due to the incompressibility of the Laughlin states) and a deep minimum at a wavevector close to  $kl_B \sim 1$  where  $k$  is the in-plane wavevector of the electronic excitation. This minimum in the excitation spectrum occurs due to a peak in the structure factor of the correlated electron liquid. The theoretical treatment used by Girvin *et al.* follows Feynman's theory of superfluid helium [80] and the minimum in the excitation spectrum is referred to as the magnetoroton minimum in analogy with the roton minimum of superfluid  $^4\text{He}$ . That a theoretical approach applied to a boson system such as superfluid helium can be applied to a low-dimensional fermion system in a strong magnetic field is, at first sight, surprising. The basic reason for the validity of this approach is that single particle excitations of the system are extremely high in energy as they involve promoting an electron to the next Landau level. This results in the low-lying excitations of the system being collective excitations.

For a Landau level filling factor of  $1/m$ , the charged excitations of the fluid correspond to isolated vortices that carry a fractional charge of  $e/m$ . Direct experimental evidence for such fractional charges has been provided by noise experiments in the fractional quantum Hall regime [81, 82]. These charge vortices are the excitations at the high wavevector limit of the excitation spectrum. Magnetorotons can be considered as bound pairs of positive and negative vortices and so carry no net charge. It has also been predicted that the excitations close to zero wavevector are bound pairs of magnetorotons [79].

Only a few of the observed fractional quantum Hall states occur at filling factors of the form  $1/m$  more generally the fractional quantum Hall state is signified by a plateau in the Hall resistance with a value of  $h/\nu e^2$  where  $\nu = p/(2rp \pm 1)$  is the Landau level filling factor,  $p$  and  $r$  are integers, and a vanishing longitudinal resistivity,  $\rho_{xx}$ . In the simplest case  $r = 1$  and  $p = 1, 2, 3, \dots$  corresponding to series of fractions  $\nu = 1/3, 2/5, 3/7, \dots$  and  $\nu = 1, 2/3, 3/5, \dots$  Fig. 3.16 shows the longitudinal and transverse resistivities for a high-mobility sample. The longitudinal resistivity  $\rho_{xx}$  follows an Arrhenius law over several orders of magnitude and suggests that the longitudinal resistivity is due to the creation of quasiparticles, thermally activated across a finite energy gap. This energy gap would presumably be related to the value of the energy gap at large wavevectors as the magnetotransport experiments are sensitive to charged quasiparticles. Experiments carried out by various groups, for instance [84], confirmed that the energy gaps vary as  $B^{1/2}$ , as expected, but the absolute value of the energy gap was always less than the theoretical value. As the discrepancy was less for samples of high mobility it is thought that disorder must play a role in reducing the effective energy gap. However, a detailed theoretical treatment of the influence of disorder has proved elusive.

Laughlin's picture describes the states such as  $1/3, 1/5$ , and the particle-hole conjugate states such as  $2/3$ . It does not describe the complete family of observed FQHE states. The explanation of the hierarchy of FQHE states has been best explained in terms

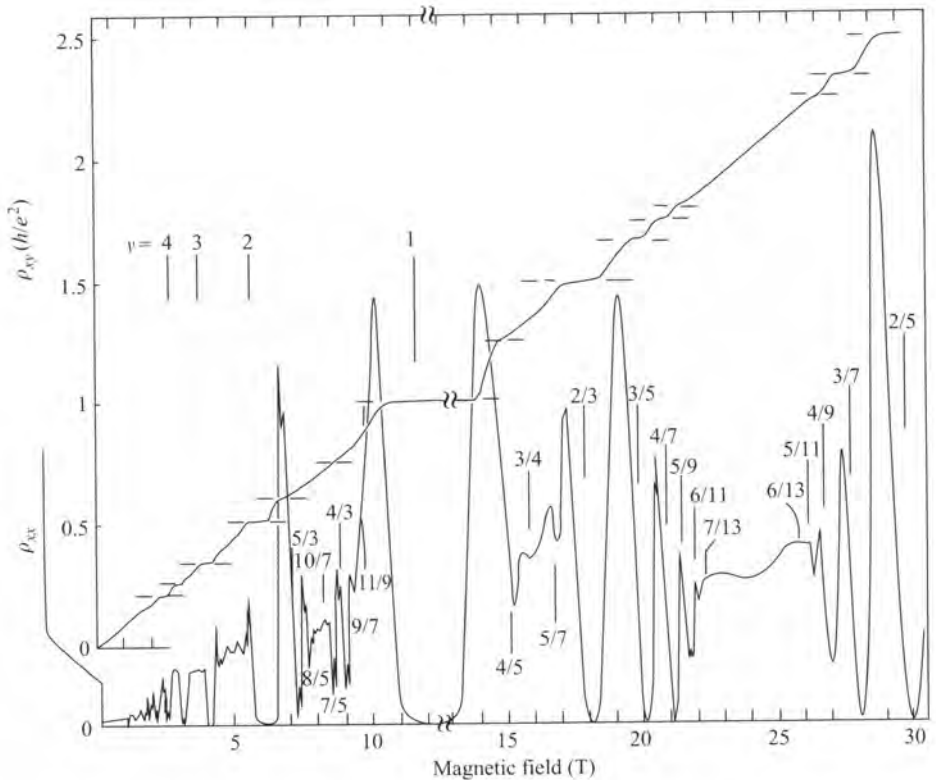


**Fig. 3.16** Longitudinal resistivity  $\rho_{xx}$  and transverse (Hall) resistivity  $\rho_{xy}$  of a high-mobility 2DEG as a function of magnetic field. The figure is a compilation of two different traces. Comparing this figure with Fig. 3.2 it can be seen that the integer plateaux are narrower than in a low-mobility sample and that extra plateaux in the Hall resistance occur at particular fractional filling factors. Note the symmetric behaviour of the longitudinal resistivity around  $\nu = 1/2$  (24 T) and the qualitative similarity to the low-field Shubnikov-de Haas oscillations. These features are due to the presence of the composite fermion Fermi surface at  $\nu = 1/2$  [83].

of new quasiparticles known as composite fermions. An introduction to the theory of composite fermions can be found in several texts such as that given by Nicholas [85]. Halperin *et al.* [5] revolutionized the picture of the FQHE by describing in detail the consequences of transforming the description of the system using a Chern–Simons gauge transformation as that of a quasiparticle which consists of an electron attached to  $2m$  flux quanta. Once such a transformation has been made the new quasiparticles behave as weakly interacting independent particles. Such a composite quasiparticle is still a fermion and for example at  $\nu = 1/2$  a composite fermion consisting of two flux quanta and one electron moves on average in an effective magnetic field of zero. The most surprising thing about this new picture is that the mean field approximation works so well. Halperin *et al.* proposed the existence of composite fermion Fermi surfaces at  $\nu = 1/2m$ . This proposal explained anomalous SAW measurements which will be described later in this chapter. The FQHE is then described as the IQHE of the composite fermions.

If we start at  $\nu = 1/2m$  the composite fermions move on average in a residual, or effective, magnetic field  $B^*$  of zero. As we move away from this special filling factor the composite fermions experience an effective magnetic field given by the difference of the applied external magnetic field,  $B$ , and the mean field of the composite fermions. The effective field is therefore given by

$$B^* = B - 2m\phi_0 n_s \quad (3.4)$$

where  $\phi_0$  is the magnetic flux quantum. The existence of this field leads to quantization of the composite fermions energies due to the formation of Landau levels with the same degeneracies as the single particle states. The energy separation of these composite fermion Landau levels is given by a cyclotron energy

$$E = \hbar e B^* / M^* \quad (3.5)$$

where  $M^*$  is the effective mass of the composite fermion which can be an order of magnitude greater than the cyclotron effective mass of the independent electrons in the semiconductor due to the interaction with the magnetic flux. Recent measurements by Kukushkin *et al.* [86] have directly measured the cyclotron absorption of composite fermions.

Prior to 1993, Jain had considered the properties of composite fermions and bosons (quasiparticles consisting of an electron bound to an odd number of flux quanta) [87] his research group has also lead the calculation of the dispersion curves of low-lying excitations using the composite fermion picture. The excitations are described as excitons of the composite fermion Landau levels and quantitative predictions of the dispersion curves have been made. The most striking qualitative difference from the earlier work of Girvin *et al.* (which can only describe the behaviour at simple fractions) is that in general there can be multiple magnetoroton minima. Whilst both theories predict a single minima at  $\nu = 1/3$ , at  $\nu = 2/5$  two minima are predicted by the composite fermion theory.

### 3.7 Electron-phonon interaction in the fractional quantum Hall regime

In this section we consider the nature of the interaction of phonons with 2DEGs at even filling factors such as  $\nu = 1/2$  and also at odd filling factors corresponding to fractional quantum Hall states.

#### 3.7.1 Close to even-denominator states

Khveshchenko and Reizer [88] consider the interaction between composite fermions and acoustic phonons at even-denominator fractions such as  $\nu = 1/2, 1/4, \dots$ . If a variation in the carrier density is induced by the phonon interaction then, in the composite fermion picture, it will be accompanied by a variation in the gauge field. This modifies the interaction between the carriers and the phonons. At temperatures below 1 K, the piezoelectric interaction in GaAs is expected to dominate the interaction between the acoustic

phonons and the 2DEG. For a 2DEG, at zero magnetic field, the unscreened matrix element that describes coupling of the 2DEG to the acoustic phonons by a piezoelectric interaction is

$$M_{\lambda}^{\text{PE}}(q) = ee_{1,4} \left( \frac{A_{\lambda}}{2\rho s_{\lambda} q} \right)^{1/2} \quad (3.6)$$

where  $q = (q_{\parallel}, q_z)$  is the 3D phonon momentum,  $\rho$  is the bulk density of GaAs,  $s_{\lambda}$  is the speed of sound with polarization  $\lambda$ ,  $e_{1,4}$  is the non-zero component of the piezoelectric tensor which relates the local electrostatic potential to a lattice displacement, and  $A_{\lambda}$  is the anisotropy factor. The authors conclude that this interaction is screened by a dynamic dielectric function so that in the random phase approximation the matrix element is given by  $M_{\lambda}^{\text{PE}}(q)/\epsilon(\omega, q_{\parallel})$ , where the dynamic dielectric function

$$\epsilon(\omega, q_{\parallel}) = 1 + H(q_{\parallel})V_{\text{ee}}(q_{\parallel})\Pi_{00}(\omega, q_{\parallel}) \quad (3.7)$$

in which the 2D Coulomb potential is given by  $V_{\text{ee}}(q_{\parallel}) = 2\pi e^2/\epsilon_0 q_{\parallel}$ , the scalar 2D polarization function  $\Pi_{00}(\omega, q_{\parallel})$ , and  $H(q_{\parallel})$  is the form factor of the carriers in the potential well that confines them in the  $z$ -direction.

In the case of composite fermions, the polarization matrix is altered, which has important effects on the phonon–composite fermion coupling. The composite fermion–phonon matrix element becomes

$$M_{\lambda}^{\text{cf}} = \frac{M_{\lambda}^{\text{PE}}(q)}{\epsilon_{\text{cf}}(\omega, q_{\parallel})} \left( 1 + (2i\pi\Phi)H(q_{\parallel})\frac{\mathbf{v} \times \mathbf{q}_{\parallel}}{q_{\parallel}^2} \Pi_{00}(\omega, q_{\parallel}) \right) \quad (3.8)$$

where

$$\epsilon_{\text{cf}}(\omega, q_{\parallel}) = 1 + H\Pi_{00}V_{\text{ee}} + H^2(2\pi\Phi/q_{\parallel})^2\Pi_{00}\Pi_{\perp}. \quad (3.9)$$

The form of the scalar CF polarization factor  $\Pi_{00}(\omega, q)$  is similar to that of ordinary electrons. The transverse vector component arises from the Chern–Simons gauge transformation and is given by

$$\Pi_{\perp}(\omega, q_{\parallel}) = \chi_{\text{cf}}q_{\parallel}^2 + i\omega\sigma_{\text{cf}}(q_{\parallel}) \quad (3.10)$$

where  $\chi_{\text{cf}}$  is of the order of the composite fermion Fermi velocity and  $\sigma_{\text{cf}}(q_{\parallel})$  is given by the product of this Fermi velocity and the composite Fermion diffusion coefficient if  $q_{\parallel}l_{\text{cf}} < 1$  ( $l_{\text{cf}}$  is the composite fermion mean free path) and  $k_{\text{F,cf}}/(2\pi q_{\parallel})$  otherwise ( $k_{\text{F,cf}}$  is the Fermi wavevector of the composite fermions). As the composite fermions are spin polarized at even-denominator filling factors  $k_{\text{F,cf}} = \sqrt{2}k_{\text{F}}$  where  $k_{\text{F}}$  is the Fermi wavevector of ordinary electrons.

Several other key parameters for composite fermions differ from those of ordinary conduction band electrons. The composite fermion effective mass is predicted to be over 10 times that of conduction band electrons and the transport times are decreased by at least a factor of 10. This results in a much lower mobility for composite fermions compared with ordinary electrons in zero magnetic field. These parameters will be discussed further in the context of the SAW experiments below. It is found that well below the Debye temperature,  $T_{\text{D}}$  ( $\sim 10$  K), the temperature below which all the components of the phonon momentum are determined by temperature, the ratio of the phonon-limited

composite fermion mobility to phonon-limited electron mobility varies as  $(T/T_D)^2$ . The authors use their results to consider phonon drag thermopower, SAW attenuation, and hot electron energy loss rate. They find that in all cases the temperature dependence is weaker than band electrons or enhanced by a numerical factor related to the ratio of SAW attenuation at zero field and that at even-denominator filling factors. Noting that in the energy loss experiments reported by Chow [37] the filling factor in the fractional quantum Hall regime that was used was close to  $3/8$ , they speculate that a possible reason for the observed increase in the strength of the electron–phonon coupling could be due to the proximity of the even-denominator state.

Ballistic phonon experiments to be discussed in more detail below have not observed any qualitative effects due to the existence of a composite fermion Fermi surface or the altered form of the piezoelectric interactions. The experiments find that the electron–phonon interaction is reduced above a certain heater temperature. The value and form of this interaction is consistent with the cut-off caused by momentum conservation in the growth direction. The effective thickness of the 2DEG calculated from these experiments is consistent with theoretical estimates [89].

### 3.7.2 Odd-denominator states

Two complementary experimental methods that have probed the energy gap close to fractional quantum Hall states are resonant Raman scattering and phonon absorption studies. The resonant Raman scattering has been used to observe the extrema in the dispersion curve of the magnetorotons [90, 91] and, for a range of small in-plane wavevectors below  $kl_B \sim 0.1$ , wavevectors have been resolved by tilting the sample [92]. At higher wavevectors, coupling is thought to be due to the weak disorder in the sample activating modes for which the excitation wavevector is larger than the light scattering wavevector. Such experiments require great care and experimental skill, as the energy shifts observed are typically in the region of 0.2–0.4 meV and it is important to rule out other optical interactions as the cause of the features observed. The results of the experiments are in good agreement with theoretical predictions once allowance has been made for the finite thickness of the 2DEG, which significantly reduces the energy gap. More details of these experiments can be found in the references given.

In this section we shall focus instead on ballistic phonon absorption experiments. These experiments have been used to study the interaction between non-equilibrium acoustic phonons and the magnetorotons. Here the term magnetorotons is used to describe the low-lying collective excitations of the FQHE state even when multiple minima are predicted by composite fermion theory [93]. The energy of acoustic phonons matches the energy scales of the FQHE energy gaps. Unlike resonant Raman scattering there is also the hope that the wavevector of the magnetoroton created by the absorption of a phonon can also be resolved as the in-plane component of the phonon wavevector can match the deepest minimum in the magnetoroton dispersion curve. The complication in such experiments is the strong focusing of the acoustic phonons as they traverse the crystal prior to interacting with the 2DEG. We shall return to the implications of the phonon focusing towards the end of this section; for the moment we shall consider the GaAs crystal to be an isotropic acoustic medium.

Experimentally a pulse of non-equilibrium phonons is injected into the substrate of the GaAs from a thin film of metal that has been deposited on the opposite side of the substrate to the 2DEG. The wafers used in the experiments are typically 2 mm thick (rather than the more usual 0.5 mm) to increase the time of flight of the ballistic phonons from the heater to the 2DEG. When the phonons impinge on the 2DEG a small number of them are absorbed. Measurements of the rate at which energy is absorbed by the electrons contains important spectroscopic information about the states of the 2DEG. The ideal experiment would be to observe the transmission of the phonons through the 2DEG. However, as the proportion of phonons absorbed is estimated to be less than one in a million another experimental arrangement has been used. The 2DEG is patterned into a long meandering track in which the longitudinal resistance is greatly enhanced relative to the Hall resistance due to the length of the sample. By measuring the variation of the two-terminal resistance in the FQHE the time variation of the electron temperature can be determined [89] as the acoustic phonons are absorbed by the 2DEG. By adjusting the temperature of the heater, the spectrum of phonons injected into the substrate can be varied altering the spectrum of phonons which impinge on the 2DEG.

A theoretical framework in which to analyse the experimental results has been provided by Benedict *et al.* [94]. Before the injection of the non-equilibrium phonons, the 2DEG and the substrate are in thermal equilibrium at a temperature  $T_0$ . The phonon pulse propagates ballistically across the substrate as the energy of the phonons (corresponding to a frequency less than 200 GHz) is too small to be affected by isotope scattering in the substrate. The substrates are sufficiently thick that the longitudinal (LA) and transverse acoustic (TA) phonons spatiotemporally separate with the LA phonons arriving at the 2DEG before TA phonons in the same direction. A small proportion of the phonons are absorbed by the 2DEG raising its temperature,  $T_e$ , above that of the substrate. The 2DEG is always close the surface of the sample and so, on the time scale of the experiments, the phonons encounter the surface of the substrate and the 2DEG at the same time. When phonons hit a free surface they undergo a variety of processes including specular reflection, diffuse scattering, and mode conversion. In the experimental signal the effects of reflection are clearly visible with peaks in  $T_e$  corresponding to the absorption of twice and quadruple reflected phonons. At times long compared with the time of flight and duration of the pulse of phonons, the 2DEG cools towards the original starting temperature as the heat injected into the system is removed by dilution refrigeration.

The two coupling mechanisms which can couple phonons to the 2DEG are the piezoelectric interaction and the deformation potential interaction as discussed in Chapter 2. As the absorption is expected to be dominated by the existence of the magnetoroton minimum, the fractional quantum Hall energy gap  $\Delta(k)$  is modelled as

$$\Delta(k) \sim \Delta^* + \frac{(k - k^*)^2}{2\mu} \quad (3.11)$$

$$\mu^{-1} = \left( \frac{d^2 \Delta(k)}{dk^2} \right)_{k=k^*} \quad (3.12)$$

where variables with asterisks are values at the magnetoroton minimum.

For the case where  $T_e \ll T_h$ , the rate at which energy is transferred from the phonon pulse to the incompressible liquid can be obtained from Fermi's golden rule which leads to the straightforward interpretation that the process involved is the direct conversion between phonons and magnetorotons with a matrix element that includes the structure factor of the liquid, a factor that describes the extent of the 2DEG in the growth direction and piezoelectric and deformation potential coupling elements. By considering only the case where  $T_e, T_h \ll \Delta^*/k_B$  stimulated emission of phonons by the 2DEG can be neglected. The model confirms that the phonon–magnetoroton conversion process is subject to the conservation of in-plane wavevector and energy. Therefore a useful picture of phonon absorption is one in which the phonon absorption occurs where the dispersion curves of the magnetorotons and phonons cross (noting that it is the in-plane momentum of the phonons that is important). This is illustrated in Fig. 3.4. If the dispersion curves do not cross then there will be no phonon absorption by the mechanisms discussed here. The matrix element for phonon–magnetoroton conversion is maximum close to the magnetoroton minimum. If the range of in-plane phonon momenta intersects the magnetoroton dispersion only above the magnetoroton minimum then the intersection closest to the magnetoroton minimum will dominate the conversion process. The caveat is that phonon focusing complicates the relationship between geometric direction of phonon propagation in the sample and the in-plane wavevector of the phonons. This complicates the interpretation of angle-resolved experiments.

On the experimentally accessible time scales ( $\sim 10$  ns) the electron system will always be in local equilibrium at a some well-defined temperature,  $T_e$ , as the electron–electron interaction times are orders of magnitude smaller than this. The experimental results are interpreted as a variation in  $T_e(t)$ . The resistance of the sample as a function of temperature is obtained from a transport experiment in which the equilibrium temperature of the whole device is varied whilst the current through the device is kept constant. When a phonon pulse of duration  $\tau_p$  impinges on the 2DEG an energy  $dE = \alpha P_h \tau_p$  is transferred to the electron system.  $P_h$  is the power dissipated from the heater in the form of ballistic phonons and  $\alpha$  is the relative number of phonons absorbed by the 2DEG. For  $T_e \ll \Delta^*/k_B$ ,  $\alpha$  is independent of the electron temperature [89]. If the 2DEG was at a temperature  $T_0$  before the phonon pulse and rises to temperature  $T_1$  after the phonon pulse then

$$\int_{T_0}^{T_1} \frac{C(T_e)}{\alpha} dT_e = P_h \tau_p \quad (3.13)$$

where  $C(T_e)$  is the specific heat of the 2DEG.

As the power dissipated in the heater and the duration of the voltage pulse applied to the heater is known, we can calculate the normalized heat capacity,  $C(T_e)/\alpha$ , experimentally. For a constant power  $P_h$ , the maximum electron temperature attained by the 2DEG,  $T_1$  is measured for different substrate temperatures  $T_0$ . The quantity  $C(T_e)/\alpha$  can then be calculated using an iterative method. Figure 3.17 shows the result of such a measurement at  $\nu = 1/3$  for a 2DEG with an areal density of  $1.16 \times 10^{15} \text{ m}^{-2}$  and a mobility of  $150 \text{ m}^2 \text{ V}^{-1} \text{ s}^{-1}$ . It is found that the heat capacity varies linearly at low temperature and rises quickly above 300 mK. The expected variation would be an exponential temperature dependence  $\sim \exp(-\Delta^*/k_B T)$ . The sharp rise can be attributed to such a form, but other power law variations fit the data with a similar level of significance. The origin of the

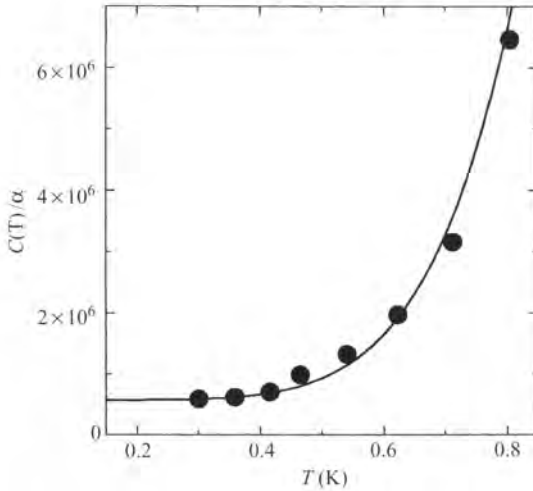


**Fig. 3.17** Relative specific heat of the 2DEG at  $\nu = 1/3$  normalized to the fraction of phonons absorbed. The solid line is a power law fit with terms in  $T$  and  $T^7$ . The linear variation is thought to be due to compressible localized states due to disorder in the sample. The rapid rise at higher temperatures reflects the presence of the magnetoroton energy gap. (After [89].)

linear variation with temperature below 300 mK is probably due to compressible states in the sample. The origin of such states is unclear but possible causes include spin excitations, sample inhomogeneity, and edge states. In transport experiments only the extended density of states at the Fermi level matters, whereas the heat capacity includes localized states as well.

Once the normalized heat capacity is known, by keeping  $T_0$  constant and varying the heater power the variation of the energy absorbed by the 2DEG can be calculated as a function of the heater temperature. The details of these experiments are described in [89, 95–97]. A representative result is shown in Fig. 3.18. The best fit to the data is a temperature dependence of the form  $[\exp(\Delta^*/k_B T) - 1]^{-1}$ , that is proportional to the number of phonons close to an energy  $\Delta^*$ . Theoretical values of  $\Delta^*$  are usually expressed in the form  $c \times e^2/4\pi\epsilon_0\epsilon l_B$ . The theoretical prediction at  $\nu = 1/3$  for an infinitely thin 2DEG is  $c = 0.063(3)$ . Allowing for the thickness of the 2DEG this value is reduced to 0.035(5). The experimentally determined value was in excellent agreement with this value at 0.036(5).

The magnetorotons created by phonon absorption are neutral quasiparticles and, to alter the conductivity of the sample, scattering of charged quasiparticles must occur. Equilibration within compressible regions will be dominated by quasiparticle scattering and therefore very rapid compared with the time scales of the experiment. The mechanisms by which this occurs in incompressible regions are unclear. What is known is that the curvature of the dispersion curve prevents magnetorotons created by phonon absorption from absorbing other low-energy phonons and so reaching sizes greater than  $\sim 3/l_B$  [98]. Hence this process will not lead to free charged quasiparticles. Two other mechanisms worthy of consideration are second-order processes such as two-phonon absorption [99]

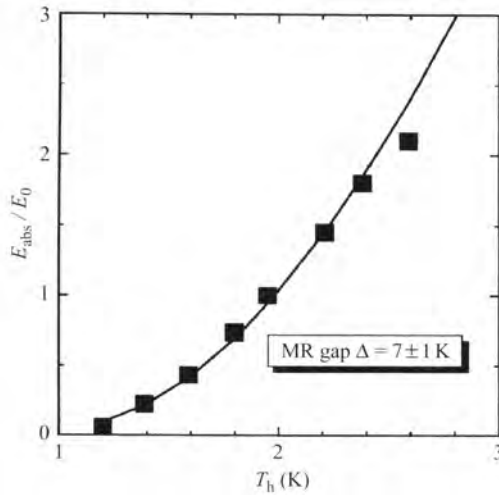


**Fig. 3.18** Dependence of the energy absorbed by the 2DES on the heater temperature  $T_h$  at  $\nu = 1/3$ . The solid line shows the fitted behaviour for phonon absorption at a well-defined energy, taken to be the magnetoroton gap,  $\Delta^*$ . (After [89].)

and collisions between magnetorotons. Experimentally, the phonon energy absorbed as a function of the pulse duration has been measured [89]. At  $\nu = 1/2$  the absorbed energy saturates with a characteristic time of 70 ns. In saturation the rate of phonons absorbed and emitted by the 2DEG are equal and so the 2DEG does not absorb any net energy even if the phonons are present for longer. At  $\nu = 1/3$  the energy absorbed by the 2DEG increases proportionally to the pulse duration with no saturation up to times as long as 300 ns. The conclusion to be drawn from this is that the magnetorotons created by phonon absorption do not come into a dynamic equilibrium with the ballistic phonons by emitting phonons of the same energy and wavevector. Instead they heat the 2DEG internally without phonon emission into the substrate. Scarola *et al.* [93] found good agreement between the theoretically predicted energy gap and the results of Zeitler *et al.* [89].

In a later series of experiments Devitt *et al.* [95–97] studied a sample in which the area of the 2DEG and the heaters was reduced sufficiently that angle-resolved measurements were possible at  $\nu = 2/5$ . This allowed the resolution of LA and TA interactions with the 2DEG (Fig. 3.19). The value of the  $\nu = 2/5$  magnetoroton minimum deduced from this experiment was  $c = 0.025(3)$  in reasonable agreement with the theoretically predicted value of  $c = 0.032(3)$  corrected for the effect of finite thickness. The experiment did not have sufficient angular resolution to resolve the two minima for  $\nu = 2/5$ . In the experiments of Zeitler *et al.* [89] the area of the 2DEG was too large to resolve the difference between LA and TA phonons clearly. Therefore the value of the energy gap at  $\nu = 1/3$  obtained in this study could be due to the absorption of either LA or TA phonons. In Devitt *et al.* [96] it was reported that angular resolved measurements at  $\nu = 1/3$  could only be reconciled with the earlier results of Zeitler *et al.* if it is assumed that the LA phonons dominate the absorption in these earlier experiments. The TA phonon absorption signals from the angle-resolved study give a magnetoroton energy

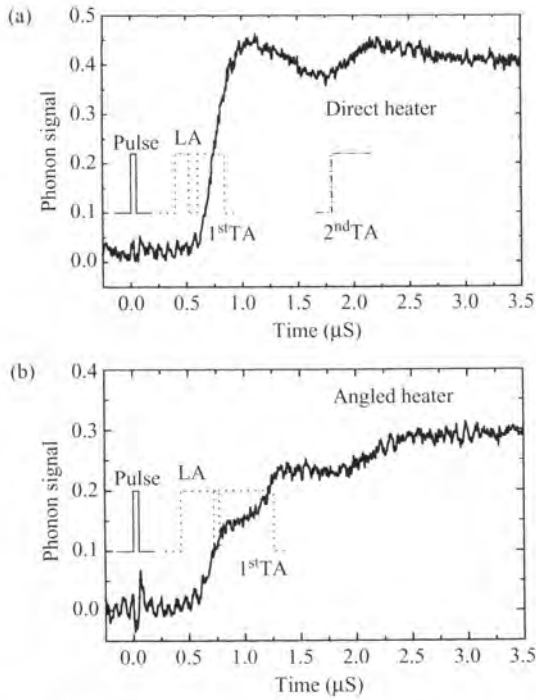


**Fig. 3.19** Angle-resolved time of flight data at  $\nu = 2/5$  with a base temperature of 180 mK and a heater temperature of 1.2 K. (a) For the heater directly under the sample no LA signal is seen, but strong rises in electron temperature are observed due to absorption of TA phonons. The LA phonons are focused out of the straight across direction whereas the TA phonons are focused into this crystallographic direction. Ballistic transport of the phonons across the wafer is demonstrated by the signal caused by the second arrival of the phonon pulse at the 2DEG. (b) For a heater placed at an angle to the sample, clear signals from the LA and TA phonons are observed. The duration of the phonon pulse at the 2DEG is largely determined by geometric considerations. [97].

gap approximately half the theoretically expected value. One explanation of this fact is that the absolute value of the energy gap for  $\nu = 1/3$  in this sample is well above the  $1/a_0$  cut-off mentioned at the beginning of this chapter. Therefore the electron-phonon coupling will be reduced and it is possible that a two-phonon process becomes the dominant process resulting in the phonon determined energy gap being measured at half the theoretical value. The results for  $\nu = 2/5$  are in good agreement with theory and in this case the absolute energy gap is sufficiently low in energy that the  $1/a_0$  cut-off will not be a major factor. Figure 3.20 shows the experimentally measured energy gaps as a function of in-plane wavevector. The points due to the TA phonon absorption have been placed at the expected wavevector position of the magnetoroton minimum as the phonon focusing results in a wide range of in-plane wavevectors interacting with the TA modes. Therefore it is expected that the magnetophonon minimum will dominate the phonon absorption. The range of LA wavevectors is estimated from the geometry of the sample as the LA modes are only weakly focused.

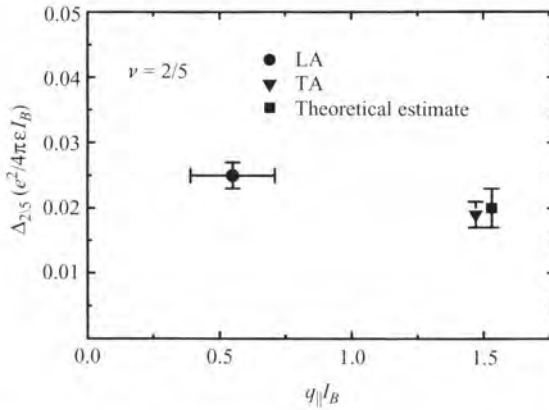


**Fig. 3.20** Dispersion curve at  $\nu = 2/5$  determined from angle-resolved phonon absorption measurements. The uncertainty in the wavevector in the LA phonon absorption is due to geometric factors. The energy is expressed in terms of reduced units as explained in the text. The TA phonon pulse has a wide range of wavevectors due to phonon focusing and so it has been placed at the maximum probable value of the in-plane wavevector [97]. The theoretical estimate is taken from Scarola *et al.* [93].

The ballistic phonon experiments have been very useful in helping to verify the magnetoroton picture of the FQHE. This technique, whilst lacking the energy resolution of resonant Raman scattering, is so far the only technique that has demonstrated the ability to make wavevector-resolved measurements close to the magnetoroton minimum. Unlike magnetotransport measures of the energy gap the values determined by phonon absorption do not appear to need correction for the effects of disorder. Refinements of the phonon absorption technique could lead to absolute measurements of the specific heat of a single 2D layer of electrons, and observation of a  $2k_{F,cf}$  cut-off in the electron–phonon interaction due to the presence of a composite fermion Fermi surface with diameter  $2k_{F,cf}$ . By modelling the effects of crystal anisotropy more carefully it should also be possible to improve the experimental determination of the magnetoroton dispersion curve and the details of the electron–phonon interaction between LA and TA phonons and the 2DEG.

### 3.8 SAW studies of quantum Hall states

#### 3.8.1 Introduction to SAWs

GaAs is a piezoelectric crystal so it is straightforward to generate and propagate SAWs along particular crystallographic directions and these then travel along the stress-free surface of the crystal. As an applied electric field causes mechanical strain within the crystal, an interdigital transducer (IDT) can be used to apply a spatially periodic electric field to the surface. If the frequency of the applied electric field is such that the resulting surface waves reinforce within the IDT then a detectable SAW will propagate from the transducer. The wave can then be detected by an identical IDT a short distance

(typically 1–5 mm) away along the direction of propagation. The SAW carries oscillating electric and strain fields with it, the energy of the wave being localized within a few wavelengths of the surface. If the SAW travels over a region with a finite conductivity then the velocity of the SAW is altered slightly by the presence of the carriers and the wave is attenuated due to energy absorption by the carriers. In this way SAW experiments can be used to probe the conductivity of a 2D carrier gas (2DCG) at finite frequency and wavevector. The coupling between the SAW and the 2D carriers is non-linear so that a DC drag effect known as the acoustoelectric effect occurs in which a dc voltage is set up between two contacts to the 2DEG by the presence of the SAW. In this section we shall review the SAW studies on a single layer 2DEG in which the carriers are trapped in a quantum well or heterojunction. Other studies which have been carried out include bilayer systems in which the carriers are in close proximity to each other [100] and low-field studies in which the 2DCG has been patterned into wires or dots [101]. In strong acoustoelectric fields the optical properties of the 2DEG can be affected [102].

The theory of SAW propagation and generation can be found in many texts [103]. There are many types of surface wave which can be excited including Rayleigh waves and pseudo-surface waves. In a Rayleigh wave the particles of the solid move in elliptical paths with both longitudinal and transverse strains. The wave is localized to within a few wavelengths of the surface. For the case of an anisotropic crystal the SAW propagates strongly only in certain crystallographic directions and can be strongly focused. For certain directions an SAW exists which has properties similar to a Rayleigh wave but with a higher velocity and electromechanical coupling coefficient. These modes are known as pseudo-surface modes and occur in directions where it is impossible to match the surface boundary conditions exactly. The energy of the pseudo-SAW flows parallel to the surface with the wave energy within a few wavelengths of the surface. However, whereas the Rayleigh wave is a true surface mode which, in the absence of scattering, will propagate without loss across the surface, the pseudo-SAW has a bulk wave component which causes a leakage of energy in the direction away from the surface. For an infinitely long sample the pseudo-SAW energy at the surface will leak from the surface mode into a bulk acoustic mode. In real samples this loss of energy at the surface is insignificant. Most SAW experiments in which the transducers are fabricated on the GaAs substrate use pseudo-SAW modes as the electromechanical coupling constant is strongest in these directions.

For a weakly piezoelectric material such as GaAs, the electromechanical coupling constant can be defined by considering two limiting cases. In the first case the solution of the wave equation is found for a piezoelectric medium in which the surface conductivity is infinite. The infinite conductivity causes the electric fields to vanish at the surface and the solution is similar to that in a non-piezoelectric medium. The velocity of the wave in this case is denoted as  $v_\infty$ . The second limiting case is where the substrate and surface are insulating and the elastic constant is enhanced by the longitudinal electric field in the material with a resulting SAW velocity,  $v$ . The electromechanical coupling constant,  $k_{\text{eff}}^2$ , is defined as,

$$k_{\text{eff}}^2 = \frac{2(v - v_\infty)}{v_\infty}. \quad (3.14)$$

The electromechanical coupling constant,  $k_{\text{eff}}^2$ , of GaAs is small compared with materials such as lithium niobate used in commercial SAW devices. In the [110] direction on the (001) plane of GaAs,  $k_{\text{eff}}^2 = 6.4 \times 10^{-4}$ . The small value of coupling constant increases the technical difficulty of experiments on GaAs as the signals that are detected are much weaker than on lithium niobate. The solution has been to use low-noise amplifiers and to average the detected signal using, for example, boxcar integrators.

### 3.8.2 SAW interaction with 2DEGs

If carriers are present in the piezoelectric medium the longitudinal electric field of the SAW can interact with the carriers resulting in a loss of energy from the acoustic wave and dispersion due the relaxation of the carriers after perturbation by the SAW. This situation was described by Hutson and White [104]. For the case of a 2D carrier system in which the free carriers are contained in a thin sheet near the surface of the substrate, with a thickness much less than the wavelength of the SAW, Adler [105] gives expressions for the dispersion and attenuation of the SAW which for the case of a 2DEG in a high magnetic field become

$$\frac{\Delta v}{v} = \frac{k_{\text{eff}}^2}{2} \frac{1}{1 + (\sigma_{xx}/\sigma_m)^2} \quad (3.15)$$

$$\Gamma = q_s \frac{k_{\text{eff}}^2}{2} \frac{(\sigma_{xx}/\sigma_m)}{1 + (\sigma_{xx}/\sigma_m)^2} \quad (3.16)$$

where  $\sigma_{xx}$  is the longitudinal conductivity of the 2D carriers,  $q_s$  the wavevector of the SAW, and  $\sigma_m$  is a characteristic conductivity given by

$$\sigma_m = v_\infty \varepsilon_0 (\varepsilon_1 + \varepsilon_2) \quad (3.17)$$

where  $\varepsilon_1$  and  $\varepsilon_2$  are the relative dielectric constants of the half-spaces above and below the surface. In the [110] direction on the free (100) surface of GaAs this results in a characteristic conductivity,  $\sigma_m$ , of  $3.3 \times 10^{-7} \Omega^{-1}$ .

The physical interpretation of the equations is that at high values of the longitudinal conductivity, the carriers screen out the piezoelectric interaction and the interaction between the carriers and the SAW is weak. In this case the SAW velocity is that of an acoustic wave without piezoelectric stiffening. If the sheet conductivity is very low then the interaction is also weak and the piezoelectric interaction is largely unscreened; the SAW velocity approaches the velocity in an insulating piezoelectric material. The maximum interaction occurs when  $\sigma_{xx} = \sigma_m$ . For this conductivity the maximum attenuation of the SAW occurs and the velocity is midway between the maximum and minimum acoustic velocities. Figure 3.21 shows the variation of the attenuation and dispersion with the longitudinal conductivity.

Whilst the low-frequency longitudinal conductivity of the 2DEG can be obtained directly using the annular, Corbino, geometry on samples used for SAW studies, Hall bars are usually used instead so that the SAW passes along the length of the Hall bar. In this geometry the longitudinal conductivity,  $\sigma_{xx}$ , can be calculated knowing the longitudinal

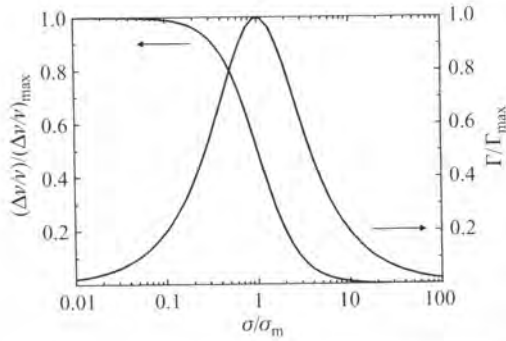


**Fig. 3.21** SAW attenuation and velocity shift as a function of the diagonal conductivity,  $\sigma_{xx}$ , of a 2DEG, normalized to  $\sigma_m$ . The attenuation passes through a maximum when  $\sigma_{xx} = \sigma_m$  leading to a characteristic double peak in the attenuation at well-developed quantum Hall filling factors.

and transverse resistivities,  $\rho_{xx}$  and  $\rho_{xy}$  respectively, using the tensor relation

$$\sigma_{xx} = \frac{\rho_{xx}}{\rho_{xx}^2 + \rho_{xy}^2}. \quad (3.18)$$

The maximum value of the attenuation,  $\Gamma_{\max} = (qs k_{\text{eff}}^2)/4$  and the maximum value of the fractional change in velocity,  $(\Delta v/v)_{\max} = (k_{\text{eff}}^2)/2$ , allow us to write a relation between the attenuation and dispersion

$$\left(\frac{\Gamma}{2\Gamma_{\max}}\right)^2 + \left(\frac{\Delta v/v}{(\Delta v/v)_{\max}} - \frac{1}{2}\right)^2 = \left(\frac{1}{2}\right)^2 \quad (3.19)$$

which leads to a graph known as a Cole–Cole plot in which the normalized attenuation is plotted against a normalized velocity shift. The result is a semicircle centred on  $\Gamma/(2\Gamma_{\max}) = 0$ ,  $(\Delta v/v)/((\Delta v/v)_{\max}) = 1/2$ . This graph is characteristic of a relaxation interaction with one relaxation time. All velocity and attenuation data from different values of longitudinal conductivity should lie on this semicircle if the relaxation approximation is valid.

Conventional low-frequency transport measurements which rely on the passage of a current through the sample only probe the extended states, that is those states that can carry the current from one current contact to the other. SAW measurements, on the other hand, allow the measurement of the conductivity of the sample as a whole including that due to localized states. SAW also probes the conductivity at well-defined finite frequencies and wavevectors; some of the most illuminating SAW studies of low-dimensional systems have looked at how the attenuation and dispersion of the SAW changes with frequency. Finally non-linearities in the SAW–carrier interaction lead to non-linearities in the attenuation and dispersion and give rise to a drag effect known as the acoustoelectric effect. These effects are discussed in the following sections.

### 3.8.3 SAW interaction with integer quantum Hall states

SAWs have been especially useful in the QHE regime because at low Landau level filling factors in general, and at the filling factors of the IQHE and FQHE in particular, the longitudinal conductivity of the 2DEG,  $\sigma_{xx}$ , decreases to values of the same order or lower than  $\sigma_m$ . Without this fortunate coincidence SAW would not be a very productive way of studying the 2DEG as the dispersion and attenuation due to the carriers would be very weak. The first studies of SAW interactions in the QHE regime were carried out by Wixforth and co-workers [106, 107] who studied a 2DEG formed in a modulation-doped heterojunction with an areal density of  $3.2 \times 10^{15} \text{ m}^{-2}$  and a mobility of  $517,000 \text{ cm}^2 \text{ V}^{-1} \text{ s}^{-1}$ . The experiments were carried out at 70 MHz and the pseudo-SAWs were propagated along the [110] direction of the (001) plane of the sample. When the 2DEG enters a quantum Hall state  $\rho_{xx}$  tends towards zero whilst  $\rho_{xy}$  takes a finite quantized value. This results in  $\sigma_{xx}$  also tending to zero. As  $\sigma_{xx}$  falls below  $\sigma_m$  the attenuation reaches its maximum and then falls again as  $\sigma_{xx}$  continues to fall, resulting in characteristic double peaks in the attenuation as the magnetic field sweeps the Landau level through the Fermi level of the 2DEG (Fig. 3.22). The results of these first experiments were in reasonable agreement with the relaxation model of the interaction although some anomalous behaviour was noted such as the maximum

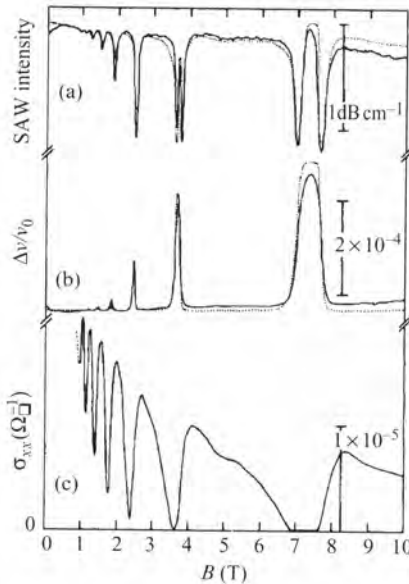


**Fig. 3.22** (a) SAW transmitted intensity, (b) SAW velocity shift, and (c) diagonal conductivity,  $\sigma_{xx}$ , for a 2DEG in the quantum Hall regime at 4.2 K with an SAW wavelength of  $33 \mu\text{m}$  [107]. The conductivity was calculated from the values of  $\rho_{xx}(B)$  and  $\rho_{xy}(B)$  measured in a Hall bar geometry. The dotted curves are the predicted SAW characteristics calculated from the low-frequency diagonal conductivity.  $\nu = 1$  is just above 7 T. Note that the conductivity measured by the SAW is higher than the low-frequency conductivity close to  $\nu = 1$ . This is due to localized states.

attenuation increasing with magnetic field. They also investigated the effect of inhomogeneity within the sample on the SAW characteristics. Small areas of the sample were illuminated to create regions of persistently increased carrier density and hence inhomogeneity in the sample. The results of the SAW experiments were successfully modelled by assuming the carrier distribution to consist of several independent, homogeneous regions. These experiments illustrate one of the important differences between quasi-DC transport experiments and SAW experiments mentioned earlier. The SAW probes the whole area of the sample, whilst the conventional transport experiments may only provide information about the edge states of the sample. This allows the SAWs to be used as sensitive probes of localized states.

In the original study of Wixforth *et al.* [106] the transducer was fabricated on the same GaAs substrate as the 2DEG. In a later series of experiments by other researchers such as Drichko *et al.* [108–112], SAW transducers were also fabricated on a lithium niobate crystal which was then placed in intimate contact with the semiconductor sample being studied. There are several differences between the two methods besides the obvious differences in the velocity of sound and coupling constants. For SAW created and propagated on GaAs the 2DEG experiences both the piezoelectric interaction and the deformation potential interaction, whereas for the lithium niobate propagated SAW the 2DEG only experiences a piezoelectric interaction. A disadvantage of using a separate crystal is that care must be taken to minimize the gap between the lithium niobate and the semiconductor crystal. Even after this it is hard to measure what this gap is. To couple the electric fields in the lithium niobate effectively to the semiconductor, the gap must be less than the wavelength of the SAW. This limits the applicability of the technique to low frequencies unless special attention is made to the mounting of the semiconductor crystal to the lithium niobate. Rotter *et al.* [113] have epitaxially mounted thinned wafers of GaAs to lithium niobate and obtained intimate contact between the sample and the transducer allowing strong high-frequency piezoelectric fields to be generated inside the semiconductor. Strong piezoelectric fields can have a highly non-linear effect on the properties of the 2D layer of carriers, for example Rocke *et al.* [102] demonstrated acoustically driven storage of light in a quantum well. The intense acoustic fields generated using SAW were used to dissociate optically generated excitons and trap the resulting electron–hole pairs in a moving lateral potential superlattice created by the SAW. This increased the radiative lifetime by several orders of magnitude. When the 2D carriers break up into strips of 2DEG moving at the speed of sound, further increases in the intensity of the SAW causes a decrease in the absorption coefficient and the system appears to be transparent to the SAWs [114, 115]. High-frequency SAWs have also been used to enable single electrons to be carried through a quantum dot formed by a pair of split gates. The aim of these experiments is to make a current standard in which the frequency of the SAW controls the rate of flow of electrons [116–123] (see also Chapter 6).

When the 2DEG is in the centre of the Hall plateau, the Fermi level lies in the tail of localized states between Landau levels. Drichko *et al.* [108] studied the discrepancies between the AC conductivity measured by SAW and quasi-DC transport experiments. They found that at the maxima in the conductivity when the Fermi energy lies in the centre of the extended states, the two conductivities were equal. At all other magnetic fields the AC conductivity was higher. At integer filling factors as  $\sigma_{xx}$  tends to zero the

AC conductivity also reaches a minimum value; however, it can be at least an order of magnitude higher than the quasi-DC measure. They attribute the attenuation of the SAW in this region to localized states. Rampton *et al.* [124] studied the frequency dependence of the SAW attenuation and dispersion at  $\nu = 1$  to obtain information on the lifetime of the localized states. The results were interpreted using the theory of Rampton *et al.* [125] in which the deformation potential interaction between the localized states and the SAW is considered. The relaxation times for the carriers was found to be of the same order as the transport relaxation times in zero field, which at the 350 mK temperature of the experiment were around 100 ps for a 2DEG sample and 20 ps for a 2DHS.

Kagan [126] has derived a fuller treatment for the attenuation and dispersion of the SAW by 2DEGs. The theory considers many effects including the finite air gap between a semiconductor substrate and a lithium niobate piezotransducer, the contribution of the deformation and piezoelectric interactions, and the influence of the diffusivity of the carriers on the SAW as well as the surface conductivity. In 2DEGs the diffusivity is believed to be an insignificant factor in SAW propagation [108]. Kagan derives a different deformation potential interaction to that of Rampton *et al.* [125] and explains that this expression will dominate the interaction considered by these authors. It would be interesting to apply this theory to the results of Rampton *et al.* [124] to see whether with the relevant experimental parameters inserted into the new expressions the interpretation of the experiments is altered.

In another study of the localized states in the centre of a Hall plateau, Drichko *et al.* [112] measure the high-frequency conductivity of GaAs heterostructures in the integer quantum Hall regime. These heterostructures were Si  $\delta$ -doped samples and one of the findings of the experiments is that under conditions of low 2DEG conductivity, the AC conductivity is dominated by the conductivity of the doping layer. After accounting for the effects of this Si  $\delta$ -doping layer, they find that the conductivity at  $\nu = 2$  is due to hopping conduction between mainly nearest neighbour sites (although the parameter values suggest that more remote sites will also retain some influence). The localization length is found to scale with the magnetic length and so is consistent with the picture of nearest neighbour hopping. One advantage the SAW studies have over quasi-DC experiments of the localization length is that SAW attenuation enables it to be measured closer to the centre of the Hall plateaux. A quantitative analysis of the SAW dispersion resulting from the presence of the two conducting layers is not given as the theoretical description for such a situation is unknown.

The experiments just discussed are not the only study of SAW propagation over two conducting layers. Takagaki *et al.* [127, 128] report measurements of the real and imaginary conductivities in asymmetric double quantum well samples in which the widths of the narrow and wide quantum wells are 10 and 15 nm respectively. The barrier separating the wells is 3 nm thick. For the maximum carrier density in the system, around  $1 \times 10^{16} \text{ m}^{-2}$ , a small number of carriers are present in the excited subband whose wave function is concentrated in the narrow quantum well. For lower carrier densities this narrow quantum well is largely unoccupied and the ground state wave function is concentrated in the wide well. The carrier density was adjusted by the persistent photoconductivity effect. A Cole–Cole plot shows that the relaxation approximation is not obeyed well at integer quantum Hall plateaux. This is attributed to the SAW wavelength (1.9  $\mu\text{m}$ ) which is small compared with the elastic mean free path (8.5  $\mu\text{m}$ )

as the relaxation approximation is only valid for wavelengths long compared with the mean free path.

At higher carrier densities the excited subband can have a small population of carriers in it and is therefore just below the Fermi energy. Ignoring the self-consistency of the potential in the structure for a moment, we can see that the lowest Landau level of the second subband crosses the higher Landau levels of the lowest subband. This means that electron transfer might be expected between the two subbands as the magnetic field is raised and the Fermi energy oscillates between the lowest Landau level of the second subband and the Landau levels of the ground state subband. However, as the wells are spatially separated this transfer from one state to another will cause a significant change in the potential. Therefore self-consistency tends to minimize the charge transfer. The barrier also has an effect on the Fermi level. It may act to pin the Fermi level to donor levels in the barrier which would lead to a constant value of  $\sigma_{xx}$  in the second subband even though successive Landau levels in the groundstate subband are depopulated. The attenuation and dispersion of the SAW have several unusual features when the propagation is over such a sample with the second subband slightly populated. The first is that a significant smoothly varying magnetic field dependent background is observed in the SAW transmission even when DC measurements suggest that  $\sigma_{xx} \gg \sigma_m$ . The second is that whilst DC conductivity measurements show no unusual behaviour, the SAW transmission and velocity shift measurements show sudden spikes at the middle of higher field Hall plateaux when the filling factor is an integer, for example  $\nu = 6$  (Fig. 3.23). Using the single layer theory the increase in transmission and the increase

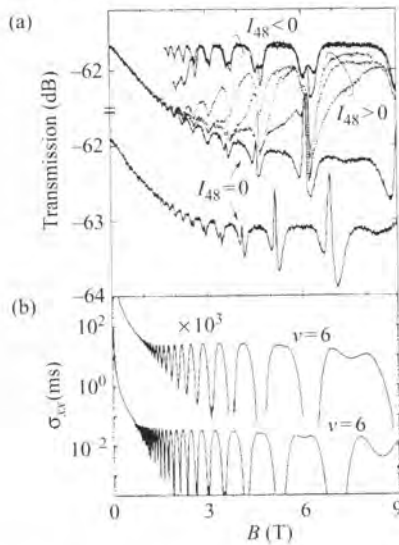


**Fig. 3.23** (a) Transmission amplitude of SAWs in a device with an SAW frequency of 1.56 GHz for two electron densities when second subband is populated. Note the abrupt enhancement of the transmission at 5.2 T and 6.9 T for the lower curve. The upper curves show the change in SAW transmission when a DC current is passed through the sample. The polarity of the current has an effect on the SAW transmission. (b) Diagonal conductivity  $\sigma_{xx}$  measured when  $I_{48} = 0$  at the two electron densities shown in (a). No anomalous behaviour is observed [128].

in velocity would be interpreted as a sudden decrease in the conductivity of the sample. However, no sudden change in the DC conductivity is observed. Similar SAW behaviour has been seen in a double-layer hole gas sample [129] which showed parallel conduction close to  $\nu = 2$ . In this case, however, the quasi-DC behaviour also showed anomalous behaviour. In the case of the asymmetric quantum well sample applying a current through the sample can both remove the slowly varying background and the anomalous features at integer filling factors. The direction of the applied current matters, which may suggest that it is the electric field within the sample that is important rather than the magnitude of the current. The features do coincide with the expected positions for magnetic population/depopulation of the Landau levels and only occur when the second subband is populated by a low density of carriers. A detailed explanation for the effects is still lacking, however, and demonstrates that theories used to investigate single layers of electrons may not be directly extended to double layers where the carriers can interact with each other and the coupling to the SAW piezoelectric field in one layer may be affected by screening in the other.

Double-layer hole systems, in which the carrier density in each layer is closely matched, have been investigated by Dunford *et al.* [100]. The results have proved, so far, to be unexplainable on the basis of the single layer theory. A strong magnetic field dependent background attenuation and velocity shift are observed which increase with the strength of the magnetic field. The magnitudes and the frequency dependence are inconsistent with the theory of SAW interaction given at the start of this section [130]. The theoretical description of the electronic properties of bilayer carrier systems is outside the scope of this review and the reader is referred to two dedicated review articles [131, 132].

In the discussion of SAW experiments up to this point we have assumed that the 2D electron system is spin polarized and that this does not have an influence on the high-frequency conductivity measured by SAW. Tilke *et al.* [133] have studied the validity of the relaxation time approximation in an AISb/InAs/AISb heterostructure using the proximity coupled SAW technique. The 2DEG in the sample is a low-mobility disordered carrier system with a small carrier effective mass of  $0.023 m_e$ . The small effective mass leads to large Landau level splittings and therefore giant quantum oscillations in the attenuation and dispersion of the SAW despite the low mobility of the sample. The relatively large effective  $g$ -factor ( $g = -15$ ) for carriers in the 15 nm InAs quantum well allows the resolution of spin-polarized odd-integer Landau levels. SAWs with frequencies between 0.2 and 2.5 GHz were generated using specially designed IDTs. The results demonstrate a clear violation of the relaxation expressions around  $\nu = 5$  and 7, the highest two odd-integer Landau levels measured. Results for even-integer Landau levels obey the relaxation approximation equations well. At  $\nu = 5$  and 7, the attenuation is higher than predicted whilst the velocity shift is lower than predicted. Another finding is that for these filling factors the observed widths of the  $\Delta v/v$  peaks narrow as the frequency is increased. This is in qualitative agreement with a prediction by Aleiner *et al.* [134] that such narrowing will occur if the SAW wavelength approaches the localization length of the 2DEG. A Cole–Cole plot is shown (Fig. 3.24) which demonstrates that the relaxation approximation is invalid but that there is nothing to indicate an imaginary finite frequency conductivity. The origin of the effect is unknown and this very clear effect deserves further study. Any model to describe these effects has to include a factor

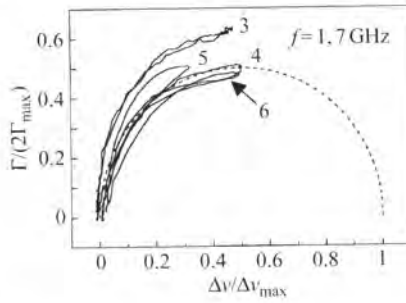


**Fig. 3.24** Cole–Cole plot of the normalized SAW attenuation versus the normalized velocity shift. The expected theoretical curve fits the even-integer filling factors but not the odd integers. The fact that all the curves follow semicircular patterns means that there is no indication of an imaginary part to the diagonal conductivity [133].

which differentiates between odd and integer filling factors and explains the observed frequency dependences. Recent work on lower density 2DHGs has found qualitatively similar behaviour in GaAs heterostructures [130].

### 3.8.4 SAW interaction close to even-denominator fractional quantum Hall states

One of the breakthroughs in the understanding of the FQHE followed high-frequency SAW studies close to  $\nu = 1/2$ . In 1990 Willett *et al.* [135] discovered an anomalous decrease in the velocity and attenuation of short-wavelength SAWs at filling factors close to  $\nu = 1/2$ . This decrease in the velocity and attenuation implies that the conductivity of the 2DEG at these short wavelengths is higher than that predicted by quasi-DC transport measurements. These results were explained by Halperin *et al.* [5] as being due to a composite fermion Fermi surface at  $\nu = 1/2$ . Because of the importance of these results and others that followed they have been described in detail in other review articles (see e.g. [136]) and for this reason these experiments will only be described briefly here. In what follows we shall focus on the behaviour of velocity shift as this can be measured with greater accuracy than the attenuation.

Following the initial discovery of the anomalous decrease in the SAW velocity and transmission around  $\nu = 1/2$ , it was discovered that the higher the frequency (the shorter the wavelength) of the SAW, the stronger the anomalous shift in the velocity and attenuation. At 300 MHz there is almost no sign of the anomalous feature, whereas it is clearly visible at 900 MHz and even stronger at 1.5 GHz (Fig. 3.25). As well as getting deeper, the width, in magnetic field, of the feature also increases with the frequency. As the frequency is increased the feature also persists to temperatures as high as 700 mK at 1.5 GHz.

The key to understanding these results is the formation of a composite fermion Fermi surface at  $\nu = 1/2$  with wavevector  $k_{F,cf} = (4\pi n_s)^{1/2}$ . For a system with impurity scattering the sheet conductivity,  $\sigma_{xx}(k)$ , is predicted to be determined by the quasiparticle

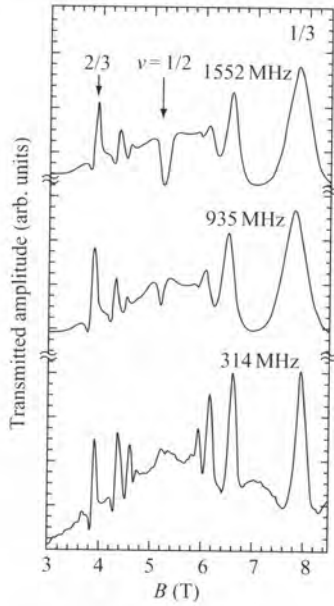


**Fig. 3.25** Transmitted SAW amplitudes for three SAW frequencies of 314, 935, and 1552 MHz. At  $\nu = 1/2$  a minimum can be seen to develop as the frequency of the SAW is increased. This minimum in the SAW transmission is accompanied by a minimum in the SAW velocity and cannot be explained by low frequency conductivity measurements [136].

transport mean free path  $l$  [136]:

$$\sigma_{xx}(k) = \frac{e^2}{8\pi\hbar} \frac{k}{k_{F,cf}} \quad \text{for } kl \gg 2 \quad (3.20)$$

$$\sigma_{xx}(k) = \frac{e^2}{8\pi\hbar} \frac{1}{k_{F,cf} l} \quad \text{for } kl < 2. \quad (3.21)$$

These equations describe a transition from mean free path limited conductivity at small wavevectors to a wavevector-dependent regime in which the conductivity increases linearly with wavevector and is independent of the transport mean free path. Thus if the conductivity can be probed on shorter length scales than the mean free path, it will appear to be enhanced. The SAW creates high-wavevector electric fields within the sample and so measures this enhanced conductivity. The early SAW results showed obvious enhancement for SAW wavelengths  $\sim 3 \mu\text{m}$  leading to an estimate for the composite fermion mean free path of  $\sim 1 \mu\text{m}$ . This mean free path is much smaller than the electron mean free path at zero field because the effect of gauge field scattering is included in the composite fermion mean free path. Later results by Kennedy [137] suggest that the composite fermion mean free path for a hole gas is around half that of the electron system.

Whilst the SAW wavevector at which the effect appears leads to an estimate of the mean free path, the Fermi wavevector can be estimated from the width of the velocity dip in magnetic field. At magnetic fields which deviate from the filling factor of  $1/2$  by

$\Delta B$  the excitations will execute cyclotron motion. The radius  $R_c^*$  of the semi-classical orbits is given by

$$R_c^* = \frac{\hbar k_{F,cf}}{e \Delta B}. \quad (3.22)$$

When  $\Delta B = 0$  the composite particle experiences, on average, no magnetic field and so it moves solely in the direction of SAW propagation—this is the condition for maximum enhancement of the conductivity. At small non-zero values of  $\Delta B$ , a composite fermion executes cyclotron motion and a component of its velocity is perpendicular to the SAW propagation direction. This reduces the enhanced conductivity. At sufficiently high values of  $\Delta B$  the composite fermion motion is effectively orthogonal to the SAW propagation direction and so there is no longer any enhanced conductivity. A simple model of this behaviour suggests that for the width at half-maximum  $R_c^* = \lambda/2$  where  $\lambda$  is the SAW wavelength. This leads to a prediction that the width of the enhanced conductivity feature will increase linearly with wavevector as

$$\frac{\Delta B}{B} = \frac{\hbar k_{F,cf}}{\pi e} k. \quad (3.23)$$

This equation agrees qualitatively with experiment and predicts the expected value of the Fermi wavevector to within a constant of proportionality that is close to one. One small point that should be mentioned is that to get agreement between the high-frequency SAW results and the relaxation approximation equations the value of  $\sigma_m$  is used as a fitting parameter and can differ from the theoretical value given before by up to a factor of 2. The origin of this change in value is unclear.

Halperin *et al.* [5] predicted that at sufficiently high SAW wavevectors (compared with the reciprocal of the quasiparticle mean free path) geometric resonance between the SAW and the cyclotron orbits of the composite fermions would be observed. This commensurability effect assumes that the SAW presents a static wave to the 2DEG. This requires the cyclotron frequency of the composite fermions to be much greater than the SAW frequency and that the Fermi velocity of the composite fermions to be much higher than the SAW velocity. These restrictions impose an upper limit on the composite fermion effective mass of around  $m_e$ , the bare electron mass, given the conditions under which the geometric resonance is observed experimentally. As usual for commensurability oscillations, the composite fermion must execute at least one complete cyclotron orbit without scattering if the effect is to occur. This meant that even higher SAW frequencies and wavevectors were required to allow the effect to occur [138, 139]. Figure 3.26 shows a comparison between experiment and theory using a 10.7 GHz SAW [139]. The agreement is striking and provides strong evidence in favour of the existence of a composite fermion Fermi surface. The position of the minima in the geometric resonance can be used to obtain an estimate of the Fermi wavevector that is in excellent agreement with theory. Shilton *et al.* [140] have demonstrated geometric resonances using the acoustoelectric effect with electrons in small magnetic fields.

The upper limit placed on the composite fermion mass by the geometric resonance experiments is in disagreement with quasi-DC transport measurements in which the composite fermion mass is estimated from Shubnikov–de Haas oscillations [139]. These experiments typically find a higher effective mass. This area is controversial and the

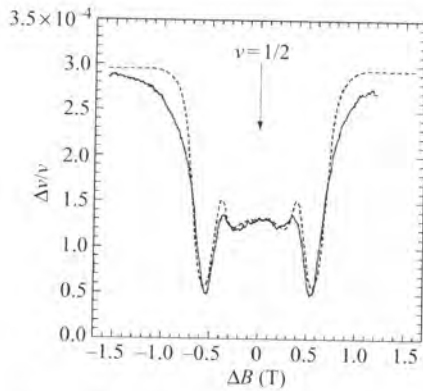


**Fig. 3.26** SAW velocity shift versus magnetic field for 10.7 GHz SAW near  $\nu = 1/2$ . Principal and secondary geometric resonances are present. The temperature is 130 mK. The dashed curve is the theoretical fit to the data assuming a 1 per cent variation in the carrier density across the sample [139].

extraction of the mass from low-frequency transport measurements is not straightforward. Nevertheless the possibility remains that the high-frequency effective mass is smaller than the low-frequency effective mass.

In later experiments Willett *et al.* [141] studied SAW propagation across a 2DEG in which a periodic modulation of the carrier density could be induced electrostatically using a gate in the form of an array of metallic lines. The inspiration for this experiment is the fact that if the composite fermion density is modulated then there must be associated modulations in the gauge field. For propagation perpendicular to the lines of the gate no variation in the SAW propagation was seen. However, when the SAW propagated along the lines of the gate, the minimum in the SAW velocity at  $\nu = 1/2$  could be turned into a maximum by reducing the density of carriers under the gate. This effect is only seen for gate wavelengths less than  $\sim 2 \mu\text{m}$ . Below this wavelength no dependence is seen and above this wavelength the effect quickly drops to zero. The SAW frequency is unimportant to the effect with low SAW frequencies still sensitive to the effect. The gate wavelength points to the importance of the imposed wavevector of the electric field being small compared with the reciprocal of the composite fermion mean free path. For a gate wavelength of  $1.3 \mu\text{m}$ , as the voltage applied to the gate is increased the peak effect at  $1/2$  is turned on (Fig. 3.27). A further increase in the voltage turns the effect off again. In contrast, for a gate wavelength of  $0.9 \mu\text{m}$  no decrease in the magnitude of the peak at  $1/2$  is seen for large bias voltages.

There have been several theoretical attempts to explain this effect [142, 143]. The treatments have examined composite fermion transport in a semi-classical picture using the Boltzmann equation. Both calculations find that under the conditions of the experiments described above there will be a peak in the velocity at a filling factor of  $1/2$ . However, the calculations find that the peak at  $\nu = 1/2$  is caused by a drop in the background around  $1/2$  rather than an increase in the velocity at  $1/2$  with little change to the velocity measurement at  $1/2$  in disagreement with the experimental results. The origin

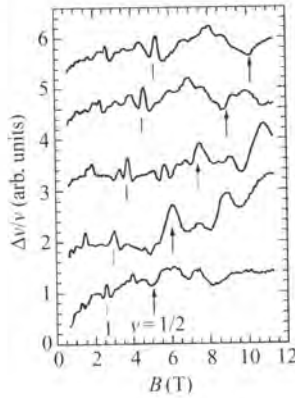


**Fig. 3.27** SAW velocity shift versus magnetic field for a gate period of  $1.3 \mu\text{m}$ . The SAW wavelength is  $0.75 \mu\text{m}$ . The figure shows the behaviour for a large density modulation. The bias voltages relative to the bottom trace are  $+690$ ,  $+530$ ,  $+340$ , and  $+170$  mV from the upper to the lower curves. The data have been offset for clarity. Note how the feature at  $\nu = 1/2$  develops into a strong increase in velocity and then decreases again as the voltage is increased further [141].

of this discrepancy is unclear. A more recent theoretical treatment has been given by Zimbovskaya and Birman [144].

At other even-denominator filling factors such as  $\nu = 1/4$ ,  $3/2$ , and  $3/4$  similar features in the velocity shift to those described above have been seen with geometric resonance being demonstrated at  $\nu = 1/4$  and minima in the SAW velocity observed at  $\nu = 3/2$ , and  $3/4$ . Recently Willett *et al.* [145] have reported studies around  $\nu = 5/2$ . This is an especially important study as at low temperatures the FQHE has been observed at  $\nu = 5/2$  at very low temperatures [146], the only even-denominator filling factor for which the FQHE is known to occur. Theoretical descriptions of this state have centred around paired composite fermions. The first step in experimentally verifying the theoretical description is to establish the validity of the composite fermion picture when several Landau levels are filled and to show the existence of a composite fermion Fermi surface. The SAW experiments were carried out at 280 mK, above the temperature at which the FQHE state forms. Using SAW frequencies of 5.8 GHz and above the signature of a composite fermion Fermi surface was observed (Fig. 3.28), consistent with a picture in which composite fermions pair up at a lower temperature to form the FQHE liquid state. Further SAW experiments are needed at lower temperatures to follow the development of the fractional quantum Hall state.

The discovery of the composite fermion Fermi surface has revolutionized the understanding of the FQHE. SAW experiments remain one of the most useful probes of even-denominator filling factor states. The recent study around  $\nu = 5/2$  demonstrates that SAWs have the potential to continue providing important insights into the fascinating quantum liquid states of low-dimensional systems.

### 3.8.5 SAW interaction with the high magnetic field insulating phase

At temperatures less than around 200 mK and at filling factors less than  $\nu = 1/5$  for high-mobility electron systems and  $\nu = 1/3$  for high-mobility hole systems the

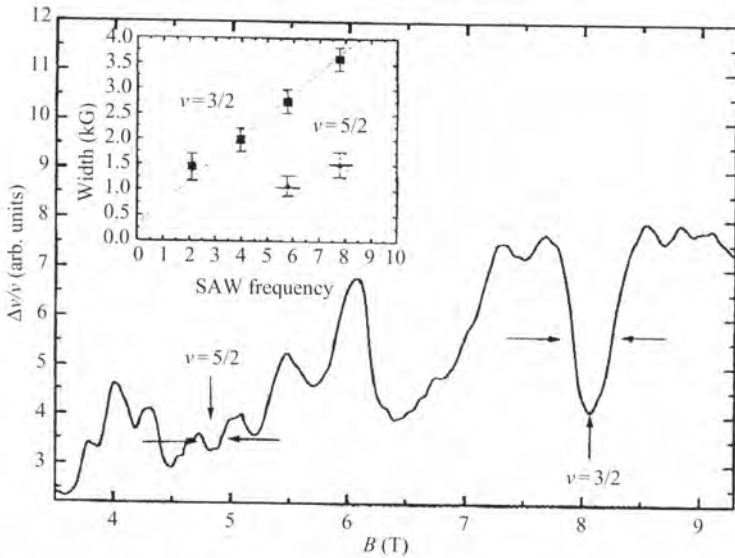


**Fig. 3.28** SAW velocity shift in the region of  $\nu = 5/2$  and  $\nu = 3/2$  in an extremely high-mobility 2DEG. The SAW measurement was made at 7.8 GHz at 280 mK. The inset plots the width of the features for different SAW frequencies at  $\nu = 3/2$  and  $5/2$ . The velocity minima measured at 7.8 GHz close to  $\nu = 5/2$  appear to exhibit some structure rather than being simple minima. It is unlikely that the structure is due to geometric resonance as no features are seen at  $\nu = 3/2$  [145].

low-dimensional systems become insulating. One of the features of these systems is the existence of low-lying excitation modes known as magnetophonons. Evidence for magnetophonons has been largely provided by microwave experiments [147]–[151]. There has been one SAW experiment which observed absorption of SAW by these modes [152]. The experiment demonstrates the usefulness of Cole–Cole plots in interpreting SAW data. Figure 3.29 shows the Cole–Cole plot at fixed magnetic field as the temperature is varied for several SAW frequencies. It is apparent that at particular temperatures the data break off from the semicircle expected of a relaxation mechanism. The manner in which the data break away from the semicircle indicates that the SAW dispersion curve has crossed the magnetophonon excitation curve, the inset shows the lowest temperature deviation of the measured velocity shift from the relaxation curve. As can be seen the magnetophonon mode is found to occur at about 1 GHz. Unfortunately in order to see higher wavevector absorptions the SAW dispersion curve would have to cross the magnetophonon curve again. If this occurs it will only happen at very high SAW frequencies and depending on the exact form of the magnetophonon excitation curve it may not happen at all. This is why microwave experiments are much more useful for the insulating phase as a meander transmission line can generate microwave fields with spatial harmonics of the meandering transmission line guaranteeing that there will be multiple crossings of the magnetophonon excitation curve [148].

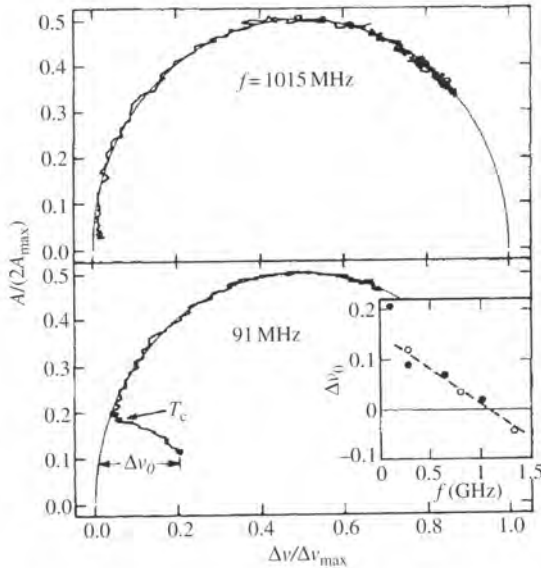


**Fig. 3.29** A Cole–Cole plot of normalized attenuation versus normalized velocity shift at two different SAW frequencies for a constant magnetic field ( $\nu = 0.167$ ) as the temperature is varied. The inset shows the deviation of the velocity shift at the lowest temperature for two samples as a function of frequency [152].

### 3.8.6 Acoustoelectric studies of the quantum Hall states

When an SAW passes over a 2DEG, as well as affecting the velocity and transmission of the SAW, DC voltages and currents can be generated by non-linear interactions in the 2DEG. The effect is related to thermopower measurements. The first studies of the acoustoelectric effect were conducted by Esslinger *et al.* [153]. The experiments measured the acoustoelectric voltages and currents induced by the SAW in a Hall bar geometry. To measure the voltages, a voltmeter was attached between the relevant contacts in an ‘open’ geometry, whilst to measure the currents the induced current flowed out of the contacts into a current amplifier in a ‘shorted’ geometry. To help with the measurement of the signal the SAW generated by the transducers was AM or FM modulated at low frequencies to turn the SAW on and off. The currents and voltages could then be measured using standard lock-in-amplifier techniques.

In the shorted geometry the longitudinal acoustoelectric current,  $J_x$ , and transverse voltage,  $V_y^s$ , were measured. It was found that  $J_x$  exhibited oscillations that resembled those of the SAW attenuation with double peak structures observed at well-developed integer quantum Hall filling factors. As  $\sigma_{xx}$  tended to zero, so the longitudinal acoustoelectric current also tended to zero. The ratio  $V_y^s/J_x$  was used to define an acoustoelectric Hall resistance. At high Landau levels this was found to be quantized into plateaux identical to the low-frequency Hall resistance, but at  $\nu = 4$  and 6 an asymmetric signal was seen.

In the open geometry the longitudinal and transverse voltages,  $V_x$  and  $V_y$  respectively, were measured. The longitudinal voltage behaved in a similar fashion to  $J_x$ . The transverse voltage displayed bipolar peaks at  $\nu = 1, 2,$  and  $4$ . Theoretical work by Fal'ko *et al.* [154] explains the major features of the experiments. The model assumes that the conductivities  $\sigma_{xx}$  and  $\sigma_{xy}$  are local quantities of the 2DEG on the scale of the SAW wavelength. The SAW is considered to induce a change in the density of the 2DEG and by accounting for the screening of the SAW field by the 2DEG and relating the local current to the electric field and the gradient of the charge density, the induced current components can be calculated. To obtain a DC component of the current a non-linearity is required to rectify the AC current; in this model the non-linearity is due to the variation of the conductivity with the carrier density. Using the measured low-frequency resistivity tensor the acoustoelectric response can be estimated. A comparison between theory and experiment shows that satisfactory agreement is obtained (Fig. 3.30) [155].

Kennedy *et al.* carried out investigations of longitudinal and transverse acoustoelectric voltages in Hall bar structures made from high-mobility hole gases [156] in the fractional quantum Hall regime. They discovered that for filling factors less than one the transverse and longitudinal acoustoelectric fields  $E_y$  and  $E_x$ , respectively, have a derivative relationship to each other, namely

$$E_y = \alpha_E B \frac{dE_x}{dB} \quad (3.24)$$

where  $\alpha_E$  is a sample-dependent constant of the order of 0.02. This is similar to the relationship seen between low-frequency conductivity tensor components and

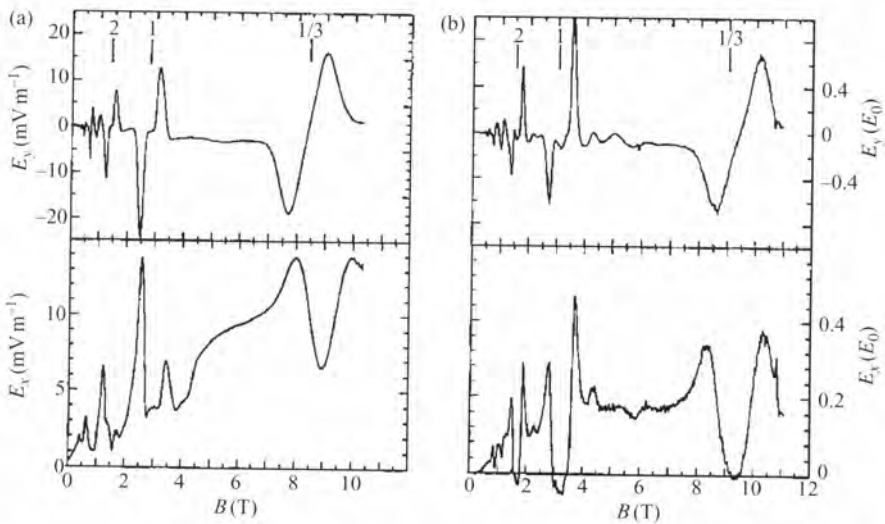


**Fig. 3.30** A comparison between (a) experimental and (b) theoretically predicted acoustoelectric fields [155]. The frequency of the SAW was 144 MHz and the temperature was 0.5 K. The longitudinal field is denoted by  $E_x$  and the transverse field by  $E_y$ . The theoretical predictions are made on the basis of the low frequency conductivity and the theory of ref. [154]. As the intensity of the SAW is not known the predicted acoustoelectric fields have an unknown scaling factor.

thermopower components [157–160]. The origin of this effect is thought to be due to inhomogeneity in the sample. Kennedy *et al.* have also shown that the acoustoelectric effect is a sensitive probe of the composite fermion Fermi surface, observing well-developed features in the acoustoelectric effect close to  $\nu = 1/2$  at SAW frequencies which only show very weak features in the velocity shift and attenuation of the SAW. The origin of this sensitivity is unclear but may be related to the model of Fal'ko *et al.* in which the derivative of the conductivity with respect to filling factor is an important element in determining the acoustoelectric current.

Preliminary results of acoustoelectric experiments on bilayer hole systems have recently been published [161]. The results show bipolar longitudinal acoustoelectric voltages which are currently not understood but may be related to results found for other drag experiments in bilayer systems [162, 163].

### 3.9 Conclusions

Phonon emission in the integer quantum Hall regime occurs predominantly from the two current entry and exit corners of the device ('hot spots'). At breakdown, dissipation starts along dissipative filaments crossing the sample width. Phonons emitted from the corners of 2DEGs in magnetically quantized Si-MOSFETS consist largely of cyclotron phonons arising from inter-Landau level transitions. These are essentially forbidden by momentum conservation in GaAs heterostructures and it seems likely that at low electron temperatures, phonon emission takes place via two-phonon processes, although this has not yet been verified experimentally. Absorption processes by 2DEGs in Si-MOSFETS and GaAs heterostructures also differ markedly. Inter-Landau level transitions have been observed in Si-MOSFETS, but not yet in GaAs heterostructures except at edges where the energy required is much less. This difference in the behaviour of 2DEGs in the two material systems is largely due to the differences in their effective masses and hence in the extent of their electron wave functions. Since holes in GaAs have appreciably larger effective masses, phonon interaction with magnetically quantized 2DHGs in GaAs is expected to behave more like the interaction with 2DEGs in Si than in GaAs but rather little work has been done so far to support this.

Phonon-induced intra-Landau level transitions are important in both types of material system if at least one Landau level is partially filled. This is the case if the Fermi energy is located inside a Landau level or if electrons are thermally excited to upper levels to a significant degree. One or more of these conditions normally applies within the hot spot corners and also in the bulk of the 2DEG above breakdown. This also seems likely to be the case in 2DHGs.

In strong magnetic fields the electron-phonon coupling increases in strength and varies as  $T^4$  rather than as  $T^5$ . This is due to breakdown of momentum conservation due to frequent collisions between the carriers and the intrinsic disorder in the sample. At a filling factor of  $1/2$  theoretical predictions suggest that the presence of composite fermions will alter the electron-phonon coupling. Whilst SAW experiments certainly see interesting behaviour at  $\nu = 1/2$  ballistic phonon experiments have not seen any anomalous behaviour. This may be due to a lack of sensitivity of these experiments at

$\nu = 1/2$  because the temperature dependence of the longitudinal resistance of the 2DEG is small at this filling factor.

In the fractional quantum Hall regime ballistic phonon experiments have measured the magnetoroton energy gaps and find good agreement with theoretical estimates. Angle-resolved measurements have resulted in the first measurements of the dispersion curve of the magnetoroton excitations in which the in-plane momentum is known, albeit with significant uncertainties caused by the size of the device and phonon focusing in the substrate.

SAWs have been a very important probe of 2DEGs in the quantum Hall regime. The ability of SAW experiments to measure local properties of the 2DEG at high frequencies and short length scales means that they can provide unique insight into the quantum Hall system. The most significant SAW experiments have been those of Willett and co-workers. These experiments led to the discovery of the composite fermion Fermi surface and continue to provide important insights, most recently at  $\nu = 5/2$ . Whilst the simple relaxation model provides a satisfactory framework for analysing results most of the time, there are situations when significant deviations from this model have been seen. Further theoretical work to correct this model would be of benefit. Acoustoelectric effects occur when non-linearities in the 2DEG cause rectification of induced acoustoelectric currents. The effects of sample inhomogeneity and the composite fermion Fermi surface can be seen in acoustoelectric measurements.

In summary, phonon and SAW techniques provide important insights into the quantum Hall regime. Phonon emission and absorption show where dissipation is occurring in the samples and allow the measurement of energy gaps at finite wavevectors at fractional quantum Hall filling factors. SAW measurements can study localized states and the high-frequency conductivity of the 2DEG which has provided the cleanest probe of the properties of composite fermions. Future directions in this area include improving the modelling of the phonon absorption in the FQHE to include phonon anisotropy effects, SAW measurements at  $\nu = 5/2$  at temperatures below 100 mK, and studies of bilayer systems. To understand bilayer systems well it is clear that new theoretical models are needed to account for the screening of one layer by the other.

## Acknowledgements

We are very grateful to Drs K.A Benedict, A.J. Kent, and F.F. Ouali and Prof. F.W. Sheard for helpful comments and discussion during the writing of this chapter and to all the students, postdoctoral researchers, and colleagues who have made the study of these effects such a pleasurable experience.

## References

1. Ezawa, Z.F. (2000). *Quantum Hall effects*, World Scientific, Singapore.
2. Yoshioka, D. (2002). *The quantum Hall effect*, Springer-Verlag, Heidelberg.
3. Laughlin, R.B. (1983). *Phys. Rev. Lett.*, **50**, 1395.
4. Jain, J.K. (1992). *Adv. Phys.*, **41**, 105.

5. Halperin, B.I., Lee, P.A., and Read, N. (1993). *Phys. Rev.*, **B47**, 7312.
6. Cage, M.E., Field, B.F., and Dziubar, R.F. (1985). *IEEE Trans. Instrum. Meas.*, **34**, 301.
7. Hartland, A., Jones, K., Williams, J.M., Gallagher, B.L., and Galloway, T. (1991). *Phys. Rev. Lett.*, **66**, 969.
8. Prange, R.E. and Girvin, M.L. (eds) (1990). *The quantum Hall effect* (2nd edn), Springer-Verlag, New York.
9. Chakraborty, T. and Pietiläinen, P. (1995). *The quantum Hall effect* (2nd edn), Springer-Verlag, Berlin.
10. Das Sarma, T. and Pinczuk, A. (eds) (1997). *Perspectives in quantum Hall effects*, Wiley, New York.
11. Dietsche, W. (1999). *Pers. Comm.*
12. Xin, Z., Ouali, F.F., Challis, L.J., Salce, B., and Cheng, T.S. (1996). *Physica*, **B219–220**, 56.
13. Toombs, G.A., Sheard, F.W., Neilson, D., and Challis, L.J. (1987). *Solid State Commun.*, **64**, 577.
14. Maslov, D.L., Levinson, Y.B., and Badalian, S.M. (1992). *Phys. Rev.*, **B46**, 7002.
15. Fal'ko, V.I. and Challis, L.J. (1993). *J. Phys. C: Solid State Phys.*, **5**, 3945.
16. Uchimura, N. and Uemura, Y. (1979). *J. Phys. Soc. Jpn.*, **47**, 1417.
17. Iordanskii, S.V. and Muzykantskii, B.A. (1989). *Zh. Eksp. Teor. Fiz.*, **96**, 1783. (*Sov. Phys. JETP*, **69**, 1006.)
18. Tamura, S. and Kitagawa, H. (1989). *Phys. Rev.*, **B40**, 8485.
19. Benedict, K.A. (1991). *J. Phys. C.*, **3**, 1279.
20. Benedict, K.A. (1992). *J. Phys. C.*, **4**, 4083.
21. Eisenstein, J.P., Gossard, A.C., and Narayanamurti, V. (1987). *Phys. Rev. Lett.*, **59**, 1341.
22. Kent, A.J., Hardy, G.A., Hawker, P., and Hurley, D.C. (1990). In *Phonons 89*, (ed. S. Hunklinger, W. Ludwig, and G. Weiss), p. 1010, World Scientific, Singapore.
23. Eaves, L. and Sheard, F.W. (1986). *Semicond. Sci. Technol.*, **1**, 346.
24. Ebert, G., v. Klitzing, K., Ploog, K., and Weimann, W. (1983). *J. Phys. C.*, **16**, 5441.
25. Blik, L., Braun, E., Hein, G., Kose, V., Niemeyer, J., Weimann, G., and Schlapp, W. (1986). *Semicond. Sci. Technol.*, **1**, 110.
26. Kawaji, S. (1996). *Semicond. Sci. Technol.*, **11**, 1546.
27. Eaves, L. (1998). *Physica*, **B256–258**, 47.
28. Komiyama, S., Takamasu, T., Hiyamizu, S., and Sasa, S. (1985). *Solid State Commun.*, **54**, 479.
29. Büttiker, M. (1988). *Phys. Rev.*, **B38**, 9375 and private communication.
30. Komiyama, S. and Hirai, H. (1989). *Phys. Rev.*, **B40**, 7767.
31. Van Son, P.C. and Klapwijk, T.M. (1990). *Europhys Lett.*, **12**, 429.
32. Komiyama, S., Hirai, H., Ohsawa, M., Matsuda, Y., Sasa, S., and Fujii, T. (1992). *Phys. Rev.*, **B45**, 11085.
33. Riess, J. (1993). *Physica*, **B190**, 366.
34. Halperin, B.I. (1982). *Phys. Rev.*, **B25**, 2185.
35. Shik, A.Y. (1992). *Fiz. Tekh. Poluprov.*, **26**, 855. (*Sov. Phys. Semicond.*, **26**, 481).
36. McKitterick, D.J., Shik, A., Kent, A.J., and Henini, M. (1994). *Phys. Rev.*, **B49**, 2585.
37. Chow, E., Wei, H.P., Girvin, S.M., and Shayegan, M. (1996). *Phys. Rev. Lett.*, **77**, 1143.
38. Jasiukiewicz, Cz., Lehmann, D., and Paszkiewicz, T. (1992). *Z. Phys.*, **B86**, 225.
39. Jasiukiewicz, Cz., Paszkiewicz, T., and Lehmann, D. (1994). *Z. Phys.*, **B96**, 213.
40. Lehmann, D. (1994). In *Die kunst of phonons* (ed T. Paszkiewicz and K. Rapcewicz), p. 211, Plenum, New York.
41. Gañza, W.M., Jasiukiewicz, Cz., Kent, A.J., Lehmann, D., Paszkiewicz, T., Strickland, K.R., and Strickland, R.E. (1996). *Semicond. Sci. Technol.*, **11**, 1030.
42. Fontein, P.F., Hendriks, P., Blom, F.A.P., Wolter, J.H., Giling, L.J., and Beenakker, C.W.J. (1992). *Surf. Sci.*, **263**, 91.

43. Knott, R.G., Dietsche, W., v. Klitzing, K., Eberl, G., and Ploog, K. (1995). *Semicond. Sci. Technol.*, **10**, 117.
44. Wakabayashiji, J. and Kawaji, S. (1978). *J. Phys. Soc. Jpn.*, **44**, 1839.
45. Russell, P.A., Ouali, F.F., Hewett, N.P., and Challis, L.J. (1990). *Surf. Sci.*, **229**, 54.
46. Ouali, F.F., Challis, L.J., and Cooper, J.J. (1992). *Semicond. Sci. Technol.*, **7**, 606.
47. Klass, U., Dietsche, W., and v. Klitzing, K. (1991). *Z. Phys.*, **B82**, 351.
48. Xin, Z., Ouali, F.F., Challis, L.J., Cooper, J., Jezierskii, A., and Henini, M. (1994). *Semicond. Sci. Technol.*, **9**, 800.
49. Xin, Z., Ouali, F.F., Challis, L.J., Jezierskii, A., and Henini, M. (1995). In *High magnetic fields in the physics of semiconductors* (ed. D. Heiman), p. 138, World Scientific, Singapore.
50. Dietsche, W., Dietzel, F., Klass, U., and Knott, R. (1993). In *Phonon scattering in condensed matter VII* (ed. M. Meissner and R.O. Pohl), p. 345, Springer-Verlag, Berlin.
51. Kent, A.J. (1991). *Physica*, **B169**, 356.
52. Wilks, J. and Betts, D.S. (1987). *An introduction to liquid helium (2nd edn)*, Oxford University Press, Oxford.
53. Knott, R.G. (1994). Ph.D. thesis, University of Stuttgart.
54. Klass, U. (1992). Ph.D. thesis, University of Stuttgart.
55. Kent, A.J., Rampton, V.W., Newton, M. I., Carter, P.J.A., Hardy, G.A., Hawker, P., Russell, P.A., and Challis L.J. (1988). *Surf. Sci.*, **196**, 410.
56. Cooper, J., Challis, L.J., Ouali, F.F., and Mellor, C.J. (1995). *Phys. Rev.*, **B51**, 70.
57. Burger, W. and Lassmann, K. (1984). *Phys. Rev. Lett.*, **53**, 2035.
58. Roshko, S. and Dietsche, W. (1996). *Solid State Commun.*, **98**, 453.
59. Roshko, S., Dietsche, W., and Challis, L.J. (1998). *Phys. Rev. Lett.*, **80**, 3835.
60. Hawker, P., Kent, A.J., Challis, L.J., Henini, M., and Hughes, O.H. (1989). *J. Phys. Condens. Matter*, **1**, 1153.
61. Gornik, E., Schwartz, R., Tsui, D.C., Gossard, A.C., and Wiegmann, W. (1981). *Solid State Commun.*, **98**, 453.
62. v. Klitzing, K., Ebert, G., Kleinmichel, N., Obloh, H., Dorda, G., and Weimann, G. (1985). In *Proc. Int. Conf. of the physics of semiconductors* (ed. J.D. Chadi and W.A. Harrison), p. 271, Springer-Verlag, New York.
63. Gornik, E., Seidenbusch, W., Christanell, R., Lassnig, R., and Pidgeon, C.R. (1988). *Surf. Sci.*, **196**, 339.
64. Diebel, E., Sigg, H., and v. Klitzing, K. (1991). *Infrared Phys.*, **32**, 69.
65. Zinov'ev, N.N., Fletcher, R., and Challis, L.J. (1994). *Phys. Rev.*, **B49**, 14466.
66. Kawano, Y., Hisanaga, Y., and Komiyama, S. (1999). *Phys. Rev.*, **B59**, 12537.
67. Kent, A.J., McKitterick, D.J., Challis, L.J., Hawker, P., Mellor, C.J., and Henini, M. (1992). *Phys. Rev. Lett.*, **69**, 1684.
68. Kent, A.J., Hardy, G.A., Hawker, P., Rampton, V.W., Newton, M.I., Russell, P.A., and Challis, L.J. (1988). *Phys. Rev. Lett.*, **61**, 180.
69. Kappus, W. and Weis, O. (1973). *J. Appl. Phys.*, **44**, 1947.
70. Rösch, F. and Weis, O. (1977). *Z. Phys.*, **B27**, 33.
71. Roshko, S., Zhitomirsky, V., Cooper, U., Wiesner, W., Dietsche, W., and Eberl, K. (1996). *Physica*, **B219-230**, 16.
72. Wiesner, U., Roshko, S., Dietsche, W., v. Klitzing, K., and Eberl, K. (1997). In *High magnetic fields in the physics of semiconductors II*, Vol. 1 (ed. G. Landwehr and W. Ossau), pp.23-6, World Scientific, Singapore.
73. Challis, L.J., (1995). *J. Phys. C: Solid State Phys.*, **6**, 481.
74. Schulze-Wischeler, F., Zeitler, U., Hohls, F., Haug, R.J., Reuter, D., and Wieck, A.D. (2002). *Physica*, **E12**, 474.
75. Kershaw, Y.M., Bending, S., Dietsche, W., and Eberl, K. (1996). *Semicond. Sci. Technol.*, **11**, 1036.

76. Dietzel, F., Dietsche, W., and Ploog, K. (1993). *Phys. Rev.*, **B48**, 4713.
77. Dietzel, F., Klass, U., Dietsche, W., and Ploog, K. (1994). In *Die kunst of phonons*, (ed. T. Paszkiewicz and K. Rapcewicz), pp. 189–200, Plenum, New York.
78. Tsui, D.C., Stormer, H.L., and Gossard, A.C. (1982). *Phys. Rev. Lett.*, **48**, 1559.
79. Girvin, S.M., MacDonald, A.H., and Platzman, P.M. (1986). *Phys. Rev.*, **B33**, 2481.
80. Feynman, R.P. and Cohen, M. (1956). *Phys. Rev.*, **102**, 1189; Feynman, R.P. (1972). *Statistical mechanics*, W.A. Benjamin, Reading, MA.
81. Saminadayar, L., Glattli, D.C., Jin, Y., and Etienne, B. (1997). *Phys. Rev. Lett.*, **79**, 2526.
82. de Picciotto, R., Reznikov, M., Heiblum, M., Umansky, V., Bunin, G., and Mahalu, D. (1997). *Nature*, **389**, 162.
83. Willett, R.L., Eisenstein, J.P., Stormer, H.L., Tsui, D.C., Gossard, A.C., and English, J.H. (1982). *Phys. Rev. Lett.*, **59**, 1776.
84. Willett, R.L., Stormer, H.L., Tsui, D.C., Gossard, A.C., and English, J.H. (1988). *Phys. Rev.*, **B37**, 8476.
85. Nicholas, R.J. (1997). In *Electron: a centenary volume* (ed. M. Springford), pp. 237–56, Cambridge University Press, Cambridge.
86. Kukushkin, I.V., Smet, J.H., von Klitzing, K., and Wegscheider, W. (2002). *Nature*, **415**, 409.
87. Jain, J.K. (1997). In *Perspectives in quantum Hall effects* (ed. S. Das Sarma and A. Pinczuk), pp. 265–05, Wiley, New York; Jain, J. K. (2000). *Phys. Today*, **53**, 39.
88. Khveshchenko, D.V. and Reizer, M.Yu. (1997). *Phys. Rev. Lett.*, **78**, 3531.
89. Zeitler, U., Devitt, A.M., Digby, J.E., Mellor, C.J., Kent, A.J., Benedict, K.A., and Cheng, T. (1999). *Phys. Rev. Lett.*, **82**, 5333.
90. Pinczuk, A. (1997). In *Perspectives in quantum Hall effects* (ed. S. Das Sarma and A. Pinczuk), pp. 307–41, Wiley, New York.
91. Davies, H.D.M., Harris, J.C., Ryan, J.F., and Turberfield, A.J. (1997). *Phys. Rev. Lett.*, **78**, 4095.
92. Kang, M., Pinczuk, A., Dennis, B.S., Pfeiffer, L.N., and West, K.W. (2001). *Phys. Rev. Lett.*, **86**, 2637.
93. Scarola, V.W., Park, K., and Jain, J.K. (2000). *Phys. Rev.*, **B61**, 13064.
94. Benedict, K.A., Hills, R.K., and Mellor, C.J. (1999). *Phys. Rev.*, **B60**, 10984.
95. Devitt, A.M., Roshko, S.H., Zeitler, U., Mellor, C.J., Kent, A.J., Benedict, K.A., Cheng, T., and Henini, M. (2000). *Physica*, **E6**, 47.
96. Devitt, A.M., Roshko, S.H., Kent, A.J., Benedict, K.A., Mellor, C.J., and Henini, M. (2002). *Physica*, **B316**, 101.
97. Devitt, A.M. (2000). Ph.D. thesis, University of Nottingham.
98. Benedict, K.A. and Hills, R.K. (2001). *Phys. Rev.*, **B6323**, 235304.
99. Apalkov, V.M. and Portnoi, M.E. (2002). *Phys. Rev.*, **B66**, 121303.
100. Dunford, R.B., Gates, M.R., Mellor, C.J., Rampton, V.W., Chauhan, J.S., Middleton, J.R., and Henini, M. (2002). *Physica*, **B316**, 219.
101. Nash, G.R., Bending, S.J., Boero, M., Grambow, P., Eberl, K., and Kershaw, Y. (1996). *Phys. Rev.*, **B54**, R8337; Nash, G.R., Bending, S.J., Boero, M., Grambow, P., Eberl, K., and Kershaw, Y. (1997). *Phys. Rev.*, **B55**, 10120; Nash, G.R., Bending, S.J., Boero, M., Riek, M., and Eberl, K. (1999). *Phys. Rev.*, **B59**, 7649; Nash, G.R., Bending, S.J., Riek, M., and Eberl, K. (2001). *Phys. Rev.*, **B63**, 113316.
102. Roche, C., Zimmermann, S., Wixforth, A., Kotthaus, J.P., Bohm, G., and Weimann, G. (1997). *Phys. Rev. Lett.*, **78**, 4099.
103. Oliner, A.A. (ed.) (1978). *Acoustic surface waves*, Springer-Verlag, Berlin, New York.
104. Hutson, A.R. and White, D. (1962). *J. Appl. Phys.*, **33**, 40.
105. Adler, R. (1971). *IEEE Trans. Sonics Ultrason.*, **SU-18**, 115.
106. Wixforth, A., Kotthaus, J.P., and Weimann, G. (1986). *Phys. Rev. Lett.*, **56**, 2104.
107. Wixforth, A., Scriba, J., Wassermeier, M., Kotthaus, J.P., Weimann, G., and Schlapp, W. (1989). *Phys. Rev.*, **B40**, 7874.

108. Drichko, I.L., Dyakonov, A.M., Kreshchuk, A.M., Polyanskaya, T.A., Savelev, I.G., Smirnov, I.Y., and Suslov, A.V. (1997). *Semiconductors*, **31**, 384.
109. Drichko, I.L. and Smirnov, I.Y. (1997). *Semiconductors*, **31**, 933.
110. Drichko, I.L., D'Yakonov, A.M., Smirnov, I.Y., Preobrazhenskii, V.V., and Toropov, A.I. (1999). *Semiconductors*, **33**, 892.
111. Drichko, I.L., Diakonov, A.M., Preobrazhenskii, V.V., Smirnov, I.Y., and Toropov, A.I. (2000). *Physica*, **B284**, 1732.
112. Drichko, I.L., Diakonov, A.M., Smirnov, I.Y., Galperin, Y.M., and Toropov, A.I. (2000). *Phys. Rev.*, **B62**, 7470.
113. Rotter, M., Ruile, W., Scholl, G. and Wixforth, A. (2000). *IEEE Trans. Ultrason. Ferroelectr. Freq. Control*, **47**, 242.
114. Govorov, A.O., Kalameitsev, A.V., Rotter, M., Wixforth, A., Kotthaus, J.P., Hoffmann, K.H., and Botkin, N. (2000). *Phys. Rev.*, **B62**, 2659.
115. Govorov, A.O., Kalameitsev, A.V., Kovalev, V.M., Kutschera, H., and Wixforth, A. (2001). *Phys. Rev. Lett.*, **87**, 226803.
116. Shilton, J.M., Mace, D.R., Talyanskii, V.I., Galperin, Y., Simmons, M.Y., Pepper, M., and Ritchie, D.A. (1996). *J. Phys. Condens. Matter*, **8**, L337.
117. Shilton, J.M., Talyanskii, V.I., Pepper, M., Ritchie, D.A., Frost, J.E.F., Ford, C.J.B., Smith, C.G., and Jones, G.A.C. (1996). *J. Phys. Condens. Matter*, **8**, L531.
118. Talyanskii, V.I., Shilton, J.M., Pepper, M., Smith, C.G., Ford, C.J.B., Linfield, E.H., Ritchie, D.A., and Jones, G.A.C. (1997). *Phys. Rev.*, **B56**, 15180.
119. Cunningham, J., Talyanskii, V.I., Shilton, J.M., Pepper, M., Simmons, M.Y., and Ritchie, D.A. (1999). *Phys. Rev.*, **B60**, 4850.
120. Cunningham, J., Talyanskii, V.I., Shilton, J.M., Pepper, M., Kristensen, A., and Lindelof, P.E. (2000). *Phys. Rev.*, **B62**, 1564.
121. Cunningham, J., Talyanskii, V.I., Shilton, J.M., Pepper, M., Kristensen, A., and Lindelof, P.E. (2000). *Physica*, **B280**, 493.
122. Cunningham, J., Talyanskii, V.I., Shilton, J.M., Pepper, M., Kristensen, A., and Lindelof, P.E. (2000). *J. Low Temp. Phys.*, **118**, 555.
123. Robinson, A.M., Talyanskii, V.I., Pepper, M., Cunningham, J.E., Linfield, E.H., and Ritchie, D.A. (2002). *Phys. Rev.*, **B65**, 045313.
124. Rampton, V.W., Kennedy, I., Mellor, C.J., Bracher, B., Henini, M., Foxon, C.T., and Harris, J.J. (2001). *Semicond. Sci. Technol.*, **16**, 136.
125. Rampton, V.W., McEnaney, K.B., and Kozorezov, A.G. (1992). *Semicond. Sci. Technol.*, **7**, 641–7.
126. Kagan, V.D. (1997). *Semiconductors*, **31**, 407.
127. Takagaki, Y., Wiebicke, E., Friedland, K.J., and Ploog, K.H. (2002). *Jpn. J. Appl. Phys. Part 1*, **41**, 2583.
128. Takagaki, Y., Wiebicke, E., Friedland, K.J., and Ploog, K.H. (2001). *Semicond. Sci. Technol.*, **16**, 144.
129. Gates, M.R., Dunford, R.B., Mellor, C.J., Rampton, V.W., Chauhan, J.S., Middleton, J.R., and Henini, M. (2001). *Physica*, **B298**, 70.
130. Gates, M.R. (2002). Ph.D. thesis, University of Nottingham.
131. Eisenstein, J.P. (1997). In *Perspectives in quantum Hall effects* (ed. S. Das Sarma and A. Pinczuk), pp. 265–305, Wiley, New York.
132. Girvin, S.M. and MacDonald, A.H. (1997). In *Perspectives in quantum Hall effects* (ed. S. Das Sarma and A. Pinczuk), pp. 265–305, Wiley, New York.
133. Tilke, A., Rocke, C., and Wixforth, A. (1999). *Physica*, **E5**, 41.
134. Aleiner, I.L. and Shklovskii, B.I. (1994). *Int. J. Mod. Phys.*, **B8**, 801.
135. Willett, R.L., Paalanen, M.A., Ruel, R.R., West, K.W., Pfeiffer, L.N., and Bishop, D.J. (1990). *Phys. Rev. Lett.*, **65**, 112.
136. Willett, R.L. (1997). *Adv. Phys.*, **46**, 447, Taylor & Francis Ltd., [www.tandf.co.uk/journals](http://www.tandf.co.uk/journals).

137. Kennedy, I. (1998). Ph.D. thesis, University of Nottingham.
138. Willett, R.L., Ruel, R.R., West, K.W., and Pfeiffer, L.N. (1993). *Phys. Rev. Lett.*, **71**, 3846.
139. Willett, R.L., West, K.W., and Pfeiffer, L.N. (1995). *Phys. Rev. Lett.*, **75**, 2988.
140. Shilton, J.M., Mace, D.R., Talyanskii, V.I., Simmons, M.Y., Pepper, M., Churchill, A.C., and Ritchie, D.A. (1995). *J. Phys. Condens. Matter*, **7**, 7675.
141. Willett, R.L., West, K.W., and Pfeiffer, L.N. (1997). *Phys. Rev. Lett.*, **78**, 4478.
142. von Oppen, F., Stern, A., and Halperin, B.I. (1998). *Phys. Rev. Lett.*, **80**, 4494.
143. Mirlin, A.D., Wolfle, P., Levinson, Y., and Entin-Wohlman, O. (1998). *Phys. Rev. Lett.*, **81**, 1070.
144. Zimbovskaya, N.A. and Birman, J.L. (1999). *Int. J. Mod. Phys.*, **B13**, 859.
145. Willett, R.L., West, K.W., and Pfeiffer, L.N. (2002). *Phys. Rev. Lett.*, **88**, 066801.
146. Willett, R., Eisenstein, J.P., Stormer, H.L., Tsui, D.C., Gossard, A.C., and English, J.H. (1987). *Phys. Rev. Lett.*, **59**, 1776.
147. Andrei, E.Y., Deville, G., Glattli, D.C., Williams, F.I.B., Paris, E., and Etienne, B. (1988). *Phys. Rev. Lett.*, **60**, 2765; Andrei, E.Y., Deville, G., Glattli, D.C., Williams, F.I.B., Paris, E., and Etienne, B. (1989). *Phys. Rev. Lett.*, **62**, 973.
148. Williams, F.I.B., Wright, P.A., Clark, R.G., Andrei, E.Y., Deville, G., Glattli, D.C., Probst, O., Etienne, B., Dorin, C., Foxon, C.T., and Harris, J.J. (1991). *Phys. Rev. Lett.*, **66**, 3285; Williams, F.I.B., Deville, G., Glattli, D.C., Andrei, E.Y., Etienne, B., and Paris, E. (1992). *Phys. Rev. Lett.*, **68**, 2105.
149. Li, C.C., Engel, L.W., Shahar, D., Tsui, D.C., and Shayegan, M. (1997). *Phys. Rev. Lett.*, **79**, 1353.
150. Li, C.C., Yoon, J., Engel, L.W., Shahar, D., Tsui, D.C., and Shayegan, M. (2000). *Phys. Rev.*, **B61**, 10905.
151. Ye, P.D., Engel, L.W., Tsui, D.C., Lewis, R.M., Pfeiffer, L.N., and West, K. (2002). *Phys. Rev. Lett.*, **89**, 176802.
152. Paalanen, M.A., Willett, R.L., Littlewood, P.B., Ruel, R.R., West, K.W., Pfeiffer, L.N., and Bishop, D.J. (1992). *Phys. Rev.*, **B45**, 11342.
153. Esslinger, A., Wixforth, A., Winkler, R.W., Kotthaus, J.P., Nickel, H., Schlapp, W., and Losch, R. (1992). *Solid State Commun.*, **84**, 939.
154. Fal'ko, V.I., Meshkov, S.V., and Iordanskii, S.V. (1993). *Phys. Rev.*, **B47**, 9910.
155. Esslinger, A., Winkler, R.W., Rocke, C., Wixforth, A., Kotthaus, J.P., Nickel, H., Schlapp, W., and Losch, R. (1994). *Surf. Sci.*, **305**, 83.
156. Kennedy, I., Rampton, V.W., Mellor, C.J., Bracher, B.H., Henini, M., Wasileski, Z.R., and Coleridge, P.T. (1998). *Physica*, **B251**, 36.
157. Simon, S.H. and Halperin, B.I. (1994). *Phys. Rev. Lett.*, **73**, 3278.
158. Tieke, B., Fletcher, R., Zeitler, U., Geim, A.K., Henini, M., and Maan, J.C. (1997). *Phys. Rev. Lett.*, **78**, 4621.
159. Simon, S.H. and Cooper, N.R. (1997). *Phys. Rev.*, **B56**, R7116.
160. Simon, S.H. (1998). *Physica*, **B258**, 23.
161. Dunford, R.B., Gates, M.R., Mellor, C.J., Rampton, V.W., Chauhan, J.S., Middleton, J.R., and Henini, M. (2002). *Physica*, **E12**, 462.
162. Lok, J.G.S., Kraus, S., Pohlt, M., Dietsche, W., von Klitzing, K., Wegscheider, W., and Bichler, M. (2001). *Phys. Rev.*, **B63**, 041305.
163. von Oppen, F., Simon, S.H., and Stern, A. (2001). *Phys. Rev. Lett.*, **87**, 106803.



# 4 Carrier–phonon interactions in semiconductor quantum dots and wires

S.A. Cavill, P. Hawker, and A.J. Kent

---

## 4.1 Introduction

So far this book has been concerned with the interaction of phonons with two-dimensional (2D) carrier systems. In this chapter we will move on to consider the interaction of phonons with one- and zero-dimensional (1D and 0D) carrier systems, respectively known as quantum wires (QWRs) and quantum dots (QDs). Such systems are interesting for the new physics that they display. In short QWRs, for example, ballistic electron transport has been seen [1], and possible evidence for the existence of the Luttinger liquid state has been obtained in clean, long QWRs [2]. In the Luttinger liquid, electron–electron interactions lead to the formation of a collective 1D state in which spin charge separation occurs. QDs, with their discrete electron energy level spectrum, exhibit atom-like electron configurations (artificial atoms) [3] and coupled QDs can behave like artificial molecules [4]. However, the interest is not purely academic because QWRs and QDs also have a number of potentially exciting technological applications. Owing to the nature of the density of electron states in QWRs, which is sharply peaked at the 1D subband edge ( $k = 0$ ), QWR lasers should have improved spectral characteristics and a lower threshold current than quantum well lasers [5]. QWRs may also be used to make a current standard [6] and this is discussed in Chapter 6. QDs too may be used as the basis of improved optoelectronic devices due to their discrete density of states. It is expected that in QD lasers the threshold current will be lower and show less temperature dependence than in quantum well devices [7]. High-power and high-efficiency QD lasers have been demonstrated [8] as have single photon detectors with applications in quantum cryptography [9]. Electron states in QDs could also be used as quantum bits in quantum computers [10]. All these applications make use of the quantum nature of the carrier states, but even conventional devices are now approaching the size (tens of nanometres) where quantum confinement may unintentionally influence their performance.

Of course, just as in the case of the other systems considered in this book, the interactions of phonons with carriers in QWRs and QDs can have a strong effect on device properties. In optoelectronic devices phonons play a part in non-radiative processes, for example carrier relaxation and non-radiative recombination. Phonon scattering also gives rise to broadening of spectral lines and leads to dephasing of carrier states. Although most of the basic concepts are the same as for 2D carrier–phonon interactions, the additional carrier confinement gives rise to some interesting differences. The most notable of these is the so-called phonon bottleneck effect [11, 12]. Reducing the dimensionality of the carrier system has the effect of reducing the phase space for carrier scattering. Corresponding to each new direction of carrier confinement a form factor arises in the

electron–phonon scattering rate. This imposes a restriction (cut-off) on the magnitude of the momentum component in that given direction of a phonon that can be emitted or absorbed. To illustrate the effect of this, we consider the simple case of an infinite rectangular confinement potential of width  $W$ . The maximum phonon wavevector component in the confinement direction is given by  $q_{\max} \sim \pi/W$ . Additionally, the confinement breaks up the carrier energy spectrum into a set of discrete levels,  $E_n = \pi^2 N^2 \hbar^2 / 2m^* W^2$ . We see that, for interlevel transitions, as  $W$  is reduced the energy  $\hbar\omega = E_{N'} - E_N$  of the emitted phonon increases as  $W^{-2}$ , while the momentum cut-off increases more slowly, as  $W^{-1}$ . Since, for acoustic phonons,  $sq = \omega$ , it becomes increasingly difficult for a phonon to be emitted or absorbed as  $W$  gets smaller. For optic phonons the momentum cut-off does not present a problem, but the narrow energy dispersion means that the carrier level spacing must lie very close to the optic phonon energy for emission or absorption to take place. This could have very serious consequences for carrier relaxation in QDs. However, in QWRs, the continuous carrier energy spectrum along the wire direction lifts the restrictions a little.

Following a brief discussion of how practical QWRs are formed and the electronic states in QWRs, and a brief review of their transport properties (Sections 4.2.1–4.2.3), in Section 4.2.4 we will consider the theory of acoustic phonon–carrier interactions. Here we will focus on acoustic phonon interactions which are relevant to the phonon absorption experiments described in Section 4.2.5 and the emission experiments considered in Section 4.2.6. The theory is well very developed in the literature and the typical approach follows closely the methods described in Chapter 2 for 2D carrier gases. We will therefore limit our discussion to the main results. The experimental development of the subject is comparatively immature. This is in part due to the difficulty in fabricating suitable devices and, as discussed, the fact that transport measurements are not good probes of carrier–phonon interaction in QWRs. In Sections 4.2.5 and 4.2.6 we will consider the phonon spectroscopy measurements that have been done so far. The reader is referred to the literature for reviews of optical measurements of relaxation at high carrier energies.

Quantum dots are considered in Section 4.3. Again, in keeping with the emphasis of this book, we will limit our discussion to ballistic phonon measurements. There is a large literature relating to optical measurements to which the interested reader is referred. Here the discussion will focus on how phonon measurements are helping to identify the processes which bypass the phonon bottleneck.

## 4.2 Electron–phonon interaction in QWRs

Before considering the details of electron–phonon interactions in QWRs, we will briefly review how practical QWRs are formed and the fundamental properties of 1D electronic systems.

### 4.2.1 Formation of QWRs

QWRs are formed by confining the motion of the electrons in two orthogonal directions within lengths comparable with or less than their de Broglie wavelengths. This is usually done by applying a lateral confining potential to a two-dimensional electron gas (2DEG).

The most widely used confinement techniques involve etching or gating but other techniques, such as  $v$ -groove and cleaved edge overgrowth which form both vertical ( $z$ ) and lateral ( $x$ ) confinement during growth, have also been used and are described in ref. [13]. In deep etched wires [14], parts of the GaAs layer containing the 2DEG are etched away to leave a narrow strip in which the electrons are brought into close proximity with the vacuum level. Surface atoms are slightly reorganized from their bulk positions producing a number of acceptor states which become filled by 2DEG electrons. The electrons in the 2DEG move in response to the electric field from the trapped electrons producing a depletion region near the surface. This removes the electrons in the wire away from the damage created by etching but this damage still dominates the electronic properties in narrow wires. In shallow etched QWRs [15], the surface layer is thinned, but the etch is stopped before it reaches the depth of the 2DEG. The 2DEG is depleted in the regions that are close to the etched surface and this provides the confinement. The electrons are removed further from the etch damage than in deep-etched wires leading to improved electronic properties.

Another commonly used technique is that of the split gate. This has two advantages over the etch method: it does not damage the structure and it allows the QWR width to be varied. This technique was first used by Thornton *et al.* [16] and Zheng *et al.* [17]. Lateral confinement of the 2DEG is achieved by fabricating a metal gate on the surface substrate. The gate is split in the middle so that when a negative voltage is applied, electrons under the gate are depleted leaving a narrow conducting channel under the split. The electrons in this channel are confined by an electrostatic potential which is approximately parabolic [18]. The width of the wire,  $W$ , can be varied by changing the applied voltage to the gate. The main drawback to all the above techniques is that  $W$  has to be determined experimentally.

#### 4.2.2 Electronic states in QWRs

Most of the experimental work considered in the following sections used QWRs formed by the split gate technique so that the wires were confined in the  $x$ -direction by a potential which has the approximate form

$$V(x) = \frac{m^* \omega^2 x^2}{2} \quad (4.1)$$

where  $\omega = \hbar/m^*W$ . The electron wavefunction  $\Psi$  can be written

$$\Psi = \psi(z)U(x) \exp(iky) \quad (4.2)$$

where  $U(x)$ ,  $\psi(z)$  are the eigenstates in the  $x$ - and  $z$ -directions ( $z$  is the growth direction),  $\exp(iky)$  is the plane wave solution for free electron motion in the  $y$ -direction along the wire and  $k = k_y$ .

$U(x)$  is given by

$$\left[ \frac{-\hbar^2}{2m^*} \frac{\partial^2}{\partial x^2} + V(x) \right] U(x) = EU(x) \quad (4.3)$$

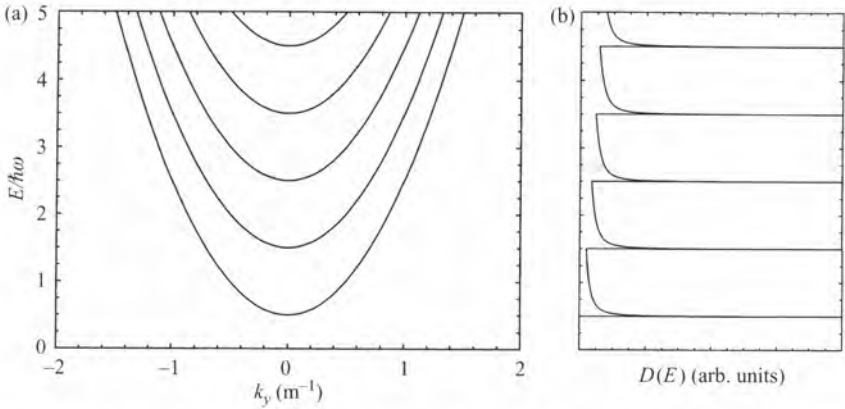


**Fig. 4.1** The energy dispersion  $E(k)$  and density of states of a QWR showing the 1D subbands.

which has the form of the Schrödinger equation for a simple harmonic oscillator with the well-known solution

$$U_N(x) = \left( \frac{\alpha}{\sqrt{\pi} 2^N N!} \right)^{1/2} \exp\left(-\frac{\alpha^2 x^2}{2}\right) H_N(\alpha x) \quad (4.4)$$

where  $\alpha = 1/W$ ,  $N$  is a positive integer, and  $H_N(\alpha x)$  is the  $N$ th order Hermite polynomial. The eigenvalues are given by Eq. (4.5) with

$$E_N = \left(N + \frac{1}{2}\right) \hbar\omega. \quad (4.5)$$

Hence, as can be seen in Fig. 4.1, lateral confinement causes a single 2D subband to be split into a series of 1D subbands of index  $N$ .

The energy of the electronic system is now quantized in two dimensions,  $x$  and  $z$ . In the  $z$ -direction, the confinement length  $a_0$  is usually sufficiently small that the second subband is essentially unoccupied at low temperatures. This is not normally the case in the  $x$ -direction where the confinement is much weaker,  $W \gg a_0$ , so many 1D subbands may be occupied. It is usual to take the zero point of energy to be the bottom of the first 2D subband (motion in the  $z$ -direction) and hence to express the total energy of an electron in the  $N$ th 1D subband by

$$E_N(k) = E_N + \frac{\hbar^2 k^2}{2m^*}. \quad (4.6)$$

It is of interest to consider the effect on the wave function and energy levels of replacing the parabolic confinement potential by that for an infinite square well of the form

$$\begin{aligned} V(x) &= 0 & \text{for } 0 < x < W \\ V(x) &= \infty & \text{otherwise.} \end{aligned} \quad (4.7)$$

Substitution into Eq. (4.3) leads to the familiar solution

$$U_N = \frac{1}{\sqrt{W}} \sin(k_x x) \quad (4.8)$$

with  $k_x = N\pi/W \dots$  where  $N$  is again a positive integer and

$$E_N = \frac{\hbar^2 N^2 \pi^2}{2m^* W^2}. \quad (4.9)$$

Plots of  $U_N$  for parabolic and infinite square well potentials are given in Fig. 4.2 along with the energies of the states. As can be seen, for a given  $W$ , the infinite square well potential gives stronger confinement than a parabolic potential. The confinement has important consequences for the electron-phonon interaction and is discussed later.

The strong effect of electron confinement on the density of states (DOS) has already been seen in previous chapters. For a 2D system the DOS is independent of energy within a given subband, but the additional effect of lateral confinement produces a dramatic change.

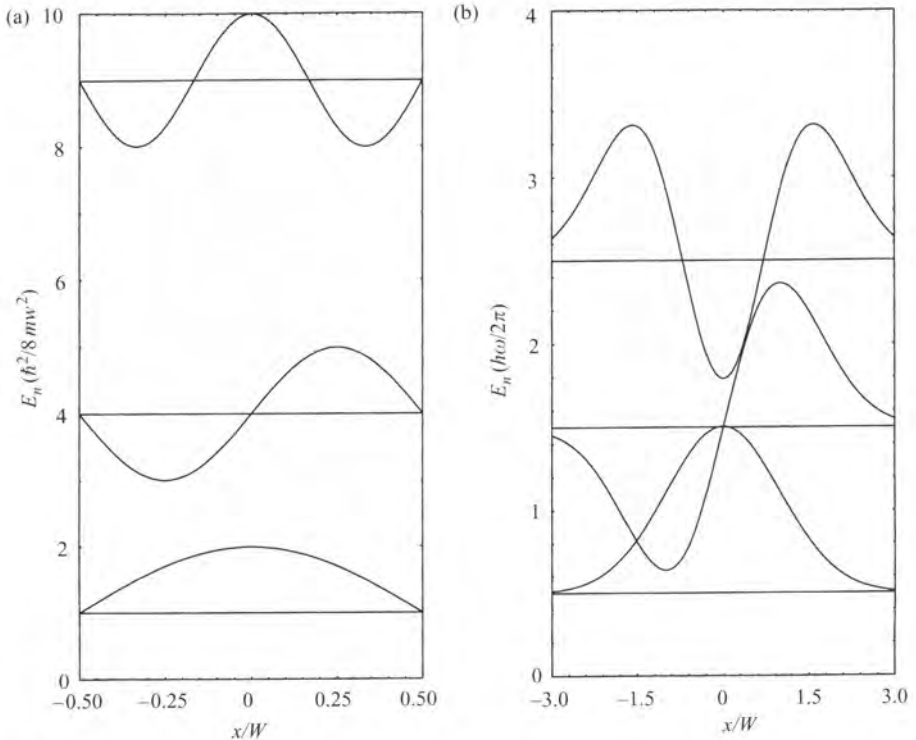


**Fig. 4.2** The wave functions and energy levels for a QWR calculated assuming (a) an infinite square well potential, (b) a parabolic potential.

In  $k$ -space the DOS per unit length,  $D(k) dk$ , is given by

$$D(k) dk = \frac{1}{2\pi} dk \quad (4.10)$$

and for free electron motion in the  $y$ -direction, this becomes

$$D(E) dE = g_s g_v D(k) dk \quad (4.11)$$

and so

$$D(E) = g_s g_v \frac{1}{2h} \sqrt{\frac{2m^*}{E - E_N}} \quad (4.12)$$

where  $g_s$  and  $g_v$  are the spin and valley degeneracy respectively.  $D(E)$  has a singularity at the bottom of each subband as shown in Fig. 4.1. This is broadened by carrier scattering in real systems but the DOS is still strongly peaked at  $E_N$ .

### 4.2.3 Electron transport in QWRs

A perfect QWR is never realized because of scattering events in and near the channel which break the translational symmetry. The frequency of these scattering events gives rise to different regimes of transport which are set by the length of the wire,  $L$ , the wire width,  $W$ , the elastic mean free path,  $l_e$ , and the inelastic scattering length,  $l_\phi$ . We consider the two transport regimes corresponding to ballistic and diffusive motion.

#### 4.2.3.1 Ballistic regime

Short QWRs such as point contacts are defined by  $l_\phi, l_e > L, W$ . In this regime no scattering takes place in the wire and, since the only potential felt by the electrons is at its boundaries, the quantum states extend from one end of the wire to the other.

Let us consider the case of two reservoirs which are joined together by an ideal QWR, see Fig. 4.3. The reservoir on the left-hand side has a slightly higher chemical potential,  $E_F + \delta\mu$ , than that on the right,  $E_F$ . This can be achieved by creating a small difference in the electron density between the two reservoirs or by applying a small voltage.

The total current  $I_N$  carried by the  $N$ th subband or channel is given by [19]

$$I_N = e \int_{E_F}^{E_F + \delta\mu} v_g(E) D(E) dE \quad (4.13)$$

where  $v_g$  is the electron group velocity.

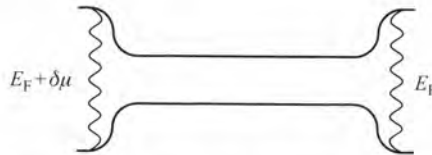


**Fig. 4.3** A 1D channel connecting two 2D electron reservoirs at different chemical potentials.

The group velocity and density of states can be written

$$D(E) = g_s g_v \left( \frac{2\pi}{h} \frac{dE_N(k)}{dk} \right)^{-1} \quad (4.14)$$

$$v_g = \frac{1}{h} \frac{dE_N(k)}{dk} \quad (4.15)$$

so, apart from a constant factor, they cancel out in the expression for the current to give

$$I_N = e \frac{g_s g_v}{h} \delta\mu. \quad (4.16)$$

We can now move away from the ideal quantum wire by including scattering. This can only produce changes in  $k$  and, for elastic scattering, this can only be from  $k$  to  $-k$ . So scattering can be accounted for by assuming part of the injected current is reflected back into the left hand reservoir. If the fraction of  $I_N$  transmitted to the right hand reservoir is  $T_N$  the total current in the channel becomes

$$I = \frac{g_s g_v e}{h} \delta\mu \sum_{N=1}^{N_{\max}} T_N \quad (4.17)$$

where  $N_{\max}$  corresponds to the highest occupied subband. Since  $\delta\mu = eV$ , where  $V$  is the potential across the wire, we can define a conductance

$$G = \frac{I}{V} = \frac{g_s g_v e^2}{h} \sum_{N=1}^{N_{\max}} T_N \quad (4.18)$$

which is the Landauer formula [20].

The ideal wire is then a special case of the Landauer formula when the transmission coefficients of all  $N$  channels is equal to unity. We then have

$$G = \frac{I}{V} = \frac{g_s g_v e^2 N_{\max}}{h} \quad (4.19)$$

that is all channels contribute equally to the conductance.

In the ballistic regime, as the negative gate voltage on a split gate is increased, the QWR becomes narrower and the energy separation between 1D subbands increases. This causes the number of subbands occupied to fall in integer steps as the subbands move through the Fermi energy and gives rise to the steps in the conductance as a function of gate bias shown in Fig. 4.4.

#### 4.2.3.2 Diffusive regime

Diffusive transport occurs in long QWRs in which the elastic mean free path is small compared with the channel dimensions, that is  $l_e < W, L$ . Elastic scattering by impurities and defects now dominates the transport properties, the concept of 1D channels no longer has meaning since there are no states that extend from one end of the wire to the other, and the steps in conductance against gate bias become smeared out. In this regime the electrons are localized to a length  $l_{\text{loc}}$  and electron transport through the wire can only take place as a result of scattering between the localized states.

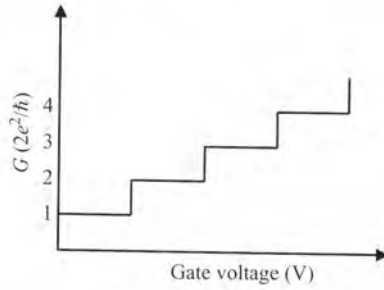


**Fig. 4.4** The conductance of a QWR as a function of the negative gate voltage applied to the split gate.

#### 4.2.4 Theory of the electron–phonon interaction in ideal QWRs

The changes to the electron wave functions and energy levels resulting from the 1D confinement modify the electron–phonon interaction and hence the transport properties of QWRs [21].

Let  $\psi_a(r)$  be the initial eigenstate of an electron which is scattered by a phonon of mode  $q$  into an eigenstate  $\psi_b(r)$ . The potential experienced by the electron due to the phonon mode  $q$  is

$$V_q(r, t) = V_{+q}(r) \exp(i\omega_q t) + V_{-q}(r) \exp(-i\omega_q t). \quad (4.20)$$

Fermi's golden rule gives the transition rate (the scattering probability per unit time) to be

$$\begin{aligned} \frac{1}{\tau_a} = \frac{2\pi}{\hbar} \sum_b \sum_q [ & |\langle \psi_b | V_{+q} | \psi_a \rangle|^2 (N_q + 1) \delta(E_b - E_a + \hbar\omega_q)] \\ & + [ |\langle \psi_b | V_{-q} | \psi_a \rangle|^2 (N_q) \delta(E_b - E_a - \hbar\omega_q)] \end{aligned} \quad (4.21)$$

where  $N_q$  is the number of phonons present in the mode. The first and second terms describe electron scattering by phonon emission (stimulated and spontaneous) and absorption respectively. The delta functions ensure conservation of energy. We limit the discussion to acoustic modes since the experimental work described later has been carried out at temperatures  $T \ll 100$  K. The electron–phonon interaction due to optical modes has been reviewed in [22]. We will also make the approximation that the wire structures do not modify the acoustic modes allowing the use of the bulk phonon approximation. This is entirely justified when considering wires formed using the split gate technique. The changes that occur in free-standing nanostructures are discussed in Chapter 8.

$$|\langle \psi_b | V_q | \psi_a \rangle|^2 = |\langle U'(x) | V_q | U(x) \rangle|^2 |\langle \exp(-ik'_y y) | V_q | \exp(ik_y y) \rangle|^2 |\langle \psi'_z | V_q | \psi_z \rangle|^2 \quad (4.22)$$

which, apart from constants, includes the products of two form factors. That in the  $z$ -direction (see Chapter 2) is given by

$$|Z|^2 = |\langle \psi'_z | V_q | \psi_z \rangle|^2 [1 + (q_z a_0)^2]^{-3}. \quad (4.23)$$

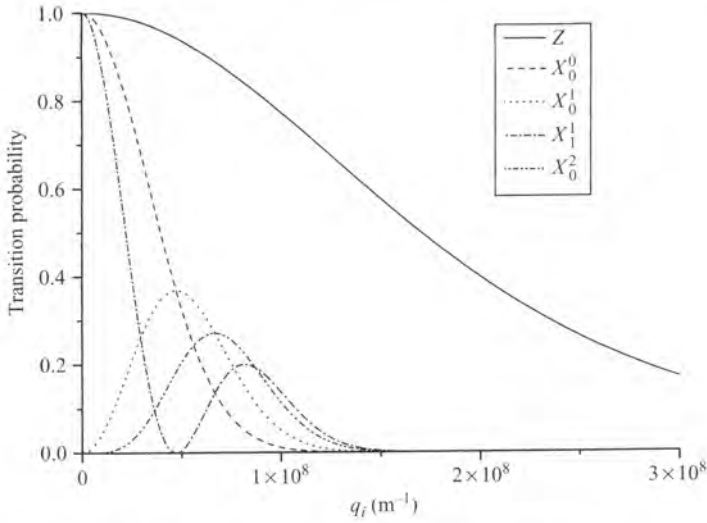


**Fig. 4.5** Examples of the  $x$ - and  $z$ -direction form factors (transition probabilities) for electron-phonon transitions in a QWR. The  $z$ -direction form factor is for the lowest intrasubband transition while intra- and intersubband transitions are included for the  $x$ -direction.

In the  $x$ -direction the form factor for intrasubband transitions within the  $N$ th subband and assuming parabolic confinement is given by

$$\begin{aligned} |X_N^M|^2 &= |\langle U'_x | V_q | U_x \rangle|^2 \left| \int_{-\infty}^{\infty} \left( \frac{\alpha}{2^N N! \sqrt{\pi}} \right)^{1/2} \left( \frac{\alpha}{2^M M! \sqrt{\pi}} \right)^{1/2} \right. \\ &\quad \times H_N(\alpha x) H_M(\alpha x) \exp(-\alpha^2 x^2 - i q_x x) dx \Big|^2. \end{aligned} \quad (4.24)$$

Normally several subbands have to be taken into account. For intrasubband transitions within the lowest subband this becomes

$$|X_0^0|^2 = \exp(-q_x^2 x^2). \quad (4.25)$$

Examples of  $x$ -direction form factors for  $N = 0$  to  $N = 2$  intrasubband and intersubband transitions and a  $z$ -direction intrasubband form factor are plotted in Fig. 4.5 [23]. The form factors provide a quantitative statement of the uncertainty principle relating to the emission or absorption of a phonon. For intrasubband transitions, the only possible change in the electron momentum is in the  $y$ -direction so classical conservation of momentum requires the emitted or absorbed phonon to have momentum precisely in the  $y$ -direction as well. However, the form factors show that phonons can in fact be emitted or absorbed with non-zero values of  $q_x$ ,  $q_z$  provided  $q_x < W^{-1}$  and  $q_z < a_0^{-1}$ . The form factors equal one when  $q_x = 0$  and  $q_z = 0$  but fall with increasing  $q$ . Intersubband transitions result in a change in  $k_x$  so the maximum in the form factor is no longer at  $q_x = 0$ . This can be seen in the  $M = 1$  and  $M = 2$  to  $N = 0$  transition form factors.

The greater the difference between  $M$  and  $N$ , the larger the change in  $k_x$ , so the peak in the form factor moves to higher wavevectors. The oscillations seen in the  $x$ -direction form factors are due to the oscillating term in the perturbing potential being successively in and out of phase with the oscillations in the electron wave function.

For free motion in the  $y$ -direction

$$|Y|^2 = | \langle \exp(-ik'_y y) | V_{\pm q} | \exp(ik_y y) \rangle |^2 = \left| \int_{-\infty}^{\infty} \exp[iy(k_y - k'_y \pm q_y)] dy \right|^2 \quad (4.26)$$

which is zero except for the case where  $k_y - k'_y \pm q_y = 0$  when it becomes

$$|Y|^2 = \delta(k_y - k'_y \pm q_y) \quad (4.27)$$

corresponding to the classical conservation of momentum.

We can now write down an expression for the overall interaction term including the  $q$ -dependence of the perturbing potentials. For deformation potential (DP) coupling

$$|M_k^{k'}|^2 = \left( \frac{\hbar \Xi_d^2 q \cdot \hat{\epsilon}}{2\rho\Omega s} \right) |X|^2 |Z|^2 \delta(k_y - k'_y \pm q_y) \quad (4.28)$$

and for piezoelectric (PE) coupling

$$|M_k^{k'}|^2 = \left( \frac{\hbar}{\rho\Omega s} \right) \left( \frac{ee_{14}}{\epsilon} \right)^2 |X|^2 |Z|^2 \left( \frac{q_x q_y \hat{\epsilon}_z + q_y q_z \hat{\epsilon}_x + q_x q_z \hat{\epsilon}_y}{q^5} \right) \delta(k_y - k'_y \pm q_y) \quad (4.29)$$

where  $\Xi_d$  and  $e_{14}$  are coupling constants (see Chapter 2),  $s$  is the sound velocity and  $\hat{\epsilon}_i$  the polarization vector components.

The above analysis neglects screening of the electron–phonon interaction. The dielectric function for a truly 1D system was derived by Williams and Bloch [24] and is basically the same as that given for a 2D system in Chapter 2 (Eq. 2.39) except that  $q_{\parallel}$  is replaced by  $q_y$ . In a quasi-1D system, there is no translational invariance and a different approach must be used. Lee and Spector [25] calculated the dielectric function for a cylindrical wire. The feature specific to 1D systems is a singularity in the screening function at  $q_y = 2k_F$  ( $k_F$  is the Fermi wavevector) which is characteristic of the Peierls transition. At higher temperatures and/or when scattering is present, the singularity is smoothed. In other respects the behaviour of the dielectric function is similar to that in systems of higher dimensionality. Screening is very effective for low wavevectors and high 1D electron densities.

#### 4.2.4.1 Phonon absorption

As already noted, the form factors in the  $x$ - and  $z$ -directions give rise to cut-offs in wavevector with the result that, to an approximation, intrasubband transitions can only occur if

$$q_z \leq \frac{1}{a_0} \quad (4.30)$$

$$q_x \leq \frac{1}{W}. \quad (4.31)$$

Since  $W > a_0$  the cut-off for  $q_x$  is more severe than that for  $q_z$  and so absorption of large perpendicular wavevector phonons ( $q_{\perp} > 1/W$  where  $q_{\perp}^2 = q_x^2 + q_z^2$ ) is only possible when incident close to the  $z$ -axis.

The absorption process is characterized by conservation of momentum,  $\mathbf{k}' = \mathbf{k} + \mathbf{q}$ , and energy

$$E_M = E_N + \hbar s q \quad (4.32)$$

where  $E_M$  is the final electron energy in subband  $M$  and  $E_N$  is the initial electron energy in subband  $N$ .

$E_M$  and  $E_N$  are given by

$$E_M = \frac{\hbar^2 k'^2}{2m^*} + (M + 1/2)\hbar\omega \quad (4.33)$$

$$E_N = \frac{\hbar^2 k^2}{2m^*} + (N + 1/2)\hbar\omega. \quad (4.34)$$

Momentum conservation in the  $y$ -direction requires  $k'_y = k_y + q_y$ , so from Eqs (4.32), (4.33), and (4.34) we obtain

$$kq_y + \frac{q_y^2}{2} + \frac{m^*\omega(M - N)}{\hbar} - \frac{m^*sq}{\hbar} = 0. \quad (4.35)$$

Inter- and intrasubband transitions can be either 'forward' or 'backward' according to whether the initial and final electron wavevectors are parallel (forward) or antiparallel (backward). Some possible transitions are illustrated in Fig. 4.6. The maximum value

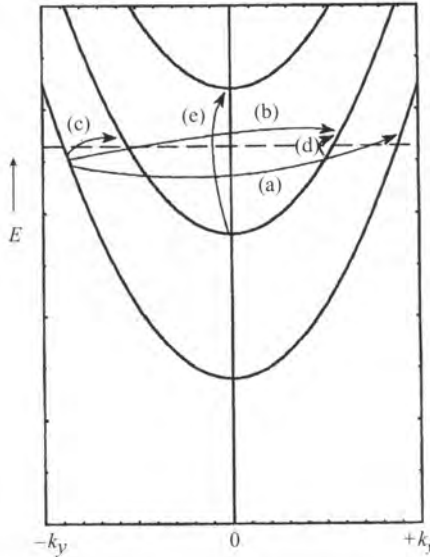


**Fig. 4.6** Some possible intra- and intersubband transitions in a QWR arising from the absorption of a phonon.

of  $q_y$  corresponds to the backscattered transition (a) and is obtained by setting  $M = N$  in Eq. (4.35) and making the approximation that the phonon energy is small compared with the electron energy so that

$$kq_y + \frac{q_y^2}{2} \approx 0. \quad (4.36)$$

For  $k = k_F$  this gives

$$q_y(2k_F + q_y) \approx 0 \quad (4.37)$$

with solutions  $q_y = 0$  and  $-2k_F$ . So the maximum value of  $q_y$  is approximately  $2k_F$  as in 2D systems.

Blencowe and Shik [26] have shown that the change in conductance of a perfect quantum wire (i.e. point contact),  $\Delta G$ , resulting from the absorption of non-equilibrium phonons is given by

$$\Delta G_N = \frac{-e^2}{\pi \hbar} L \frac{m^*}{\hbar k} W_N^b(k) \quad (4.38)$$

where  $W_N^b(k)$  is the probability per unit time of a single backscattering event. The authors assume that the electrons are completely degenerate, that is  $T_e = 0$  K, and evaluate at the Fermi energy which gives

$$\Delta G = -\frac{e^2 L m^* C}{(2\pi)^3 \hbar^3} \sum_{M,N} \frac{1}{\sqrt{E_F - E_N}} \iint \frac{dq_x dq_z q^n N_q |Z|^2 |X_N^M|^2}{\sqrt{E_F - E_M + \hbar s q}} \quad (4.39)$$

where  $C$  is the electron-phonon coupling constant and  $n = +1$  for DP coupling and  $-1$  for PE coupling. The terms  $(E_F - E_N)^{-1/2}$  and  $(E_F - E_M + \hbar s q)^{-1/2}$  are the initial and final DOSs and  $q_y$  has a fixed value approximately equal to  $-\sqrt{2m^*}(\sqrt{E_F - E_N} + \sqrt{E_F - E_M})/\hbar$ , which becomes  $|q_y| = 2k_F$  for intrasubband transitions.

Figure 4.7 shows the  $k$ -dependence of the phonon scattering rate,  $W_0$ , for the first subband. The scattering rate peaks when the electron energy coincides with the subband edge and the 1D DOS reaches a maximum. From Eq. (4.39) it can also be shown that the phonoconductivity is always negative in an ideal wire which follows since scattering can only decrease the transmission coefficients  $T_N$ ; this had also been noted earlier by Gurevich *et al.* [27] in their calculations of the reduction in the conductivity of an ideal QWR resulting from the absorption of equilibrium phonons.

The work of Blencowe and Shik [26] was also extended to phonoconductivity in long (non-ideal) wires, where elastic scattering from impurities and defects is important. At low temperatures this should dominate the resistivity  $\rho$  and might be expected to lead to temperature-independent and vanishingly small values of  $\Delta G$ . However, measurements of  $\rho$  in narrow wires have shown that, below a critical temperature,  $\rho$  starts to rise with decreasing temperature. This difference in behaviour, also seen in 2D and 3D systems, is attributable to the assumption leading to constant resistivity that the memory of the electron phase is completely destroyed in a scattering event. This is reasonable for inelastic scattering but not for elastic scattering and one effect of this is that weak localization occurs and that the probability for backscattering is enhanced. Weak localization is most intuitively described in the following treatment by Bergmann [28]. The probability for

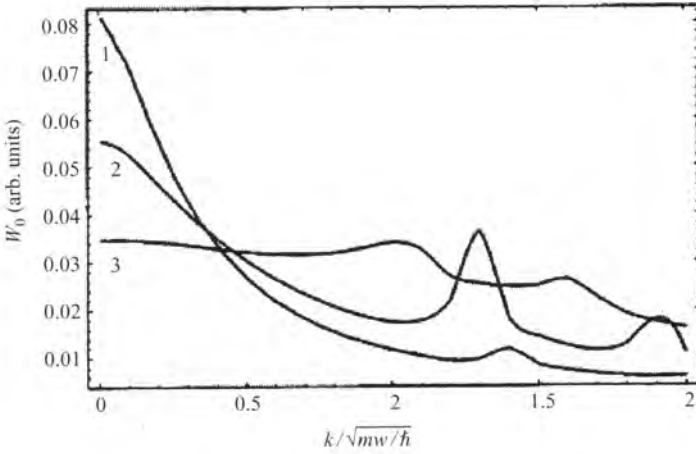


**Fig. 4.7** The  $k$ -dependence of the phonon scattering rate for the first subband showing the peaks that occur when the electron energy coincides with the subband edge. Curves are shown for three wire widths (Blencowe and Shik [26]).

motion from an initial starting point  $r$  to another position  $r'$  is given by the classical path probability plus an interference term:

$$P(r, r', t) = \sum_i |A_i|^2 + \sum_{i \neq j} A_i A_j^*. \quad (4.40)$$

If  $r \neq r'$ , the phase of different paths is generally uncorrelated and the interference term averages out. However, when  $r = r'$ , the contributions to the interference term can be grouped into time-reversed pairs. Time-reversal invariance leads to equal probabilities for counter-propagating pairs so that the interference term is non-zero. This enhanced probability reduces the conductivity and the magnitude of the weak localization correction to the conductivity,  $\delta\sigma$ , is proportional to the probability of return to the initial starting point [29]; the conductivity is related to the conductance by the usual expression  $\sigma = LG/W$ . Inelastic scattering destroys the coherence and its effect on the weak localization correction depends on whether it is sufficiently strong enough for the diffusion to be 2D,  $l_\phi \ll W$ , or whether it remains 1D  $l_\phi \gg W$ , where  $l_\phi$ , the phase coherence length (inelastic scattering length), is given by  $l_\phi = (D\tau_\phi)^{1/2}$  and  $D$  and  $\tau_\phi$  are respectively the diffusion constant and the inelastic lifetime. Expressions for the weak localization correction given in ref. [29] are

$$\delta\sigma = -\frac{g_s g_v e^2}{4\pi\hbar} \ln\left(1 + \frac{\tau_\phi}{\tau_e}\right) \quad \text{for 2D} \quad (4.41)$$

and

$$\delta\sigma = -\frac{g_s g_v e^2}{2\pi\hbar} \frac{l_\phi}{W} \left[ 1 - \left(1 + \frac{\tau_\phi}{\tau_e}\right)^{-1/2} \right] \quad \text{for 1D} \quad (4.42)$$

so that  $\delta\sigma \rightarrow 0$  as  $\tau_\phi \rightarrow 0$  as expected.

Weak localization can also be destroyed by the application of a weak magnetic field. The magnetic field gives rise to a phase difference between the counter-propagating pairs destroying the constructive interference. In a magnetic field, paths which take longer than a so-called magnetic relaxation time  $\tau_B$  to complete no longer contribute to the interference term because of the phase difference produced between the two paths of a counter-propagating pair. When  $\tau_B$  becomes comparable with  $\tau_\phi$ , the magnetic field starts to reduce the weak localization correction and this is completely quenched when  $\tau_B \ll \tau_\phi$  so that

$$\sigma(B \gg B_c) - \sigma(B = 0) = -\delta\sigma(B = 0) \quad (4.43)$$

where  $B_c$  is the critical field value when  $\tau_B = \tau_\phi$ . So magnetoresistance measurements can be used to determine  $\tau_\phi$ . Since  $\tau_e$  can be estimated from experiments at slightly higher temperatures where weak localization effects are negligible,  $\tau_\phi$  can also be obtained from Eq. (4.42).

This weak localization has a major effect on the change in conductivity resulting from incident non-equilibrium phonons. The phonoconductivity still oscillates with the Fermi energy  $E_F$ , but since the increase in inelastic scattering produced by the phonons produces an increase in conductivity, the phonon-induced changes are now always positive in contrast to the changes produced in ideal wires. With  $E_F < E_1$ , so that only the first subband is occupied, the change in conductance is given [26] by

$$\Delta G \approx -\frac{e^2}{\pi\hbar} v_F \sqrt{\tau_e} \left( \sqrt{W_{h0}^{-1}} - \sqrt{W_{a0}^{-1}} \right) \quad (4.44)$$

where  $W_{h0}$  and  $W_{a0}$  are respectively the non-equilibrium and equilibrium electron-phonon scattering rates and  $v_F$  is the Fermi velocity. When the temperature of the non-equilibrium phonon source (heater) is much larger than the ambient temperature we can neglect  $W_{h0}^{-1}$  in the above expression and

$$\Delta G \approx \frac{e^2}{\pi\hbar} v_F \sqrt{\tau_e W_{a0}^{-1}}. \quad (4.45)$$

This indicates that the change in conductance should saturate at high heater temperatures and also suggests that non-equilibrium phonon measurements may be used to measure the weak localization correction directly.

#### 4.2.4.2 *Phonon emission*

The requirements of energy and momentum conservation for phonon emission are similar to those for absorption. However, one additional restriction that needs to be included is that the energy of the emitted phonon cannot exceed  $\sim k_B T_e$  where  $T_e$  is the electron temperature in the wire. Phonon emission is characterized by  $\mathbf{k} = \mathbf{k}' + \mathbf{q}$  and, using similar considerations to those for absorption, we obtain

$$-\frac{q_y^2}{2} + kq_y - \frac{m^*sq}{\hbar} + \frac{m^*\omega(M-N)}{\hbar} = 0. \quad (4.46)$$

The restriction  $\hbar sq \lesssim k_B T_e$  places additional limits on  $q_x$  and  $q_z$  and, since  $W > a_0$ , the momentum cut-off is largely determined by the relative values of  $k_B T_e / \hbar s$  and  $1/a_0$ .

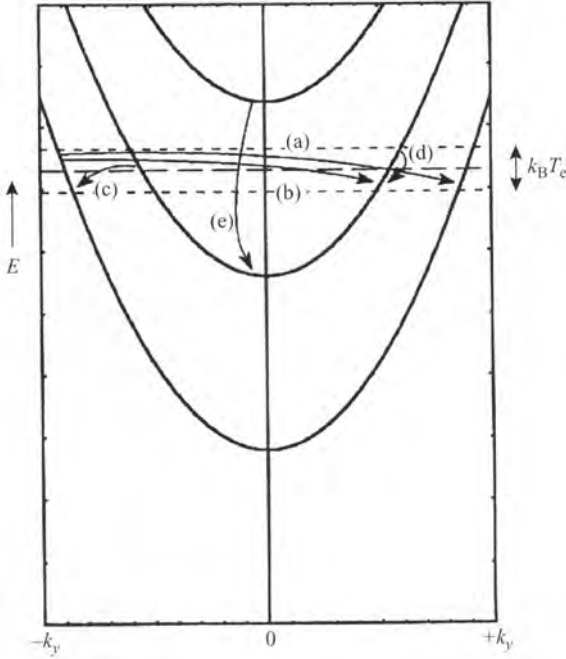


**Fig. 4.8** Some possible intra- and intersubband transitions in a QWR arising from the emission of a phonon. Transitions (a) to (d) assume the phonon energy  $\lesssim k_B T_e$ .

For a GaAs heterostructure, a typical value of  $a_0 \approx 3$  nm and  $k_B T_e / \hbar s \lesssim 1/a_0$  for  $T_e \lesssim 15$  K so, for near normal incidence,  $q_z$  is determined by  $T_e$  at low temperatures. However, at temperatures at which  $k_B T_e \gg (\hbar s)/W$  (but  $< (\hbar s)/a_0$ ),  $q_x$  is determined by the  $1/W$  cut-off. Phonons are emitted perpendicular to the plane of the 2DEG since  $q_z \gg q_x, q_y$ . The possible transitions are shown in Fig. 4.8.

At lower temperatures where  $(\hbar s)/W \gg k_B T_e$ ,  $q_x$  is determined by the thermal cut-off which gives  $q = k_B T_e / \hbar s$ . As can be seen from Fig. 4.5, the form factors for intersubband transitions become vanishingly small at small  $q$ . The component  $q_y$  is given by Eq. (4.46) with  $M = N$ . Following the procedure of Shik and Challis [30] we can neglect the  $q_y^2$  term since

$$k_N \gtrsim W^{-1} \gg k_B T_e / \hbar s \gtrsim q \quad (4.47)$$

leaving

$$|q_y| \approx \frac{m^* s q}{k_N \hbar} = \frac{m^* k_B T_e}{\hbar^2 k_N}. \quad (4.48)$$

The only allowed transitions are shown by (d) in Fig. 4.8 and correspond to forward scattering. Since  $q_x, q_z \sim k_B T_e / \hbar s$  which is greater than  $q_y$  the phonons are emitted almost perpendicular to the length of the wire and isotropically in the  $x$ - and  $z$ -directions.

The energy loss rate per electron for a wire with a parabolic confinement potential was shown to be

$$Q = (vL)^{-1} \sum_q \hbar s W(q) \left[ \frac{1 - \exp[\hbar s q (1/k_B T_e - 1/k_B T)]}{1 - \exp(-\hbar s q / k_B T)} \right] \quad (4.49)$$

where  $v$  is the number of electrons per unit length and  $W(q)$  is the probability per unit time of spontaneous emission of a phonon  $q$ . For deformation potential coupling and at low temperatures this becomes

$$Q \propto [T_e^5 - T^5] \sum_N \frac{1}{[E_F - \hbar\omega(N + 1/2)]}. \quad (4.50)$$

The energy loss rate evidently oscillates with  $E_F$  and peaks when  $E_F$  coincides with a subband edge. At higher temperatures  $k_B T_e > \hbar s / W$ , the energy loss rate becomes

$$Q \propto [T_e^4 - T^4] \sum_{n,m} \frac{1}{[E_F - \hbar\omega(N + 1/2)]^{1/2}} \frac{1}{[E_F - \hbar\omega(M + 1/2)]^{1/2}} \quad (4.51)$$

which now includes the possibility of intersubband scattering.  $Q$  again oscillates with  $E_F$  and peaks at subband edges but its temperature dependence is less in power by one since  $q_x$  is now limited by  $1/W$  and so independent of  $T_e$ . At even higher temperatures  $k_B T_e \gg \hbar s q_{\max}$  ( $q_{\max}$  is the largest wavevector at which interaction is possible under all momentum cut-offs) the temperature dependence associated with  $q_z$  also vanishes and since

$$N_q \sim \frac{k_B T}{\hbar s q} \quad (4.52)$$

$Q$  becomes proportional to  $T_e$  [30]. This is known as the equipartition regime.

This short summary of the theoretical results is not intended to be a review of all the work in this area and indeed the acoustic phonon relaxation rate from QWRs has also been treated by a number of other authors [12, 31–35]. In 1990 Bocklemann and Bastard [12] studied an InGaAs wire embedded in InP. They also found that in 1D systems the phonon scattering rate, the mean LA phonon energy, and the energy loss rate exhibit oscillations about their corresponding 2D values as the electron density is changed, see Fig. 4.9, and is again the result of the peak in the 1D DOS. The oscillations weaken with increasing electron density as more subbands drop below the Fermi level and the wire begins to lose its 1D nature. Das Sarma and Campos [31] found that the power loss per carrier from GaAs wires should be comparable with the 2D case at higher temperatures, see Fig. 4.10. However, at lower temperatures, the occupation number of the phonons which dominate backscattering, that is those with  $q_y = 2k_F$ , lie on the tail of the Bose–Einstein distribution so the scattering time is given by

$$\tau \propto \exp(2\hbar s k_F / k_B T) \quad (4.53)$$

and the power loss decreases exponentially with temperature, which contrasts sharply with the Bloch–Grüneisen  $T^5$  dependence expected in 2D and 3D cases. In a later paper, though, Senna and Das Sarma [32] noted that the exponential dependence neglects the

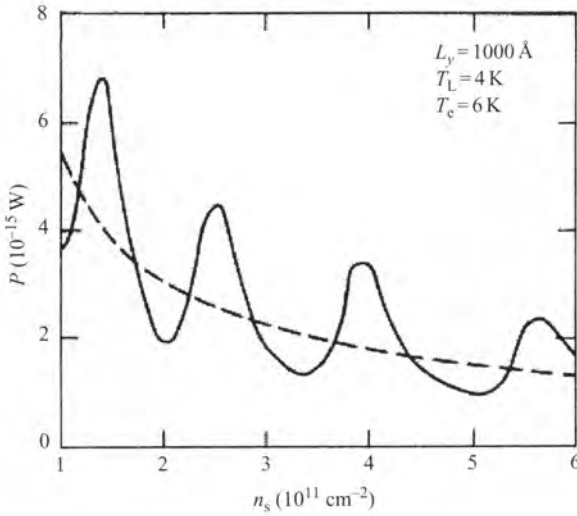


**Fig. 4.9** Power loss per electron from 1D (solid) and 2D (dashed) systems calculated as a function of the electron sheet density (Bocklemann and Bastard [12]). The electron and lattice temperatures were assumed to be 6 and 4 K respectively.

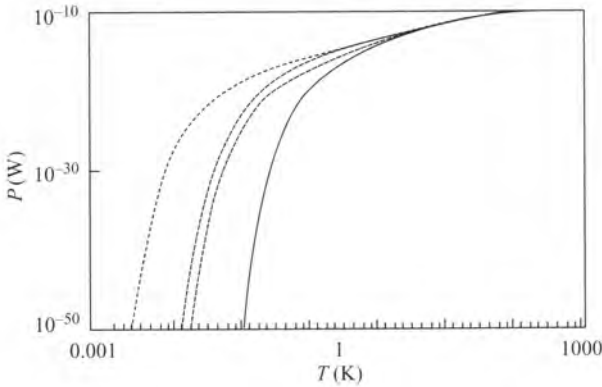


**Fig. 4.10** The power loss from a 1D electron system as a function of electron temperature (Das Sarma and Campos [31]). Curves are shown for electron densities ranging from  $0.1 \times 10^7 \text{ m}^{-1}$  (dashed line) to  $5 \times 10^7 \text{ m}^{-1}$  (thick solid line).

many-body effect on the phonon dispersion produced by the electron-phonon interaction. The resulting broadening allows energy relaxation to occur over a wide range of frequencies leading to a  $T^5$  power loss as in 2D and 3D systems.

#### 4.2.5 Experimental studies of phonon absorption by QWRs

In principle, it should be possible to investigate the effect of phonon scattering on the electron transport in a QWR from the temperature dependence of the mobility provided

the temperatures are sufficiently high for this process to be dominant. In practice, however, scattering from ionized impurities dominates up to quite high temperatures. The phonon contribution eventually dominates but, as pointed out by Blencowe [21], by then many subbands are thermally populated and the wire has lost its 1D character. It is of note, though, that recent measurements [36] in the range 1–9 K of the energy loss rate from quasi-1D InGaAs wires showed a weak temperature dependence  $T^{1.4}$ . In this temperature range the Bloch–Grüneisen criterion is never met and to our knowledge there has been no experimental data in the Bloch–Grüneisen regime. However, the authors point out that the energy loss rate is greater for the quasi-1D wire than for a corresponding 2D system over the same temperature range and attribute this to an enhanced electron–phonon interaction due to singularities in the 1D DOS.

Non-equilibrium phonon pulses provide a convenient way of maintaining the 1D character since the phonon distribution can be varied at a fixed electron temperature. The phonons are produced as heat pulses using techniques described in Chapter 2 and elsewhere in this book. Naylor *et al.* [37–39] were the first to use this approach to study the electron–phonon interaction in QWRs. The wire, formed by the split gate technique, was subjected to phonon pulses generated by a thin film heater on the opposite side of the substrate. The incident pulses caused a transient change in the device conductance. Figure 4.11 shows the experimental setup.

The experiments were performed on two devices which were fabricated from a GaAs/Al<sub>x</sub>Ga<sub>1-x</sub>As heterostructure with a 2DEG density of  $4.4 \times 10^{15} \text{ m}^{-2}$  and a mobility of  $100 \text{ m}^2 \text{ V}^{-1} \text{ s}^{-1}$  at 4.2 K. Both devices were from the same wafer but the first device had a channel length of approximately  $10 \mu\text{m}$ , comparable with the electron mean free path in the heterostructure, while the second was constructed as a point contact so that the channel length was much shorter than the mean free path. A  $2 \times 1 \text{ mm}^2$  area of the 2DEG was defined by etching and ohmic contacts were made at its ends. Gates with a split of width  $400 \text{ nm}$  were fabricated over the centre of the devices by electron beam lithography (EBL). The phonon source ( $100 \times 10 \mu\text{m}^2$ ) was a thin film of CuNi on the

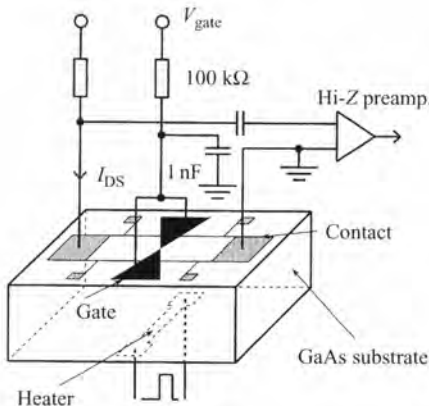


**Fig. 4.11** The experimental arrangement for measuring the absorption of non-equilibrium phonons by a QWR.

polished back face of the wafer. Infrared front-back alignment was used to position the heater directly opposite the split gate with its long axes perpendicular.

The sample was mounted in a cryostat at 1.3 K. Non-equilibrium phonons were generated by applying short ( $\approx 50$  ns) voltage pulses to the heater. The heater temperatures,  $T_h$ , for different power inputs and hence the characteristic temperatures of the non-equilibrium phonon distributions, were calculated by acoustic mismatch theory. A constant current was passed through the device and the phonon-induced changes in the conductivity were obtained by measuring the transient voltage across the device with a high-speed digitizer and signal averager.

The results of the two devices are considered separately.

#### 4.2.5.1 Short wire (quantum point contact)

The short wire was fabricated using standard techniques. Its conductance, shown in Fig. 4.12, shows clear steps at integer values of  $2e^2/h$  showing its 1D character. The figure also shows well-defined oscillations in its phonoconductivity with gate voltage,  $V_G$ , with maxima coinciding with the steps in the DC conductance. The experiment was carried out at constant bias current and the phonon-induced change in device resistance,  $\Delta R = -\Delta G/G^2$ , was measured. The phonoconductivity is negative; the phonons cause a decrease in conductance, as predicted theoretically, see Section 4.2.4. However, the size of the response ( $\sim 0.01G_0$ ) [37] is about two orders of magnitude larger than calculated by Blencowe and Shik [26] leading Hawker *et al.* to propose an alternative model. In this model the phonons, absorbed in the 2DEG area close to the point contact, lead to an increase in the temperature of the reservoirs. Warm electrons are then injected into the point contact where some relax and are thus scattered leading to a decrease in conductance. More recent work by Lehmann *et al.* [40], has shown, however, that the size of the response is in good agreement with the direct backscattering model if acoustic anisotropy is taken into consideration (see Chapter 2). Acoustic anisotropy permits

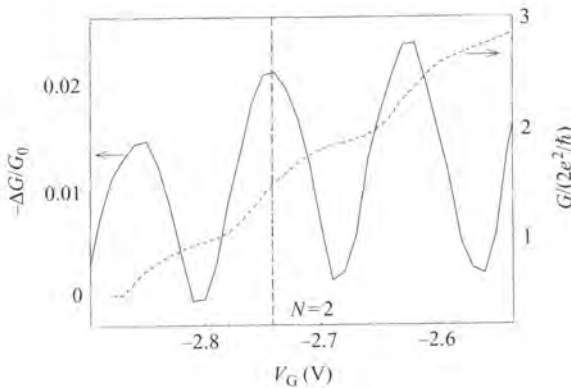


**Fig. 4.12** The phonon-induced change in conductance  $\Delta G/G^2$  of a short quantum wire (point contact) as a function of split gate bias,  $V_G$ . The dashed line shows the conductance (Hawker *et al.* [37]).

deformation potential coupling to the transverse phonons having non-zero components of  $q_y$  that are strongly focused towards the wire.

#### 4.2.5.2 Long wire

Figure 4.13 shows the conductance–gate voltage characteristics of the device [38]. Since localization effects are expected to dominate in these long wires, the conductance step at high gate biases ( $V_G \approx -0.7$  V) at a value of  $\sim 2e^2/h$  was attributed to short regions of the wire where the width had been reduced by inhomogeneity. The response of the device to a phonon pulse is shown in Fig. 4.14, for  $V_G = -0.5$  V,  $I_{DS} = 100$  nA, and  $T_h = 14$  K. The initial negative spike seen in the data is the residual capacitive breakthrough of the electrical excitation pulse and can be used as a measure of the start of the pulse. The rising edge of the phonon-induced conductivity starts about 80 ns after the start of the pulse, the expected time of flight for LA phonons. However, because

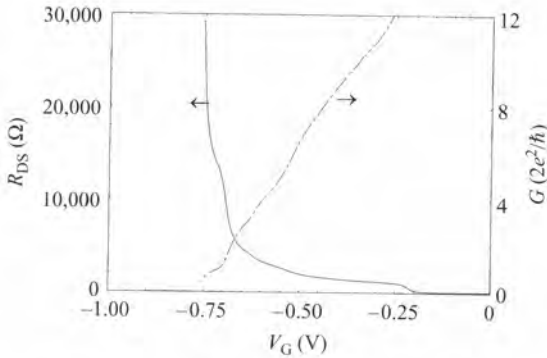


**Fig. 4.13** The two-terminal resistance  $R_{DS}$  and conductance of a long QWR as a function of gate bias voltage (Kent *et al.* [38]).

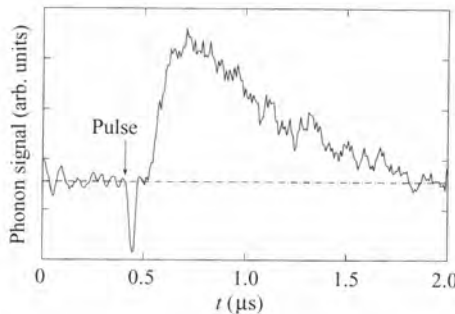


**Fig. 4.14** The phonon signal as a function of time resulting from the change in conductance of a long QWR. The signal was produced by a 50 ns pulse of non-equilibrium phonons with a start time shown by the arrow (Kent *et al.* [38]).

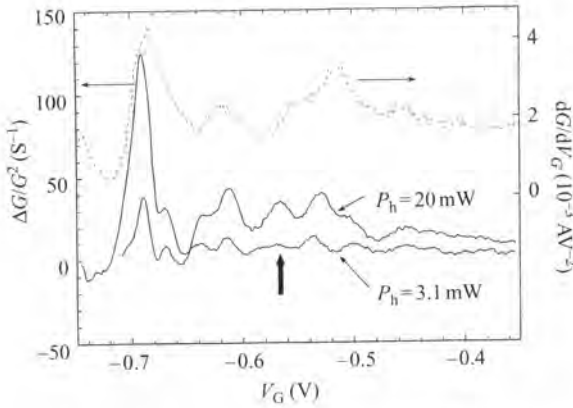


**Fig. 4.15** The phonon-induced change in conductance,  $\Delta G/G^2$ , of a long QWR as a function of split gate bias,  $V_G$ . Data are shown for heater powers of 3.1 and 20 mW. The dashed line shows  $dG/dV_G$  and the vertical arrow indicates the peak attributed to intersubband transitions (Kent *et al.* [38]).

of the poor signal-to-noise ratio and the long time constant of the measuring system ( $\sim 1 \mu\text{s}$ ) it was not possible to separate the two modes and the broad leading edge of the signal was attributed to both LA and TA modes. The absence of a signal at zero bias current showed that the signal observed was not the result of thermopower as seen by Molenkamp *et al.* [41] and other spurious sources of the signal were also ruled out. It was concluded that the signal was due to an increase in conductivity produced by the non-equilibrium phonons. The increase is consistent with weak localization:  $\tau_\phi$  is reduced by the inelastic scattering by non-equilibrium phonons resulting in an increase in the conductance. The existence of weak localization was confirmed by measurements showing negative magnetoresistance.

Figure 4.15 shows that the phonoconductivity signal oscillates as the negative gate voltage is increased. The peaks coincide with peaks in  $dG/dV_G$  (also shown). Peaks in  $dG/dV_G$  occur when  $E_F$  coincides with the edge of a 1D subband in the short ballistic regions present at various points along the length of the inhomogeneous wire. The coincidence of the peaks in phonoconductivity and  $dG/dV_G$  suggest that the electron-phonon interaction is proportional to the DOS as expected [26].

The increase in amplitude with power of all but one of the peaks shown in Fig. 4.15 is slower than linear. This was provisionally attributed to the increase in the average value of  $q$  compared with the cut-offs but not explored in detail. Interestingly, though, the amplitude of the peak indicated by the arrow increased more rapidly with heater temperature than the others and its position did not coincide with a peak in  $dG/dV_G$ . It was proposed that the peak was due to a near vertical phonon-induced intersubband transition similar to transition (e) of Fig. 4.6. Its amplitude showed thermally activated behaviour varying as  $\exp(-\Delta/k_B T_h)$  for  $\Delta > k_B T_h$  so that values for the 1D subband separation could be obtained. The value obtained in this way at  $V_G = -0.55 \text{ V}$  was 3 meV which, from Eq. (4.1), corresponds to

a wire width of 20 nm, in reasonable agreement with that obtained from other methods [42].

#### 4.2.6 Experimental studies of phonon emission from QWRs

Although there have been many theoretical papers describing phonon emission in QWRs, for example [28, 35], there has been very little experimental work. This is not surprising since the power emitted by a wire is proportional to its length and 1D electron density and in practice is too small to detect even with sensitive superconducting bolometers. An experiment has been carried out, though, by Kent *et al.* [43] using an array of 100, 100  $\mu\text{m}$  long, split gate wires formed by EBL from a GaAs/Al<sub>x</sub>Ga<sub>1-x</sub>As heterostructure. At  $V_G = -1.5$  V, the average wire width and 1D electron density were shown by magnetotransport techniques [44] to be 50 nm and  $1.5 \times 10^8 \text{ m}^{-1}$  respectively. Their experimental setup shown in Fig. 4.16 is quite similar to that for phonon absorption. The heater on the back surface of the substrate is replaced by a superconducting bolometer, and the electrons are heated above the lattice temperature by applying a 20 ns voltage pulse to the device. The electrons relax by emitting acoustic phonons which are detected as a transient change in bolometer resistance. One drawback of this technique, not encountered with the absorption experiments, is that the lattice temperature is restricted to the normal–superconducting transition range of the detector (about 2 K).

Figure 4.17 shows the bolometer response at different excitation powers. At low powers, there is no evidence of an LA mode signal and the signal is dominated by the TA mode. This suggested that the cut-off in the electron–phonon interaction was occurring at a relatively low phonon wavevector so that piezoelectric coupling was dominant. Similar effects have also been seen in 2DEGs [45]. At high powers, the signal develops a long tail which is attributable to the downconversion of the optic phonons that would be emitted at higher temperatures  $\sim 50$  K. This occurred at a power input of about 0.2 pW/electron for the wire array, an order of magnitude less than for a 2D heterojunction, and it was suggested that this was due to the additional restriction arising from the  $x$ -direction form factor. However, measurements to examine the effect of wire width on the power per electron at the onset of optic phonon emission are needed before any definite conclusions can be made.

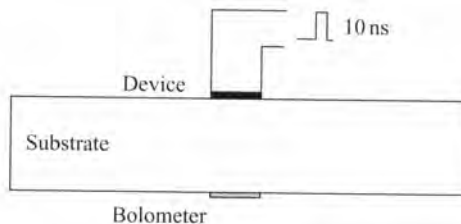


**Fig. 4.16** The experimental arrangement for measuring the phonon emission from an array of QWRs.

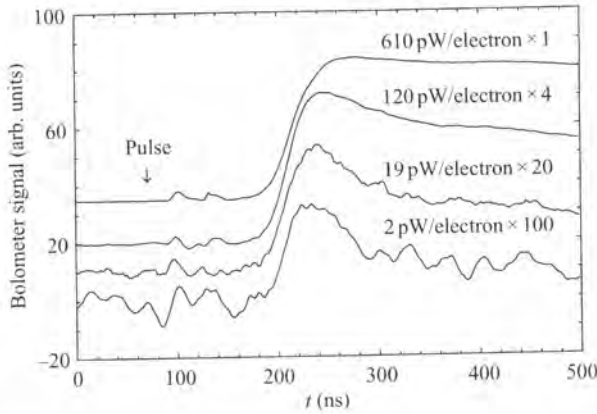


**Fig. 4.17** The bolometer signal from a phonon pulse emitted by an array of QWRs. Data are shown for power inputs to the wires ranging from 2 to 610 pW per electron (Kent *et al.* [43]).

### 4.3 QDs

In this section we will consider carrier–phonon interactions in QDs. The discussion will focus on carrier relaxation processes and, in particular, the predicted phonon bottleneck effects. However, we first briefly review the structure and properties of QDs.

#### 4.3.1 Fabrication and basic properties of QD structures

QDs have been formed by deep etching or gating of 2DEG structures as discussed in relation to QWR formation in Section 4.2.1 or by a combination of both methods. These techniques have the advantage of allowing some control of the size and shape of the dot. However, the minimum dot size and the maximum dot density are restricted by the state of the art in lithography. Practical devices require structures having a high dot density and strong carrier confinement in a dot of small dimensions ( $\sim 10$  nm). Such structures are produced using techniques that rely on self-organization at semiconductor surfaces [46]. As an example, we will briefly consider the In(Ga)As QD system which has been the subject of much recent interest. The In(Ga)As system exhibits efficient interband optical transitions and the relatively small effective mass enhances quantum size effects. These characteristics are favourable both for optoelectronic applications and fundamental studies. The In(Ga)As systems has been used in the phonon experiments described later in this chapter.

Self-organized (or self-assembled) InAs QDs in GaAs are formed by the Stranski–Krastanov growth mode. There is a 7 per cent lattice mismatch between InAs and GaAs and so a layer of InAs grown epitaxially on a GaAs substrate is under strain. At low coverages, less than about 1.8 monolayers (MLs), growth is 2D. However, at higher coverages, the strain is relaxed by the formation of 3D islands. As the coverage is increased further, these islands grow into full-size QDs. The size and shape of the dots depends critically on the growth parameters: deposition rate, temperature, etc., and

whether the dots are on the surface or capped by an overlayer of GaAs. Capped or embedded dots, which are most relevant from a practical point of view, are typically 'lens' shaped with a height of about 3–5 nm and a width of around 15–25 nm. These have a typical density of  $\sim 10^{15} \text{ m}^{-2}$  and sit on top of the 'wetting layer' which is left over from the initial 2D growth, see Fig. 4.18.

The 3D confinement leads to discrete atom-like energy states for the electrons and holes. Exact calculation of the carrier wave functions and energy states in real dots is difficult due to uncertainties regarding the size, shape, and composition [47]. However, a very rough picture may be obtained by assuming the dot is pure InAs in GaAs, with no alloying at the interfaces, and has an idealized shape, such as a square slab. Figure 4.19 shows the energy levels calculated for such a dot having a height of 3 nm and a side

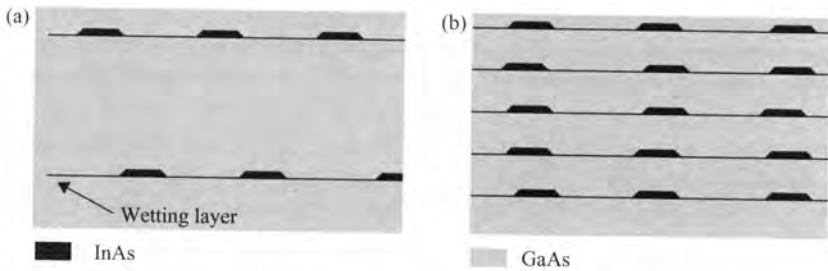


**Fig. 4.18** Schematic diagram of an InAs in GaAs QD structure. In (a) the multiple layers of dots are well separated and there is no coupling between them. In (b) the dot layers are much closer together and are coupled electrically. Furthermore, due to the effect of the strain fields the coupled dots grow in columns.

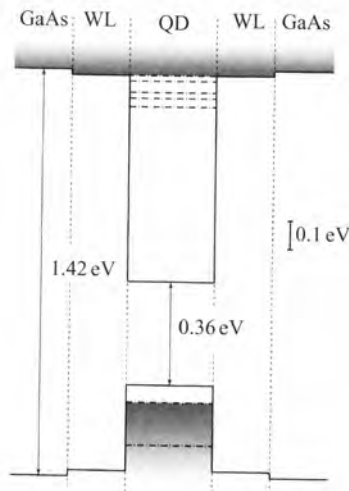


**Fig. 4.19** Energy-level structure of an idealized InAs QD in GaAs. The dot is pure InAs and in the shape of a square slab, 20 nm side and 3 nm thick. The band discontinuity is shared 70 : 30 between the conduction and valence bands respectively. Because they are so close together, the hole energy levels are not shown separately in the figure.

of 20 nm which are fairly typical dimensions for the In(Ga)As system. We see the electron levels are separated by a few tens of millielectronvolts and all states in the dot correspond to the lowest subband for motion in the  $z$ -(growth) direction. Owing to the higher effective mass of holes, the hole energy levels are much closer together; only a few meV separates them and so they cannot be shown individually on this scale. Instead the lowest levels corresponding to the two allowed  $z$ -subbands are indicated. For electrons and holes, the discrete energy levels inside the dot merge to a continuum of levels in the 2D wetting layer. In the example shown, the ground state recombination luminescence energy would be 1.0 eV which is fairly typical for InAs QD systems.

#### 4.3.2 Phonon bottleneck

The 'phonon bottleneck' was postulated to explain the poor luminescence efficiencies measured in early experiments [48]. It was based on the following argument (applicable only to one-phonon processes) [5]. Excited electrons and holes relax down to the ground state by emission of phonons, finally recombining and emitting a photon. Owing to the discrete density of states in QDs, emission of longitudinal optic (LO) phonons is only possible if the energy difference between two confined states,  $\Delta E$ , is, by coincidence, exactly equal to the zone-centre LO phonon energy,  $\hbar\omega_{LO}$ . Coupling to acoustic phonons is restricted to low frequencies (closely spaced dot levels) due to momentum conservation considerations and is expected to be weak. Owing to their larger mass and closer spaced energy levels, holes can relax to the ground state more rapidly than electrons. The electrons in excited levels are thus unable to recombine with ground state holes due to orthogonality. So, the phonon bottleneck is expected to lead to a reduction of luminescence efficiency. However, more recent measurements on self-organized InAs dots show quite high luminescence efficiencies and it was suspected that the poor efficiency measured in the early experiments was really due to damage caused when fabricating the dot structures.

#### 4.3.3 Theoretical work

A number of processes which could possibly shortcut the phonon bottleneck effect have been postulated and discussed in the literature. These include: multiphonon effects [49]; intradot Auger relaxation [50]; Auger-type processes involving electrons and holes, sometimes called electron-hole pair (EHP) relaxation; defect-assisted relaxation [51]; and the formation of coupled electron-phonon (resonant polaron) modes [52]. None of these processes provides a completely satisfactory explanation of the observed relaxation/luminescence. Naively, one might imagine that the rare event of an LO phonon emission is immediately followed by a coherent reabsorption, the result being that the electron-phonon system exhibits undamped 'Rabi' oscillations, or, put simply, undamped oscillations between a carrier and a carrier plus LO phonon state. In more detail, the oscillations described are reversible oscillations between the states  $|e_2, 0\rangle$  and  $|e_1, 1_q\rangle$ , where  $|e_1\rangle$  and  $|e_2\rangle$  are the unperturbed QD carrier states, separated by energy  $\hbar\omega_{LO}$ , and  $|1_q\rangle$  is associated with the one-LO phonon continuum. Such oscillations are exactly analogous to the vacuum Rabi oscillations observed in Rydberg atoms confined in a high-Q cavity [53]. In [52] anharmonicity is invoked to provide a damping mechanism

by which the polaron (coupled carrier–LO phonon mode) is coupled to the two-phonon reservoir allowing polaron relaxation. Multiphonon emission, specifically simultaneous emission of an LO and LA phonon, relaxes the bottleneck condition ( $\Delta E = \hbar\omega_{\text{LO}}$ ) to an extent. Emission becomes possible for a small range of  $\Delta E$  centred around  $\hbar\omega_{\text{LO}}$ , but the probability that a given QD will satisfy the condition is still small. Auger processes—carrier–carrier scattering events in which an electron/hole is able to relax within the QD while a second electron/hole is excited to a higher energy state—may be important at high carrier densities where there is more than one carrier per QD, but will not be significant at lower densities. Defect-mediated relaxation can give rise to significant emission rates at low temperatures (where defect-related processes might have been expected to be frozen out) due to tunnelling through the defect activation barrier for capture and emission. However, this is only possible if the QDs and defects are strongly correlated in position, something which has not been conclusively demonstrated.

Carrier relaxation by direct electron–phonon coupling will be affected by an additional momentum cut-off in comparison with the QWR case. In the InAs QD/GaAs substrate system, QDs are typically pancake-shaped with a diameter and height of order 20 nm and 5 nm respectively and momentum conservation again limits emission in a given direction to phonons with  $q < \hbar/d$ , where  $d$  is the appropriate confinement length. This leads to cut-offs for emission normal and parallel to a QD of the stated dimensions to  $q_{\perp} < 2 \times 10^8 \text{ m}^{-1}$  and  $q_{\parallel} < 5 \times 10^7 \text{ m}^{-1}$  respectively. So the range of available  $q$  values for in-plane emission is considerably more limited than for emission normal to the QDs. Thus, emission, if it occurs, should tend to be directed normal to the QD layer. In energy terms, emission will be limited to acoustic phonons of  $< 1 \text{ meV}$  or zone-centre LO phonons with energy  $\sim 30 \text{ meV}$ . The former requires the existence of a closely spaced ladder of carrier states, not expected in a QD, while the latter can only occur if the QD confined states are separated by exactly the LO phonon energy (phonon bottleneck).

#### 4.3.4 Techniques

The experimental techniques most commonly used for studying the carrier relaxation in QDs are time-resolved photoluminescence (PL), time-resolved PL (TRPL), and PL excitation (PLE) applied to single QDs and ensembles (for a general review of these techniques see [46, 54]). While these techniques can, as for QWRs, give information about the relaxation rates, they do not give direct information concerning the mode and wavevector of the emitted phonons. To differentiate between the possible carrier relaxation mechanisms detecting the phonons emitted is essential to be able to resolve the contributions of acoustic and optic modes. For example, if multiphonon processes are relevant, it should be possible to detect both optic and acoustic phonons with most of the energy emitted as optic phonons. Raman spectroscopy and PL excitation can resolve optic phonons in dots. However, the low energy ( $< 10 \text{ meV}$ ) of acoustic phonons means they are masked by other line broadening effects. Raman measurements are also difficult due to the low density of dots. In this chapter we shall only be reviewing the direct observations made of phonon emission from excited carriers in QD systems.

In essence, direct phonon measurements are extremely simple. Carriers are excited in the sample by a pulse of light, typically from a laser. Relaxation to the band edge

occurs accompanied by phonon emission, followed by recombination and the emission of a bandgap photon, and the phonons are detected by a superconducting bolometer. The bolometer can also be sensitive to any PL emitted during the excitation as a result of direct pair breaking but, since its response to PL will be on the time scale of the experiment ( $\sim 10$ – $100$  ns), coincident with the excitation pulse, it is easily distinguished from the phonon contribution. The various phonon modes emitted can also be distinguished from their arrival times and information on the angular dependence of the emission processes can be obtained by varying the relative positions of the excitation spot and bolometer. In practice it is not possible to move the detector so the excitation spot is scanned over the sample surface. The intensity of any given signal component (LA, TA, PL, etc.) can be extracted from the time of flight trace at each point and plotted to produce an image. This method does, of course, have the disadvantage that the set of QDs sampled changes as the excitation spot moves. For a typical excitation area of diameter  $10\ \mu\text{m}$ , the measurement samples some  $10^4$  QDs simultaneously. It can be seen that direct observation of the phonon emission in the way described can potentially give very detailed information on the phonon emission.

#### 4.3.5 Phonon experiments on QDs

Measurements using this technique have been carried out to study the phonons emitted by optically excited carriers in the self-organized InAs QD system [55]. The samples were based on an MBE-grown GaAs wafer containing 20 InAs QD layers (1.8 ML) separated by 30 nm of GaAs. (At this separation the QDs were not vertically aligned and electrically independent.) Carriers were excited in the GaAs surface layer by 12 ns pulses of  $\lambda = 524$  nm radiation from a frequency-doubled Q-switched Nd-YLF laser. The phonons and photons emitted as the carriers relaxed to the QD ground state and recombined were detected by a superconducting aluminium bolometer on the opposite side of the GaAs substrate. A typical time of flight trace is shown in Fig. 4.20. The sharp signal near  $t = 0$ , coincident with the laser pulse, is due to luminescence photons reaching the bolometer (the GaAs substrate is transparent to the dot luminescence). A short time later, corresponding to the ballistic phonon time of flight, the bolometer detects first longitudinal acoustic (LA) and then transverse acoustic (TA) phonon pulses. The ballistic TA phonons are followed by a long, slowly decaying tail. Also shown in Fig. 4.20 is the time of flight trace for optical excitation of a GaAs wafer with no dots (trace b). This latter signal is characteristic of relaxation phonons in the GaAs. Highly excited carriers relax by emitting a cascade of LO phonons before reaching the band edge, recombining with holes and emitting a bandgap photon. The LO phonons decay by a series of steps, on a picosecond timescale, ending in high energy TA phonons which propagate diffusively to the bolometer giving the long tail after the TA peak. No optically induced signal, coincident with the excitation, is evident in the ‘no dots’ sample because the substrate is highly opaque to GaAs bandgap recombination luminescence. In contrast, the QD sample trace shows relatively little tail to the ballistic TA peak, indicating that a significantly higher proportion of the energy relaxed by phonon emission is going into low-frequency acoustic modes. By analysing the two traces in Fig. 4.20 it was possible to deduce that more than 50 per cent of the energy relaxed by carriers in the QD system was emitted as acoustic phonons. Whilst it was not possible to state definitively the

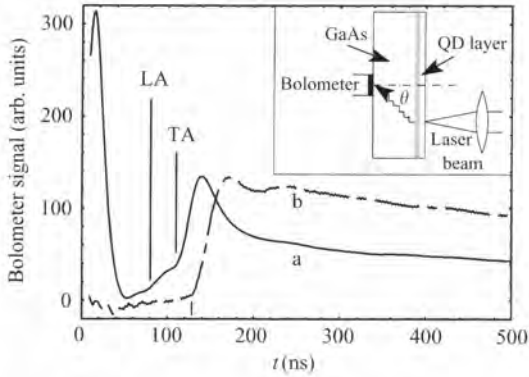


**Fig. 4.20** Bolometer signal following optical excitation of InAs/GaAs QD heterostructure (trace a, solid line). The initial peak near  $t = 0$  is due to QD luminescence reaching the detector. Signals due to the ballistic LA and TA phonons are indicated. Trace b, dashed line, shows the bolometer signal obtained by optically exciting a bare GaAs layer (no QDs). The inset shows the experimental arrangement. The data are for an excitation point directly opposite the bolometer ( $\theta = 0$ ).

nature of the mechanism which gave rise to such significant low-frequency acoustic emission, Auger scattering was suggested as a suitable candidate. Two electrons initially captured in a QD undergo a scattering event in which one carrier remains bound in the QD while the other is expelled into the wetting layer (WL) continuum of states. Energy is conserved in the process, but, once in the WL continuum, the expelled electron can undergo low-energy transitions allowing acoustic phonon emission.

These results were obtained at relatively low laser powers where the instantaneous PL bolometer response scaled linearly with laser power. At higher laser powers the PL response saturated, the LA component increased strongly relative to the TA, and the TA response itself developed a long tail. This result was explained in terms of ‘filling’ of the QDs with carriers as the density of photoexcited carriers rose. At high carrier densities further carrier capture into the QDs is only possible after recombination and is limited by the radiative recombination lifetime. The average carrier lifetime in the WL is increased as is the 2D carrier density. This has the effect of moving the in-plane momentum conservation cut-off at twice the Fermi wavevector ( $2k_F$ ) to larger phonon wavevectors. Increasing the momentum conservation cut-off favours the emission of deformation potential ( $\propto q$ )-coupled LA phonons over mainly piezoelectrically ( $\propto q^{-1}$ )-coupled TA phonons. The appearance of the TA tail was attributed to the formation of a ‘hot spot’ [56] in the excitation region.

By raster scanning the excitation spot over the sample surface and using a bolometer that is small on the scale of the wafer thickness it is possible to produce a high-resolution ‘image’ showing the angular dependence of the phonon emission. In [57] this method is used to produce images of the angular dependence of the phonon emission from multiple (10–20) layer QD structures grown on wafers with orientation (100), (311A), and (311B). For comparison purposes measurements were also made on samples fabricated on wafers with multiple InAs WLs, but no dots present, on blank, ungrown material, and also on blank wafers with a metal deposited on the surface to thermalize the excitation. Excitation

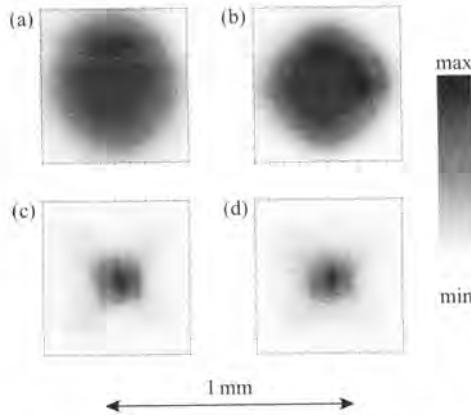


**Fig. 4.21** Images of the LA (b) and TA (d) phonon signals due to optical excitation of InAs QDs. Also shown are corresponding images produced by laser heating a metal film (a) and (c) for which the angular distribution of  $q$ -vectors of the emitted phonons is expected to be isotropic. The detectors are located at the centre of the images and the laser is scanned over a  $1 \times 1 \text{ mm}^2$  area.

of a metal film generates an isotropic distribution of low-frequency acoustic phonons allowing a better discrimination between the effect on the angular dependence of the QDs and phonon focusing within the GaAs substrate. Figure 4.21 shows images of the emitted phonon flux for the (100) sample as a function of the position of the excitation region, and equivalent images from the metal film sample. Clearly, in the QD sample the emission into both LA and TA modes is directed more narrowly normal to the QD layers than is the case for the metal film sample. This is consistent with emission from structures having a thickness of a few nm and lateral dimensions significantly larger. In a previous work [58] the QDs in this material were shown to be approximately ‘pancake’ shaped with a height of 3.3 nm and diameter 23 nm. From simple momentum conservation considerations emission in a given direction is limited to phonons with  $q < \hbar/W$  (easily shown as a consequence of the uncertainty principle), where  $w$  is the thickness of the volume in which emission occurs in the direction of emission. Calculating the ‘cut-off’ for the directions normal and parallel to the QDs gives  $q < 3 \times 10^8 \text{ m}^{-1}$  and  $q < 4 \times 10^7 \text{ m}^{-1}$  respectively. Plainly, the range of available  $q$  values allowed for in-plane emission is considerably more limited than for emission normal to the QDs. Thus, emission should be directed more narrowly normal to the QD layer as is observed. At very low excitation densities, where the probability of finding more than one electron per dot is low, the phonon emission was still observed to consist of a high proportion of subterahertz acoustic phonons. At these carrier densities Auger scattering is no longer possible and another mechanism must be responsible. A possible mechanism was proposed based on the formation of excitons in the QDs. Low-energy acoustic phonon emission requires the existence of a closely spaced ladder of energy levels. This is the case for holes but not electrons because of the difference in effective mass. The energy-level structure for the composite particle is essentially a modified combination of the free electron and hole levels. This means that the separation between exciton energy levels will be similar to that of the holes and the exciton will be able to relax to its ground state by

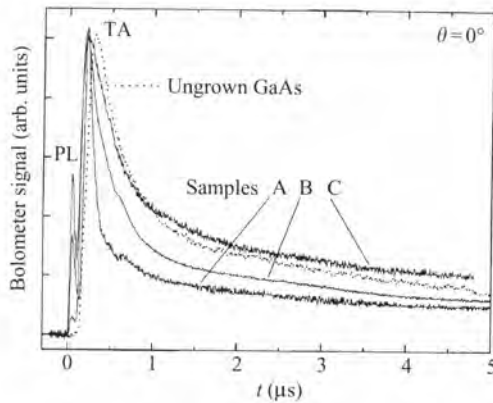


**Fig. 4.22** Phonon signals obtained by photoexcitation of (A) uncoupled, (C) strongly coupled, and (B) intermediate coupled, multiple InAs QD layers in GaAs. The bolometer was located directly opposite the excitation spot. Also shown is the signal obtained using a GaAs sample with no QDs.

emission of acoustic phonons. A proportion of these will be low-energy ballistic acoustic phonons.

In multiple layer QD structures, at sufficiently small layer separations, the strain field associated with each QD affects the growth of QDs in subsequent layers and vertical alignment occurs. The QDs form coupled stacks, see Fig. 4.18. Overlap of the carrier wave functions from adjacent QDs in a stack should give rise to additional electron and hole states in comparison to uncoupled dots. The effect of this coupling on the phonon emission was investigated in [59]. Three samples were studied having layer separations of 30 nm (A, QDs uncoupled), 2.5 nm (B), and 1.7 nm (C, QDs strongly coupled). Strong coupling of the QDs appeared to open up an efficient channel for optic phonon emission. Figure 4.22 shows normalized phonon signals measured in the three samples with the excitation spot directly opposite the bolometer ( $q = 0$ ). For comparison the normalized phonon signal from an ungrown sample is also shown. As previously, the uncoupled QD sample (A) produces a relatively sharp TA mode peak with little tail. In contrast, the TA peak observed in the strongly coupled QD sample (C) shows a well-developed tail approaching that observed in the ungrown sample. Sample B shows a tail intermediate between A and C. As discussed previously, the appearance of a strong tail of late arriving TA mode phonons is characteristic of LO mode emission. The authors attributed the increased LO emission at close QD coupling to the formation of a quasicontinuous electron energy-level spectrum resulting from the overlap of electronic wave functions in adjacent QDs. Fast carrier relaxation involving emission of LO phonons is only possible if the energy difference between two carrier levels is accidentally equal to the LO phonon energy. The additional carrier energy levels available in the closely coupled QD case increase the probability that the LO phonon emission condition can be met. In the limit of very strong coupling the electronic spectrum forms a band and the emission of LO phonons becomes possible as in the bulk GaAs case.

A common factor of the work described in [55, 57], and [59] is that the carriers were excited by photons having an energy (2.4 eV) well in excess of the GaAs bandgap

(1.5 eV). A significant proportion of the subsequent non-radiative energy loss is as LO phonons in the GaAs cladding. To an extent, this background of phonon emission obscures the energy relaxation of interest that occurs once the carriers have been captured in the WL/QD system. In [60] the background was eliminated by exciting the samples with a Ti:sapphire laser 'tuned' to the GaAs bandgap and using a wider range of excitation energy densities than was possible before. The samples investigated were fabricated from the same three wafers used in [59]. In the uncoupled QD sample, at high excitation densities (corresponding to more than one electron-hole pair per QD) the authors observed significant low-energy acoustic phonon emission. At excitation densities corresponding to one or fewer electron-hole pairs per QD this low-energy ballistic component was absent. The authors attributed its appearance at high induced carrier densities to the onset of Auger scattering, consistent with [55] in which higher excitation densities were used. Simultaneous measurements of the TRPL revealed that the QD sample with the strongest coupling exhibited the fastest PL rise and fall times, again indicative that strong coupling gives rise to additional carrier states and more rapid relaxation.

#### 4.4 Conclusions

It should be clear after reading this chapter that direct phonon studies of carrier-phonon interactions in QWRs and QDs are nowhere near as mature as in 2DEG structures. However, the measurements reviewed here demonstrate that direct phonon experiments can also give new and complementary information about 1D and 0D electronic systems. Phonon techniques are evidently more suitable for investigating carrier-phonon interactions in these systems where traditional transport and optical techniques have limited applicability due to disorder and experimental factors.

Device processing has proved the limiting factor in phonon studies of QWRs. For emission experiments large homogeneous arrays of wires are needed and absorption experiments require uniform wires with excellent electrical contacts. Nevertheless, phonon absorption experiments have confirmed theoretical estimates of carrier-phonon scattering rates and demonstrated the effects of the unique 1D density of carrier states. Phonon emission experiments have shown a reduced power loss per carrier at the onset of optic phonon emission compared with a 2DEG at the same temperature ( $T_c \approx 50$  K). This is consistent with predictions based on the phonon bottleneck model.

Whether or not a phonon bottleneck exists in QD systems is still very much an open question. Although its existence is suggested by theoretical arguments, there is no experimental evidence of the long relaxation times that would reduce the optical efficiency of self-organized InAs QDs which are likely to form the basis of practical devices. This suggests that alternative relaxation mechanisms exist, but these have, however, still to be identified. Phonon measurements of QDs clearly demonstrate that a significant proportion of the phonon emission from excited carriers in QDs appears as low-energy acoustic phonons. A necessary condition for such emission is the existence of a closely spaced ladder of carrier states. Two possible candidates for satisfying this condition have been suggested: Auger processes resulting in an ejected carrier in the WL where a continuum of states exists, or formation of a bound exciton which will possess an energy-level

structure that reflects the more closely spaced energy-level structure of the holes. It is likely that direct phonon measurements will continue to play a role in understanding the processes of carrier relaxation in QDs.

A possible future application of phonon experiments in QWR systems is in the search for the Luttinger liquid state. Phonon measurements have already been used to probe excitations of the interacting 2D electron liquid in the FQHE and have been shown to be less sensitive to the effects of disorder than are transport measurements. If the same were to be the case in QWRs, phonon spectroscopy could play a major role in investigating this elusive state of matter.

## References

1. van Wees, B.J., van Houten, H., Beenakker, C.W.J., Williamson, J.G., Kouwenhoven, L.P., van der Marel, D., and Foxon, C.T. (1988). *Phys. Rev. Lett.*, **60**, 848; Wharam, D.A., Thornton, T.J., Newbury, R., Pepper, M., Ahmed, H., Frost, J.E.F., Hasko, D.G., Peacock, D.C., Ritchie, D.A., and Jones, G.A.C. (1988). *J. Phys. C: Solid State Phys.*, **21**, 209.
2. Auslaender, O.M., Yacoby, A., de Picciotto, R., Baldwin, K.W., Pfeiffer, L.N., and West, K.W. (2002). *Science*, **295**, 825.
3. Tarucha, S., Austing, D.G., Honda, T., van der Hage, R.J., and Kouwenhoven, L.P. (1996). *Phys. Rev. Lett.*, **77**, 3613.
4. Schedelbeck, G., Wegscheider, W., Bichler, M., and Abstreiter, G. (1997). *Science*, **278**, 1792.
5. Kapon, E. (1992). *Proc. IEEE*, **80**, 398.
6. Cunningham, J., Talyanskii, V.I., Shilton, J.M., Pepper, M., Simmons, M.Y., and Ritchie, D.A. (1999). *Phys. Rev.*, **B60**, 4850.
7. Arakawa, Y. and Sakaki, H. (1982). *Appl. Phys. Lett.*, **24**, 195.
8. Sellin, R.L., Ribbat, C., Bimberg, D., Rinner, F., Konstanzer, H., Kelemen, M.T., and Mikulla, M. (2002). *Electron. Lett.*, **38**, 883.
9. Shields, A.J., O'Sullivan, M.P., Farrer, I., Ritchie, D.A., Leadbeater, M.L., Patel, N.K., Hogg, R.A., Norman, C.E., Curson, N.J., and Pepper, M. (2001). *Jpn. J. Appl. Phys.*, **40**, 2058.
10. Hu, X.D. and Das Sarma, S. (2000). *Phys. Rev.*, **A61**, 062301.
11. Benisty, H., Sotomayor-Torres, C.M., and Weisbuch, C. (1991). *Phys. Rev.*, **B44**, 10945.
12. Bockelmann, U. and Bastard, G. (1990). *Phys. Rev.*, **B42**, 8947.
13. Weisbuch, C. and Vinter, B. (1991). *Quantum semiconductor structures*, Academic Press, New York; de Picciotto, R., Störmer, H.L., Pfeiffer, L.N., Baldwin, K.W., and West, K.W. (2001). *Nature*, **411**, 51.
14. Egeler, T., Abstreiter, G., Weimann, G., Demel, T., Heitmann, D., Grambow, P., and Schlapp, W. (1990). *Phys. Rev. Lett.*, **65**, 1804.
15. Strenz, R., Roßkopf, V., Hirler, F., Abstreiter, G., Böhm, G., Tränkle, G., and Weimann, G. (1994). *Semicond. Sci. Technol.*, **9**, 399.
16. Thornton, T.J., Pepper, M., Ahmed, H., Andrews, D., and Davies, G.J. (1986). *Phys. Rev. Lett.*, **56**, 1198.
17. Zheng, H.Z., Wei, H.P., Tsui, D.C., and Weimann, G. (1986). *Phys. Rev.*, **B34**, 5635.
18. Laux, S.E., Frank, D.J., and Stern, F. (1988). *Surf. Sci.*, **196**, 101.
19. Beenakker, C.W.J. and van Houten, H. (1991). In *Solid state physics*, Vol. 44 (ed. H. Ehrenreich and D. Turnbull), pp. 1–228. Academic Press, New York.
20. Landauer, R. (1986). *IBM J. Res. Dev.*, **57**, 1761.
21. Blencowe, M.P. (2001). In *Low dimensional semiconductor structures* (ed. K. Barnham and D. Vvedensky), ch. 4, Cambridge University Press, Cambridge.
22. Stroschio, M.A. and Dutta, M. (2001). *Phonons in nanostructures*, Cambridge University Press, Cambridge.

23. Pentland, I.A. (2000). Ph.D. thesis, University of Nottingham.
24. Williams, P.F. and Bloch, A.N. (1974). *Phys. Rev.*, **B10**, 1097.
25. Lee, J. and Spector, H.N. (1985). *J. Appl. Phys.*, **57**, 366.
26. Blencowe, M. and Shik, A.Y. (1996). *Phys. Rev.*, **B54**, 13899.
27. Gurevich, V.L., Pevzner, V.B., and Hess, K. (1995). *Phys. Rev.*, **B51**, 5219.
28. Bergmann, G. (1983). *Phys. Rev.*, **B28**, 2914.
29. Chakravarty, S. and Schmid, A. (1986). *Phys. Rep.*, **140**, 193.
30. Shik, A.Y. and Challis, L.J. (1993). *Phys. Rev.*, **B47**, 2082.
31. Das Sarma, S. and Campos, V.B. (1992). *Phys. Rev.*, **B47**, 3728.
32. Senna, R. and Das Sarma, S. (1993). *Phys. Rev. Lett.*, **70**, 2593.
33. Fishman, G. (1987). *Phys. Rev.*, **B36**, 7448.
34. Mickevicius, R. and Mitin, V. (1993). *Phys. Rev.*, **B48**, 17194.
35. Xu, W. (1996). *Appl. Phys. Lett.*, **68**, 1355.
36. Sugaya, T., Bird, J.P., Ferry, D.K., Sergeev, A., Mitin, V., Jang, K.-Y., Ogura, M., and Sugiyama, Y. (2002). *Appl. Phys. Lett.*, **81**, 727.
37. Hawker, P., Pentland, I.A., Kent, A.J., Naylor, A.J. and Henini, M. (2000). *Physica*, **E6**, 522.
38. Kent, A.J., Naylor, A.J., Hawker, P., Henini, M. and Bracher, B. (1997). *Phys. Rev.*, **B55**, 9775.
39. Kent, A.J., Naylor, A.J., Hawker, P., and Henini, M. (2000). *Phys. Rev.*, **B61**, R16311.
40. Lehmann, D., Jasiukiewicz, Cz., and Kent, A.J. (2000). *Physica*, **E6**, 538.
41. Molenkamp, L.W., van Houten, H., Beenakker, C.W.J., Eppenga, R. and Foxon, C.T. (1990). *Phys. Rev. Lett.*, **65**, 1052.
42. Naylor, A.J. (1999). Ph.D. thesis, University of Nottingham.
43. Kent, A.J., Naylor, A.J., Pentland, I.A., Hawker, P., and Henini, M. (1999). *Physica*, **B263-264**, 170.
44. Berggren, K.F., Thornton, T.J., Newson, D.J., and Pepper, M. (1986). *Phys. Rev. Lett.*, **57**, 1769.
45. Hawker, P., Kent A.J., Hughes, O.H., and Challis, L.J. (1992). *Semicond. Sci. Technol.*, **7**, **B29**.
46. Bimberg, D., Grundmann, M., and Ledentsov, N.N. (1999). *Quantum dot heterostructures*, Wiley, Chichester.
47. Zunger, A. (2001). *Phys. Status Solidi*, (b) **224**, 727.
48. Arnot, H.E.G., Watt, M., Sotomayor-Torres, C.M., Glew, R., Cusco, R., Bates, J., and Beaumont, S.P. (1989). *Superlattices Microstruct.*, **5**, 459.
49. Inoshita, T. and Sakaki, H. (1996). *Physica*, **B227**, 373.
50. Ferreira, R. and Bastard, G. (1999). *Appl. Phys. Lett.*, **74**, 2818.
51. Schroeter, D.F., Griffiths, D.J., and Sercel, P.C. (1996). *Phys. Rev.*, **B54**, 1486.
52. Hameau, S., Guldner, Y., Verzelen, O., Ferreira, R., Bastard, G., Zeman, J., Lemaitre, A., and Gérard, J.M. (1999). *Phys. Rev. Lett.*, **83**, 4152; Verzelen, O., Ferreira, R., and Bastard, G. (2000). *Phys. Rev.*, **B62**, R4809.
53. Brune, M., Schmidt-Kaler, F., Maali, A., Dreyer, J., Hagle, E., Raimond, J.M., and Haroche, S. (1996). *Phys. Rev. Lett.*, **76**, 1800.
54. Masumoto, Y. and Takagahara, T. (eds) (2002). *Semiconductor quantum dots: physics, spectroscopy and applications*, Springer-Verlag, Berlin.
55. Hawker, P., Kent, A.J., and Henini, M. (1999). *Appl. Phys. Lett.*, **75**, 3832.
56. Danilchenko, B.A., Kazakovtsev, D.V., and Slutskii, M.I. (1989). *Phys. Lett. A*, **138**, 77.
57. Bellingham, R., Kent, A.J., Akimov, A.V., and Henini, M. (2001). *Phys. Status Solidi*, (b) **224**, 695.
58. Hawker, P., Kent, A.J., and Henini, M. (1999). *Physica*, **B263**, 514.
59. Kent, A.J., Akimov, A.V., Cavill, S.A., Bellingham, R.J., and Henini, M. (2002). *Physica*, **B316-317**, 198.
60. Kent, A.J., Stanton, N.M., and Henini, M. (2003). *Physics of Semiconductors 2002, Proc. 26th Int. Conf. on the physics of semiconductors* (ed. J.H. Davies and A.R. Long), ID-R2.4, Institute of Physics conference series 171, Bristol.



# 5 Phonon drag thermopower of low-dimensional systems

R. Fletcher, E. Zaremba, and U. Zeitler

---

## 5.1 General introduction

### 5.1.1 Introduction and historical background

Most of the work on the thermoelectric properties of reduced dimensionality systems has focused on the two-dimensional (2D) case. In this introductory section we will give a brief, historical survey of this work and indicate how it is related to earlier work on bulk metals and semiconductors. Readers who are unfamiliar with thermoelectricity would benefit by first reading the following section which gives an introduction to the phenomena. There are two previous reviews, one by Gallagher and Butcher [1] covering work up to 1992, and a more recent one by Fletcher [2] on magnetothermoelectric effects in semiconductors, but not confined to the 2D case.

There are a number of related thermoelectric effects, but this chapter concentrates on the thermopower  $S$ . There are two, additive and essentially independent, contributions to  $S$  from diffusion,  $S^d$ , and phonon drag,  $S^g$ , which may or may not be easily separable experimentally. The former is always present, unless coincidentally zero, but the latter, the focus of this chapter, is typically observed only at temperatures below about 100 K and arises as follows. In a temperature gradient, phonons have a non-equilibrium distribution and carry both an energy and a (crystal) momentum current in a direction down the temperature gradient. As a result of electron-phonon (e-p) collisions, momentum is transferred from the phonons to the electrons, which gives rise to an electric current in the electron gas. However, the experimental condition is that the external current must be zero, so an electric field is induced which provides an equal and opposite current. It is the ratio of this electric field to the temperature gradient that constitutes phonon drag thermopower  $S^g$ .

$S^d$  is the contribution to  $S$  that arises from the diffusive motion of the carriers in a temperature gradient. Although this chapter concentrates on  $S^g$ , we provide an elementary introduction to  $S^d$  so that experimental data may be more easily understood. When the details of electronic scattering are neglected,  $S^d$  is a direct measure of  $S_e$ , the entropy per unit area (or volume in 3D) of the carriers [3]. One finds  $S^d = -S_e/n_s e$  where  $n_s$  is the 2D areal density of the carriers and the negative sign implies negative charge carriers. This is valid for both degenerate and non-degenerate systems. Most of the data we will examine are for 2D degenerate electrons for which  $S_e/n_s = \pi^2 k_B^2 T / 3 E_F$  at zero magnetic field, where  $E_F$  is the Fermi energy.

When electronic scattering is considered,  $S^d$  also depends on the factor  $p = (\partial \ln \tau / \partial \ln E)_{E_F}$  where  $\tau$  is the momentum relaxation time of the carriers;  $p$  is of order

unity and can be of either sign. One finds

$$S^d = -\frac{\pi^2 k_B^2 T}{3eE_F}(1+p) = -\frac{S_e}{n_s e}(1+p) \quad (5.1)$$

for negative carriers, a result valid for elastic scattering and degenerate electrons. For our purposes the most important feature is that, under the stated conditions,  $S^d \propto T$ . Equation (5.1) is obtained from the well-known Mott relation [4]  $S^d = -(\pi^2 k_B^2 T/3e)(\partial \ln \sigma / \partial E)_{E_F}$  where  $\sigma$  is the conductivity considered to be a function of the electron energy  $E$ . To be valid it also requires that  $\sigma(E)$  does not vary strongly with  $E$  on the scale of  $k_B T$ .

Let us now turn back to the primary focus of the chapter, phonon drag thermopower  $S^g$ . Before the availability of 2D materials,  $S^g$  had been studied extensively in a large variety of bulk metals and semiconductors [5–7]. There are basically two approaches which have been, and still are, used to describe drag for these cases. These have also been used extensively by experimentalists to analyse and discuss 2D data and so we briefly outline them here.

In bulk metals at low temperatures, phonons are scattered primarily by electrons, so that practically all the momentum in the phonon flux is transferred to the electrons. The simplest result for  $S^g$  in this situation is

$$S^g = -f \frac{C_v}{3Ne}, \quad (5.2)$$

where  $C_v$  is the specific heat of the lattice per unit volume,  $N$  the (3D) electron density, and  $f$  is a factor which gives the fraction of the phonon crystal momentum that is absorbed by the electrons, and is of order unity as a first approximation for pure metals at low temperatures. Elementary derivations of this equation appear in many texts (e.g., Ref. [8]) and in the review of Gallagher and Butcher [1]. Note that the factor  $C_v/3$  is the entropy of the lattice per unit volume  $S_p$  at low temperatures. Thus, in the simplest case (ignoring energy-dependent carrier scattering) the result for the total thermopower is given by  $S = S^d + S^g = (S_e + fS_p)/Ne$ . There are a number of assumptions required to derive this result for  $S^g$ , but in particular it requires that all phonons can interact with the electrons (i.e. energy and momentum can always be conserved) and that only normal (N-type) e–p processes are allowed as opposed to Umklapp (U-type) processes which involve a reciprocal lattice vector. This latter restriction means that the result strictly applies only at very low temperatures, and then only to those simple metals (perhaps only the alkali metals) where the Fermi surface does not contact a Brillouin zone boundary. Under these conditions  $S^g \propto T^3$  which is easily distinguished from  $S^d \propto T$ . It is worth pointing out, anticipating the discussion to follow, that the approximate  $T^3$  dependence of  $S^g$  often seen in 2D systems over restricted temperature ranges is somewhat coincidental.

The situation in bulk semiconductors is fundamentally different from that in metals. The primary difference is that the phonon distribution is essentially unaffected by e–p scattering, that is e–p scattering is very weak in comparison with other phonon scattering processes, an assumption diametrically opposite to that for Eq. (5.2). In addition, in both degenerate and non-degenerate semiconductors, only a small range of momentum states

are occupied by the carriers so that only very long-wave phonons can interact with the electrons because of energy and momentum conservation requirements. Using classical statistics for the electrons, Herring [9] developed the following result:

$$S^g = -\frac{\Lambda s}{\mu_{ep} T} \quad (5.3)$$

for this case. The negative sign assumes the carriers are electrons,  $\mu_{ep}$  is the mobility that the electrons would have if scattered only by phonons, that is  $\mu_{ep} = e\tau_{ep}/m_e^*$  with  $\tau_{ep}$  being the momentum relaxation time of the electrons for e-p scattering,  $m_e^*$  is the effective mass of the electrons, and  $\Lambda$  and  $s$  are the phonon mean free path and velocity respectively. Interestingly, the dimensionality of the electron system is not explicit in this result, though it is implicit in  $\mu_{ep}$ .

Equation (5.3) has the important feature that it shows  $S^g$  to be intimately related to  $\tau_{ep}$ , a quantity which is normally obtained from measurements of the resistivity  $\rho$ .<sup>†</sup> In contrast, Eq. (5.2) is independent of any parameters concerning e-p scattering because e-p scattering is the overwhelmingly dominant relaxation mechanism for the phonons and the drag is 'saturated'; in principle an analogous parameter  $\tau_{pe}$ , the momentum relaxation time of phonons due to p-e scattering, appears in the factor  $f$  if phonon scattering mechanisms other than e-p are also significant. Equation (5.3) has the disadvantage that much of the essential physics is hidden in  $\mu_{ep}$ , for example the  $n_s$  and  $T$  dependences. Simple derivations of Eq. (5.3) have been given by Herring [9], Blatt [8], and Gallagher and Butcher [1]. We will give a detailed derivation of this equation for degenerate electron statistics in Section 5.1.3. Both the above expressions were initially derived only for the case of zero magnetic field.

This review is concerned with  $S^g$  in reduced dimensionality systems fabricated with semiconductors. These are usually based on heterostructures or metal-oxide-semiconductor interfaces. There are other systems that are quasi-1D and 2D but these will not be covered in detail since the theoretical development is in a more primitive state. Some organic materials and also the high-temperature superconductors are quasi-2D systems. As far as we are aware, the only thermopower data relevant to the organics are those of Yu *et al.* [10]. There is more information concerning thermopower in high-temperature superconductors, but in both cases  $S^g$  does not seem to play a significant role, or at least has not been invoked to any significant extent. Of the 1D and quasi-1D systems, there are thermopower measurements on carbon nanotubes [11], Bi [12], and AuFe [13] nanowires, and the linear chain inorganics typified by NbSe<sub>3</sub> [14–16]. Phonon drag is occasionally mentioned in the analysis of data, but usually only in a qualitative way.

As far as we are aware, the first thermoelectric measurements on a true 2D system were those of Zavaritskiĭ *et al.* (reviewed in ref. [17]). They initially examined 2D electron gases at interfaces in bicrystals and at cleaved surfaces in Ge, and later studied 2D carriers in Si-MOSFETs. All this initial work was carried out at zero magnetic field. They recognized  $S^g$  as the probable mechanism for the large magnitudes of the

<sup>†</sup> Note that other electronic relaxation times can also be defined which are generally different from the momentum relaxation time, for example the energy relaxation time.

thermopower that they observed at low temperatures. Because 2D systems are metallic at low temperatures, they interpreted their  $S^{\text{g}}$  data using Eq. (5.2). However, there were difficulties in trying to adapt this equation to 2D, for example Zavaritskiĭ used an effective 3D density of electrons  $N = n_s/L_z$  where  $L_z$  is the thickness of the 2D electron layer. Later it was shown that this should be  $N = n_s/t$  where  $t$  is the substrate thickness [18]. Another difficulty with the approach is that the 3D phonon distribution is essentially unaffected by e-p scattering, a situation much closer to the semiconductor case. This makes the factor  $f$  in Eq. (5.2) very small (perhaps  $\sim 0.01$ ). In spite of these problems, Zavaritskiĭ and co-workers were successful in identifying many of the important parameters contributing to  $S^{\text{g}}$  and had many important insights, such as the ‘Kohn anomaly’ which we mention again in Sections 5.1.3, 5.2.2, and 5.3.3.

The availability of high-quality, well-characterized GaAs/AlGaAs samples led to a surge in experimental work by many groups in the mid 1980s. Because of the discovery of the quantum Hall effect, the emphasis of experiment and theory was on the properties of 2D electrons in high magnetic fields. Theory, based on a consideration of  $S^{\text{d}}$  only, predicted that thermopower would be a direct measure of the entropy of the electron gas [19], a result in keeping with our previous comments. However, the early experimental situation was confused in that a great range of magnitudes was observed. In retrospect, it is evident that some of the published data are invalid. Furthermore, it rapidly became clear [1] that the data were dominated by  $S^{\text{g}}$  just as Zavaritskiĭ [17] had already established for Ge and Si systems. The contribution of  $S^{\text{g}}$  in these new measurements was often qualitatively interpreted in terms of Herring’s result, Eq. (5.3). This simple 3D model dating back to 1954 was first applied to 2D electron systems by Nicholas [20]. Because some of the early experimental data were incorrect, there was confusion for a number of years about whether  $S^{\text{g}}$  was dependent on sample mobility, which is primarily determined by impurity scattering at low temperatures. Equation (5.3) suggests it should not be (and indeed it is not), but this expression was regarded as an approximation and its bounds of validity were not understood. In addition  $S^{\text{g}}$  depends on  $n_s$  which varied over a wide range for different experimental groups and Eq. (5.3) does not give an explicit  $n_s$  dependence.

Closely following these experimental results, theorists began to develop detailed models of  $S^{\text{g}}$  for 2D systems. In particular, Butcher and co-workers, and Lyo, published papers on many aspects of the problem which advanced our understanding enormously. The theoretical results began to show good absolute agreement with experiment, particularly at zero magnetic field. A few calculations on  $S^{\text{g}}$  in high magnetic fields were also made and were reasonably successful, though much still remains to be done in this area.

However, the theoretical papers tended to lose contact with the early physical models, Eq. (5.2) and Eq. (5.3), though there were attempts to explore the connections [18]. In particular Eq. (5.3) indicates a relation between  $\tau_{\text{ep}}$  and  $S^{\text{g}}$  which was not obvious in the theoretical developments. Interestingly, the theory came full circle when it was shown recently that the theoretical results (specifically those at low temperatures for zero or low magnetic fields) were, in fact, essentially identical in content to Herring’s original result Eq. (5.3) [21]. Thus at low temperatures we can now determine  $\mu_{\text{ep}}$ , or equivalently  $\tau_{\text{ep}}$ , from either  $S^{\text{g}}$  and  $\rho$ , whichever is more convenient. In this connection, one of the most interesting points about  $S^{\text{g}}$  is that it is insensitive to electron-impurity scattering (cf. Eq. (5.3)) over a very wide range of carrier mobilities, even though this might be

the overwhelmingly dominant scattering mechanism in  $\rho$ . This makes it very powerful in investigating  $\tau_{ep}$  for samples where impurity scattering is so strong as to make  $\tau_{ep}$  unobservable in  $\rho$ .

Our intent in the rest of this chapter is to concentrate on the key developments which have led to our current understanding of phonon drag thermopower.

### 5.1.2 Introduction to the phenomena

In anisotropic crystals, the transport coefficients are always tensors, but are often treated as scalars for simplicity. However, when we are interested in the effects of a magnetic field  $\mathbf{B}$ , the transport coefficients must necessarily be treated as tensors, even in nearly isotropic crystals. In the linear regime (i.e. with only small displacements from the equilibrium distributions) the various measurable quantities are defined by the relations

$$\mathbf{E} = \overleftrightarrow{\rho} \mathbf{J} + \overleftrightarrow{S} \nabla T \quad (5.4)$$

$$\mathbf{U} = \overleftrightarrow{\Pi} \mathbf{J} - \overleftrightarrow{\lambda} \nabla T, \quad (5.5)$$

where  $\mathbf{E}$  and  $\nabla T$  are the electric field and temperature gradient that correspond to the applied electric current density  $\mathbf{J}$  and heat current density  $\mathbf{U}$ . The measured resistivity is  $\rho_{ij}$  and the thermal conductivity is  $\lambda_{ij}$ . Since no appreciable heat is carried by the electrons in 1D and 2D systems, only the phonons contribute to  $\lambda_{ij}$ . This is also approximately true in 3D semiconductors, but not in bulk metals. The fact that  $\lambda_{ij}$  is largely dominated by phonons implies that it may be treated as a scalar ( $\lambda$ ) for the cubic systems which we consider here. However, it should be mentioned that phonon focusing can give some considerable orientation dependence in practice [36], see Section 5.2.1. For simplicity we will neglect this anisotropy for the moment.

There are two thermoelectric tensors, the thermopower  $S_{ij}$  and the Peltier coefficient  $\Pi_{ij}$  which are related by the Onsager relation [4]  $S_{ij}(\mathbf{B}) = \Pi_{ji}(-\mathbf{B})/T$ . As far as we are aware,  $\Pi_{ij}$  has not been measured for a reduced dimensionality system and we shall not refer to it again.  $S_{ij}$  is obtained by measuring  $\mathbf{E}$  with a known temperature gradient and the condition  $\mathbf{J} = 0$ . The fact that  $\lambda$  and  $S_{ij}$  are measured under the same conditions is very convenient in that both can be determined at the same time.

Theoretically one deals with a different set of coefficients because one is interested in calculating the currents that arise in response to applied fields. Thus,

$$\mathbf{J} = \overleftrightarrow{\sigma} \mathbf{E}' - \overleftrightarrow{\epsilon} \nabla T \quad (5.6)$$

$$\mathbf{U} = \overleftrightarrow{\pi} \mathbf{E}' - \overleftrightarrow{\kappa} \nabla T. \quad (5.7)$$

Here, the conductivity is  $\overleftrightarrow{\sigma} = (\overleftrightarrow{\rho})^{-1}$  and we can take  $\kappa_{ij} = \lambda_{ij} = \lambda \delta_{ij}$ . Strictly speaking these relations are not exact because the various quantities are determined under different conditions, but in practice any differences seem to be negligible. The quantities  $\epsilon_{ij}$  and  $\pi_{ij}$  are the relevant thermoelectric tensors to be calculated, but again the Onsager relation [4]  $\epsilon_{ij}(\mathbf{B}) = \pi_{ji}(-\mathbf{B})/T$  means that only one of these need be considered. The quantity  $\mathbf{E}'$  is the gradient of the electrochemical potential but the chemical part  $\nabla\mu/e$  is not observed experimentally [4, 22] (cf. Eq. (5.4), which is written in terms of  $\mathbf{E}$ ).

With a magnetic field applied along  $\hat{z}$  perpendicular to the plane of the 2D gas (the most common geometry), and assuming isotropy of the phonons and electrons in the  $xy$ -plane, there are two measurable components of  $S_{ij}$ , the Seebeck coefficient  $S_{xx}$ , and the Nernst–Etingshausen coefficient  $S_{yx}$  which are given by

$$S_{xx} = E_x / \nabla T_x = \rho_{xx} \epsilon_{xx} - \rho_{yx} \epsilon_{yx} \quad (5.8)$$

$$S_{yx} = E_y / \nabla T_x = \rho_{yx} \epsilon_{xx} + \rho_{xx} \epsilon_{yx}. \quad (5.9)$$

( $S_{zz}$  cannot be measured in a single 2D electron gas but it might be measurable in a superlattice of many 2D layers.) In principle, each thermoelectric coefficient  $\epsilon_{ij}$  has two components, arising from diffusion and phonon drag, which leads to analogous components in the measured quantities  $S_{ij}$ .

### 5.1.3 Theory of phonon drag thermopower

In a typical heterostructure, the electrons (or holes) are confined in a 2D plane and in the ideal (i.e. disorder-free) limit their states are characterized by a 2D wavevector  $\mathbf{k}$  and a subband index  $n$ . For the most part we shall consider conduction band states having a parabolic dispersion with an isotropic effective mass  $m_e^*$ . In this situation, the conduction band envelope wavefunction  $\psi_{\mathbf{k},n}(\mathbf{r})$  consists of a plane wave factor  $\exp(i\mathbf{k} \cdot \mathbf{r})$  and a subband wavefunction  $\phi_n(z)$  which describes the confinement of the electron in the perpendicular direction.

The electrons of interest interact with, and scatter from, impurities and phonons. These are the scattering processes determining the transport properties of the system. In a semi-classical description, the non-equilibrium state of the electrons is specified by the phase-space distribution function  $f_\alpha(\mathbf{r})$  where we use the notation  $\alpha \equiv (\mathbf{k}, n)$  to identify the electronic states. For a steady-state situation, this distribution function satisfies the Boltzmann equation

$$\mathbf{v}_\alpha \cdot \nabla f_\alpha - \frac{e}{\hbar} (\mathbf{E} + \mathbf{v}_\alpha \times \mathbf{B}) \cdot \nabla_{\mathbf{k}} f_\alpha = \left. \frac{\partial f_\alpha}{\partial t} \right|_{\text{imp}} + \left. \frac{\partial f_\alpha}{\partial t} \right|_{\text{ph}}, \quad (5.10)$$

where the two terms on the right-hand side account for impurity and phonon scattering, respectively. We assume that the electric and magnetic fields are static and uniform, with the magnetic field oriented perpendicular to the plane of the 2D electron gas. To a good approximation in most cases, the electron velocity,  $\mathbf{v}_\alpha = (1/\hbar) \nabla_{\mathbf{k}} E_\alpha \simeq \hbar \mathbf{k} / m_e^*$ , is independent of the subband index  $n$ .

The impurity scattering term is given by

$$\left. \frac{\partial f_\alpha}{\partial t} \right|_{\text{imp}} = \sum_{\alpha'} W_{\alpha\alpha'}^{(\text{imp})} [f_{\alpha'}(1 - f_\alpha) - f_\alpha(1 - f_{\alpha'})], \quad (5.11)$$

where  $\alpha' = (\mathbf{k}', n')$  and the impurity scattering rate is

$$W_{\alpha\alpha'}^{(\text{imp})} = \frac{2\pi}{\hbar} |\langle \alpha | V | \alpha' \rangle|^2 \delta(E_\alpha - E_{\alpha'}). \quad (5.12)$$

The bar denotes a configuration average of the screened impurity potential  $V(\mathbf{r})$ . Similarly, the phonon scattering term is given by [23]

$$\left. \frac{\partial f_\alpha}{\partial t} \right|_{\text{ph}} = \sum_{\alpha'} [f_{\alpha'}(1 - f_\alpha)P_{\alpha'\alpha} - f_\alpha(1 - f_{\alpha'})P_{\alpha\alpha'}] \quad (5.13)$$

with

$$P_{\alpha\alpha'} = \frac{2\pi}{\hbar} \sum_{\mathbf{q}, i} |M_{\alpha\alpha'}(\mathbf{q}, i)|^2 [N_{\mathbf{q}, i} \delta(E_{\alpha'} - E_\alpha - \hbar\omega_{\mathbf{q}, i}) + (N_{-\mathbf{q}, i} + 1) \delta(E_{\alpha'} - E_\alpha + \hbar\omega_{\mathbf{q}, i})]. \quad (5.14)$$

The summation runs over both the 3D phonon wavevector  $\mathbf{q}$ , with components parallel ( $q_\parallel$ ) and perpendicular ( $q_z$ ) to the 2D electron gas, and the polarization index  $i$ ;  $\omega_{\mathbf{q}, i}$  is the phonon frequency and  $N_{\mathbf{q}, i}$  is the non-equilibrium phonon occupation number.  $P_{\alpha\alpha'}$  is the total rate for an electron making a transition from  $\alpha$  to  $\alpha'$  with the absorption ( $N_{\mathbf{q}, i}$ ) or emission ( $N_{-\mathbf{q}, i} + 1$ ) of a phonon. The e-p matrix element has the property  $M_{\alpha\alpha'}(\mathbf{q}, i) = M_{\alpha'\alpha}^*(-\mathbf{q}, i)$  and is proportional to  $\delta_{\mathbf{k}', \mathbf{q}_\parallel + \mathbf{k}}$ , due to momentum conservation in the plane of the 2D electron gas. It also includes a subband matrix element  $I_{nn'}(q_z) \equiv \int \phi_n^*(z) \exp(iq_z z) \phi_{n'}(z) dz$ . The detailed form of  $M_{\alpha\alpha'}(\mathbf{q}, i)$  depends on the nature of the interaction. In systems such as GaAs/AlGaAs, the acoustic phonon deformation potential and piezoelectric interaction are the interactions of interest. It should be emphasized, however, that in all cases the bare e-p interaction must be screened by the dielectric matrix  $\epsilon_{nn'}(q)$  of the 2D electron gas. An example of how this is done in the calculation of hot electron energy loss rates is given by Ma *et al.* [24].

The above equations have been written in a form which is useful for situations with multiple subbands. However, most experimental work has dealt with samples having a single occupied subband and we therefore restrict ourselves to this situation in the following. In this case, the subband index  $n$  is superfluous and the state label  $\alpha$  is simply  $\mathbf{k}$ . The solution to Eq. (5.10) is obtained by linearizing about a local equilibrium (le) Fermi distribution, namely

$$f_{\mathbf{k}}(\mathbf{r}) = f_{\mathbf{k}}^{\text{le}}(T(\mathbf{r}), \mu(\mathbf{r})) - \frac{\partial f_{\mathbf{k}}^0}{\partial E_{\mathbf{k}}} \Phi_{\mathbf{k}}, \quad (5.15)$$

where  $T(\mathbf{r}) = T + \delta T(\mathbf{r})$  is the local temperature and  $\mu(\mathbf{r}) = \mu + \delta\mu(\mathbf{r})$  is the local chemical potential. The thermodynamic equilibrium distribution at temperature  $T$  and chemical potential  $\mu$  will be denoted by  $f_{\mathbf{k}}^0 = \{\exp[\beta(E_{\mathbf{k}} - \mu)] + 1\}^{-1}$ , with  $\beta = 1/k_B T$ . The deviation from local equilibrium is written in the form shown for later convenience. Similarly, the phonon distribution is expanded as

$$N_{\mathbf{q}, i} = N_{\mathbf{q}, i}^{\text{le}} - \frac{\partial N_{\mathbf{q}, i}^0}{\partial(\hbar\omega_{\mathbf{q}, i})} G_{\mathbf{q}, i}, \quad (5.16)$$

where  $N_{\mathbf{q}, i}^0 = \{\exp[\beta\hbar\omega_{\mathbf{q}, i}] - 1\}^{-1}$  is the equilibrium Bose distribution at temperature  $T$ . We shall assume that the non-equilibrium phonon distribution  $G_{\mathbf{q}, i}$  is established

by a temperature gradient and is insensitive to the interactions of the phonons with the electronic system. However, phonon drag thermopower arises directly from the interaction of the electrons with the non-equilibrium distribution of phonons.

Substituting these forms of the electron and phonon distributions into Eq. (5.10), we obtain the linearized equation (details of the derivation of the phonon scattering terms can be found in the work of Cantrell and Butcher [23])

$$\mathbf{v}_k \cdot \nabla T \frac{\partial f_k^0}{\partial T} - e \mathbf{v}_k \cdot \mathbf{E}' \frac{\partial f_k^0}{\partial E_k} + \frac{e}{\hbar} \mathbf{v}_k \times \mathbf{B} \cdot \nabla_k \Phi_k \frac{\partial f_k^0}{\partial E_k} = \frac{\partial f_k}{\partial t} \Big|_{\text{imp}} + \frac{\partial f_k}{\partial t} \Big|_{\text{ph}} \quad (5.17)$$

where the effective electric field  $\mathbf{E}'$  is now the gradient of the electrochemical potential,  $\mathbf{E} + \nabla\mu/e$ . The impurity scattering term is given by

$$\frac{\partial f_k}{\partial t} \Big|_{\text{imp}} = - \sum_{k'} W_{kk'}^{(\text{imp})} (\Phi_{k'} - \Phi_k) \frac{\partial f_k^0}{\partial E_k} \quad (5.18)$$

while the phonon scattering term consists of two parts

$$\frac{\partial f_k}{\partial t} \Big|_{\text{ph}} = \frac{\partial f_k}{\partial t} \Big|_{\text{ph},1} + \frac{\partial f_k}{\partial t} \Big|_{\text{ph},2}, \quad (5.19)$$

with

$$\begin{aligned} \frac{\partial f_k}{\partial t} \Big|_{\text{ph},1} &= \beta \sum_{k',q,i} (\Phi_{k'} - \Phi_k) (\Gamma_{kk'}(\mathbf{q}, i) + \Gamma_{k'k}(\mathbf{q}, i)) \\ &\equiv - \sum_{k'} W_{kk'}^{(\text{ph})} (\Phi_{k'} - \Phi_k) \end{aligned} \quad (5.20)$$

and

$$\frac{\partial f_k}{\partial t} \Big|_{\text{ph},2} = -\beta \sum_{k',q,i} G_{q,i} [\Gamma_{kk'}(\mathbf{q}, i) - \Gamma_{k'k}(\mathbf{q}, i)]. \quad (5.21)$$

The quantity

$$\Gamma_{kk'}(\mathbf{q}, i) = \frac{2\pi}{\hbar} |M_{kk'}(\mathbf{q}, i)|^2 f_k^0 (1 - f_{k'}^0) N_{q,i}^0 \delta(E_{k'} - E_k - \hbar\omega_{q,i}) \quad (5.22)$$

represents the equilibrium rate at which an electron in the state  $\mathbf{k}$  is scattered to  $\mathbf{k}'$  with the absorption of a phonon of energy  $\hbar\omega_{q,i}$ .

The first two terms on the left-hand side of Eq. (5.17) are inhomogeneous terms which drive the distribution function away from equilibrium. For a given non-equilibrium phonon distribution  $G_{q,i}$ , the term  $\partial f_k / \partial t|_{\text{ph},2}$  is likewise a known inhomogeneous term in the equation. Since the transport equation is linear in the non-equilibrium distribution  $\Phi_k$ , each of these terms can be considered independently and gives rise to its respective non-equilibrium electron distribution. In other words, the distribution function can be written as

$$\Phi_k = \Phi_k^{(E)} + \Phi_k^{(\nabla T)} + \Phi_k^{(\text{ph})}, \quad (5.23)$$

where the superscripts denote the source of the different contributions to the total. Thus, for example, the contribution  $\Phi_k^{(E)}$  arising from the imposed electric field is the solution of

$$-e\mathbf{v}_k \cdot \mathbf{E}' + \frac{e}{\hbar} \mathbf{v}_k \times \mathbf{B} \cdot \nabla_k \Phi_k^{(E)} = - \sum_{k'} \left( W_{kk'}^{(\text{imp})} + W_{kk'}^{(\text{ph})} \right) \left( \Phi_{k'}^{(E)} - \Phi_k^{(E)} \right). \quad (5.24)$$

The term  $W_{kk'}^{(\text{ph})}$  represents the scattering of non-equilibrium electrons from the thermal distribution of phonons and has the effect of equilibrating the electrons to the lattice. At low temperatures, the phonons are frozen out and the scattering is dominated by the impurity term  $W_{kk'}^{(\text{imp})}$ . In this case one can rigorously justify the neglect of  $W_{kk'}^{(\text{ph})}$  and the conductivity is governed by impurity scattering. However, with increasing temperature, phonon scattering becomes more important and eventually becomes the dominant scattering mechanism. In the transition from impurity to phonon-limited mobility both scattering mechanisms have to be included and the solution of the kinetic equation becomes exceedingly difficult.

It is therefore useful to begin by considering a sufficiently low temperature for which  $W_{kk'}^{(\text{ph})}$  can be neglected. In addition, we assume  $B = 0$ . In this case, the exact solution of the resulting equation has the form

$$\Phi_k^{(E)}(B = 0) = -e\tau_{\text{imp}}(E_k) \mathbf{v}_k \cdot \mathbf{E}', \quad (5.25)$$

where the (weakly) energy-dependent impurity transport lifetime is

$$\frac{1}{\tau_{\text{imp}}(E_k)} = \frac{m_c^*}{2\pi\hbar^3} \int_0^{2\pi} (1 - \cos\theta) \overline{|k|V|k'|^2} d\theta. \quad (5.26)$$

Here,  $\theta$  is the angle between  $\mathbf{k}$  and  $\mathbf{k}'$ , and since the scattering is elastic,  $k = k'$ . The factor  $(1 - \cos\theta)$  has the effect of preferentially weighting large-angle scattering. Once the distribution is known, the electric current is calculated from

$$\mathbf{J}^{(E)} = -\frac{2e}{A} \sum_k \mathbf{v}_k \left( -\frac{\partial f_k^0}{\partial E_k} \right) \Phi_k^{(E)}, \quad (5.27)$$

where the factor of 2 accounts for electron spin and  $A$  is the sample area. Inserting Eq. (5.25) into Eq. (5.27), we have

$$\begin{aligned} \mathbf{J}^{(E)} &= \frac{2e^2}{A} \sum_k \left( -\frac{\partial f_k^0}{\partial E_k} \right) \tau_{\text{imp}}(E_k) \mathbf{v}_k \mathbf{v}_k \cdot \mathbf{E}', \\ &= \int dE \left( -\frac{\partial f^0}{\partial E} \right) \overleftrightarrow{\sigma}(E) \cdot \mathbf{E}', \end{aligned} \quad (5.28)$$

where the energy-dependent impurity conductivity is given by

$$\overleftrightarrow{\sigma}(E) = \frac{e^2 E \tau_{\text{imp}}(E)}{\pi \hbar^2} \overleftrightarrow{1} \equiv \sigma_0(E) \overleftrightarrow{1}. \quad (5.29)$$

At low temperatures the derivative of the Fermi function acts as a delta function at  $E = E_F$  and we obtain the usual Drude conductivity  $\sigma_0(E_F) = ne^2\tau_{\text{imp}}(E_F)/m_e^*$ .

The situation with a magnetic field is a bit more complicated, but the calculation can still be carried through exactly. One simply finds that the energy-dependent conductivity becomes a non-diagonal tensor  $\sigma_{ij}(E; B)$  with components

$$\begin{aligned}\sigma_{xx}(E; B) &= \sigma_{yy}(E; B) = \frac{\sigma_0(E)}{1 + (\omega_c\tau_{\text{imp}}(E))^2}, \\ \sigma_{yx}(E; B) &= -\sigma_{xy}(E; B) = \omega_c\tau_{\text{imp}}(E)\sigma_{xx}(E).\end{aligned}\quad (5.30)$$

The calculation of  $\Phi_k^{(\nabla T)}$  proceeds in a similar way and leads to the diffusion thermopower. It is apparent from Eq. (5.17) that the effect of the temperature gradient term is obtained with the replacement  $e\mathbf{E}' \rightarrow (E_k - \mu)\nabla T/T$  in Eq. (5.28). This gives the diffusion current

$$\mathbf{J}^{(\nabla T)} = \frac{1}{e} \int dE \left( -\frac{\partial f^0}{\partial E} \right) (E - \mu) \vec{\sigma}(E; B) \frac{\nabla T}{T}, \quad (5.31)$$

and the diffusion thermoelectric tensor

$$\epsilon_{ij}^d = \frac{\pi^2 k_B^2 T}{3e} \left. \frac{d\sigma_{ij}(E; B)}{dE} \right|_{\mu}. \quad (5.32)$$

We next consider the effect of the non-equilibrium phonon scattering term  $\partial f_k/\partial t|_{\text{ph},2}$ . This term depends on the non-equilibrium phonon distribution and is responsible for the phonon drag thermopower. To obtain the phonon distribution we make use of the following phonon kinetic equation:

$$\mathbf{v}_p(\mathbf{q}, i) \cdot \nabla N_{\mathbf{q},i} = \left. \frac{\partial N_{\mathbf{q},i}}{\partial t} \right|_{\text{coll}} \equiv -\frac{1}{\tau_p} (N_{\mathbf{q},i} - N_{\mathbf{q},i}^{\text{le}}), \quad (5.33)$$

where the phonon relaxation time  $\tau_p$  is a parameter characterizing boundary and impurity scattering. In principle it is a function of  $\mathbf{q}$  and  $i$  but for simplicity we take it to be a constant which can be obtained from the phonon thermal conductivity. With our earlier definition of  $G_{\mathbf{q},i}$ , Eq. (5.33) implies that

$$G_{\mathbf{q},i} = -\frac{\hbar\omega_{\mathbf{q},i}}{T} \tau_p \mathbf{v}_p(\mathbf{q}, i) \cdot \nabla T. \quad (5.34)$$

Within an isotropic Debye model, the phonon velocity is given by  $\mathbf{v}_p(\mathbf{q}, i) = s_i \hat{\mathbf{q}}$  where the sound speed has a common value  $s_{\text{TA}}$  for the two transverse modes and a distinct value  $s_{\text{LA}}$  for the longitudinal mode. The distribution function in Eq. (5.34) has the property  $G_{-\mathbf{q},i} = -G_{\mathbf{q},i}$ , which is the asymmetry one would expect in a situation with a net flux of phonons.

Substituting Eq. (5.34) into Eq. (5.21), we find

$$\left. \frac{\partial f_k}{\partial t} \right|_{\text{ph},2} = \frac{\hbar}{k_B T^2} \nabla T \cdot \sum_{k', \mathbf{q}, i} s_i \Lambda_i \mathbf{q} [\Gamma_{kk'}(\mathbf{q}, i) + \Gamma_{k'k}(-\mathbf{q}, i)], \quad (5.35)$$

where  $\Lambda_i = s_i \tau_{\text{ph}}$  is the phonon mean free path. Only the in-plane projection  $\mathbf{q}_{\parallel}$  of the phonon wavevector  $\mathbf{q}$  contributes to the sum and so only the temperature gradient in the plane of the 2D electron gas is relevant. Furthermore, the summation over  $\mathbf{k}'$ ,  $\mathbf{q}$ , and  $i$  results in a vector quantity which by symmetry must be along the direction defined by the vector  $\mathbf{k}$ . Thus, Eq. (5.35) can be written as

$$\left. \frac{\partial f_{\mathbf{k}}}{\partial t} \right|_{\text{ph},2} = \frac{\hbar \mathbf{k} \cdot \nabla T}{k_{\text{B}} T^2} \sum_{\mathbf{k}', \mathbf{q}, i} s_i \Lambda_i \left( \frac{\mathbf{k} \cdot \mathbf{q}}{k^2} \right) [\Gamma_{\mathbf{k}\mathbf{k}'}(\mathbf{q}, i) + \Gamma_{\mathbf{k}'\mathbf{k}}(-\mathbf{q}, i)]. \quad (5.36)$$

This equation is beginning to look like the second term on the left-hand side of Eq. (5.17). To make this correspondence more apparent we write [21]

$$\left. \frac{\partial f_{\mathbf{k}}}{\partial t} \right|_{\text{ph},2} = e \mathbf{v}_{\mathbf{k}} \cdot \mathbf{E}^{(\text{ph})}(E_{\mathbf{k}}) \frac{\partial f_{\mathbf{k}}^0}{\partial E_{\mathbf{k}}}, \quad (5.37)$$

where we have introduced an effective electric field defined as

$$\mathbf{E}^{(\text{ph})}(E_{\mathbf{k}}) = \sum_i \frac{m_{\text{e}}^* s_i \Lambda_i}{e \tau_{\text{ep}}^i(E_{\mathbf{k}})} \frac{\nabla T}{T}. \quad (5.38)$$

Appearing in this expression is an energy-dependent e-p relaxation time  $\tau_{\text{ep}}^i(E)$  which is defined as

$$\frac{1}{\tau_{\text{ep}}^i(E_{\mathbf{k}})} = \beta \left( \frac{\partial f_{\mathbf{k}}^0}{\partial E} \right)^{-1} \sum_{\mathbf{k}', \mathbf{q}, i} \left( \frac{\mathbf{k} \cdot \mathbf{q}}{k^2} \right) [\Gamma_{\mathbf{k}\mathbf{k}'}(\mathbf{q}, i) + \Gamma_{\mathbf{k}'\mathbf{k}}(-\mathbf{q}, i)]. \quad (5.39)$$

Equation (5.37) is very suggestive. It clearly shows that the non-equilibrium flow of phonons along the 2D electron gas imparts momentum to the electrons in much the same way as an externally applied electric field. The only difference is that this phonon drag field is energy dependent and thus acts differently on electrons with different energies. However, this presents no formal problem if the dominant scattering mechanism is elastic impurity scattering. In this case the Boltzmann equation can be solved at a fixed energy which leads to the energy-dependent impurity conductivity  $\sigma_{ij}(E; B)$  introduced earlier. Thus, following Eq. (5.28), the current density arising from the phonon drag field can be written down immediately as

$$\mathbf{J}^{(\text{ph})} = \int dE \left( -\frac{\partial f^0}{\partial E} \right) \overleftrightarrow{\sigma}(E; B) \mathbf{E}^{(\text{ph})}(E). \quad (5.40)$$

It should of course be remembered that  $\mathbf{E}^{(\text{ph})}(E)$  is proportional to the temperature gradient, and, as such, the phonon drag current contributes to the thermoelectric coefficients  $\epsilon_{ij}^{\text{g}}$ . In particular, we have

$$\epsilon_{ij}^{\text{g}}(B) = \sum_i \frac{m_{\text{e}}^* s_i \Lambda_i}{e T} \int dE \left( -\frac{\partial f^0}{\partial E} \right) \frac{\sigma_{ij}(E; B)}{\tau_{\text{ep}}^i(E)}. \quad (5.41)$$

This is a very useful result and it is worthwhile repeating the physical circumstances under which it may be expected to be valid. First, it is derived for the assumed form of the non-equilibrium phonon distribution given in Eq. (5.34). This form has in fact been used in most of the detailed calculations of the phonon drag thermopower. The second assumption is that the mobility is impurity limited. As a result, the energy-dependent impurity conductivity is the relevant quantity which enters. As we shall see, neither of these assumptions is very restrictive and we shall argue that this expression has a somewhat broader range of validity than the present derivation might suggest.

The calculation of the phonon drag thermoelectric tensor given by Eq. (5.41) simplifies at low temperatures where the electron gas is degenerate. In this limit, factors having a weak energy dependence can be evaluated at the Fermi energy and removed from the energy integral. This applies to the conductivity, which, as seen from Eq. (5.29), has an explicit factor of  $E$ , as well as an energy dependence coming from the impurity transport lifetime. The latter is typically assumed to have some power law dependence  $E^p$ , which is again relatively weak. On the other hand,  $\tau_{\text{ep}}^i(E)$  has a strong energy dependence since it is determined by inelastic phonon collisions, and, as such, it must be treated more carefully. Evaluating the impurity conductivity at  $E = E_F$ , the thermoelectric tensor becomes [21]

$$\epsilon_{ij}^g(B) = - \sum_i \frac{m_e^* s_i \Lambda_i}{eT} \left\langle \frac{1}{\tau_{\text{ep}}^i} \right\rangle \sigma_{ij}(B), \quad (5.42)$$

where the average lifetime is given by

$$\left\langle \frac{1}{\tau_{\text{ep}}^i} \right\rangle \equiv \int dE \left( -\frac{\partial f^0}{\partial E} \right) \frac{1}{\tau_{\text{ep}}^i(E)}. \quad (5.43)$$

The phonon drag thermopower tensor, defined as  $\vec{S}^g(B) = \vec{\rho}(B) \vec{\epsilon}^g(B)$ , is therefore given by  $\vec{S}^g(B) = S^g \vec{1}$  with

$$S^g = - \sum_i \frac{m_e^* s_i \Lambda_i}{eT} \left\langle \frac{1}{\tau_{\text{ep}}^i} \right\rangle. \quad (5.44)$$

To this level of approximation, the phonon drag thermopower is a diagonal tensor *independent* of the magnetic field. This result was first discovered numerically [25], but the present derivation shows that it is a consequence of the thermoelectric tensor being a scalar multiple of the conductivity. A weak magnetothermopower would arise, however, if higher order terms in the expansion of  $\sigma_{ij}(E; B)$  about  $\mu$  are retained.

In the original work of Cantrell and Butcher [23],  $\tau_{\text{ep}}$  does not appear in  $S^g$ , but an explicit formal expression for the thermopower is given. Their expression follows on manipulation of the thermal average in Eq. (5.43). Using Eq. (5.39), we have

$$\left\langle \frac{1}{\tau_{\text{ep}}^i} \right\rangle = \frac{2\pi \hbar^2}{m_e^* k_F^2 k_B T A} \sum_{k, k', q} (-\mathbf{k} \cdot \mathbf{q}_{\parallel}) [\Gamma_{kk'}(\mathbf{q}, i) + \Gamma_{k'k}(-\mathbf{q}, i)]. \quad (5.45)$$

In obtaining this expression we have changed the energy integration in Eq. (5.43) into a sum over  $\mathbf{k}$  and have replaced the factor  $k^{-2}$  by  $k_F^{-2}$ . If we next interchange  $\mathbf{k}$  and  $\mathbf{k}'$  in the second term of the sum and set  $\mathbf{q} \rightarrow -\mathbf{q}$ , the averaged lifetime can be written

$$\left\langle \frac{1}{\tau_{\text{ep}}^i} \right\rangle = \frac{2\pi \hbar^2}{m_e^* k_F^2 k_B T A} \sum_{\mathbf{k}, \mathbf{k}', \mathbf{q}} \mathbf{q}_{\parallel} \cdot (\mathbf{k}' - \mathbf{k}) \Gamma_{\mathbf{k}\mathbf{k}'}(\mathbf{q}, i). \quad (5.46)$$

Since  $\mathbf{k}$  and  $\mathbf{k}'$  are in the plane of the gas, the vector dot product is equivalent to  $\mathbf{q} \cdot (\mathbf{k}' - \mathbf{k})$ . By substituting Eq. (5.46) into Eq. (5.44), we finally obtain the expression

$$S^{\text{g}} = \frac{2\pi m_e^* \tau_{\text{ph}}}{e k_F^2 k_B T^2 A} \sum_{\mathbf{k}, \mathbf{k}', \mathbf{q}, i} \hbar \omega_{\mathbf{q}, i} \mathbf{v}_{\text{p}}(\mathbf{q}, i) \cdot (\mathbf{v}_{\mathbf{k}} - \mathbf{v}_{\mathbf{k}'}) \Gamma_{\mathbf{k}\mathbf{k}'}(\mathbf{q}, i). \quad (5.47)$$

This is the form used by Cantrell and Butcher in their calculations.

The averaged lifetime in Eq. (5.46) can be simplified further by making use of the result for  $\Gamma_{\mathbf{k}\mathbf{k}'}(\mathbf{q}, i)$  in Eq. (5.22). Noting that  $|M_{\mathbf{k}\mathbf{k}'}(\mathbf{q}, i)|^2 = |M(\mathbf{q}, i)|^2 \delta_{\mathbf{k}', \mathbf{k} + \mathbf{q}_{\parallel}}$ , we then obtain

$$\left\langle \frac{1}{\tau_{\text{ep}}^i} \right\rangle = \frac{8\pi^2}{\hbar k_F^2 k_B T A} \sum_{\mathbf{k}, \mathbf{q}} E_{\mathbf{q}_{\parallel}} |M(\mathbf{q}, i)|^2 N_{\mathbf{q}, i}^0 f_{\mathbf{k}}^0 (1 - f_{\mathbf{k} + \mathbf{q}_{\parallel}}^0) \delta(E_{\mathbf{k} + \mathbf{q}_{\parallel}} - E_{\mathbf{k}} - \hbar \omega_{\mathbf{q}, i}). \quad (5.48)$$

This is a particularly convenient form since all of the  $\mathbf{k}$  dependence is contained in the delta and Fermi functions. The result of the  $\mathbf{k}$  summation for a strongly degenerate gas ( $\beta\mu \gg 1$ ) is

$$\left\langle \frac{1}{\tau_{\text{ep}}^i} \right\rangle = \frac{1}{\hbar E_{\text{F}}^{3/2}} \sum_{\mathbf{q}} E_{\mathbf{q}_{\parallel}} |M(\mathbf{q}, i)|^2 F(\beta \hbar \omega_{\mathbf{q}, i}) \frac{\theta(E_{\mathbf{q}_{\parallel}} - \gamma)}{\sqrt{E_{\mathbf{q}_{\parallel}} - \gamma}}, \quad (5.49)$$

where  $\gamma = (E_{\mathbf{q}_{\parallel}} - \hbar \omega_{\mathbf{q}, i})^2 / (4E_{\text{F}})$  and  $F(y) = y N^0(y) [N^0(y) + 1]$  [26, 27]. The square root in the denominator arises from the angular average of the transition density of states. If the inelasticity of phonon scattering is ignored ( $\hbar \omega_{\mathbf{q}, i} \rightarrow 0$ ), we have  $\sqrt{E_{\mathbf{q}_{\parallel}} - \gamma} \propto \sqrt{2k_{\text{F}} - q}$ , and the integrand exhibits a square root singularity at  $q = 2k_{\text{F}}$ . This is sometimes identified as a Kohn anomaly although it should be noted that it is here associated with the density of states and not with singularities in the screening function.

The expression in Eq. (5.49) allows one easily to extract the low-temperature behaviour of the phonon drag thermopower, the so-called Bloch limit. This is done by simply determining the power of the wavenumber dependence in the limit  $q \rightarrow 0$ . The summation gives  $q^3$ , the energy-dependent factors give an additional factor of  $q$ , and the  $e$ - $\text{p}$  matrix element behaves as  $q^M$  for a total power of  $q^{4+M}$ . For the screened deformation potential coupling we have  $M = 3$  while for screened piezoelectric coupling we have  $M = 1$ . As a result, we have  $\langle 1/\tau_{\text{ep}} \rangle \propto T^7$  and  $T^5$  for deformation and piezoelectric coupling, respectively, and the corresponding low-temperature behaviour of the thermopower is  $T^6$  and  $T^4$  [28]. Thus the dominant contribution at low  $T$  is due to piezoelectric coupling, as observed experimentally. The prefactors for these  $T$  dependences have been given by Stormer *et al.* [29] and we reproduce them here in [30]. If the interactions are *unscreened*, the powers of  $T$  are reduced by 2 and do not agree with experiment.

With increasing temperature the equilibrium phonon scattering rate becomes more important and the term  $W_{kk'}^{(\text{ph})}$  in Eq. (5.24) cannot be neglected in comparison with the impurity collision rate. To see what happens in this situation, we consider Eq. (5.24) in the  $B = 0$  limit. The distribution function can still be expressed in the form given in Eq. (5.25), but now the impurity lifetime is replaced by a combined transport lifetime  $\tau_{\text{tr}}(E_k)$ . Equation (5.24) can then be written as

$$1 = \sum_{k'} \left[ \tau_{\text{tr}}(E_k) - \frac{\mathbf{k} \cdot \mathbf{k}'}{k^2} \tau_{\text{tr}}(E_{k'}) \right] (W_{kk'}^{(\text{imp})} + W_{kk'}^{(\text{ph})}), \quad (5.50)$$

where we have again made use of the assumed isotropy of the electronic and phonon states. The equation is an integral equation determining the energy dependence of the transport lifetime. It has recently been argued [31] that the energy dependence for *combined* impurity–phonon scattering is weak at all temperatures, which implies that the solution of Eq. (5.50) is

$$\frac{1}{\tau_{\text{tr}}(E_k)} = \frac{1}{\tau_{\text{imp}}(E_k)} + \sum_i \frac{1}{\tau_{\text{ep}}^i(E_k)}, \quad (5.51)$$

where  $\tau_{\text{imp}}$  and  $\tau_{\text{ep}}^i$  are given by Eqs (5.26) and (5.39), respectively. Although the e–p lifetime is strongly energy dependent at low temperatures [31], this form of Matthiessen’s rule for the transport lifetime is valid provided the weakly energy-dependent impurity lifetime is dominant. At higher temperatures, the phonon scattering rate is dominant but in this temperature range the e–p lifetime itself becomes weakly energy dependent. Thus in either limit, Eq. (5.51) can be averaged over energy with respect to the weight function  $(-\partial f^0/\partial E)$  without changing the value of the final result. In other words, we can take

$$\frac{1}{\tau_{\text{tr}}} = \frac{1}{\tau_{\text{imp}}} + \sum_i \left\langle \frac{1}{\tau_{\text{ep}}^i} \right\rangle \quad (5.52)$$

as the lifetime determining the transport mobility of the electrons,  $\mu_{\text{tr}} = e\tau_{\text{tr}}/m_e^*$ . The important conclusion is that the e–p lifetime contributing to the mobility is precisely the same as the lifetime appearing in the phonon drag thermopower. This is true even though the latter is caused by the non-equilibrium distribution of phonons in contrast to the situation for the mobility.

So far, everything has been based on the semi-classical Boltzmann equation. Such a formulation of the thermoelectric coefficients is inadequate in describing oscillatory behaviour in a magnetic field or strong localization (though we believe it is still adequate to describe weak localization effects [21]). In both of these cases, the electronic states  $\alpha$  are no longer characterized by a wavevector  $\mathbf{k}$  and the current cannot be written as a sum over momentum eigenstates. In this situation, it is convenient to approach the problem from a complementary point of view, namely the calculation of the phonon heat current induced by a non-equilibrium distribution of electrons [9]. This heat current is given by

$$\mathbf{U}_{\text{p}} = \sum_{\mathbf{q}, i} \hbar \omega_{\mathbf{q}, i} \mathbf{v}_{\text{p}}(\mathbf{q}, i) N_{\mathbf{q}, i} \quad (5.53)$$

where the phonon distribution  $N_{\mathbf{q},i}$  is determined by the phonon transport equation

$$\left. \frac{\partial N_{\mathbf{q},i}}{\partial t} \right|_{\text{el-ph}} + \frac{1}{\tau_p} (N_{\mathbf{q},i} - N_{\mathbf{q},i}^0) = 0, \quad (5.54)$$

This differs from Eq. (5.33) since now the phonons are assumed to be driven out of equilibrium as a result of collisions with electrons which are carrying a current induced by an electric field. In this situation, the e-p scattering rate is given by

$$\left. \frac{\partial N_{\mathbf{q},i}}{\partial t} \right|_{\text{el-ph}} = \sum_{\alpha\alpha'} \left[ P_{\alpha'\alpha}^{(\text{em})} f_{\alpha'} (1 - f_{\alpha}) - P_{\alpha\alpha'}^{(\text{abs})} f_{\alpha} (1 - f_{\alpha'}) \right], \quad (5.55)$$

where the electron state labels  $\alpha$  and  $\alpha'$  in general include spin. The quantities  $P_{\alpha\alpha'}^{(\text{abs})}$  and  $P_{\alpha\alpha'}^{(\text{em})}$  are respectively the absorption and emission parts of the total phonon transition rate given in Eq. (5.14). The phonon heat current is now determined to lowest order in the electric field by making use of Eq. (5.15) and linearizing Eq. (5.55). We thus find that Eq. (5.55) reduces to

$$\left. \frac{\partial N_{\mathbf{q},i}}{\partial t} \right|_{\text{el-ph}} = \beta \sum_{\alpha\alpha'} \Gamma_{\alpha\alpha'}(\mathbf{q}, i) (\Phi_{\alpha'} - \Phi_{\alpha}), \quad (5.56)$$

and, as a result, the phonon heat current takes the form

$$\mathbf{U}_p = \beta \sum_{\alpha\alpha', \mathbf{q}, i} \hbar \omega_{\mathbf{q},i} \tau_p \mathbf{v}_p(\mathbf{q}, i) \Gamma_{\alpha\alpha'}(\mathbf{q}, i) (\Phi_{\alpha'} - \Phi_{\alpha}). \quad (5.57)$$

It is important to emphasize that this result is based on the assumption of independent electrons, and is generally valid to lowest order in the e-p coupling.

In the case of plane wave states, one can check that the impurity scattering distribution in Eq. (5.25) gives rise to a Peltier coefficient  $\pi^{\mathcal{E}} = T\epsilon^{\mathcal{E}}$  where  $\epsilon^{\mathcal{E}}$  is given by Eq. (5.42). This of course is to be expected on the basis of the Onsager reciprocity relations. The key to applying Eq. (5.57) more generally is the determination of the non-equilibrium distribution  $\Phi_{\alpha}$ . This is difficult to do rigorously and is the source of the main uncertainty that arises in the calculations.

One application of Eq. (5.57) has been to the problem of magnetoquantum oscillations of the phonon drag thermopower in the quantum Hall regime [32–34]. We should state at the outset that the calculations that have been done do not treat fully the physics associated with the quantum Hall effect and its implications for transport phenomena. We shall content ourselves with a discussion of the assumptions made and what conclusions these assumptions lead to.

The calculations start by considering ideal Landau states in the presence of a uniform electric field,  $E$ . In the absence of the electric field, the magnetic states carry no current since the electrons undergo cyclotron motion, but in the presence of the field, each state acquires a drift velocity  $v_d = E/B$  in a direction perpendicular to the field. If one ignores the complications of disorder, this so-called  $E$  cross  $B$  drift results in a Hall conductance  $\sigma_{yx} = n_s e/B$ . Furthermore, the energy of a magnetic state is given to first order in the field by  $E_{\alpha} = E_{\alpha}^0 + eEx_{\alpha}$ , where  $x_{\alpha} = \langle \alpha | x | \alpha \rangle$ . It is then assumed that the occupation

of the state  $\alpha$  is unchanged from its equilibrium value  $f^0(E_\alpha^0)$  in the absence of the field. This implies that the deviation from the true equilibrium distribution  $f^0(E_\alpha)$  is equal to  $[-df^0(E_\alpha)/dE_\alpha]eEx_\alpha$ , and hence  $\Phi_\alpha = eEx_\alpha$ . This result is used in Eq. (5.57) to evaluate the thermoelectric tensor  $\pi_{ij}^g$ . In carrying out the calculations, the effect of disorder is taken into account in an *ad hoc* manner by using a Gaussian approximation for the Landau level density of states.

When the theoretical  $\pi_{yx}$  coefficient is combined with the experimental resistivity to generate  $S_{xx}^g$ , theory qualitatively reproduces the oscillatory behaviour observed [33,34] although the detailed  $B$  dependence is not correct. The situation for  $S_{yx}^g$ , however, is at variance with the experimental findings since the model predicts  $\pi_{xx}^g = 0$ . This deficiency is not apparent in  $S_{xx}^g$  since  $\pi_{yx}^g$  gives the dominant contribution to the latter. The problem with  $S_{yx}^g$  can only be resolved by taking into account explicitly the effect of the localized states between Landau levels.

#### 5.1.4 Experimental techniques

As we have already mentioned,  $\Pi_{ij}$  has not been investigated experimentally and all investigations have involved  $S_{ij}$ . Thus the main experimental problem is to determine  $\mathbf{E}$  and  $\nabla T$  accurately as a function of temperature and/or magnetic field. Both AC and DC techniques are possible, but the latter are the most common except perhaps at very low temperatures where the thermal inertia of the system becomes very low. Experimental systems to measure  $S_{ij}$  for small samples over a wide range of temperature and magnetic field have been described in the literature [35–39].

The sample must be in high vacuum to prevent heat loss, and the leads used in connecting to the thermometers and sample contacts must be chosen to prevent any appreciable heat flow which could disturb the measurement conditions. In principle, one must also choose leads which have a negligible thermopower compared with the sample, unless suitable corrections are made. The alloy manganin, which is commercially available as wire in many sizes, satisfies these requirements. Pure metals such as copper and gold are a poor choice.

The potential difference has usually been determined using commercial voltmeters which are available with sensitivities down to about 1 nV and input impedances in the  $G\Omega$  range. These are useful for sample resistances  $R_s$  up to several hundreds of kilohms. A problem that has often gone unrecognized in the measurements is the effect of the bias current  $i_b$  of the voltmeter input amplifier. All amplifiers require a small current to bias their input devices. In commercial instruments this can be as high as 50 pA. The combination of  $i_b$  and  $R_s$  gives a spurious offset voltage of  $i_b R_s$  which is added to the true signal being measured. Typically, this is eliminated by measuring the difference in voltage with the temperature gradient turned off and on. However, when  $R_s$  is a function of  $T$  (and perhaps also  $B$ ) the elimination of the offset voltage requires that the average temperature of the sample is the same whether the temperature gradient is on or off. Electrometers are designed to reduce  $i_b$  to very low levels, but this is obtained at the expense of sensitivity. In principle this problem can be completely eliminated by using AC rather than DC methods, providing the preamplifier is AC coupled.

The measurement of temperature and temperature difference presents its own problems, especially in the presence of high magnetic fields. We shall not pursue this matter in detail here, but refer the reader to ref. [2] where some of the difficulties and solutions have been described. Note that, because of the problems that can arise with thermometry, it has become customary to use the experimental data to evaluate the thermal conductivity of the substrate. These results can then be compared with previously published experimental data, which are available for a wide variety of materials, and this acts as a useful check on accuracy.

## 5.2 Experimental results at zero magnetic field

### 5.2.1 Survey of results

Early work on  $S$  (which we can treat as a scalar here) in 2D systems was typically limited to a range of temperatures of  $\sim 1.4$ –20 K. Diffusion and drag were not readily separated because the former is not unambiguously identifiable in this range. Nevertheless, the temperature dependence of  $S$  and its large magnitude were clear indicators that  $S^g$  was dominant [35, 40–42]. Another clue was the fact that the condition of the substrate surfaces was found strongly to affect the observed magnitude of  $S$  [43, 44]. The surface next to the 2D layer always has a specular appearance, but the opposite surface is typically left as a matt finish. Polishing this second surface gave a very large increase in the observed magnitude of  $S$ . This is caused by the increase in phonon mean free path  $\Lambda$  giving an increase in  $S^g$  (see Eq. (5.3) or (5.44)).

There were a number of first-principles calculations of  $S^g$  for comparison with the experimental data [23, 28, 45, 46]. Because the thermal conductivity  $\lambda$  of the substrates was usually measured along with  $S$ ,  $\Lambda$  was available for use in the calculations. It usually turned out that in GaAs/AlGaAs heterostructures grown on semi-insulating GaAs substrates the experimentally measured  $\Lambda$  is primarily determined by boundary scattering<sup>‡</sup> (which is often not the case for Si-MOSFET samples). Some of the early calculations did not include electronic screening of the e–p interaction, but it is now clear that this is essential to obtain accurate results, especially at low temperatures.

The first experiments which unambiguously showed  $S^d$  and  $S^g$  were those of Ruf *et al.* [48] on GaAs/AlGaAs down to 0.2 K. They analysed their data assuming  $S^g \propto T^3$  at low temperatures. Their data were in the Bloch limit below about 1 K so the dependence should be  $T^4$  as outlined in Section 5.1.3, but the data were not quantitatively compared with theory.

The simplest behaviour of  $S^g$  is seen in the Bloch limit and this has recently been investigated experimentally for both GaAs/AlGaAs samples [36] and Si-MOSFETs [49]. In the former, piezoelectric scattering is dominant so we expect  $S^g \propto T^4$ . The first experiments where the  $T^4$  dependence was observed unambiguously were by Zeitler *et al.* [50] and the result was confirmed by Tieke *et al.* [36, 51]. Data from the latter

<sup>‡</sup> It should be noted that even weak unintentional Cr doping in semi-insulating GaAs can lead to an additional phonon scattering process in the substrate [47]. The experimentally measured  $\Lambda$  to be used for the calculation can then be slightly different from its pure boundary scattering limit.

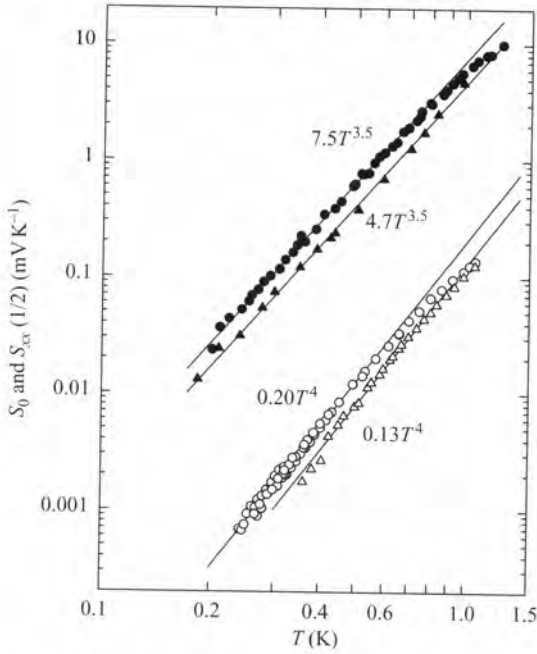


**Fig. 5.1** Measured thermopower  $S_{xx}$  of two GaAs/AlGaAs samples at zero field (open symbols) and in a magnetic field at filling factor  $\nu = \frac{1}{2}$  (closed symbols). The two samples are oriented along different crystallographic directions but have similar densities  $n_s = 1.75 \times 10^{15} \text{ m}^{-2}$ . From Ref. [36]

experiments are shown in Fig. 5.1. Not only do they have the correct low-temperature dependence but the coefficient is also in good accord with theory with no free parameters (the analysis used the accepted value of the piezoelectric coupling coefficient in GaAs,  $h_{14} = 1.2 \times 10^9 \text{ V m}^{-1}$ ). The experiments were carried out using substrates aligned along two different directions. Because of phonon focusing,  $\Lambda$  is different for the two directions and this is reflected in both  $\lambda$  and  $S^g$ .

In Si-MOSFET samples, where the piezoelectric coefficient is zero, only deformation potential scattering contributes to  $S^g$ . This should result in  $S^g \propto T^6$  in the Bloch limit which was found to be so experimentally [49]. The absolute values agreed well with those calculated, again with no free parameters. In this case  $S^g$  decreases so rapidly with temperature that it becomes very small compared with  $S^d$  by about 0.8 K, whereas in the GaAs/AlGaAs system,  $S^g$  is typically dominant down to 0.3 K or below. It is interesting that the use of  $S^g$  now provides the most accurate way of measuring the phonon-limited mobility,  $\mu_{ep}$ , in the low-temperature limit. Indeed, in the Si-MOSFET case, experiment and theory now agree that  $\mu_{ep} \propto T^{-7}$ , but this has never been observed in  $\rho$ . We note that at the time that  $S^g \propto T^6$  was observed experimentally for Si-MOSFETs in ref. [49], it was not known that Eq. (5.44) was exact so the connection with  $\mu_{ep}$  was not made. In GaAs/AlGaAs,  $\mu_{ep} \propto T^{-5}$  and this has been seen in  $\rho$ , but only in very high-mobility samples where impurity scattering was reduced to a very low level [29, 52]. It is important

to stress that the mobility of the sample does not affect  $S^g$ , except at the very lowest mobilities where the e-p interaction is modified, a situation we shall mention again later.

As the temperature rises beyond the point where  $\langle q \rangle \simeq 2k_F$  (where  $\langle q \rangle$  is an average phonon wavenumber), there is a steady drop in the temperature exponent of  $\mu_{ep}^{-1}$  for both piezoelectric and deformation scattering and one finally finds  $\mu_{ep} \propto T^{-1}$  at high temperatures. According to Eq. (5.3), this implies  $S^g$  becomes constant. However, this is not seen because  $\Lambda$ , and hence  $S^g$ , begins to decrease rapidly with increasing temperature. Many systems have been investigated under conditions where the transition from low to high temperatures takes place, but these can be quantitatively analysed only by numerical methods. The first systems studied were GaAs/AlGaAs heterojunctions and Si-MOSFETs where good agreement between theory and experiment was found [28, 42, 45].

The work has since been extended to a variety of systems. An interesting case is that of holes in both GaAs/AlGaAs and Si/SiGe because the hole band structure is more complicated than that for electrons. The first data on holes in GaAs/AlGaAs were those of Bayot *et al.* [37] and were taken at very low temperatures ( $\sim 0.04$ – $0.14$  K). They indicated both  $S^d$  and  $S^g$  but no quantitative study of the latter was made. An experimental and theoretical study was made later by Tsaousidou *et al.* [53] for two other samples over the range 0.2–1.0 K. The agreement of theory and experiment was excellent with no adjustable parameters.

The available experimental data for holes in Si/SiGe cover the range of 3–20 K [54] but the theory did not provide a good description of the data, especially at low temperatures. The same authors have also measured  $S$  for Si samples which have single  $\delta$ -doped layers of boron and antimony [55], the former giving a hole 2D gas and the latter an electron 2D gas. In both cases, the deformation potentials required to fit the data appear to be unrealistically large and inconsistent with previous values for Si, unless unscreened interactions are used, which is not physically reasonable. However, the samples do not appear to be well characterized and it seems likely that at least two subbands might be populated so that the single band analysis that was made is probably inadequate. Another feature that suggests further investigation might be useful is that these samples have extremely low mobility ( $0.02$ – $0.05 \text{ m}^2 \text{ V}^{-1} \text{ s}^{-1}$ ) so that they are likely to be in the dirty limit at low temperatures (i.e.  $\langle q \rangle l < 1$ , where  $l$  is the electron-impurity mean free path). We mention this limit again in Section 5.2.3.

At high temperatures, boundary scattering becomes negligible and phonons are primarily brought into equilibrium by phonon-phonon scattering (perhaps augmented at intermediate temperatures by impurity scattering) which gives a rapidly falling  $\Lambda$  and eventually  $S^g$  should tend to zero. It is of interest to examine  $S^g$  under these conditions but there are only two, relevant, experimental publications, both dealing with GaAs/AlGaAs. The first examined relatively high-mobility and low-density samples that became non-degenerate at rather low temperatures [38]. The second dealt with a system where the mobility was very low (so that impurity scattering dominated over the whole temperature range) and the density was so high that the sample remained degenerate to high temperatures [56]; these characteristics ensure that  $S^d \propto T$ , with a constant coefficient, over a wide range of temperatures so that it is easily separated from  $S^g$ .

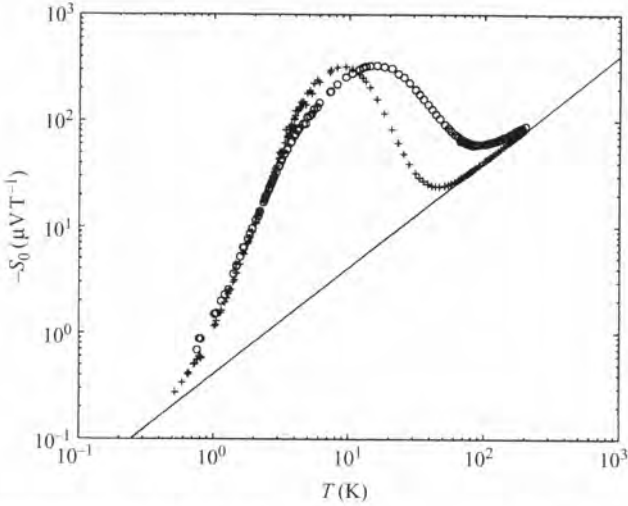


**Fig. 5.2** Measured (circles) and calculated (crosses) thermopower  $S_{xx}$  ( $B = 0$ ) for a high-density GaAs/AlGaAs sample ( $n_s = 3.6 \times 10^{16} \text{ m}^{-2}$ ) at zero field. The calculations take the phonon mean free path  $\Lambda$  from experimental data on the thermal conductivity  $\lambda$ . The straight line is  $S^d$ . From ref. [56].

Figure 5.2 shows data from the second study. The straight line is  $S^d$  estimated from the asymptotic linear behaviour of  $S$  at high temperatures, and the hump superposed on this is  $S^e$ . The calculated  $S^e$  has no free parameters. It takes  $\Lambda$  from the measured  $\lambda$  of the substrate and uses established parameters for both piezoelectric and deformation potential e-p scattering. The agreement between theory and experiment is excellent up to about 10 K, but the theoretical results rapidly tend to zero above this whereas the experimental  $S^e$  persists to much higher temperatures. Wu *et al.* [57] have used a somewhat different theoretical formalism but find essentially the same result. The discrepancy is probably due to the fact that all the phonons in the substrate contribute to  $\lambda$ , but  $S^e$  results only from those phonons which can interact with electrons and is thus primarily determined by phonons of long wavelength. Calculations of  $\lambda$  at high temperatures typically assume that when equilibrium is established among the various phonon normal modes by N- and U-type phonon-phonon scattering, all modes have the same relaxation time, but the present data indicate that  $\Lambda$  continues to depend strongly on wavelength.

### 5.2.2 Kohn anomalies

As mentioned in the theory section, the Kohn anomaly is the name given to the effect on the phonon dispersion curves of bulk metals arising from a singularity in the electronic screening of the ion-ion interaction at  $q_{\parallel} = 2k_F$ . In papers on 2D phonon drag thermopower, it has become customary to refer to a feature related to the same condition  $q_{\parallel} = 2k_F$  as a Kohn anomaly. As seen in Eq. (5.49), the expression for  $\langle 1/\tau_{ep} \rangle$ , and hence  $S^e$ , contains a square root singularity. This arises from the following mechanism.

The e-p interaction is subject to conservation of crystal momentum in the plane of the 2D gas. At low temperatures, where phonon energies are small compared with  $E_F$ , the in-plane component of phonon crystal momentum,  $q_{\parallel}$ , essentially bridges two points on the Fermi circle. The density of final states increases with  $q_{\parallel}$  and exhibits a square root singularity at  $q_{\parallel} = 2k_F$ , beyond which it drops sharply to zero (cf. ref. [1]). This gives  $S^g$  a noticeable structure as a function of temperature.

At low temperatures the magnitude of the average phonon momentum  $\langle q \rangle$  increases linearly with  $T$ , according to  $\hbar s_i \langle q \rangle \simeq 5k_B T$ . Thus, we might expect that  $S^g$  will show an anomaly at  $T_{KA} \simeq 2\hbar k_F s_i / 5k_B$ . This will be superposed on a rapidly increasing  $S^g$  and so in analysing the experimental data it is customary to divide out most of the intrinsic temperature dependence. In this region  $S^g$  varies roughly as  $T^3$ , so plotting  $S^g/T^3$  as a function of  $T$  should reveal a peak at  $T_{KA}$ . Often  $S^g/\lambda$  is plotted because  $\lambda$  reflects both the  $T^3$  dependence, and also any variation due to  $\Lambda$  (but see our comments above concerning  $\Lambda$ ). However, the precise position of the peak in such a plot can only be obtained by numerical calculation and the equations given here should be regarded only as semi-quantitative estimates. Figure 5.3 shows an example for a GaAs/AlGaAs heterojunction [50]. The normalized thermopower  $S/T^3$  at zero magnetic fields displays a clear maximum around a temperature  $T_{KA} \approx 0.5$  K as expected from the above relation (using a transverse sound velocity of about  $3000 \text{ m s}^{-1}$ ).

The effect was first predicted by Zavaritskiĭ *et al.* [17,59] who used it to determine  $k_F$  in Si-MOSFET grown on a (111) surface and hence deduce the valley degeneracy. Since then it has been demonstrated on many occasions: Gallagher *et al.* in MOSFETs [35,42], Zeitler *et al.* [60] for electrons in GaAs/AlGaAs, Crump *et al.* [58] for holes in GaAs/AlGaAs, Hyndman *et al.* [61] for a p-type double quantum well. A similar

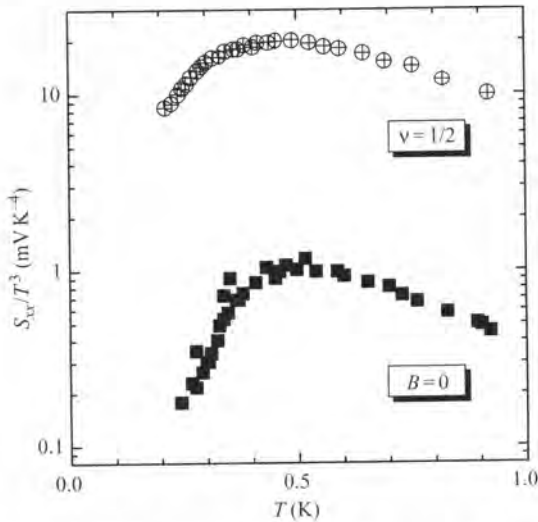


**Fig. 5.3** Kohn anomaly of electrons at zero field and composite fermions at  $\nu = \frac{1}{2}$  seen in the normalized thermopower  $S_{xx}/T^3$  for a 2D electron gas with a low electron concentration  $n_s = 0.43 \times 10^{15} \text{ m}^{-2}$ . The data are based on fig. 4 in ref. [50].

Kohn anomaly has also been observed in a magnetic field when the lowest Landau level is half-filled; this is attributed to the phonon drag thermopower of composite fermions (CFs) and will be mentioned again in Section 5.3.3. An example is given in Fig. 5.3. For a fully spin-polarized system, the Fermi wavevector is increased by a factor of  $\sqrt{2}$  compared with a spin degenerate system. As a consequence  $T_{KA}$  might be expected to shift to approximately 0.7 K for CFs. However, the precise position of the maximum also depends on the details of the e–p coupling (see our comments above) and the degree of spin polarization and this may explain why clear shifts by a factor of  $\sqrt{2}$  have not been observed experimentally [50, 58].

### 5.2.3 Weak and strong localization

Boltzmann transport theory assumes that there are no interference effects from successive scattering events. On the other hand, if the electron scattering is elastic, as it typically is from impurities, then the wave function is not randomized by collisions and the various possible electron paths are subject to interference effects. This mechanism was shown to decrease the conductivity (and hence also diffusivity) as calculated by the usual Boltzmann formalism, and the effect is therefore known as weak localization (WL). Only inelastic collisions (typically electron–electron (e–e) scattering at low temperatures, but e–p scattering and spin-flip scattering can also be relevant) can randomize the wave function and terminate the interference effects. The corrections are most pronounced in low-conductivity samples and have been extensively studied in a variety of systems, including 2D gases [62, 63].

If we express the Boltzmann value of conductivity as  $\sigma_0 = \pi k_F l_{\text{imp}} (e^2/2\pi^2 h) = \pi k_F l_{\text{imp}} \sigma_N$ , where  $l_{\text{imp}}$  is the elastic mean free path (the electron scattering is dominated by impurities in the samples of interest here), and denote the WL correction as  $\Delta\sigma_{\text{WL}}$ , then the corrected conductivity is

$$\sigma = \sigma_0 + \Delta\sigma_{\text{WL}} = \sigma_N [\pi k_F l_{\text{imp}} - \ln(l_{\text{in}}/l_{\text{imp}})] \quad (5.58)$$

where  $l_{\text{in}}$  is the inelastic mean free path. Because  $l_{\text{in}}$  is usually taken to have a power law dependence on temperature, say  $l_{\text{in}} \propto 1/T^p$ , then  $\Delta\sigma_{\text{WL}} = p\sigma_N \ln T$ . The above equation shows that WL effects are significant compared with  $\sigma_0$  only when  $k_F l_{\text{imp}}$  is low, which implies very low-mobility samples since  $\mu_{\text{imp}} = (e/h)(k_F l_{\text{imp}}/n_s)$ . There is also a correction due to e–e effects which can mimic the above behaviour, but we do not consider this here.

Corrections have been predicted to occur in  $S^{\text{d}}$ , but these have not yet been seen in either 2D or 3D. However, in a series of experimental papers, Syme and Pepper [64] reported that both  $S^{\text{g}}$  and  $\sigma$  had essentially the same correction factor (though of opposite sign), namely

$$\frac{\Delta S_{\text{WL}}^{\text{g}}}{S^{\text{g}}} = -\frac{\Delta\sigma_{\text{WL}}}{\sigma}. \quad (5.59)$$

Because  $S^{\text{g}} = \epsilon^{\text{g}}/\sigma$ , this result implies that  $\epsilon^{\text{g}}$  is unaffected by WL. The strong intrinsic temperature dependence of  $S^{\text{g}}$  makes it impractical to look for a correction varying as  $\ln T$ . Instead, Syme and Pepper used the fact that a low magnetic field perpendicular to

the plane of the 2D gas reduces the WL correction. The dependence of  $\sigma$  on magnetic field  $B$  is found to be

$$\sigma = \sigma_N \left[ \pi k_F l_{\text{imp}} + \psi \left( \frac{1}{2} + \frac{\hbar}{2eBl_{\text{in}}l_{\text{imp}}} \right) - \psi \left( \frac{1}{2} + \frac{\hbar}{2eBl_{\text{imp}}^2} \right) \right] \quad (5.60)$$

where  $\psi$  is the digamma function. As  $B \rightarrow \infty$ ,  $\sigma$  goes to the Boltzmann value. (Note that any effects in  $\sigma$  or  $S$  arising from the Lorentz force are typically very small in these experiments because the sample mobilities are very low; at the same time the field required to decrease  $\Delta\sigma_{\text{WL}}$  strongly is also very low.) It was changes in  $S$  and  $\sigma$  as a function of field that were compared by Syme and Pepper and claimed to be essentially equivalent. The strong temperature dependence of  $S$  implied that it was dominated by  $S^{\text{g}}$ . The sample used was a Si-MOSFET grown on a sapphire substrate, a procedure which introduces many defects and gives a very low mobility.

More recently, Miele *et al.* [21] repeated the experiment but used samples based on a AlGaAs/GaAs/AlGaAs quantum well  $\delta$ -doped with a Si layer within the GaAs well to give the requisite low mobility. As seen in Fig. 5.4, they found that  $S$  showed no significant field dependence compared with  $\sigma$ , a result directly contradictory to that reported by Syme and Pepper. Again the results were dominated by  $S^{\text{g}}$ .

The only microscopic calculation of the effect of WL on  $S^{\text{g}}$  is that by Afonin and Galperin [65] but this was claimed to be valid only at very low magnetic fields. However, Miele *et al.* [21] gave a semi-classical argument based on Eq. (5.44) which suggested that  $S^{\text{g}}$  should be unaffected by WL. Basically the idea is that all the quantum interference effects can be incorporated into the momentum relaxation time  $\tau$  which is dominated by impurity scattering. This appears in both  $\sigma$  and  $\epsilon^{\text{g}}$  in exactly the same way, but their ratio  $S^{\text{g}} = \epsilon^{\text{g}}/\sigma$  is insensitive to WL. The original paper should be consulted for more details. If this explanation is correct, there are probably other situations where drag may be affected by WL. Thus, the acoustoelectric effect will presumably reflect WL, as will phonon coupling (drag) of currents between two parallel layers of different mobility.

If the mobility of the sample is continuously reduced, a point is reached where the e-p interaction is expected to be modified by the intense impurity scattering. This happens approximately when  $\langle q \rangle l_{\text{imp}} < 1$  and is referred to as the dirty limit. The physical effect is a reduction in the effectiveness of screening by the electrons due to their very low diffusivity. The problem has been considered in detail for the piezoelectric interaction [66, 67] and it was predicted that the limiting low-temperature dependence (in the Bloch limit) of  $S^{\text{g}}$  would change from  $T^4$  in the pure limit,  $\langle q \rangle l_{\text{imp}} > 1$ , to  $T^3$  in the dirty limit. As we noted earlier,  $\hbar s_i \langle q \rangle \simeq 5k_{\text{B}}T$  so that the transition should occur when  $T \simeq \hbar s_i / 5k_{\text{B}}l_{\text{imp}} = s_i e / (5\mu_{\text{imp}}k_{\text{B}}\sqrt{2\pi n_s})$ . For example, if  $n_s = 2 \times 10^{15} \text{ m}^{-2}$ ,  $\mu_{\text{imp}} = 0.1 \text{ m}^2 \text{ V}^{-1} \text{ s}^{-1}$ ,  $s_i \simeq 3000 \text{ m s}^{-1}$  (transverse phonons in GaAs) then  $T \simeq 0.6 \text{ K}$ . Thus, this is typically a low-temperature transition, even when using very low-mobility samples. The transition has recently been observed experimentally [68] in GaAs/AlGaAs samples. The temperature dependence of the energy relaxation time of the electrons was also predicted to change; this has also been observed though the absolute magnitude appears to agree with theory only when the sample conductivity is not too low (see ref. [69] and references therein).

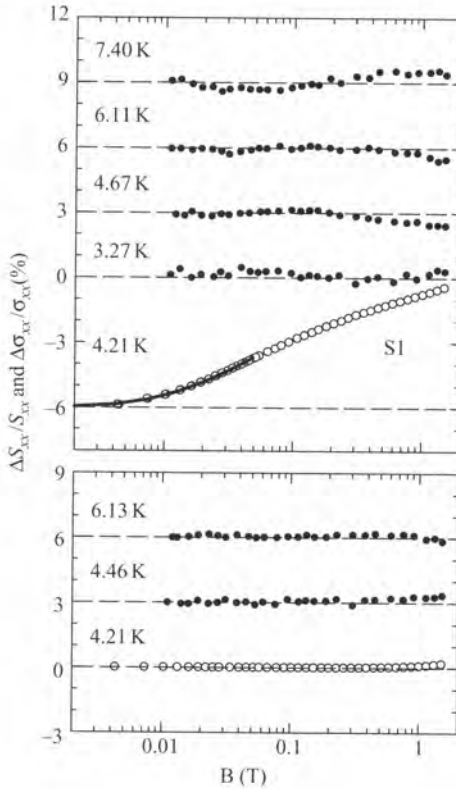


**Fig. 5.4** Measured relative changes (in %) in the thermopower  $S_{xx}$  (filled circles) and conductivity  $\sigma_{xx}$  (open circles) as a function of magnetic field  $B$  for a GaAs/AlGaAs sample ( $n_e = 3.6 \times 10^{16} \text{ m}^{-2}$ ,  $\mu_{\text{imp}} \approx 0.12 \text{ m}^2 \text{ V}^{-1} \text{ s}^{-1}$ ). The upper panel shows data for  $B$  perpendicular to the sample, the lower panel for  $B$  parallel to the sample. The changes in  $\sigma_{xx}$  are due to weak localization. From Ref. [21].

In the case of e-p deformation potential scattering, it has been predicted that no changes will occur in the e-p scattering in going from the clean to the dirty limit [66,67]. Si-MOSFETs have only deformation potential scattering and measurements on  $S$  are available for this system [70] which span the clean to dirty limit transition. However, there is a major complication in that high-mobility Si-MOSFETs, and many other 2D systems, appear to undergo a metal-insulator transition in the region of  $k_F l_{\text{imp}} \sim 1$ . Such a transition is not expected to occur according to scaling results for non-interacting electrons, and the origin of this transition has not been established as yet. Earlier data on  $S^g$  in low-mobility Si-MOSFETs [35] also exist and should not show the metal-insulator transition, but the sample conductivities are not available so the data cannot be analysed quantitatively.

We should mention that the literature concerning the transition from the clean to dirty limit in 3D has a long history. Zavaritskiĭ [17] was the first to consider this problem in 2D systems and used earlier 3D results as a guide. We will not pursue the details here

because we believe that the more recent results discussed above are more relevant to the 2D situation.

As the energy associated with the random impurity potential in the sample becomes stronger compared with  $E_F$ , there comes a point when one expects a crossover from weak localization to strong localization (often referred to as exponential localization). At this point the electrons become localized in space and transport current only if they are excited to delocalized states or if transitions between the localized states occur. In general the localized states have a range of different energies and so transitions between them require inelastic processes to conserve energy. In principle there will be transitions between nearest neighbour sites as well as between sites further apart. The latter turns out to be the most probable and this is known as variable range hopping (VRH). Excitation to delocalized states will be likely only at higher temperatures and VRH should always dominate at sufficiently low temperature.

Our interest is in what happens to  $S$  under these conditions. There are predictions for both  $S^d$  and  $S^g$ , but we will discuss only the latter. Because  $S^g$  requires the conservation of crystal momentum, and this will not hold for e-p scattering between localized states, we expect  $S^g$  to be zero under these conditions [71, 72].  $S^g$  will presumably exist when excitation to delocalized states occurs, but there is no published theory for this case as yet. Experiments on  $S$  are very difficult under these circumstances because of the high resistivities of the samples. The only relevant experimental data that we are aware of are those on low-mobility Si-MOSFETs by Gallagher *et al.* [35] and high-mobility Si-MOSFETs by Fletcher *et al.* [70]. The former probably reached into the region of interest, but resistivity data are not available. As noted above, the latter show a metal-insulator transition. The resistivities are metallic at high electron densities (i.e. the resistivity decreases with temperature) and there is a transition to activated behaviour at lower densities (the samples become insulating at low temperatures); as density is decreased in the insulating region, there is a progressive change in resistivity from simple activated behaviour, implying excitation of the carriers to delocalized states, to a temperature dependence which indicates VRH. Interestingly,  $S^g$  appears to be present over the whole range of densities. As yet there is no experimental evidence that  $S^g$  goes to zero in the VRH regime, as predicted.

## 5.3 Behaviour of 2D systems in magnetic fields

### 5.3.1 Classical high-field limit

We deal only with the case of a perpendicular magnetic field. There is some early work with a parallel field which has been reviewed by Gallagher and Butcher [1]. Equation (5.44) is a semi-classical prediction and ignores Landau quantization. It predicts that  $S_{xx}^g$  is independent of  $B$  and  $S_{yx}^g$  is zero. The same predictions have also been made by Zianni *et al.* [25]; in that work small corrections to these results were calculated, but these are now believed to be negligible. The semi-classical, high-field condition is reached when  $\omega_c \tau_{tr} > 1$  where  $\tau_{tr}$  is the momentum relaxation time. On the other hand, Landau levels becomes visible when  $\omega_c \tau_q > 1$  where  $\tau_q$  is the quantum relaxation time. In typical heterostructures based on GaAs/AlGaAs,  $\tau_{tr}$  is about an order of magnitude

larger than  $\tau_q$ . Thus, in these and many other systems, one can reach classically high magnetic fields well before Landau quantization becomes visible. In Si-MOSFETs the two relaxation times are very similar so the two regimes are not so readily separated. From an experimental point of view, we should also be aware that the diffusion thermopower  $S_{ij}^d$  is field dependent; one finds that Eq. (5.1) is replaced by [56]

$$S_{xx}^d = -\frac{S_c}{ne} \left( 1 + \frac{p}{1 + (\omega_c \tau_{tr})^2} \right) \quad (5.61)$$

$$S_{yx}^d = -\frac{S_c}{ne} \left( \frac{p\omega_c \tau_{tr}}{1 + (\omega_c \tau_{tr})^2} \right). \quad (5.62)$$

With typical GaAs/AlGaAs samples,  $S^g \gg S^d$  at zero field over the temperature range where nearly all the early data have been obtained, and this should remain so for  $S_{xx}^g$  and  $S_{xx}^d$  in the semi-classical field regime. All the early GaAs/AlGaAs data on thermopower used high-mobility samples ( $\mu_{tr} > 10 \text{ m}^2 \text{ V}^{-1} \text{ s}^{-1}$ ) so that  $\omega_c \tau_{tr} = \mu_{tr} B$  reaches 1 for  $B \leq 0.1 \text{ T}$ . This low-field region was not examined in detail (there was no prediction for the semi-classical behaviour at that time) though in retrospect we see that the available results were consistent with  $S_{xx}$ , and hence  $S_{xx}^g$ , being independent of  $B$  as predicted.

The first measurements specifically to investigate the semi-classical regime were made on a very low-mobility GaAs/AlGaAs sample [56] ( $\mu_{tr} \simeq 0.13 \text{ m}^2 \text{ V}^{-1} \text{ s}^{-1}$  and  $\tau_{tr} \approx \tau_q$ ) and  $S_{xx}^g$  was found to be accurately independent of  $B$  up to  $\omega_c \tau_{tr} \sim 1$  over a wide range of temperatures. This was the case even when weak localization had a strong effect on  $\rho_{xx}$  as already seen in Fig. 5.4. At high temperatures  $S_{xx}^d$  became visible and the observed field dependence was interpreted in terms of Eq. (5.61). A strong field dependence seen for  $S_{xx}$  in Si-MOSFETs at low magnetic fields was not initially understood [34, 73], but it was later shown that a contribution from  $S_{xx}^d$  as predicted by Eq. (5.61) completely accounts for this [74].

We should mention that high-mobility GaAs/AlGaAs samples often show [75] a strong decrease of  $\rho_{xx}$  which varies as  $B^2$ . This has been ascribed to e-e interaction. As far as we are aware there are no data on  $S_{xx}$  for such samples.

The situation with regard to the early data on  $S_{yx}^g$  in this regime was not clear. We now know that, contrary to Eq. (5.44), both GaAs/AlGaAs samples [56] and Si-MOSFETs [74] do exhibit an anomalous contribution to  $S_{yx}$  which is almost certainly due to drag. Butcher and Tsaousidou [76] have suggested that this might be caused by anisotropy in both the phonon and electron systems, but there is no direct proof of this. If this explanation is correct, there should also be a field-dependent contribution to  $S_{xx}^g$ , though its magnitude has not yet been calculated. Inhomogeneity effects have also been invoked to explain the behaviour of  $S_{yx}^g$  at high  $B$  (see Section 5.3.2), but the theory requires high-field conditions and there is no reason to believe that this mechanism is still significant at low  $B$ . Interestingly, Eq. (5.44) is equally appropriate to 3D. For bulk HgSe doped with Fe,  $S_{yx}^g$  was not detected [39]; this difference between 2D and 3D behaviour is puzzling.

To put the matter in perspective we should recall that Eq. (5.9) shows that  $S_{yx}^g$  arises from two terms, the drag components of which should precisely cancel according to Eq. (5.42). An estimate suggests that a difference of only about 10 per cent in the drag components of the two terms would be all that is required to reproduce the observations in GaAs/AlGaAs samples [56]. This is a relatively small discrepancy which suggests that

all the components of  $\epsilon_{ij}^g$  and  $\rho_{ij}$  are actually rather close to the theoretical predictions. Other information which suggests that Eq. (5.42) is basically correct is provided by data on InAs/GaSb samples [77]. These are unusual in having electron and hole gases on opposite sides of the interface, which results in a complex behaviour for the measured  $S_{ij}$  and  $\rho_{ij}$ . On the other hand, an analysis in terms of  $\epsilon_{ij}$  and  $\sigma_{ij}$  (which are readily obtained from the data) shows that the situation is basically very simple. As a first approximation one can ignore scattering between the electron and hole states so that  $\epsilon_{ij}$  and  $\sigma_{ij}$  are then simply the sum of the contributions from the individual electron and hole systems. Fortunately, the electron and hole systems have very different mobilities so that their contributions are easily separated. It is found that the experimental data on these coefficients can be accurately fitted to the expected behaviour with very few parameters.

### 5.3.2 Integer quantum Hall regime

In the first part of this section we will give a brief overview of  $S_{xx}$  in quantizing magnetic fields. A more detailed review can be found in ref. [1]. The second part will concentrate on recent developments concerning the Nernst–Etingshausen coefficient  $S_{yx}$ .

Initially the theories considered only diffusion and it was predicted that in the quantum Hall (QH) regime, in the limit where disorder broadening of the Landau levels is less than  $k_B T$ ,  $S_{xx}^d$  would measure the electronic entropy per unit charge [19] (consistent with our comments in Section 5.1.1). Both  $S_{xx}^d$  and  $S_{yx}^d$  were predicted to show magnetoquantum oscillations with amplitudes of order of 10–100  $\mu\text{V K}^{-1}$ . However, the measured  $S_{xx}$  were found to have considerably higher values [40, 41, 48] and also a much stronger temperature dependence than predicted from diffusion. We have already mentioned that  $S$  in 2D systems at zero or low magnetic field is largely dominated by phonon drag, and this was found to remain true in quantizing magnetic fields. Most of the data available, in particular in GaAs/AlGaAs heterojunctions where piezoelectric e–p scattering is very effective down to low temperatures, are dominated by phonon drag for 2D electron systems [2, 33, 40, 41, 48] as well as in 2D hole systems for  $T > 0.1$  K [58, 78, 79]. The situation in Si-MOSFETs [34, 73] is less clear because there is only deformation coupling in this case, and this becomes very small below 1 K.

In Section 5.2.1 we mentioned that further evidence for the dominance of phonon drag in zero magnetic field was gained from using polished substrates [43, 44] and from measuring  $S_{xx}$  in different crystallographic directions [36]. Extending such experiments to quantizing magnetic fields confirmed that phonon drag remains the dominant mechanism in the experimentally measured  $S_{xx}$ .

These experimental results triggered the development of theories dealing with the calculation of  $S_{ij}^g$  in quantizing magnetic fields [32, 80, 81]. These followed the formalism outlined in the theory section (Eq. (5.53) and the following paragraphs). Including both deformation potential and piezoelectric scattering for the GaAs/AlGaAs case, good agreement of the models with the experimental data on  $S_{xx}^g$  available at that time was found. An example of such a comparison between theory and experiment is shown in Fig. 5.5 [32]. Disorder broadened Landau levels were used in the initial calculations but these did not reproduce the observed behaviour  $S_{xx}^g \sim 0$  over a finite magnetic field

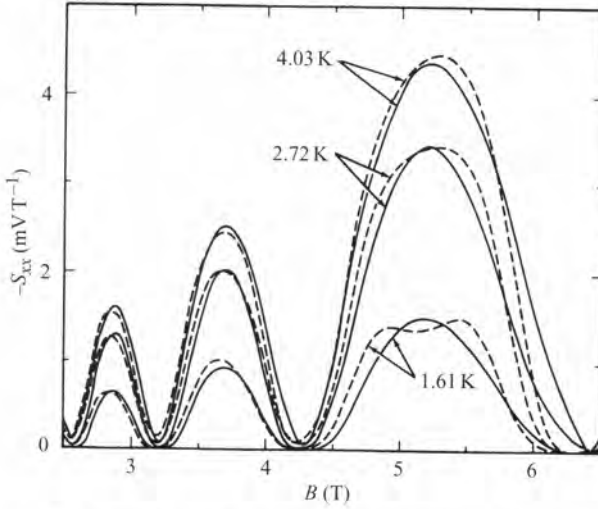


**Fig. 5.5** Comparison of the calculated phonon drag thermopower  $S_{xx}^g$  (solid lines) in the QH regime with experimental data (dashed lines) on a GaAs/AlGaAs sample. From ref. [32].

range where the Fermi energy is situated in the localized states between two Landau levels. To obtain agreement it was necessary to assume that only the extended states near the centre of a Landau level contributed to the scattering of phonons.

Butcher and co-workers attempted a more complete comparison of experiment and theory for both components  $S_{xx}^g$  and  $S_{yx}^g$  with both Si-MOSFETs [34] and GaAs/AlGaAs heterostructures [33]. They calculated the microscopic quantities  $\pi_{yx}^g$  and  $\pi_{xx}^g$  and compared them with experimental data determined from the measured transport tensors  $S_{ij}$  and  $\rho_{ij}$ . Good agreement was found for  $\pi_{yx}^g$ , and hence also for  $S_{xx}^g$  because the second term in Eq. (5.8) is negligibly small. However, the theory predicted  $\pi_{xx}^g = 0$ , which is incompatible with the experimental fact that  $S_{yx}$  is comparable in size with  $S_{xx}$ . Theory also could not account for the fact that the magneto-oscillations in  $S_{yx}$  were phase shifted by  $\pi/2$  relative to the oscillations in  $S_{xx}$ . This observation was already expressed qualitatively in an early paper of Zeitler *et al.* as ‘ $S_{yx}$  resembles the derivative of  $S_{xx}$  with respect to magnetic field’ [60]. The situation was confusing since it had been predicted that  $S_{yx}^d$  had this property, but the experiments were clearly dominated by  $S_{yx}^g$ . Recently it was realized that this qualitative statement could be made quantitative with the empirical rule [82], namely

$$S_{yx} = \alpha_S B \frac{dS_{xx}}{dB}, \quad (5.63)$$

where  $\alpha_S$  is a dimensionless constant. Figure 5.6 shows a comparison of experimentally measured  $S_{yx}$  with Eq. (5.63) where it is seen that with a single fit parameter  $\alpha_S$  all the features of  $S_{yx}$  are accurately reproduced by this equation.

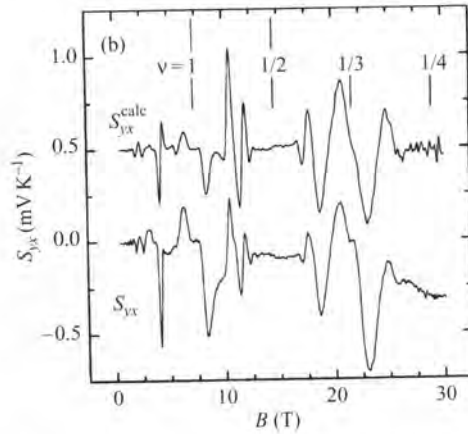


**Fig. 5.6** Comparison of the experimentally measured  $S_{yx}$  in the FQH regime (bottom) with the calculated values using Eq. (5.63) and  $\alpha_S = 0.027$  (top). The calculated trace is offset by  $0.5 \text{ mV K}^{-1}$  for clarity. From ref. [82].

A similar relation had already been noticed for resistivity (see references in [82]) where

$$\rho_{xx} = \alpha_r B \frac{d\rho_{xy}}{dB}. \quad (5.64)$$

Again  $\alpha_r$  is a constant very similar to  $\alpha_S$  for a broad range of parameters. These similarities suggest that the origin of the magnetoquantum oscillations in  $S_{yx}$  and  $\rho_{xx}$  is universal. A promising explanation for the latter was given by Simon and Halperin [83]. They proposed that, even in the limit of vanishing  $\rho_{xx}$  on a microscopic scale, oscillations will be observed in  $\rho_{xx}$  measured on macroscopic scales caused by fluctuations in  $\rho_{xy}$  due to inhomogeneities. The prefactor  $\alpha_r$  is then related to the relative variation of  $\rho_{xy}$  on such a macroscopic scale. It was suggested that a similar analysis might be applied to thermoelectric effects [82] and this was later confirmed by Simon and Cooper [84]. Here  $S_{yx}^g$  is expected to vanish on a microscopic scale. However, when inhomogeneities cause a variation of  $S_{xx}^g$  on a macroscopic scale this is reflected in a finite value of  $S_{yx}^g$  when measured on such length scales. The universality of the above derivative relations for resistance and thermopower is also underlined by the fact that an analogous relation was found in studies of surface acoustic waves [85].

### 5.3.3 Fractional quantum Hall regime

As far as we are aware, thermopower data covering the fractional quantum Hall (FQH) regime are available only for GaAs/AlGaAs heterostructures. The first experiments systematically exploring this regime are those of Zeitler *et al.* [60] and Bayot *et al.* [37]. These and later experiments show a strongly temperature-dependent thermopower, at least for temperatures down to 150 mK [36, 58, 60], indicating that phonon drag again plays a dominant role. In 2D hole gases a transition into a linear temperature dependence

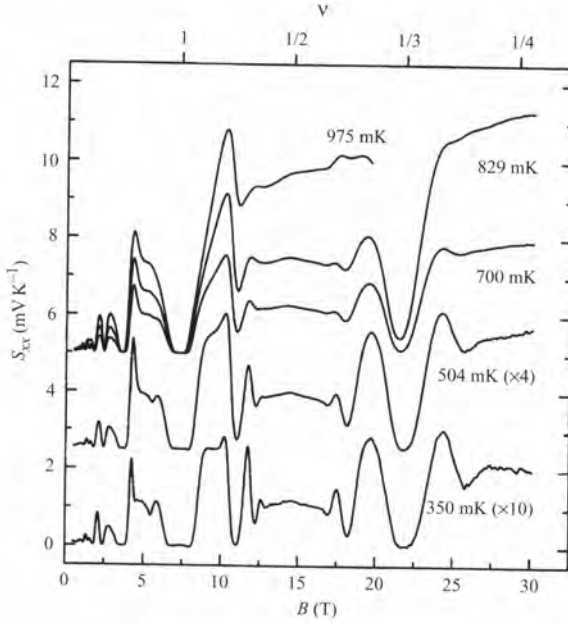


**Fig. 5.7** The magnetic field dependence of  $S_{xx}$  of a GaAs/AlGaAs sample at various temperatures. The density is  $n_s = 1.75 \times 10^{15} \text{ m}^{-2}$ . The data show both IQH and FQH regimes but, in particular, notice the plateaux around  $\nu = \frac{1}{2}$ . For clarity the curves for  $T \geq 600 \text{ mK}$  are offset by  $5 \text{ mV K}^{-1}$  and that at  $504 \text{ mK}$  by  $2.5 \text{ mV K}^{-1}$ . Also note the magnification factors for the low-temperature data. From ref. [36].

was found for  $T < 100 \text{ mK}$  perhaps caused by the diffusion contribution at the lowest temperatures [78, 79].

In retrospect, even the first thermopower experiments revealed the new quasiparticle states that appear in this regime. Apart from minima due to the appearance of odd-denominator FQH states, for example at filling factor  $\nu = \frac{1}{3}$ ,  $S_{xx}$  is essentially constant. Two plateau-like regions for  $1 > \nu > \frac{1}{3}$  and  $\frac{1}{3} > \nu > \frac{1}{5}$  were evident, which differ by roughly a factor of 2 in magnitude. The authors of this figure noted that ‘ $\nu = 1/3$  acts as a boundary between two different states’ [60]. Later these states were identified as the CFs [86] formed at  $\nu = 1/2$  and  $\nu = 1/4$  [36, 50, 51]. Figure 5.7 shows a typical trace of  $S_{xx}$  covering both IQH and FQH regimes [36] where plateaux around  $\nu = \frac{1}{2}$  and  $\nu = \frac{1}{4}$  develop as a signature of CFs.

At  $\nu = \frac{1}{2}$  each CF consists of one electron with two flux quanta attached to it. At  $\nu = \frac{1}{4}$  four flux quanta attached to an electron form a different CF state. The CF theory regards these even-denominator filling factors as occurring at an effective zero magnetic field for the new quasiparticles. At slightly different fields the CFs are subject to an effective magnetic field of only the difference in the fields. Therefore, the plateaux in  $S_{xx}$  around  $\nu = \frac{1}{2}$  and  $\nu = \frac{1}{4}$  can be interpreted as the ‘low-field’ semi-classical thermopower of CFs. Equation (5.44) predicts that  $S_{xx}^{\text{e}}$  for electrons is independent of  $B$ . If these semi-classical arguments remain valid here, then the CFs at  $\nu = \frac{1}{2}$  and  $\nu = \frac{1}{4}$  would be

expected to result in two plateau-like regions in  $S_{xx}$  around these filling factors, just as observed.

The identification of  $S_{xx}$  in the FQH regime as the thermopower of CFs opened new possibilities to probe the fundamental properties of these quasiparticles. It was shown in Section 5.2.1 that at zero field  $S_{xx}^g \propto T^4$  for electrons where piezoelectric scattering is dominant in the low-temperature Bloch limit, that is when  $\langle q \rangle \ll 2k_F$ . In this low-temperature limit, Tieke *et al.* [36, 51] measured the temperature dependence of  $S_{xx}$  for CFs at several even-denominator filling factors and compared it with zero-field data [36, 50, 51]. At  $\nu = \frac{1}{2}$  it was found that  $S_{xx} \propto T^{3.5 \pm 0.5}$  with no evidence of any diffusion contribution. The authors concluded that piezoelectric scattering was still the dominant mechanism and that the description of  $S_{xx}$  at  $\nu = \frac{1}{2}$  as the ‘zero-field’ phonon drag thermopower of CFs is indeed valid.

The appearance of a Kohn anomaly [50, 58] at even-denominator Landau level filling also supports these arguments. An example is shown in Fig. 5.3. Taking this a step further, the appearance of a Kohn anomaly is strong evidence that the CFs forming at even-denominator filling factors do indeed have a Fermi ‘surface’ and can therefore be described as fermionic quasiparticles in an effective zero magnetic field as predicted by theory [86].

It turned out that  $S_{xx}$  at  $\nu = \frac{1}{2}$  not only shows a fermion-like behaviour, but has a magnitude identical to that at  $\nu = \frac{3}{2}$  at low enough temperatures [51]. This is strong evidence that identical CFs, each composed of an electron with two flux quanta attached to it, form at these two filling factors. A similar identity of  $S_{xx}$  is also found for  $\nu = \frac{3}{4}$  and  $\nu = \frac{1}{4}$  pointing to the existence of the same type of quasiparticle, a CF formed by electron and four flux quanta, at these filling factors [36].

A theory for the coupling of phonons to CFs, and specifically for  $S_{xx}^g$ , was proposed by Khveshchenko and Reizer [66]. They showed that the CF gauge field modifies the piezoelectric coupling to the phonons. Tsaousidou *et al.* [87] used this theory to evaluate  $S_{xx}^g$  at  $\nu = \frac{1}{2}$  numerically and found excellent agreement with the experiments of Tieke *et al.* [36] if a quasiparticle mass  $m_{CF} = 1.5m_e$  was assumed ( $m_e$  is the free electron mass). More recently Tsaousidou and Tribelis [88] extended the calculations to the  $\nu = \frac{3}{2}$  state and showed that the phonon drag at low temperatures is indeed the same as that for the  $\nu = \frac{1}{2}$  state as had been experimentally reported.

Tieke *et al.* [36] also used the semi-classical relation between  $S_{xx}^g$  and  $\tau_{cp}$  in Eq. (5.44) to calculate the phonon-limited mobility for CFs,  $\mu_{cp}^{CF}$ , at  $\nu = \frac{1}{2}$  (as well as for electrons as mentioned earlier in Section 5.2.1). A strong discrepancy between  $\mu_{cp}^{CF}(T)$  as obtained from  $S_{xx}$  and that from resistivity was found. It was initially argued [66] that this discrepancy might be due to the fact that the two experiments were in two different regimes: that is by assuming that the resistivity experiments were performed in the clean limit ( $\langle q \rangle l_{imp} > 1$ ) but that  $S_{xx}^g$  experiments were in the dirty limit ( $\langle q \rangle l_{imp} < 1$ ). However the later calculations of Tsaousidou *et al.* [87] giving good agreement with  $S_{xx}^g$  use a Boltzmann approach and Eq. (5.44) is believed to be generally valid in this case. It should also be mentioned that estimates of  $\langle q \rangle l_{imp}$  make it unlikely the measurements of  $S_{xx}^g$  were in the dirty limit [36].

Strictly speaking,  $S_{xx}$  is not precisely constant in the plateaux regions in Fig. 5.7. In particular at  $\nu = \frac{1}{2}$  a weak maximum in  $S_{xx}$  is observed at low temperatures [51]. This

maximum is symmetric around the magnetic field where  $\nu = \frac{1}{2}$ , again underlining the idea that around  $\nu = \frac{1}{2}$  the CFs are subject to an effective magnetic field. A comparable feature is not observed for the resistivity  $\rho_{xx}$  which is dominated by impurity scattering. It was initially thought that  $S_{xx}^g$  had a linear dependence on  $m_{CF}$  and that the weak maximum was due to a logarithmically diverging  $m_{CF}$  predicted by CF theory at zero effective field [86]. However, the calculations of Tsaousidou *et al.* [87] suggest that  $S_{xx}^g$  is only weakly dependent on  $m_{CF}$  in the temperature range of interest, so the origin of the weak maximum remains an open question.

Experimental data are also available for 2D hole gases. Whereas Bayot and co-workers [37, 78, 79] mainly concentrated on diffusion, Crump *et al.* [58] examined phonon drag, identified by the appearance of a clear Kohn anomaly in the thermopower. A feature unique to  $S_{xx}$  of holes appeared around  $\nu = \frac{1}{3}$  and  $\nu = \frac{2}{3}$ . At low temperatures, typically below 500 mK,  $S_{xx}$  displays a clear minimum around these filling factors. At higher temperature this minimum turns into a maximum. Crump *et al.* explained this effect by a strong screening of the CF-phonon interaction.

We finally mention that, in the FQH regime, the oscillating contribution to  $S_{yx}$  continues to obey Eq. (5.63). However, a strong monotonic contribution to  $S_{yx}$  proportional to  $S_{xx}$  is also present, and this is probably phonon drag. Depending on the electron concentration the ratio  $S_{yx}/S_{xx}$  is typically between of 20 per cent and 40 per cent [60, 82]. The origin of this additional background to  $S_{yx}$  is not understood. However, it is interesting that it is only present in the FQH regime and may be related to the formation of CFs. Perhaps a strongly anisotropic coupling of the phonons to the CFs may be responsible for the observations.

## 5.4 Conclusions and outlook

The thermopower of 2D systems is probably far better understood at the quantitative level than is the case for most 3D materials. The understanding of the thermopower of bulk metals has always been fraught with difficulties. In particular, the analysis of the magnetic field dependence typically remains at a qualitative level. Bulk semiconductors are better understood than metals, but even so it is difficult to find cases where the agreement between theory and experiment is as impressive as one often finds in 2D.

There are many instances where 2D systems have provided almost model systems to test theories of diffusion and drag quantitatively. We mention here some of their many advantages: (a) the use of a gate on the sample which allows the electronic density to be varied over a wide range; (b) the fact that the occupied energy bands are often very simple; (c) the absence of e-p U-processes which leads to a big simplification compared with bulk metals; (d) the ease with which the carrier mobility can be changed without changing the properties of the phonons. This allows us to probe  $S^g$  at very low mobilities where the e-p coupling is changing or where the electronic states begin to localize. Such experiments are usually not possible in 3D where the changes in mobility or localization are typically induced by adding impurities to the lattice which also quenches phonon drag.

Nevertheless, there are many areas that remain to be investigated or understood and we have tried to draw attention to some of them in this chapter. In particular, there are

outstanding problems in the theory of phonon drag thermopower in the region dominated by Landau levels. On the experimental side, much remains to be done in the regime of very low-mobility samples, especially in the region of strong localization. Other areas where we have little or no information on phonon drag are: experiments on 1D wires (cf. the theory of Tsousidou and Butcher [89]); quantum point contacts [90, 91]; the effects of periodic modulation of 2D gases, both theoretically and experimentally; experiments on superlattices to compare with the available theory [92].

In summary, we have made many advances in our understanding of reduced dimensionality thermopower, but there is still wide scope for fundamental and exciting discoveries in the future.

## References

- Gallagher, B.L. and Butcher, P.N. (1992). In *Handbook on semiconductors* (series ed. T.S. Moss), Vol. I (vol. ed. P.T. Landsberg), p. 817. Elsevier, Amsterdam.
- Fletcher, R. (1999). *Semicond. Sci. Technol.*, **14**, R1.
- Ioffe, A.F. (1956). *Semiconductor thermoelements and thermoelectric cooling*, Infosearch, London.
- Ziman, J.M. (1960). *Electrons and phonons*, Clarendon Press, Oxford.
- Barnard, R.D. (1972). *Thermoelectricity in metals and alloys*, Taylor and Francis, London.
- Blatt, F.J., Schroeder, P.A., Foiles, C., and Greig, D. (1974). *Thermoelectric power of metals*, Plenum, New York.
- Mahan, G.D. (1998). In *Solid state physics*, Vol. **51** (ed. H. Ehrenreich and F. Spaepen), p. 81, Academic Press, New York.
- Blatt, F.J. (1968). *Physics of electronic conduction in solids*, McGraw-Hill, FL, New York.
- Herring, C. (1954). *Phys. Rev.*, **96**, 1163.
- Yu, R.C., Chiang, L., Upasani, R., and Chaikin, P.M. (1990). *Phys. Rev. Lett.*, **65**, 2458.
- Hone, J., Ellwood, I., Muno, M., Mizel, A., Cohen, M.L., Zettl, A., *et al.* (1998). *Phys. Rev. Lett.*, **80**, 1042.
- Heremans, J. and Thrush, C.M. (1999). *Phys. Rev.*, **B59**, 12579.
- Strunk, C., Henny, M., Schönenberger, C., Neuttiens, G., and Van Haesendonck, C. (1998). *Phys. Rev. Lett.*, **81**, 2982.
- Hundley, M.F. and Zettl, A. (1987). *Solid State Commun.*, **61**, 587.
- Stokes, J.P., Bloch, A.N., Janossy, A., and Gruner, G. (1984). *Phys. Rev. Lett.*, **52**, 372.
- Kagohashi, T., Takarada, T., Hasegawa, H., Katumata, Y., Kuga, M., Okamoto, H., *et al.* (1999). *J. Phys. Condens. Matter*, **11**, 6373.
- Zavaritsky, N.V. (1984). *Physica B&C*, **126**, 369.
- Smith, M.J. and Butcher, P.N. (1990). *J. Phys. Condens. Matter*, **2**, 2375.
- Jonson, M. and Girvin, S.M. (1984). *Phys. Rev.*, **B29**, 1939.
- Nicholas, R.J. (1985). *J. Phys. C: Solid State Phys.*, **18**, L695.
- Miele, A., Fletcher, R., Zaremba, E., Foxon, C.T., and Harris, J.J. (1998). *Phys. Rev.*, **B58**, 13181.
- Gurevich, Yu.G., Titov, O.Yu., Logvinov, G.N., and Lyubimov, O.I. (1995). *Phys. Rev.*, **B51**, 6999.
- Cantrell, D.G. and Butcher, P.N. (1987). *J. Phys. C: Solid State Phys.*, **20**, 1985; 1993.
- Ma, Y., Fletcher, R., Zaremba, E., D'Iorio, M., Foxon, C.T., and Harris, J.J. (1991). *Phys. Rev.*, **B43**, 9033.
- Zianni, X., Butcher, P.N., and Kearney, M.J. (1994). *Phys. Rev.*, **49**, 7520.
- Price, P.J. (1984). *Solid State Commun.*, **51**, 607.

27. Price, P.J. (1981). *Ann. Phys. (NY)*, **133**, 217.
28. Lyo, S.K. (1988). *Phys. Rev.*, **B38**, 6345.
29. Stormer, H.L., Pfeiffer, L.N., Baldwin, K.W., and West, K.W. (1990). *Phys. Rev.*, **B41**, 1278.
30. The low-temperature forms of the electron-phonon scattering rates in Eq. (5.49) are the following. (a) Deformation potential:  $\langle 1/\tau_{ep} \rangle_{\text{def}} = (3.7! \zeta(7)/2^5 \pi) g \Xi_d^2 (k_B T)^7 / (\hbar s_l)^8$ ; (b) Longitudinal piezoelectric:  $\langle 1/\tau_{ep} \rangle_{\text{pl}} = (63.5! \zeta(5)/2^{11} \pi) g (eh_{14})^2 (k_B T)^5 / (\hbar s_l)^6$ ; (c) Transverse piezoelectric:  $\langle 1/\tau_{ep} \rangle_{\text{pt}} = (87.5! \zeta(5)/2^{11} \pi) g (eh_{14})^2 (k_B T)^5 / (\hbar s_l)^6$ . Here,  $\Xi_d$  is the deformation potential interaction,  $eh_{14}$  the piezoelectric interaction, and  $g = m_e^* / \hbar k_F^3 \rho q_s^2$  with  $\rho$  the mass density of the crystal and  $q_s = m_e^* e^2 / 2\pi \epsilon_s \epsilon_0 \hbar^2$  the 2D screening constant where  $\epsilon_s$  is the relative permittivity. We note that (c) gives the sum of the transverse piezoelectric scattering rates for both transverse phonon branches.
31. Tsaousidou, M., Butcher, P.N., and Triberis, G.P. (2001). *Phys. Rev.*, **B64**, 165304.
32. Lyo, S.K. (1989). *Phys. Rev.*, **B40**, 6458.
33. Fromhold, T.M., Butcher, P.N., Qin, G., Mulimani, B.G., Oxley, J.P., and Gallagher, B.L. (1993). *Phys. Rev.*, **B48**, 5326.
34. Qin, G., Fromhold, T.M., Butcher, P.N., Mulimani, B.G., Oxley, J.P., and Gallagher, B.L. (1993). *J. Phys. Condens. Matter*, **5**, 1355.
35. Gallagher, B.L., Gibbings, C.J., Pepper, M., and Cantrell, D.G. (1987). *Semicond. Sci. Technol.*, **2**, 456.
36. Tieke, B., Fletcher, R., Zeitler, U., Henini, M., and Maan, J.C. (1998). *Phys. Rev.*, **B58**, 2017.
37. Bayot, V., Ying, X., Santos, M.B., and Shayegan, M. (1994). *Europhys. Lett.*, **25**, 613.
38. Cyca, B.R., Fletcher, R., and D'Iorio, M. (1992). *J. Phys. Condens. Matter*, **4**, 4491.
39. Tieke, B., Fletcher, R., Maan, J.C., Dobrowolski, W., Mycielski, A., and Wittlin, A. (1996). *Phys. Rev.*, **B54**, 10565.
40. Fletcher, R., Maan, J.C., and Weimann, G. (1985). *Phys. Rev.*, **B32**, 8477.
41. Fletcher, R., Maan, J.C., Ploog, K., and Weimann, G. (1986). *Phys. Rev.*, **B33**, 7122.
42. Gallagher, B.L., Oxley, J.P., Galloway, T., Smith, M.J., and Butcher, P.N. (1990). *J. Phys. Condens. Matter*, **2**, 755.
43. Fletcher, R., D'Iorio, M., Moore, W.T., and Stoner, R. (1988). *J. Phys. C: Solid State Phys.*, **21**, 2681.
44. Fletcher, R., D'Iorio, M., Sachrajda, A.S., Stoner, R., Foxon, C.T., and Harris, J.J. (1988). *Phys. Rev.*, **B37**, 3137.
45. Smith, M.J. and Butcher, P.N. (1989). *J. Phys. Condens. Matter*, **1**, 1261; 4859.
46. Okuyama, Y. and Tokuda, N. (1990). *Phys. Rev.*, **B42**, 7078.
47. Xin, Z., Ouali, F.F., Challis, L.J., Salce, B., and Cheng, T.S. (1996). *Physica*, **B219-220**, 56.
48. Ruf, C., Obloh, H., Junge, B., Gmelin, E., Ploog, K., and Weimann, G. (1988). *Phys. Rev.*, **B37**, 6377.
49. Fletcher, R., Pudalov, V.M., Feng, Y., Tsaousidou, M., and Butcher, P.N. (1997). *Phys. Rev.*, **B56**, 12422.
50. Zeitler, U., Tieke, B., Wiegers, S.A.J., Maan, J.C., Fletcher, R., Fal'ko, V.I., *et al.* (1995). In *High magnetic fields in the physics of semiconductors* (ed. D. Heiman), p. 38, World Scientific, Singapore.
51. Tieke, B., Zeitler, U., Fletcher, R., Wiegers, S.A.J., Geim, A.K., Maan, J.C., *et al.* (1996). *Phys. Rev. Lett.*, **76**, 3630.
52. Kang, W., He, S., Pfeiffer, L.N., Baldwin, K., and West, K.W. (1995). *Phys. Rev. Lett.*, **75**, 4106.
53. Tsaousidou, M., Butcher, P.N., Crump, P.A., Hyndman, R.J., and Gallagher, B.L. (1998). In *Proc. 24th Int. Conf. on physics of semiconductors, Jerusalem, 1998* (ed. D. Gershoni), p. 1239, World Scientific, Singapore (Preprint cond-mat/0004274).
54. Miranov, O.A., Gerleman, I.G., Phillips, P.J., Parker, E.H.C., Tsaousidou, M., Butcher, P.N., *et al.* (1997). *Thin Solid Films*, **294**, 182.

55. Agan, S., Miranov, O.A., Parker, E.H.C., and Whall, T.E. (2000). *Semicond. Sci. Technol.*, **15**, 551.
56. Fletcher, R., Harris, J.J., Foxon, C.T., Tsaousidou, M., and Butcher, P.N. (1994). *Phys. Rev.*, **B50**, 14991.
57. Wu, M.W., Horing, N.J.M., and Cui, H.L. (1996). *Phys. Rev.*, **B54** 5438.
58. Crump, P.A., Tieke, B., Barraclough, R.J., Gallagher, B.L., Fletcher, R., Maan, J.C., et al. (1996). *Sur. Sci.*, **361/2**, 50.
59. Gusev, G.M., Zavaritskiĭ, N.V., Kvon, Z.D., and Yurgens, A.A. (1984). *Pis'ma Zh. Éksp. Teor. Fiz.*, **40**, 275 [*JETP Lett.*, **40**, 1056].
60. Zeitler, U., Maan, J.C., Wyder, P., Fletcher, R., Foxon, C.T., and Harris, J.J. (1993). *Phys. Rev.*, **B47**, 16008.
61. Hyndman, R.J., Stoddart, S.T., Tieke, B., Lok, J.G.S., Gallagher, B.L., Geim, A.K., et al. (1998). *Physica*, **B249–251**, 745.
62. Lee, P.A. and Ramakrishnan, T.V. (1985). *Rev. Mod. Phys.*, **57**, 287.
63. Altshuler, B.L. and Aronov, A.G. (1985). In *Electron-electron interactions in disordered systems* (ed. A.L. Efros and M. Pollack), p. 1, North-Holland, Amsterdam.
64. Syme, R.T. and Pepper, M. (1989). *J. Phys. Condens. Matter*, **1**, 2747.
65. Afonin, V.V. and Galperin, Yu.M. (1992). *Phys. Rev.*, **B46**, 7915.
66. Khveshchenko, D.V. and Reizer, M. (1997). *Phys. Rev. Lett.*, **78**, 3531.
67. Khveshchenko, D.V. and Reizer, M. (1997). *Phys. Rev.*, **B56**, 15822.
68. Fletcher, R., Tsaousidou, M., Coleridge, P.T., Feng, Y., and Wasilewski, Z.R. (2002). *Physica*, **E12**, 478.
69. Fletcher, R., Feng, Y., Foxon, C.T., and Harris, J.J. (2000). *Phys. Rev.*, **B61**, 2028.
70. Fletcher, R., Pudalov, V.I., Radcliffe, A.R., and Possanzinin, C. (2001). *Semicond. Sci. Technol.*, **16**, 386.
71. Pollak, M. and Friedman, L. (1985). In *Localization and the metal-insulator transition* (ed. H. Fritzsche and D. Adler), p. 347, Plenum, New York.
72. Zvyagin, I.P. (1991). In *Hopping transport in solids* (ed. M. Pollak and B. Shklovskii), p. 143, North-Holland, Amsterdam.
73. Oxley, J.P., Gallagher, B.L., Galloway, T., Butcher, P.N., Fromhold, T.M., Mulimani, B.G., et al. (1990). In *Proc. 20th Int. Conf. on physics of semiconductors, Thessaloniki, 1990* (ed. E.M. Anastassakis and J.D. Joannopoulos), p. 853, World Scientific, Singapore.
74. Fletcher, R., Pudalov, V.M., and Cao, S. (1998). *Phys. Rev.*, **B57**, 7174.
75. Beenakker, C.J.W. and van Houten, H. (1991). In *Solid state physics* (ed. H. Ehrenreich and D. Turnbull), Vol. **44**, p. 1, Academic, New York.
76. Butcher, P.N. and Tsaousidou, M. (1998). *Phys. Rev. Lett.*, **80**, 1718.
77. Cao, S., Fletcher, R., Lakrimi, M., Mason, N.J., Nicholas, R.J., and Walker, P.J. (1996). *Phys. Rev.*, **B54**, 5684.
78. Ying, X., Bayot, V., Santos, M.B., and Shayegan, M. (1994). *Phys. Rev.*, **B50**, 4969.
79. Bayot, V., Grivei, E., Manoharan, H.C., Ying, X., and Shayegan, M. (1995). *Phys. Rev.*, **B52**, 8621.
80. Kubakaddi, S.S., Butcher, P.N., and Mulimani, B.G. (1989). *Phys. Rev.*, **B40** 1377.
81. Sankeshwar, N.S., Kubakaddi, S.S., Mulimani, B.G., and Butcher, P.N. (1990). *J. Appl. Phys.*, **68**, 5919.
82. Tieke, B., Fletcher, R., Zeitler, U., Geim, A.K., Henini, M., and Maan, J.C. (1997). *Phys. Rev. Lett.*, **78**, 4621.
83. Simon, S.H. and Halperin, B.I. (1994). *Phys. Rev. Lett.*, **73**, 3278.
84. Simon, S.H. and Cooper, N.G. (1997). *Phys. Rev.*, **B56**, 7116.
85. Kennedy, I., Rampton, V.W., Mellor, C.J., Bracher, B.H., Henini, M., Wasilewski, Z.R., et al. (1998). *Physica*, **B249–251**, 36.
86. Halperin, B.I., Lee, P.A., and Read, N. (1993). *Phys. Rev.*, **B47**, 7312.
87. Tsaousidou, M., Butcher, P.N., and Kubakaddi, S.S. (1999). *Phys. Rev. Lett.*, **83**, 4820.

88. Tsaousidou, M. and Triberis, G.P. (2002). *Physica*, **E12**, 112.
89. Tsaousidou, M. and Butcher, P.N. (1997). *Phys. Rev.*, **B56**, R10044.
90. Shklyarevskii, O.I., Jansen, A.G.M., Hermsen, J.G.H., and Wyder, P. (1986). *Phys. Rev. Lett.*, **57**, 1374.
91. Kozub, V.I. and Rudin, A.M. (1994). *Phys. Rev.*, **B50**, 2681.
92. Kubakaddi, S.S., Mulimani, B.G., and Butcher, P.N. (1992). *Semicond. Sci. Technol.*, **7**, 1344 (and references therein).

# 6 Phonon-assisted tunnelling

F.F. Ouali and L.J. Challis

## 6.1 Introduction

In this chapter we discuss the roles of phonon-assisted tunnelling and, to a lesser extent, phonon scattering, in two related types of low-dimensional semiconducting structure: resonant tunnelling devices (RTDs) and superlattices. Interest in these two types of structures developed rapidly in the early 1970s following two seminal papers by Esaki and Tsu. The first, in 1970 [1], considered the possibility of miniband conduction in superlattices (SLs) and predicted that they should exhibit negative differential conductivity (NDC). Then, in 1973, they proposed the double-barrier resonant tunnelling device or diode (DBRTD) as the electronic analogue of the Fabry–Pérot etalon in optics [2] with the barriers treated as partially reflecting mirrors of electronic waves. As in an etalon, the transmission should be resonantly enhanced when an integral number of half-wavelengths can be fitted into the cavity (Fig. 6.1) and should equal one if the two barriers have the same transmission probability at resonance. The advent and improvement of techniques such as molecular beam epitaxy (MBE) led to the growth of monolayers with very sharp interfaces and made it possible for Chang *et al.* to test this proposal for a DBRTD soon after it was made [3]. The existence of resonant tunnelling was apparent as a weak feature in the  $I(V)$  characteristic of a GaAs/AlGaAs DBRTD. A few months later, Esaki and Chang [4] reported the first unambiguous demonstration of NDC in a GaAs/AlAs SL. The first measurements on triple-barrier (double quantum well-QW) resonant tunnelling devices (TBRTDs) were made in 1986 by Nakagawa *et al.* [5].

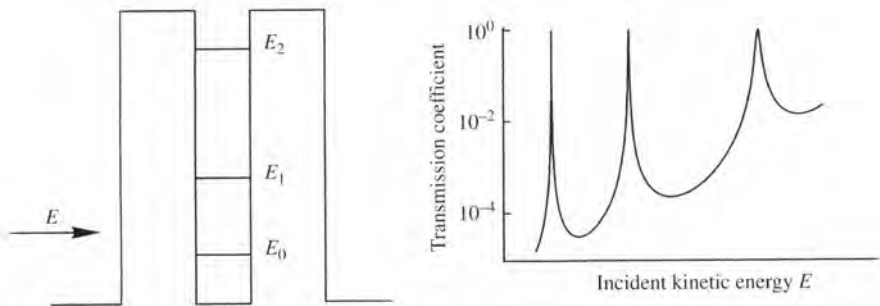


**Fig. 6.1** Transmission coefficient  $T(E)$ , where  $E = E_z$ , of a symmetric DBRTD with a 3D emitter calculated from the global coherent model using the expression given by Toombs and Sheard [17].

Phonon-assisted tunnelling is a process in which the tunnelling of an electron or hole through a barrier or barriers is accompanied by the absorption or emission of a phonon. An electron with in-plane wavevector  $\mathbf{k}$  and energy  $E_{\mathbf{k}}$  tunnels into a quantum well and, simultaneously, a phonon of wavevector  $\mathbf{q}$  and energy  $\hbar\omega_{\mathbf{q}}$  is absorbed or emitted. The most striking manifestation of this process is the production of replicas of resonant features in  $I(V)$ . If a resonant feature occurs at a bias at which electrons of energy  $E_{\mathbf{k}}$  reach some critical value, additional resonant features may occur at lower and higher bias values when the same electrons are aligned with levels lower or higher by  $\hbar\omega_{\mathbf{q}}$ . These replica peaks or satellite lines in  $I(V)$  are often referred to as anti-Stokes and Stokes peaks respectively in analogy with Raman scattering. Phonon-assisted tunnelling can occur both for optic modes, predominantly LO although much weaker TO phonon-assisted tunnelling should also occur, and for acoustic modes, both LA and TA. In RTDs, the emission peak involving LO phonons can be seen directly in  $I(V)$  and was first reported in 1987 in a DBRTD [6] and shortly afterwards in a TBRTD [7]. (The LO phonon emission seen earlier by Hickmott *et al.* [8] when electrons are injected into GaAs as a result of tunnelling through a single barrier was the first such observation in  $I(V)$  but was the result of hot electron relaxation rather than phonon-assisted tunnelling.)

Phonon-assisted tunnelling involving acoustic modes has only been seen by differential techniques, techniques in which a change in  $I(V)$  is produced by a change in phonon occupation number at the device. This was the approach used in the first observation of acoustic phonon-assisted tunnelling which was in a DBRTD [9] and also in subsequent work on a TBRTD [10]. The reason why the effects of acoustic phonon-assisted tunnelling are less marked than those of the LO phonon process can be attributed to the weaker electron-phonon coupling of acoustic modes together with the broader frequency range of modes involved in the assisted processes.

In SLs, LO phonon-assisted tunnelling has not been seen directly as a satellite peak in  $I(V)$ . The process does, however, contribute significantly to the transport and can be seen by applying magnetic fields  $\mathbf{B}$  parallel to the tunnel current  $\mathbf{I}$ . The first measurements of this type were by Higman *et al.* [11] and a more detailed investigation was made by Müller *et al.* [12] who observed a number of resonant peaks in the photoconductivity some of which could be attributed to LO phonon-assisted tunnelling between Landau levels. Studies of assisted tunnelling in SLs by acoustic phonons have been reported by Cavill *et al.* [13, 14]. This whole area of phonon-assisted tunnelling has also been one of substantial theoretical interest which in some cases preceded the experimental work.

This chapter mainly focuses on the physics of the assisted tunnelling processes occurring in RTDs and but also considers the effect of these on device performance. What appear to be the first reports of phonon-assisted tunnelling in quantum dots are included in the section on RTDs. A section on transport effects related to phonon-assisted tunnelling includes short descriptions of coherent phonon generation in SLs and of the effect of surface acoustic waves on single electron transport through quantum wires which has metrological significance as well as intrinsic interest. Finally a brief comparison is made with photon-assisted tunnelling which has been studied experimentally and theoretically in some detail.

## 6.2 DBRTDs and TBRTDs

The physics of RTDs has attracted considerable interest both experimentally and theoretically and a comprehensive review of this work up to 1995 is given in the book by Mizuta and Tanoue [15]. An example of an  $I(V)$  characteristic for a DBRTD is shown in Fig. 6.2 for the case of a 2D emitter [16]. From a threshold bias value, the current rises to a resonant peak and then falls rapidly (NDC) to a minimum where its value is referred to as the valley current. It may then rise again to a second peak, and possibly others if the well contains more than one state. The first attempts at modelling  $I(V)$  used the global coherent model. In this relatively simple approach, the transmission coefficient through the system is calculated by solving Schrödinger's equation for a potential that only depends on position. The so-called transfer matrix method [2, 17] was used together with the WKB approximation for systems with no analytical solutions [17, 18]. The model assumes that energy, and momentum parallel to the plane of the barriers ( $\hbar\mathbf{k}$ ), are both conserved in the tunnelling processes. For a 3D emitter and at  $T = 0$  K, current starts to flow at a bias which aligns the Fermi level in the emitter  $E_F$  with the ground state energy level in the QW,  $E_0$ , and becomes resonant when the ground state energy level in the emitter (the conduction band edge  $E_c$  in this 3D case) coincides with  $E_0$ . At the resonance peak, the tunnel current density is given by [17]

$$J = (E_F - E_0^c) \left( \frac{e^2 m_e^* v_z}{2\pi \hbar^2 w} \right) \left( \frac{T_E T_C}{T_E + T_C} \right) \quad (6.1)$$

where  $E_F$  and  $E_0^c$  are respectively the energies, measured from  $E_c$ , of the Fermi level in the emitter and of the ground state level  $E_0$  in the QW.  $v_z = (2E_0/m_e^*)^{1/2}$ ,  $m_e^*$  is the electron effective mass,  $w$  is the width of the QW and the last bracket expresses the total transmission coefficient through the device in terms of  $T_E$  and  $T_C$ , the transmission coefficients for the emitter and collector barriers respectively. The current falls

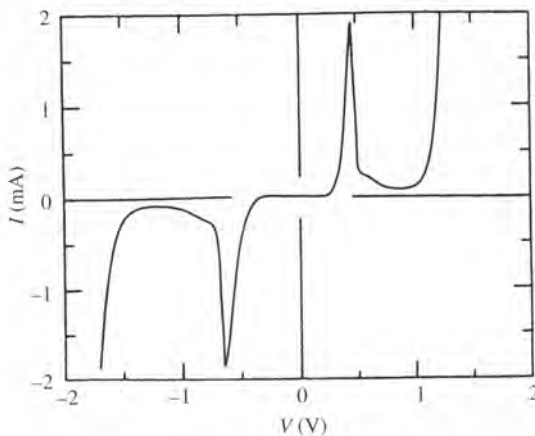


**Fig. 6.2**  $I(V)$  characteristic for a DBRTD with a 2D emitter [16]. (This figure and all the others in this chapter are for GaAs/AlGaAs or GaAs/AlAs devices.)

discontinuously beyond resonance, although in practice this becomes a region of NDC since scattering relaxes the  $k$  conservation rule. The behaviour is somewhat different for a 2D emitter. Resonance again occurs when  $E_c$  and  $E_0$  are aligned and, since the  $z$ -component of motion is now quantized in both emitter and well,  $I(V)$  becomes a delta function. However  $k$  conservation is again relaxed by scattering and this allows tunnelling to start when  $E_F$  reaches  $E_0$  as for 3D emitters and also broadens the discontinuous fall above resonance into a more gradual decrease.

Although this model provides a good qualitative description of the tunnelling, it assumes a single wave function throughout the barrier and well regions of the device which is an oversimplification because of the random phase changes produced by inelastic scattering processes including electron–electron scattering within the QW. To allow for this, Luryi [19] proposed the sequential tunnelling model illustrated in Fig. 6.3(a). Tunnelling through the device is now assumed to take place in two stages: from the emitter to the well and then from the well to the collector. It is again assumed that energy and in-plane momentum are conserved in both tunnelling processes but the two stages are treated as incoherent processes. Interestingly the  $I(V)$  characteristics calculated using this model for both symmetric and asymmetric barriers are exactly the same as those calculated using the global coherent model [17, 20, 21] provided the width  $E_F$  of the distribution of energies in the emitter region is greater than  $\hbar/\tau_t$  where  $\tau_t^{-1} = \tau_d^{-1} + \tau_s^{-1}$  and  $\tau_d$  is the dwell time (the time an electron spends in the well before tunnelling into the collector) and  $\tau_s$  the scattering time in the well.

Luryi used the diagram shown in Fig. 6.3(b) to illustrate the increase in  $I$  with bias in a DBRTD with a 3D emitter. As before, tunnelling starts when  $E_F$  reaches  $E_0$ . Now if at some bias, occupied emitter levels of energy  $E$  coincide with  $E_0$ , tunnelling occurs from all those states between  $E$  and  $E_F$  whose kinetic energy in the  $z$ -direction is of value  $\hbar^2 k_z^2 / 2m_c^* = E_0^c$ . Their  $k$  values must therefore lie between 0 and  $[2m_c^*(E_F - E_0^c)/\hbar^2]^{1/2}$  so the states are those whose wavevectors end at points within the shaded disc. As the bias increases, the disc moves towards the equatorial plane resulting in an increase in the number of electrons taking part in the tunnelling. This reaches a maximum when  $E_c$  is aligned with  $E_0$  resulting in a peak in the current. Since further transitions are forbidden,

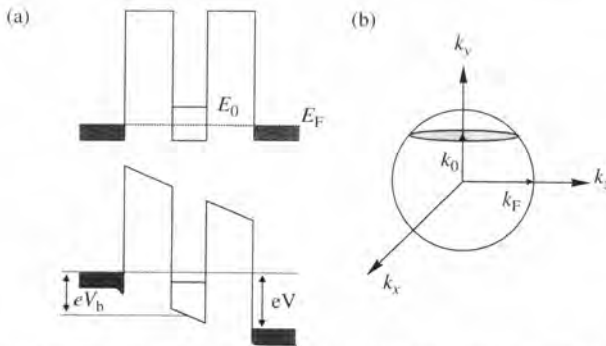


**Fig. 6.3** Sequential tunnelling model of a DBRTD with a 3D emitter: (a) the effect of bias ( $eV_b$  is the energy of the lowest filled emitter state with respect to the bottom of the quantum well and not the highest as shown), (b) the Fermi surface  $E_F(k)$  of the 3D emitter; the shaded disc contains the end points of the  $k$ -vectors of the electrons that can tunnel resonantly [19].

this is followed by a drop in current which would be discontinuous at  $T = 0$  K and in the absence of scattering.

Scattering not only changes the nature of the tunnelling through the device but also leads to reductions in both the peak value and the peak-to-valley ratio. Scattering within the well can also result in effects associated with the degree of thermalization that occurs during transport. The scattering is produced by extrinsic centres: impurities, interface roughness, and disorder; as well as by intrinsic effects: phonons and other electrons. The effect of extrinsic centres has been greatly reduced over the years as a result of improved device quality, and electron and phonon scattering are expected to play an ever-increasing role in determining the properties of tunnelling devices.

While the above models provide good qualitative explanations of  $I(V)$ , further refinements need to be introduced to obtain quantitative agreement. The most important is to include the electrostatic effect of the negative charge  $Q$  that begins to build up in the well once tunnelling starts, and steadily increases with current since  $Q = I\tau_{wc}$  where  $\tau_{wc}^{-1}$  is the tunnelling rate from the well to the collector. The presence of the charge reduces the proportion of the potential drop that occurs across the first barrier,  $V_b/V$ , so that additional bias, proportional to  $Q$ , is needed to achieve the same energy-level alignment. These electrostatic effects produce a non-linear extension in the bias range between the threshold and peak of  $I(V)$  and they can also lead to bistability. They have been modelled both by using the Bardeen Hamiltonian [22] and by using self-consistent calculations based on the Wigner distribution function and Hartree potentials. In principle, allowance also needs to be made for the fact that the electrons taking part in the transport are not in equilibrium, although calculations made by various techniques suggest this has little effect on the form of  $I(V)$  [15].

Resonant tunnelling in TBRTDs has been investigated in both symmetric (QWs of equal width) and asymmetric devices. In most of the work, including the first [5], a thick central barrier is used and resonant peaks in  $I(V)$  are seen when the ground state energy in the well nearer to the emitter, QW1, is aligned with the energy of successive excited states in the further well, QW2. Measurements on devices with a narrow central barrier show interestingly different behaviour, however [23], since the formation of two coupled states, the lower being the symmetric state and the upper, asymmetric, becomes a significant factor. Symmetry requires that these states are equally distributed between the wells for  $V = 0$ . However, this is broken by the application of bias and, if the sense of this is to raise the uncoupled level in QW1 relative to that in QW2, the upper and lower states become concentrated in QW1 and QW2 respectively.  $I(V)$  now has two peaks of very different size, with the smaller peak at lower bias, and these are attributed to tunnelling from the emitter into the further and nearer wells respectively.

The improvement in the quality of RTDs has been driven by their possible applications and considerable experimental and theoretical effort has been directed towards the development and optimization of a number of different devices. Their negative differential conductance made it possible to design new types of device and the importance of their high speed was demonstrated when Sollner *et al.* [24] showed their potential as detectors and mixers at frequencies as high as 2.5 THz. Since then a variety of electronic and optoelectronic devices have been devised and tested. These are discussed in some detail elsewhere [15] but we note that some of the earlier work on electronic devices included multistable devices, three terminal transistors, and logic devices [25–27] and

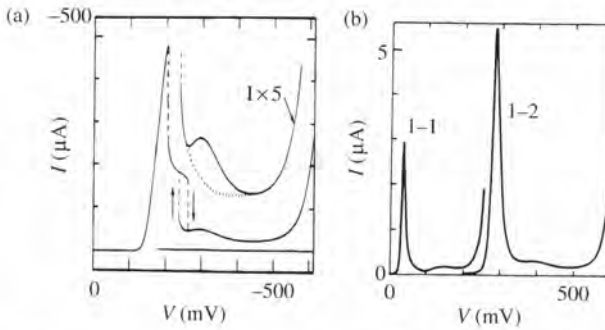


**Fig. 6.4** LO phonon-assisted tunnelling peak in the  $I(V)$  characteristics of a (a) DBRTD [6] and (b) TBRTD [7].

that demonstrations have been made of oscillators with frequencies up to 712 GHz [28] and of switches with switching times down to 1.7 ps [29]. Optoelectronic devices such as optical switches [30] and modulators [31] have also been investigated in some detail.

### 6.2.1 LO phonon-assisted tunnelling in RTDs

As already noted, the first experimental observations of LO phonon-assisted tunnelling were made by Goldman *et al.* [6] and Bando *et al.* [7] who observed a weak feature in  $I(V)$  above the main resonance in GaAs/AlGaAs DBRTDs and TBRTDs respectively (Fig. 6.4). The feature was attributed to assisted tunnelling as a result of LO phonon emission. Since then, the effect has been intensively studied and information obtained on aspects such as the modes involved and how these vary with the form of the device, the probability of two-phonon-assisted tunnelling, and the relative sizes of phonon-assisted tunnelling and elastic tunnelling (tunnelling involving elastic scattering; this is normally taken to include quasielastic scattering by acoustic phonons since the energy changes are usually  $\ll \hbar\omega_{\text{LO}}$ ). If the subband spacing is greater than  $\hbar\omega_{\text{LO}}$ , scattering by LO phonon emission is also the dominant relaxation process for electrons injected into excited QW states resulting in relaxation times less than 1ps [32–36].

### 6.2.2 Experimental investigations of LO phonon-assisted tunnelling in RTDs

Most of the detailed information on LO phonon-assisted tunnelling has been obtained from transport measurements made in magnetic fields parallel to the tunnel current. The fields enhance and sharpen the assisted peaks in  $I(V)$  making them easier to compare with peaks resulting from elastic scattering. Studies have been made on a number of different material systems and structures but the discussion here focuses on those showing the clearest features. For DBRTDs, these are n-type GaAs/AlGaAs or GaAs/AlAs devices with 2D emitters [37–44]; there appear to be no reports of observations of LO phonon-assisted tunnelling in p-type DBRTDs such as those studied by Hayden *et al.* [45]. The nature of the emitter is less important for those TBRTDs in which the main features

in  $I(V)$  are due to resonant tunnelling between the two QWs [46]. DBRTDs will be considered first.

In a magnetic field  $\mathbf{B} \parallel \mathbf{I}$ , the in-plane kinetic energy in both the emitter and well is quantized into Landau levels (LLs) so that the total kinetic energies are:  $E_c + (n + \frac{1}{2})\hbar\omega_c$  and  $E_0 + (n' + \frac{1}{2})\hbar\omega_c$  where  $\omega_c = eB/m_e^*$  is the cyclotron frequency and  $E_0$ ,  $n$ , and  $n'$  are respectively the ground state energies measured from the conduction band edges and the LL quantum numbers in the emitter and well. The selection rule  $\Delta k = 0$  for  $B = 0$  becomes  $n = n'$  in a magnetic field so the condition for resonant tunnelling is still  $E_c = E_0$ . However, as at  $B = 0$ , the selection rule governing in-plane motion is relaxed by scattering and, if the possibility of LO phonon-assisted transitions is included, the condition for 'resonant tunnelling' becomes

$$E_c = E_0 + (n' - n)\hbar\omega_c + p\hbar\omega_{LO} \quad (6.2)$$

where  $p = 0, 1$ , and  $2$  for transitions involving the emission of zero, one, and two LO phonons respectively.

At low temperatures, the transitions  $\Delta n = n' - n = 0, 1, 2, \dots$  give rise to periodic structure in the  $I(V)$  characteristics emerging both from the main ( $p = 0$ ) and LO phonon peaks ( $p = 1$ ). Figure 6.5(a) shows data for device III of Leadbeater *et al.* [37] and the positions of the peaks for device II with a wider well are shown by Landau fans in Fig. 6.5(b). The resonant peak ( $p = 0, \Delta n = 0$ ) occurs at 70 mV in this structure and line  $E_1$  shows the  $p = 0, \Delta n = 1$  transition. The  $LO_0$  peak at 160 mV is readily attributed to a phonon-assisted transition  $p = 1, \Delta n = 0$ , and the  $LO_1$  to  $LO_6$  peaks, to phonon-assisted transitions between different LLs ( $\Delta n > 0$ ). Figure 6.5(a) shows there are in fact two different  $LO_0$  phonon peaks in this device (III) and this will be discussed shortly. The interest at this point, though, is to note that these phonon-assisted peaks are both somewhat larger than line  $E_1$  resulting from elastic tunnelling and that the  $LO_0$  peaks are appreciably sharper than in zero field. These effects are evidently due to the

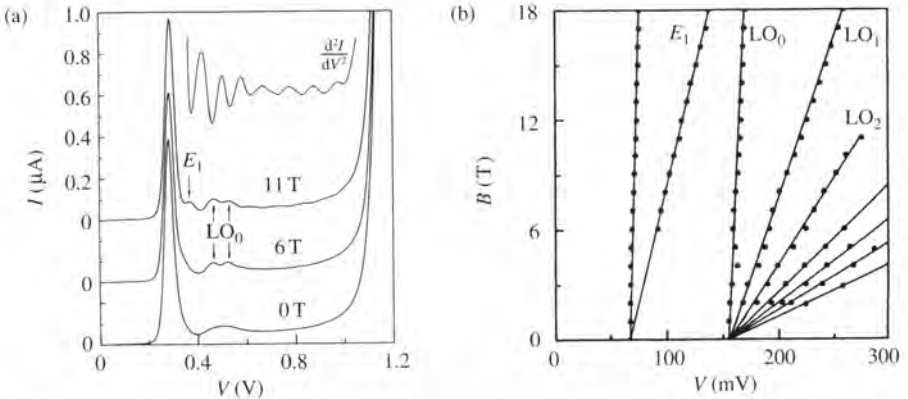


**Fig. 6.5** Oscillatory structure in the  $I(V)$  characteristic of a DBRTD in magnetic fields ( $\mathbf{B} \parallel \mathbf{I}$ ): (a)  $I(V)$  for device III at  $B = 0, 6$ , and  $11$  T and  $d^2I/dV^2$  at  $11$  T; (b) fan chart showing the positions of the peaks in  $I(V)$  for device II as a function of  $B$  [37].

change in the density of states produced by a magnetic field. This enhances the current at the transition frequencies and reduces it in between and this also has the effect of increasing the peak-to-valley ratio. Similar effects have been seen by other groups and for example  $\Delta n \leq 7$  transitions have been seen by Chen *et al.* [39].

From the voltage difference corresponding to the energy,  $\hbar\omega_c$ , separating the  $\Delta n = 0$  and 1 transitions given in Fig. 6.5(b) it can be shown that  $V_b \sim V/3$  for these bias values ( $V$  is the bias across the whole structure) and hence that the voltage separation of  $LO_0$  from the resonant peak corresponds to an LO phonon energy  $\sim 35$  meV. This is close to that of LO phonons in bulk GaAs (35.3 meV [47]) suggesting the mode involved is GaAs-like. A similar analysis for the two phonon peaks in Fig. 6.5(a) shows that one is of similar energy and so GaAs-like while the other is AlAs-like since its energy,  $\sim 48$  meV, is close to that of LO phonons in AlAs (50.1 meV [47]). Later work confirmed this result that in some structures AlAs- and GaAs-like phonons can both give rise to assisted tunnelling [38, 39, 41–43]. Leadbeater *et al.*'s work [37] suggested that the probability of AlAs-like phonon transitions decreased strongly with well width since they were present in their devices I and III with narrow wells, 5.0 and 5.8 nm, but not in II which was nominally identical to I apart from its well width of 11.7 nm. Support for this came from measurements by Boebinger *et al.* [38] showing that, although there appeared to be an AlAs-like assisted transition in a sample with a 10 nm well, it was appreciably weaker than that due to the GaAs-like mode. However, Chen *et al.* [39] observed relatively strong AlAs-like phonon-assisted transitions in a 12 nm well, which suggests the probability of these transitions is also influenced by other parameters. (The well widths used in the work of Goodings *et al.* [43] and Turley *et al.* [42] were 6 and 8 nm respectively).

Measurements [16, 42] on asymmetric DBRTDs (barriers of unequal width) showed that the phonon-assisted peaks are more pronounced when the bias direction places the thicker barrier between the well and the collector. This suggests that the probability of the process increases with the dwell time and this would also account for the fact that, in two symmetric devices, the assisted peak was larger in the device with the thicker barriers [43]. These results imply that the electron–phonon interaction mostly takes place in the well rather than the emitter. The nature of the modes involved and the strengths of the various transitions are discussed further in the next section.

The LO phonon coupling to the electrons renormalizes the energy states both in zero and magnetic fields (polaron and magnetopolaron effects) leading to anti-crossings when  $\Delta n \hbar\omega_c = p \hbar\omega_{LO}$  [48–50]. No anti-crossing effects at a bias voltage corresponding to the energy of  $\omega_{LO}$  phonons were seen at  $B \sim 11$  T, the field at which  $2\omega_c = \omega_{LO}$  (GaAs-like phonons) [37, 38], nor at  $B \sim 23$  T at which  $\omega_c = \omega_{LO}$  [38]. However, Figure 6.6 showing data by Boebinger *et al.* [38] obtained using pulsed magnetic fields up to 44 T, shows that the  $2\omega_c = \omega_{LO}$  and  $\omega_c = \omega_{LO}$  anti-crossings can both be seen at a bias corresponding to  $2\omega_{LO}$ . The absence of observable effects at  $\omega_{LO}$  is attributed to the fact that, when  $p = 0$ , the  $\Delta n = 1, 2$  transitions at  $\omega_c$  and  $2\omega_c$  are forbidden in the absence of elastic scattering and so are relatively weak. The fact that effects can be seen at  $2\omega_{LO}$  is attributable to the greater strength of the allowed  $\Delta n = 1, p = 1(\omega_c + \omega_{LO})$  and  $\Delta n = 2, p = 1(2\omega_c + \omega_{LO})$  transitions which anti-cross with the  $\Delta n = 0, p = 2(2\omega_{LO})$  transition. Figure 6.6 also shows that the  $2\omega_{LO}$  peak is not detectable at  $B = 0$  but is at high fields presumably because of the enhancement of the density of states and also

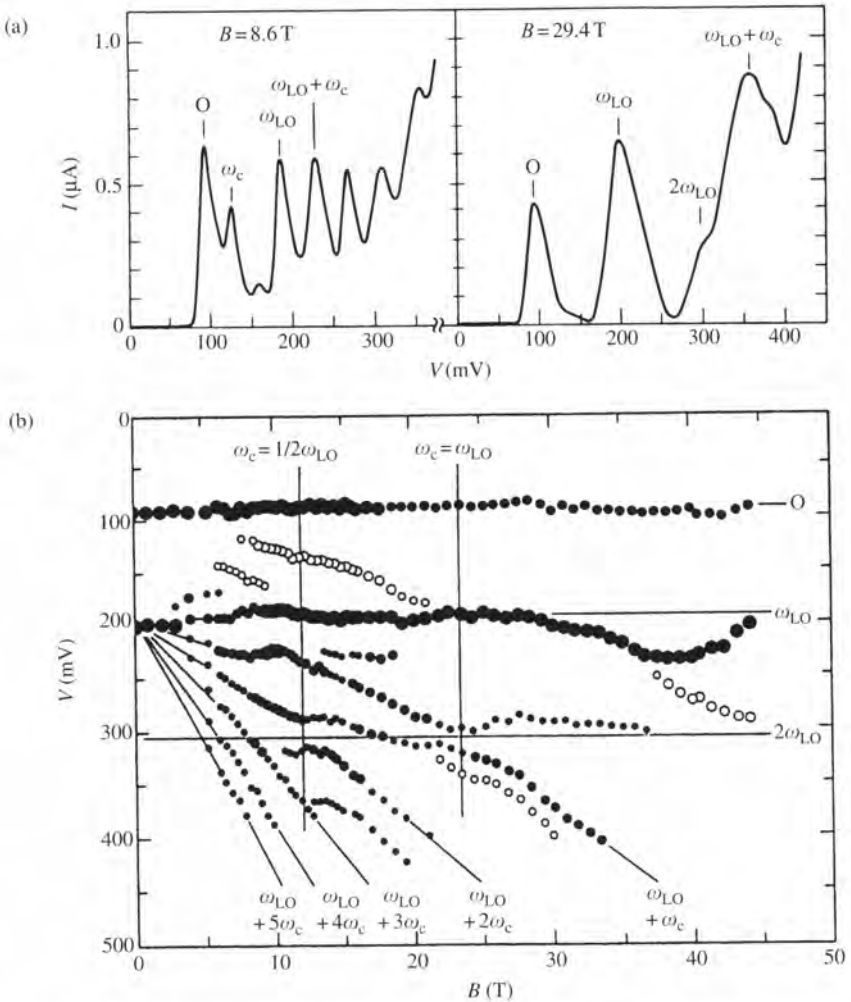


**Fig. 6.6** Oscillatory structure in the  $I(V)$  characteristic of a DBRTD in magnetic fields ( $B \parallel I$ ): (a)  $I(V)$  for  $B = 8.6$  and  $29.4\text{ T}$ ; (b) fan chart showing the positions of the peaks in  $I(V)$  as a function of  $B$ ; the open, filled, and larger filled circles indicate increasing peak size [38].

because the background scattering is suppressed. Pronounced magnetopolaron effects involving both GaAs-like and AlAs-like phonons have also been seen by Chen *et al.* [39].

Results for TBRTDs with thick central barriers show very similar effects to those for DBRTDs. The first work on magnetotunnelling by Bando *et al.* [7] was followed by two other studies [51, 52] and the measurements up to  $30.5\text{ T}$  by Rascol *et al.* [51] showed GaAs-like LO phonon-assisted peaks with  $\Delta n \leq 6$ . Later work at  $0.3\text{ K}$  by Wirner *et al.* [46] showed a series of sharp GaAs- and AlAs-like LO phonon-assisted peaks with  $\Delta n \leq 4$  plus a GaAs-like phonon peak at  $2\omega_{\text{LO}}$ . An LO phonon peak was also seen in a TBRTD with a thin central barrier [23] and attributed to assisted tunnelling into

the higher energy state of the coupled wells. LO phonon emission has also been seen in magnetic fields up to 50 T in two asymmetric TBRTDS with thin central barriers [53]. One device showed an LO phonon-assisted peak associated with tunnelling from the emitter to the nearer well, while in the other device a peak was attributed to a double resonance, approximately resonant tunnelling from the emitter to the nearer well coinciding with LO phonon-assisted tunnelling between the two wells.

The effects of LO phonon-assisted tunnelling in GaAs/AlGaAs RTDs have also been seen in a number of optical experiments. A small increase in the photoluminescence (PL) linewidth at the LO phonon peak in  $I(V)$  of a DBRTD observed by Skolnick *et al.* [54] was attributed to charge build-up in the well associated with the rise in current caused by the increased tunnelling rate. The first optical experiments on asymmetric double QW structures with thick central barriers (not strictly TBRTDs since no tunnelling takes place through the outer barriers) suggested the assisted tunnelling between the two QWs was predominantly due to impurities [55]. However, the demonstration by Oberli *et al.* [56, 57] that the decay time of the luminescence from the ground state subband in the wide well had a minimum when its energy under bias was greater by  $\sim 48$  meV than that of the same subband in the narrow well appeared to show convincingly that a phonon-assisted process was dominant. This interpretation was supported by Monte Carlo simulations [58] although the experiments of Alexander *et al.* [59] might suggest that LO phonons play a less important role. The importance of phonon-assisted tunnelling was, however, finally confirmed by similar measurements by four other groups [60–63]. Ozaki *et al.* [63] also carried out Raman measurements and showed that the intensity of the Stokes line and hence the density of LO phonons had a maximum at the bias at which the tunnelling time had a minimum. PL measurements were also made on a symmetric TBRTD with a thin central barrier and provided further evidence for LO phonon-assisted tunnelling [23]. One somewhat surprising feature in some of the experiments on devices with thicker central barriers [56, 57, 62] is that the energy of the mode involved in the tunnelling is  $\sim 50$  meV suggesting an AlAs-like mode rather than a GaAs-like mode, while in others it was  $\sim 36$  meV suggesting a GaAs-like mode [60, 61, 63] which seems more in line with the results from several transport measurements. The energy of the mode does not appear to correlate with barrier thickness as would be suggested by the theoretical studies described in the next section. Theoretical support for an AlAs-like mode in the work of Oberli *et al.* was given by Rucker *et al.* [64].

An interesting effect of the electron–phonon interaction in a GaAs/AlGaAs QW laser was demonstrated by measurements of time-resolved PL at 77 K by Benjamin *et al.* [65]. There had been a number of previous reports [66] (see also references in Benjamin *et al.*) indicating the occurrence of laser emission at the frequency  $\sim(\hbar\omega - \hbar\omega_{\text{LO}})$  of a phonon sideband to the main line at  $\hbar\omega$ . However, this was the first work to show that the lower frequency emission was delayed by between 20 and 100 ps with respect to that at  $\hbar\omega$ , supporting the view that it is indeed a phonon sideband and not the result of processes such as impurity scattering etc. Since, remarkably, the intensity of the sideband is only slightly lower than that at  $\hbar\omega$ , it was concluded that the LO phonon emission must also be a stimulated process. Benjamin *et al.* suggested that the time needed for the phonon occupation number  $N_q$  to reach the threshold value may be partly responsible for the delay, the rest being due to the lower probability of phonon-assisted recombination.

Finally we note recent work that demonstrates the importance of both optic and acoustic phonon-assisted tunnelling in the characteristics of vertical gated silicon p-i-n diodes [69].

### 6.2.3 Theoretical investigations of LO phonon-assisted tunnelling in RTDs

The first theoretical analysis of LO phonon-assisted tunnelling in DBRTDs was by Wingreen *et al.* [67, 68] who calculated the transmission coefficient at zero temperature using a Green's function approach and showed that the contribution to the current from this process had a peak in the valley region in qualitative agreement with the experimental observations of Goldman *et al.* [6]. This work on DBRTDs has been followed by many other studies using a wide range of methods including perturbation theory, Green's functions, transmission matrices, Monte Carlo methods, and Landauer's approach [70–85] and by studies on TBRTDs using perturbation theory and Green's functions respectively [86–88] (a fuller list of the earlier work is given by Turley *et al.* [79]). The work of Cai *et al.* [70], for example, used a 1D model to show that it was possible to obtain solutions for tunnelling at finite temperatures which demonstrate that the assisted tunnelling leads to phonon replicas in the transmission coefficient either side of the resonant peak and displaced from it by  $\pm\hbar\omega_{LO}$ . The 3D model used by Chevoir and Vinter [76] illustrates the approach used in some of the other calculations referred to above. They assumed the sequential model and calculated the currents due to interface roughness, alloy disorder, and intersubband scattering as well as those by acoustic and LO phonon scattering. To simplify the problem, only the most important scattering transitions were considered in each case. The current  $I$  through the device is assumed to be limited by tunnelling from emitter to well and for phonon scattering is calculated in the Born approximation using Fermi's golden rule together with the Fröhlich Hamiltonian to describe the coupling to LO phonons. The approach is broadly similar to that used earlier by Tsu and Döhler [89] to calculate acoustic phonon-assisted current. They were considering an SL but in one limit they used a 'two-well model' which is equivalent to treating the SL as a series of DBRTDs. The calculation is described in some detail in Section 6.3.6. For LO phonons, the coupling term  $C(q)(\propto q^{1/2})$  used to describe deformation potential coupling to acoustic phonons is replaced by  $\alpha_q$ , the electron–LO phonon coupling strength, which, in the Fröhlich model, is given by

$$\alpha_q = \frac{\alpha_{LO}}{q}, \quad \alpha_{LO} = \left[ \frac{e^2 \hbar \omega_{LO}}{2 \epsilon_s \epsilon_0 \Omega} \right]^{1/2} \quad (6.3)$$

where  $\epsilon_p^{-1} = \epsilon_\infty^{-1} - \epsilon_s^{-1}$  ( $\epsilon_\infty$ ,  $\epsilon_s$  are the high-frequency and static relative permittivities) and  $\Omega$  is the volume of the device ( $\alpha_q$ , which has the dimensions of energy, should not be confused with the dimensionless Fröhlich constant,  $\alpha$  of Section 2.3.2.). The effect of the inverse  $q$ -dependence of  $\alpha_q$  is to weight the interaction strongly towards a narrow frequency band of modes with  $q \sim 0$  leading to a comparatively sharp feature in  $I(V)$ . Chevoir and Vinter's results for LO phonon-assisted tunnelling reproduce the phonon replica in the valley current (Fig. 6.7), and the calculated values for the low-temperature peak-to-valley ratio agree reasonably well with the experimental results for a GaAs/AlGaAs DBRTD [6].

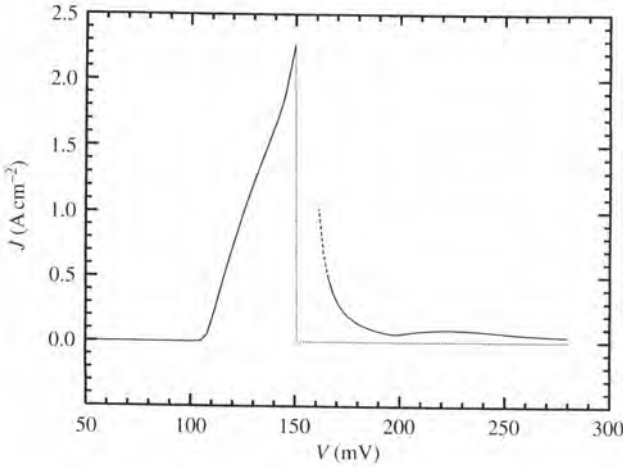


**Fig. 6.7** Calculated  $J(V)$  characteristic for the DBRTD structure measured by Goldman *et al.* [6] showing the LO phonon-assisted tunnelling peak [76].

Most of this earlier theoretical work assumed the assisted tunnelling was due to bulk phonons. However, the localization of the optical phonons within the semiconductor layers (confined modes) or at the interface between two layers (interface modes) has been considered in some of the more recent treatments [42, 64, 74, 79, 81] which compare the contributions to the phonon-assisted current from localized modes described by the dielectric continuum model (a recent description of this model has been given in the books by Ridley [90] and Stroscio and Dutta [91]). Mori *et al.*'s analysis [74] was for the five modes they expected to be of greatest importance and they investigated two symmetric GaAs/AlAs DBRTDs of different barrier width. The modes they considered were the confined LO mode in the GaAs well and four LO interface modes, two GaAs-like ( $S_0^\pm$ ) and two AlAs-like ( $S_1^\pm$ ), the most significant evidently being those whose amplitudes peak at the interfaces of the barrier between the emitter and the well:  $+/-$  refer to the barrier-emitter and barrier-well interfaces respectively. The contribution is determined by the quantity  $\alpha_i(q_{\parallel})F_i(q_{\parallel})$  which is shown in Fig. 6.8 as a function of  $q_{\parallel}w$  for each of the two DBRTDs ( $q_{\parallel}$  is the in-plane component of  $\mathbf{q}$ ,  $\alpha_i(q_{\parallel})$  is the coupling strength,  $F_i(q_{\parallel})$  is the square of the phonon matrix element between the  $z$ -components of the electronic states involved in the tunnelling, and  $w$ , called  $a$  in their paper, is the well width). For the thicker barrier device, the LO AlAs-like interface mode,  $S_1^-$ , dominates at intermediate values,  $0.5 < q_{\parallel}w < 1.5$ , while the LO GaAs-like interface mode,  $S_0^+$ , and the LO GaAs confined mode dominate at low,  $q_{\parallel}w \lesssim 0.5$ , and high values,  $q_{\parallel}w \gtrsim 1.5$ , respectively. However, for the narrower barrier device, the LO GaAs interface mode  $S_0^+$  and the LO GaAs confined mode again dominate at low and high values of  $q_{\parallel}w$  (in this case for  $q_{\parallel}w \lesssim 1$  and  $q_{\parallel}w \gtrsim 1$  respectively) and the contributions of the two AlAs-like interface modes are relatively small over the whole range. Figure 6.9 shows the sizes of the GaAs- and AlAs-like peaks in the  $I(V)$  characteristics resulting from these modes. They are of comparable size for the DBRTD with the thicker barrier but the AlAs-like peak is appreciably smaller in the narrow barrier device.

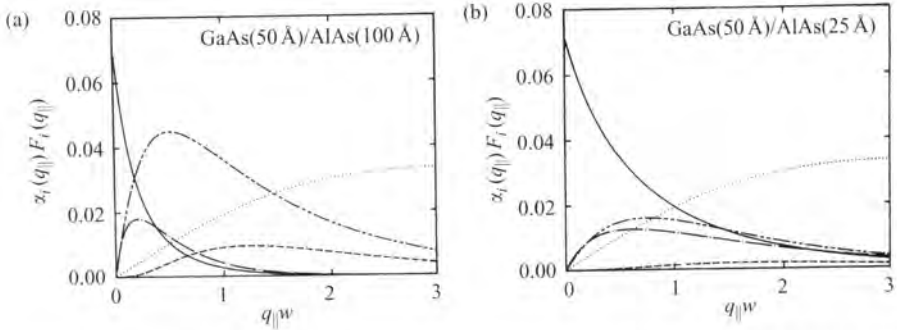


**Fig. 6.8** Contribution to the electron–phonon interaction ( $\alpha_i(q_{\parallel})F_i(q_{\parallel})$ ) of five localized modes:  $S_0^+$  = full,  $S_0^-$  = broken,  $S_1^+$  = chain,  $S_1^-$  = double dotted chain, and confined LO mode = dotted curve. The data are for two GaAs/AlAs DBRTDs with the same well width  $w = 5$  nm but different barrier widths (a) 10 nm (b) 2.5 nm [74].

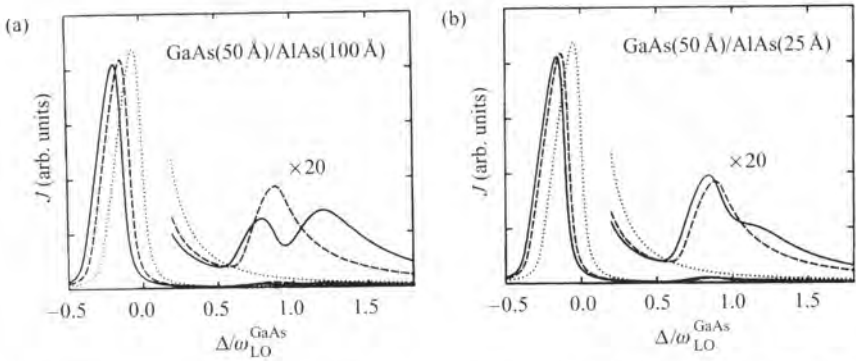


**Fig. 6.9** (a) and (b) show  $J(\Delta/\omega_{LO})$  for the two DBRTDs defined in Fig. 6.8. The solid curves are calculated for the localized modes of Fig. 6.8 and show both GaAs- and AlAs-like peaks, the dashed curves assume interaction with GaAs bulk modes only, and the dotted curves assume no electron–phonon interaction [74].

Turley and Teitsworth [79] carried out similar calculations on an asymmetric GaAs/AlAs DBRTD with an 8 nm well and barriers of 3.3 and 4.5 nm. They considered the effects of 14 localized modes: the five considered by Mori *et al.* plus the TO GaAs confined mode in the well, the LO and TO confined modes in each of the AlAs barriers, and four asymmetric interface modes (two GaAs-like and two AlAs-like:  $A_0^{\pm}$  and  $A_1^{\pm}$  in the notation of Mori *et al.* with  $A$  denoting asymmetric modes) plus the GaAs LO half-space mode [92] in the emitter (the LO half-space mode in the collector is evidently unlikely to contribute significantly to phonon-assisted tunnelling). Their conclusions differ somewhat from those of Mori *et al.* in that only two of the five modes they calculated to be of greatest importance were those listed above,  $S_1^-$  and the confined mode in the well, and two modes not considered by Mori *et al.*, the LO GaAs-like interface mode  $A_0^-$  and the LO GaAs half-space mode in the emitter, were of comparable importance and the LO AlAs-like interface mode  $A_1^+$  was significant though somewhat weaker. Their results indicate that the size of the peak in  $I(V)$  from the two dominant AlAs-like modes

should be appreciably smaller than that from the three dominant GaAs-like modes so the contributions of the additional modes does not in fact change this aspect of Mori *et al.*'s conclusions for the narrow barrier device whose dimensions are closest to theirs. Turley and Teitsworth report that they have also investigated RTDs with a range of dimensions and conclude that the contribution of TO modes is always relatively small and that the AIAs-like peaks that have been seen in experiments are due to interface modes and not to confined modes in the AIAs barriers [79] as had earlier been suggested [6, 37].

The effect on the size of the phonon-assisted peak of changes in the transmission coefficient  $T_C$  of the collector barrier has been investigated by Lake *et al.* [93]. They used an analytical model which agreed well with numerical simulations and were able to account for the experimental observation that the ratio of the heights of the phonon and resonant tunnelling peaks increases as  $T_C$  is reduced by increasing the width of the collector barrier [16, 42, 43]. The basis of their explanation is that the emitter transmission coefficient for phonon-assisted transitions, written as  $gT_E$ , is appreciably less than its value  $T_E$  for the corresponding resonant transitions:  $g \ll 1$ . The heights of the phonon and resonant peaks are proportional to  $gT_ET_C/(gT_E + T_C)$  and  $T_ET_C/(T_E + T_C)$  respectively, so while the height of resonant peak starts to decrease rapidly once  $T_C \lesssim T_E$ , the phonon peak remains approximately unchanged until  $T_C$  has fallen to the much lower value of  $gT_E$  which is rarely reached in practice.

Theoretical work on assisted tunnelling in magnetic fields involving phonon emission, and the anti-crossing that occurs as a result of the electron-phonon coupling [48–50] has already been referred to in the previous section. Bø *et al.* [94] (see also Nazhi Zou *et al.* [95]) extended this to include the phonon absorption processes that become significant as the temperature is raised. They considered the situation where the ground state LL in the emitter is aligned with the same LL in the well. For  $\omega_c \neq \omega_{LO}$ , only the resonant tunnelling peak is seen but, when  $\omega_c = \omega_{LO}$ , an electron can tunnel either resonantly into the ground state level or inelastically into the first excited LL by absorbing a phonon. The mixing of these two coherent processes leads to broad inelastic peaks either side of the crossing point at  $\omega_c = \omega_{LO}$  whose heights increase rapidly with temperature and whose widths are proportional to  $B^{1/2}$ . The gap between these two peaks is due to anti-crossing as in the emission process, but the interesting difference for the absorption process is that the resonant elastic tunnelling peak at the crossing point survives when electron-phonon interaction is present.

Finally we note the interesting suggestion that the LO phonon absorption that takes place when current flows through a suitably biased TBRTD could be used as an effective way of cooling optoelectronic devices [96].

#### 6.2.4 Acoustic phonon-assisted tunnelling in RTDs

From the work on LO phonons, it seemed likely that acoustic phonons of frequency  $\omega_q$  incident normally on the RTD should also produce phonon-assisted replicas in  $I(V)$  separated from the resonant peak by  $eV_b = \hbar\omega_q$ . However, the effect of acoustic phonon-assisted tunnelling on transport in RTDs is appreciably less pronounced than that by optic phonons and has only been seen by differential techniques: techniques in which a change in  $I(V)$  is produced by a change in phonon intensity ( $N_q$ ) at the device. The first experimental work was reported in 1995 [9] although theoretical interest in this problem started somewhat earlier.

### 6.2.5 Experimental investigations of acoustic phonon-assisted tunnelling

It has not yet been possible to do experiments with quasi-monochromatic phonons and the investigations have been carried out using phonons emitted by heated metal films evaporated onto the substrate. The phonons have a broad Planckian energy distribution with a peak at  $\hbar\omega_q \sim 2.8k_B T_h$ , where  $T_h$  is the heater temperature [9, 97, 98]. The work has not been reported in a full publication so will be discussed here in some detail.

The transient change in current,  $\Delta I$ , produced by phonons of wavenumber  $q$  should be proportional to  $W(q)g(q)N_q^*(T_h)$  where  $W(q)$  is the probability of assisted tunnelling by phonon absorption/stimulated emission and  $g(q)$  is the phonon density of states. The occupation numbers at the RTD,  $N_q^*(T_h)$ , are less than those at the heater,  $N_q(T_h)$ , since only a proportion of the phonons reach the device and some of these are delayed as a result of scattering by isotopes and impurities. So  $N_q^*(T_h) = aN_q(T_h)$  where  $a < 1$  and  $N_q(T_h) = [\exp(\hbar\omega_q/k_B T_h) - 1]^{-1}$ . In GaAs and AlGaAs, the dominant interaction between electrons and LA and TA phonons at these frequencies is through deformation potential coupling (this has been demonstrated for off-axis TA phonons by Lehmann *et al.* [99]) so that  $W(q) \propto q$  in the absence of screening and neglecting any  $q$ -dependence that may arise from interaction with the layered structure. So if phonons of energy  $\hbar\omega_q$  produce phonon-assisted tunnelling when the emitter and well levels are separated by  $eV_b$  then, for  $g(q) \propto q^2$ ,  $\Delta I(V_b) \propto q^3 N_q$  which corresponds to a Planckian energy distribution with a peak at  $eV_b \sim 2.8k_B T_h$ . Hence the phonon replicas should be displaced from the resonant peak by  $V_b \sim \pm 2.8k_B T_h/e$ . We note, however, that this assumes that the phonons are incident close to the normal which is not usually the case because of the finite sizes of the DBRTD and heater. These define the range of incident angles of the phonon group velocities and for TA modes incident around the [001] focusing direction, the incident angles of the  $q$ -vectors may extend up to  $\theta_{\max} \sim 15$  degree or more [14].

The experimental setup is shown schematically in Fig. 6.10. The RTDs are GaAs/AlGaAs devices grown by MBE on [001] 400  $\mu\text{m}$  semi-insulating substrates, etched down to a mesa of area  $50 \times 50 \mu\text{m}^2$  or smaller and contacts made to the emitter and collector. The back of the substrate is polished and a  $60 \times 600 \mu\text{m}^2$  constantan heater evaporated opposite the device. The sample is either in a vacuum or in liquid helium at a temperature of 1.3 or 4.2 K. Non-equilibrium acoustic phonons are generated from the heater by applying electrical pulses typically of duration 100 ns although longer pulses were used in the first experiments. The heater temperature during the pulse,  $T_h$ , is estimated from the input power using acoustic mismatch theory [100]. The resulting transient change in the tunnel current,  $\Delta I$ , is measured as a function of applied bias.

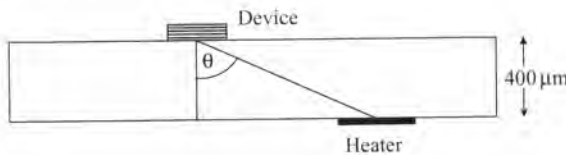


**Fig. 6.10** Experimental arrangement for measuring the change in tunnel current  $\Delta I(V)$  through an RTD or SL due to non-equilibrium acoustic phonons from a heater at temperature  $T_h$  [14].

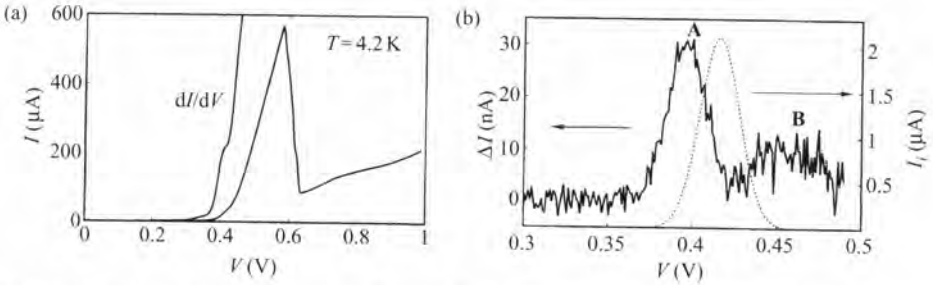


**Fig. 6.11** Phonon-assisted tunnelling through the donor state of a DBRTD with a 2D emitter (a)  $I(V)$  and  $dI/dV$  characteristics of the device, the shoulder in  $dI/dV$  is attributed to donor tunnelling; (b)  $\Delta I(V)$  due to non-equilibrium phonons from a heater at  $T_h = 15$  K. The dashed line shows the impurity (donor) peak  $I_i(V)$  extracted from  $I(V)$  [9].

The first measurements of  $\Delta I(V)$  [9] were on an undoped DBRTD with a 2D emitter and a QW of width 5.0 nm. Its  $I(V)$  characteristic, Fig. 6.11(a), shows that the main resonant peak has a small shoulder at 0.415 V. This can be seen more clearly in  $dI/dV$  and was attributed to resonant tunnelling through the ground state of Si donors in the well. Si diffuses from the contact layers during growth and, since the spacer layer was thin (2.5 nm), a significant concentration would have diffused through the layer and barrier into the nominally undoped well [101]. The phonon signal  $\Delta I(V)$  is shown as a solid line in Fig. 6.11(b). Also shown is a dotted line which is the current component,  $I_i(V)$ , obtained by extracting the shoulder in Fig. 6.11(a) from the total current,  $I(V)$ .  $I_i(V)$  is attributed to current tunnelling through the donor impurities. It can be seen that  $\Delta I(V)$  has a minimum at a bias equal to that of the peak in  $I_i(V)$  with two peaks **A** and **B** either side attributed to assisted tunnelling. The lower peak **A** is attributed to phonon absorption and the upper peak **B**, which is smaller and less well defined than the lower, to stimulated phonon emission [9]. The main resonance in  $I(V)$  was bistable, which complicated its response to phonons, and this first study concentrated on the donor resonance.

These initial measurements were extended to DBRTDs with a QW of width 9.0 nm which was  $\delta$ -doped with Si to  $\sim 4 \times 10^9 \text{cm}^{-2}$  [97, 98]. The donor resonance can now be seen as a clear feature in  $I(V)$  shown in the inset to Fig. 6.12 at  $B = 0$  and 15 T ( $B \parallel I$ ). The magnetic field produces a large increase in the bias at the main resonance presumably as a result of an increase in the charge stored in the well; an explanation for this has been given by Eaves *et al.* [102]. There is also an increase in the threshold bias. Figure 6.12 also shows  $\Delta I(V)$  at various fields  $B \leq 15$  T produced by a phonon pulse from a heater at  $T_h = 10$  K. Two peaks, **A** and **B**, are again observed either side of a minimum which coincides with the donor peak for all values of  $B$  and in zero field, these appear to be identical to the very much smaller signals seen by Ouali *et al.*. As  $B$  increases, the first peak, **A**, follows the minimum to lower voltages while **B** is in fact seen to consist of two peaks **B** and **C** which overlap in zero field. The lower peak, **B**, also follows the minimum to lower voltages while **C**, which is appreciably larger, lies just above the threshold for tunnelling into the QW bound state and follows it closely with increasing  $B$ . For  $B > 5$  T, a new broad peak, **D**, appears below the main resonant peak in  $I(V)$  and follows it with increasing  $B$ .

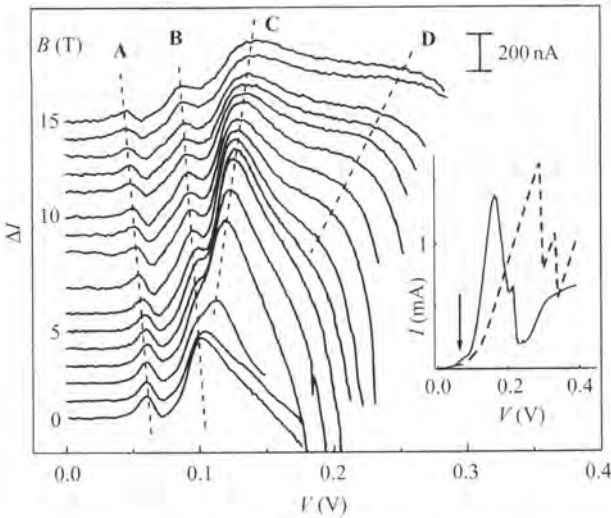


**Fig. 6.12**  $\Delta I(V)$  for a DBRTD with a 2D emitter due to non-equilibrium phonons from a heater at  $T_h = 10$  K for  $B \leq 15$  T ( $B \parallel I$ ). The inset shows  $I(V)$  for  $B = 0$  (solid line) and 15 T (dashed line); the arrow shows the position of the donor peak [98].

The movements of the peaks relative to the donor and bound state levels suggest **A** and **B** are the result of phonon-assisted tunnelling through the donor level (**A** due to absorption, **B** to stimulated emission) and **C** and **D** are associated with the bound state level. This was confirmed by comparing data for  $\delta$ -doped devices with that for a device with a nominally undoped QW. This had a much thicker (20 nm) spacer layer than that in the device of Ouali *et al.* in order to reduce the Si concentration diffusing into the QW during growth, and this seems to have been effective since there was no detectable donor contribution in  $I(V)$ . Peaks **A** and **B** could not be detected in  $\Delta I(V)$  but **C** and **D** could both be seen as the field was increased.

Measurements were also made of the positions of the peaks as a function of heater temperature  $T_h$  for  $5 < T_h < 10.5$  K. Figure 6.13 shows that, for the DBRTD of Ouali *et al.*, the position of **A** varies nearly linearly with,  $T_h$  with a slope  $\sim 9.3k_B/e$ . The analysis given earlier suggests that the phonon-assisted peaks should be separated from the minimum by  $V_b \sim \pm 2.8k_B T_h/e$  which, for a leverage factor  $V/V_b$  of 3, becomes  $V \sim \pm 8.4k_B T_h/e$  in reasonable agreement with the experimental value. The analysis did not, however, include factors such as the range of angles over which the phonons are incident and the cut-offs in the electron-phonon interaction associated with the finite size of the donor wavefunction in the in-plane and  $z$ -directions. The first of these restricts the interaction to phonons with in-plane wavenumbers  $q_{\parallel} = q \sin \theta \lesssim 1/a_0$ , where  $a_0 \sim 10$  nm is the donor Bohr radius of GaAs, and for TA phonons of energy  $\sim 2$  meV ( $\sim 2.8k_B T_h$  at  $T_h \sim 8$  K), this corresponds to  $\theta \lesssim 6$  degrees. The second cut-off limits the interaction to phonons with  $q_z \sim q \lesssim 2\pi/w$  or  $hw_q \lesssim 2.7$  meV ( $T_h \sim 11$  K) which is satisfied for the dominant TA phonons over much of the experimental range. It was not possible to obtain accurate data for **B/C** because of its small size but the shift with  $T_h$  appeared to be less than that in **A**. Any shift in the position of **A** with  $T_h$  was, however,

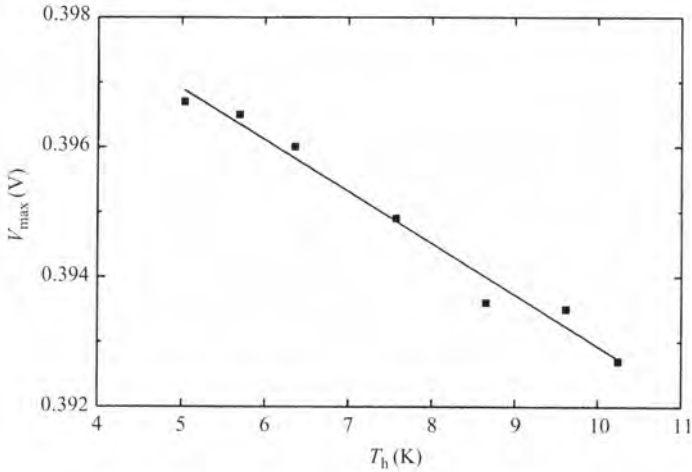


**Fig. 6.13** Bias voltage  $V_{\max}$  at the maximum of peak **A** in Fig. 6.11(b) plotted against  $T_h$ ; the line fitted to the data has a slope of  $9.3k_B/e$  [9].

too small to measure in the experiments on  $\delta$ -doped devices and Hill *et al.* tentatively suggested this might be the result of greater inhomogeneous broadening in their device. It is not clear, though, why this should be larger in a  $\delta$ -doped device than in one in which the donors are randomly distributed and a more convincing explanation [103] is that it is due to the wider QW width  $w$  of the  $\delta$ -doped devices, 9.0 nm rather than 5.0 nm, which limits the interaction to TA phonons of energy  $\lesssim 1.5$  meV ( $T_h \lesssim 6$  K). Donor-level broadening does seem likely, though, to be the reason why the separations of the peaks from the minimum are appreciably larger than the phonon energies in all of the measurements. This will be discussed in Section 6.2.6 [98, 104, 105]

We next discuss the intrinsic peaks **C** and **D**. The broad peak **D**, which occurs just below the main resonance at all magnetic fields, was attributed to phonon-assisted tunnelling through the QW bound state as a result of phonon absorption (its large breadth could be due to the angular range of the incident phonons). The position of peak **B/C** did not change significantly with  $T_h$  in zero magnetic field even in the Ouali *et al.* device. Furthermore it occurs just above the threshold for tunnelling into the QW bound state at all magnetic fields and, at this bias value,  $I(V)$  seems likely to be very sensitive to the electron temperature in the 2D emitter. Hill *et al.* concluded that peak **C** is the result of a rise in electron temperature in the emitter produced by the incident phonons and its size is broadly in line with a simple model [103] using estimates for  $\Delta T_e$  obtained from measurements of phonon absorption in a 2D electron gas [106]. (These values for  $\Delta T_e$  are appreciably larger than earlier estimates [9] based on calculations by Price [107].)

Experimental evidence that peak **A** is not due to heating comes from the increase in  $I(V)$  when the sample temperature is raised from 1.3 to 4.2 K. In this case the phonon and electron temperatures are both raised by 3 K but the form and position of  $\Delta I(V)$  were found to be the same as in the non-equilibrium measurements (Fig. 6.11(b)) where only the phonon temperature is changed significantly. This strongly suggests that the

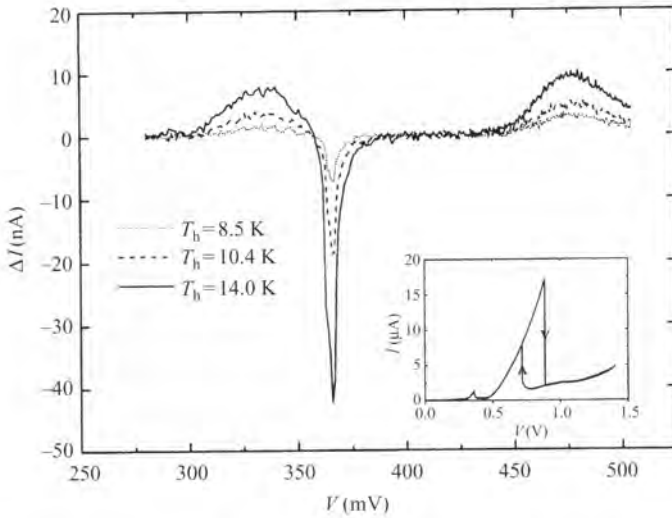


**Fig. 6.14**  $\Delta I(V)$  for a symmetric TBRTD due to non-equilibrium phonons for different values of  $T_h$ . The left and right hand peaks are attributed to assisted tunnelling by phonon absorption and emission respectively; the minimum coincides with the peak in  $I(V)$  shown in the inset (after Cavill *et al.* [10]).

changes in  $I(V)$  associated with the rise in electron temperature are much smaller than those associated with phonon-assisted tunnelling. We also note that theoretical work by Kral *et al.* [104] to be discussed later, indicates that the form of  $I(V)$  for heating would be very different from that observed.

Measurements have also been made on a symmetric TBRTD with two 5.9 nm QWs separated by a narrow (0.9 nm) central barrier [10]. The  $I(V)$  characteristic is similar to that found earlier [23] and values of the phonon signal  $\Delta I(V)$  in the region of the lower bias peak in  $I(V)$  are shown in Fig. 6.14 for different heater temperatures  $T_h$ . The minimum coincides with the position of the maximum in  $I(V)$  and peaks occur either side of the minimum. The peaks are small,  $\Delta I \sim 1$  nA for  $T_h = 8.5$  K ( $\Delta I/I \sim 0.01$ ), compared with 60 nA for peak A of the DBRTD of Ouali *et al.*, so the signals are noisy and the movement in their position with  $T_h$  could not be measured with any precision. The position of the upper peak appeared to increase in bias by  $\sim 3$  mV as  $T_h$  increased from 8.5 to 14 K as expected for assisted tunnelling for phonon emission, but it was not possible to see if there is a similar decrease of  $\sim 3$  mV in the lower peak although it could not be excluded. The charge build-up should be very small for this first peak so, if the potential drop across the QW is small, that across the first barrier should be  $V_b \sim V/2$  (it was initially suggested it might be much smaller [10]) and a shift of 3 mV would correspond to  $e\Delta V_b \sim 3.3k_B\Delta T_h$ . The most that can be said therefore is that the data are not inconsistent with phonon-assisted tunnelling. No  $\Delta I(V)$  measurements were made in the region of the higher peak in  $I(V)$  where the current changes should be appreciably larger.

These experiments indicate that RTDs have potential as tuneable spectrometers for phonons. However, they also demonstrate that this is only the case for phonons with  $q \lesssim 2\pi/w$  where  $w$  is the effective QW width of the device. This was not the case for some of the devices examined and it would be of interest to make further experiments on  $\delta$ -doped DBRTDs with narrower QWs and also on TBRTDs in the region of the larger peak.

We conclude this section by noting that acoustic phonon-assisted tunnelling would also appear to play a role in the properties of quantum dots. The coupling to nearby defects that this provides has been calculated to be efficient enough to provide a relaxation path for excited electrons [108] and so circumvent the predicted phonon bottleneck. It has also been suggested that the same mechanism accounts for the slow carrier replenishment of self-assembled quantum dots observed in exciton luminescence [109]. In addition, piezoelectrically generated acoustic phonons produced by microwave radiation have been shown to contribute to the assisted electron transfer between two coupled quantum dots formed by lateral confinement of a 2D electron gas [110].

### 6.2.6 Theoretical investigations of acoustic phonon-assisted tunnelling in RTDs

Since acoustic phonon-assisted tunnelling between the emitter and QW of a DBRTD differs only in detail from that between the two QWs of a TBRTD, we consider them together. The first theoretical analyses were on DBRTDs and treated the phonon-assisted tunnelling as an elastic scattering process [76, 111]. Roblin and Liou [111] found that the phonon contribution to the transmission coefficient was greatest in the valley region. It also displaced the resonant peak to slightly lower bias values so that  $\Delta I(V)$  has a positive peak just below resonance and becomes negative just below the peak and, although both these features are consistent with the data of Hill *et al.* in magnetic fields [98], it seems unlikely that this type of approach could explain other features of the work.

The first analysis to treat the phonon-assisted scattering as an inelastic process was by Tsu and Döhler [89]. They were interested in the assisted process in SLs but their limiting case was of the tunnelling between neighbouring wells, their so-called two-well model, and so is directly applicable to RTDs. The details of the model will be discussed in Section 6.3.6 but at this stage we note that interference effects arising from the formation of coupled states lead to size-dependent oscillations in the transition probability for phonon-assisted tunnelling. The probability becomes zero, antiresonant, for  $q_z = 0$ ,  $2l\pi/d$  ( $l = 1, 2, 3, \dots$ ) and  $2l\pi/w$  ( $l = 2, 3, 4, \dots$  but not  $l = 1$ ), and cuts off when  $q_z > 2\pi/w$  ( $w$  is the well width and  $d$  the distance between the centres of the two wells).

The first treatment specifically aimed at RTDs was by Vasko *et al.* [112] and was an investigation of the spontaneous LA phonon emission that occurs as a result of assisted tunnelling between the two QWs of symmetric and asymmetric TBRTDs when for example a voltage pulse is applied across the device to produce an energy separation between the ground states of  $\Delta$ . They used an approach similar to that of the two-well model (although were evidently unaware of the earlier work on SLs) and again found that the form of the emission is complicated by size-dependent oscillations. In general, the phonon-assisted interwell transition is followed by one or more intrawell transitions as the electron relaxes to the lowest empty state (we assume for the moment  $T = 0$  K and  $\Delta \gg E_F$ ). The total energy emitted as phonons in these two processes

must be  $\sim \Delta$  but the proportion emitted in interwell and intrawell transitions depends on the emission angle of the interwell phonon. For interwell phonons emitted close to the normal,  $\theta \sim 0$ ,  $q_{\parallel}$ , and so  $\Delta k \sim 0$  so that  $\hbar\omega_q$  (inter)  $\sim \Delta$ . Hence the energy of any phonon(s) emitted in intrawell transitions following the tunnelling is  $\ll \hbar\omega_q$  (inter). The situation is reversed, however, if the phonons are emitted at larger angles  $\theta \rightarrow \pi/2$ . Since the final state now has energy  $\sim \Delta$ , the interwell phonons emitted have momentum  $\hbar q \sim \hbar k$  (final)  $\sim (2m_e^* \Delta)^{1/2}$  and so have energy  $\hbar\omega_q$  (inter)  $\sim (2m_e^* s^2 \Delta)^{1/2}$ . This is  $\ll \Delta$  for values of  $\Delta$  of a few meV ( $2m_e^* s^2 \sim 18(8) \mu\text{eV}$  for LA (TA) phonons in GaAs) so that most of the phonon energy is emitted during the relaxation that follows the tunnelling.

So whether the total intensity of the emission is largely due to interwell or intrawell phonons depends on the angular distribution of the interwell phonons and, if most of the interwell emission occurs at low angles, interwell phonons should form the larger part of the total emission. Detailed calculations confirmed this for degenerate systems but the proportion of intrawell transitions was found to rise with temperature and to become comparable in size with that of interwell transitions for non-degenerate systems.

The frequency distribution of interwell phonons emitted at all but the larger angles is expected to be strongly affected by the size-dependent oscillations in the transition probability. Their energies are  $\sim \Delta$ , so for  $\Delta$  values of a few meV,  $q_z \sim 2\pi/w, 2\pi/d$  for typical structure dimensions and plots of the frequency distribution [112] have maxima at frequencies equal to those of the resonant peaks in the transition probability. This is no longer the case at larger angles, however, since now  $q_z \ll 2\pi/w, 2\pi/d$ . The authors give a number of useful asymptotic expressions which provide information on the parametric dependence of the frequency distribution in various limits. The work was extended to magnetic fields by Raichev and Vasko [113] who showed that magneto-oscillations should occur in the acoustic phonon relaxation rate between the two QWs with antiresonances at  $\Delta + n\hbar\omega_c = 2l\pi\hbar s/d$  ( $n$  and  $l$  are integers) when the wavevector component  $q_z$  of the phonons responsible for the relaxation satisfies  $q_z = 2l\pi/d$ . Similar effects have also been found in SLs [114].

The first study of the change in current  $\Delta I$  in an RTD produced by an incident beam of phonons was by Kozub and Rudin [115]. They were interested in the potential such a system might have as a spectroscopic detector and considered a device designed so that the tunnel current was small in the absence of phonons. This was an asymmetric TBRTD with narrow and wide wells with ground state levels of energy  $E_N$  and  $E_W$  respectively. The well widths were chosen so that, for zero bias,  $E_N$  lies above the Fermi level in the contacts while  $E_W$  lies below so that its well is filled to the same Fermi level. At  $T \sim 0$  K, very little current can flow when a small bias is applied in either direction because of the position of  $E_N$ . However, an assisted current can result from the absorption of phonons of sufficient energy. For phonons incident normally this requires  $\hbar\omega_q = \Delta = E_N - E_W$  but as the angular distribution increases, transitions become possible for a range of phonon energies. The lowest energy is  $\hbar\omega_q = \Delta - E_F = E_N - E_W - E_F$  where  $E_F$  is measured from  $E_N$ . If  $\theta < \theta_{\max}$ , the position of the upper phonon energy is set by transitions from  $E_W$  to states in the narrow well with  $k = q \sin \theta_{\max}$  and hence energy  $E_N + (\hbar q \sin \theta_{\max})^2 / 2m_e^*$ . So  $\Delta - E_F \lesssim \hbar\omega_q \lesssim \Delta + (\Delta^2 / 2m_e^* s^2) \sin^2 \theta_{\max}$  if  $\sin \theta_{\max} \ll 1$ . For LA (TA) modes in GaAs and  $\Delta = 2$  meV, the upper limit is  $\hbar\omega - \Delta = (200) 500 \sin^2 \theta_{\max}$  meV so that the spectral response to phonons with

$q$ -vectors within an angle of 8 (5) degrees from the normal would have a halfwidth (HWHM)  $\sim 1$  meV if  $E_F$  is kept small. However, since  $\Delta I$  rises rapidly below the maximum, better resolution than this suggests should be achievable by for example modulating the bias voltage. Since the spectral width  $\propto 1/m_e^*$ , this might also be reduced by using hole states, although these would be more strongly affected by inhomogeneous broadening. Kozub and Rudin note that a more effective way is to confine the electrons to quantum dots or, as had been suggested by other authors, to apply magnetic fields perpendicular to the QW planes. They also studied the phonon emission arising from assisted tunnelling and confirmed that, although it took place over a wide energy range, the phonons emitted close to the normal had energy  $\sim \Delta$  and its angular distribution could be restricted by electrostatic or magnetic confinement. We note that the formation of coupled states is not included in their treatment, so no effects arise from size-dependent oscillations in the transition probability.

Further calculations on the effect of quantizing magnetic fields on phonon-assisted tunnelling rates were made by Bø and Galperin [116], in this case on a DBRTD. They assumed a coherent tunnelling model and used a Green's function transmission method [68] to calculate  $I$ . The other principal assumptions are deformation potential coupling, electron-phonon interaction taking place in the QW,  $\omega_q \ll \omega_c$  so that tunnelling is restricted to the lowest LLs, and negligible electron heating in the emitter. Their calculations showed that Stokes and anti-Stokes phonon replicas should be present for both 2D and 3D emitters and Fig. 6.15(a) shows an example for a DBRTD with a 3D emitter. Four peaks in  $\Delta I(V)$  are seen to occur, two positive and two negative. Figure 6.15(b) for the two lower bias peaks shows that the form of  $\Delta I$  is sensitive to both the mean frequency and the distribution of the incident phonons which again demonstrates that in magnetic fields, these devices have potential as phonon spectrometers. Their results also indicate that the electron-phonon coupling strength and, hence, the strength of the phonon-induced current,  $\Delta I$ , increases with  $B$ . This would appear to be the case in the experiments of Hill *et al.* for the peak, **D**, attributed to phonon-assisted tunnelling through the bound state. However, the experimental peak is very broad and the DBRTD parameters etc. used in the experiments differ appreciably from those used in the calculations so quantitative comparison is not possible.

A treatment of phonon-assisted tunnelling through a donor state has been made by Kral *et al.* [104] using Green's functions. It again assumed the interaction to be with LA phonons via deformation potential coupling and that it took place in the QW. However, it was now with donor electrons confined within a QW of width  $w$  with wave functions

$$\phi(r) = \sqrt{\frac{2}{\pi w a_0}} \exp\left(-\frac{x^2 + y^2}{2a_0^2}\right) \cos\left(\frac{\pi z}{w}\right); \quad -\frac{w}{2} < z < \frac{w}{2}. \quad (6.4)$$

The in-plane radius of the donors,  $a_0$ , is taken to be 10 nm and their levels are assumed to have a halfwidth  $\gamma$  due to inhomogeneous broadening. The emitter and collector are taken to be 2D with  $E_F$  (emitter) = 1 meV and the phonons are assumed to be incident normally. The electron temperature is kept constant throughout. The non-equilibrium phonon distribution that occurs when phonons are emitted by a heater at  $T_h$  was modelled in various ways: one for example used a weighted equilibrium phonon occupation number

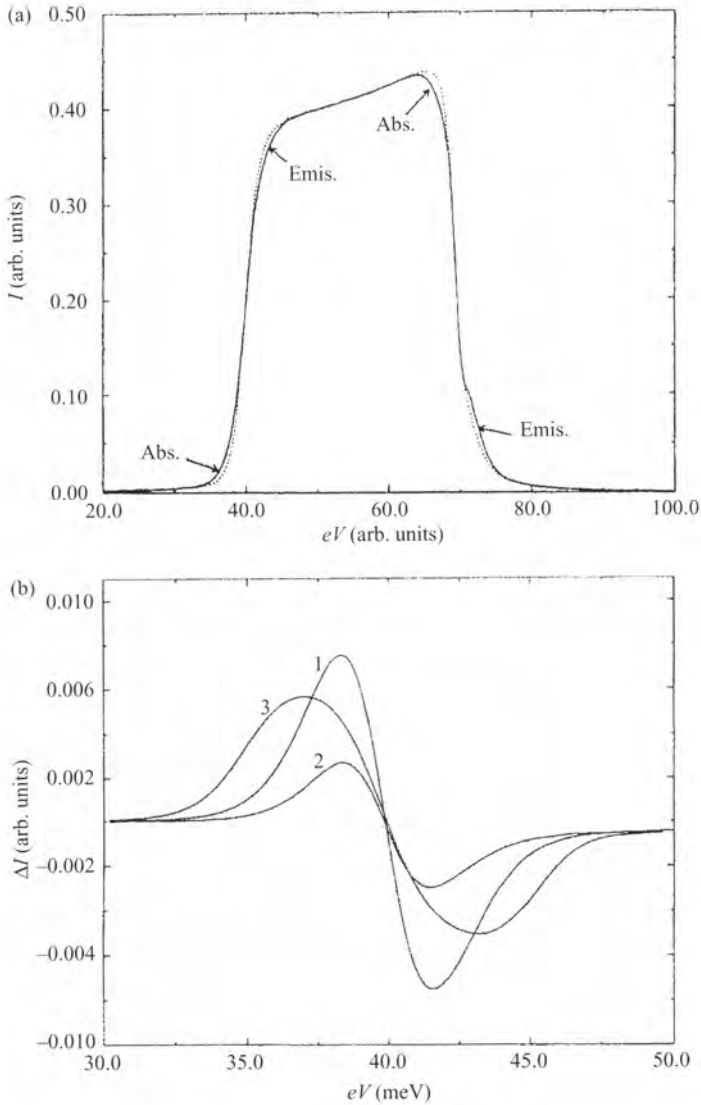


**Fig. 6.15** Calculated values of the effect of assisted tunnelling due to acoustic non-equilibrium phonons on  $I(V)$  for DBRTD (a)  $I(V)$  with (solid line) and without (dotted line) non-equilibrium phonons with a distribution corresponding to  $T_{\text{eff}} = 30$  K; (b)  $\Delta I(V)$  (additional current due to phonons) for (1)  $T_{\text{eff}} = 15$  K, (2)  $T_{\text{eff}} = 8$  K (2), and (3) for a Gaussian distribution centred at  $\hbar\omega_0 = 2.5$  meV [116].

at the DBRTD,  $(1 - c)N_q(T) + cN_q(T_h)$ , where  $c$  is a fitting parameter. The response to monochromatic phonons was also considered and confirmed that the interaction was restricted to phonons with  $q_z \lesssim 2\pi/w$  as expected. The changes in tunnel current  $\Delta I(V)$  produced by increases in the energy,  $\hbar\omega_q$ , of non-equilibrium phonons shown in Fig. 6.16 are qualitatively similar to those seen in the experiments [98]. There are two peaks due

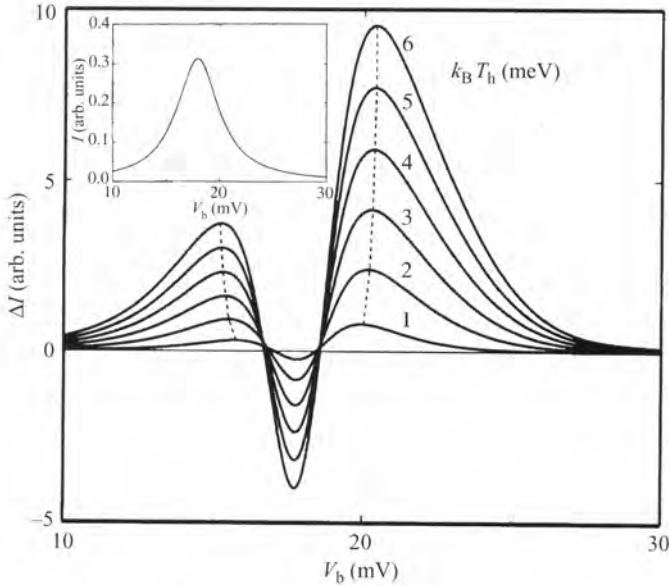


**Fig. 6.16** Calculated values of  $\Delta I(V_b)$  for current tunnelling through the donor state of a DBRTD due to non-equilibrium phonons from a heater at temperature  $T_h$  ( $V_b$  is the potential drop over the first barrier). The inset shows  $I(V_b)$  (after Král *et al.* [105]).

to assisted tunnelling by phonon absorption and stimulated emission respectively and the minimum at resonance results from a shift of the oscillator strength to the phonon replicas. It is also found that when  $\hbar\omega_q \ll \gamma$ , the phonon peaks are located at energies from the minimum and with widths which are both  $\gg \hbar\omega_q$  as observed. However, in this limit, the position of the peaks only changes weakly with  $\hbar\omega_q$  in contrast with the experimental results and the strong sensitivity to  $\hbar\omega_q$  only occurs when  $\hbar\omega_q \gtrsim \gamma$  as in this case. Another discrepancy is that, for all sensible parameters, the values of  $\Delta I(V)$  are 10–100 times smaller than those observed in reference [98]. Kral *et al.* found, however, that the increase in electron temperature in the emitter produced by phonon absorption (electron heating) leads to a change  $\Delta I(V)$  appreciably bigger than that calculated for phonon-assisted tunnelling although its form, Fig. 6.17, is clearly very different from that observed experimentally. It was pointed out, though [104], that the Coulomb potential from the ionized donors in the QW should produce localized states in the emitter and close to the barrier with binding energies of several meV [117]. So, since the electron concentration in the emitter is small, most of the tunnelling might be taking place from these states and, if so,  $\Delta I(V)$  would be very much less sensitive to electron heating than that calculated. We conclude that the model, with some refinements to reduce the effect of electron heating, can account for the form of  $\Delta I(V)$  but further work is needed to explain the movement of the phonon peaks with frequency. It would be interesting to extend the calculations to phonons incident over a range of angles although it is not clear that this would have a large effect since, as noted earlier, interaction can only take place for phonons with  $q_{\parallel} < 1/a_0$ .

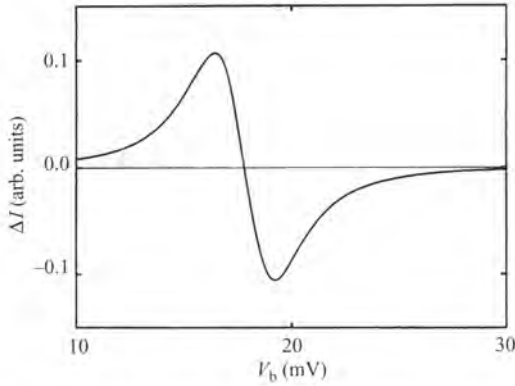


**Fig. 6.17** Calculated values of  $\Delta_S I(V_b)$  for current tunnelling through the donor state of a DBRTD caused by heating the emitter electrons from 1 to 1.1 K [105].

### 6.3 SLs

In a semiconductor SL, the additional periodicity of the lattice potential splits the conduction and valence bands into a series of minibands separated by minigaps for electron motion parallel to the  $z$ -direction of growth (Fig. 6.18). The miniband width  $\Delta_M$  is proportional to the overlap integral between neighbouring wells and so decreases rapidly with barrier thickness. The energy dispersion  $E_i(k_z)$  of electrons within the  $i$ th miniband can readily be calculated using techniques such as the Kronig–Penney model or, more accurately, using a  $\mathbf{k} \cdot \mathbf{p}$  calculation. The corresponding eigenstates are Bloch functions which, in a perfect SL and for small applied electric fields, would extend throughout the length  $L = Nd$  of the SL ( $N$  is the number of periods of length  $d$ ). However, in practice the extent of the eigenstates is limited to a coherence length determined by disorder. For thick barriers, where coupling between wells is weak,  $E_i(k_z)$  is harmonic with

$$E_i(k_z) = \frac{\Delta_M^i}{2} \left[ 1 - (-1)^i \cos(k_z d) \right] \quad i = 1, 2, \dots \quad (6.5)$$

where  $\Delta_M^i$  is the width of the  $i$ th miniband and varies very approximately as  $1/w^2$ .

The nature of the electron transport through the conduction band of an SL depends mainly on the relative sizes of six energies:  $\Delta_M^1$  (corresponding to  $i = 1$ ) which typically falls in the range  $\sim 0.1$  and 100 meV,  $E(k_z)$ , the energy difference  $\Delta = eFd$  between neighbouring wells produced by an electric field  $F$  parallel to the SL axis, the structural and dynamic broadening  $\hbar/\tau$  ( $\tau$  is the mean collision time) which is typically a few meV (6 meV for  $\tau = 0.1$  ps) though it varies with the quality of the SL and the temperature, the thermal broadening  $k_B T$  which increases from 0.1 to 25 meV over the range  $1 < T < 300$  K, and, in magnetic fields, the cyclotron energy,  $\hbar\omega_c$ , which for example is 17 meV for electrons in GaAs at  $B = 10$  T.

For small values of  $F$ , transport takes place through the minibands. This form of transport was first proposed by Esaki and Tsu and analysed using a semi-classical Drude model [1]. In the absence of scattering, the electrons would carry out Bloch oscillations

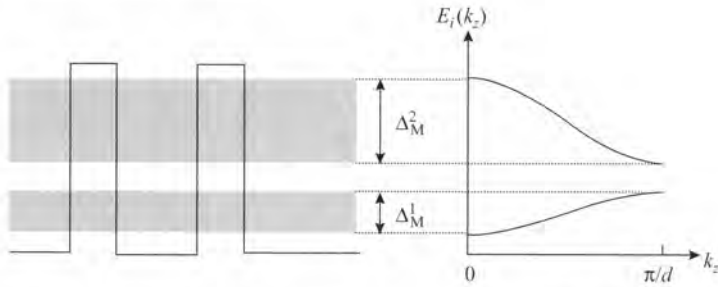


**Fig. 6.18** The miniband structure of an SL arising from the form of the dispersion curve  $E_i(k_z)$ .

of period  $\tau_B = \hbar/eFd$ . However, if the scattering rate  $\tau^{-1} > \tau_B^{-1}$ , the oscillations are suppressed and the electrons are accelerated up the miniband and so acquire a drift velocity. The resulting current  $I(V)$  increases with  $F$  but reaches a peak at a value of field  $F_c$  given by  $eF_c d = \hbar/\tau$  and then falls. The peak occurs when the electrons have an average value of  $\langle k_z \rangle \sim 1/d$ , close to the point of inflection in  $E_i(k_z)$  at  $\pi/2d$  at which the effective mass changes sign. Indeed this change in sign when  $F > F_c$  is the origin of the fall in electron drift velocity (NDC). Since the current is proportional to the scattering time, the conductivity is normally *reduced* by processes such as phonon scattering.

The first experimental demonstration of miniband transport was by Esaki and Chang [4] who measured the differential conductance of a doped SL with narrow barriers and hence wide minibands. Since then it has been studied extensively by both transport and optical techniques [118]. Overall it is found that the Esaki–Tsu model, which assumes a constant value for  $\tau$  and neglects the thermal broadening of the electron distribution, provides a good qualitative description of the transport process and a value for  $F_c$  in reasonable agreement with experiment. However, more precise descriptions can be obtained using the Boltzmann equation and including thermal broadening together with more realistic descriptions of the scattering processes. This work has been reviewed by Sibille [118] and we also note the work of Ignatov *et al.* [119] which distinguishes the rather different roles that elastic and inelastic (phonon) scattering can have on the drift velocity.

The electric field  $F$  tilts the minibands and, at higher fields, it is no longer possible for electrons to travel ballistically from one end of the SL to the other. Instead, the eigenstates become localized within a distance  $\lambda = \Delta_M/eF$  [1, 4] and this splits each miniband into a ladder of levels separated by  $eFd$  that are well defined if  $eFd > \hbar/\tau$  which corresponds to  $F > F_c$ . These ladder states, each centred on different wells, are known as Wannier–Stark (WS) states [120] and transport takes place by hopping between them [89]. If  $F$  is large, so that the localization length  $\sim d$ , hopping is essentially limited to states centred on neighbouring wells, but in lower fields it can also occur to wells further away. The hopping can be either by phonon-assisted tunnelling or by an elastic process involving impurity or disorder scattering with the subsequent emission of one or more phonons. The contribution by phonon-assisted tunnelling indicates that the electron–phonon interaction normally *increases* the conductivity in the WS regime in marked contrast to its effect on miniband transport.

The discussion so far assumes that the minibands are relatively wide and so well defined with  $\Delta_M \gtrsim \hbar/\tau$ . Somewhat surprisingly, though, the form of  $I(V)$  found experimentally at low fields remains qualitatively the same when the minibands become narrow with  $\Delta_M \lesssim \hbar/\tau$  [121]. In this regime, the electron scattering rate  $\tau^{-1}$  is greater than the coherent tunnelling rate so that miniband transport would not seem possible and indeed most of the states should be localized within the QWs for all values of  $F$ . It has been shown theoretically, however, that the current  $I(V)$  resulting from tunnelling between these localized states should still have a peak at  $eF_c d = \hbar/\tau$  followed by NDC [122]. Transport in this regime is referred to as sequential tunnelling as in the analogous case in RTDs where it has already been noted that the global coherent model and the sequential model lead to identical  $I(V)$  characteristics. It has been suggested, though, that disorder in the SL would result in a mobility edge in the minibands so that, even under these conditions, there could be a parallel conduction path due to extended states passing through parts of the SL through which miniband transport can still take place [123].

The discussion has also assumed that the electron density in the SL is too small to affect the nature of the transport. This is not always the case, however. Doping, or optical excitation or indeed charge flowing under bias from the emitter to the wells can all result in sufficient space charge to produce significant modifications in the transport properties particularly in weakly coupled SLs. These were first seen by Esaki and Chang [4] who observed that, in doped SLs, the single current peak followed by NDC seen in undoped SLs is now followed by a whole series of peaks. They attributed this to the formation and expansion of static electric field domains. At the first current peak, the system switches from a single domain throughout the SL in which the field is constant to two (or more) domains of significantly different field strength separated by a domain boundary which contains space charge to provide the field gradient. This is shown schematically in Fig. 6.19. Miniband transport occurs in the low field domain while, in the high-field domain, the potential energy drop between neighbouring wells is  $eFd \sim E_2 - E_1$  ( $E_1$  and  $E_2$  are the energies of the ground and first excited subbands in the well), close to the condition for resonant tunnelling. As the bias is increased, a peak occurs in the differential conductance as the tunnelling becomes resonant and this is followed by a nearly discontinuous fall, NDC. There is then an adjustment in the electric field distribution as the high-field domain suddenly expands by one period at the expense of the low-field domain to bring the field in the high-field domain back below resonance. The

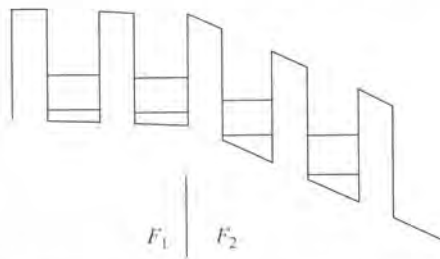


Fig. 6.19 The low-field and high-field domains in an SL containing space charge.

process is then repeated leading to the series of conductance peaks seen experimentally. At somewhat lower electron densities, however, the position of the domain boundary becomes unstable leading to oscillating currents,  $I = I(\omega_0 t)$ , so that the series of peaks in  $I(V)$  is replaced by a plateau in the time-averaged current. The period of the oscillations is equal to the time the domain boundary takes to travel the length of the SL and the corresponding frequency can vary over a wide range (a few MHz to  $\sim 100$  GHz) depending on the domain velocity and the SL length [124, 125]. The formation of high-field domains and their stability and time evolution, have been subjects of intensive study both theoretically and experimentally. This work has been reviewed by Grahn [124] and also reported in more recent papers [126, 127].

This introduction has focused on the properties of SLs of most relevance to studies of phonon-assisted tunnelling. However, ever since the pioneering work of Esaki and Tsu, SLs have provided a convenient laboratory in which a variety of techniques have been used to study a much wider range of static and dynamic phenomena. These studies include the very demanding and often contentious experiments carried out to demonstrate the existence of both Bloch oscillations and localization [128]. The properties of SLs also seem likely to result in a range of device applications although in most cases these are presently at an early stage of development. These include applications based on NDC such as oscillators based on the domain motion discussed above [129] and terahertz detectors [130, 131]. The highest frequency reported for oscillators to date is  $\sim 100$  GHz [125] but it is thought that it may be possible to extend this to frequencies approaching 1 THz. Optical devices include the quantum cascade laser [132, 133, 135, 136], now a working device, light modulators, and electrooptic devices based on WS localization (for a review see Agulló-Lopez *et al.* [138]). LO phonon emission leading to intersubband relaxation has a significant effect on optical device performance and phonon-assisted tunnelling is an essential element in the operation of the quantum cascade laser.

### 6.3.1 Phonon scattering in SLs

The effect of phonon scattering on transport in SLs was first considered theoretically in the 1970s [89, 139, 140] and has subsequently been studied intensively both theoretically and experimentally by many authors. As already noted, the electron-phonon interaction normally reduces the conductivity in the miniband transport regime and, at higher temperatures, if acoustic phonon scattering is dominant, the conductivity varies inversely with its scattering rate. So if as expected the main coupling is through the deformation potential, the scattering rate  $\propto T^2$  [139] and the conductivity  $\propto T^{-2}$ .

Optic phonon scattering can also have significant effects on miniband transport although, in zero magnetic field, scattering involving transitions within a miniband should only be possible in rather wide minibands for which  $\Delta_M > \hbar\omega_{LO}$  and this is supported by experiment [141]. It seems, however, that this constraint can be relaxed by a magnetic field applied parallel to the SL axis. The resulting localization of the in-plane motion effectively creates an array of 1D SLs. If now the separation of the LLs  $\hbar\omega_c < \Delta_M$ , electrons can obtain sufficient energy from the applied electric field to emit an LO phonon even if  $\Delta_M < \hbar\omega_{LO}$  as a result of being elastically scattered from one LL to the one above and so on [142]. Indeed in this case LO phonon emission assists the conduction process since, without the relaxation it provides, the electrons would

be unable to obtain significant average momentum along the axis. Eaves *et al.* [142] showed, however, that when the magnetic field was increased so that  $\hbar\omega_c > \Delta_M$  the conduction at low temperatures was strongly suppressed since it was no longer possible for electrons to be elastically scattered to the next LL. The details of the mechanism have been clarified by recent Monte Carlo simulations [143] although further experimental work in the region  $\hbar\omega_c \sim \Delta_M$  would evidently be of interest.

At higher temperatures, as  $k_B T$  approaches  $\hbar\omega_{LO}$ , magnetophonon oscillations are seen in the resistivity of SLs for magnetic fields  $\mathbf{B} \parallel \mathbf{I}$ . For example, the oscillations seen in a GaAs/AlGaAs SL at temperatures between 150 and 300 K are attributed to LO phonon scattering from the lowest LL to the next two:  $n\hbar\omega_c = \hbar\omega_{LO}$  ( $n = 1$  and  $2$ ) [144]. The oscillations are much more pronounced than in bulk material if  $\hbar\omega_c > \Delta_M$  because of the much smaller density of final states between the LLs.

### 6.3.2 LO phonon-assisted tunnelling in SLs

While the effect of LO phonon-assisted tunnelling can be seen directly in the  $I(V)$  characteristic of RTDs, this is not the case in SLs, although the process does contribute significantly to the transport current. It is also a critically important element in the operation of the quantum cascade laser (QCL) in which the emission wavelength is determined by the separation of quantum confined levels within the conduction band rather than by the bandgap as in conventional QW lasers [145]. The role of phonon-assisted tunnelling in QCLs is outlined below before a more general review of the tunnelling process is given.

Kazarinov and Suris first discussed the possibility of using SLs to amplify electromagnetic waves in 1971 [146] but the first successful QCL was not produced until 1994 by Faist *et al.* [132] following considerable experimental and theoretical endeavour. Faist *et al.*'s laser had 25 stages each consisting of an n-doped compositionally graded SL as injector plus a triple well active region built from heterojunctions of  $\text{Al}_{0.48}\text{In}_{0.52}\text{As}/\text{Ga}_{0.47}\text{In}_{0.53}\text{As}$ . The compositional grading is designed so that under the operating bias the conduction band in the SL is nearly flat. This results in efficient conduction, and injection into the first well, QW1, of the active region is very rapid. Figure 6.20 shows the band diagram of the first two stages. Electrons are injected into the ground state (labelled 3) of a narrow QW, QW1, make an assisted tunnelling transition into the ground state (labelled 2) of a wider well, QW2, and then to the ground state (labelled 1) of QW3 before tunnelling into the next SL. The energy separation of levels 3 and 2 is of energy  $E_3 - E_2 \gg \hbar\omega_{LO}$  so that LO-phonon-assisted transitions are to states of large  $\hbar k$  ( $E_3 - E_2 = 295$  meV in their device and  $\hbar\omega_{LO} \sim 34$  meV in GaInAs). Hence phonon-assisted tunnelling is only possible for LO phonons of large in-plane momentum so is relatively slow with  $\tau_{32} \sim 4.3$  ps and a radiative transition of energy  $E_3 - E_2$  occurs. The assisted tunnelling rate from level 2 to 1 is, however, much much faster with  $\tau_{21} \sim 0.6$  ps because  $E_2 - E_1 \sim \hbar\omega_{LO}$  and the tunnelling time out of state  $n = 1$  is even shorter ( $\lesssim 0.5$  ps). So population inversion occurs between levels 3 and 2. The emission of photons in the first active region by the (much slower) phonon-assisted process stimulates the emission of photons in the second leading to a cascade and hence to laser action which can be tailored to occur over a relatively broad spectral range.

Since their invention, QCLs have shown impressive improvements in device performance and now cover the range 3.4–70  $\mu\text{m}$ . Pulsed QCLs with a maximum power to date

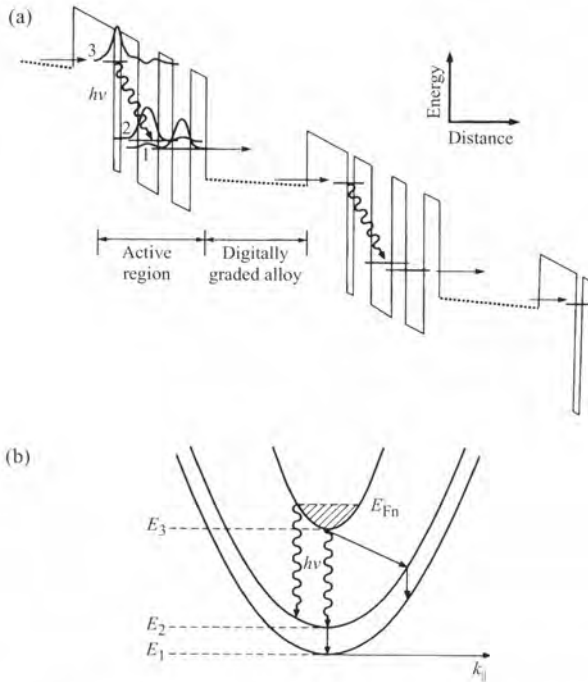


**Fig. 6.20** (a) Energy levels of a section of a quantum cascade laser: electrons are injected into level 3, make a radiative transition to level 2 followed by a LO phonon-assisted transition to level 1; (b)  $E(k_{\parallel})$ : radiative and phonon-assisted transitions are shown by wavy and straight arrows respectively [132].

of 0.6 W can operate at room temperature and indeed are the only room-temperature solid-state lasers operating in the range 5–11  $\mu\text{m}$ . Improvements in the performance of CW QCLs are equally impressive. Until recently, though, they had to be operated below room temperature but this is no longer the case [134] and room-temperature CW QCLs seem likely to be available commercially in the near future. Recent developments have been reviewed by Capasso *et al.* and Cartlidge [135–137] and include QCLs based on GaAs/AlGaAs heterostructures and also QCLs with an SL as the active region with the potential of generating much higher powers than conventional QCLs. Applications which could be extensive include astronomy, biomedical diagnostics, chemical sensing, high-resolution spectroscopy, medical imaging, and wireless communications.

The first detailed observations of phonon-assisted tunnelling were in magnetotransport measurements including work on magnetophotconductivity. These studies were on SLs with narrow minibands and, as already noted, were made by Higman *et al.* [11] and Müller *et al.* [12].

### 6.3.3 Experimental and theoretical investigations of LO phonon-assisted tunnelling in SLs

The effects of phonon-assisted tunnelling in SLs were first seen as magneto-oscillations ( $B \parallel I$ ) in the  $I(V)$  characteristics of a weakly coupled GaAs/AlGaAs SL at helium

temperatures [11]. The miniband width  $\Delta_M$  was small, 0.15 meV, so that transport occurs by hopping and, at  $B = 0$ ,  $I(V)$  has a peak when the first miniband in one well is aligned with the second in the neighbouring well ( $E_1 = E_2$ ). When  $B$  was increased at this bias, the current fell and then rose to broad peaks centred at  $\sim 8$  T and  $\sim 12$  T. In a magnetic field, the condition for assisted tunnelling is evidently

$$eFd = (n' - n)\hbar\omega_c + p\hbar\omega_{LO} \quad (6.6)$$

where the electric field  $F$  is measured from the value needed to bring  $E_1$  and  $E_2$  into coincidence. So the two peaks were tentatively attributed to optic phonon-assisted tunnelling between levels separated respectively by  $3\hbar\omega_c$  ( $n - n' = \Delta n = 3$ ,  $p = 1$ ) and  $2\hbar\omega_c$  ( $\Delta n = 2$ ,  $p = 1$ ), an energy of  $\sim 42$  meV. The authors suggested the tunnelling was due to an AIAs-like TO phonon. However, in the light of later work, it seems more likely to have been an LO phonon either GaAs-like or AIAs-like of energy  $\sim 36$  or 50 meV respectively.

Müller *et al.* [12] obtained very detailed information of this process by measuring the photocurrent  $I(V)$  in a weakly coupled SL ( $N = 40$ ). Bias could be applied between highly doped regions either end of the SL and, by doping one  $p^+$  and the other  $n^+$ , reverse bias could be used to ensure that very little current flowed in the absence of optical excitation. This technique ensures that there are equal numbers of electrons and holes in the SL and so reduces the broadening that results from the non-uniform electric fields that are present if there is an excess of one type of carrier. It also allows time-dependent measurements and so studies of the electron dynamics to be made although the work described here concerns the peak values of the current. Four resonances were seen in  $I(V)$  at  $B = 0$  (Fig. 6.21(a)), two attributed to resonant tunnelling (between

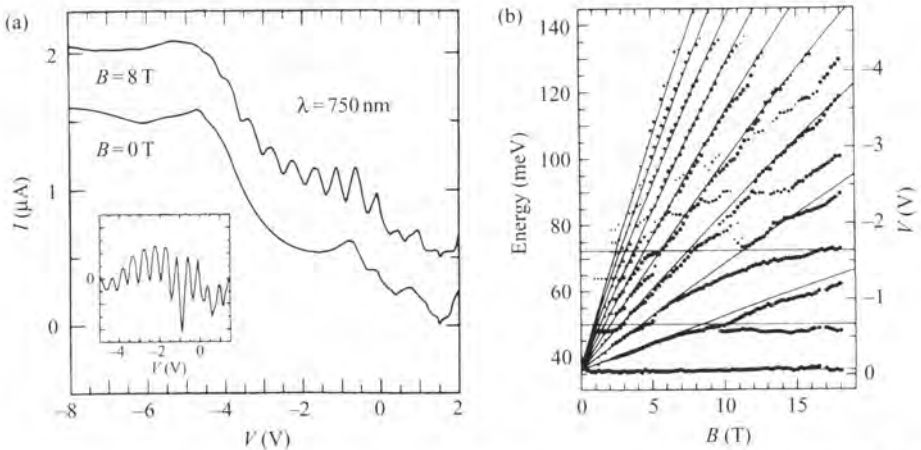


**Fig. 6.21** Oscillatory structure in the photocurrent  $I(V)$  through an SL in magnetic fields  $B \parallel I$  [12]. (a)  $I(V)$  at  $B = 0$  and 8 T (the curves are displaced by  $0.5 \mu\text{A}$ ). The additional structure at 8 T is emphasized in the inset which shows the difference between the two curves. (b) Fan diagram showing the position of the peaks as a function of  $B$ .

the first and second minibands of both the conduction and valence bands) and two to assisted tunnelling involving GaAs-like LO phonons. Application of magnetic fields resulted in a large number of additional oscillations, whose period agreed well with the cyclotron energy. Some of the observed transitions were attributable to elastic transitions ( $p = 0$ ) and others to LO phonon-assisted tunnelling ( $p = 1$ ) with values of  $\Delta n$  from 0 to 9 as shown in the fan diagrams in Fig. 6.21(b). Transitions involving the emission of two LO phonons ( $p = 2$ ) or a zone-folded acoustic phonon [147] were also observed. The results could be explained quantitatively if allowance were made for both the non-parabolicity of the conduction band and the magnetopolaron effects that are apparent in the figure.

As the temperature is raised, the contribution of LO phonon-assisted tunnelling to  $I(V)$  should increase once  $k_B T \gtrsim \hbar\omega_{LO}$  because of the increasing importance of both stimulated emission and absorption. However, resonant tunnelling from excited minibands could also start to become significant and, to study the relative importance of these two effects, Müller *et al.* [148] made  $I(V)$  measurements of the photocurrent in two GaAs/AlAs SLs at temperatures up to 300 K. The SLs had the same barrier width but the wells were of different thickness with energy separations between the two lowest minibands of samples A and B of 96 and 40 meV respectively. As the temperature was raised, the assisted peaks in sample A increased in size relative to the resonant tunnelling peaks and no further peaks appeared. It seems clear therefore that these are phonon-assisted transitions  $E_1 \rightarrow E_i + \hbar\omega_{LO}$  ( $i = 1, 2, 3$ ). Similar peaks were also observed in sample B but, in this case, new peaks appeared when  $T \gtrsim 120$  K, one even becoming larger than the nearby resonant  $E_1 = E_2$  peak and another lying close to a phonon-assisted peak. The relative size of these two types of peak evidently depends on the ratio of the excitation energy of the first excited miniband to  $\hbar\omega_{LO}$  and, since the excitation energy is much lower in sample B, it seems likely that these new peaks are due to resonant transitions from the first excited miniband (thermally induced resonant transitions) rather than to phonon-assisted transitions.

For wide minibands and in zero magnetic field, phonon-assisted tunnelling only becomes significant at higher electric fields  $F$  when hopping in the WS regime replaces miniband conduction. Since transitions might now take place to wells some distance away, a general expression for the energy of the  $n$ th LL of the lowest subband in the  $\nu$ th well can be written

$$E_{n,\nu} = \nu e F d + \left(n + \frac{1}{2}\right) \hbar\omega_c + E_1 \quad (6.7)$$

where  $\nu = 0, \pm 1, \pm 2, \dots$  is the WS or well index and  $E_1$  is the energy of the lowest subband for  $\nu = 0$ . So the condition for elastic transitions is now  $\Delta \nu e F d = \Delta n \hbar\omega_c$  and this becomes  $\Delta \nu e F d = \Delta n \hbar\omega_c + p \hbar\omega_{LO}$  for LO phonon-assisted tunnelling. These are known as Stark–cyclotron resonances (SCRs) and Stark–cyclotron–phonon resonances (SCPRs) respectively and both have been investigated theoretically in some detail including the effect of terahertz irradiation [149–152]. The first observation of SCRs was in a GaAs/AlGaAs structure with  $\Delta_M = 23$  meV: a series of peaks in  $I(V)$  occurred at bias values corresponding to  $\Delta \nu = 1$  and  $\Delta n = 1$  to 4 [153] but SCR transitions up to  $\Delta \nu = 4$  have since been reported in a GaAs/AlAs structure with  $\Delta_M = 8$  meV demonstrating that significant hopping is occurring to wells up to 40 nm

away [154]. Lyanda-Geller and Leburton [155] reanalysed the data of Canali *et al.* and showed that for  $\Delta n = 3$  the peaks deviated from a linear dependence on  $F$  by an amount which oscillated with  $F$  and attributed this to the effect of anti-resonances in the intrawell acoustic phonon scattering as a result of Bragg reflection [114]. This will be discussed further in Section 6.3.4. As already noted, a range of SPCR transitions ( $\Delta v = 1$ , with  $p = 1$ ,  $\Delta n = 1$  to 9) have been seen in narrow miniband SLs [12] but not, however, in wide minibands (the broad peak seen by Nogaret *et al.* in the structure with  $\Delta_M = 8$  meV was attributed to a  $\Delta v = 1$  LO phonon-assisted transition ( $p = 1$ ) but was between states with the same LL index ( $\Delta n = 0$ )) [154]. The absence of SPCR transitions in wide miniband SLs might be the result of elastic scattering which has been shown theoretically to dampen the phonon resonances [152] although it is not clear why the effects of this should be greater than in narrow miniband SLs. It seems more likely to be because of the large values of  $eFd$  required for the  $\Delta n > 0$  transitions. These would result in strong WS localization and hence weaken the overlap between neighbouring WS states.

#### 6.3.4 Acoustic phonon-assisted tunnelling in SLs

The first experimental observations of acoustic phonon-assisted tunnelling in SLs was by Cavill *et al.* [10, 14] but the first theoretical work in this area was published nearly 25 years earlier by Tsu and Döhler [89].

#### 6.3.5 Experimental investigations of acoustic phonon-assisted tunnelling in SLs

The approach is similar to that for RTDs although two complementary techniques were used. In one, a  $50 \times 500 \mu\text{m}^2$  constantan film evaporated onto the substrate is heated electrically with 50–100 ns pulses while in the other, which provided better time and hence mode resolution, a  $50 \mu\text{m}$  diameter area of an extended film is heated by a 12 ns focused laser pulse [14]. The well and barrier widths of the 50 period GaAs/AlAs SLs were respectively 5.9 and 3.9 nm, the latter chosen to provide weak coupling with  $\Delta \sim 0.7$  meV [156] and the layers were etched down to a  $100 \mu\text{m}$  diameter mesa. The structure was uniformly doped with Si to  $2 \times 10^{16} \text{cm}^{-3}$  corresponding to  $E_F \sim 0.3$  meV in the wells although this is expected to increase under bias because of charge injection from the  $n^+$  contacts as discussed earlier. These were of very different size, the lower being an extended layer while the upper had the diameter of the mesa. The current  $I(V)$  starts at a threshold bias,  $V_0^{(1)} \sim 50$  mV, and becomes asymmetric with peaks at  $V_c = -275$  and  $+700$  mV. This suggests that some of the bias is being dropped across part of the SL although the reason for this is not understood. The existence of a series of peaks in  $I(V)$  for  $V < 0$  but not  $V > 0$  shows that stable domain formation is not possible when  $V > 0$  but is when  $V < 0$ . This indicates that  $E_F$  is larger under bias for  $V < 0$  as might be expected since the electron injection is from a contact of much greater area [124].

Figure 6.22 also shows  $\Delta I(V)$  for the two bias directions. For  $V > 0$ , the phonons were generated using an electrically heated film and for  $V < 0$ , using an optically

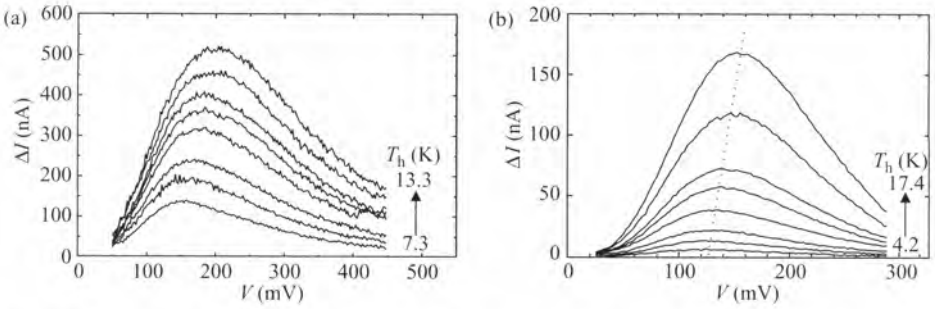


**Fig. 6.22**  $\Delta I(V)$  for an SL produced by TA phonons for (a)  $V > 0$  and (b)  $V < 0$ . The phonons were from electrically and optically heated films respectively [14].

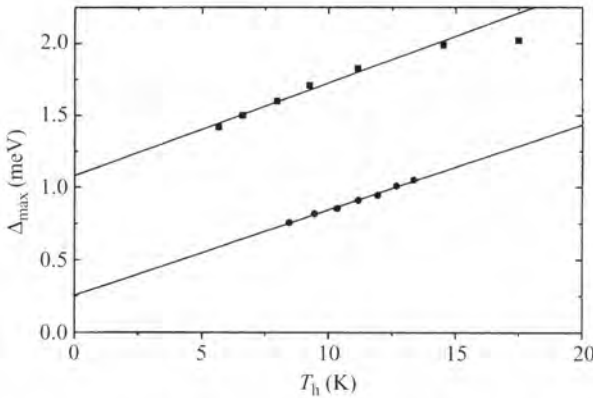


**Fig. 6.23**  $\Delta_{\max}(T_h)$  for  $V > 0$  and  $V < 0$ . The slopes are the same to within experimental accuracy but the intercepts differ appreciably [14].

heated film; the differences in size of  $\Delta I(V)$  is attributed largely to the different areas of the two films. Figure 6.23 shows the corresponding plots of  $\Delta_{\max}(T_h)$  where  $\Delta = \alpha(V - V_0^{(1)})/50$  is the energy drop between neighbouring wells and  $\Delta_{\max}$  is its value at the peak of  $\Delta I(V)$ .  $\alpha = 1$  for  $V < 0$  but 0.35 for  $V > 0$  to allow for the potential drop across part of the SL. The slope of  $\Delta_{\max}(T_h)$  is  $0.7k_B$  for both directions but the intercepts are very different: 0.25 meV for  $V < 0$  and 1.1 meV for  $V > 0$ , and possible reasons for this are discussed later. Cavill *et al.* [14] argued that, for phonons incident normally and if  $q_z$ -dependent factors associated with the periodicity of the SL structure are neglected, the transition probability for stimulated phonon emission should  $\propto q^3 N_q$  as in RTDs leading to  $\Delta I(V) \propto \omega_q^3 N_q$ , where  $\hbar\omega_q = \Delta$ , which has a maximum at  $\Delta_{\max} \approx 2.8k_B T_h$ , appreciably greater than the value of  $0.7k_B T_h$  found experimentally.

The linear dependence of  $\Delta_{\max}$  on the dominant phonon frequency shows that the SL device acts as a spectrometer and Cavill *et al.* confirmed this using the time-delayed phonons in the heat pulse as a source of phonons of higher frequency than those arriving

ballistically (the scattering that delays the phonons increases strongly with frequency). They were not, however, able to measure the spectral halfwidth although it is evidently no larger than that of the source and so  $\leq k_B T_h$ . These measurements were made using phonons generated by laser heating and, by moving the laser spot away from the point opposite the SL, they were also able to investigate how the signals varied with the incident angle of the phonons. Their measurements were made with relatively low-frequency phonons ( $\nu_{\max} \sim 450$  GHz) which should mostly travel ballistically through the substrate. They found that the signal fell in size as  $\theta$  increased and this could be explained by the fall in intensity due to the decreasing proportion of phonons incident on the device. However, they were unable to explain why  $V_{\max}$  remained approximately constant. They also demonstrated that the form of  $I(V)$  in a magnetic field of 6.5 T was similar to that in zero field.

Cavill *et al.* suggested that the surprisingly large signal they observed,  $\Delta I/I \sim 0.03$  for phonons from the laser heater at  $T_h \sim 13$  K, could be evidence for phonon amplification. They argued that, since stimulated phonon emission is likely to provide the dominant contribution to  $\Delta I$ , and since phonons from the heater pass through 100 wells (50 before reflection at the top surface and 50 after), amplification could be significant. They also noted that Glavin *et al.* [157, 158] had shown that competing loss mechanisms should be weak at low temperatures. They obtained an upper limit to  $\Delta I/I$  if no amplification occurred by estimating  $\Delta I/I_{\text{sp}}$  where  $I_{\text{sp}}$  is the contribution to  $I$  from spontaneous phonon emission, the dominant process of phonon-assisted current when no phonons are incident from the heater.  $\Delta I$  is the additional current resulting from stimulated emission by the phonons from the heater so  $\Delta I/I_{\text{sp}}$  should approximately equal  $N^*(T_h)/1$  where  $N^*(T_h)$  is the occupation number of phonons from the heater at the peak of their energy distribution. Now stimulated and spontaneous emission transitions follow the same selection rules and their calculations suggest that they are both only possible for emission angles  $\theta \lesssim 25$  degrees. This is in fact larger than the range of angles  $\theta \lesssim 5$  degrees ( $\tan \theta \lesssim 25/400$ ) at which phonons from the optically heated film would arrive if they were emitted isotropically and travelled ballistically from a point on the heater. However, the strong focusing of the TA phonons into directions close to the [001] direction increases the intensity by  $\sim 20$  and this increases  $\theta$  from 5 degrees to  $\sim 25$  degrees showing that approximately all allowed transitions can be stimulated by phonons from the heater. So from this they conclude that  $\Delta I/I_{\text{sp}} \sim N_q(T_h)/1 = 0.06$  for a heater at 13 K. This does not allow for the scattering in the substrate of the higher frequency phonons from the heater which they estimate approximately halves the intensity of ballistic phonons and, when this is included, their estimate for the change in current becomes  $\Delta I/I_{\text{sp}} \sim N_q(T_h)/2 = 0.03$ . Now the total current  $I$  contains contributions from spontaneous emission due to TA and LA modes plus that from elastic scattering and, making the usual assumption that the elastic contribution is dominant, they conclude that  $\Delta I/I \ll 0.03$ . The change  $\Delta I/I \sim 0.03$  seen experimentally therefore might suggest that phonon amplification is occurring. Phonon amplification has been observed in a number of other systems, most recently in optically pumped magnetic ions in dielectrics for phonon frequencies  $\nu < 100$  GHz [159] and in two-level systems in glasses for  $\nu < 1$  GHz [160], but has not apparently previously been seen above 100 GHz. Discussion of this earlier work is included in a popular review by Watson [161].

### 6.3.6 Theoretical investigations of the effect of acoustic phonon-assisted tunnelling on transport in SLs

The first theoretical treatment of the effect of acoustic phonons on hopping transport between the WS states of the lowest miniband was made by Tsu and Döhler [89] and is outlined below (we also note recent work by Rott *et al.* [162]). The current,  $I_{\nu\nu'}$ , due to an electron in well  $\nu$  making a transition to well  $\nu'$  as a result of phonon emission or absorption is given as

$$I_{\nu\nu'} = eA \sum_{k,k'} d(\nu' - \nu) [f_k(1 - f_{k'})W_{\nu\nu'} - f_{k'}(1 - f_k)W_{\nu'\nu}] \quad (6.8)$$

where  $\mathbf{k}$  and  $\mathbf{k}'$  are the in-plane components of the electron wavevectors in the two wells,  $W_{\nu\nu'} = W_{\nu\nu'}^+ + W_{\nu\nu'}^-$  is the transition rate between the two states due to a phonon  $\mathbf{q}$  (+/- refers to emission/absorption), and  $\nu' - \nu = 1, 2, 3, \dots$ . Since the intrawell scattering rate is much faster than the tunnelling rate, the Fermi functions  $f_k$  and  $f_{k'}$  are those for the lattice temperature,  $T$ , to a good approximation. Now  $W_{\nu\nu'} = W_{\nu'\nu} \exp[-\beta(\nu' - \nu)eFd]$ , where  $\beta = 1/k_B T$  so that Eq. 6.8 can be written

$$I_{\nu\nu'} = eA \sum_{k,k'} d(\nu' - \nu) f_k(1 - f_{k'}) W_{\nu\nu'}^\pm \{1 - \exp[-\beta(\nu' - \nu)eFd]\}. \quad (6.9)$$

For deformation potential coupling:

$$W_{\nu\nu'}^\pm = \frac{2\pi}{\hbar} C^2(q) \sum_{\mathbf{q}} |\langle \psi' | \exp(i\mathbf{q} \cdot \mathbf{r}) | \psi \rangle|^2 \left( N_{\mathbf{q}} + \frac{1}{2} \pm \frac{1}{2} \right) \times \delta(E_{\nu'}(\mathbf{k}') - E_{\nu}(\mathbf{k}) \mp \hbar\omega_{\mathbf{q}}) \quad (6.10)$$

where  $C(q) = i\Xi(\hbar q/2\rho\Omega_s)^{1/2}$ ,  $\Xi$  is the deformation potential energy, and  $|\psi\rangle = |\nu, \mathbf{k}\rangle$ . Using electron wave functions which allow for the periodicity of the SL but not that of the bulk semiconductor they obtain, for transitions between ground states

$$\langle \psi' | \exp(i\mathbf{q} \cdot \mathbf{r}) | \psi \rangle \sim J_{\nu-\nu'} \left( \frac{\Delta_M}{eFd} \sin \frac{q_z d}{2} \right) \frac{\sin\left(\frac{1}{2}q_z w\right)}{\frac{1}{2}q_z w} \times \frac{1}{1 - (q_z w/2\pi)^2} \times \delta_{\mathbf{k}', \mathbf{k} \pm \mathbf{q}_{\parallel}} \quad (6.11)$$

where  $q_z$  is the  $z$ -component of the phonon wavevector,  $w$  is the width of the quantum well,  $J_k$  is the Bessel function of order  $k$ , and  $\delta_{\mathbf{k}', \mathbf{k} \pm \mathbf{q}_{\parallel}}$  requires  $q_{\parallel}^2 = k'^2 + k^2 - 2kk' \cos \beta$  where  $\beta$  is the angle between  $\mathbf{k}$  and  $\mathbf{q}$ ; the miniband width,  $\epsilon_1$  in their notation, has been replaced by  $\Delta_M$ .

At low fields, the WS states may extend over several wells so that hopping can occur between wells some distance apart. However, at higher fields, or at all fields if the barriers are sufficiently thick, hopping is dominated by nearest neighbour transitions leading to a two-well model,  $\nu' - \nu = 1$  and so  $(\nu' - \nu)eFd = (\hbar^2/2m_e^*)(k^2 - k'^2) \mp \hbar\omega_{\mathbf{q}}$ . So in

this limit, and assuming the uncoupled well states are those for infinite barrier height, they obtain

$$M(q) = \langle \psi' | \exp(iq_z z) | \psi \rangle \sim \left( \frac{\alpha}{\Delta} \right) \sin \left( \frac{q_z d}{2} \right) \frac{\sin \left( \frac{1}{2} q_z w \right)}{\frac{1}{2} q_z w} \times \frac{1}{1 - (q_z w / 2\pi)^2} \quad (6.12)$$

where  $\alpha$  is the coupling between the wells and  $\Delta = eFd$ . For large electric fields,  $\Delta \gg \Delta_M$ , Eq. (6.11) becomes identical to (6.12), if  $\Delta_M$  is replaced by  $2\alpha$ , since  $J_1(\delta) \sim \frac{1}{2}\delta$  for  $\delta \rightarrow 0$ . This can be seen in the calculated values shown in Fig. 6.24 which also shows that the current falls quite rapidly at high fields. Differences in the currents calculated from the two models appear at low fields,  $eFd = \Delta < \Delta_M$ . The electron wave functions now extend over several wells and it is interesting that for the same value of  $F$  the current from next nearest neighbour hopping is in fact greater at low fields than that from nearest neighbour hopping (curves 2 and 1 respectively in Fig. 6.24). The phonons involved in the assisted tunnelling in next nearest neighbour hopping evidently have twice the energy ( $2\Delta$ ) of those involved in nearest neighbour hopping so the larger current can presumably be attributed to the larger density of phonon modes and electron-phonon coupling at these energies. This would suggest that the contribution to the current from further wells should also be considered although of course only at the lower fields.

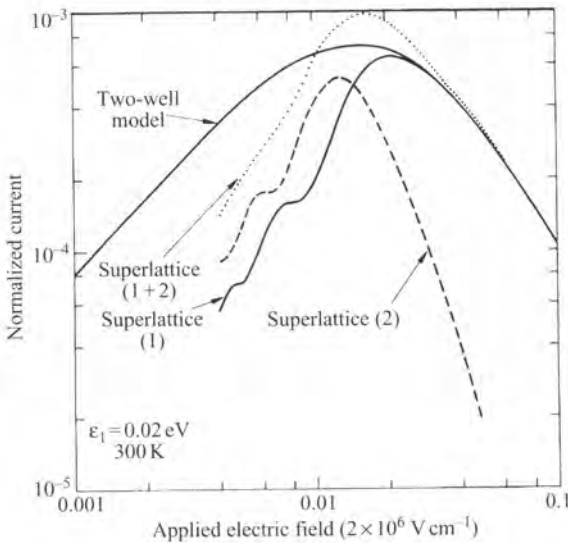


**Fig. 6.24** Calculated values of the normalized current  $I(F)$  through an SL due to acoustic phonon-assisted tunnelling as a function of electric field  $F$ : (1) nearest neighbour transitions,  $I_1$ ; (2) next-nearest neighbour transitions  $I_2$ . The dotted curve shows  $I_1 + I_2$  and the solid curve shows  $I(F)$  calculated using the two-well model. The actual current is  $AI(F)$  where  $A$  is temperature dependent [89].

It can also be seen that the nearest neighbour and next nearest neighbour currents both oscillate, though with different wavelengths. This is evidently associated with the fact that the Bessel functions  $J_1(x)$  and  $J_2(x)$  are oscillatory functions and these oscillations persist when  $J_1^2(x)$  and  $J_2^2(x)$  are averaged over all  $q_z$ . However, the oscillations in the total current are very much smaller because the two sets of oscillations partially cancel.

Before discussing further work in this area we consider the dependence of the transition probability  $W \propto |\langle \psi' | \exp(iq_z z) | \psi \rangle|^2$  on  $q_z$ . It can be seen from Eq. (6.12) that  $W$  oscillates and is 0 (anti-resonant) for  $q_z = 0, 2l\pi/d$  ( $l = 1, 2, 3, \dots$ ) and  $2l\pi/w$  ( $l = 2, 3, 4, \dots$  but not  $l = 1$ ). However, since it also falls as  $q_z^{-4}$  when  $q_z > 2\pi/w$ , the higher anti-resonances will probably be difficult to observe. The anti-resonance at  $q_z = 0$  occurs because  $|\psi\rangle$  and  $|\psi'\rangle$  are orthogonal and that at  $q_z = 2l\pi/d$  would arise from phonon Bragg reflection by the SL causing them to be equivalent to phonons with  $q_z = 0$  (zone folding). This can only be the correct explanation, though, if there are differences in the acoustic properties of the barrier and the well. This was not assumed in Tsu and Döhler's model and in this case  $W$  vanishes at  $q_z = 2l\pi/d$  because of electron Bragg scattering [114, 155]: by zone folding one of the  $k$  vectors, the matrix element for  $q_z = 2l\pi/d$  becomes identical to that for  $q_z = 0$ . The reason for the anti-resonances at  $q_z = 2l\pi/w$  ( $l = 2, 3, 4, \dots$ ) is apparent from a comparison of the phonon waveforms at these values with the ground state electron wave function of wavelength  $w$ . It can be seen that the interactions from the positive and negative phonon displacements will cancel at these values of  $q_z$ . (This also happens at  $q_z = 2\pi/w$  but is offset by the resonance in the interaction when the phonon wavelength matches the wavelength  $w$  of  $\sin^2(\frac{1}{2}q_z w)$ .) Colvard *et al.* [147] pointed out some years ago that, if the acoustic properties of the barrier and well are different, anti-resonances should also occur at  $q_z = l\pi/d$  for the (001) direction when the phonon energies  $\hbar\omega_q$  lie in the gap of the spectrum of the zone-folded acoustic phonons. However, the effect of these relatively narrow gap widths should usually be much less than those associated with Bragg reflection [163] so could be difficult to detect experimentally.

None of these anti-resonances is apparent in the curves shown in Fig. 6.24. This is to be expected at  $q_z = l\pi/d$  since the acoustic properties were assumed to be uniform and the reason the others are too small to be seen is presumably because the phonons of wavenumber  $q$  are emitted at all angles corresponding to a wide range of  $q_z$ . This is not the case in magnetic fields, however, as was pointed out by Lyanda-Geller and Leburton [114]. These two authors extended Tsu and Döhler's work for the two-well model to the case where magnetic fields are applied parallel to the SL axis leading to quasi-1D SLs (called 'quantum box' SLs by Lyanda-Geller and Leburton). In an electric field  $F$ , the probability of phonon-assisted tunnelling between the partially filled ground state LLs in neighbouring wells was shown to be proportional to

$$|\langle \psi' | \exp(i\mathbf{q} \cdot \mathbf{r}) | \psi \rangle|^2 = V_q^2 F_{11}(\mathbf{q}_{\parallel}) J_1^2 \left( \frac{\Delta_M}{\Delta} \sin \frac{q_z d}{2} \right) \quad (6.13)$$

where  $F_{11}(\mathbf{q}_{\parallel}) = |\langle n = 0 | \exp(i\mathbf{q}_{\parallel} \cdot \mathbf{r}_{\parallel}) | n = 0 \rangle|^2 \propto \exp(-q_{\parallel}^2 l_B^2)$ ,  $l_B$  is the magnetic length, and, as before  $J_1(\Delta_M/\Delta) \sim \Delta_M/2\Delta$  when  $\Delta \gg \Delta_M$  (their miniband width  $4\Delta$  becomes  $\Delta_M$  in the present notation). Energy conservation requires  $\hbar\omega_q = \Delta$  and so  $q = \Delta/\hbar s$  and the form of  $F_{11}(\mathbf{q}_{\parallel})$  shows that the probability of phonon-assisted

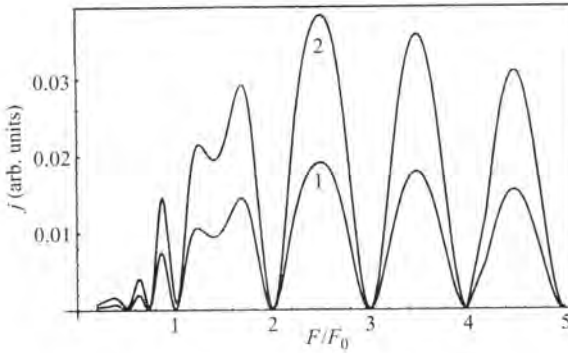


**Fig. 6.25** Calculated values of the current  $I(F/F_0)$  produced by LO phonon-assisted tunnelling in a quasi-1D SL (quantum box) for  $F_0 = 2.17 \times 10^5 \text{ V m}^{-1}$  and (1)  $B = 6 \text{ T}$  and (2)  $12 \text{ T}$  [114].

transitions is only significant for  $q_{\parallel} \lesssim l_B^{-1}$ . So, if  $\Delta/\hbar s \gg l_B^{-1}$  or  $\Delta^2 \gg \hbar\omega_c m_e^* s^2$ , the phonons are emitted at angles close to the normal to the SL with  $q_z \sim q \sim \Delta/\hbar s$ . The values of  $F$  needed to satisfy this condition for magnetic fields normally available are readily achievable. However, the condition that the system is strongly magnetically quantized and hence that  $\hbar\omega_c$  is large compared with other linewidths such as that from inhomogeneous broadening may be more demanding.

This analysis indicates that, as in zero field,  $I(V)$  should oscillate with anti-resonances at  $q_z \sim \Delta/\hbar s = 2n\pi/d$  and we recall that a similar result was found in TBRTDs [113]. In SLs, these anti-resonances occur at fields  $F = nF_0$  where  $F_0 = 2\pi\hbar s/ed^2$  (Fig. 6.25) although would be damped by disorder or if hopping to next nearest neighbours is significant. Recent evidence for their existence appeared to have been obtained by Nogaret *et al.* [163] in the  $I(V)$  characteristics of three GaAs/AlAs SLs. Two of the SLs had the same period  $d_1 = 10.6 \text{ nm}$  but different barrier-to-width ratios while the third had a different period  $d_2 = 17.3 \text{ nm}$ . Measurements were made in the WS regime and in magnetic fields up to 23 T applied parallel to the current and at higher fields they observed a series of well-defined oscillations whose periods (separations in voltage) were independent of  $B$  but scaled with  $1/d$ . The positions of the minima were broadly consistent with those arising from electron Bragg reflection as discussed earlier and were used to obtain data in quite good agreement with the LA phonon dispersion curve for GaAs suggesting that the hopping was by LA phonon-assisted tunnelling as expected. However, the authors have since revised this interpretation since it is not supported by their more recent data on SL structures with a wider range of  $d$ . They suggest the effects that are seen may be related to charge build-up in successive QWs, that is to the formation of static domains [164].

### 6.3.7 Theoretical investigations of the effect of non-equilibrium acoustic phonons on transport in SLs

The first theoretical treatment of phonon-assisted tunnelling in an SL was by Glavin *et al.* [158] for LA modes and is an extension of the two-well model [89] to the situation where the incident phonons have a temperature  $T_h$  higher than that of the electrons  $T$ .

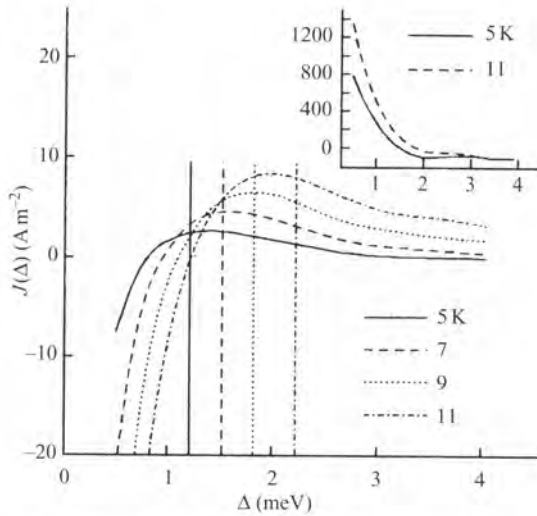


**Fig. 6.26** The current density response  $\Delta J(\Delta)$  to LA phonons calculated for an SL for a range of heater temperatures  $T_h$ . The inset shows  $\Delta J_s(\Delta)$  due to electron heating [158].

Glavin *et al.* also calculate the change in current  $\Delta I_s(V)$  associated with the tunnel current  $I_s(V)$  that arises from elastic scattering followed by phonon emission.  $\Delta I_s(V)$  is caused by an increase in electron temperature resulting from the absorption of non-equilibrium phonons (electron heating) and is device dependent since its size is evidently proportional to  $I_s(V)$  and so the electron scattering rate. They also point out that, since electron heating is relatively weak for phonons incident at angles  $\theta \lesssim s/v_F$  ( $v_F$  is the Fermi velocity), the relative importance of this process,  $\Delta I_s(V)/\Delta I(V)$ , depends on the angular distribution of the phonons. Glavin *et al.* found that  $\Delta I_s$  falls steadily with increasing bias, Fig. 6.26, in line with the decrease in  $I_s(V)$  and eventually becomes negative, presumably reflecting the fact that a rise in electron temperature increases the average value of the difference in  $\mathbf{k}$  between the initial and final states of the tunnelling transition. The sign and form of the calculated value of  $\Delta I_s(V)$  is very different from that observed experimentally and suggests the contribution to  $\Delta I(V)$  from electron heating is small in these devices compared with that by phonon-assisted tunnelling.

The summations over  $\mathbf{q}$  and  $\mathbf{k}, \mathbf{k}'$  in the calculation of the current due to phonon-assisted tunnelling can be done in either order and Glavin *et al.* in fact use the opposite order to Tsu and Döhler. So they write the transient change in current  $\Delta I$  due to phonon-assisted tunnelling as

$$\Delta I = eA \sum_{\mathbf{q}} W(\mathbf{q}) N_{\mathbf{q}}^*(T_h) \quad (6.14)$$

where the transition probability,  $W(\mathbf{q}) = W_+^+ + W_-^- - W_+^- - W_-^+$ , is the sum of the probabilities of the four possible stimulated emission and absorption processes shown in Fig. 6.27 (spontaneous emission is omitted since this is not affected by the incident phonons); the superscript  $+/-$  again indicates emission/absorption and the subscript, the direction of the electron current with respect to the bias. Since only a proportion

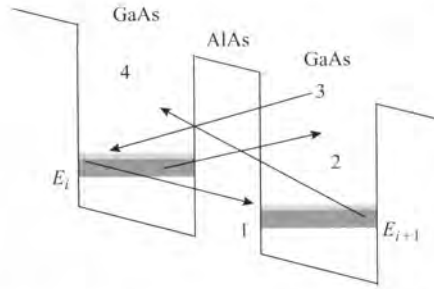


**Fig. 6.27** The four phonon-assisted tunnelling processes between the neighbouring wells of an SL [14].

of the phonons from the heater are incident on the device, Cavill *et al.* [14] write the occupation number as  $N_q^* = a N_q$  where  $a < 1$ . For simplicity,  $a$  is assumed to be constant, so its introduction only reduces the size of  $\Delta I$  from that given by Glavin *et al.* and not its form. (They also write a term  $N_q^*(T_h) - N_q^*(T)$  in place of  $N_q^*(T_h)$  to make  $\Delta I = 0$  when  $T_h = T$  but later omit  $N_q^*(T)$  since it has little effect on  $\Delta I$ .)

$$W(\mathbf{q}) = \frac{2\pi}{\hbar} C^2(q) |M(q_z)|^2 \sum_{\mathbf{k}, \mathbf{k}'} \delta_{\mathbf{k}, \mathbf{k}' \mp \mathbf{q}_{\parallel}} \times \delta(E_{\mathbf{k}} - E_{\mathbf{k}'} \mp \hbar\omega_q) \times f_{\mathbf{k}}(1 - f_{\mathbf{k}'}). \quad (6.15)$$

$\psi, \psi'$  and  $\mathbf{k}, \mathbf{k}'$  are respectively the electron wave functions and in-plane wavevector components of the initial and final states in the two neighbouring wells involved in the tunnelling and  $M(q_z)$  is given in Eq. (6.12).

For phonons incident at angles  $\theta \leq \theta_{\max}$ , the change in current is the sum of the changes due to the two emission and two absorption terms and each can be written

$$\Delta I(\Delta) = KA \int_0^{\theta_{\max}} \int_0^{\infty} \int_{E_m}^{\infty} \frac{|M(q \cos \theta)|^2 q^2 N_q(T_h) f(E)(1 - f(E \mp \hbar\omega_q \pm \Delta))}{(E - E_m)^{1/2}} d\theta dq dE \quad (6.16)$$

where the signs before  $\hbar\omega_q$  and  $\Delta$  are respectively the reverse of and equal to those of the superscript and subscript of the particular term in  $W(q)$ ,

$$K = \frac{ea \Xi_d^2 m_e^{*3/2}}{8\pi^4 2^{1/2} \hbar^3 \rho_s}$$

and  $E_m$  is the minimum value of  $E$  for which tunnelling is possible for phonons  $q$  incident at angle  $\theta$ . For a particular value of  $\Delta$ , conservation of energy and in-plane momentum determines the two values of  $k \cos \beta$  that can interact with a phonon  $q$  incident at angle  $\theta$ :

$$k \cos \beta = \frac{m^*}{\hbar^2 q_{\parallel}} \left( \frac{\hbar^2 q_{\parallel}^2}{2m^*} \pm \hbar\omega_q \mp \Delta \right) \quad (6.17)$$

where  $\beta$  is the angle between  $\mathbf{k}$  and  $\mathbf{q}_{\parallel}$ . In this case, the signs before  $\hbar\omega_q$  and  $\Delta$  are respectively equal to and the reverse of those of the superscript and subscript of

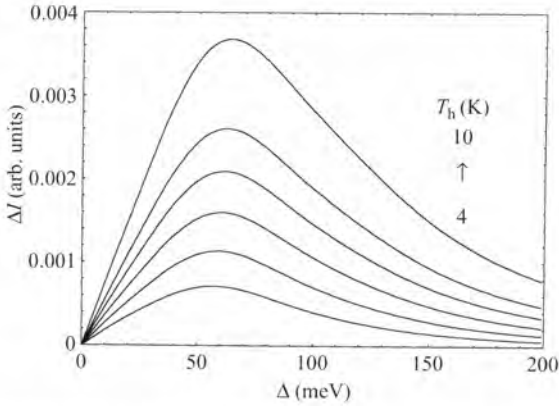


**Fig. 6.28** The current response  $\Delta I(\Delta)$  to TA phonons calculated for an SL for a range of heater temperatures  $T_h$  and for  $E_F$  values of (a) 0.3 and (b) 1.0 meV [14].

the particular term in  $W(q)$ . The minimum electron energy  $E_m$  at which interaction is possible with phonons of wavenumber  $q$  incident at angle  $\theta$  occurs when  $\beta = 0$  and is given by

$$E_m = \frac{m^*}{2\hbar^2 q_{\parallel}^2} \left( \frac{\hbar^2 q_{\parallel}^2}{2m^*} \pm \hbar\omega_q \mp \Delta \right)^2 \quad (6.18)$$

where  $q_{\parallel} = q \sin \theta$ . The integral over  $E$  is integrated by parts to avoid the singularity at  $E = E_m$ .

Figure 6.28 shows  $\Delta I(\Delta)$  for TA phonons and a range of heater temperatures  $T_h$  assuming  $T = 1.5$  K,  $w = 6$  nm,  $d = 10$  nm,  $m_e^* = 0.067m_e$ ,  $E_F = 0.6$  meV, and  $\theta_{\max} = 10$  degrees. It can be seen that  $\Delta I(\Delta)$  has a qualitatively similar form to that observed experimentally (Fig 6.22) but the peaks occur at appreciably lower bias values which vary less strongly with  $T_h$ . The values of the bias at the peaks can be expressed approximately as  $\Delta_{\max} \sim 0.25k_B T_h + 1.1$  meV. The intercept  $\Delta_{\max}^0$  is therefore similar to the measured value of 1.1 meV for  $V < 0$  but much greater than that of 0.25 meV for  $V > 0$  and the calculated values are essentially independent of  $E_F$ . For these parameters, the calculated slope is appreciably smaller than the measured value of 0.7 but approaches this value for  $E_F = 1.0$  meV. The authors point out though, that quantitative agreement might not be expected since they have not included a number of factors such as anisotropy in both phonon propagation (phonon focusing) and the electron–phonon interaction, piezoelectric coupling, and the possibility of phonon amplification arising from the strong stimulated phonon emission processes. Qualitatively similar results were found for LA phonons, the main difference being that the calculated slopes and intercepts are somewhat bigger than those for TA phonons.

Because of the potential the SL device has for phonon spectroscopy, calculations were also made of  $\Delta I(\omega_0)$  at fixed  $\Delta$  and  $\Delta I(\Delta)$  at fixed  $\omega_0$  for a quasi-monochromatic beam of phonons of frequency  $\omega_0$  by replacing the thermal distribution by a Gaussian,  $\exp[-\gamma(\omega - \omega_0)^2]$  with  $\gamma = 1000s^{-2}$ . These show that the oscillatory structure of  $W(q)$  has a marked effect on both  $\Delta I(\omega_0)$  and  $\Delta I(\Delta)$  and contributes to the relatively weak

dependence of  $\Delta_{\max}$  on  $T_h$ . The calculations of  $\Delta I(\omega_0)$  show that the dominant process for phonons incident near to the normal is stimulated emission with  $\hbar\omega_0 \sim \Delta$  but that, as  $\theta$  increases, lower frequency transitions with  $\hbar\omega_0 < \Delta$  become of greater importance and absorption processes also start to become significant. The data also show that the spectroscopic resolution  $\Delta\nu$  (HWHM)  $\sim 100$  GHz.

## 6.4 Related transport processes

Finally we consider three processes which have features related to those of phonon-assisted tunnelling.

### 6.4.1 Coherent phonon generation

Coherent acoustic phonons at frequencies of several hundred gigahertz have been generated by ultrafast optical excitation of GaAs/AlGaAs QWs [165] and superlattices [166–173]; the work has recently been reviewed by Dekorsy *et al.* [174]. The generation process, thought to be impulsively stimulated Raman scattering, involves the formation of an electron–hole pair accompanied by the creation of an LA phonon. It could not occur in bulk material because of the large phonon momentum involved but becomes possible in SLs where zone folding of the acoustic branches leads to the existence of relatively high-frequency phonons with  $q \sim 0$ . These correspond to the unfolded zone boundaries at  $q = 2l\pi/d$  and hence to frequencies  $\nu = ls_{\text{LA}}/d$  ( $s_{\text{LA}}$  is the LA sound velocity) which, for  $l = 1$ , is typically around 500 GHz for the structures that have been used. Weak generation at twice this frequency,  $l = 2$ , has also been detected. There are also weaker sidebands at  $q \sim 2k$  (laser) produced by backscattering. In the first experiments [166, 168–171], the presence of the phonons was detected by studying the reflection of a probe pulse from the surface following the excitation pulse. The amplitude of the reflected signal was seen to oscillate because of the phonon modulation of the refractive index at a dominant frequency of  $\nu = s_{\text{LA}}/d$  together with the weaker components described above. The oscillations decayed in a few nanoseconds presumably because the modes confined within the SL leak into propagating modes in the substrate. The existence of phonons at distances  $\sim 500$  nm away from the SL was demonstrated using an optical two-colour pump–probe technique [172] and more recently they have been shown to traverse the 400  $\mu\text{m}$  substrate [173]. The oscillations in the surface reflectivity of the sample following a laser pulse at a wavelength of  $\lambda = 767$  nm are shown in Fig. 6.29 and Fig. 6.30 shows examples of the signals detected by a superconducting bolometer on the opposite side of the substrate [173]. The arrival times of LA and TA phonons are indicated; the initial large peak is attributable to optical excitation of the bolometer. For  $\lambda > 767$  nm, the only phonon signal is a strong, slowly rising TA peak resulting from the decay of LO phonons generated in the bulk GaAs by the relaxation of the hot carriers before they recombine [175]. At shorter wavelengths, carrier excitation becomes possible in the SL and an LA signal appears. This increases in size until  $\lambda \sim 750$  nm. The signal could in principle be due either to incoherent LA phonons resulting from carrier relaxation in the wells or to quasi-monochromatic coherent LA

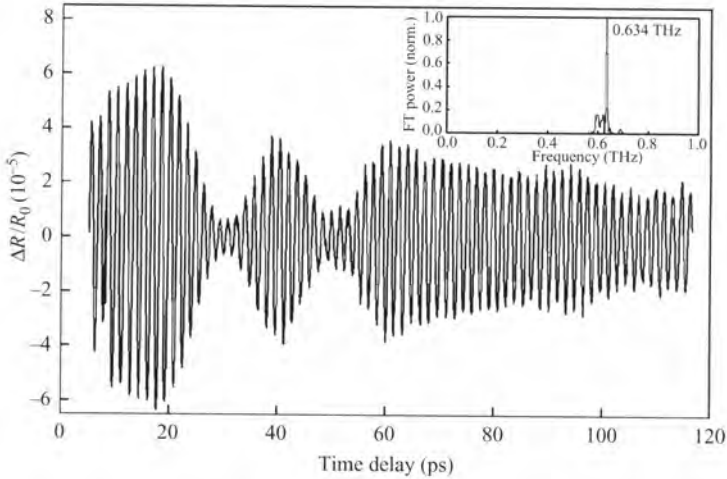


**Fig. 6.29** Time dependence of the fractional change in reflectivity of an SL device following irradiation by a femtosecond laser of wavelength  $\lambda = 767$  nm [173]. The inset shows the Fourier transform of  $\Delta R/R_0$ .

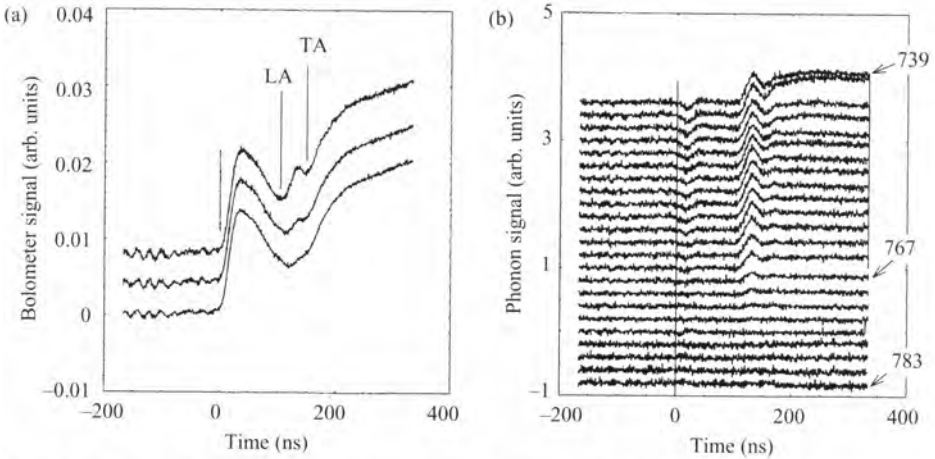


**Fig. 6.30** Change in voltage  $\Delta V(t)$  across a superconducting bolometer due to phonons emitted from an SL following irradiation by a femtosecond pulse of wavelength  $\lambda$ ; carrier excitation in the QWs is possible for  $\lambda \leq 767$  nm. (a)  $\lambda = 785$  (lowest curve), 767, and 755 nm; (b)  $\lambda$  decreasing in 2 nm steps from 783 nm (lowest curve) to 739 nm (highest curve). The LA signal appears once carrier excitation in the QWs becomes possible [173].

phonons resulting from the decay of the confined modes in the SL. Hawker *et al.* demonstrated that it could not be due to incoherent emission by showing that the emission of LA phonons from a single well had a very much wider angular distribution than that observed. They concluded that they had detected the decay of the confined modes. In a second experiment, a 2.0 mm GaAs substrate was used as a phonon filter to show that the phonons producing the LA signal mostly had frequencies  $> 600$  GHz. This appears

to confirm they are indeed the result of quasi-monochromatic phonon generation rather than the result of carrier relaxation [176].

It has also been suggested by Makler and co-workers (see references in Camps and Makler [177]) that [111] GaAs/AlGaAs DBRTDs could be used to obtain beams of coherent TA phonons at frequencies  $\sim 2$  THz. The LO phonons emitted into GaAs as a result of assisted tunnelling are known to decay predominantly into an LO phonon at the L-point of the Brillouin zone plus a zone-edge 2 THz TA phonon emitted in the opposite [111] direction [178, 179]. The LO phonons and zone-edge TA phonons would both be confined within the QW by multiple reflection and Makler and co-workers suggest that the decay into these modes could be predominantly a stimulated process and that their leakage into bulk modes in the substrate would result in a beam of coherent 2 THz TA phonons. Glavin *et al.* [157, 180, 181] have suggested that tuneable coherent phonon emission should occur from SLs as a result of population inversion under bias. Possible experimental evidence for phonon amplification in SLs resulting from this population inversion has been discussed briefly in Section 6.3.5.

#### 6.4.2 Surface acoustic waves

There has recently been considerable interest in the process called SETSAW, single electron transport by surface acoustic waves (SAWs), in which electrons are transported through pinched-off 1D channels connecting two 2D regions [182, 183]. A typical arrangement shown as an inset to Fig. 6.31 [182] consists of a split gate structure above a 2D electron gas formed within a GaAs/AlGaAs heterostructure. A 1D channel of length  $\sim 1 \mu\text{m}$  can be created by applying negative bias to the gate and exhibits quantized conductance at low temperatures [184, 185] as discussed in Chapters 4 and 8. The channel is pinched off by sufficient negative bias but a current can still be made to pass

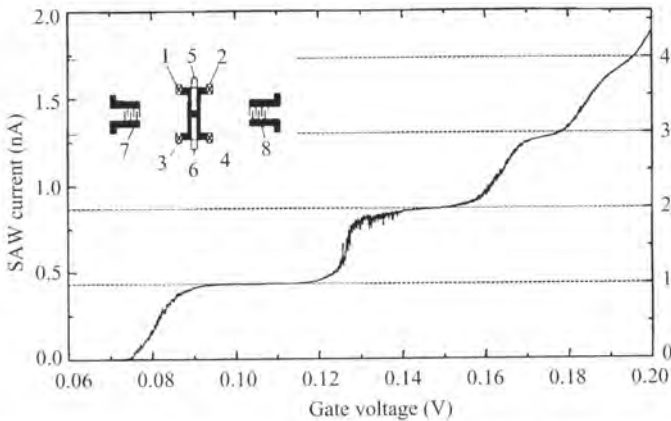


**Fig. 6.31** The current passing through a pinched-off 1D channel produced by an SAW as a function of gate voltage (after Janssen and Hartland [186]). Inset: a typical experimental arrangement showing the ohmic contacts to the 1D channel, 1–4, split gate, 5–6, and SAW transducers, 7–8 [182].

if a SAW of frequency  $f$  ( $\sim 1$  GHz) is launched towards and parallel to it. Piezoelectric coupling results in the SAW being accompanied by potential modulation of wavelength  $\lambda \sim 1 \mu\text{m}$  and, if its positive amplitude is greater than the negative potential from the gate, electrons flow into that region resulting in the formation of one or more quantum dots within the channel, each containing a small number of electrons  $n_d$ . The dots travel along the channel at the speed of sound leading to a quantized current  $I = n_d e f$ .  $n_d$  can be varied by changing the gate voltage or SAW amplitude causing the current to pass through a series of current plateaux as shown in Fig. 6.31 [186]. The process has been studied and analysed in detail in a number of papers listed by Robinson and Barnes [187]. The precision of the current measurement that has been achieved so far is about 1 part in  $10^4$  [188] but there are encouraging indications that this could be greatly improved if the electron temperature  $T_e$  in the dots could be reduced towards that of the rest of the device [189]. In present arrangements  $T_e \sim 10$  K or more because of RF heating [186] and, since the precision should fall rapidly with  $T_e$  [190], the figure of 1 part in  $10^7$  needed to establish a current standard might well be achievable if the heating could be reduced.

SAW-assisted transport has also been observed in a specially designed DBRTDs [191] and these first results suggest that this type of structure could have considerable potential for signal processing. This could include the use of counter-propagating SAW beams to convolute two signals.

#### 6.4.3 Photon-assisted tunnelling

The processes of acoustic phonon-assisted tunnelling considered in this chapter have evident similarities to those of photon-assisted tunnelling (PAT) in low-dimensional semiconducting structures though differences arise from the very much larger photon velocity and correspondingly smaller photon momentum. The small momentum  $\hbar q$ , and hence small in-plane momentum  $\hbar q \sin \theta$ , means that angular spread of the incident RF radiation would not lead to broadening as in the phonon case and also that the values of  $q_z$  are too small to produce oscillations in the transition probability. Another consequence of the large velocity is that the oscillating electric field is now approximately uniform across the device and so its effect is to modulate the bias potential. At the lower frequencies ( $\leq 600$  GHz in the work by Zeuner *et al.* [192]) non-linearities in  $I(V)$  lead to rectification but, at higher frequencies, this classical regime is replaced by PAT. Electron-photon coupling is very much weaker than electron-phonon coupling and, in all the work so far, tuneable free electron lasers have been used to provide the high RF intensity required to produce detectable effects. These sources can in fact provide sufficiently high intensities to generate multiphoton transitions.

PAT between the WS states of a doped SL was first observed by Guimaraes *et al.* [193] and has since been investigated in some detail [192, 194]. For one-photon transitions, the assisted peak occurs at a value  $\Delta$  (the energy separation between neighbouring levels) which increases linearly with  $\hbar\omega$  and with a slope of 1 and an intercept  $\sim 1.5$ – $2$  meV attributed to variations in well width (the doping of these sample is appreciably less than those used for the acoustic phonon-assisted tunnelling experiments and corresponds to a zero bias value of  $E_F \sim 0.1$  meV). The results can be well explained in terms of the model by Tucker [195, 196]. The predominant assisted process at higher bias was

shown to be due to stimulated emission and this can result in photon amplification at temperatures as high as room temperature [194]. At low bias, absorption becomes predominant resulting in a negative contribution and hence a negative current  $I$  [192] rather than the negative  $\Delta I$  predicted, though not yet observed, in the phonon measurements. PAT has also been seen in resonant tunnelling devices [197] and quantum dots [198].

## 6.5 Conclusions

Assisted tunnelling by optic and acoustic phonons is a natural accompaniment to any tunnelling process though is not always readily observable. The effects due to LO phonons are much more evident in experimental data than those of acoustic phonons, particularly in resonant tunnelling devices where the LO emission process gives rise to a pronounced peak in the  $I(V)$  characteristic [6, 7]. More detailed information on this process in RTDs, such as the probability of two-phonon emission and of the hybridization effects arising from the electron-phonon coupling, has been obtained from measurements of  $I(V)$  in quantizing magnetic fields [37–39, 41–43] and optical techniques have been used to demonstrate the effects the process has on the charge stored in the wells [54]. There has also been a range of theoretical investigation starting with the work of Wingreen [67, 68] and the main features of the assisted tunnelling seem reasonably well understood. However, further work is needed to determine which localized modes are of most importance under various conditions [74, 79]. Modes associated with the barriers and the wells are readily distinguishable by their frequencies but this is not the case for the different types of mode of the same frequency and new techniques will be needed to identify these. The LO phonon process is less evident in tunnelling in SLs and has received appreciably less experimental and theoretical attention than in RTDs. In magnetic fields, LO phonon-assisted tunnelling in SLs with narrow minibands gives rise to oscillations in  $I(V)$ , Stark-cyclotron phonon resonances [12]. The conditions for seeing such resonances become more demanding with increasing mini bandwidth because the large electric fields that need to be applied reduce the overlap between the Wannier-Stark states in neighbouring wells.

Experimental work on acoustic phonon-assisted tunnelling in RTDs [9, 97, 98] and SLs [14] has so far only been carried out by one group although there have been a number of theoretical studies [76, 89, 111–116, 155, 158]. The effects are much less pronounced than those of LO phonons and have only been seen using differential techniques in which a change in  $I(V)$  is produced by a change in phonon occupation number. Using this approach it is possible to see  $\Delta I(V)$  peaks in assisted tunnelling for both phonon absorption and emission. The bias at which the absorption peak occurs for transitions through a donor level in a DBRTD has been shown to vary linearly with phonon frequency demonstrating that it could be used as a phonon spectrometer. The changes are much smaller in a TBRTD [10]. The emission peak in an SL also moves approximately linearly with phonon frequency and, since its size is greater than in a RTD, SL devices look particularly promising for phonon spectroscopy in both zero and quantizing magnetic fields. The larger signals have tentatively been attributed to phonon amplification [14] but further work would be needed to establish this. Amplification should also reduce the

spectral linewidth of the response and it would be interesting to measure this using a narrow-band phonon source.

The most significant practical application of LO phonon-assisted tunnelling to date is in the quantum cascade laser [132] which uses the dependence of the assisted tunnelling rates on the transition energy to achieve population inversion. The uses of acoustic phonon-assisted tunnelling seem likely to be more limited but one promising application is in the SL phonon spectrometer. This could in principle be used to study the frequency distributions of phonons emitted from hot electrons in quantum wires and quantum dots as well as from 2D gases in zero and quantizing magnetic fields. Acoustic phonon-assisted tunnelling may also have a key role to play in circumventing the phonon bottleneck in the relaxation of quantum dots [108] although this has not yet been demonstrated experimentally. It might also enhance the performance of particle detectors which use the fact that phonons are emitted following particle collisions within solids or liquid helium at low temperatures ( $\sim 100$  mK) [199]. The predominantly optic phonons that are emitted decay rapidly into non-equilibrium acoustic phonons whose spectrum is expected to be characteristic of the initial particle [200]. If this proves to be correct, it might be possible to use the measured phonon spectrum to separate the signals from different types of particle. It has also been suggested [201] that, just as coherent megahertz ultrasonics has been used to produce holograms of, for example, a foetus, coherent terahertz acoustic phonons might be used to produce holograms of nanostructures. These authors also suggested that modulated beams of coherent terahertz acoustic phonons could be used to transmit information from one circuit component to another over very short distances within devices and that phonon beams could be used for high-resolution lithography using nanometre resolution 'phonoresists' made from material with a soft mode close to the beam frequency. These last three suggestions are speculative but would clearly be of very considerable interest if they could be realized. Assisted transport by surface acoustic waves (SAWs) may have a number of applications within a shorter time scale, perhaps within the next five to ten years. SAW-assisted transport through pinched-off 1D channels appears to offer a promising route to the development of a current standard [182, 183, 186–188, 190] and SAW transport through specially designed DBRTDs has a number of properties of potential value in signal processing [191].

## Acknowledgements

We are very grateful to Professors Koung-An Chao, Laurence Eaves, and Fred Sheard for very helpful comments and discussions. LJC wishes to acknowledge with thanks the award of a Leverhulme Emeritus Fellowship which provided support for FFO during the writing of this chapter.

## References

1. Esaki, L. and Tsu, R. (1970). *IBM J. Res. Dev.*, **14**, 61.
2. Tsu, R. and Esaki, L. (1973). *Appl. Phys. Lett.*, **22**, 562.

3. Chang, L.L., Esaki, L., and Tsu, R. (1974). *Appl. Phys. Lett.*, **24**, 593.
4. Esaki, L. and Chang, L.L. (1974). *Phys Rev Lett.*, **33**, 495.
5. Nakagawa, T., Inamoto, H., Kojima, T., and Ohta, K. (1986). *Appl. Phys. Lett.*, **49**, 73.
6. Goldman, V.W., Tsui, D.C., and Cunningham, J.E. (1987). *Phys. Rev.*, **B35**, 9387.
7. Bando, H., Nakagawa, T., Tokumoto, H., Ohta, K., and Kajimura, K. (1987). *Jpn. J. Appl. Phys.*, **26** (supplement **26-3**), 765.
8. Hickmott, T.W., Solomon, P.M., Fang, F.F., Stern, F., Fischer, R., and Morkoc, H. (1984). *Phys. Rev. Lett.*, **52**, 2053.
9. Ouali, F.F., Zinov'ev, N.N., Challis, L.J., Sheard, F.W., Henini, M., Steenson, D.P., and Strickland, K.R. (1995). *Phys. Rev. Lett.*, **75**, 308.
10. Cavill, S.A., Kent, A.J., Challis, L.J., Ouali, F.F., and Henini, M. (1999). *Physica*, **B272**, 171.
11. Higman, T.K., Favaro, M.E., Miller, L.M., Emmanuel, M.A., and Coleman, J.J. (1989). *Appl. Phys. Lett.*, **54**, 1751.
12. Müller, W., Grahn, H.T., Haug, R.J., and Ploog, K. (1992). *Phys. Rev.*, **B46**, 9800.
13. Cavill, S.A., Akimov, A., Ouali, F.F., Challis, L.J., Kent, A.J., and Henini, M. (1999). *Physica*, **B263-4**, 537.
14. Cavill, S.A., Challis, L.J., Kent, A.J., Ouali, F.F., Akimov, A.V. and Henini, M. (2002). *Phys. Rev.*, **B66**, 235320.
15. Mizuta, H. and Tanoue, T. (1995). *The physics and applications of resonant tunnelling diodes*, Cambridge University Press, Cambridge.
16. Leadbeater, M.L., Alves, E.S., Eaves, L., Sheard, F.W., Henini, M., Hughes, O.H., and Toombs, G.A. (1988). *Semicond. Sci. Technol.*, **3**, 1060.
17. Toombs, G.A. and Sheard, F.W. (1990). In *Electronic properties of multilayers and low-dimensional semiconductor structures* (ed. J.M. Chamberlain, L. Eaves, and J.C. Portal), pp. 257-82. Plenum, New York.
18. Ricco, B. and Azdel, M.Ya. (1984). *Phys. Rev.*, **B29**, 1970.
19. Luryi, S. (1985). *Appl. Phys. Lett.*, **22**, 490.
20. Payne, M.C. (1986). *J. Phys. C: Solid State Phys.*, **19**, 1145.
21. Weil, T. and Vinter, B. (1987). *Appl. Phys. Lett.*, **50**, 1281.
22. Sheard, F.W. and Toombs, G.A. (1988). *Appl. Phys. Lett.*, **52**, 1288.
23. Turner, T.S., Martin, P.M., Eaves, L., Evans, H.B., Harrison, P.A., Henini, M., Hughes, O.H., Whittaker, D.M., Buckle, P.D., Fisher, T.A., Skolnick, M.S., and Hill, G. (1994). *Solid St. Electron.*, **37**, 721.
24. Sollner, T.C.L.G., Goodhue, W.D., Tannenwald, P.E., Parker, C.D., and Peck, D.D. (1983). *Appl. Phys. Lett.*, **43**, 588.
25. Capasso, F. and Kiehl, R.A. (1985). *J. Appl. Phys.*, **58**, 1366.
26. Bonnefoi, A.R., McGill, T.C., and Burnham, R.D. (1985). *IEEE Electron Device Lett.*, **EDL-6**, 636.
27. Potter, R.C., Lakhani, A.A., Beyea, D., Hier, H., Hempfling, E., and Fathimulla, A. (1988). *Appl. Phys. Lett.*, **52**, 2163.
28. Brown, E.R., Söderström, J.R., Parker, C.D., Mahoney, L.J., Molvar, K.M., and McGill, T.C. (1991). *Appl. Phys. Lett.*, **58**, 2291.
29. Özbay, E., Bloom, D.M., Chow, D.H., and Schulman, J.N. (1993). *IEEE Electron Device Lett.*, **14**, 400.
30. Kan, S.C., Harshman, P.J., Lau, K.Y., Wang, Y., and Wang, W.I. (1996). *IEEE Photonics Technol. Lett.*, **8**, 641.
31. Figueiredo, J.M., Stanley, C.R., Boyd, A.R., Ironside, C.N., McMeekin, S.G. and Leite, A.M.P. (1999). *Appl. Phys. Lett.*, **74**, 1197.
32. Tatham, M.C., Ryan, J.F., and Foxon, C.T. (1989). *Phys. Rev. Lett.*, **63**, 1637.
33. Grahn, H.T., Schneider, H., Rühle, W.W., von Klitzing, K., and Ploog, K. (1990). *Phys. Rev. Lett.*, **64**, 2426.

34. Heberle, A.P., Rühle, W.W., and Köhler, K. (1992). *Phys. Status Solidi* (b), **173**, 381.
35. Shah, J. (1992). In *Spectroscopy of nonequilibrium electrons and phonons* (ed. V. Shank and B.P. Zakharchenya), pp. 57–112. Elsevier, Amsterdam.
36. Hunsche, S., Leo, K., Kurz, H., and Köhler, K. (1994). *Phys. Rev.*, **B50**, 5791.
37. Leadbeater, M.L., Alves, E.S., Eaves, L., Henini, M., Hughes, O.H., Celeste, A., Portal, J.C., Hill, G., and Pate, M.A. (1989). *Phys. Rev.*, **B39**, 3439.
38. Boebinger, G.S., Levi, A.F.J., Schmitt-Rink, S., Passner, A., Pfeiffer, L.N., and West, K.W. (1990). *Phys. Rev. Lett.*, **65**, 235.
39. Chen, J.G., Yang, C.H., Yang, M.J., and Wilson, R.A. (1991). *Phys. Rev.*, **B43**, 4531.
40. Gobato, Y.G., Chevoir, F., Berroir, J.M., Bois, P., Guldner, Y., Nagle, J., Vieren, J.P., and Vinter, B. (1991). *Phys. Rev.*, **B43**, 4843.
41. Pritchard, R.E., Harness, P.C., Cury, L., Portal, J.C., Khamsehpor, B., Truscott, W.S., and Singer, K.E. (1991). *Semicond. Sci. Technol.*, **6**, 626.
42. Turley, P.J., Wallis, C.R., Teitworth, S.W., Li, W., and Bhattacharya, P.K. (1993). *Phys. Rev.*, **B47**, 12640.
43. Goodings, C.J., Mizuta, H., and Cleaver, J.R.A. (1994). *J. Appl. Phys.*, **75**, 2291.
44. Teitworth, S.W., Turley, P.J., Wallis, C.R., Li, W., and Bhattacharya, P.K. (1994). *Semicond. Sci. Technol.*, **9**, 508.
45. Hayden, D.K., Eaves, L., Henini, M., Maude, D.K., Portal, J.C., and Hill, G. (1992). *Appl. Phys. Lett.*, **60**, 1474.
46. Wirner, C., Awano, Y., Mori, T., Yokoyama, N., Nakagawa, T., Bando, H., and Muto, S. (1996). *Appl. Phys. Lett.*, **69**, 1596.
47. Madelung, O. (ed.) (1996). *Semiconductors-basic data*, Springer-Verlag, Berlin.
48. Das Sarma, S. (1984). *Phys. Rev. Lett.*, **52**, 859; (1984). **52**, 1570 (E).
49. Larsen, D.M. (1984). *Phys. Rev.*, **B30**, 4087.
50. Peeters, F.W. and Devreese, J.T. (1985). *Phys. Rev.*, **B31**, 3689.
51. Rascol, J.J.L., Martin, K.P., Ben Amor, S., Higgins, R.J., Celeste, A., Portal, J.C., Torabi, A., Harris, H.M., and Summers, C.J. (1990). *Phys. Rev.*, **B41**, 3733.
52. Asahi, H., Tewardt, M., Syme, R.T., Kelly, M., Law, V.J., Mace, D.R., Frost, J.E.F., Ritchie, D.A., Jones, G.A.C., and Pepper, M. (1991). *Appl. Phys. Lett.*, **59**, 803.
53. Macks, L.D., Brown, S.A., Clark, R.G., Starrett, R.P., Reed, M.A., Deshpande, M.R., Fernando, C.J.L., and Frensley, W.R. (1996). *Phys. Rev.*, **B54**, 4857.
54. Skolnick, M.S., Hayes, D.G., Simmonds, P.E., Higgs, A.W., Smith, G.W., Hutchinson, H.J., Whitehouse, C.R., Eaves, L., Henini, M., Hughes, O.H., Leadbeater, M.L., and Halliday, D.P. (1990). *Phys. Rev.*, **B41**, 10754.
55. Liu, H.W., Ferreira, R., Bastard, G., Delande, C., Palmier, J.F., and Etienne, B. (1989). *Appl. Phys. Lett.*, **54**, 2082.
56. Oberli, D.Y., Shah, J., Damen, T.C., Tu, C.W., Chang, T.Y., Miller, D.A.B., Henry, J.E., Kopf, R.F., Sauer, N., and Di Giovanni, A.E. (1989). *Phys. Rev.*, **B40**, 3028.
57. Oberli, D.Y., Shah, J., Damen, T.C., Kuo, J.M., Henry, J.E., Lary, J., and Goodnick, S.M. (1990). *Appl. Phys. Lett.*, **56**, 1239.
58. Lary, J., Goodnick, S.M., Lugli, P., Oberli, D.Y., and Shah, J. (1989). *Solid State Electron.*, **32**, 1283.
59. Alexander, M.G.W., Nido, M., Rühle, W.W., and Köhler, K. (1990). *Phys. Rev.*, **B41**, 12295.
60. Matsuo, T., Tsuchiya, M., Schulman, J.N., and Sakaki, H. (1990). *Phys. Rev.*, **B42**, 5719.
61. Devaud, B., Chomette, A., Clerot, F., Auvray, P., Regreny, A., Ferreira, R., and Bastard, G. (1990). *Phys. Rev.*, **B42**, 7021.
62. Roussignol, Ph., Vinattieri, A., Carraresi, L., Colocci, M., and Fasolino, A. (1991). *Phys. Rev.*, **B44**, 8873.
63. Ozaki, S., Feng, J.M., Park, J.H., Osako, S., Kubo, H., Morifuji, H.M., Mori, N.N., and Hamaguchi, C.J. (1998). *J. Appl. Phys.*, **83**, 962.
64. Rucker, H., Lugli, P., Goodnick, S.M., and Lary, J. (1992). *Semicond. Sci. Technol.*, **7**, B98.

65. Benjamin, S.D., Lo, Y.C., and Kolbas, R.M. (1991). *Appl. Phys. Lett.*, **59**, 351.
66. Holonyak, N. Jr, Kolbas, R.M., Laidig, W.D., Altarelli, M., Dupuis, R.D., and Dakpus, P.D. (1979). *Appl. Phys. Lett.*, **34**, 502.
67. Wingreen, N.S., Jacobsen, K.W., and Wilkins, J.W. (1988). *Phys. Rev Lett.*, **61**, 1396.
68. Wingreen, N.S., Jacobsen, K.W., and Wilkins, J.W. (1989). *Phys. Rev.*, **B40**, 11834.
69. Sedlmaier, S., Schulze, J., Sulima, T., Fink, C., Tolksdorf, C., Bayerstadler, A., Eisele, I., Wang, P.-F., Hilsenbeck, K., and Hansch, W. (2002). *Mater. Sci. Eng.*, **B89**, 116.
70. Cai, W., Zheng, T.F., Hu, P., Yadahin, B., and Lax, M. (1989). *Phys. Rev. Lett.*, **63**, 418.
71. Chevoir, F. and Vinter, B. (1989). *Appl. Phys. Lett.*, **55**, 1859.
72. Jonson, M. (1989). *Phys. Rev.*, **B39**, 5924.
73. Rudberg, B.G.R. (1990). *Semicond. Sci. Technol.*, **5**, 328.
74. Mori, N., Taniguchi, K., and Hamaguchi, C. (1992). *Semicond. Sci. Technol.*, **7**, B83.
75. Zou, N. and Chao, K.A. (1992). *Phys. Rev Lett.*, **69**, 3224.
76. Chevoir, F. and Vinter, B. (1993). *Phys. Rev.*, **B47**, 7260.
77. Fu, Y. and Willander, M. (1993). *J. Appl. Phys.*, **74**, 3261.
78. Grein, C.H., Runge, E., and Ehrenreich, H. (1993). *Phys. Rev.*, **B47**, 12590.
79. Turley, P.J. and Teitsworth, S.W. (1994). *Phys. Rev.*, **B50**, 8423.
80. Lake, R., Klimeck, G., Bowen, R.C., Fernando, C., Moise, T., Kao, Y.C., and Leng, M. (1996). *Superlattices Microstruct.*, **20**, 279.
81. Shi, J.J., Sanders, B.C., and Pan, S.H. (1998). *Eur. Phys. J.*, **B1**, 113.
82. Zu Wei Yan, Liang, X.X., and Ban, S.L. (2001). *Phys. Rev.*, **B64**, 125321.
83. Torres, I.E.F.F., Pastawski, H.M., and Makler, S.S. (2001). *Phys. Rev.*, **B64**, 193304.
84. Jun-jie Shi, Sanders, B.B., Shao-hua Pan, and Goldys, E.M. (2001). *Physica*, **E10**, 535.
85. Zu Wei Yan and Liang, X.X. (2002). *J. Appl. Phys.*, **91**, 724.
86. Weil, T. and Vinter, B. (1986). *J. Appl. Phys.*, **60**, 3227.
87. Liu, L.-J., Du, Y.-T., and Lin, T.-H. (1996). *Phys. Rev.*, **B54**, 1953.
88. Khan-ngern, S. and Larkin, I.A. (2000). *Phys. Lett.*, **A266**, 209.
89. Tsu, R. and Döhler, G. (1975). *Phys. Rev.*, **B12**, 680.
90. Ridley, B.K. (1997). *Electrons and phonons in semiconductor multilayers*, Cambridge University Press, Cambridge.
91. Stroschio, M.A. and Dutta, M. (2001). *Phonons in nanostructures*, Cambridge University Press, Cambridge.
92. Mori, N. and Ando, T. (1989). *Phys. Rev.*, **B40**, 6175.
93. Lake, R., Klimeck, G., and Datta, S. (1993). *Phys. Rev.*, **B47**, 6427.
94. Bø, Ø.L., Galperin, Yu., and Chao, K.A. (1995). *Phys. Rev.*, **B52**, 8893.
95. Nazhi, Zou, Galperin, Yu., and Chao, K.A. (1993). *Phys. Rev. Lett.*, **71**, 1756.
96. Dogonkin, E.B. and Zegrya, G.G. (2001). *Pis'ma Eksp. Teor. Fiz.*, **74**, 346 [*JETP Lett.*, **74**, 312].
97. Moskalenko, E.S., Hill, D.N., Ouali, F.F., Challis, L.J., Sheard, F.W., and Henini, M. (1997). In *High magnetic fields in the physics of semiconductors* (ed. G. Landwehr and W. Ossau), pp. 453, World Scientific, Singapore.
98. Hill, D.N., Cavill, S.A., Moskalenko, E.S., Ouali, F.F., Akimov, A.V., Challis, L.J., Kent, A.J., Sheard, F.W., and Henini, M. (1997). *Phys. Status Solidi* (b), **204**, 431.
99. Lehmann, D., Jasiukiewicz, C., and Kent, A.J. (1998). *Physica*, **B251**, 718.
100. Kappas, W. and Weiss, O. (1973). *J. Appl. Phys.*, **44**, 1947.
101. Sakai, J.W., Fromhold, T.M., Beton, P.H., Eaves, L., Henini, M., Main, P.C., and Sheard, F.W. (1993). *Phys. Rev.*, **B48**, 5664.
102. Eaves, L., Foster, T.J., Leadbeater, M.L., and Maude, D.K. (1992). In *Resonant tunnelling in semiconductors: physics and application*, NATO Advanced Study Institute Series B: Vol. 227 (ed. L.L. Chang, E.E. Mendez, and C. Tejedor), p. 229, Plenum, New York.
103. Cavill, S.A. (2000). Ph.D. thesis, University of Nottingham.

104. Král, P., Sheard, F.W., Ouali, F., Hill, D.N., Akimov, A.V., and Challis, L.J. (1998). *Physica*, **E2**, 191.
105. Král, P., Sheard, F.W., and Ouali, F.F. (1998). *Phys. Rev.*, **B57**, 15428.
106. Kent, A.J. (1996). Private communication.
107. Price, P.J. (1985). *Physica*, **B134**, 164.
108. Schroeter, D.F., Griffiths, D.J., and Sercel, P.C. (1996). *Phys. Rev.*, **B54**, 1486.
109. Türeci, V., Rodt, S., Heitz, R., Strassburg, U., Pohl, U.W., and Bimberg, D. (2001). *Phys. Status Solidi (b)*, **B224**, 643.
110. Qin, H., Holleitner, A.W., Eberl, K., and Blick, R.H. (2001). *Phys. Rev.*, **B64**, 241302(R).
111. Roblin, P. and Liou, W.-R. (1993). *Phys. Rev.*, **B47**, 2146.
112. Vasko, F.T., Balev, O.G., and Vasilopoulos, P. (1993). *Phys. Rev.*, **B47**, 16433.
113. Raichev, O.E. and Vasko, F.T. (1994). *Phys. Rev.*, **B50**, 12199.
114. Lyanda-Geller, Y. and Leburton, J.-P. (1995). *Phys. Rev.*, **B52**, 2779.
115. Kozub, V.I. and Rudin, A.M. (1994). *Phys. Rev.*, **B49**, 5710.
116. Bø, Ø.L. and Galperin, Yu. (1996). *J. Phys. Condens. Matter*, **8**, 8595.
117. Monozon, B.S. (1998). Private communication.
118. Sibille, A. (1995). In *Semiconductor superlattices* (ed. H.T. Grahn), pp. 29–97, World Scientific, Singapore.
119. Ignatov, A.I., Renk, R.F., and Dodin, E.P. (1993). *Phys. Rev. Lett.*, **70**, 1996.
120. Wannier, G.H. (1960). *Phys. Rev.*, **117**, 432.
121. Grahn, H.T., von Klitzing, K., Ploog, K., and Döhler, G.H. (1991). *Phys. Rev.*, **B43**, 12094.
122. Wacker, A. and Jauho, A.-P. (1998). *Phys. Rev. Lett.*, **80**, 369.
123. Fertig, H.A. and Das Sarma, S. (1990). *Phys. Rev.*, **B42**, 1448.
124. Grahn, H.T. (1995). In *Semiconductor superlattices* (ed. H.T. Grahn), pp. 205–50, World Scientific, Singapore.
125. Schomburg, E., Henini, M., Chamberlain, J.M., Steenson, D.P., Brandl, S., Hofbeck, K., Renk, K.F., and Wegscheider, W. (1999). *Appl. Phys. Lett.*, **74**, 2179.
126. Wacker, A. and Jauho, A.P. (1998). *Superlattices Microstruct.*, **23**, 297.
127. Schomburg, E. (1999). In *Terahertz spectroscopy and applications II* (ed. M.S. Sherwin and J.M. Chamberlain), pp. 89–96, SPIE, Bellingham, WA.
128. Agulló-Rueda, F. and Feldman, J. (1995). In *Semiconductor superlattices* (ed. H.T. Grahn), pp. 205–50, World Scientific, Singapore.
129. Hadjazi, M., Palmier, J.F., Sibille, A., Wang, H., Paris, E., and Mollot, F. (1993). *Electron. Lett.*, **29**, 648.
130. Winnerl, S., Schomburg, E., Grenzer, J., Regl, H.-J., Ignatov, A.A., Semenov, A.D., Renk, K.F., Pavel'ov, D.G., Koschurinov, Yu., Melzer, B., Ustinov, V., Ivanov, S., Schaposchnikov, S., and Kop'ev, P.S. (1997). *Phys. Rev.*, **B56**, 10303.
131. Schomburg, E., Brandl, S., Winnerl, S., Renk, F.K., Ledentsov, N.N., Ustinov, V.M., Zhukov, A., Kop'ev, P.S., Hübers, H.-W., Schubert, J., Röser, H.P., Rosenauer, A., Litvinov, D., Gerthsen, D., and Chamberlain, J.M. (2000). *Physica*, **E7**, 814.
132. Faist, J., Capasso, F., Sivco, D., Sirtori, C., Hutchinson, A.L., and Cho, A.Y. (1994). *Science*, **264**, 553.
133. Faist, J., Capasso, F., Sirtori, C., Sivco, D., Hutchinson, A.L., and Cho, A.Y. (1997). *Nature*, **387**, 777.
134. Beck, M., Hofstetter, D., Aellen, T., Faist, J., Oesterle, U., Illegems, M., Gini, E., and Melchior, H. (2002). *Science*, **295**, 5553.
135. Capasso, F., Gmachl, C., Sivco, D.L., and Cho, A.Y. (1999). *Phys. World*, **12**, 27.
136. Capasso, F., Gmachl, C., Paiella, R., Tredicucci, A., Hutchison, A.L., Sivco, D.L., Baillargeon, J.N., Cho, A.Y., and Liu, H.C. (2000). *IEE J. Sel. Top. Quantum Electron.*, **6**, 931.
137. Cartlidge, E. (2002). *Phys. World*, **15**, 10.

138. Agulló-Lopez, F., Cabrera, J.M., and Agulló-Rueda, F.F. (1994). *Electrooptics*, Academic Press, New York.
139. Shmelev, G.M., Chaikovskii, I.A., and Min Shon Chan (1976). *Phys Status Solidi* (b), **76**, 811.
140. Hess, K. (1979). *Appl. Phys. Lett.*, **35**, 484.
141. von Plessen, G., Meier, T., Feldman, J., Göbel, E.O., Thomas, P., Goosen, K.W., Kuo, J.M., and Kopf, R.F. (1994). *Phys. Rev.*, **B49**, 14058.
142. Eaves, L., Murphy, H.M., Nogaret, A., Stoddard, S.T., Main, P.C., Henini, M., Mori, N., Hamaguchi, C., Maude, D.K., and Portal, J.C. (1999). *Physica*, **B272**, 190.
143. Mori, N., Hamaguchi, C., Eaves, L., and Main, P.C. (2001). *Physica*, **B298**, 329.
144. Noguchi, H. and Sakaki, H. (1992). *Phys. Rev.*, **B45**, 12148.
145. Chow, W.W., Koch, S.W., and Sargent, M. III. (1994). *Semiconductor-laser physics*, Springer-Verlag, Berlin.
146. Kazarinov, R.F. and Suris, R.A. (1971). *Fiz. Tekh. Poluprov.*, **5**, 797 [*Sov. Phys. Semicond.*, **5**, 707].
147. Colvard, C., Merlin, R., Kein, M.V., and Gossard, A.C. (1980). *Phys. Rev. Lett.*, **45**, 298.
148. Müller, W., Bertram, D., Grahn, H.T., von Klitzing, K., and Ploog, K. (1994). *Phys. Rev.*, **B50**, 10998.
149. Ferreira, R. (1991). *Phys. Rev.*, **B43**, 9336.
150. Hong Shon, N. and Nazareno, H.N. (1996). *Phys. Rev.*, **B53**, 1937.
151. Bryskin, V.V. and Kleinert, P. (1999). *Phys. Rev.*, **B59**, 8152.
152. Bryskin, V.V. and Kleinert, P. (1999). *Physica*, **B269**, 163.
153. Canali, L., Lazzarino, M., Sorba, L., and Beltram, F. (1996). *Phys. Rev. Lett.*, **76**, 3618.
154. Nogaret, A., Eaves, L., Main, P.C., Henini, M., Maude, D.K., and Portal, J.C. (1997). *Phys. Status Solidi* (b), **204**, 374.
155. Lyanda-Geller, Y. and Leburton, J.-P. (1998). *Physica*, **E2**, 73.
156. Bastard, G. and Ferreira, R. (1989). In *Spectroscopy of semiconductor microstructures*, NATO Advanced Study Institute Series B: Physics 206 (ed. G. Fasol and A. Fasolino), pp. 333–45, Plenum, New York.
157. Glavin, B.A., Kochelap, V.A., and Linnik, T.L. (1999). *Appl. Phys. Lett.*, **74**, 3525.
158. Glavin, B.A., Kochelap, V.A., and Linnik, T.L. (2000). *Pis'ma Eksp. Teor. Fiz.*, **71**, 280 [*JETP Lett.*, **71**, 191].
159. Fokker, P.A., Dijkhuis, J.I., and de Wijn, H.W. (1997). *Phys. Rev.*, **B55**, 2925.
160. Baumhoff, S., Prieur, J.-Y., and Joffrin, J. (1999). *Physica*, **B263–4**, 34.
161. Watson, A. (1999). *New Sci.*, **161**, 37.
162. Rott, S., Linder, N., and Döhler, G. (2002). *Phys. Rev.*, **B65**, 195301.
163. Nogaret, A., Eaves, L., Main, P.C., Henini, M.D., Maude, K., Portal, J.C., Molineri, E., and Beaumont, S.P. (1998). *Solid State Electron.*, **42**, 1489.
164. Eaves, L. (2000). Private communication.
165. Baumberg, J.J., Williams, D.A., and Köhler, K. (1997). *Phys. Rev. Lett.*, **78**, 3358.
166. Yamamoto, A., Mishina, T., and Masumoto, Y. (1994). *Phys. Rev. Lett.*, **73**, 740.
167. Iwazaka, Y., Mishina, T., Masumoto, Y., and Nakayama, M. (1996). In *Proc. 23rd Int. Conf. on physics of semiconductors* (ed. M. Scheffler and R. Zimmerman), pp. 701–4, World Scientific, Singapore.
168. Mizoguchi, K., Matsutani, K., Nakachima, S., Dekorsy, T., Kurz, H., and Nakayama, M. (1997). *Phys. Rev.*, **B55**, 9336.
169. Mizoguchi, K., Matsutani, K., Hase, M., Nakachima, S., and Nakayama, M. (1998). *Physica*, **B249–51**, 887.
170. Mishina, T., Iwazaki, Y., Masumoto, Y., and Nakayama, M. (1998). *Solid State Commun.*, **107**, 281.
171. Bartels, A.A., Dekorsy, T., Kurz, H., and Köhler, K. (1999). *Phys. Rev. Lett.*, **82**, 1044.
172. Mizoguchi, K., Hase, M., and Nakachima, S. (1999). *Phys. Rev.*, **B60**, 8262.

173. Hawker, P., Kent, A.J., Challis, L.J., Bartels, A., Dekorsy, T., Kurz, H., and Köhler, K. (2000). *Appl. Phys. Lett.*, **77**, 3209.
174. Dekorsy, T., Cho, G.C., and Kurz, H. (2000). In *Light scattering in solids VIII* (ed. M. Cardona and G. Güntherodt), pp.169–209, Springer-Verlag, Berlin.
175. Ulbrich, R.G., Narayanamurti, V., and Chin, M.A. (1980). *Phys. Rev. Lett.*, **45**, 1432.
176. Stanton, N.M., Challis, L.J., Henini, M., and Kent, A.J. (2002). *Appl. Phys. Lett.*, **81**, 3497.
177. Camps, I. and Makler, S.S. (2000). *Solid. State Commun.*, **116**, 191.
178. Vallée, F. and Bogani, F. (1991). *Phys. Rev.*, **B43**, 12049.
179. Vallée, F. (1994). *Phys. Rev.*, **B49**, 2460.
180. Glavin, B.A., Kochelap, V.A., Linnik, T.L., Kim, K.W., and Strocio, M.A. (2002). *Phys. Rev.*, **B65**, 085303.
181. Glavin, B.A., Kochelap, V.A., Linnik, T.L., Kim, K.W., and Strocio, M.A. (2002). *Phys. Rev.*, **B65**, 085304.
182. Shilton, J.M., Talyanskii, V.I., Pepper, M., Ritchie, D.A., Frost, J.E.F., Ford, C.J.B., Smith, C.G., and Jones, G.A.C. (1996). *J. Phys. Condens. Matter*, **8**, L531.
183. Talyanskii, V.I., Shilton, J.M., Pepper, M., Smith, C.G., Ford, C.J.B., Linfield, E.H., Ritchie, D.A., and Jones, G.A.C. (1997). *Phys. Rev.*, **B56**, 15180.
184. Wharam, D.A., Thornton, T.J., Newbury, R., Pepper, M., Ahmed, H., Frost, J.E.F., Hasko, D.G., Peacock, D.C., Ritchie, D.A., and Jones, G.A.C. (1998). *J. Phys. Condens. Matter*, **21**, L209.
185. van Wees, B.J., van Houten, H., Beenakker, C.W.J., Williamson, J.G., Kouwenhoven, L.P., van der Marel, D., and Foxon, C.T. (1988). *Phys. Rev. Lett.*, **60**, 848.
186. Janssen, T.J.B.M. and Hartland, A. (2001). *IEEE Trans. Instrum. Meas.*, **50**, 227.
187. Robinson, A.M. and Barnes, C.H.W. (2001). *Phys. Rev.*, **B63**, 165418.
188. Janssen, T.J.B.M. and Hartland, A. (2000). *Physica*, **B284–8**, 1790.
189. Fletcher, N.E., Janssen, T.J.B.M., and Hartland, A. (2002). *IEE Proc. Sci. Meas. Technol.*, **149**, 299.
190. Flensburg, K., Niu, Q., and Pustilnik, M. (1999). *Phys. Rev.*, **B60**, R16291.
191. Talyanskii, V.I., Hutchinson, A.B., Batov, I.E., Ritchie, D.A., and Linfield, E.H. (1999). *J. Appl. Phys.*, **86**, 2917.
192. Zeuner, S., Keay, B.J., Allen, S.J. Jr, Maranowski, K.D., Gossard, A.C., Bhattacharya, U., and Rodwell, M.J.W. (1996). *Phys. Rev.*, **B53**, R1717.
193. Guimaraes, P.S.S., Keay, B.J., Kaminski, J.P., Allen, S.J. Jr, Hopkins, P.F., Gossard, A.C., Florez, L.T., and Harbison, J.P. (1993). *Phys. Rev. Lett.*, **70**, 3792.
194. Zeuner, S., Allen, S.J. Jr, Maranowski, K.D., and Gossard, A.C. (1996). *Appl. Phys. Lett.*, **69**, 2689.
195. Tucker, J.R. (1979). *IEEE J. Quantum Electron.*, **QE-15**, 1234.
196. Wacker, A. and Jauho, A.-P. (1997). *Phys. Status Solidi (b)*, **204**, 73.
197. Drexler, H., Scott, J.S., Allen, S.J. Jr, Campman, K.L., and Gossard, A.C. (1996). *Appl. Phys. Lett.*, **67**, 2816.
198. Kouwenhoven, L.P., Jauhar, S., Orenstein, J., McEuen, P.L., Nagamune, Y., Motohisa, J., and Sakaki, H. (1994). *Phys. Rev. Lett.*, **73**, 3443.
199. Probst, F., Frank, M., Cooper, S., Colling, P., Dummer, D., Ferger, P., Forster, G., Nucciotti, A., Seidel, W., and Stodolksy, L. (1995). *J. Low Temp. Phys.*, **100**, 69.
200. Sadoulet, B., Cabrera, B., Maris, H.J., and Wolfe, J.P. (1990). In *Phonons 89* (ed. S. Hunklinger, W. Ludwig, and G. Weiss), pp. 1383–93, World Scientific, Singapore.
201. Makler, S.S., Vasilevsky, M.I., Anda, E.V., Tuyarot, D.E., Weberszpil, J., and Pastawski, H.M. (1998). *J. Phys. C: Solid State Phys.*, **10**, 5905.

# 7 Exciton–phonon interaction in quantum wells

A.V. Akimov

---

## 7.1 Introduction

Free electrons and holes created in a semiconductor as a result of optical excitation are coupled to each other by Coulomb interaction. These coupled electron–hole pairs are called excitons and may be considered as free quasiparticles analogous to other elementary excitations in solids. In the simplest case the system of exciton levels may be compared with those of the hydrogen atom. But, in contrast to an atom in a crystalline lattice, an exciton is a mobile quasiparticle which has momentum. The properties of excitons have some common features with the properties of carriers in semiconductors. However, the neutrality, finite lifetime, and Bose statistics make the overall behaviour of excitons very different from those of free electrons and holes.

There is a very substantial body of literature devoted to excitons and most optical phenomena seen in semiconductors involve in some way the existence of exciton states. So when two-dimensional (2D) semiconductor structures first became available in the early 1980s, it was not surprising that 2D excitons should be one of the most attractive subjects of study. In the present chapter we are aiming to give an introduction rather than a comprehensive review of all the properties of 2D excitons and refer the reader to books and review articles devoted to excitons in low-dimensional semiconductor nanostructures [1–4].

Our main interest here is to review the role that acoustic phonons play in exciton dynamics. The effect of the exciton–phonon interaction on many optical properties is in fact comparable in significance with that of the electron–phonon interaction. We plan to show that excitons may become a powerful tool for phonon spectroscopy experiments providing valuable information about the dynamical properties of phonons in semiconductor nanostructures. This partly arises because the 10–100 nm wavelengths of terahertz and subterahertz acoustic phonons are comparable in magnitude with the typical dimensions of semiconductor nanostructures.

The chapter is divided into five sections. Section 7.1 describes briefly the main properties of excitons and could be skipped by readers who have already worked in this field. In Section 7.2 we describe the basic properties of the exciton–phonon interaction and review experimental and theoretical work in this area. Section 7.3 is concerned with non-equilibrium acoustic phonons in single quantum wells (QWs). It gives details of experimental work and also presents the results of calculations describing the effect of phonons on the energy distribution of 2D excitons. Section 7.4 describes the experiments and results of theoretical analysis on the interaction of excitons with acoustic phonons in coupled double quantum wells and Section 7.5 draws conclusions from all this work and discusses prospectives for future studies.

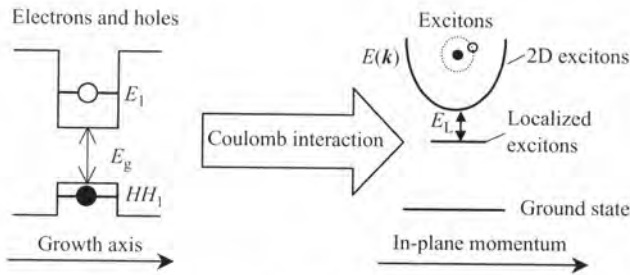


**Fig. 7.1** Representation of exciton formation in QWs.

### 7.1.1 Exciton spectrum in quantum wells

The complete calculation of the energy spectrum of 2D excitons is a complicated task, since it has to take account of the complex structure of the valence band in most semiconductors [1]. Here we use a simplified approach which, however, provides a good basis for the analysis of the exciton–phonon interaction.

Figure 7.1 shows schematically the formation of exciton states in a single quantum well as a result of the Coulomb interaction between a free electron and a heavy hole with ground state QW energies  $E_1$  and  $HH_1$  respectively. The energy of the lowest exciton state may be written as

$$E(\mathbf{k}) = E_g + E_1 + HH_1 - E_B + \frac{\hbar^2 k^2}{2m^*}, \quad (7.1)$$

where  $\mathbf{k}$  is the exciton wavevector in the plane of the QW,  $E_g$ , the energy gap in the bulk material,  $m^* = m_e^* + m_{hh}^*$ , the effective (transport) exciton mass, and  $m_e^*$  and  $m_{hh}^*$ , the effective electron and heavy hole in-plane masses respectively.

The important term in Eq. (7.1) is the exciton binding energy  $E_B$ . For the ideal 2D case,  $E_B$  can be shown to be [5]

$$E_B = \frac{2e^4 \mu}{\hbar^2 \varepsilon}, \quad (7.2)$$

where  $\varepsilon$  is the static dielectric constant and  $\mu$  is a reduced exciton mass. In this perfect 2D limit,  $E_B$  is four times bigger than in the 3D case, so 2D excitons are more strongly bound than the corresponding 3D quasiparticles. In practice, however, excitons are not ideally 2D and  $E_B$  depends on the QW width. For infinite QW barriers it has been shown that  $E_B$  increases smoothly from its 3D to its 2D value with decreasing QW width [6, 7]. However, the ideal 2D value is never reached for finite barriers and  $E_B$  is predicted to reach a maximum value at a finite value of QW width and then to fall as the width is reduced still further. These theoretical predictions have been tested by a number of different research groups using GaAs/AlGaAs structures and the work has been reviewed by Cingolani and Ploog [2].  $E_B$  was found to increase from 6 meV in 30 nm QWs to about 15 meV in QWs with widths down to a few nanometres. The Bohr radius,  $a_0$ , for a 2D exciton is defined, as in a shallow impurity, as the average radius of the electron orbit. In 10 nm GaAs/Al<sub>0.4</sub>Ga<sub>0.6</sub>As QWs,  $a_0$  has a value of 12 nm and increases to 15 nm in 20 nm QWs [2].

The 2D excitons are mobile in the plane of the QW and characterized by a wavevector  $\mathbf{k}$  and kinetic energy

$$E_k = \frac{\hbar^2 k^2}{2m^*}. \quad (7.3)$$

They have a band spectrum with a constant density of states similar to that of 2D electrons and holes. If the kinetic energy  $E_k$  exceeds  $E_B$  the excitons become resonant with the continuum of electron and hole states so that high-energy excitons are likely to dissociate into free carriers. Dissociation becomes significant at elevated temperatures  $k_B T \gtrsim E_B$ , so in GaAs/AlGaAs QWs with  $E_B \sim 10$  meV excitons are mostly bound at liquid nitrogen temperatures ( $k_B T \sim 6$  meV) but mostly dissociated at room temperature ( $k_B T \sim 25$  meV) although even at room temperature some excitonic features can still be seen.

The exciton envelope function in a state with wavevector  $\mathbf{k}$  can be written as

$$\Psi_{\mathbf{k}}(\mathbf{r}_e, \mathbf{r}_h) = \exp(i\mathbf{k} \cdot \mathbf{R}_{\parallel}) F(\rho) \varphi_e(z_e) \varphi_h(z_h), \quad (7.4)$$

where  $\mathbf{r}_e, \mathbf{r}_h$  are the electron and hole positions,  $\mathbf{R}_{\parallel}$  is the position of the exciton centre of mass,  $\rho = (\mathbf{r}_e - \mathbf{r}_h)_{\parallel}$  where  $\parallel$  indicates the vector component in the QW plane,  $F(\rho)$  is a function describing the relative electron–hole motion,  $z$  is the growth direction of the structure, and  $\varphi_e(z_e)$  and  $\varphi_h(z_h)$  are the electron and hole wave functions for the first size-quantized level. In the simplest variational approach,

$$F(\rho) = \sqrt{\frac{2}{\pi a_0^2}} \exp\left(-\frac{\rho}{a_0}\right) \quad (7.5)$$

and Eqs (7.4) and (7.5) are used in analysis of the exciton–phonon interaction.

In reality the 2D exciton spectrum is much more complicated than suggested by these expressions and includes excited exciton states. Some of these correspond to the excited hydrogen-like states associated with the first size-quantized levels of the electron and hole [1]. Their binding energies are much smaller than those of the ground state so that their levels lie very close to the electron–hole continuum. They are very difficult to detect in GaAs/AlGaAs QWs and do not play a significant role in the exciton–phonon interaction. Other groups of excited exciton states are associated with excited electron and hole subbands. Many of these states are well defined and have been studied by optical spectroscopy [2]. The first excited exciton band arises from the light hole (*LH*) exciton which is formed by an electron in the first size-quantized level  $E_1$  together with a light hole of energy  $LH_1$ . The binding energy for light hole excitons is almost the same as for heavy hole excitons, although their transport masses are different. The energy separation between light and heavy hole excitons increases with decreasing QW width and closely follows the energy separation between the light and heavy hole states,  $LH_1 - HH_1$ . In 10 nm GaAs/AlGaAs QWs this energy has a value  $\sim 10$  meV. The overlap between heavy and light hole excitons considerably complicates detailed analysis of the exciton spectrum [1].

Up to now we have only been describing free excitons. In real QW structures excitons can bind to impurities or structural defects forming localized exciton states and this leads to an excess exciton binding energy  $E_L$  as can be seen by the horizontal line in

Fig. 7.1. Effects of localization on impurities are readily seen in bulk material but are in fact very difficult to detect in narrow undoped GaAs/AlGaAs QWs. However, the localization effects due to interface defects in QWs are clearly observed at liquid helium temperatures. This strong localization does not occur, however, in wide ( $>5$  nm) high-quality QWs and in this case the excitons may be considered as free quasiparticles. In interpreting experimental results, it is important to take into account the likely degree of localization. For instance, in studies of the interaction of 2D excitons with phonons, the exciton gas may be roughly considered as free if the excess binding energy  $E_L$  of the localized excitons is much smaller than the energy of phonons  $\hbar\omega \gg E_L$ .

The main experimental method used to study 2D excitons is optical spectroscopy, in particular optical absorption and reflection, photoluminescence (PL), and photoluminescence excitation (PLE) techniques. The absorption technique gives valuable information on the spectrum of the exciton states which is usually quite easy to interpret. Its disadvantage, however, is that it is sometimes difficult to separate absorption in the QW from that in the substrate. This could in principle be done by etching off most of the substrate but this turns out to be difficult to do without introducing strains into the QW layer. This problem evidently does not arise in reflection experiments although, in this case, interpretation is sometimes complicated by interference effects [4]. In high-quality QWs absorption and reflection experiments are only sensitive to free excitons because the density of localized states is negligible. The most complete information about the exciton spectrum in QWs is in fact obtained from PL measurements preferably in combination with PLE. Readers interested in optical techniques best adapted to provide information about the dynamical properties of excitons are referred to the book by Henneberger *et al.* [3].

Optical transitions involving exciton states in QWs are governed by selection rules [1]. For example, the requirement that momentum is conserved in interactions between photons and excitons leads to the important conclusion that only excitons with  $k \approx 0$  are optically active. The result of this is that an optical spectrum usually consists of narrow lines at the energies corresponding to the minima of the excitonic bands.

It is useful to mention two more characteristics of optical transitions involving 2D excitons. The first is the increase in oscillator strength caused by 2D confinement [8]. The second is the absence of polariton effects in single QWs. The polariton effects, which are commonly seen in 3D exciton spectra, are due to the strong exciton–photon interaction and important when the wavelength of the coupled exciton–photon excitation (polariton) is bigger than the thickness of the medium in which the polariton is propagating. In the 2D case the thickness of a QW is so small that polariton effects may be neglected.

### 7.1.2 Exciton PL

Exciton PL can be either excited directly or via the electron–hole continuum. Direct or resonant excitation can be difficult technically and is usually only done when it is important that the exciton should be excited instantaneously from the bottom of an exciton band or in order to exclude the influence of free photoexcited carriers [9]. It is much easier in fact to excite the 2D exciton gas (2DExG) by optically creating electron–hole pairs bound to free excitons on a picosecond timescale [10]. By appropriately selecting

the wavelength used for the optical excitation, the electron-hole pairs may either be excited solely in the QWs (under-barrier excitation) or in both the QWs and the barriers (above-barrier excitation). In typical stationary PL experiments, the excitation light is incident close to the normal of the QW plane and the density of optical excitation on the surface of the sample lies in the range of  $I_0 = 10^{-1}$ – $10$  W cm $^{-2}$  leading to an exciton sheet density of less than  $n_s \sim 10^8$ – $10^{10}$  cm $^{-2}$ .

Exciton PL has very high quantum efficiency at low temperatures. Indeed in high-quality GaAs/AlGaAs QW structures the value of the quantum efficiency is thought to be very close to one although it is very difficult to measure absolutely. Because of this high efficiency, the PL signal may be readily detected using standard optical techniques although a high-resolution spectrometer and photon counting registration system is usually preferred. To illustrate the technique and resulting spectrum we describe work on samples grown at the University of Nottingham [11, 12]. The samples were obtained from a wafer containing six GaAs single QWs of different thickness  $w$  (2.5, 5.1, 10.2, 19.5, 29.7, and 39.9 nm) grown on a semi-insulating LEC (001) GaAs substrate of thickness 0.4 mm. The QWs are separated from each other by 20 nm (Al $_{0.33}$ Ga $_{0.67}$ )As barriers. The structures were grown by molecular beam epitaxy at a substrate temperature of 630°C.

The measurements were made in a helium flow cryostat at temperatures  $T_0 \geq 4.5$  K and a CW Ar laser (514 nm) was used to form the 2D exciton gas. The laser beam was focused down to a 100  $\mu$ m spot onto the surface containing the QWs and, by using neutral filters, the intensity could be varied over the range  $I_0 = 1$ – $50$  W cm $^{-2}$  corresponding to exciton sheet densities from  $n_s < 10^9$  cm $^{-2}$  to  $\sim 10^{10}$  cm $^{-2}$ . The PL spectra from the 2DExGs were analysed by a double-grating monochromator which, together with a photomultiplier and photon counting system, provided a spectral resolution of 0.1 meV.

The PL spectra for two lattice temperatures ( $T_0 = 4.5$  and 15 K) and two excitation densities ( $I_0 = 2$  and 20 W cm $^{-2}$ ) are shown in Fig. 7.2. Each spectrum contains several sharp  $H$  lines corresponding to photon energies  $E_H = 1.519, 1.525, 1.550, 1.612,$  and  $1.715$  eV which can readily be attributed to radiative recombination of the heavy hole free exciton in QWs with  $w = 29.7, 19.5, 10.2, 5.1,$  and  $2.5$  nm respectively. The spectral widths of the exciton PL lines for  $T_0 = 4.5$  K are 0.3 meV and 5.4 meV for 29.7 nm and 2.5 nm QWs respectively, which demonstrate that QWs are of high interface quality.

The PL  $L$  lines seen in Fig. 7.2 are due to free excitons associated with light holes. These lines are clearly seen in 29.7 and 19.5 nm QWs at sufficiently elevated temperature and the strong temperature dependence of their intensity indicates that the exciton energy distribution is very sensitive to the number of occupied phonon states. This fact is widely used in experiments using non-equilibrium acoustic phonons (Section 7.3). The low-energy satellites ( $B$  lines) which accompany some free exciton  $H$  lines can also be seen in Fig. 7.2. Their intensity increases superlinearly with  $I_0$  and the lines quench at elevated temperatures (Fig. 7.2). The origin of these  $B$  lines is not completely clear and seems to be sample dependent; in these samples, they could only be seen when the excitation was above-barrier. This appeared to suggest that in these samples the  $B$  lines were associated with excitons localized by defects in the barrier whose charge state is influenced by the above-barrier illumination. In wide QWs, the total PL intensity is almost independent of temperature for  $T_0 < 30$  K but then starts to fall. However, for narrow (2.5 nm) QWs, it starts to decrease at lower temperatures as can be seen from the data in Fig. 7.2.

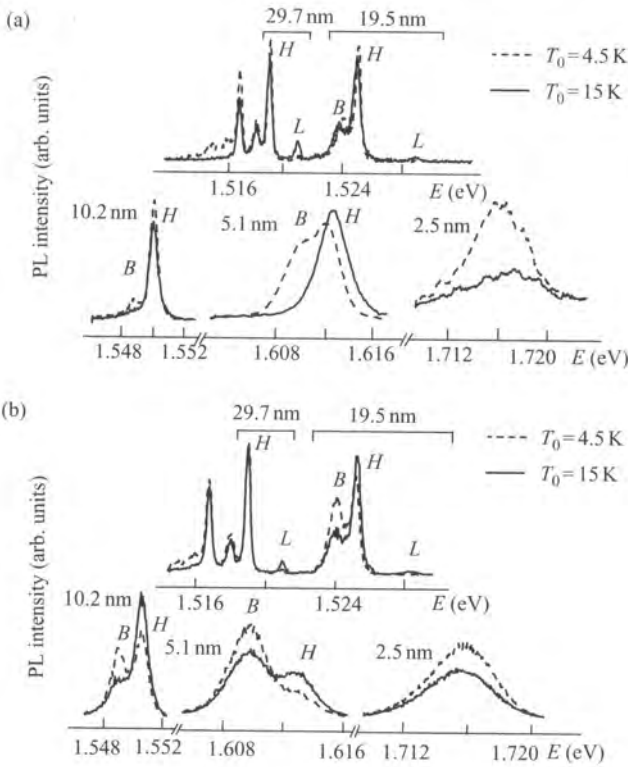


**Fig. 7.2** PL spectra in a series of GaAs/AlGaAs QWs of different thicknesses taken at two lattice temperatures,  $T_0 = 4.5$  K and 15 K. Data are shown for two laser intensities (a)  $I_0 = 2 \text{ W cm}^{-2}$  and (b)  $I_0 = 20 \text{ W cm}^{-2}$ . Luminescence from heavy and light hole free excitons is indicated as *H* and *L* respectively and that from bound excitons by *B* [12].

This behaviour is related to the temperature dependence of the exciton lifetime and will be discussed shortly.

Excitons have a finite lifetime  $\tau_0$  which is governed by both radiative and non-radiative recombination processes. In GaAs QWs, the radiative lifetime for strongly localized excitons has a value  $\tau_R^B \sim 10^{-9}$  s. For free excitons the situation is more complicated and, as a result, has been widely studied experimentally and analysed in some detail. A qualitative appreciation of the process can be readily seen from Fig. 7.3. The wide vertical arrow represents the allowed radiative transitions taking place from excitons with  $k \approx 0$ . If we create an exciton resonantly at the bottom of the exciton band, the exciton will emit a photon in a time  $\tau_R (k = 0) \sim 10^{-11}$  s [13]. Such fast radiative recombinations are described as superradiance phenomena and were first predicted theoretically by Hanamura [14]. Non-resonantly excited excitons first need to reach the bottom of the band in order to emit a photon. This relaxation process requires time so the total radiative lifetime  $\tau_R$  is greater than that of resonantly excited excitons. The interplay between radiative recombination from the bottom of the exciton band and inelastic exciton-phonon transitions governs the temperature dependence of the mean radiative lifetime,  $\tau_R$ , for

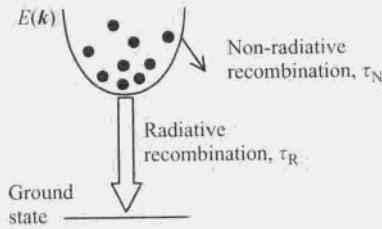


**Fig. 7.3** Diagram demonstrating radiative and non-radiative recombination of excitons. The radiative process is allowed only for excitons with  $k \approx 0$ .

2D exciton gases. Theoretical studies [15, 16] predicted that  $\tau_R$  should increase linearly with temperature and this was later confirmed by experimental work on GaAs/AlGaAs QWs which showed

$$\tau_R = AT_0, \quad (7.6)$$

where  $A$  increases from  $2.2 \times 10^{-11}$  s K $^{-1}$  for 4 nm QWs to  $6.5 \times 10^{-11}$  s K $^{-1}$  for 18 nm QWs [17]. Equation (7.6) is in fact only valid if the excitons are in equilibrium with the lattice at  $T_0$  and, since it also assumes that  $\tau_R(k=0) \ll AT_0$ , it no longer applies at very low temperatures ( $T_0 \lesssim 1$  K).

In analysing exciton kinetics we cannot always neglect the non-radiative channel for exciton recombination characterized by a time  $\tau_N$  (Fig. 7.3). The mechanisms of non-radiative recombination are not yet well understood. There may be multiphonon relaxation or Auger-like processes which involve the defects but it is not known at present which type(s) are of most importance in QW structures. However, it does seem likely that the non-radiative recombination largely takes place in the barriers rather than in the QWs since the barriers are usually of alloy material and so have a much higher density of defects. As a result,  $\tau_N$  will be smaller in narrow QWs because the exciton wave function penetrates deeper into the barrier and it should decrease with increasing  $T_0$  since the depth of penetration should increase with the kinetic energy of the exciton. An additional effect is that localized excitons become free at elevated temperatures and so more easily diffuse towards a defect. In summary, then,  $\tau_N$  should fall with decreasing QW width and increasing temperature.

It can readily be shown that the intensity  $I$  of the free exciton luminescence measured in stationary PL experiments is given by

$$I = \frac{\tau_R^{-1}}{\tau_R^{-1} + \tau_N^{-1}} g, \quad (7.7)$$

where  $g$  is the generation rate of free excitons. In wide QWs,  $\tau_R^{-1} \gg \tau_N^{-1}$  and we enter the limit of high quantum efficiency in which  $I$  does not depend on  $T_0$ . In the opposite limit of narrow QWs,  $\tau_R^{-1} \ll \tau_N^{-1}$  and  $I \propto \tau_R^{-1} \tau_N$  and, since both  $\tau_R^{-1}$  and  $\tau_N$  decrease with increasing  $T_0$ ,  $I$  should also fall as the temperature increases. This then explains the decrease in PL intensity with temperature observed for 2.5 nm QWs (Fig. 7.2), and the absence of similar effects in wider QWs. The temperature quenching of the PL in narrow QWs has been used in studies of the exciton-phonon interaction (Section 7.3.1).

### 7.1.3 Exciton transport

All excitons are mobile quasiparticles but the transport properties of resonantly and non-resonantly excited excitons differ appreciably and require different approaches. Resonant excitation in single QWs leads to coherent transport effects which are of considerable fundamental interest. The reader is referred to the paper by Vledder *et al.* [13] and references therein for further discussion of these processes. Transport of non-resonantly excited excitons in QWs can, however, be considered as a 2D diffusion process with diffusivity  $D$ . The mean scattering time,  $\langle\tau\rangle$ , and mobility,  $\mu$ , may be obtained from measured values of  $D$  using

$$\langle\tau\rangle = \frac{m^*D}{k_B T} \quad (7.8)$$

$$\mu = \frac{eD}{k_B T}, \quad (7.9)$$

where  $m^*$  is a transport exciton mass and  $T$  is the temperature of the 2D exciton gas which is taken to equal the lattice temperature,  $T = T_0$ .

Studies of exciton transport require sophisticated optical techniques and so contrast markedly with those of carrier transport which often only require the passage of electrical current through the device. One of the most comprehensive investigations of exciton transport has been carried out by Hillmer *et al.* [18] who studied GaAs/AlGaAs QWs using time of flight techniques. The devices were optically masked leaving a small unmasked area from which the transient PL signal was detected. A range of masks was used and from the decay times of the signals from each of them it was possible to determine the exciton lifetime  $\tau_0$  and the diffusivity  $D$ . Other optical picosecond pump-probe techniques which have been successfully used to study exciton transport include: an optical transient grating technique [19, 20]; time-resolved, space-imaged Raman spectroscopy [21]; and pump-probe transient reflection [13].

These studies all show that  $D$  decreases rapidly with decreasing QW width. In narrow QWs ( $w =$  several nanometers) and at low temperatures ( $T < 50$  K) it has not been possible to detect exciton transport in GaAs/AlGaAs samples, prepared without interruption of growth at the interface. However, transport has been detected in somewhat wider QWs ( $w = 10$  nm) with  $D \sim 1 \text{ cm}^2 \text{ s}^{-1}$  at  $T \sim 10$  K, which corresponds to  $\mu \sim 10^3 \text{ cm}^2 \text{ V}^{-1} \text{ s}^{-1}$  [18, 20].  $D$  increases with width and, for  $w = 74$  nm and at  $T = 80$  K, the mobility  $\mu \simeq 2 \times 10^4 \text{ cm}^2 \text{ V}^{-1} \text{ s}^{-1}$  is close to that of hole mobilities in QWs [18].

The transport properties of free excitons are governed by the scattering processes. The mean scattering time  $\langle\tau\rangle$  includes two contributions:

$$\langle\tau^{-1}\rangle = \langle\tau_{\text{ph}}^{-1}\rangle + \langle\tau_{\text{e}}^{-1}\rangle, \quad (7.10)$$

where  $\langle\tau_{\text{ph}}^{-1}\rangle$  is the result of inelastic scattering of excitons by phonons and  $\langle\tau_{\text{e}}^{-1}\rangle$  is due to elastic scattering of excitons by defects. Phonon scattering dominates at high exciton temperatures ( $T \gtrsim 100$  K) while defect scattering dominates at low  $T$ . There is at present no well-developed theory to describe the elastic scattering. The main mechanism was assumed to be interface-roughness scattering with  $\langle\tau_{\text{e}}^{-1}\rangle \simeq B\sqrt{T}/w^2$ , where  $B$  is a

temperature-independent constant [20] although experiments [18] showed a somewhat stronger dependence on  $w$ , with  $\mu \propto \langle \tau_e^{-1} \rangle \propto w^{-2.5}$ . The constant  $B$  was estimated by Oberhauser *et al.* [20] to be  $B = 9 \times 10^{-6} \text{ m}^2 \text{ s}^{-1} \text{ K}^{-0.5}$ . Later work by Hillmer *et al.* [22] showed that the low-temperature mobility was significantly greater ( $\mu = 4 \times 10^3 \text{ cm}^2 \text{ V}^{-1} \text{ s}^{-1}$  in 5 nm QWs) and independent of  $T$  in QWs prepared with growth interruption. It is suggested therefore that interface roughness scattering is less important in high-quality growth-interrupted QW samples and that the low-temperature transport properties of these is determined by elastic barrier–alloy–disorder scattering. The exciton–phonon scattering time will be discussed in detail in the next section.

## 7.2 Role of phonons in exciton dynamics

In the previous section it has already been shown that phonons influence a number of properties of excitons. An increase in phonon density induces an increase in the population of excited exciton states and can also lead to quenching of the PL in narrow QWs (Section 7.1.2). Phonons affect the transport properties of excitons, particularly at elevated temperatures when the exciton–phonon scattering rate becomes greater than the scattering rate due to impurities and defects (Section 7.1.2). Phonon interactions with 3D exciton systems can also lead to a number of other interesting effects such as self-trapping [23] and phonon-assisted luminescence [24] but these have not yet been seen in 2D systems so will not be discussed further here. In this section we present the basic equations for the exciton–phonon interaction and give a review of experimental and theoretical studies of the exciton–phonon interaction.

The basic approach used in analysing the 2D exciton–phonon interaction is similar to that used for electrons and holes [25] and, as already noted, does not have the complication of the significant polariton effects that occur in the 3D case [26]. The main differences arise from the fact that: (a) excitons are Bose particles so that Bose–Einstein or frequently Boltzmann statistics are used to describe their equilibrium distribution; (b) since their density is usually low ( $n_s < 10^{10} \text{ cm}^{-2}$ ) and the exciton–exciton interaction is relatively weak, significant departures from thermal equilibrium can occur within the 2D exciton gas so that it is not always possible to define an exciton temperature (see Section 7.3) in the way that is for a degenerate 2D electron gas; (c) excitons have a finite lifetime; (d) exciton interaction with optical phonons results in both scattering and in their dissociation into uncoupled electron–hole pairs.

### 7.2.1 Scattering and relaxation of 2D excitons by acoustic phonons

The exciton–phonon interaction is an inelastic scattering process involving the absorption or emission of a phonon and corresponding changes in the exciton kinetic energy  $E_k$  and wavevector  $k$ . The dependence of the exciton–phonon transition rate on phonon mode and wavevector is more complicated than that of the electron–phonon interaction. Both of course require conservation of energy and momentum but the symmetry of the exciton state depends on the type and excitation state of the exciton, and hence on the particular combination of electron and hole eigenstates. The present discussion will

focus on GaAs/AlGaAs QWs in which the acoustic mismatch between the QW and barrier materials is so small that the acoustic phonons may be considered as 3D.

The two mechanisms responsible for the exciton–phonon interaction are those responsible for acoustic phonon interaction with free carriers: deformation potential (DP) and piezoelectric (PE) coupling. However, the Hamiltonian for exciton–phonon coupling includes phonon interaction with both holes and electrons and, for excitons in GaAs, this increases the matrix element for DP coupling but decreases it for PA coupling in comparison with the corresponding values for free carriers. A third mechanism, the ‘ripple mechanism’, arising from phonon-induced dynamical modulation of the QW width has also been considered theoretically [27, 28]. However there is as yet no experimental evidence that it makes a significant contribution to the interaction.

Detailed theoretical studies of the exciton–phonon interaction in QWs have been made by a number of groups. The first investigation was made by Takagahara [29] in order to understand energy transfer in GaAs/AlGaAs heterostructures. Energy relaxation times of 2D excitons in GaAs QWs were also calculated by Basu and Ray [30]. Calculations made by Vaas [31] for GaAs QWs show that, at temperatures as low as  $T \geq 1$  K, DP coupling dominated PA coupling in single QWs. Thilagan and Singh [32] showed that interaction between 2D excitons via virtual phonon exchange is quite significant in narrow QWs. The electric field dependence of the exciton–phonon interaction in a QW was first studied by Thilagan and Singh [33] and analysis of the dependence of the DP and PA interactions on the phonon polarization (LA, TA) and wavevector has been given by Oh and Singh [34]. It can be seen from this summary that the energy loss rate for 2D excitons in QWs has been calculated in detail by a number of authors and it is of note that the rates obtained differ appreciably. This is partly due to differences in the values assumed for the deformation potential but is also due to the different approximations made in the various treatments. Lee *et al.* [35] used a simplified approach and obtained an analytical expression for the scattering rate of excitons with  $k = 0$  which is often used to analyse the experimental results:

$$\tau_{\text{ph}}^{-1} = B_{\text{ph}} \frac{T_0}{w}, \quad (7.11)$$

where the proportionality factor  $B_{\text{ph}} \simeq 50 \text{ m K}^{-1} \text{ s}^{-1}$  does not depend on  $T_0$  and  $w$ . Because of its simplicity, this expression is often used to obtain approximate values and, for example, at  $T_0 = 10$  K and  $w = 10$  nm, it gives  $\tau_{\text{ph}} \simeq 20$  ps.

In the present section we limit the discussion to a basic treatment of the exciton–phonon DP coupling and refer the reader to the references given above for further details of the interaction. The probability of exciton–phonon transitions taking place within a volume  $V$  is given by Fermi’s golden rule:

$$W_{\mathbf{k} \rightarrow \mathbf{k}'} = \frac{2\pi}{\hbar} \sum_{\mathbf{q}, j} \left| M_{\mathbf{k} \rightarrow \mathbf{k}'}^{\mathbf{q}, j} \right|^2 \left( N_{\mathbf{q}, j} + \frac{1 \pm 1}{2} \right) \delta(E_{\mathbf{k}'} - E_{\mathbf{k}} \pm \hbar\omega(\mathbf{q}, j)), \quad (7.12)$$

where  $M_{\mathbf{k} \rightarrow \mathbf{k}'}^{\mathbf{q}, j}$  is the matrix element of the  $\mathbf{k} \rightarrow \mathbf{k}'$  transition involving emission (+) or absorption (–) of an acoustic phonon with polarization  $j = \text{LA, TA}$ , wavevector  $\mathbf{q}$ , and

frequency  $\omega(\mathbf{q}, j) = s_j q$ ;  $s_j$  is the sound velocity, and  $N_{\mathbf{q}, j}$  are the phonon occupation numbers which, in equilibrium, are given by the Bose-Einstein distribution:

$$N_{\mathbf{q}, j} = \left[ \exp\left(\frac{\hbar\omega}{kT_0}\right) - 1 \right]^{-1}, \quad (7.13)$$

where  $T_0$  is the lattice temperature.

The DP interaction Hamiltonian for creation (annihilation) of an acoustic phonon of wavevector  $\mathbf{q}$  and mode  $j$  can be written as

$$\begin{aligned} H_{\text{ex-ph}}^{\text{DP}} &= H_{\text{e-ph}}^{\text{DP}} + H_{\text{h-ph}}^{\text{DP}} \\ &= \sqrt{\frac{\hbar}{2\rho_0\Omega s_j q}} i q \left[ \Xi_e \exp(\mp i \mathbf{q} \cdot \mathbf{r}_e) + \Xi_h \exp(\mp i \mathbf{q} \cdot \mathbf{r}_h) \right], \end{aligned} \quad (7.14)$$

where  $\Xi_e$ ,  $\Xi_h$  are the electron and hole DP constants,  $\rho_0$  is the material density,  $\Omega$  is the volume, and we note that the DP Hamiltonian for holes is anisotropic:

$$H_{\text{h-ph}}^{\text{DP}} = \left( a + \frac{b}{2} \right) (u_{xx} + u_{yy}) + (a - b) u_{zz}, \quad (7.15)$$

where  $a$  and  $b$  are constants and the diagonal components of the deformation tensor are

$$u_{\alpha\alpha} = \sqrt{\frac{\hbar}{2\rho_0\Omega s_j q}} i \mathbf{e}_\alpha^{(q,j)} q_\alpha \exp(\mp i \mathbf{q} \cdot \mathbf{r}_h),$$

where  $\mathbf{e}^{(q,j)}$  is the polarization unit vector. Hence  $\Xi_h$  in Eq. (7.14) is a function of the angle between  $\mathbf{q}$  and the plane of the QW:

$$\Xi_h(\mathbf{q}) = \begin{cases} a + \frac{b}{2} - \frac{3}{2}b \left( \frac{q_z}{q} \right)^2 \\ -\frac{3}{2}b \left( \frac{q_z q_{\parallel}}{q^2} \right). \end{cases} \quad (7.16)$$

If we assume crystalline isotropy, the conduction electrons only interact with LA phonons and  $\Xi_e$  vanishes for TA modes. The signs of  $\Xi_e$ ,  $a$ , and  $b$  differ in various reference sources due to different definitions and thus care must be taken using Eqs (7.14), (7.15), and (7.16). For example, for GaAs, the values for  $\Xi_e$ ,  $a$ , and  $b$  should be taken with the same signs.

The matrix elements can be calculated using the exciton wave functions given in Eq. (7.4):

$$M_{\mathbf{k} \rightarrow \mathbf{k}'}^{q,j} = \langle \Psi_{\mathbf{k}} | H_{\text{ex-ph}} | \Psi_{\mathbf{k}'} \rangle \quad (7.17)$$

and substituting into Eq. (7.12) we obtain the expression for the transition probability

$$W_{\mathbf{k} \rightarrow \mathbf{k}'}^{\text{DP}} = \frac{\Xi^2(\mathbf{q})}{\hbar \rho_0 S_0 s_j^2} \left( N_{s_j q} + \frac{1 \pm 1}{2} \right) \frac{q^2}{q_z} \Theta(q - q_{\parallel}), \quad (7.18)$$

where energy and momentum conservation require

$$q = \frac{\hbar}{2m^*s_j} |k^2 - k'^2|, \quad q_{\parallel} = |\mathbf{k} - \mathbf{k}'|, \quad q_z = \sqrt{q^2 - q_{\parallel}^2} \quad (7.19)$$

and  $S_0$  is the sample area.  $\Theta(x)$  is the Heaviside step-function:

$$\Theta(x) = \begin{cases} 1, & x \geq 0, \\ 0, & x < 0. \end{cases}$$

The effective exciton DP constant is given by

$$\Xi(\mathbf{q}) = \frac{\Xi_e Z_e(q_z)}{\left[1 + \left(\frac{m_h^*}{2m^*} q_{\parallel} a_0\right)^2\right]^{3/2}} + \frac{\Xi_h(\mathbf{q}) Z_h(q_z)}{\left[1 + \left(\frac{m_e^*}{2m^*} q_{\parallel} a_0\right)^2\right]^{3/2}}, \quad (7.20)$$

$Z_{e,h}$  are the overlap integrals or form factors defined as

$$Z_{e,h}(q_z) = \int_{-\infty}^{\infty} dz \varphi_{e,h}^2(z) \exp(iq_z z), \quad (7.21)$$

and  $m_e^*$ ,  $m_h^*$  are the electron and hole effective masses. If we use the approximation that the QW barriers are infinitely high

$$Z_e(q_z) = Z_h(q_z) = \frac{\sin(q_z w/2)}{(q_z w/2) [1 - (q_z w/2\pi)^2]}, \quad (7.22)$$

where, as before,  $w$  is the QW width.

Equation (7.18) gives the probability of a phonon-induced exciton transition  $\mathbf{k} \rightarrow \mathbf{k}'$  but present transport and optical techniques can only measure quantities related to this probability and integrated over many transitions. For example, a quantity that is often measured is the scattering time  $\tau_{\text{ph}}$  of a thermalized ensemble of excitons. Lee *et al.* [35] determined this quantity from the temperature dependence of the luminescence linewidth and, in a similar approach by Schultheis *et al.* [36], it was obtained from the temperature dependence of the dephasing time of the exciton resonance. Hillmer *et al.* [18] and Oberhauser *et al.* [20] determined  $\tau_{\text{ph}}$  from studies of exciton diffusion (see Eq. (7.8)) and Damen *et al.* [37] measured the temporal evolution of the exciton luminescence and obtained  $\tau_{\text{ph}}$  from an analysis of the rise time ( $\tau \approx 30$  ps). The results of these experiments agree qualitatively with the theoretical studies and the values obtained for  $\tau_{\text{ph}}$  can be roughly described by Eq. (7.11).

These experimental studies were aimed at obtaining values of the exciton scattering rate and relaxation time but provide little information on specific features of the exciton–phonon interaction like the selection rules (Eq. (7.19)) and form factor (Eq. (7.21)) which distinguish the 2D case from the exciton–phonon interaction in bulk material. This information can be more readily obtained from experiments with non-equilibrium acoustic phonons which will be described in Section 7.3.

### 7.2.2 Phonon wind effect on excitons

Since momentum is conserved in exciton-phonon interactions, an exciton gas may acquire momentum-exciton drag if the distribution of phonons with which it is interacting has an anisotropic momentum distribution. This phenomenon, which is well known for carriers in 3D and 2D semiconductors, is called the phonon wind effect. Experiments where the phonon wind (drag) effect plays an important role are described in Chapters 2, 3, and 5. The simplest case is the drag of quasiparticles caused by a flux of non-equilibrium acoustic phonons. Phonon momentum is transferred to the quasiparticles, which start drifting in the direction of the phonon flux. The most widely studied example for neutral quasiparticles is of exciton droplets in bulk Ge [38] and the drag effect has also been studied directly by imaging the exciton-droplet cloud [39]. Because of their diffusion and finite lifetime, the effect is less pronounced for free excitons than for exciton droplets but it has been seen in Ge [40], CdS [41], and Si [42]. A comprehensive review of the experiments and theory of the drag effect in optically excited 3D semiconductors has been given by Keldysh and Sibeldin [43]. In 2D semiconductor structures, the phonon wind effect is thought to be one of the factors inhibiting the Bose condensation of 2D excitons that should occur at high densities. The excitation of a high-density exciton gas is accompanied by the creation of non-equilibrium phonons. These propagate into the 'cold' part of the sample dragging the excitons with them and hence causing the exciton cloud to expand and so reduce its density.

Despite the importance of the effect this illustrates, the phonon wind effect has not been yet been studied in detail in 2D. However, the following experiment demonstrates qualitatively its role on the exciton dynamics in QWs. In conventionally grown GaAs QWs, the lateral motion of excitons is difficult to detect directly because the typical diffusion length of free excitons is only  $\sim 1 \mu\text{m}$ . To overcome this problem, Moskalenko *et al.* [44] used GaAs QWs in which the growth was interrupted to allow atoms to redistribute in the plane of the interface. The most noteworthy feature of these QWs is the presence of large flat islands where the QW has an additional thickness of one monolayer which are separated by several micrometres [45]. The shift in the PL line resulting from this additional thickness makes it possible to detect optically the density of the excitons in different islands and thus to monitor the motion of excitons from one island to another. This gives the possibility of studying the phonon wind effect on excitons in GaAs QWs.

The experimental arrangement is shown in Fig. 7.4. The sample consisting of a 10 nm GaAs/Al<sub>0.33</sub>Ga<sub>0.67</sub>As QW structure grown on a 0.4 mm semi-insulating GaAs substrate is mounted in a helium flow cryostat whose temperature could be varied above 4.5 K. A phonon generator (h) consisting of a  $1.5 \times 1 \text{ mm}^2$ , 20 nm thick constantan film is evaporated on the polished side of the substrate opposite the QWs. The QWs are illuminated by a laser beam focused to a  $100 \mu\text{m}$  spot which creates a 2D exciton gas of sheet density  $n_s$  up to  $10^{10} \text{ cm}^{-2}$ . The constantan film is heated by 200 ns current pulses producing pulses of non-equilibrium phonons which propagate through the substrate and strike the excitons. Phonon-induced changes in the exciton luminescence are observed and found to depend strongly on the mean angle of incidence of the phonons on the 2D exciton gas; this could be varied by moving the laser-illuminated area relative to the heater.

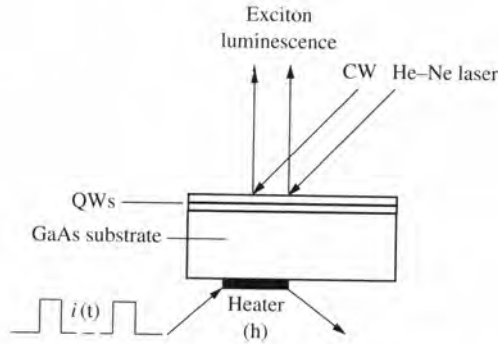


**Fig. 7.4** Experimental arrangement used for phonon wind experiments.

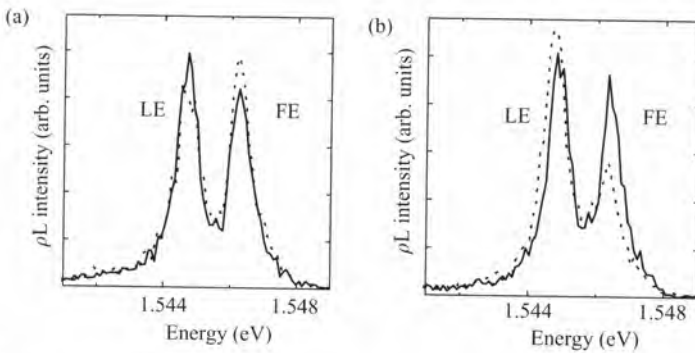


**Fig. 7.5** PL spectra in a 10 nm GaAs/Al<sub>0.33</sub>Ga<sub>0.67</sub>As QW measured in the absence (solid lines) and in the presence (dashed lines) of non-equilibrium phonons. Spectral lines corresponding to free and ‘localized’ excitons are indicated as FE and LE respectively: (a) laser spot located opposite the heater and phonon wind on 2D excitons does not occur; (b) laser spot is shifted to one side of the heater to produce a phonon wind [44].

The solid lines in Fig. 7.5 show luminescence spectra for  $n_s \sim 10^{10} \text{ cm}^{-2}$  and a bath temperature of 4.5 K and are typical for high values of  $n_s$ . Figure 7.5(a) shows data with the laser spot opposite the heater and (b) with it shifted to one side. The solid lines, which show the spectra in the absence of non-equilibrium phonons, are essentially independent of the position of the illuminated area as expected. The lines at 1.5444 and 1.5460 eV are readily attributable to excitons in QWs differing in thickness by one monolayer. The higher energy line is evidently from free excitons (FEs) in the thinner parts of the QWs while the lower energy line is due to so-called ‘localized’ excitons (LEs) in the microscopic islands which are thicker by one monolayer [45]. The sharpness of the sharp LE line shows that the islands have lateral sizes greater than the exciton Bohr radius.

The dashed lines in Fig. 7.5 show the effect of the phonon pulses; the PL was measured during a 500 ns interval gated to coincide with the arrival and duration of the phonon pulse. It can be seen that the effect of the phonon pulses is very different in Fig. 7.5(a) and (b). In Fig. 7.5(a) for phonons incident near to the normal, the intensity from the

LEs falls while that of FEs rises. However, exactly the opposite occurs when phonons are incident obliquely (Fig. 7.5(b)).

Since the area of the islands is only a small fraction of the total it seems probable that most of the excitons are generated in the main (thin) part of the QW and the relatively large population of the lower energy LEs is the result of capture from the diffusing FEs. The efficiency of this FE  $\rightarrow$  LE capture depends on the ratio of the mean distance  $L_i$  between islands and the diffusion length of the FEs,  $L_d = (D\tau_0)$ , where  $D$  is the diffusion coefficient and  $\tau_0$  is the lifetime of the FEs. A pulse of normally incident phonons evidently excites excitons from the lower energy LE states in the islands to the higher energy FE states outside. This process also occurs if the bath temperature is raised. It is clear, however, that when the same phonons are incident obliquely another more effective process takes place. The phonons now have momentum parallel to the plane of the QW and the transfer of momentum to the excitons by the phonon wind effectively enhances the FE diffusion rate and so increases the probability of FE capture in the island regions. This process is clearly more effective than LE excitation since it leads to a decrease in the FE population and a corresponding increase in that of the LEs.

The main problem in studying the phonon wind effect on excitons in QWs is the control of the morphology of the semiconductor structures used in the experiments. The experiments described above provide qualitative evidence that the phonon wind effect is present but detailed studies of this interesting phenomenon have still to be done.

### 7.2.3 Role of optic phonons in exciton dynamics

In polar semiconductors like GaAs, excitons are coupled to optic phonons through the Fröhlich interaction and the resulting matrix elements are appreciably greater than those for acoustic phonons. However, because of their high energy ( $\hbar\omega_{LO} = 34$  meV in GaAs), the role of optic phonons in exciton dynamics is relatively unimportant at low temperatures and, since the exciton binding energy  $E_B \ll \hbar\omega_{LO}$ , very few excitons exist at high temperatures ( $k_B T \gtrsim \hbar\omega_{LO}$ ) where the optic phonon population is much greater. But there is an interval of intermediate temperatures ( $100 \text{ K} < T < 200 \text{ K}$ ) in which excitons can still be observed in GaAs/AlGaAs QWs and the population of optic phonons is sufficient to influence their dynamics.

The influence of optic phonons on the luminescence linewidths of GaAs QWs was first studied by Lee *et al.* [35] both experimentally and theoretically. Their calculations show that for heavy hole excitons the contribution to the PL width from optical phonons becomes equal to that from acoustic phonons at  $T = 200$  K. For light hole excitons this happens at even higher temperatures. The effect of optic phonons on the exciton diffusion was analysed by Hillmer *et al.* [18] who showed that it was greatest in wide QWs. Thus in 15 nm QWs the exciton mobility from optic phonon scattering becomes equal to that from acoustic phonon scattering at  $T \approx 150$  K, while in 4 nm QWs this does not happen until  $T \approx 200$  K. So quantum confinement produces a relative decrease in optic phonon scattering, or, in other words, acoustic phonons are more dominant in exciton scattering in QWs than in bulk material.

Optic phonons can, however, play an important role in the relaxation of hot excitons at all temperatures. Peaks are often seen in the excitation spectrum of exciton luminescence at photon energies equal to  $E(k=0) + p\hbar\omega_{LO}$ , where  $E(k=0)$  is the energy at the

bottom of the exciton band and  $p$  is an integer. This indicates the formation of hot excitons with kinetic energy much larger than  $E_B$  which relax rapidly by emitting LO phonons and this relaxation process essentially determines the lifetime of hot excitons. This effect is well known for bulk II–VI semiconductors and can also be seen in resonant Raman scattering [46]. The creation of hot excitons and their relaxation by LO phonon emission in confined structures was first demonstrated in II–VI QWs [47, 48] but has not been seen in GaAs QWs. Blom *et al.* [49] measured the dependence of the PL exciton rise time on the optical excitation energy in thin ( $w = 2.6$  nm) GaAs/AlGaAs QWs and showed that LO phonons are involved in the formation of excitons but through the relaxation of hot carriers rather than of excitons. The role of LO phonons in exciton formation in GaAs QWs has been studied theoretically by Oh *et al.* [50]. They derived an expression for the rate of formation of an exciton as a function of carrier density, temperature, and the wavevector of the exciton centre of mass and showed that the rate was greatest at non-zero exciton wavevectors.

### 7.3 Heating of 2D exciton gas by non-equilibrium acoustic phonons

In this section we shall show that quantum confinement of excitons in QWs strongly influences their energy distribution in the presence of non-equilibrium phonons. The effect of non-equilibrium phonons on their energy distribution can be understood in terms of the selection rules and the effect of confinement (Eq. (7.19)) together with the form factor (Eq. (7.21)) of the exciton–phonon matrix element (Eq. (7.17)). In Section 7.3.1 we present the results of experiments investigating the effect of heating a 2DExG by non-equilibrium phonons which clearly reveals the distinctive features of the exciton–phonon interaction associated with the lowering of the dimensions [11, 12]. In Section 7.3.2, we show that the qualitative conclusions of this work is supported by theoretical analysis [51, 52].

#### 7.3.1 Effect of non-equilibrium phonons on exciton luminescence in GaAs/AlGaAs QWs (experiment)

The experimental arrangement is shown in Fig. 7.6. The samples were those described in Section 7.1.2 and their PL spectrum at two temperatures and two excitation powers is shown in Fig. 7.2. Non-equilibrium phonons are produced by electrically pulse heating, to temperature  $T_h$ , a thin constantan film,  $h$ , at the surface of the GaAs substrate opposite the GaAs/AlGaAs QWs. The bath temperature  $T_0 = 4.5$  K. Low-energy phonons,  $\hbar\omega < 2\text{--}4$  meV, propagate through the substrate ballistically and those with phonon wavevectors  $\mathbf{q}$  within an angle  $\vartheta_{\max}$  defined by the geometry (see Fig. 7.6) are incident on the 2DExG created in the QWs by laser illumination. Higher energy phonons,  $\hbar\omega \gtrsim 2\text{--}4$  meV, are very unlikely to reach the 2DExG ballistically because of the strong scattering in the GaAs substrate [53]. The cut-off energy,  $\hbar\omega = 2\text{--}4$  meV, between ballistic and diffusive propagation depends on the thickness and quality of the substrate [53, 54].

Qualitatively, the transient effect of non-equilibrium phonons on the exciton PL is expected to be similar to that of a temperature rise (see Section 7.1.2) suggesting that

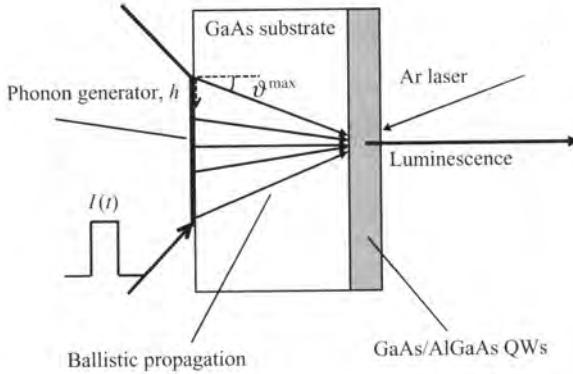


Fig. 7.6 Scheme of experiment with non-equilibrium phonons.

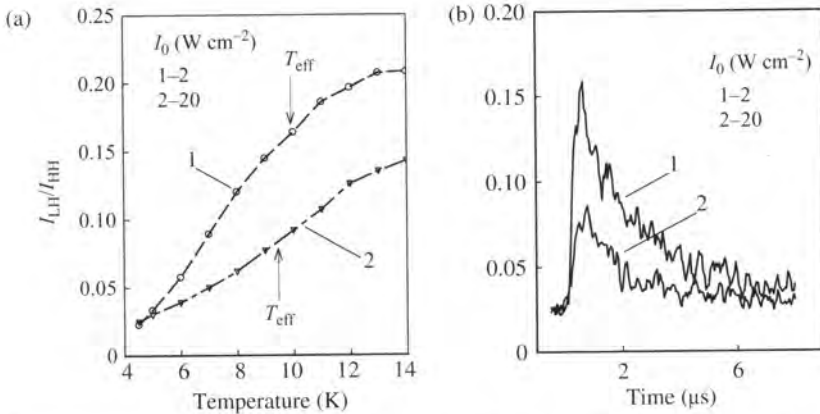
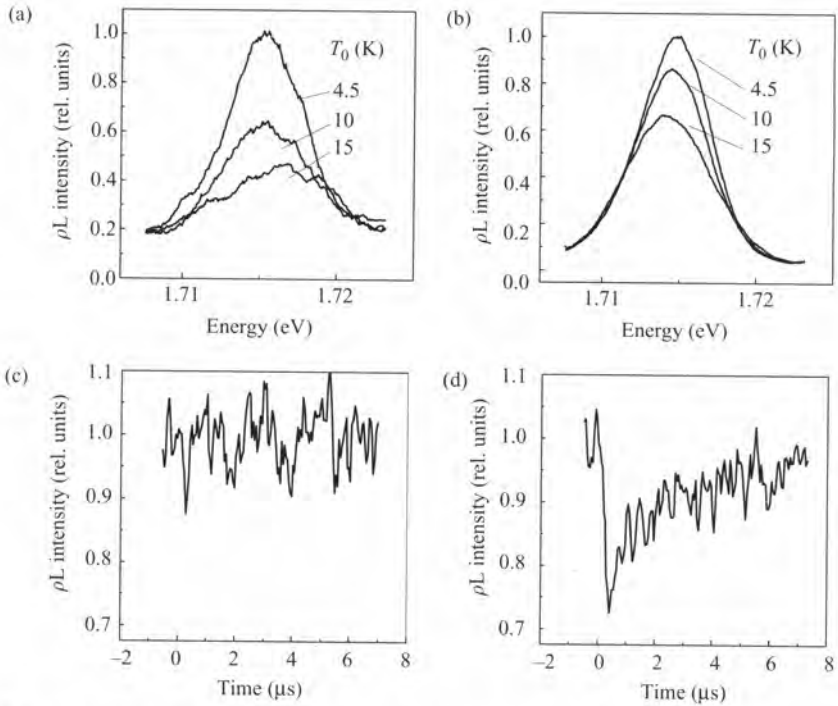


Fig. 7.7 The ratio of  $I_{\text{LH}}/I_{\text{HH}}$  of PL intensities from light hole and heavy hole excitons in a 29.7 nm GaAs/AlGaAs QW for two laser intensities  $I_0$ : the temperature dependence of the ratio measured in thermal equilibrium and (b) the time dependence of the ratio following a  $0.5 \mu\text{s}$  phonon pulse. The vertical arrows in (a) show the maximum effective temperature of the 2DExG,  $T_{\text{eff}}$ , following the phonon pulse [12].

an effective non-equilibrium phonon temperature  $T_{\text{eff}}$  can be defined from the equilibrium temperature that produces the same change in PL. Figure 7.7 shows an example of this approach for a 29.7 nm QW. Figure 7.7(a) shows the equilibrium temperature dependence of the ratio of the PL intensities for light (LH) and heavy hole (HH) excitons and Fig. 7.7(b) shows the time evolution of the same ratio induced by non-equilibrium phonons; the data are shown for two excitation densities. It can be seen that the maximum values of the ratio in Fig. 7.7(b) correspond to the temperatures  $T_{\text{eff}}$  shown by the vertical arrows in Fig. 7.7(a). A similar approach was used for a 19.5 nm QW. However, it is not possible to use this technique for narrow QWs since the LH-FE splitting is too large and thermal quenching of PL is used instead. As noted earlier, this quenching is due to the non-radiative exciton recombination that becomes increasingly important as



**Fig. 7.8** Equilibrium PL spectra ((a) and (b)) and the time dependences of phonon-induced PL changes ((c) and (d)) in a 2.5 nm GaAs/AlGaAs QW: ((a) and (c)) laser intensity  $I_0 = 2 \text{ W cm}^{-2}$ ; ((b) and (d))  $I_0 = 20 \text{ W cm}^{-2}$ . From comparison equilibrium ((a) and (b)) and non-equilibrium ((c) and (d), respectively) data an effective temperature,  $T_{\text{eff}}$ , in the presence of phonon pulse is obtained [12].

the temperature is raised (see Section 7.1.2). An example for a 2.5 nm QW is given in Fig. 7.8 for low, (a) and (c), and high, (b) and (d), excitation densities. The upper curves show the temperature dependence of the PL and the lower curves show the time evolution of the non-equilibrium phonon-induced signals. As before,  $T_{\text{eff}}$  is obtained by comparing the maximum change produced by non-equilibrium phonons with the changes produced by increasing the temperature.

Values for  $T_{\text{eff}}$  obtained in this way for a particular value of heater temperature are shown in Table 7.1 together with calculated values (see Section 7.3.2). It can be seen that  $T_{\text{eff}}$  depends significantly on both the QW width and the 2DExG sheet density,  $n_s$ . The dependence of  $T_{\text{eff}}$  on  $n_s$  is particularly strong for the narrowest QW ( $w = 2.5 \text{ nm}$ ) falling from 12.5 K at  $\sim 10^{10} \text{ cm}^{-2}$  to  $< 6 \text{ K}$  at  $n_s \sim 10^9 \text{ cm}^{-2}$ . This dependence of  $T_{\text{eff}}$  on both  $w$  and  $n_s$  indicates clearly that the 2DExG is not operating as a bolometric detector of non-equilibrium phonons but rather that the heating of the 2DExG is determined by the selection rules for exciton–phonon transitions. These rules, together with the fixed spectrum of the non-equilibrium phonons, determine the value of  $T_{\text{eff}}$  and its dependence on  $w$  and  $n_s$ .

**Table 7.1** Calculated and experimental  $T_{\text{eff}}(\text{K})$  for QWs of different thickness, obtained in the limit of high and low  $n_s$ 

$d$ (nm)		29.7	19.5	2.5
$E_{LH}$ (meV)		1.9	4.1	
High $n_s$	LA	7.3	8.6	9
	TA	9.1	10.1	10.3
	exp.	9.5	10.5	12.5
Low $n_s$	LA	8.2	7.7	
	TA	9.4	9.5	
	exp.	9.5	9.5	<6

### 7.3.2 Energy distribution of excitons in the presence of non-equilibrium phonons

To understand these results, Golub *et al.* [51] and later Scherbakov and Akimov [52] analysed the energy distribution function  $f(E)$  of a 2DExG in the presence of non-equilibrium phonons to investigate how it, and hence  $T_{\text{eff}}$ , depend on  $w$  and  $n_s$ . An analysis of  $f(E)$  is also of practical importance in seeing how semiconductor structures could be used as phonon spectrometers. When the exciton lifetime  $\tau_R$  (see Section 7.1.2) is much longer than the exciton-phonon scattering time  $\tau_{\text{ph}}$  (see Section 7.2), which is the case for GaAs QWs at  $T \geq 10$  K, the 2DExG is in equilibrium with the non-equilibrium phonons and exciton creation and radiative recombination can be neglected. At low excitation densities, exciton-exciton interaction processes can also be neglected and the kinetic equation can be written

$$\sum_{k'} [W_{k' \rightarrow k} f(E_{k'}) - W_{k \rightarrow k'} f(E_k)] = 0, \quad (7.23)$$

where  $k$  is the exciton wavevector in the QW plane and  $E_k$  is the exciton kinetic energy (Eq. (7.3)). The probability  $W_{k \rightarrow k'}$  for the  $k \rightarrow k'$  exciton-phonon transition is given by Eq. (7.18) and so does not include piezoelectric coupling (Section 7.2.1).

We next consider the case of high excitation densities. We can no longer neglect the exciton-exciton interaction processes so the kinetic equation for  $f(E_k)$  cannot be written in the form of Eq. (7.23). However, if the probability of exciton-exciton collisions is much greater than that of exciton-phonon relaxation, the 2DExG is in thermal equilibrium at an effective temperature  $T_{\text{eff}}$  and  $f(E_k)$  can be written as

$$f(E_k) = \exp\left(-\frac{E_k}{k_B T_{\text{eff}}}\right) \quad (7.24)$$

and since, in equilibrium, the power absorbed from the non-equilibrium phonons must equal that emitted, the equation for  $f(E_k)$  becomes

$$\sum_{k, q, j} f(E_k) \hbar s_j q W_{k \rightarrow k'}^+ f(E_k) = \sum_{k, q, j} f(E_k) \hbar s_j q W_{k \rightarrow k'}^- f(E_k), \quad (7.25)$$

where  $W_{k \rightarrow k'}^+$  and  $W_{k \rightarrow k'}^-$  are the probabilities of phonon absorption and emission respectively. The solution of this equation gives the effective temperature  $T_{\text{eff}}$ .

The calculations were carried out separately for the TA (DP mechanism) and LA phonons emitted by a heater at temperature  $T_h$ . The phonon occupation numbers are given by

$$N_{q,j} = \left\{ \exp \left[ \frac{\hbar s_j q}{k_B T(\mathbf{q})} \right] - 1 \right\}^{-1}. \quad (7.26)$$

It was assumed that phonon scattering in the substrate leads to a cut-off in the incident spectrum at  $\omega_0$  so that, for  $\omega < \omega_0$ ,  $T(\mathbf{q}) = T_h$  for  $n\pi - \vartheta^{\text{max}} < \vartheta < n\pi + \vartheta^{\text{max}}$  ( $n = 0, 1$ ;  $n = 1$  allows for specular reflection from the upper surface of the QWs) and  $T(\mathbf{q}) = T_0$  ( $T_0$  is the bath temperature), and for  $\omega > \omega_0$ ,  $T(\mathbf{q}) = T_0$  at all other angles. To reflect the experimental conditions (see Section 7.3.1), the calculations were carried out for  $T_h = 12$  K,  $T_0 = 4.5$  K, and  $\vartheta^{\text{max}} = 45$  degrees and for  $m_c^* = 0.067m_e$ ,  $m_h^* = 0.15m_e$  ( $m_e$  is the free electron mass),  $a_0 = 10$  nm,  $\Xi_e = 7.3$  eV,  $a = 6.7$  eV,  $b = 2$  eV,  $s_{\text{LA}} = 5 \times 10^3$  m s<sup>-1</sup>, and  $s_{\text{TA}} = 3 \times 10^3$  m s<sup>-1</sup>.

We first discuss the values of  $f(E)$  obtained at low  $n_s$  which are given in Fig. 7.9 for QWs of different thickness. Figure 7.9(a) assumes that all phonons leaving the heater travel ballistically so only includes the angular dependence of  $N_q$  and omits a cut-off in the phonon energy spectrum at  $\omega_0$  ( $\hbar\omega_0 \gg k_B T_h$ ). The calculations show that for wide QWs,  $f(E)$  falls well below the equilibrium Boltzmann distribution (dashed line) but steadily approaches it as  $w$  decreases and lies very close to it for  $w = 2.5$  nm. This behaviour is attributable to the angular dependence of the matrix element for the exciton–phonon interaction, Eq. (7.16). Energy and momentum conservation require  $q_{\parallel} < 2k$  to be satisfied in the 2DExG plane and the effect of the overlap integral, Eq. (7.21), in the direction perpendicular to the 2DExG plane is to limit the interaction primarily to phonons with  $q_z < \pi/w$ . For thin QWs,  $2k \ll \pi/w$ , and the exciton–phonon matrix element becomes strongly anisotropic; this behaviour is similar to that of the electron–phonon interaction. So  $f(E)$  is dominated by the absorption and emission of phonons whose wavevectors  $\mathbf{q}$  lie close to the normal to the 2DExG plane and is barely affected by the absence of phonons from  $h$  with  $\vartheta > \vartheta^{\text{max}}$  as a result of the experimental geometry. Hence in thin QWs, the heating of the 2DExG in the experiments should be the same as if it were located very close to  $h$ , which explains why  $f(E)$  approaches the equilibrium function. For thick QWs,  $2k \sim \pi/w$ , and the transition probability is much less anisotropic (at least for LA phonons) than it is for thin QWs. This means that the 2DExG interaction is only weakly dependent on the incident angle of the phonons (with the exception of  $\vartheta = 0$  where it vanishes). So since the experimental geometry means that phonon absorption can only take place within angles  $-\vartheta^{\text{max}} < \vartheta < \vartheta^{\text{max}}$  and  $\pi - \vartheta^{\text{max}} < \vartheta < \pi + \vartheta^{\text{max}}$ , whereas emission can occur at all angles, the 2DExG heating is less effective in thick QWs.

Figure 7.9(b) shows the results of calculations made including a high-energy cut-off in  $N_q$  at  $\hbar\omega_0 = 2$  meV. For thick QWs, this has little effect on  $f(E)$  (compare curve 4 in Fig. 7.9(a) with curve 3 in Fig. 7.9(b)) but it becomes significant as  $w$  decreases and this is attributable to the dependence of the overlap integral Eq. (7.21) on  $w$ . As already noted, the exciton–phonon interaction is only effective when  $q_z < \pi/w$  so that few phonons with  $\omega > s_j \pi/w$  can induce exciton transitions. So if  $\omega_0 > s_j \pi/w$  (as it is for

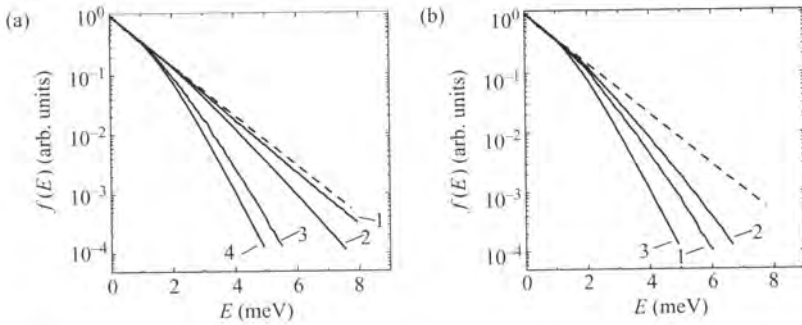


**Fig. 7.9** The energy distribution of excitons interacting with non-equilibrium LA phonons calculated for QWs of different thicknesses: (a) neglecting the high-energy cut-off,  $w$  (nm): 1, 2.5; 2, 10.0; 3, 20.0; 4, 30.0; (b) including a high-energy cut-off  $\hbar\omega_0 = 2$  meV,  $w$  (nm): 1, 2.5; 2, 10.0; 3, 30.0. The dashed line shows an equilibrium Boltzmann distribution at  $T = 12$  K [52].

thick QWs), the 2DExG is heated as if there were no high-energy cut-off in the spectrum of non-equilibrium phonons, and  $f(E)$  is not affected by the cut-off. But for thin QWs, transitions resulting in phonon emission occur at frequencies up to  $\omega \sim s_j\pi/w$ , whereas those involving phonon absorption only occur up to  $\omega = \omega_0 < s_j\pi/w$  because of the cut-off. So at energies  $E > \hbar\omega_0$ , the heating of 2DExGs in thin QWs is less effective than it is in thick QWs. This effect is particularly pronounced for an isotropic  $N_q$  distribution [51].

The results of calculations made for high  $n_s$  are given in Table 7.1 and show that now  $T_{\text{eff}}$  increases with decreasing  $w$ . A qualitative explanation of this effect is similar to that proposed for the case of low  $n_s$  and is related to the dependence of the matrix element of the exciton–phonon interaction on the angle of incidence. The results of numerical calculations are in good agreement with experimental data (Section 7.3.1) although the experimental values of  $T_{\text{eff}}$  lie closer to the values calculated for TA phonons. For low  $n_s$ , it was found that  $f(E)$  cannot be described by a single temperature, so in comparing the calculations with the experiment, it is necessary to look rather carefully at the way in which  $T_{\text{eff}}$  is determined in the experiments. For thick QWs,  $T_{\text{eff}}$  is derived from a comparison of the luminescence intensity ratios for LH and HH excitons. Due to elastic and exciton–phonon transitions between HH and LH free excitons it is reasonable to assume that the LH luminescence intensity directly reflects the value of  $f(E)$  for HH excitons at  $E = E_{\text{LH}}$  ( $E_{\text{LH}}$ , the energy gap between the LH and HH exciton lines, is given in Table 7.1 for thick QWs). Then  $T_{\text{eff}}$  can be calculated from the expression

$$T_{\text{eff}} = -\frac{E_{\text{LH}}}{k_{\text{B}} \ln(f(E_{\text{LH}})/f(0))}. \quad (7.27)$$

Finally we note that the fact that any heating of 2DExGs in QWs with  $w = 2.5$  nm (Section 7.3.1) at low  $n_s$  was too small to measure appears to be particularly interesting and could not be explained by theory. This might suggest that exciton localization effects become important in this limit and it would be interesting to extend the theory to include this possibility.

## 7.4 Acoustic phonon-assisted tunnelling in double QWs

In this section we consider exciton–phonon transitions accompanied by exciton tunnelling. As a model system we take a double QW (DQW) which is one of the simplest semiconductor structures in which carriers and excitons can tunnel through a thin barrier. We first (Section 7.4.1) describe the exciton energy-level system in a DQW and give an example of its luminescence spectrum. In Section 7.4.2 we present experimental results which provide information about the energy relaxation rate between the different exciton states. Finally in Section 7.4.3 we discuss the mechanisms of energy relaxation which involve both exciton tunnelling and exciton–phonon transitions.

### 7.4.1 Energy levels and PL spectrum in DQWs

DQWs consist of two QWs separated by a thin (several nanometres) barrier (Fig. 7.10(a)). At low temperatures, the carriers are bound in excitons which can be either direct or indirect. A direct exciton (DX) is formed by an electron and hole from the same QW, while in an indirect exciton (IX) the electron and hole are located in different QWs (Fig. 7.10(a)). IXs have radiative lifetimes up to  $10^{-4}$  s [55] which greatly exceed those of DXs ( $\sim 10^{-9}$  s) and the binding energies of IXs are less than those of DXs.

The relative positions of the energy levels of the excitons can be tuned by changing the electric field applied perpendicular to the plane of the DQW and this is shown schematically in Fig. 7.10(b). The IX is a dipole so its energy levels vary linearly with electric field, while those of the DX are almost independent of electric fields  $F < 10$  kV cm $^{-1}$ . At some values of electric field the energies of different exciton states become equal, leading to the resonances seen in Fig. 7.10(b). The dashed circles show resonances between pairs of exciton states associated with electrons in different QWs while the hole is located in the same QW (the narrow or the wide well) and the dashed triangles show resonances between pairs of excitons in which only the holes are located in different QWs. The resonance between a pair of exciton states in which both the electron and the hole are located in different QWs is shown by a dashed square. Near to resonance, anti-crossing can occur as a result of tunnelling and the resulting exciton wave functions become admixtures of the DX and IX eigenstates. This phenomenon has been observed

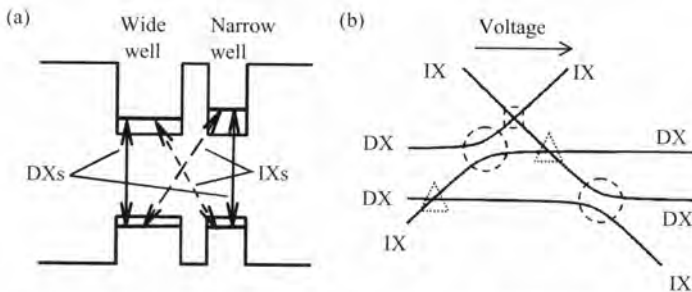


**Fig. 7.10** (a) Diagram showing the formation of direct (DX) and indirect (IX) excitons in a DQW; (b) schematic illustration of the electric field dependence of the exciton energy levels in a DQW.

experimentally in DQWs by several groups (e.g. see [56] and references therein), but only for the pair of exciton states with different electron eigenstates (dashed circles in Fig. 7.10(b)). The energy splitting at the other resonances appears to be too small to measure.

Both DX and IX in GaAs/AlGaAs DQWs are optically active and can be observed using optical techniques such as absorption, reflection, and PL, and the reader is referred to a review of the earlier work by Shah [57]. Here we describe the results of PL studies on slightly asymmetric DQWs carried out by Akimov *et al.* [56] which includes further references to work in this area. The two GaAs QWs with widths of 9.61 and 10.18 nm are separated by a 3.82 nm  $\text{Al}_{0.33}\text{Ga}_{0.67}\text{As}$  barrier. Figure 7.11 shows the CW PL spectra measured at  $T = 20$  K for a range of values of voltage  $V$  applied to the DQW. Four narrow PL lines are observed whose intensity and position depend on  $V$  in agreement with the scheme in Fig. 7.10. PL lines 1 and 2 correspond to excitons formed by a hole in the wide QW while lines 3 and 4 correspond to excitons with a hole in the narrow QW. The anti-crossing regions due to electron tunnelling are clearly seen at  $V = 1.4$  V and 2.3 V. Further details of the temperature and electric field dependences may be found in their paper. In the next section we show that studies of the relative intensities of the exciton PL lines provide information about the exciton relaxation processes.

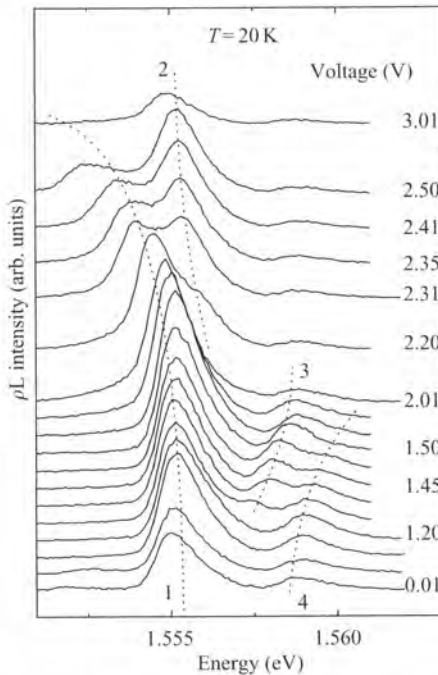


**Fig. 7.11** PL spectra of a GaAs/AlGaAs DQW measured at  $T = 20$  K for different voltages applied to the structure. Dotted lines show the position of exciton resonances as a function of applied voltage [63].

### 7.4.2 Experimental studies of energy relaxation of excitons in DQWs

The exciton–phonon interaction in DQWs results in two types of transition involving the emission or absorption of phonons: transitions within one exciton band and transitions between different exciton bands. The first type of transition is similar to the exciton–phonon transitions in single QWs (Sections 7.2 and 7.3) and is only slightly modified near the DX–IX resonances. The second type of exciton–phonon transition includes electron or hole tunnelling and will be discussed in more detail.

The optic phonon-assisted tunnelling process, which evidently requires the energy separation  $\Delta$  between two exciton levels to exceed the optic phonon energy, is very efficient with tunnelling times between 10 and 100 ps depending on the barrier width [10, 58–61]. Acoustic phonon-assisted tunnelling becomes more important near the DX–IX resonances where the energy separations are much less than the optic phonon energy and was first studied experimentally by Mazurenko *et al.* [62] and Akimov *et al.* [63] by measuring the relative intensities of the PL lines associated with exciton tunnelling. The experiments were carried out on the DQW structure described earlier whose PL spectrum is shown in Fig. 7.11. Figure 7.12(a) shows a fragment of the PL spectrum measured at  $T = 10$  K near the DX–IX resonance. The ratio of PL intensities  $I_2/I_1$  of exciton lines 1 and 2 evidently depends on the thermal populations of the lower and higher energy exciton states and hence on the lattice temperature  $T$ , and it can readily be shown that in thermal equilibrium and when the energy of DX is higher by  $\Delta$  than that of IX

$$\frac{I_2}{I_1} = \frac{\Delta + (\Delta^2 - \delta^2)^{1/2}}{\Delta - (\Delta^2 - \delta^2)^{1/2}} \exp\left(-\frac{\Delta}{k_B T}\right), \quad (7.28)$$

where  $\delta$  is the energy separation at resonance ( $\delta = 1.3$  meV for the DQW studied experimentally). Figure 7.12(b) shows experimental data at  $T = 10$  K and there is seen to be good agreement with the equilibrium dependence  $I_2/I_1$  calculated using Eq. (7.28) and shown by the solid line. Similar agreement was obtained at higher temperatures [62, 63]. From this it can be concluded that this pair of excitons reaches thermal equilibrium with the phonon system during the exciton lifetime ( $\tau_R \sim 10^{-9}$  s) and hence that the exciton–phonon transition rate  $w_{1\rightleftharpoons 2} \gg 10^9$  s $^{-1}$ .

The transition in this case involves the tunnelling of an excitonic electron and very different results were obtained for pairs of excitons involving the tunnelling of an excitonic hole. The PL spectra clearly show that these pairs never attain thermal equilibrium so that the hole tunnelling rate must be less than  $10^9$  s $^{-1}$ . The much slower tunnelling rate for the excitonic hole can readily be attributed to its greater effective mass.

### 7.4.3 The role of elastic scattering in the energy relaxation of excitons

Energy relaxation of excitons in DQWs by acoustic phonon emission and involving tunnelling takes place through the two parallel channels shown in Fig. 7.13. These involve either a one-step transition, I (Fig. 7.13(a)), where energy and momentum are conserved with the change in energy and momentum of the exciton being given to the emitted phonon; or a two-step transition, II (Fig. 7.13(b)), which allows for the fact that, in real DQWs, excitons are scattered by defects, particularly interface roughness. The

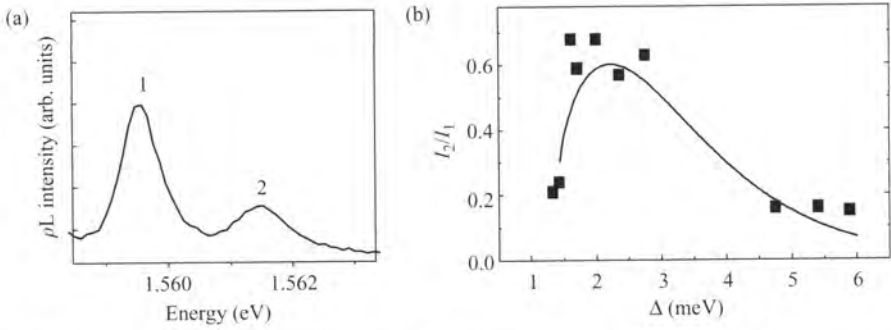


**Fig. 7.12** (a) PL spectrum of a GaAs/AlGaAs DQW measured near the IX/DX resonance at  $T = 10$  K; (b) the ratio of PL intensities  $I_2/I_1$  as a function of energy separation  $\Delta$  between corresponding exciton states: measured (symbols) and calculated from Eq. (7.28) (solid line) [63, 64].

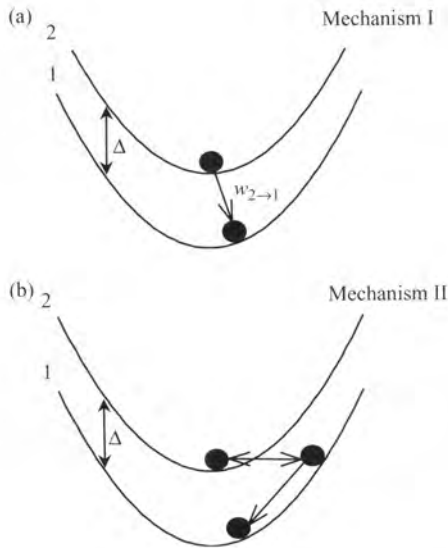


**Fig. 7.13** Diagram showing two mechanisms of exciton energy relaxation by acoustic phonon emission in DQWs: (a) one-step mechanism (I); (b) two-step mechanism (II) including elastic tunnelling of excitons.

transition II takes place in two stages. In the first, an exciton tunnels elastically from one QW to another (horizontal arrow in Fig. 7.13(b)), the momentum change being associated with the elastic scattering. This process is followed by phonon emission leading to exciton relaxation within the same exciton band (oblique arrow in Fig. 7.13(b)).

The experiments described in the previous section provide approximate values for the total energy relaxation rate involving tunnelling but neither these, nor the non-equilibrium

phonon experiments [63], give information on the relative importance of the two processes so that at present we rely on theoretical analysis. Calculations have been made by Mazurenko and Akimov [64] for symmetric DQWs at  $T = 0$ .

It is easy to show that for one-step transitions (Fig. 7.13(a)) the matrix element for holes is equal to zero [64] so transitions can only occur as a result of the interaction of phonons with excitonic electrons. The calculations show that the energy relaxation rate is governed by the interaction of excitons with both LA and TA phonons through DP and PA coupling respectively. The relaxation time increases with the energy separation  $\Delta$  of the exciton states and, in a DQW structure with parameters similar to that used in the experiments (Section 7.4.2),  $w_{2 \rightarrow 1}^{-1}(\text{I}) = 1.4 \times 10^{-10}$  s at resonance,  $\Delta = \delta = 1.3$  meV, but increases to  $1.4 \times 10^{-9}$  s for  $\Delta = 3.5$  meV. For two-step transitions, the elastic tunnelling rate  $w_e$  is the controlling parameter and this evidently depends on the quality of the DQW structure. For structures of high quality, such as those used in the experiments, Mazurenko and Akimov [64] estimate  $12 \text{ ps} < w_e^{-1} < 60 \text{ ps}$  and for these obtained  $w_{2 \rightarrow 1}^{-1}(\text{II}) = (5.1\text{--}9.9) \times 10^{-11}$  s at resonance and  $(2.4\text{--}5.9) \times 10^{-10}$  s for  $\Delta = 3.5$  meV. These are appreciably smaller than the values calculated for one-step transitions suggesting that the two-step process is dominant in the relaxation. The calculated rates also exceed the radiative exciton rate  $w_R \sim 10^9 \text{ s}^{-1}$  in agreement with the observation that the pairs of exciton states coupled by the tunnelling of excitonic electrons reach thermal equilibrium (Section 7.4.2).

The one-step exciton–phonon transition may, however, become dominant in particular situations because of the very different angular dependences of the exciton–phonon interaction matrix elements for the one- and two-step transitions. For DP coupling, the one-step process mostly leads to phonons of energy  $\hbar\omega \approx \Delta$  emitted perpendicular to the plane of the QW. However the phonon emission in the two-step process is similar to that in single QWs for which phonon emission perpendicular to the plane of DQW is forbidden by energy and momentum conservation. Since similar results apply to phonon absorption this may all be very important in phonon spectroscopy experiments with ballistic phonons where the direction of the phonon flux is well defined. We conclude that it may be possible to use exciton PL in DQWs and other tunnelling devices for phonon spectroscopy experiments as described in Chapter 6. However, this will depend on whether indeed it is possible to confine the phonons to near-normal incidence and so avoid the dominance of two-step transitions which would destroy the spectral resolution of the spectrometer.

## 7.5 Conclusions and outlook

In the present chapter we have described some fundamental aspects of the properties of excitons in quantum wells and the important role that the exciton–phonon interaction plays in their dynamics. The exciton–acoustic phonon scattering rate is surprisingly sensitive to the 2D confinement of the exciton states in nanometre layers given the 3D character of the acoustic phonons. An important feature of this confinement is the resulting anisotropy of the matrix element for the exciton–phonon interaction. Experiments with non-equilibrium phonons (Section 7.2) are found to provide a useful approach for observing specific features of the exciton–phonon interaction in a 2D exciton gas.

Studies of excitons and of exciton–phonon dynamics are not only of fundamental interest but also shed light on the structural and other properties of semiconductor nanostructures. The position and width of the exciton resonances provides information on the width of quantum well layers and the quality of the material and the interfaces since exciton scattering arises from impurities and interface defects as well as from phonons and free carriers. These latter intrinsic processes are likely to be of increasing importance as device quality improves so an understanding of exciton–phonon scattering is an important aspect in the characterization of semiconductor nanostructures. Optical techniques for studying excitons in tunnelling nanostructures (double quantum wells, superlattices) may also find application in phonon spectroscopy experiments.

Excitons may also provide a powerful tool for studying the interaction of phonons with magnetic excitations. For example, in semi-magnetic nanostructures with giant Zeeman splittings, excitonic techniques have been used to study the phonon and Mn spin dynamics in CdMnTe quantum wells [65–67]. This activity is directly connected with attempts to design spintronic devices.

The next step in studies of the exciton–phonon interaction is to investigate 1D and 0D nanostructures (quantum wires and quantum dots respectively) although the exciton spectrum of these is still not completely understood (see [68] and references therein). However, it is clear that excitons in quantum dots are completely localized by the 3D confinement so the exciton–phonon interaction should be significantly different from that in quantum wells since the excitons have to relax through closely separated exciton levels. Relaxation of carriers in quantum dots is believed to be inhibited by the so-called phonon bottleneck effect [69] and it is interesting therefore to consider whether relaxation of composite particles, excitons, may provide a more efficient route [70]. Due to its closely spaced levels the exciton may be able to relax all the way down to its ground state by the emission of low-energy phonons.

## Acknowledgements

I am very grateful to the people with whom I worked to obtain the experimental and theoretical results presented in the chapter: L.J. Challis, L.E. Golub, A.A. Kaplyanskii, D.A. Mazurenko, E.S. Moskalenko, A.V. Scherbakov, and A.L. Zhmodikov.

## References

1. Bastard, G. (1988). *Wave mechanics applied to semiconductor heterostructures*, Les editions de physique, Les Ulis, France.
2. Cingolani, R. and Ploog, K. (1991). *Adv. Phys.*, **40**, 535.
3. Henneberger, F., Schmitt-Rink, S., and Gobel, E. (1993). *Optics of semiconductor nanostructures*, Academic Verlag, Berlin.
4. Ivchenko, E.L. and Pikus, G.E. (1997). *Superlattices and other heterostructures, symmetry and optical phenomena* (trans. G.P. Skrebtsov), Springer Series in Solid-State Sciences, Vol. 110 (2nd edn), Springer-Verlag, Berlin.
5. Shinada, M. and Sugano, S. (1966). *J. Phys. Soc. Jpn*, **21**, 1936.
6. Miller, R.C., Kleinman, D.A., Tsang, W.T., and Gossard, A.C. (1981). *Phys. Rev.*, **B24**, 1134.

7. Greene, L. and Bajaj, K.K. (1983). *Solid State Commun.*, **45**, 831.
8. Andreani, L.C. and Pasquarello, A. (1988). *Europhys. Lett.*, **6**, 259.
9. Vinattieri, A., Shah, J., Damen, T.C., Kim, D.C., Pfeiffer, L.N., Maialle, M.Z., *et al.* (1994). *Phys. Rev.*, **B50**, 10868.
10. Strobel, R., Eccleston, R., Kuhl, J., and Köhler, K. (1991). *Phys. Rev.*, **B43**, 12564.
11. Moskalenko, E.S., Akimov, A.V., Zhmodikov, A.L., Kaplyanskii, A. A., Cheng, T.S., and Hughes, O.H. (1994). *Phys. Solid State*, **36**, 1668.
12. Moskalenko, E.S., Zhmodikov, A.L., Akimov, A.V., Kaplyanskii, A.A., Challis, L.J., Cheng, T.S., and Hughes, O.H. (1995). *Ann. Phys.*, **4**, 127.
13. Vledder, P., Akimov, A.V., Dijkhuis, J.I., Kusano, J., Aoyagi, Y., and Sugano T. (1997). *Phys. Rev.*, **B56**, 15282.
14. Hanamura, E. (1988). *Phys. Rev.*, **B38**, 1228.
15. Ridley, B.K. (1990). *Phys. Rev.*, **B41**, 12190.
16. Andreani, L.C., Tassone, F., and Bassani, F. (1991). *Solid State Commun.*, **77**, 641.
17. Martinez-Pastor, J., Vinattieri, A., Carraresi, L., Colocci, M., Roussignol, Ph., and Weimann, G. (1993). *Phys. Rev.*, **B47**, 10456.
18. Hillmer, H., Forchel, A., Hansmann, S., Morohashi, M., Lopez, E., Meier, H.P., *et al.* (1989). *Phys. Rev.*, **B39**, 10901.
19. Hegarty, J. and Sturge, M.D. (1985). *J. Opt. Soc. Am.*, **B2**, 1143.
20. Oberhauser, D., Pantke, K.-H., Hvam, J.M., Weimann, G., and Klingshirn, C. (1993). *Phys. Rev.*, **B47**, 6827.
21. Tsen, K.T., Sankey, O.F., and Morkoc, H. (1990). *Appl. Phys. Lett.*, **57**, 1666.
22. Hillmer, H., Forchel, A., Sauer, R., and Tu, C.W. (1990). *Phys. Rev.*, **B42**, 3220.
23. Rashba, E.I. (1982). In *Excitons, modern problems in condensed matter sciences*, Vol. 2 (ed. E.I. Rashba and M.D. Sturge), pp. 543–602, North-Holland, Amsterdam.
24. Permogorov, S.A. (1982). In *Excitons, modern problems in condensed matter sciences*, Vol. 2 (ed. E.I. Rashba and M.D. Sturge), pp. 177–203, North-Holland, Amsterdam.
25. Ridley, B.K. (1999). *Quantum processes in semiconductors* (4th edn.), Clarendon Press, Oxford.
26. Tait, W.C. and Weiher, R.L. (1969). *Phys. Rev.*, **178**, 1404.
27. Vasko, F.T. and Mitin, V.V. (1995). *Phys. Rev.*, **B52**, 1500.
28. Knipp, P.A. and Reinecke, T.L. (1995). *Phys. Rev.*, **B52**, 5923.
29. Takagahara, T. (1985). *Phys. Rev.*, **B31**, 6552.
30. Basu, P.K. and Ray, P. (1992). *Phys. Rev.*, **45**, 1907.
31. Vaas, E. (1993). *Z. Phys.* **B90**, 401.
32. Thilagam, A. and Singh, J. (1993). *Phys. Rev.*, **B48**, 4636.
33. Thilagam, A. and Singh, J. (1997). *J. Lumin.*, **72–74**, 397.
34. Oh, I.-K., and Singh, J. (2000). *J. Lumin.*, **85**, 233.
35. Lee, J., Koteles, E.S., and Vassell, M.O. (1986). *Phys. Rev.*, **B33**, 5512.
36. Schultheis, L., Honold, A., Kuhl, J., Köhler, K., and Tu, C.W. (1986). *Phys. Rev.*, **B34**, 9027.
37. Damen, T.C., Shah, J., Oberli, D.Y., Chelma, D.S., Cunningham, J.E., and Kuo, J.M. (1990). *Phys. Rev.*, **B42**, 7434.
38. Bagaev, V.S., Keldysh, L.V., Sibeldin, N.N., and Tsvetkov, V.A. (1976). *Sov. Phys. JETP*, **43**, 362.
39. Greenstein, M., and Wolfe, J.P. (1978). *Phys. Rev. Lett.*, **41**, 715.
40. Etienne, B., Voos, M., and Benoit à la Guillaume, C. (1979). In *Proc. 14th Int. Conf. on physics of semiconductors, Edinburgh, 1978* (ed. B.L.H. Wilson), p. 387, Institute of Physics, Bristol.
41. Zinoviyev, N.N., Ivanov, L.P., Kozub, V.I., and Yaroschetskii, I.D. (1983). *Sov. Phys. JETP*, **57**, 1027.
42. Akimov, A.V., Kaplyanskii, A.A., and Moskalenko, E.S. (1991). *Physica*, **B169**, 382.

43. Keldysh, L.V., and Seldin, N.N. (1986). In *Nonequilibrium phonons in nonmetallic crystals*, Modern Problems in Condensed Matter Sciences, Vol. 16 (ed. W. Eisenmenger, and A.A. Kaplyanskii), pp. 455–686, North-Holland, Amsterdam.
44. Moskalenko, E.S., Akimov, A.V., Kaplyanskii, A.A., Zhmodikov, A.L., Challis, L.J., Cheng, T.S., *et al.* (1996). *Physica*, **B219&220**, 59.
45. Herman, M.A., Bimberg, D., and Christen, J. (1991). *J. Appl. Phys.*, **70**, R1.
46. Permogorov, S.A. (1975). *Phys. Status Solidi* (b), **68**, 9.
47. Collet, J.H., Kalt, H., Dang, L.S., Cibert, J., Saminadayar, K., and Tatarenko, S. (1991). *Phys. Rev.*, **B43**, 6843.
48. Stanley, R.P., Hegarty, J., Fischer, R., Feldmann, J., Göbel, E.O., Feldman, R.D., *et al.* (1991). *Phys. Rev. Lett.*, **67**, 128.
49. Blom, P.W.M., van Hall, P.J., Smith, C., Cuypers, J.P., and Wolter J.H. (1993). *Phys. Rev. Lett.*, **71**, 3878.
50. Oh, I.-K., Singh, J., Thilagam, A., and Vengurlekar, A.S. (2000). *Phys. Rev.*, **B62**, 2045.
51. Golub, L.E., Scherbakov, A.V., and Akimov, A.V. (1996). *J. Phys. Condens. Matter*, **8**, 2163.
52. Scherbakov, A.V. and Akimov, A.V. (1999). *Phys. Solid State*, **41**, 1564.
53. Ramsbey, M.T., Tamura, S., and Wolfe, J.P. (1992). *Phys. Rev.*, **B46**, 1358.
54. Xin, Z., Ouali, F.F., Challis, L.J., Salce, B., and Cheng, T.S. (1996). *Physica*, **B219&220**, 56.
55. Golub, J.E., Kash, K., Harbison, J.P. and Florez, L.T. (1990). *Phys. Rev.*, **B41**, 8564.
56. Akimov, A.V., Moskalenko, E.S., Zhmodikov, A.L., Mazurenko, D.A., Kaplyanskii, A.A., Challis, L.J., Cheng, T.S., and Foxon, C.T. (1997). *Phys. Solid State*, **39**, 649.
57. Shah, J. (1993). In *Optics of semiconductor nanostructures* (ed. F. Henneberger, S. Schmitt-Rink, and E. Göbel), pp. 149–80, Akademie-Verlag, Berlin.
58. Oberli, D.Y., Shah, J., Damen, T.C., Tu, C.W., Chang, T.Y., Miller, D.A., *et al.* (1989). *Phys. Rev.*, **B40**, 3028.
59. Norris, T.B., Vodjdani, N., Vinter, B., Wiesbuch, C., and Mourou, G.A. (1989). *Phys. Rev.*, **B40**, 1392.
60. Ferreira, R., Delande, C., Liu, H.W., Bastard, G., Etienne, B., and Palmier, J.F. (1990). *Phys. Rev.*, **B42**, 9170.
61. Heberle, A.P., Ruhlet, W.W., Alexander, M.G.W., and Köhler, K. (1992). *Semicond. Sci. Technol.*, **7**, B421.
62. Mazurenko, D.A., Akimov, A.V., Moskalenko, E.S., Zhmodikov, A.L., Kaplyanskii, A.A., Challis, L.J., Cheng, T.S. and Foxon, C.T. (1996). *Acta Phys. Polon.*, **A90**, 895.
63. Akimov, A.V., Kaplyanskii, A.A., Mazurenko, D.A., Moskalenko, E. S., Zhmodikov, A.L., Challis, L.J., Cheng, T.S., and Foxon C.T. (1997). *Phys. Status Solidi* (b), **204**, 400.
64. Mazurenko, D.A. and Akimov, A.V. (2001). *Phys. Solid State*, **43**, 752.
65. Akimov, A.V., Scherbakov, A.V., Yakovlev, D.R., Ossau, W., Landwehr, G., and Wojtowicz, T. (1997). *Phys. Rev.*, **B56**, 12100.
66. Scherbakov, A.V., Akimov, A.V., Yakovlev, D.R., Ossau, W., Waag, A., Landwehr, G., *et al.* (1999). *Phys. Rev.*, **B60**, 5609.
67. Scherbakov, A.V., Akimov, A.V., Yakovlev, D.R., Ossau, W., Landwehr, G., Wojtowicz, T., *et al.* (2000). *Phys. Rev.*, **B62**, R10641.
68. Hawryak, P., Narzaev, G.A., Bayer, M., and Forchel, A. (2000). *Phys. Rev. Lett.*, **85**, 389.
69. Bensity, H., Sotomayor-Torres, C.M., and Weisbuch, C. (1991). *Phys. Rev.*, **B44**, 10945.
70. Bellingham, R., Kent, A.J., Akimov, A.V., and Henini, M. (2001). *Phys. Status Solidi* (b), **224**, 659.



# 8 Quantized thermal conductance of acoustic phonons in nanowires

M.P. Blencowe

---

## 8.1 Introduction

Mesoscopic physics might be defined as the study of certain quantum electronic phenomena, normally belonging to the atomic domain, which through the use of special microfabrication techniques are realized in structures having dimensions ranging from tens of nanometres up to micrometres (for a review, see [1]). One of the pioneering experiments in mesoscopic physics was the measurement by van Wees *et al.* [2] and Wharam *et al.* [3] of quantized steps of magnitude  $e^2/\pi\hbar$  in the conductance of point contacts in a two-dimensional electron gas (Fig. 8.1). A two-dimensional electron gas (2DEG) is formed in a GaAs/AlGaAs heterostructure. A negative voltage applied to metal point contacts defining a gate on top of the heterostructure depletes the electron gas underneath the gate, allowing only conduction through the electrostatically defined constriction between the point contacts. The experimental results are simply explained by the classic formula of Landauer [4] for the conductance  $G$  between 2DEG reservoirs smoothly separated by a constriction:

$$G = \frac{e^2}{\pi\hbar} N_c T. \quad (8.1)$$

Here  $N_c$  is the number of transverse channels available to electrons at the Fermi energy, that is the largest integer smaller than  $2w/\lambda_F$  where  $w$  is the width of the constriction and  $\lambda_F$  is the Fermi wavelength.  $T$  is the transmission probability averaged over the  $N_c$  channels. Because of the mutual cancellation of the electron group velocity and density of states terms in one dimension, they do not appear in (8.1) and in the absence of scattering the contribution to the conductance from each available channel is  $e^2/\pi\hbar$ , universal and independent of the wire band structure. As the gate voltage is made increasingly negative, the constriction width  $w$  and hence number of available channels decreases, causing the conductance to decrease in discrete steps of magnitude  $e^2/\pi\hbar$ .

It should also be possible to fabricate mesoscopic structures in which the *lattice* degrees of freedom behave in a manifestly non-classical way. Phononic analogues of various mesoscopic electron phenomena are an obvious possibility to consider. In particular, we might ask whether the thermal conductance of a dielectric wire with sufficiently small cross-section will exhibit steps of universal magnitude (i.e. expressed, apart from a numerical factor, solely in terms of Boltzmann's and Planck's constants) analogous to the electronic conductance steps observed in quantum point contacts. Such a question has a bearing on the limits quantum mechanics places on heat flow in ultrasmall wires, of

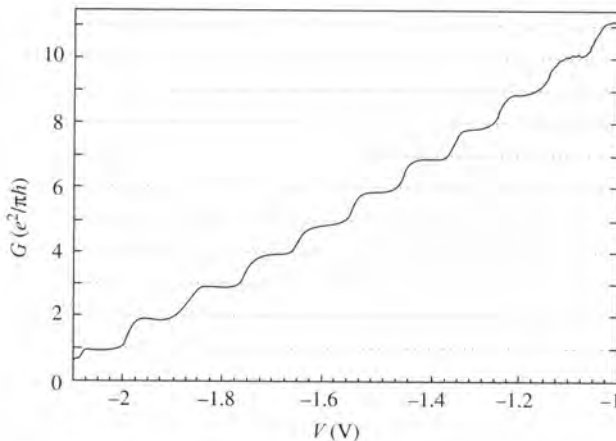


**Fig. 8.1** Point contact conductance versus gate voltage. The conductance shows plateaux at multiples of  $e^2/\pi h$ . (After van Wees *et al.* [2].)

relevance to issues of cooling with decreasing circuit component sizes and increasing component densities.

Phonon-confining mesoscopic structures are not as straightforward to realize as electron quantum wells, wires, etc. For acoustic phonons, there are no perfect thermal insulators; although confined modes may exist in a heterostructure consisting of layers of material with different elastic properties, there will always be unconfined bulk modes with the same energies. The only solution is to use *suspended* structures, that is structures which are physically separated from the substrate for most of their extent. An additional challenge is the problem of probing the phonon dynamics in the suspended structures. For example, in order to measure the thermal conductance of a suspended nanowire, a way must be found in which to heat one end of the wire while keeping the other end at a fixed temperature and also to measure the temperature difference between the two ends. As can be appreciated, it is rather more difficult to fabricate suspended nanostructures integrated with ultrasensitive probes than it is to fabricate conventional heterostructures. While the idea of a mesoscopic phonon-confining wire and realization of the first concept device [5] predates the electronic quantum conductance experiments [2, 3], because of the above difficulties it took much longer and required further advances in probe techniques before the phononic thermal conductance quantum was successfully measured [6].

In the following two sections, we will give an account of the quantum of thermal conductance, beginning with a discussion of the theory and following with a discussion of the various significant experiments.

## 8.2 Derivation of the Landauer formula for the thermal conductance

In the following we shall derive the Landauer formula for the thermal conductance of a suspended, dielectric wire [7], analogous to the electrical conductance formula (8.1).

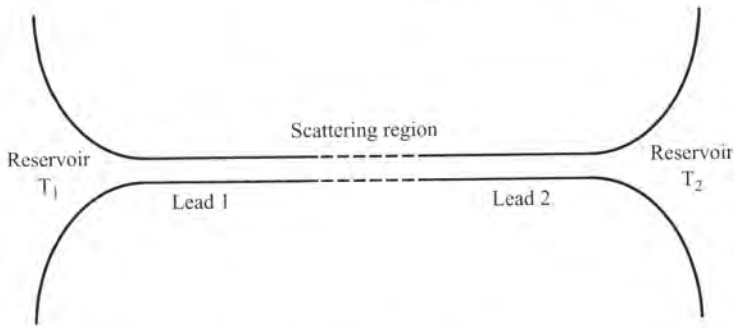


**Fig. 8.2** Schematic diagram of the model wire. The left and right reservoirs are at temperatures  $T_1$  and  $T_2$ , respectively.

No assumptions are made about the elastic moduli of the wire material. As we shall see, all the material properties dependent on the wire's mass density and elastic moduli will eventually drop out to yield the universal thermal conductance quantum. Readers not interested in the derivation may skip directly to the Landauer formula (8.20).

The model wire structure on which the calculations are based is shown in Fig. 8.2. Two very long, perfect leads (i.e. crystalline and with uniform cross-section) join a central section in which the phonon scattering occurs. The scattering may be caused by any combination of the following: a changing cross-section, surface roughness, or various internal defects. The only restriction we place on the scattering is that it be elastic. Phonon–phonon interactions are also neglected. The other ends of the leads are connected to heat reservoirs with Bose–Einstein distributions for the phonons. Perfect adiabatic reservoir–lead connections are assumed so that no scattering occurs at these connections. The wire, comprising leads and central scattering section, must be free-standing so that the phonons do not ‘leak’ out, except to the reservoirs at the ends. Furthermore, the wire is electrically insulating, so that only phonons transport heat in the wire.

Our point of departure is the classical equations of motion for the lattice dynamics of a perfect wire (i.e. no scattering) and also the expression for the classical energy current flowing in the wire. At Kelvin or lower reservoir temperatures, phonon wavelengths typically exceed several hundred angstroms, and thus the continuum approximation can be used, so that the equation of motion is just the wave equation (see e.g. [8], p. 446):

$$\rho \frac{\partial^2 u_i}{\partial t^2} - \sum_{jkl} c_{ijkl} \frac{\partial^2 u_l}{\partial x^j \partial x^k} = 0, \quad (8.2)$$

where  $\rho$  is the mass density,  $u_i$  denotes the  $i$ th component of the displacement field, and  $c_{ijkl}$  is the elastic modulus tensor of the wire material. For a free-standing wire the stress normal to the surface vanishes, so that we have the following boundary condition at the wire surface:

$$\sum_{jkl} c_{ijkl} n_j \frac{\partial u_l}{\partial x^k} \Big|_S, \quad (8.3)$$

where  $n_j$  is the  $j$ th component of the unit vector normal to the wire surface  $S$ . In terms of the displacement field and elastic modulus tensor, the energy current at a given location  $x$  is (the  $x$  coordinate runs along the length of the wire)

$$I(x, t) = -c_{xjkl} \sum_{jkl} \int_A dy dz \frac{\partial u_j}{\partial t} \frac{\partial u_l}{\partial x^k}, \quad (8.4)$$

where the integral is over the cross-sectional surface  $A$  at  $x$ .

In order to quantize Eq. (8.2), we require a complete set of normal mode solutions. For a perfect, infinitely long wire, these solutions can be written in the following form:

$$u_{n,q,i}(\mathbf{r}, t) = \frac{1}{\sqrt{2\pi}} \exp[-i(\omega_{n,q}t - qx)] \chi_{n,q,i}(y, z), \quad (8.5)$$

where  $\chi_{n,q,i}$  denotes the transverse modes,  $q$  is the longitudinal wavevector along the wire axis, and  $n$  is the subband label. In the presence of scattering, we can still construct solutions in the leads using the perfect wire solutions (8.5) as follows:

$$u_{n,q,i}^1 = \begin{cases} u_{n,q,i} + \sum_{n'} u_{n',-q',i} t_{n'n}^{11}(\omega) & \text{lead 1} \\ \sum_{n'} u_{n',q',i} t_{n'n}^{21}(\omega) & \text{lead 2} \end{cases} \quad (8.6)$$

and

$$u_{n,q,i}^2 = \begin{cases} \sum_{n'} u_{n',-q',i} t_{n'n}^{12}(\omega) & \text{lead 1} \\ u_{n,-q,i} + \sum_{n'} u_{n',q',i} t_{n'n}^{22}(\omega) & \text{lead 2,} \end{cases} \quad (8.7)$$

where  $q, q' > 0$ . The solutions  $u_{n,q,i}^1$  describe waves propagating from lead 1 to lead 2, while solutions  $u_{n,q,i}^2$  propagate from lead 2 to lead 1. The absolute value of the scattering matrix element  $t_{n'n}^{ba}(\omega)$  gives the fraction of the incident wave in lead  $a$ , with frequency  $\omega$  and subband label  $n$ , which is transmitted/reflected into lead  $b$  and subband  $n'$ . In the sum over  $n'$ , the frequency  $\omega$  is kept fixed, while  $q'$  is treated as a function of  $n'$  and  $\omega$  through the condition  $\omega_{n',q'} = \omega_{n,q} = \omega$ .

From energy conservation, the time average of the energy current  $I(x, t)$  should be independent of the position  $x$ . Substituting into the definition for the energy current (8.4) an arbitrary linear combination of solutions (8.6) and (8.7) and demanding that the time-averaged energy currents in leads 1 and 2 be the same, we obtain the following conditions on the scattering matrix elements:

$$\sum_{n''} v_{n'',q''} t_{n''n}^{11}(\omega) t_{n''n'}^{11*}(\omega) + \sum_{n''} v_{n'',q''} t_{n''n}^{21}(\omega) t_{n''n'}^{21*}(\omega) = v_{n,q} \delta_{nn'}, \quad (8.8)$$

$$\sum_{n''} v_{n'',q''} t_{n''n}^{22}(\omega) t_{n''n'}^{22*}(\omega) + \sum_{n''} v_{n'',q''} t_{n''n}^{12}(\omega) t_{n''n'}^{12*}(\omega) = v_{n,q} \delta_{nn'}, \quad (8.9)$$

and

$$\sum_{n''} v_{n'',q''} t_{n''n}^{11}(\omega) t_{n''n'}^{12*}(\omega) + \sum_{n''} v_{n'',q''} t_{n''n}^{21}(\omega) t_{n''n'}^{22*}(\omega) = 0, \quad (8.10)$$

where  $v_{n,q} = \partial\omega_{n,q}/\partial q$  is the group velocity. In the derivation of these conditions, we require the following very useful relation between the group velocity and displacement field:

$$i\pi \sum_{ijl} c_{xijl} \int_A dy dz \left( u_{n,q,i} \frac{\partial u_{n',q',l}^*}{\partial x^j} - u_{n',q',i}^* \frac{\partial u_{n,q,l}}{\partial x^j} \right) = \rho\omega_{n,q} v_{n,q} \delta_{nn'}, \quad (8.11)$$

where  $\omega_{n',q'} = \omega_{n,q}$ . This relation follows from the equations of motion (8.2).

We are now ready to quantize. In the wire leads, the displacement field operator has the solution

$$\hat{u}_i(\mathbf{r}, t) = \sum_{n,\sigma} \int_0^\infty dq \sqrt{\frac{\hbar}{2\rho\omega_{n,q}}} \left[ \hat{a}_{n,q}^\sigma u_{n,q,i}^\sigma(\mathbf{r}, t) + \hat{a}_{n,q}^{\sigma\dagger} u_{n,q,i}^{\sigma*}(\mathbf{r}, t) \right], \quad (8.12)$$

where the phonon creation and annihilation operators satisfy the commutation relations

$$\left[ \hat{a}_{n,q}^\sigma, \hat{a}_{n',q'}^{\sigma'\dagger} \right] = \delta_{\sigma\sigma'} \delta_{nn'} \delta(q - q'). \quad (8.13)$$

Substituting the field operator solution (8.12) into the energy current operator

$$\hat{I} = -\frac{1}{2} c_{xjkl} \int_A dy dz \left( \frac{\partial \hat{u}_j}{\partial t} \frac{\partial \hat{u}_l}{\partial x^k} + \frac{\partial \hat{u}_l}{\partial x^k} \frac{\partial \hat{u}_j}{\partial t} \right) \quad (8.14)$$

and then taking the expectation value of  $\hat{I}$  at any location  $x$  in leads 1 or 2, we obtain

$$\langle \hat{I} \rangle = \frac{1}{2\pi} \sum_{n,n'} \int_{\omega_{n,0}}^\infty d\omega \hbar\omega v_{n,q}^{-1} v_{n',q'} t_{n'n}^{21}(\omega) t_{n'n}^{21*}(\omega) [n_1(\omega) - n_2(\omega)], \quad (8.15)$$

where

$$n_\sigma(\omega) = \frac{1}{\exp(\hbar\omega/k_B T_\sigma) - 1}, \quad (8.16)$$

with  $T_\sigma$  the temperature of the reservoir at the end of lead  $\sigma$ . In the derivation of Eq. (8.15), use is made of relation (8.11) and conditions (8.8)–(8.10). We also use the following creation/annihilation operator expectation values:

$$\langle \hat{a}_{n,q}^{\sigma\dagger} \hat{a}_{n',q'}^{\sigma'} \rangle = n_\sigma(\omega_{n,q}) \delta_{\sigma\sigma'} \delta_{nn'} \delta(q - q'). \quad (8.17)$$

Defining

$$T_{n'n}^{21}(E) = v_{n,q}^{-1} v_{n',q'} t_{n'n}^{21}(\omega) t_{n'n}^{21*}(\omega), \quad (8.18)$$

where  $E = \hbar\omega$ , we can rewrite (8.15) as follows:

$$\langle \hat{I} \rangle = \frac{1}{2\pi\hbar} \sum_{n,n'} \int_{E_{n,0}}^\infty dE E T_{n'n}^{21}(E) [n_1(E) - n_2(E)]. \quad (8.19)$$

This is our key expression for the mean energy current. From the form of this expression and condition (8.8), we see that the matrix  $T_{n'n}^{21}(E)$  is naturally interpreted as the

probability for a phonon with energy  $E$  in subband  $n$  of lead 1 to be transmitted into subband  $n'$  of lead 2.

When the temperature difference between the reservoirs is small, that is  $|T_1 - T_2| \ll T_1, T_2$ , we can expand Eq. (8.19) to obtain the wire thermal conductance:

$$\kappa = \frac{\langle \hat{I} \rangle}{|T_1 - T_2|} = \frac{\pi k_B^2 T}{6\hbar} \sum_{n,n'} \int_{E_{n,0}/k_B T}^{\infty} d\epsilon g(\epsilon) T_{n'n}^{21}(\epsilon k_B T), \quad (8.20)$$

where  $T$  is the average temperature and

$$g(\epsilon) = \frac{3\epsilon^2 e^\epsilon}{\pi^2 (e^\epsilon - 1)^2}. \quad (8.21)$$

Equation (8.20) relates the thermal conductance to the single phonon transmission probability and thus we call this the Landauer expression for the phonon thermal conductance.

The function  $g(\epsilon)$  satisfies  $\int_0^\infty d\epsilon g(\epsilon) = 1$ . Therefore, in the absence of scattering, a given subband  $n$  contributes to the reduced conductance  $\kappa/T$  the *universal* quantum  $\pi k_B^2/6\hbar \approx 9.465 \times 10^{-13} \text{ W K}^{-2}$  in the limit  $E_{n,0}/k_B T \rightarrow 0$ . In Fig. 8.3, we show the temperature dependence of the reduced thermal conductance for perfect GaAs wires with uniform, rectangular cross-sections of various dimensions comparable with those in the experiments of Tighe *et al.* [9] and Schwab *et al.* [6]. The only GaAs wire characteristics which are needed in order to determine the conductance are the zone-centre frequencies  $\omega_{n,0}$ . These can be calculated using the elegant numerical method developed in [10]. In contrast to the quantized conductance of electronic point contacts [2, 3], there are no steplike features, a consequence of the broad nature of the Bose–Einstein distribution; at a given temperature, the exponential tails of many subband distributions contribute to the conductance, washing out the steps.

There is, however, a plateau for  $T \rightarrow 0$  where only phonons in the lowest subband with  $E_{n,0} = 0$  contribute. The plateau has the value 4 in universal quantum units, a consequence of there being four basic transverse mode types: dilatational, torsional, and two types of flexural mode [10]. The existence of this lowest plateau is a consequence of the stress-free boundary conditions at the wire surface. With hard-wall boundary conditions on the other hand, the reduced conductance would drop to zero as  $T \rightarrow 0$  and there would be no plateau.

Of course, whether or not this lowest, universal plateau can be resolved as  $T \rightarrow 0$  depends on the extent to which phonon scattering in the wire can be controlled. Scattering due to surface roughness and other wire impurities will reduce the thermal conductance below its universal value [11–13]. However, with the practical impossibility of realizing a perfectly adiabatic reservoir–wire connection, the main obstruction to observing the plateau is in fact the backscattering of reservoir phonons incident on the wire. In classical wave optics and acoustics, the same reflection phenomenon occurs for waves travelling in narrowing waveguides and is called ‘diffractive blocking’. Working with a scalar wave model, Rego and Kirczenow [14] explored the effect of various reservoir–wire geometries on the thermal conductance plateau. A catenoidal geometry of the form  $y(x) = w \cosh^2(x/L)$ , where  $w$  is the minimum width and  $L$  is the characteristic length

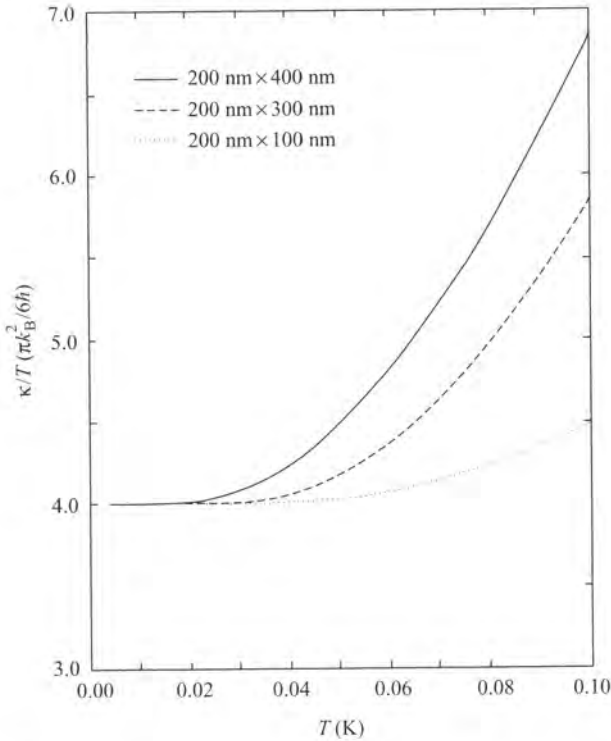


**Fig. 8.3** Reduced thermal conductance versus temperature for perfect GaAs wires with uniform rectangular cross-section 200 nm × 400 nm (solid line), 200 nm × 300 nm (dashed line), and 200 nm × 100 nm (dotted line). The reduced conductance is given in units  $\pi k_B^2/6\hbar \approx 9.465 \times 10^{-13} \text{ W K}^{-2}$ . (After Blencowe [7].)

of the catenoid, was found to give a distinct plateau over a wide temperature range, whereas a wedge-shaped reservoir–wire junction gave no resolvable plateau (Fig. 8.4).

### 8.3 Measurement of the quantum of thermal conductance

The pioneering work of Lee *et al.* [5] represented the first attempt to probe quantized phononic heat transport in suspended, electrically insulating wires of ultrasmall cross-section. The motivation came from a theoretical investigation by Kelly [15] of thermal phonon analogues of electrical transport properties of long, thin wires. However, while the possibility of a phonon waveguide is mentioned in [5], there is no discussion of the universal thermal conductance quantum  $\pi k_B^2 T/6\hbar$ . Particular attention is instead paid to thermal analogues of quantum corrections to electrical resistance due to scattering from wire impurities.

The layout of the structure is shown in Fig. 8.5. The suspended wires were fashioned out of an amorphous silicon nitride ( $\text{Si}_3\text{N}_4$ ) membrane deposited on an Si substrate.

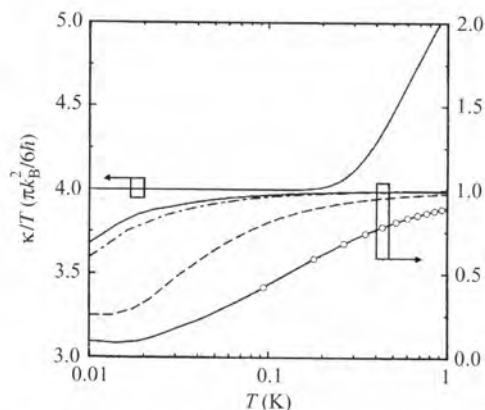


**Fig. 8.4** Left scale: reduced thermal conductance of a quantum wire with ideal contacts. Right scale: single scalar mode thermal conductance for various contact shapes; infinite catenoid for  $L = 4.6 \mu\text{m}$  (solid line), finite catenoid for  $L = 4.6 \mu\text{m}$  (dot-dashed line), finite catenoid with  $L = 0.86 \mu\text{m}$  (long-dashed line), and wedge shape with wedge angle  $= \pi/6$  (solid line with circles). (After Rego and Kirczenow [14].)

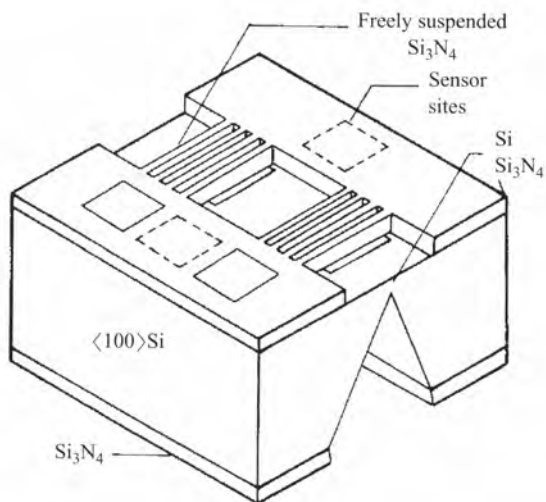


**Fig. 8.5** Schematic layout of device with freely suspended  $\text{Si}_3\text{N}_4$  wires for one-dimensional phonon transport studies. (After Lee *et al.* [5].)

Amorphous  $\text{Si}_3\text{N}_4$  was chosen for its high strength. A large array of wires was fabricated in order to improve the signal-to-noise ratio. The cross-sectional dimensions of the resulting suspended wires were determined by the membrane thickness and the lithography resolution. Figure 8.6 shows a micrograph of part of the wire array. The wires are approximately  $0.16 \mu\text{m}$  wide,  $0.14 \mu\text{m}$  thick,  $300 \mu\text{m}$  long, and have a 5 per cent linewidth variation. With such a cross-section, one would expect to observe the lowest

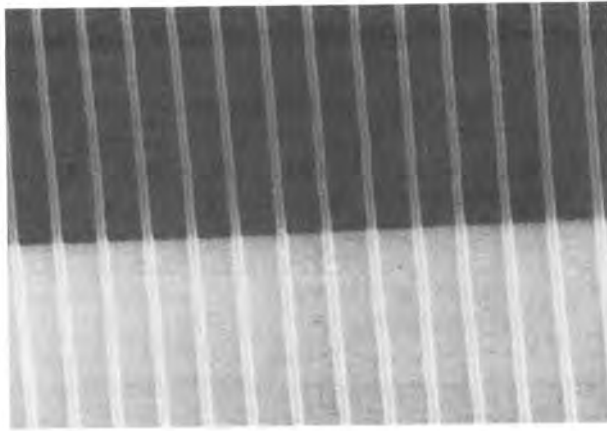


**Fig. 8.6** Scanning electron microscope (SEM) micrograph of part of an array of freely suspended  $\text{Si}_3\text{N}_4$  wires projecting over the Si support and the anisotropically etched hole. The wires are about  $1\ \mu\text{m}$  apart. (After Lee *et al.* [5].)

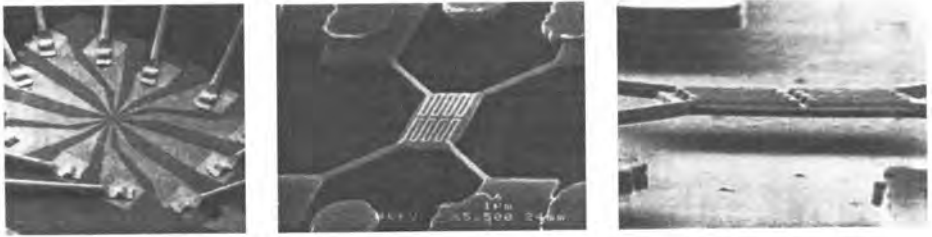


**Fig. 8.7** Scanning electron microscope micrograph of a suspended, monocrystalline device for thermal conductance measurements. The centre image, which is an enlargement of the central region of the image on the left, shows a GaAs reservoir cavity with area  $\approx 3\ \mu\text{m}^2$  which is suspended by four GaAs bridges with length  $\approx 5.5\ \mu\text{m}$  and cross-section  $\approx 200\ \text{nm} \times 450\ \text{nm}$ . Deposited on top of the reservoir are two meandering Si-doped GaAs conductors, one of which serves as a heater and the other as a thermometer. The image on the right presents an edge view of the device which is approximately  $300\ \text{nm}$  thick and suspended about  $1\ \mu\text{m}$  above the substrate. (After Tighe *et al.* [9].)

plateau region in the reduced thermal conductance  $\kappa/T$  at temperatures of a few tenths of a kelvin and below, neglecting phonon scattering. However, at the time, probe techniques were simply not sensitive enough to resolve the extremely small amount of power associated with the thermal conductance quantum: less than a picowatt below  $1\ \text{K}$ .

More than a decade went by before another attempt was made to probe low-dimensional phonon transport by Roukes and co-workers [9]. An improvement over the device of Lee *et al.* [5] was the elimination of all parasitic phonon pathways by making one of the heat reservoirs a suspended cavity, materially connected to the other, external reservoir through the suspended wires only (Fig. 8.7). The device was patterned from a GaAs heterostructure comprising three molecular beam epitaxially grown layers

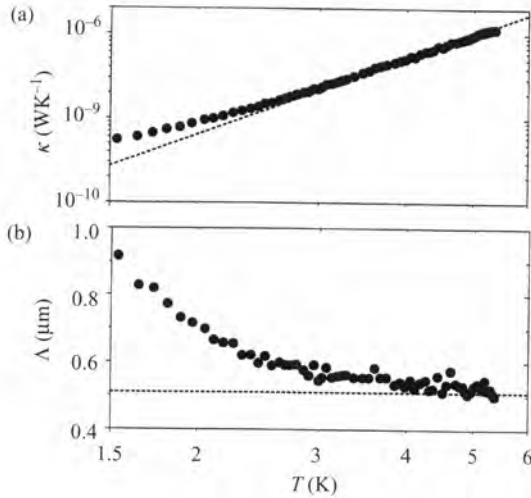


**Fig. 8.8** (a) Phononic thermal conductance from the parallel measurement of four  $200 \text{ nm} \times 300 \text{ nm}$  GaAs bridges. The dashed line represents the predictions of the Debye model for a fixed boundary-limited mean free path of  $0.51 \text{ } \mu\text{m}$ . (b) Effective mean free path deduced from the experimental data. (After Tighe *et al.* [9].)

atop an undoped GaAs substrate. The topmost epilayer was heavily Si-doped  $n^+$  GaAs, out of which two meandering electrical wire transducers were patterned, one serving as a thermal phonon reservoir through Joule heating of the central cavity, and the other functioning as a thermometer by exploiting the well-characterized temperature dependence of the weak-localization and electron–electron interaction corrections to the electrical resistance ([1], p. 34). The second epilayer was undoped GaAs, out of which the phonon wires and isolated reservoir were patterned. The removal of the third, sacrificial AlAs epilayer by chemical etching enabled the suspension of the phonon wire/cavity structure with integrated transducers.

Figure 8.8 shows the measured thermal conductance versus temperature. At the high-temperature end, the thermal conductance approaches a  $T^3$  dependence. The kinetic formula for the bulk, 3D thermal conductance of a single wire is ([16], p. 288)

$$\kappa_{3D} = \frac{C_v \bar{v} \Lambda A}{3L}, \quad (8.22)$$

where  $C_v \sim T^3$  is the Debye heat capacity,  $\bar{v}$  the averaged phonon velocity,  $\Lambda$  the phonon mean free path, and  $A$  and  $L$  are the wire cross-sectional area and length, respectively. The data are therefore consistent with bulk heat flow limited by temperature-independent surface-roughness scattering. At temperatures of a few kelvin, the dominant thermal phonon wavelength is considerably smaller than the transverse dimensions of the suspended wires ( $300 \text{ nm}$  thick by  $200 \text{ nm}$  wide), and thus one expects to be in the regime of bulk transport. Substituting into Eq. (8.22) the measured conductance, wire dimensions, and specific heat and averaged phonon velocity values for GaAs, one deduces a mean free path  $\Lambda \sim 0.5 \text{ } \mu\text{m}$ , about one-tenth the wire length. The deviation

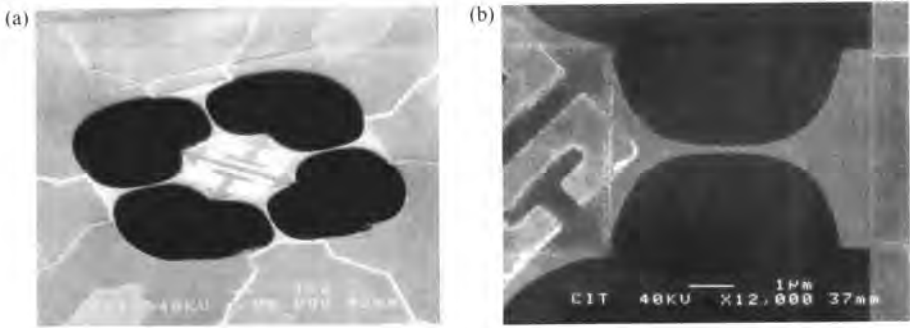


**Fig. 8.9** (a) Suspended mesoscopic phonon device comprising a  $4 \times 4 \mu\text{m}$  phonon cavity (centre) patterned from a silicon nitride membrane 60 nm thick. The 'C'-shaped objects on the cavity are thin film Cr/Au resistors, whereas in the dark areas the membrane has been completely removed. The resistors are connected to thin film Nb leads that run atop the four phonon wires and ultimately terminate at the wirebond pads. (b) Close-up of one of the freely suspended catenoidal phonon wires. The narrowest region necks down to  $<200$  nm width. (After Schwab *et al.* [17].)

from  $T^3$  with decreasing temperature does not signify reduced dimensionality for phonon transport (the temperature is still too high), but rather the increasing importance of the parasitic electronic pathways for heat transport relative to the phonons of the doped GaAs sensor wires. Because of this problem, it was not possible to probe low-dimensional phonon transport with this device.

Roukes and co-workers eliminated the parasitic electronic thermal conduction problem in a subsequent device (Fig. 8.9) by employing superconducting Nb films on top of the suspended phonon wires to contact the heater and thermometer transducers on top of the central phonon cavity [6, 17]. The device incorporated several other improvements as well, all essential for resolving the lowest, thermal conductance quantum plateau. The wires were fashioned from a silicon nitride membrane 60 nm thick, the same material used in the original device of Lee *et al.* [5], and patterned according to the catenoidal geometry  $y(x) = w \cosh^2(x/L)$  with  $L = 1.0 \mu\text{m}$  and  $w \approx 200$  nm. As discussed above, for this geometry the plateau is more pronounced than for a wedge-shaped reservoir–wire junction [14]. A stiffer material, the dominant thermal phonon wavelength in silicon nitride is larger than in GaAs at a given temperature: assuming the average sound speed  $\bar{s} \sim 6000 \text{ m s}^{-1}$  for silicon nitride gives a dominant thermal wavelength  $\lambda_{\text{th}} = \hbar \bar{s} / k_{\text{B}} T \sim 300 \text{ nm} / T$ . Thus, the transition from bulk to low-dimensional thermal phonon transport occurs at a higher temperature than in the GaAs device. For the heater and thermometer transducers, two Cr/Au thin film resistors were employed. Because of the extremely weak coupling between the Cr/Au electron gas and cavity phonons at low temperatures, it was essential that the power dissipated by the external thermometer circuitry into the Cr/Au resistor be sufficiently low so as not to heat the electron gas significantly above the cavity phonons. Otherwise, the thermometer would not give a sufficiently accurate reading of the cavity phonon temperature. For example, dissipating only  $10^{-16} \text{ W}$  into the electron gas with volume  $0.1 \mu\text{m}^3$  heats the electrons by as much as 50 mK above the cavity phonons [17]. Similarly, given the very small volume and hence heat capacity of the central phonon cavity, the DC current supplied to the heater

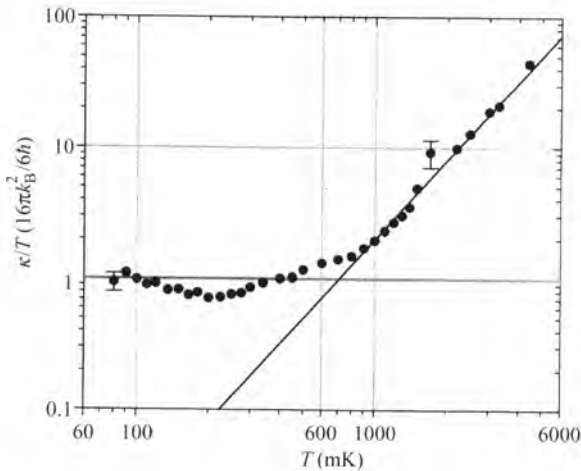


**Fig. 8.10** The measured reduced thermal conductance versus temperature. (After Schwab *et al.* [6].)

and Johnson noise from the room-temperature electronics must be sufficiently small so as to be able to heat controllably the central reservoir by temperature increments of a few tens of millikelvin above the dilution refrigerator temperature. Schwab *et al.* [17] were able to meet these conditions by employing DC SQUID-based noise thermometry, together with extensive filtering of the noise from the room-temperature electronics. The temperature of the Cr/Au resistor is obtained by measuring its Nyquist current noise using a SQUID. The power dissipated in the other, Cr/Au heater resistor is determined by employing another SQUID to measure the voltage across the resistor for given DC current. From Eq. (8.20), knowing both the power supplied to the reservoir and its temperature allows us to determine the parallel thermal conductance of the four wires.

Figure 8.10 shows the measured reduced thermal conductance versus temperature. At the high-temperature end, the data show the expected  $T^3$  dependence for bulk transport, consistent with a mean free path  $\sim 0.9 \mu\text{m}$ . As the temperature decreases, there is a crossover to a plateau-like region at about 0.8 K. The plateau value is close to 16 in units of the universal quantum. This is precisely the value one expects in the 1D regime with four parallel wires and four lowest, independent, transverse modes per wire. The crossover to the 1D regime should occur where the dominant thermal wavelength  $\lambda_{\text{th}}$  exceeds the spacing between the lowest lying modes  $\Delta\lambda \sim 2w$ . For  $w = 200 \text{ nm}$ , this estimate gives 0.8 K, in agreement with experiment. Within the experimental error, the measured thermal conductance never exceeds the universal conductance quantum in the 1D regime. Again this is consistent with theory, which predicts that the conductance quantum is the maximum possible conductance, achievable for ballistic (i.e. no scattering) transport only. The observed dip in the conductance and the recovery towards the universal upper limit at the lowest temperatures can be attributed to surface-roughness-dominated scattering. (Note that, at these low temperatures, the amorphous silicon nitride appears largely homogeneous to the long-wavelength thermal phonons.) Santamore and Cross [11–13] calculated the effects of surface roughness scattering on the thermal conductance and

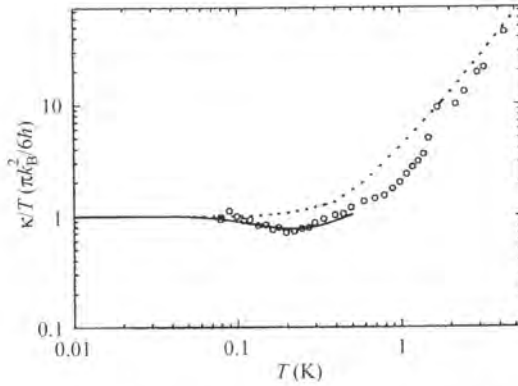


**Fig. 8.11** Thermal conductance per mode in units of the universal conductance versus temperature. Solid line: fit using roughness parameters  $a/w = 5.5$  and  $\delta/w = 0.2$ ; circles: data of Schwab *et al.* [6]. The dotted line shows the ideal conductance with no scattering. (After Santamore and Cross [13].)

were able to provide a good fit to the data for roughness amplitude and correlation length values of approximately  $\delta = 0.2w$  and  $5.5w$ , respectively (Fig. 8.11). Electron micrographs of the actual wires show surface roughness on comparable scales. Decreasing the temperature further, the reduced thermal conductance should eventually drop due to the loss of adiabatic coupling between the reservoirs and wire [14]. However, it was not possible to probe this effect in the experiment; the SQUID noise thermometer saturated at about 80 mK, preventing the accurate measurement of lower temperatures.

## 8.4 Conclusion

In this chapter we have given an account of the thermal conductance of ultrasmall, suspended dielectric wires. The thermal conductance cannot exceed  $\pi k_B^2 T / 6\hbar = 9.465 \times 10^{-13} T \text{ W K}^{-1}$  per transverse channel and equals this value in the absence of scattering. This conductance quantum is universal in the sense that it does not depend on the material properties of the suspended wire.

The experimental and theoretical investigations outlined here have been extended in several interesting directions. For instance, by using suspended carbon nanotube wires which have much smaller cross-sections than the patterned wires, it should be possible to observe the lowest thermal conductance quantum plateau at higher temperatures, thus simplifying the thermometry [18, 19]. Another direction concerns the thermal conductance of a single channel connecting two heat reservoirs which support other types of particle. For example, two black-body ovens joined by an optical fibre furnish a photonic analogue, while a quantum point contact in a 2DEG with the reservoirs held at different temperatures but at the same voltage furnishes an electronic analogue. Remarkably, it turns out that the maximum, limiting thermal conductance quantum is independent of the particle statistics as well [20, 21]. Thus, for the example of electrons in the degenerate limit and in the absence of scattering, the conductance quantum per channel is  $\pi k_B^2 T / 6\hbar$ ,

coinciding with that for phonons. The thermal conductance is therefore universal in a wider sense. This wider universality is unique to the thermal conductance: all other single channel transport coefficients depend on the particle statistics.

## References

1. Imry, J. (1997). *Introduction to mesoscopic physics*, Oxford University Press, Oxford.
2. van Wees, B.J., van Houten, H., Beenakker, C.W.J., Williamson, J. G., Kouwenhoven, L.P., van der Marel, D., and Foxon, C.T. (1988). *Phys. Rev. Lett.*, **60**, 848.
3. Wharam, D.A., Thornton, T.J., Newbury, R., Pepper, M., Ahmed, H., Frost, J.E.F., Hasko, D.G., Peacock, D.C., Ritchie, D.A., and Jones, G.A.C. (1988). *J. Phys. C: Solid State Phys.*, **21**, L209.
4. Landauer, R. (1992). *Phys. Scr.*, **T42**, 110.
5. Lee, K.L., Ahmed, H., Kelly, M.J., and Wybourne, M.N. (1984). *Electron. Lett.*, **20**, 289.
6. Schwab, K., Henriksen, E.A., Worlock, J.M., and Roukes, M.L. (2000). *Nature*, **404**, 974.
7. Blencowe, M.P. (1999). *Phys. Rev.*, **B59**, 4992.
8. Ashcroft, N.W. and Mermin, N.D. (1976). *Solid state physics*, Holt Rinehart and Winston, Philadelphia.
9. Tighe, T.S., Worlock, J.M., and Roukes, M.L. (1997). *Appl. Phys. Lett.*, **70**, 2687.
10. Nishiguchi, N., Ando, Y., and Wybourne, M.N. (1997). *J. Phys. Condens. Matter*, **9**, 5751.
11. Santamore, D.H. and Cross, M.C. (2001). *Phys. Rev.*, **B63**, 184306.
12. Santamore, D.H. and Cross, M.C. (2001). *Phys. Rev. Lett.*, **87**, 115502.
13. Santamore, D.H. and Cross, M.C. (2002). *Phys. Rev.*, **B66**, 144302.
14. Rego, L.G.C. and Kirczenow, G. (1998). *Phys. Rev. Lett.*, **81**, 232.
15. Kelly, M.J. (1982). *J. Phys. C: Solid State Phys.*, **15**, L969.
16. Ziman, J.M. (1960). *Electrons and phonons*, Oxford University Press, London.
17. Schwab, K., Arlett, J.L., Worlock, J.M., and Roukes, M.L. (2001). *Physica*, **E9**, 60.
18. Hone, J., Batlogg, B., Benes, Z., Johnson, A.T., and Fischer, J.E. (2000). *Science*, **289**, 1730.
19. Kim, P., Shi, L., Majumdar, A., and McEuen, P.L. (2001). *Phys. Rev. Lett.*, **87**, 215502.
20. Rego, L.G.C. and Kirczenow, G. (1999). *Phys. Rev.*, **B59**, 13080.
21. Krive, I.V. and Mucciolo, E.R. (1999). *Phys. Rev.*, **B60**, 1429.

# Index

- acoustic mismatch 78, 133, 199, 248  
acoustically stored light 95  
acoustoelectric effect 91, 93, 101, 105, 107, 108, 171  
Auger processes 139, 140, 142, 143, 145, 245
- backscattering 126, 130, 133, 227, 274  
ballistic electron transport 115, 120, 121, 135, 210, 280  
ballistic phonon transport 9, 10, 38, 39, 61, 62, 63, 79, 84, 85, 86, 88, 89, 90, 107, 108, 116, 141, 142, 144, 145, 218, 219, 254, 255, 258, 264  
Bardeen Hamiltonian 189  
bilayer systems 91, 98, 107, 108  
Bloch oscillations 209, 212  
Bloch-Grüneisen or Bloch limit 42, 130, 132, 161, 165, 166, 171, 179  
Boltzmann equation 32, 102, 154, 159, 162, 170, 179, 210
- carbon nanotubes 151, 281  
carrier energy relaxation—*see* electron relaxation  
Chern-Simons gauge transformation 81, 83  
coherent phonon generation 186, 227, 229  
Cole-Cole plot 93, 96, 98, 99, 104, 105  
commensurability oscillations 101  
composite fermions 60, 81, 82, 83, 84, 101, 107, 108  
  effective mass 82, 83, 103  
  Fermi surface 81, 84, 90, 99, 101, 103, 104, 108  
  Fermi velocity 83, 101  
  Landau levels 82  
  mobility 83, 84  
  pairs 103  
confinement length 118, 140  
Corbino geometry 92  
coupled wells 194, 239  
current standard 3, 4, 61, 95, 115, 230, 232  
cut-off 17, 18, 19, 22, 23, 24, 25, 39, 40, 41, 43, 44, 45, 51, 52, 58, 66, 74, 78, 79, 84, 89, 90, 116, 124, 125, 128, 129, 130, 135, 136, 140, 142, 201, 254, 258, 259
- cyclotron  
  energy 82, 209, 216  
  frequency 8, 65, 74, 101, 191  
  motion 101, 163  
  orbit 101  
  phonon 2, 64, 65, 66, 73, 74, 77, 78, 79, 107  
  resonance 9, 61, 216, 231
- dirty limit 25, 26, 167, 171, 172, 179  
double quantum wells 96, 169, 239, 260, 265  
Drude conductivity 158, 209
- edge state 66, 67, 76, 78, 87, 95  
electric field domains 211, 212, 217, 223  
electromechanical coupling coefficient 91, 92  
electron confinement 1, 16, 19, 21, 27, 42, 43, 44, 53, 115, 116, 117, 118, 119, 122, 123, 130, 137, 138, 140, 204, 206  
electron diffusion 127, 149, 154, 158, 165, 174, 178, 179, 180  
  diffusion coefficient 26, 83  
electron energy loss  
  electron temperature model 6  
  loss rate 5, 6, 7, 9, 12, 22, 26, 27, 28, 30, 31, 32, 36, 37, 41, 42, 44, 46, 47, 48, 53, 66, 67, 68, 84, 130, 131, 132, 145  
  standard model 13, 21, 27, 28, 30, 33, 41, 54  
electron localization 26, 96, 134, 180, 210, 212, 217  
  localized states 59, 61, 87, 93, 94, 95, 96, 108, 121, 164, 173, 176, 208, 210, 211  
  strong localization 26, 162, 170, 173, 181  
  weak localization 26, 127, 128, 135, 162, 170, 172, 173, 174, 278  
electron screening 2, 20, 21, 24, 26, 27, 66, 98, 106, 124, 148, 161, 165, 168, 171, 180, 198  
  dielectric function 20, 26, 33, 83, 124  
  dynamic screening 21, 26, 28  
  static screening 21, 27, 68  
electron tunnelling 52, 140, 185, 186, 187, 188, 189  
  bistability 189  
  charge build-up 194, 203, 223  
  coherent tunnelling 198, 206, 211  
  dwell time 188, 192  
  elastic tunnelling 190, 191, 192, 198, 204, 212, 213, 216, 224  
  global coherent model 185, 187, 188, 211  
  negative differential conductivity 185, 189  
  sequential tunnelling model 188, 195, 211  
  transfer matrix 187  
  electron-electron scattering 6, 10, 32, 52, 140, 142, 188, 189  
electro-optic technique 69, 73  
electron-phonon interaction  
  deformation potential coupling 2, 4, 15, 18, 22, 27, 47, 53, 85, 86, 95, 96, 124, 130, 134, 142, 155, 161, 166, 167, 168, 172, 175, 195, 199, 206, 212, 220, 248, 249  
  Fröhlich interaction 2, 27, 28, 29, 33, 37, 53, 195, 253

- electron-phonon interaction (*cont.*)
  - normal (N-type) processes 150
  - piezoelectric coupling 2, 4, 15, 19, 20, 22, 27, 52, 53, 68, 82, 83, 84, 85, 86, 90, 91, 92, 95, 96, 98, 124, 136, 142, 155, 161, 165, 166, 167, 168, 171, 175, 179, 204, 226, 230, 257
  - piezoelectric stiffening 92
  - Umklapp (U-type) processes 150
- exciton
  - confinement 242, 253, 254, 264, 265
  - diffusion 153, 246, 250, 251
  - direct excitons 260
  - dynamics 239, 247, 251, 253, 264
  - excited states 241, 247
  - free excitons 241, 242, 243, 244, 245, 246, 251, 252, 259
  - hot excitons 253, 254
  - indirect excitons 260
  - localization 240, 241, 242, 243, 244, 245, 252, 259, 265
- exciton-phonon interaction 239ff
  - ripple mechanism 248
- exciton-phonon-assisted tunnelling 259ff
- Fabry-Pérot etalon 185
- Fang-Howard parameter 43, 64
- filling factor 59, 60, 69, 70, 76, 79, 80, 81, 82, 83, 84, 93, 94, 95, 97, 98, 99, 102, 103, 105, 106, 107, 108, 166, 178, 179, 180
- flux quantum 59, 82
- form factor 16, 17, 18, 19, 21, 37, 42, 43, 44, 45, 49, 50, 65, 83, 250, 254
- fractional quantum Hall effect 60, 61, 68, 80ff
  - charge vortices 80
  - compressible states 87
  - composite fermions—see separate heading
  - even denominator states 82, 83, 84, 99, 103
  - incompressible electron liquid 87
  - insulating phase 63, 103, 104
  - Laughlin state 80
  - liquid structure factor 80, 86
  - quasiparticles 80, 81, 82, 87, 99, 101
- gate wavelength 102
- geometric resonance 101, 102, 103, 104
- Green's function approach 195, 206
- Hall angle 69
- helium drops 71, 72
- hopping conduction 26, 96, 173, 210, 215, 216, 220, 221, 223
- hydrodynamic limit 68
- integer quantum Hall effect 59, 60, 61, 68, 71, 76, 81, 94ff, 105, 107, 175
  - breakdown 61, 62, 63, 67, 69, 71, 72, 73, 107
  - dissipation 62, 67, 69, 71, 72, 73, 74, 75, 76, 107, 108
  - hot spots 62, 63, 64, 67, 69, 71, 72, 73, 74, 76, 107
- Kohn anomaly 152, 161, 168, 169, 170, 179, 180
- Landauer approach 195
  - formula 121, 269, 270, 271, 274
  - level anti-crossing 192, 198, 260, 261
  - lithium niobate 92, 95, 96
- phonon localization (confinement) 37,
  - confined modes 196ff
  - interface modes 196ff
- Luttinger liquid 115, 146
- magnetophonon 89, 104
- magnetophonon oscillations 39, 74, 213
- magnetoplasmon 61, 62
- magnetopolaron 192, 193, 216
- magneton 62, 80, 82, 84, 85, 86, 87, 88, 108
- Matthiessen's rule 162
- meander transmission line 85, 104
- metal-insulator transition 172, 173
- minibands 185, 209, 210, 211, 212, 214, 215, 216, 217, 220, 222, 226, 231
- momentum cut-off, see cut-off
- Monte Carlo approach 33, 41, 194, 195, 213
- Mott relation 150
- non-linear SAW attenuation, dispersion 91, 93
- non-radiative processes 1, 115, 145, 244, 245
- normal fluid (liquid helium) 71
- one dimensional electron gas—see quantum wire
- overlap integral 209, 250, 258
- phonoconductivity 67, 77, 78, 126, 128, 133, 135
- phonon
  - amplification 219, 226, 229, 231
  - anharmonic processes 27, 31, 37, 48, 64, 139
  - bottleneck 137, 139, 140, 145
  - Bragg reflection 217, 222
  - confinement (localization) 37, 195, 196, 197, 231
  - dielectric continuum model 37, 196
  - diffractive blocking 274
  - down conversion—see anharmonic processes
  - focussing 39, 40, 41, 42, 69, 79, 84, 86, 89, 90, 108, 143, 153, 166, 199, 219, 226
  - imaging 2, 9, 11, 40, 41, 63, 64, 66, 69, 70, 71, 72, 73, 76, 77, 79, 141, 142, 143
- phonon absorption from a magnetically quantized 2DEG
  - frequency dependence 76ff
  - inter-Landau level transitions 61, 62, 64, 66, 76, 77, 78
  - intra-Landau level transitions 76, 77, 79
  - location 76ff
  - two-phonon process 87, 89
- phonon detector
  - boron dopant atoms 74
  - cadmium sulphide (CdS) film 10, 11, 39, 40, 63, 64, 70

- carbon film 64
- carbon resistors 64
- superconducting bolometer 10, 11, 38, 39, 40, 64, 136, 141, 227, 228
- superconducting tunnel junctions 10, 11, 39, 40
- superfluid helium film 63, 69, 71, 72
- phonon drag 3, 9, 64, 75, 79, 84, 91, 93, 107, 149ff, 251, 252, 252
- phonon emission (see also electron energy loss)
- phonon emission from a magnetically quantized 2DEG
  - frequency distribution 73ff
  - inter-Landau level transitions 66, 67, 74, 97
  - intra-Landau level transitions 66, 67, 74, 107
  - location 69ff
  - two-phonon process 66, 107
- phonon sources
  - electrically heated films 9, 75, 77, 218
  - normal-metal tunnel junction 63, 64, 74, 78
  - optically heated films 9, 63, 143, 218, 219
- phonon-assisted tunnelling 67, 185ff
- antiresonances 205, 222
- phonon replica (satellite peak, side-band, Stokes, anti-Stokes peak) 186, 195, 198, 199, 206, 208
- spontaneous phonon emission 204, 219, 224
- stimulated phonon emission 194, 199, 200, 210, 206, 216, 226, 227, 229, 231
- two-phonon process 190, 231
- phonon-magnetoroton interaction 84ff
- phonon wind (see phonon drag)
- photoluminescence (PL) 2, 7, 12, 46, 140, 194, 242
- photoluminescence excitation (PLE) 140, 242
- photon-assisted tunnelling 186
- polariton 37, 242, 247
- polaron 139, 140, 192
  
- quantum cascade laser 1, 54, 212, 213, 214, 232
- quantum dots 115, 116, 137ff
  - coupled dots 114, 138, 144, 145
- quantum Hall effect (QHE)
  - fractional quantum Hall effect-see separate heading
  - integer quantum Hall effect-see separate heading
- quantum interference 127, 128
- quantum point contact 120, 126, 132, 133ff, 269, 270, 271, 274, 281
- quantum wire 1, 3, 91, 115ff, 151, 181, 186, 232, 269ff
  
- quasielastic inter-Landau level scattering (QUILLS) 67, 73, 76
- quasielastic scattering 67, 190
  
- radiative processes 95, 142, 214, 243, 244, 245, 257, 260, 264
- Raman scattering 13, 37, 84, 90, 254, 186, 227
- resonant tunnelling devices
  - double barrier (DBRTD) 185, 186, 187ff
  - triple barrier (TBRTD) 185, 186, 187ff
- roton minimum-see magnetoroton minimum
  
- Shubnikov-de Haas oscillations 8, 52, 78, 81, 101
- signal processing (SAW) 230, 232
- single electron transport 95, 186, 229
- skyrmions 79
- space charge 211
- spin excitations 79, 87
- Stark-cyclotron resonance (SCR) 216
- Stark-cyclotron-phonon resonance (SCPR) 216, 231
- superfluid (liquid helium) 64, 69, 71, 72
- superlattice 3, 11, 95, 154, 181, 185, 221, 227
- surface acoustic wave (SAW) 1, 61, 90ff, 229, 230, 232
  - Rayleigh waves 91
  - pseudo-surface waves 91, 94
- suspended nanostructures 270, 275, 276, 278, 279, 281
  - dielectric wires 269, 270, 281
  
- thermal conductance quantum 270, 271, 275, 277, 279, 281
- thermoelectric coefficients
  - Nernst-Ettingshausen coefficient 79, 154, 175
  - Onsager relation 153, 163
  - Peltier coefficient 153, 163
  - Seebeck coefficient 154
- thermopower 84, 105, 107, 149, 150, 151, 152, 153, 154, 156, 158, 160, 161, 162, 163, 164, 166, 168, 169, 170, 172, 174, 176, 177, 178, 179, 180, 181
- tuneable phonon source 64, 229
- tuneable phonon spectrometer 204
  
- variable range hopping 173
  
- Wannier-Stark localization 210, 231

# Applications

---

The electron-phonon interaction can have a significant effect on the performance of electronic and optoelectronic devices. More direct applications or possible applications arising from the interaction include

- acoustically produced holograms 232
- cooling optoelectronic devices 198
- current standard (SAW) 3, 4, 61, 95, 115, 230, 232
- particle detector 232
- "phonoresist" 232
- phonon spectroscopy
  - tuneable coherent phonon source 64, 229
  - tuneable phonon spectrometer 204
- quantum cascade laser 1, 54, 212, 213, 214, 232
- signal processing (SAW) 230, 232





